

PROCEEDINGS

**1994 U.S. WORKSHOP
ON THE PHYSICS AND CHEMISTRY
OF MERCURY CADMIUM TELLURIDE
AND OTHER IR MATERIALS**

**Edited by
Ishwara B. Bhat**

TMS
Minerals • Metals • Materials

DISTRIBUTION STATEMENT A

Approved for public release;
Distribution Unlimited

**Proceedings of the
1994 U.S. Workshop on the
Physics and Chemistry
of Mercury Cadmium Telluride
and Other IR Materials**

DISTRIBUTION STATEMENT A

Approved for public release;
Distribution Unlimited

**Proceedings of the
1994 U.S. Workshop on the
Physics and Chemistry
of Mercury Cadmium Telluride
and Other IR Materials**

**4-6 October 1994
San Antonio, Texas**

Special Editor for the Proceedings:

Ishwara B. Bhat

This book is a reprint of Volume 24, No. 9
of the *Journal of Electronic Materials*.
Hence, the pagination begins on page 1039
rather than the customary page 1.

Published for the American Vacuum Society
by The Minerals, Metals & Materials Society,
Warrendale, PA 1995

19960731 183

DISCLAIMER NOTICE



THIS DOCUMENT IS BEST QUALITY AVAILABLE. THE COPY FURNISHED TO DTIC CONTAINED A SIGNIFICANT NUMBER OF PAGES WHICH DO NOT REPRODUCE LEGIBLY.

A Publication of The Minerals, Metals & Materials Society
420 Commonwealth Drive
Warrendale, Pennsylvania 15086
(412) 776-9000

The Minerals, Metals & Materials Society is not responsible for statements or opinions and is absolved of liability due to misuse of information contained in this publication.

Printed in the United States of America
Library of Congress Catalog Number 95-80463
ISBN Number 0-87339-319-8

Authorization to photocopy items for internal or personal use, or the internal or personal use of specific clients, is granted by The Minerals, Metals & Materials Society for users registered with the Copyright Clearance Center (CCC) Transactional Reporting Service, provided that the base fee of \$3.00 per copy is paid directly to Copyright Clearance Center, 27 Congress Street, Salem, Massachusetts 01970. For those organizations that have been granted a photocopy license by Copyright Clearance Center, a separate system of payment has been arranged.

TMS
Minerals • Metals • Materials

© 1995

If you are interested in purchasing a copy of this book, or if you would like to receive the latest TMS publications catalog, please telephone 1-800-759-4867.

Proceedings of the 1994 U.S. Workshop on the Physics and Chemistry of Mercury Cadmium Telluride and Other IR Materials

Foreword	1039
<i>Ishwara B. Bhat</i>	
Two-Dimensional Molecular Beam Epitaxy of {001} CdTe on Cd and Zn Terminated {001} GaAs	1041
<i>N.K. Dhar, C.E.C. Wood, P.R. Boyd, H.K. Pollehn, M. Martinka, J.D. Benson, and J.H. Dinan</i>	
Studies on the Growth of CdTe on Si Using Ge Interfacial Layer in an Organometallic Vapor Phase Epitaxial System	1047
<i>Wen-Sheng Wang and Ishwara B. Bhat</i>	
Thermomigration of Tellurium Precipitates in CdZnTe Crystals Grown by Vertical Bridgman Method	1053
<i>T.S. Lee, J.W. Park, Y.T. Jeoung, H.K. Kim, C.H. Chun, J.M. Kim, I.H. Park, J.M. Chang, S.U. Kim, and M.J. Park</i>	
Vertical Bridgman Techniques to Homogenize Zinc Composition of CdZnTe Substrates	1057
<i>T.S. Lee, S.B. Lee, J.M. Kim, J.S. Kim, S.H. Suh, J.H. Song, I.H. Park, S.U. Kim, and M.J. Park</i>	
Assessment of the Purity of Cadmium and Tellurium as Components of the CdTe-Based Substrates	1061
<i>R. Triboulet, A. Aoudia, and A. Lusson</i>	
Molecular Beam Epitaxial HgCdTe Material Characteristics and Device Performance: Reproducibility Status	1067
<i>J. Bajaj, J.M. Arias, M. Zandian, J.G. Pasko, L.J. Kozlowski, R.E. DeWames, and W.E. Tennant</i>	
Metalorganic Chemical Vapor Deposition of HgCdTe p/n Junctions Using Arsenic and Iodine Doping	1077
<i>P. Mitra, T.R. Schimert, F.C. Case, S.L. Barnes, M.B. Reine, R. Starr, M.H. Weiler, and M. Kestigian</i>	
Real-Time Control of HgCdTe Growth by Organometallic Vapor Phase Epitaxy Using Spectroscopic Ellipsometry	1087
<i>Srikanteswara Dakshina Murthy, Ishwara Bhat, Blaine Johs, Shakil Pittal, and Ping He</i>	
Low Temperature Growth of (100) HgCdTe Layers with DtBTe in Metalorganic Vapor Phase Epitaxy	1093
<i>K. Yasuda, H. Hatano, T. Ferid, K. Kawamoto, T. Maejima, and M. Minamide</i>	

(Continued)

The Growth and Characterization of (211) and (133) Oriented (Hg,Cd)Te Epilayers (211)B GaAs by Organometallic Vapor Phase Epitaxy	1099
<i>G.J. Gouws and R.J. Muller</i>	
Improvement in HgCdTe Diode Characteristics by Low Temperature Post-Implantation Annealing	1105
<i>Akira Ajisawa and Naoki Oda</i>	
Effect of Cooling Procedure After Annealing on Electrical Properties of Cd_{0.2}Hg_{0.8}Te Epitaxial Films Grown by Liquid Phase Epitaxy	1113
<i>Z. Kawazu, S. Ochi, T. Sonoda, and S. Takamiya</i>	
Theoretical Evaluation of InTIP, InTIAs, and InTISb As Long-Wave Infrared Detectors	1119
<i>A. Sher, M. van Schilfgaarde, S. Krishnamurthy, M.A. Berding, and A-B Chen</i>	
Temperature Dependence of Band Gaps in HgCdTe and Other Semiconductors	1121
<i>Srinivasan Krishnamurthy, A.-B. Chen, A. Sher, and M. van Schilfgaarde</i>	
Defect Modeling Studies in HgCdTe and CdTe	1127
<i>M.A. Berding, A. Sher, and M. van Schilfgaarde</i>	
Process Simulation for HgCdTe Infrared Focal Plane Array Flexible Manufacturing	1137
<i>C.R. Helms, J.L. Meléndez, H.G. Robinson, S. Holander, J. Hasan, and S. Halepete</i>	
Effect of Dislocations on 1/f Noise of Long Wavelength Infrared Photodiodes Fabricated with HgCdTe Layers Grown on GaAs by Metalorganic Vapor Phase Epitaxy	1143
<i>S. Murakami, H. Nishino, H. Ebe, and Y. Nishijima</i>	
The Role of Surface Adsorbates in the Metalorganic Vapor Phase Epitaxial Growth of (HgCd)Te onto (100) GaAs Substrates	1149
<i>J. Giess, J.E. Hails, A. Graham, G. Blackmore, M.R. Houlton, J. Newey, M.L. Young, M.G. Astles, W. Bell, and D.J. Cole-Hamilton</i>	
Reaction Chemistry and Resulting Surface Structure of HgCdTe Etched in CH₄/H₂ and H₂ ECR Plasmas	1155
<i>Robert C. Keller, M. Seelmann-Eggebert, and H.J. Richter</i>	
The Interface of Metalorganic Chemical Vapor Deposition-CdTe/HgCdTe	1161
<i>Y. Nemirovsky, N. Amir, D. Goren, G. Asa, N. Mainzer, and E. Weiss</i>	
Electrical and Structural Properties of Epitaxial CdTe/HgCdTe Interfaces	1169
<i>V. Ariel, V. Garber, D. Rosenfeld, G. Bahir, V. Richter, N. Mainzer, and A. Sher</i>	
Characterization of CdTe for HgCdTe Surface Passivation	1175
<i>L.O. Bubulac, W.E. Tennant, J. Bajaj, J. Sheng, R. Brigham, A.H.B. Vanderwyck, M. Zandian, and W.V. McLevige</i>	
Bake Stability of Long-Wavelength Infrared HgCdTe Photodiodes	1183
<i>A. Mestechkin, D.L. Lee, B.T. Cunningham, and B.D. MacLeod</i>	
The Relationship Between Lattice Matching and Crosshatch in Liquid Phase Epitaxy HgCdTe on CdZnTe Substrates	1189
<i>S.P. Tobin, F.T.J. Smith, P.W. Norton, J. Wu, M. Dudley, D. DiMarzio, and L.G. Casagrande</i>	

Electron Cyclotron Resonance Plasma Etching of HgTe-CdTe Superlattices Grown by Photo-Assisted Molecular Beam Epitaxy	1201
<i>K.A. Harris, D.W. Endres, R.W. Yanka, L.M. Mohnkern, A.R. Reisinger, T.H. Myers, A.N. Klymachyov, C.M. Vitrus, and N.S. Dalal</i>	
Origin of Void Defects in $\text{Hg}_{1-x}\text{Cd}_x\text{Te}$ Grown by Molecular Beam Epitaxy	1207
<i>M. Zandian, J.M. Arias, J. Bajaj, J.G. Pasko, L.O. Bubulac, and R.E. DeWames</i>	
Analysis of Low Doping Limitation in Molecular Beam Epitaxially Grown HgCdTe(211)B Epitaxial Layers	1211
<i>P.S. Wijewarnasuriya, M.D. Lange, S. Sivananthan, and J.P. Faurie</i>	
Compositional Dependence of Cation Impurity Gettering in $\text{Hg}_{1-x}\text{Cd}_x\text{Te}$	1219
<i>José L. Meléndez, John Tregilgas, John Dodge, and C.R. Helms</i>	
A Comparison of the Diffuion of Iodine into CdTe, $\text{Hg}_{0.8}\text{Cd}_{0.2}\text{Te}$ and $\text{Zn}_{0.05}\text{Cd}_{0.95}\text{Te}$	1225
<i>E.D. Jones, J. Malzbender, N. Shaw, P. Capper, and J.B. Mullin</i>	
HgCdTe and Other Infrared Material Status in the Ukraine	1231
<i>V.K. Malyutenko</i>	
Numerical Simulation of HgCdTe Detector Characteristics	1239
<i>G.M. Williams and R.E. DeWames</i>	
The Magnetic Field Dependence of R_0A Products in n-on-p Homojunctions and p-on-n Heterojunctions from $\text{Hg}_{0.78}\text{Cd}_{0.22}\text{Te}$ Liquid Phase Epitaxy Films	1249
<i>M.C. Chen, A. Turner, L. Colombo, and D. Chandra</i>	
Magneto-Transport Characterization Using Quantitative Mobility-Spectrum Analysis	1255
<i>J. Antoszewski, D.J. Seymour, L. Faraone, J.R. Meyer, and C.A. Hoffman</i>	
Characterization of Molecular Beam Epitaxially Grown HgCdTe Epilayers by Mid-Infrared Interband Magneto-Absorption	1263
<i>P. Helgesen, R. Sizmann, T. Skauli, T. Colin, H. Steen, and S. Løvold</i>	
Photoluminescence and Raman Studies of High Quality CdTe:I Epilayers	1269
<i>N.C. Giles, Jaesun Lee, T.K. Tran, J.W. Tomm, and C.J. Summers</i>	
Status of Te-Rich and Hg-Rich Liquid Phase Epitaxial Technologies for the Growth of (Hg,Cd)Te Alloys	1275
<i>H.R. Vydyanath</i>	
Te-Rich Liquid Phase Epitaxial Growth of HgCdTe on Si-Based Substrates	1287
<i>F.T. Smith, P.W. Norton, P. LoVecchio, N. Hartle, M. Weiler, N.H. Karam, S. Sivananthan, and Y.P. Chen</i>	
Piezoelectric Effects in HgCdTe Devices	1293
<i>C.F. Wan, J.D. Luttmner, R.S. List, and R.L. Strong</i>	
1/f Noise and Material Defects in HgCdTe Diodes	1299
<i>R. Schiebel, D. Bartholomew, M. Bevan, R.S. List, and M. Ohlson</i>	
Characterization of Liquid-Phase Epitaxially Grown HgCdTe Films by Magnetoresistance Measurements	1305
<i>J.S. Kim, D.G. Seiler, L. Colombo, and M.C. Chen</i>	

Nondestructive Characterization of $\text{Hg}_{1-x}\text{Cd}_x\text{Te}$ Layers with n-p Structures by Magneto-Thermoelectric Measurements	1311
<i>J. Baars, D. Brink, C.L. Littler, and M. Bruder</i>	
Compositionally Graded HgCdTe Photodiodes: Prediction of Spectral Response From Transmission Spectrum and the Impact of Grading	1321
<i>D. Rosenfeld, V. Garber, V. Ariel, and G. Bahir</i>	
Effect of a Valence-Band Barrier on the Quantum Efficiency and Background-Limited Dynamic Resistance of Compositionally Graded HgCdTe P-on-n Heterojunction Photodiodes	1329
<i>M.H. Weiler and M.B. Reine</i>	
Author Index	1341

Foreword

The papers in this special issue of the *Journal of Electronic Materials* were presented during the 1994 U.S. Workshop on the Physics and Chemistry of Mercury Cadmium Telluride and Other IR Materials that was held at the Hyatt Regency Hill Country Resort, San Antonio, TX, October 4–6, 1994. This workshop was the thirteenth in a series which began in October 1981. Over that time, it has become the preeminent forum for open interdisciplinary discussion of scientific and technological issues concerning HgCdTe and other Hg-based IR materials.

Subject areas discussed at the 1994 workshop include substrate technology, epitaxial material growth, surface and interface properties, defects, electrical and noncontact optical characterization. Forty-three of the 57 papers presented at the workshop appear in this publication. Much of the credit goes to the referees for their careful and prompt review of the manuscripts and to the authors for choosing this forum for presenting their results. The proceedings of the first ten workshops (from 1981–91) have been published in the *Journal of Vacuum Science and Technology*. Papers from the workshop from 1992 onwards appear in special issues of *Journal of Electronic Materials*.

Ishwara B. Bhat
Electrical, Computer & Systems Engineering Department
Rensselaer Polytechnic Institute
Troy, NY 12180-3590

Special Issue Editor

Two-Dimensional Molecular Beam Epitaxy of {001} CdTe on Cd and Zn Terminated {001} GaAs

N.K. DHAR* and C.E.C. WOOD

Electrical Engineering Department, University of Maryland, College Park,
MD 20742

P.R. BOYD and H.K. POLLEHN

Army Research Laboratory, Fort Belvoir, VA 22060-5838

M. MARTINKA, J.D. BENSON, and J.H. DINAN

Night Vision & Electronic Sensors Directorate, Fort Belvoir, VA 22060

Amorphous layers of CdTe deposited on Cd or Zn terminated GaAs {001} surfaces can be recrystallized above $\sim 200^{\circ}\text{C}$. Subsequent molecular beam epitaxy of CdTe proceeds in a two-dimensional mode and leads to layers which are specular and single domain {001}. Threading dislocation density in these layers was $1\text{--}2 \times 10^5 \text{ cm}^{-2}$. Values of full width at half maximum for x-ray rocking curves were as low as 80 arc-s.

Key words: CdTe/GaAs, growth modes, molecular beam epitaxy (MBE)

INTRODUCTION

CdTe epitaxial layers on GaAs and Si have potential use as large area composite substrates for Hg based infrared focal plane arrays. Both {111} and {001} oriented epitaxial layers of CdTe on {001} GaAs have been reported.¹⁻⁷ The orientation has been shown to be determined by the preparation of the GaAs wafer surface in the growth chamber.

{111} CdTe layers have been obtained when growth occurs on atomically clean (free of native oxide) GaAs surfaces.²⁻⁵ Under the {111} CdTe growth condition, the {001} GaAs surfaces are As-deficient, and the initial coverage of Te on the GaAs surface is less than

0.8 monolayer (ML). $\langle 111 \rangle$ CdTe nucleation usually proceeds in a two-dimensional growth (2-D) mode. Compared to {001} layers, {111} layers usually have a lower density of threading dislocations, higher density of twins and point defects, and contain a mixture of {001} and {111} domains.

{001} CdTe layers have been obtained when ZnTe, Te, or residual oxides are present at the interface.⁸⁻¹⁰ Surfaces with Te coverage greater than 1 ML lead to {001} growth.^{2,3} However, $\langle 001 \rangle$ CdTe growth ordinarily proceeds by island nucleation and subsequent coalescence into uniform layers (3-D growth). {001} oriented CdTe layers are twin free, but have a high density of threading dislocations. Layers are typically nonspecular, with large number of hillocks, and contain a mixture of {001} and {111} domains. Single domain {001} CdTe has been grown on {001} GaAs only when ZnTe was used as an interfacial layer.

*Present address: Army Research Laboratory, Fort Belvoir, VA 22060.

(Received November 15, 1994; revised March 10, 1995)

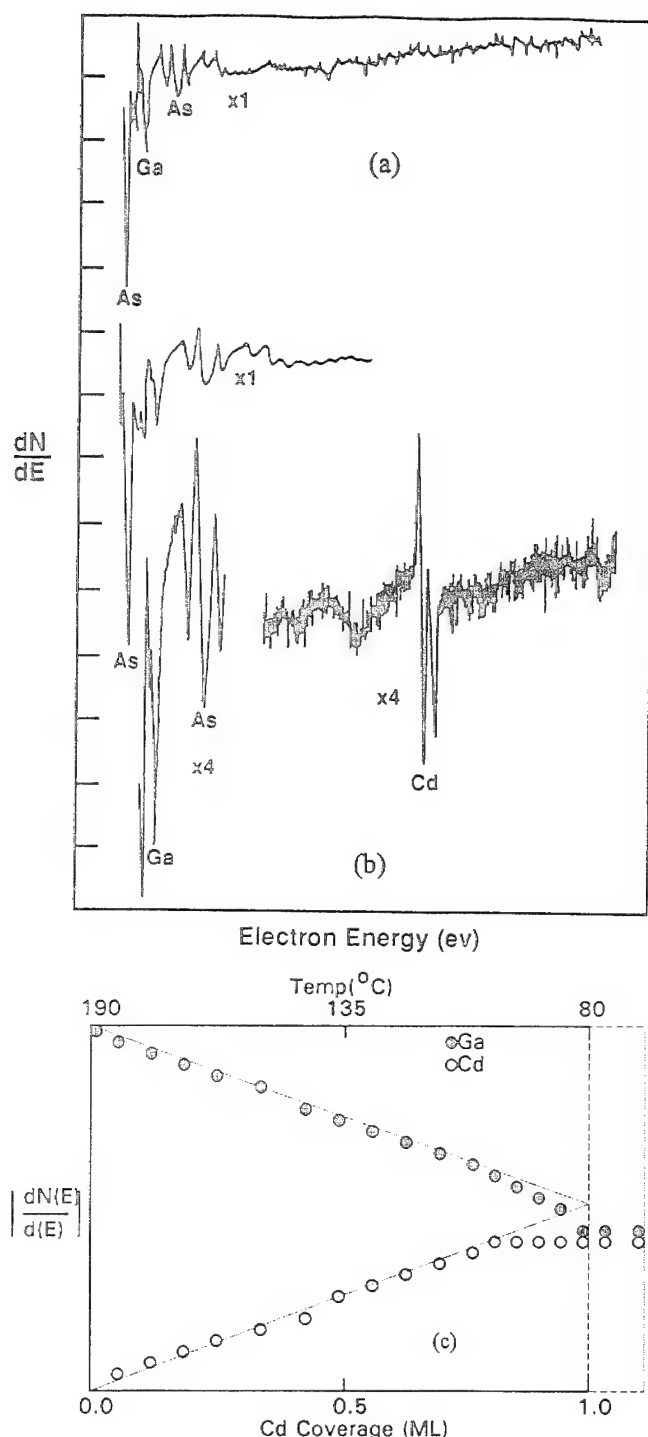


Fig. 1. *In-situ* AES during Cd pre-treatment process: (a) from a thermally clean {001} GaAs surface; (b) after the Cd treatment at 80°C; (c) peak-to-peak (P/P) magnitude of Ga (55 eV) and Cd (376 eV) Auger peaks vs surface coverage during the T_s cool down period under Cd flux. Cd surface coverage estimated to be nearly a monolayer. The Cd and Ga P/P intensities remain unchanged when substrate is subjected to Cd flux at 80°C for more than 30 min or when T_s is lowered several degrees below 80°C.

If CdTe layers are to be used for subsequent growth of HgCdTe, the {001} orientation is preferable because HgCdTe layers grown on {111} CdTe suffer from a high density of lamellar twins.^{11,12} Moreover, better

control over dopant incorporation in the HgCdTe overgrowth can be achieved for {001} layers.¹³ Although {112} orientation is another important surface that has been used successfully to grow twin free HgCdTe and controlled chemical doping, however, this paper primarily deals with CdTe epitaxy in the {001} orientation.

Growth of high quality {001} CdTe on {001} GaAs requires that the threading dislocation density be reduced. For other heteroepitaxial systems, such as ZnSe/GaAs, it has been reported that threading dislocation density can be reduced by initiating a 2-D growth mode.¹⁴ No 2-D nucleation of {001} oriented CdTe layers on {001} GaAs substrates has been reported.

All of the previously reported growth results of CdTe on GaAs (including the case of interfacial ZnTe) indicate that growth initiates from an initial atomic layer of Te at the substrate-layer interface which encourages Ga-Te bonds. Growth of CdTe by nucleation on surfaces with high Cd or Zn coverage has not previously been reported. Ekawa et al.⁶ and Mar et al.⁷ showed that only small concentrations of Cd can be adsorbed on atomically clean (H_2 annealed) GaAs surfaces and that these were always accompanied by Te, most likely adsorbed from the vacuum background. In this paper, we describe a technique for achieving 2-D nucleation, and growth of {001} CdTe on Cd or Zn terminated {001} GaAs surfaces.

EXPERIMENTAL

{001} GaAs substrates were etched in $H_2SO_4:H_2O_2:H_2O$ (5:1:1) solutions, mounted with indium on molybdenum blocks and introduced into a commercial MBE system. Temperatures were measured to within a few degree accuracy, by a thermocouple in contact with the molybdenum block. Conventional Cd, Te, CdTe, Zn, Ga, and As effusion cells were used for GaAs surface treatment and CdTe growth. Surface preparation, nucleation, and growth were monitored by 10 KV reflection high energy electron diffraction (RHEED). Surface composition was monitored *in situ* by Auger electron spectroscopy (AES). Several CdTe layers with thicknesses in the range of 3 to 6 μm were grown. Optical microscopy, x-ray diffraction spectra in the θ -2 θ mode, and double crystal x-ray rocking curve (DCRC) measurements were used to assess layer morphology, number of domains, and crystallinity, respectively. Density of threading dislocations was estimated by the average density of the etch pits (EPD) formed on the CdTe layer surfaces using a solution¹⁵ with controlled Ag^+ ions. Optical properties were qualitatively evaluated by photoluminescence (PL) measurements at 8K.

In Situ Surface Preparation

In the present work, we have sought to avoid the formation of Ga-Te bonds. Thin GaAs layers were first grown at 580°C on {001} GaAs substrates. Substrates were then cooled below 450°C under an incident arsenic flux to physically adsorb an excess monolayer

of arsenic. This was indicated by a change in the RHEED pattern from (2×4) to $c(4 \times 4)$ reconstruction and by the enhancement of the low energy arsenic Auger peak (31 eV). If the substrate temperature (T_s) is lowered to 80°C under a Cd flux with beam equivalent pressure (BEP) of 1×10^{-6} Torr, the RHEED pattern changes from the $c(4 \times 4)$ As-rich reconstruction to the (1×1) Cd-rich reconstruction. Thus, we find that at low T_s , monolayer coverage of cadmium can be achieved on As-rich $c(4 \times 4)$ {001} GaAs surfaces.

To minimize adsorption of Te on the substrate surface, Te and CdTe cells were kept at low temperatures prior to and during the Cd adsorption process. An Auger spectrum from the surface of a thermally cleaned {001} GaAs is shown in Fig. 1a. The Auger spectrum from the same surface after treating with arsenic to form the $c(4 \times 4)$ As-rich surface followed by cooling under Cd from 190 to 80°C is shown in Fig. 1b. Te was not detected from these Cd terminated surfaces. Cd (376 eV) Auger peak-to-peak intensity (coverage) increased as T_s was reduced from 190 to 80°C . The monolayer Cd coverage was estimated by monitoring the attenuation of the low energy Ga (55 eV) Auger peak-to-peak (P/P) intensity as shown in Fig. 1c. As evidenced from the data plotted in Fig. 1c, the magnitude of the Ga P/P intensity decrease with increasing coverage of Cd is commensurate with monolayer coverage. The Cd surface coverage approaches a complete monolayer at or near $T_s = 80^\circ\text{C}$. Upon reaching a monolayer, the Cd adsorption becomes self-limiting and both the Cd and Ga P/P intensities remain nearly constant.

Zn terminated GaAs surfaces were prepared in a similar way by cooling an As-stabilized (2×4) or (4×4) {001} surface from 340 to $\sim 200^\circ\text{C}$ under an incident Zn flux (BEP = $7\text{--}9 \times 10^{-7}$ Torr). The Zn-rich surface caused a (1×4) surface reconstruction. In the range of T_s between $\sim 200^\circ\text{C}$ and 80°C , it was necessary to shut off the Zn flux because of the apparent degradation of the surface. In this temperature range, the Zn terminated surfaces were cooled in Cd flux. Near 80°C , this surface also showed a (1×1) RHEED reconstruction.

On clean GaAs surfaces, Te can readily adsorb from the ambient.⁷ By simply cooling an atomically clean GaAs surface from 580 to 300°C a Te-poor (6×1) reconstructed GaAs surface can be formed.^{5,16} A Te-rich (2×1) surface can be formed on an As-rich GaAs surface as described previously in the reference.¹⁶

MBE Growth

Molecular beam epitaxial growth of CdTe was carried out on Cd and Zn terminated {001} surfaces. In an attempt to minimize Cd or Zn desorption from the surface during the CdTe growth at 310°C , an initial deposition of ~ 4 ML of CdTe (cap layer) was performed at $T_s = 80^\circ\text{C}$ with a CdTe flux of 9×10^{-7} Torr. A diffused RHEED indicated that the CdTe cap layer was amorphous. The cap layer thickness was estimated by the deposition time and by the attenuation

of the Ga (55 eV) Auger peak intensity. T_s was then raised to 310°C under the incident Cd flux. Above 200°C , the diffuse RHEED faded, a (2×1) reconstructed pattern appeared, and at 310°C a sharp (2×1) pattern was clearly visible, indicating crystallization of the amorphous cap layer. The layer was then annealed under incident Cd flux for several

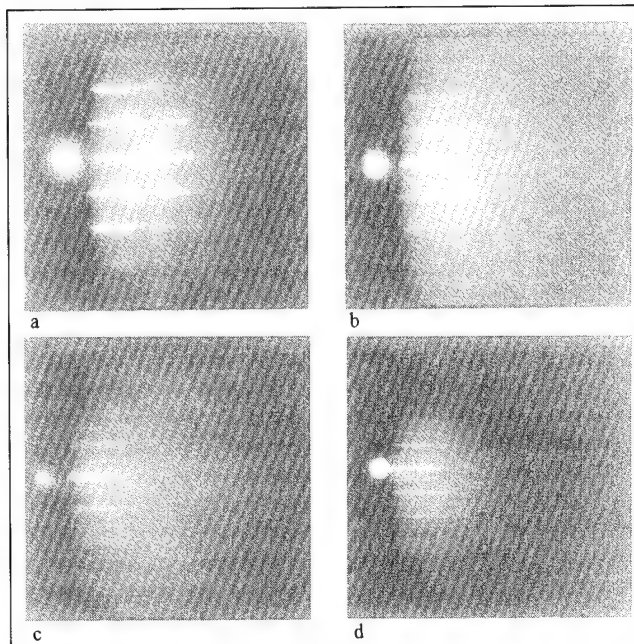


Fig. 2. Reflection high energy electron diffraction reconstructed patterns, in the $\langle 110 \rangle$ azimuth, during various steps described in the section entitled experimental: (a) Cd terminated {001} GaAs surface at 80°C , (b) recrystallized {001} CdTe on {001} GaAs at 310°C , (c) at the instant of CdTe deposition, and (d) after one minute of CdTe growth.

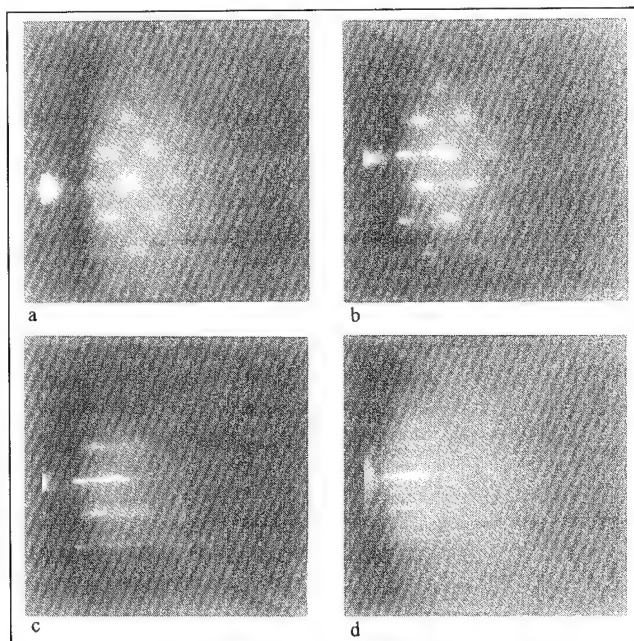


Fig. 3. Reflection high energy electron diffraction reconstructed patterns, in the $\langle 110 \rangle$ azimuth, during the conventional method of growth: (a) at the instant of deposition, (b) after 5, (c) after 10, and (d) after 30 min of {001} CdTe growth.

Table I. Effect of Surface Chemistry and Capping Temperatures on CdTe Growth on (001) GaAs

Starting Surface	Cap Layer T (°C)	Cap Layer Crystallinity	Growth Mode at 310°C	Morphology	Crystal Domain
As(2 × 4) → Te(6 × 1)	—	—	2D - (111)	Specular	Mixed
As(2 × 4) → Te(2 × 1)	—	—	3D - (001)	Rough	Mixed
As(2 × 4) → Te(2 × 1)	80–150	Poly	Poly	Very rough	—
As(4 × 4) → Cd(1 × 1)	80	Amorphous	2D-(001)	Specular	Single
As(4 × 4) → Cd(1 × 1)	80–90	Crystalline	3D-(001)	Pyramidal	Mixed
As(4 × 4) → Cd(1 × 1)	90–150	Crystalline	3D-(111)	Milky, Rough	Mixed
As(4 × 4) → Zn(1 × 4)	80	Amorphous	2D-(001)	Specular	Single
As(4 × 4) → Zn(1 × 4)	>80	Crystalline	3D-(001)	Elongated Pyramidal	Single

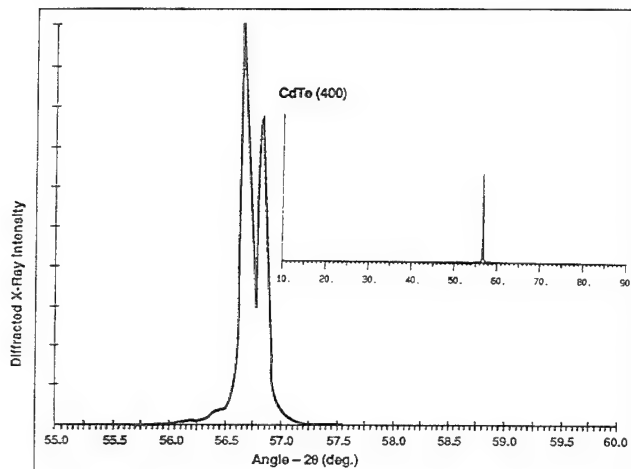


Fig. 4. X-ray θ - 2θ diffractometer scan from a 3 μm {001} CdTe grown by MBE on a Cd terminated GaAs {001} surface. The (400) reflection of the Cu $K\alpha_1$ and $K\alpha_2$ doublet is well resolved. The complete scan from 10 to 90° is shown in the inset indicating single domain {001} CdTe.

minutes and CdTe epitaxy was initiated.

For comparison with this new procedure, CdTe layers were also grown by the conventional procedure on both, the (2 × 1) and (6 × 1) Te terminated reconstructed surfaces. Conventional method was also used to grow {001} CdTe on {001} GaAs with an interfacial ZnTe layer.

RESULTS

Growth Modes

Figures 2 and 3 depict the RHEED patterns during the various steps of {001} CdTe growth on Cd terminated and Te terminated {001} GaAs surfaces, respectively. It is shown in Figs. 2a–2d that using the growth schedule described in the section on MBE growth, two-dimensional <001> CdTe growth can be promoted on Cd or Zn terminated {001} GaAs surfaces. The absence of transmission spot features in the RHEED patterns showed the CdTe layer to be substantially two dimensional as shown in Fig. 2b.

Reflection high energy electron diffraction patterns taken during {001} CdTe growth using the conventional method on (2 × 1) Te terminated reconstructed surfaces and on thin ZnTe interfacial layers (ZnTe terminated surfaces) indicated 3-D growth mode as

shown in Fig. 3a–3b. Conventional MBE growth of CdTe on the (6 × 1) Te terminated surfaces always led to {111} growth via a 2-D mode. Growth on Te terminated surfaces using the low temperature process always resulted in poor quality layers. In most cases, when thin cap layers were deposited in the temperature range of 80 to 150°C on the Te terminated surfaces, the cap layer was found (by RHEED) to be polycrystalline. Crystalline growth at 310°C for the subsequent CdTe layer was possible if the cap layers were annealed above 350°C; however, this procedure always led to <111> growth.

CdTe Layer Characteristics

The crystal orientation, morphology, and defect density of {001} CdTe layers were found to depend on the composition of the initial atomic layer and the cap layer deposition temperature. Table I presents a summary of the CdTe characteristics for various initial surface conditions and capping temperatures.

Our results of CdTe growth orientation on Te terminated surfaces were similar to those detailed in references.^{2–6} Models describing {111} growth on Te-poor surfaces can be found in references.^{17,18} CdTe growth on Te-terminated (6 × 1) surfaces proceeded in a two-dimensional mode and resulted in layers which were predominantly {111}. X-ray θ - 2θ scans from these layers showed them to be composed of mixed (111)B and (001) domains. On (2 × 1) reconstructed Te-stabilized surfaces, island nucleation dominated as shown in Figs. 3a–3d, leading to {001} CdTe growth. {001} growth on Te-rich surfaces occurs by the nucleation of twin tetrahedral unit cells as described in references.^{17,18} These layers also contained {111} domains. Etch pit density in the range of 1 to 5 × 10⁷ cm⁻² were found in these {001} oriented CdTe layers, and DCRC-FWHM values were in the range of 400–600 arc-s. CdTe conventional growth on Te terminated surfaces using a thin interfacial ZnTe layer usually produced better layers that were single domain but had elongated pyramidal surface morphology. Growth using interfacial layers of ZnTe proceeded in a 3-D mode, and the observed RHEED patterns were similar to those shown in Fig. 3. Etch pit density in these layers were in the range of 1 to 5 × 10⁶ cm⁻², and DCRC-FWHM values were in the range of 180–350 arc-s.

Molecular beam epitaxial growth on Cd or Zn termi-

nated GaAs surfaces produced specular, single crystal {001} CdTe layers with lower dislocation density. X-ray θ -2 θ scan from several of these samples indicated single domain {001} growth. A θ -2 θ x-ray diffracted intensity curve measured from CdTe layer grown on a Cd terminated surface is shown in Fig. 4. The (400) reflections of the Cu $K\alpha_1$ and $K\alpha_2$ lines are well resolved. A complete scan indicating single domain is shown in the inset of Fig. 4. (FWHM) of (400) diffraction peaks, measured using a DCRC apparatus were in the range of 80 to 150 arc-s. Etch pit density values were in the range of $1-2 \times 10^5 \text{ cm}^{-2}$.

Low temperature PL measurements were made on {001} CdTe layers grown on Cd, Zn, Te, and ZnTe terminated {001} GaAs substrates. For all layers, transitional energies of PL spectral features, except for those due to free excitons, were similar. The free excitonic peak at 1.596 eV and its excited state at 1.602 eV¹⁹ were not present in CdTe layers grown on substrates other than Cd or Zn terminated surfaces. The overall integrated PL intensity from the Cd and Zn terminated samples were one or two orders of magnitude higher than from those of the Te or ZnTe terminated samples. A representative PL spectrum measured from a CdTe layer grown on the Cd terminated surface is presented in Fig. 5. Details of the origin of various spectral features shown in this figure can be found in references.¹⁹⁻²¹ The existence of the free excitonic peak at 1.596 eV and the improved luminescence intensity suggest that the layers grown on Cd and Zn terminated surfaces had lower density of nonradiative centers and were of better quality.

DISCUSSIONS

At elevated temperatures, strain energy associated with lattice-mismatched layers is often minimized by growth in the Stransky-Krastanow mode.²² This involves surface migration of ad atoms until a supersaturated surface concentration is achieved. At this point, ad atoms and molecules unite to form three-dimensional islands. This is the case for conventional {001} MBE CdTe growth on Te terminated surfaces. As these islands grow, and eventually coalesce to form complete layer coverage, two things can be expected. First, the coalescence of these islands result in layers with rough surfaces. Secondly, island boundaries lead to threading dislocations. If the free energy difference between two crystal orientations of the epitaxial layer with respect to the substrate is small, then islands with different orientations can nucleate simultaneously on adjacent regions of the substrate resulting in mixed domain layers. This is exactly the situation that exists when {001} GaAs surfaces are prepared conventionally where they are always As-deficient. CdTe nucleation on these surfaces occurs with the formation of Ga-Te bonds that may be either in the $\langle 111 \rangle$ or $\langle 001 \rangle$ directions.^{6,17} Even in the case of growth on As-stabilized (2×8) or (2×4) GaAs surfaces, where CdTe growth is predominantly in the $\langle 001 \rangle$ direction,^{10,18} islands with $\{111\}$ orientation can nucleate.

The approach used here is to reduce the temperature to the point where kT is not sufficient to overcome the activation energy for crystalline compound formation. Thus, atomic and molecular beams condense as amorphous layers. Such deposits are conformal, uniform in thickness, and devoid of crystallographic boundaries. If these amorphous deposits are sufficiently thin, they can be recrystallized in the solid state by raising the temperature. In the present case, ~ 4 MLs of amorphous CdTe were deposited at $\sim 80^\circ\text{C}$ on Cd or Zn terminated As-rich GaAs {001} surfaces. The amorphous deposit was recrystallized into a thin CdTe layer. The orientation of the crystalline layer thus formed conforms to that of the underlying lattice. CdTe growth on this thin layer at the recrystallization temperature (310°C) results in the conventional two-dimensional step flow epitaxy. In this manner, single domain, single crystal, specular layers of CdTe with the same crystallographic orientation as the underlying GaAs substrate are obtained, vis. {001}/{001}. Furthermore, the defect density is low compared to layers grown according to conventional nucleation and growth procedures. During the process of recrystallization, dislocations are immediately formed to relax the associated strain. However, most of them extend in the plane of the interface as misfit dislocations and do not thread up through the growing layer.

This procedure works well on {001} GaAs surfaces, if formation of Ga-Te bonds are inhibited as these bonds predominantly lead to growth in the $\langle 111 \rangle$

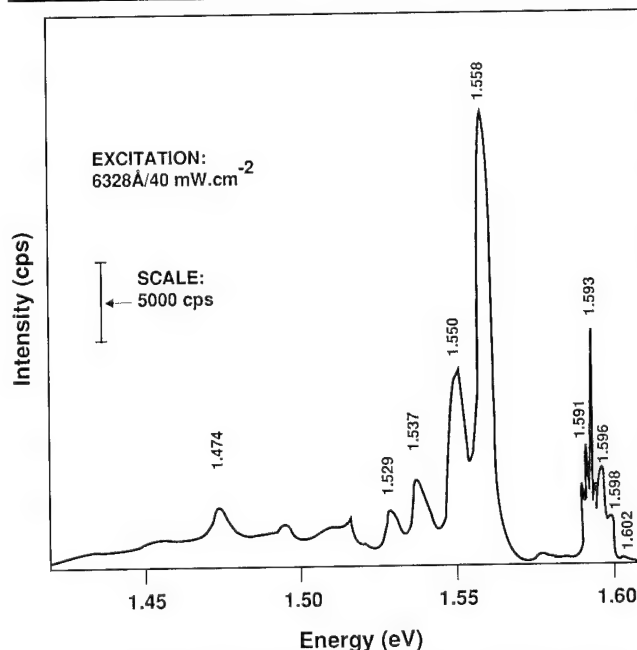


Fig. 5. Low temperature (8K) PL spectrum from {001} CdTe grown on Cd terminated {001} GaAs substrate. The photon energies (eV) emitted by electronic transitions are: 1.602 ($n = 2$, free excitonic (FE) state), 1.598 (upper polariton branch of the FE), 1.596 (FE), 1.593 (donor-bound exciton), 1.591 (acceptor-bound exciton), 1.558 (free-to-bound ($e-A^0$)), 1.550 (donor acceptor pair (DAP)), 1.537 ($e-A^0$ -LO phonon), 1.529 (DAP-LO phonon), and 1.474 (defect related complexes).

direction. Fortunately ~ 1 monolayer coverage of either Cd or Zn on As-rich surfaces suppresses the formation of Ga-Te bonds and promotes growth in the desired {001} orientation. It is not clear whether the Cd or Zn interfacial layer has any influence on the growth mode, however. This interfacial chemistry ensures that the ultra thin crystallized CdTe 'template' is in the {001} orientation. Since this 'template' is most likely relaxed and two dimensional, the subsequent CdTe growth proceeds in a 2D growth mode.

CONCLUSIONS

{001} CdTe epitaxy was achieved on thin ($\sim 12\text{\AA}$) recrystallized CdTe layers deposited on Cd or Zn terminated {001} GaAs. Growth proceeded in a 2-D mode and layers so produced were specular and single domain. {001} CdTe epitaxy was also achieved on Te-rich or ZnTe terminated {001} GaAs using the conventional MBE procedure. The conventional growth always led to 3-D growth mode and layers had defect densities at least an order of magnitude higher than layers grown in a 2-D mode. Predominately {111} CdTe epitaxy with multiple domains was produced on Te terminated {001} GaAs surfaces.

ACKNOWLEDGMENTS

This work was funded in part by the U.S. Army Research Laboratory DIRF-1994.

REFERENCES

1. J.M. Ballingall, M.L. Wroge and D.J. Leopold, *Appl. Phys. Lett.* 48, 1273 (1986).
2. R.D. Feldman, R.F. Austin, A.H. Dayem and E.H. Westerwick, *Appl. Phys. Lett.* 49, 797 (1986).
3. Y. Gobil, J. Cibert, K. Saminadayar and S. Tatarenko, *Surf. Sci.* 211/212, 969 (1989).
4. R. Srinivasa, M.B. Panish and H. Temkin, *Appl. Phys. Lett.* 50, 1441 (1987).
5. S. Tatarenko, J. Cibert, Y. Gobil, G. Feuillet, K. Saminadayar, A.C. Chami and E. Ligeon, *Appl. Surf. Sci.* 41/42, 470 (1989).
6. M. Ekawa, K. Yasuda, S. Sone, Y. Sugiura, M. Saji and A. Tanaka, *J. Appl. Phys.* 67, 6865 (1990).
7. H.A. Mar, K.T. Chee and N. Salanski, *Appl. Phys. Lett.* 44, 237 (1984).
8. H. Shtrikman, M. Oron, A. Raizman and G. Cinader, *J. Electron. Mater.* 17, 105 (1988).
9. R.D. Feldman, R.F. Austin, D.W. Kisker, K.S. Jeffers and P.M. Bridenbaugh, *Appl. Phys. Lett.* 48, 248 (1986).
10. N. Otsuka, L.A. Kolodziejski, R.L. Gunshor, S. Dutta, R.N. Bicknell and J.F. Schetzina, *Appl. Phys. Lett.* 46, 860 (1985).
11. P. Capper, C.D. Maxey, P.A.C. Whiffin and B.C. Easton, *J. Cryst. Growth* 96, 519 (1989).
12. J.P. Faurie, R. Sporken, S. Sivanathan and M.D. Lang, *J. Cryst. Growth* 111, 698 (1991).
13. W.S. Wang, H. Ehsani and I. Bhat, *J. Electron. Mater.* 22, 873 (1993).
14. S. Guha, H. Munekata, F.K. LeGoues and L.L. Chang, *Appl. Phys. Lett.* 60, 3220 (1992).
15. Morio Inoue, Iwao Teramoto and Shigetoshi Takayanagi, *J. Appl. Phys.* 33, 2578 (1962).
16. N.K. Dhar, P.R. Boyd, P.M. Amirtharaj, J.H. Dinan and J.D. Benson, *SPIE Proc.* 2228, 44 (1994).
17. G. Cohen-Solal, F. Bailly and M. Barbe, *Appl. Phys. Lett.* 49, 1519 (1986).
18. S. Tatarenko, K. Saminadayar, J. Cibert, Y. Gobil, G. Cohen-Solal and F. Bailly, *SPIE Proc.* 944, 2 (1988).
19. Z.C. Feng, M.J. Bevan, W.J. Choyke and S.V. Krishnaswamy, *J. Appl. Phys.* 64, 2595 (1988).
20. N.K. Dhar, P. Boyd, M. Martinka, J.D. Benson, J.H. Dinan and A.A. Iliadis, *Mater. Res. Soc. Symp. Proc.* 263, 359 (1992), and references therein.
21. Z.C. Feng, M.G. Burke and W.J. Choyke, *Appl. Phys. Lett.* 53, 128 (1988).
22. D.J. Eaglesham and M. Cerullo, *Phys. Rev. Lett.* 64, 1943 (1990), and references therein.

Studies on the Growth of CdTe on Si Using Ge Interfacial Layer in an Organometallic Vapor Phase Epitaxial System

WEN-SHENG WANG and ISHWARA B. BHAT

Electrical, Computer and Systems Engineering Department, Rensselaer Polytechnic Institute, Troy, New York 12180

Epitaxial CdTe layers were grown using organometallic vapor phase epitaxy on Si substrates with a Ge buffer layer. Ge layer was grown in the same reactor using germane gas and the reaction of germane gas with the native Si surface is studied in detail at low temperature. It is shown that germane gas can be used to "clean" the Si surface oxide prior to CdTe growth by first reducing the thin native oxide that may be present on Si. When Ge layer was grown on Si using germane gas, an induction period was observed before the continuous layer of Ge growth starts. This induction period is a function of the thickness of the native oxide present on Si and possible reasons for this behavior are outlined. Secondary ion mass spectrometry (SIMS) data show negligible outdiffusion and cross contamination of Ge in CdTe.

Key words: CdTe, organometallic vapor phase epitaxy (OMVPE), Ge interfacial layer

INTRODUCTION

The heteroepitaxial growth of CdTe on Si has attracted increased attention recently since the resulting layer can be used as substrates for subsequent HgCdTe growth. Growth of high quality CdTe directly on Si has already been demonstrated by molecular beam epitaxy (MBE).^{1,2} However, direct growth of CdTe on Si is difficult by organometallic vapor phase epitaxy (OMVPE) because it is difficult to maintain "clean" Si surface in an OMVPE system. We had reported earlier that high quality, single crystal CdTe can be grown on Si substrates in an atmospheric pressure OMVPE reactor if a thin layer of Ge is first grown on Si prior to CdTe growth.³ If the Ge layer is not present, we would get only polycrystalline CdTe layers. We speculated that the Ge layer "protects" the Si surface from the residual contaminants such as

H₂O and O₂ present in the reactor. We also found that the conditions used for the Ge interfacial layer growth is critical for obtaining high quality CdTe layers. For example, deposition of Ge using germane at low temperature is necessary to grow high quality CdTe layers. It is believed that this step reduces the Si native oxide (Si₂O₃) to Si³⁻⁵ and coats it with Ge.

In order to understand the reaction mechanism, we have carried out a more detailed study of this "in-situ cleaning step" at low temperature (<500°C). Since Ge and CdTe were grown in the same reactor, secondary ion mass spectrometry (SIMS) was carried out to measure the depth profile of Ge in CdTe. Finally, photoluminescence spectra at 10K of a 5 μm thick CdTe grown on Si was carried out to determine its optical quality.

EXPERIMENTAL DETAILS

The growth of Ge and CdTe were carried out in a 2 inch diameter horizontal reactor operated at atmo-

(Received November 1, 1994; revised January 10, 1995)

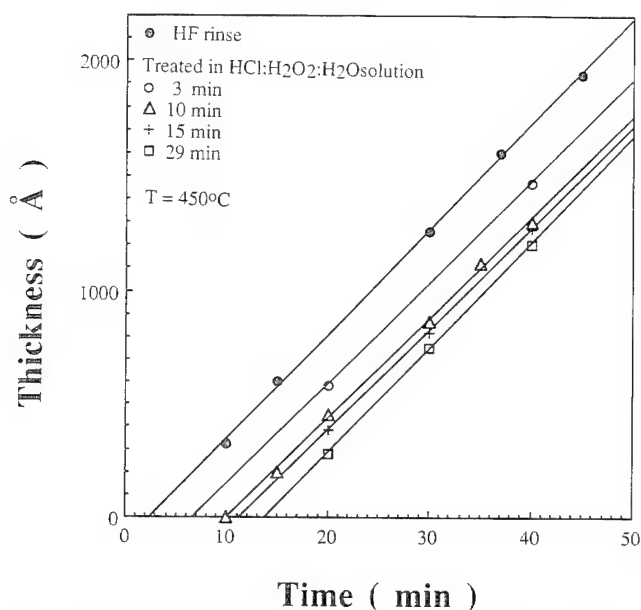


Fig. 1. The thickness of Ge layer grown on Si as a function of time at 450°C. The substrate was treated in $\text{HCl}:\text{H}_2\text{O}_2:\text{H}_2\text{O}$ solution at 80°C for different times prior to growth.

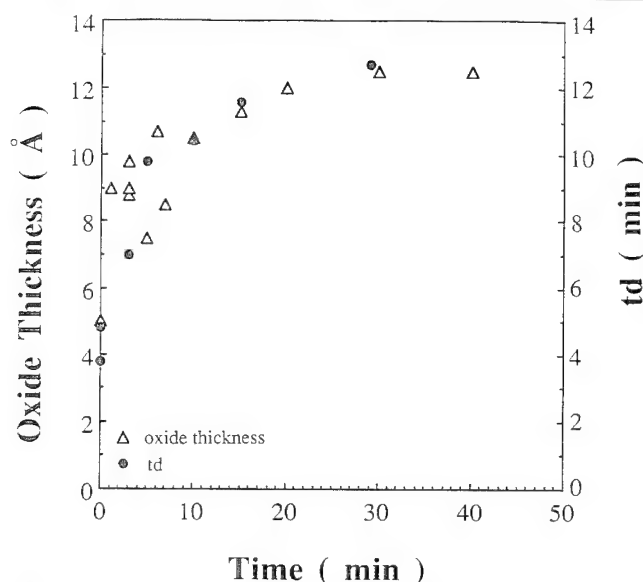


Fig. 2. The thickness of the native oxide layer on Si as a function of time treated in $\text{HCl}:\text{H}_2\text{O}_2:\text{H}_2\text{O}$ solution at 80°C. Δ represents the native oxide thickness; \circ represents the induction time, t_d of growth.

spheric pressure. The detailed conditions for the growth of CdTe was reported elsewhere.³ The precursor used for Ge growth was germane gas (GeH_4), diluted in hydrogen (0.5% germane in H_2). To investigate the role of GeH_4 in Si surface cleaning, a systematic growth study was carried out. The growth temperature ranged from 350 to 480°C.

Three kinds of surface treatments were used for this study:

- A final treatment in dilute HF solution.
- A final treatment in $\text{HCl}:\text{H}_2\text{O}_2:\text{H}_2\text{O}$ solution with a volume ratio 1:1:4 at 80°C. This step will grow a thin layer of native oxide.
- 900Å thick SiO_2 grown on Si.

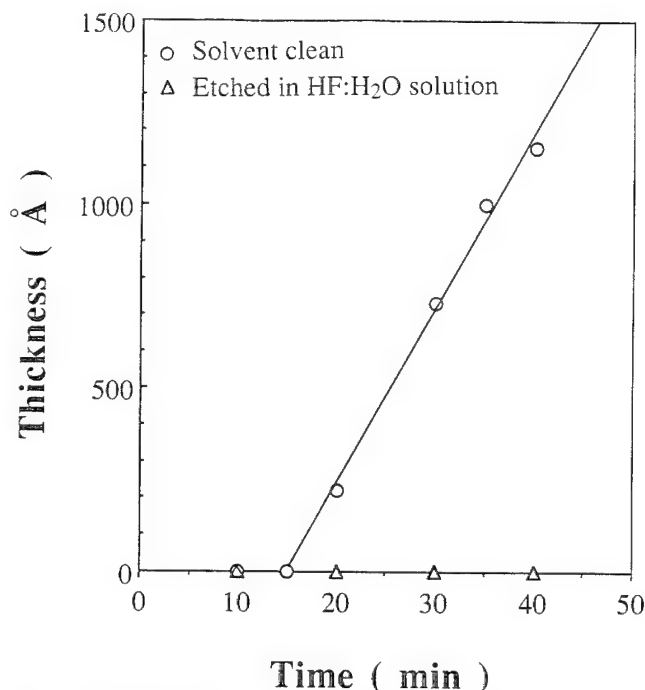


Fig. 3. Ge layer thickness on SiO_2 covered Si as a function of time. Δ represents a final dip in HF solution; \circ represents only solvent clean without HF final dip. Ge growth is observed if only solvent clean of SiO_2 is carried out prior to growth.

The thickness of the Ge layer was measured by the alpha-step profiler.

RESULTS AND DISCUSSIONS

If the Si substrate is covered with any residual native oxide (Si_xO_y), a "delay period" was seen before any continuous film growth is observed. For example, Ge growth starts almost immediately if the Si substrate is finally treated in dilute HF solution that removes any residual native oxide and passivates the surface by hydrogen termination. However, it takes about 10 min at 450°C before Ge growth starts if native Si oxide (Si_xO_y) is intentionally grown using $\text{HCl}:\text{H}_2\text{O}_2:\text{H}_2\text{O}$ solution. The delay time we observed was thought to be caused by the time required to reduce Si_xO_y by adsorbed germane molecules. We speculate that Ge growth starts when all the Si_xO_y is desorbed. A similar delay period (more than 20 min) was observed on silane pyrolysis on Si at 830°C.⁶ This period was attributed to the difficulty of nucleation on SiO_2 remaining on the surface. It was proposed that Si from silane reacts with SiO_2 to form volatile SiO which desorbs.

To investigate whether the induction period is related to the oxide thickness, we prepared samples by treating them in $\text{HCl}:\text{H}_2\text{O}_2:\text{H}_2\text{O}$ solution for various times. The thickness of the Ge layer grown at 450°C as a function of the growth time is shown in Fig. 1. The induction period depends on the length of times these samples underwent treatment in $\text{HCl}:\text{H}_2\text{O}_2:\text{H}_2\text{O}$ solution. For example, for samples treated for 30 min in $\text{HCl}:\text{H}_2\text{O}_2:\text{H}_2\text{O}$ solution, the induction period was 14 min, whereas for samples treated for 3 min, the

induction period was only 7 min. The thickness of the grown native oxide on Si is independently estimated using spectroscopic ellipsometry. The native oxide thickness as a function of the treatment time in $\text{HCl}:\text{H}_2\text{O}_2:\text{H}_2\text{O}$ solution is shown in Fig. 2. The observed induction periods for different native oxide thicknesses are also shown in Fig. 2 for comparison. The induction time increased monotonically with the native oxide thickness. It appears that the induction period is related to the time required for the reduction of native oxide by germane gas.

Another possible mechanism for the presence of delay period before continuous Ge growth starts is the time required for surface nucleation.⁷ If this is the case, then the induction time should not depend on the thickness of the native oxide. However, in our results, this induction time is a function of the native oxide thickness. Additionally, we carried out Ge growth on Si coated with 900Å thick thermal oxide. The thickness of the Ge layer as a function of growth time is shown in Fig. 3. No continuous Ge film is observed on SiO_2 even though the growth time is as long as one hour, provided the SiO_2/Si is freshly dipped in dilute HF solution prior to growth. From these experiments, it is clear that Ge will not nucleate easily on oxide-covered Si substrates at low temperature. Therefore, it appears that the induction time of Ge growth is related to the removal of the native oxide on the Si surface.

In order to understand the mechanism of oxide removal by germane, the Ge growth experiments were repeated at various temperatures in the range 350 to 480°C. In these experiments, the native oxide was intentionally grown on the Si substrate by treating in $\text{HCl}:\text{H}_2\text{O}_2:\text{H}_2\text{O}$ solution for 10 min. The thickness of the native oxide is estimated to be around 10Å. An induction time was observed for reach growth temperature. Since the oxide thickness was kept constant, the inverse of induction time is proportional to the etching rate of the oxide. The inverse of induction time as a function of temperature is shown in Fig. 4. An activation energy of 21 kcal/mol is observed and can be related to the removal of oxide prior to Ge growth.

It was reported previously by several workers that both Ge and GeH_4 can remove the Si native oxide.^{4,5} However, it was not clear which species dominate this reaction. For example, in the case of oxide removal by GeH_4 , it is possible that GeH_4 decomposes first, followed by the reaction of Ge and the oxide. Another scenario is that GeH_4 can react directly with the native oxide. If GeH_4 can decompose first, then the energy required for this activated process should be less than the activation energy we observed, namely, 21 kcal/mol. In order to understand this reaction, the Ge growth rate as a function of temperature was studied. The growth rate was calculated from the slope of thickness vs growth time curve. The result is shown in Fig. 5. Two distinct regimes are observed. The growth at high temperature is probably diffusion limited.⁸ On the other hand, the growth at low tem-

perature is probably controlled by the surface reaction. The decomposition of GeH_4 at the heated surface (heterogeneous decomposition) may dominate the surface reaction.^{4,8} Thus, the activation energy for the decomposition of GeH_4 is 38 kcal/mol. This value is close to the reported values by other workers. Tamaru et al.⁹ reported 41.5 kcal/mol for the decomposition of GeH_4 in a closed system. Recently, Cunningham et

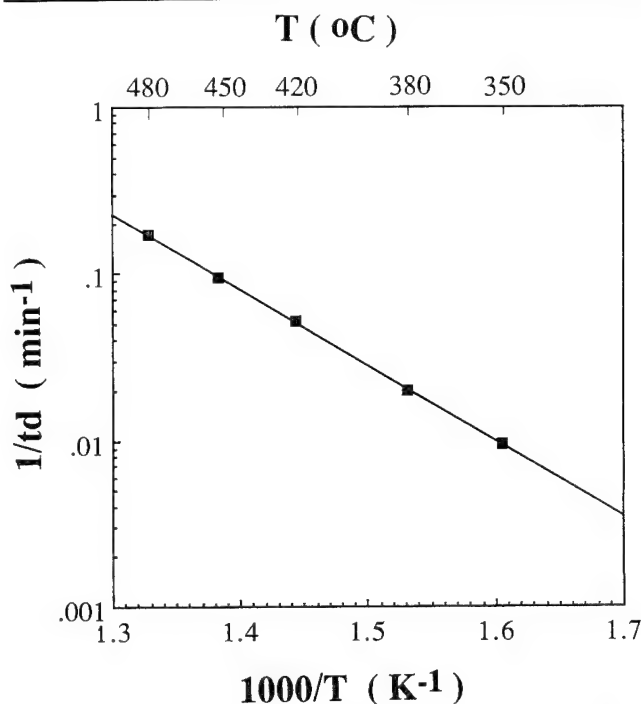


Fig. 4. The induction period of Ge growth as a function of temperature. The Si wafer was treated in $\text{HCl}:\text{H}_2\text{O}_2:\text{H}_2\text{O}$ solution at 80°C for 10 min prior to Ge growth.

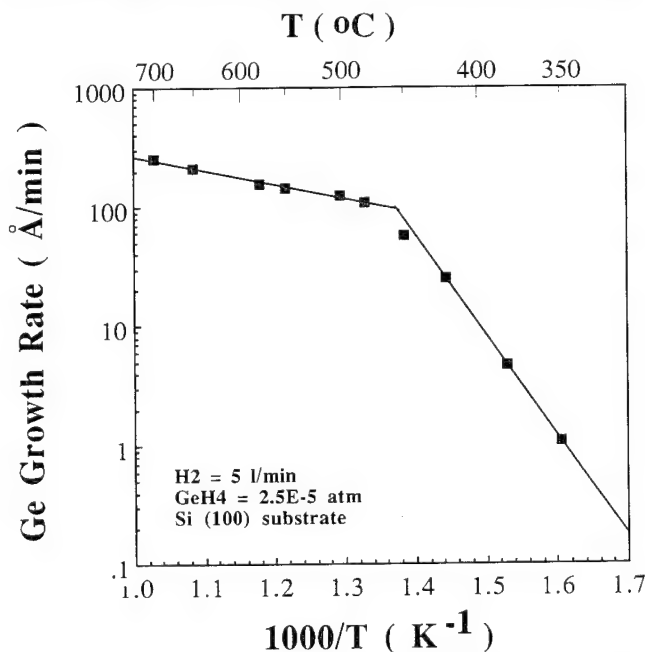


Fig. 5. The growth rate of Ge on Si as a function of temperature. The Ge partial pressure was 2.5×10^{-5} Torr.

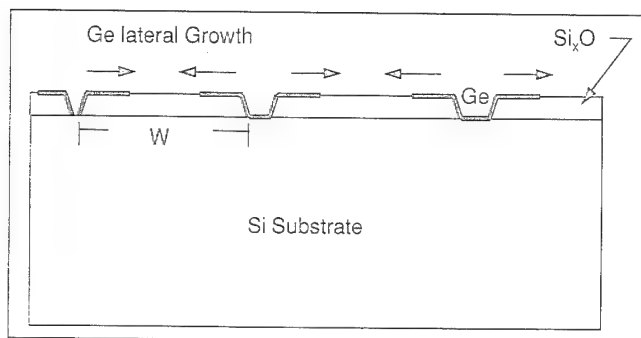


Fig. 6. A schematic picture showing Ge growth on discontinuous native oxide. The delay period for the continuous Ge layer can be related to the time required for the lateral growth of Ge on Si_xO_y .

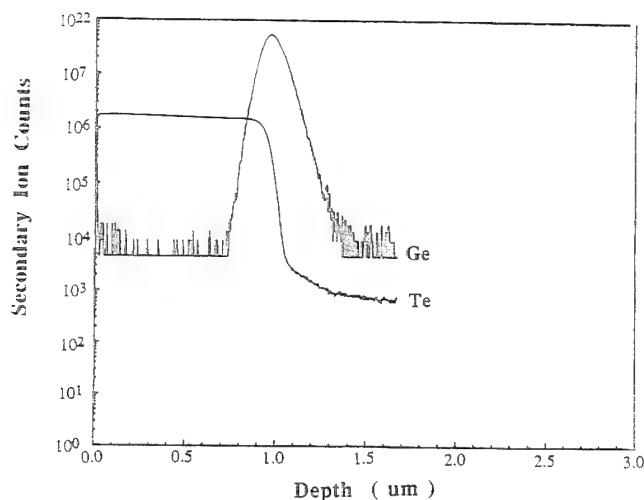
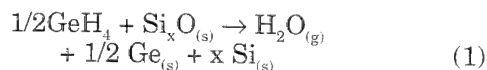


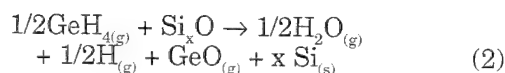
Fig. 7. Secondary ion mass spectroscopy profile of 1 μm thick CdTe on Ge/Si. The CdTe was grown at 360°C.

al.¹⁰ reported 33 kcal/mol for the decomposition of GeH_4 in UHV-CVD system using He as the carrier gas.

In our study, the activation energy of the reaction between SiO_x and GeH_4 is smaller than the activation energy of GeH_4 decomposition. Thus, it can be concluded that the mechanism for oxide removal is the direct reaction between GeH_4 and SiO_x , and not the one between Ge and SiO_x . However, the exact reaction between GeH_4 and SiO_x is still not clear. Takahashi et al.⁵ have observed that the reduction rate of SiO_x by GeH_4 is proportional to the square root of GeH_4 gas pressure in a closed system. This relation means that two oxygen atoms in the oxide are reduced by one molecule of GeH_4 gas. They suggested that the reaction equation could be



and/or



In reaction (1), the Ge layer may form before the

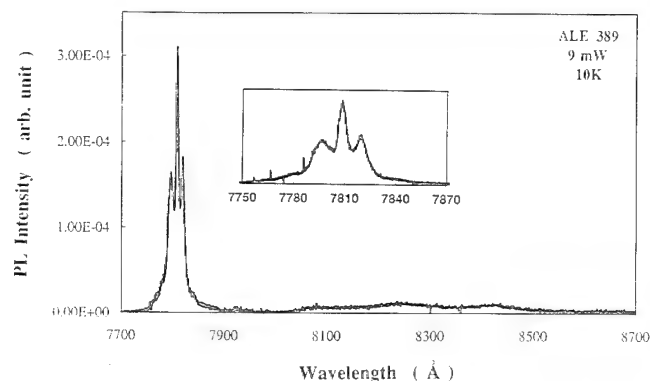


Fig. 8. The photoluminescence spectra at 10K of a 5 μm thick CdTe grown on Si with ZnTe/Ge buffer layer. The ZnTe layer was grown to obtain (100) oriented CdTe.

native oxide is totally removed. Ge can continuously grow on this Ge-covered surface. Thus, the induction time corresponds to only partial removal of the oxide. In this case, the induction time should be independent of the thickness of the native oxide, which is opposite to our result. Therefore, the GeH_4 may reduce the Si surface oxide by forming volatile GeO . Based on the available data, these conclusions are speculative at present.

An alternative mechanism may exist, which will result in the delay period we have seen. Note that the thickness of the Si_xO_y layer was measured using spectroscopic ellipsometry. Here, we assume that the Si_xO_y is uniformly grown on Si and covers the whole Si surface. In practice, a discontinuous film of Si_xO_y may grow in island form, but spectroscopic ellipsometry measurement will give us only an average thickness. Therefore, the delay period we observed could be due to the time required for the lateral growth of Ge on the discontinuous SiO_x instead of the time required for the removal of Si_xO_y , as schematically shown in Fig. 6. This delay period is directly related to the width of the Si native oxide W , which can be a direct function of the treatment time in $\text{HCl}:\text{H}_2\text{O}_2:\text{H}_2\text{O}$ solution. CdTe layers grown on Si that are treated in $\text{HCl}:\text{H}_2\text{O}_2:\text{H}_2\text{O}$ solution as a final step were polycrystalline. This result supports the above lateral growth mechanism. We cannot conclusively say which mechanism is the correct one at this moment. Thus, more measurements, such as transmission electron microscopy (TEM), will be needed to determine which mechanism is dominant here.

One main concern when both Ge and CdTe is grown in the same reactor is the cross contamination of Ge in CdTe. The SIMS data of a CdTe layer grown on Ge/Si at 360°C are shown in Fig. 7. It is clear that no outdiffusion of Ge into CdTe is seen. In addition, contamination of CdTe from residual Ge in the reactor is negligible (below the detection limit) even though the same reactor was used for both Ge and CdTe growth. Since Ge deposition is kinetically limited and deposits only on the Si surface, the residual Ge in the reactor is negligible. Any deposited Ge on the substrate (if any) will have low enough vapor pressure at 360°C so that Ge contamination of CdTe layer is low.

High quality CdTe can be grown on Si using the low temperature grown Ge interfacial layer. Figure 8 shows the PL spectra at 10K of a 5 μm thick CdTe layer grown on Si. An Ar-ion laser (4880Å) with source power of 9 mW was used. The spectra was dominated by strong excitonic emission at 1.588 eV. The position of this exciton has shifted from the more typical 1.596 eV found in bulk CdTe. The shift of the excitonic emission was also observed on CdTe/GaAs/Si grown by hot wall epitaxy¹¹ and attributed to residual strain the film. The weak defect emission at 1.472 eV and its phonon replica were also observed. The low intensity of defect emission compared to the excitonic emission indicates that the CdTe layer on Si is of high optical quality.

CONCLUSIONS

In summary, the nature of reaction between germane gas and native Si_xO on Si is studied in more detail. The induction period observed before a continuous film of Ge starts to grow on Si is related to the thickness of the native oxide film present. It appears that the induction period is related to the time required to remove any residual native oxide by the reduction reaction of SiO_x germane gas. An alternative possibility is that the Ge nucleates at the pin holes that may be present in the oxide and the induction period is related to the time required for the Ge nuclei to coalesce by lateral growth. The SIMS data show negligible outdiffusion and cross contamination of Ge in CdTe.

ACKNOWLEDGMENT

The authors would like to thank Professor S.P. Murarka for allowing to use his alpha-step profiler, Dr. Hung-Dah Shih of Texas Instruments for SIMS results, and J. Barthel for technical assistance. Partial support was provided by a gift from Texas Instruments. This support is gratefully acknowledged.

REFERENCES

1. R. Sporken, Y.C. Chen, S. Sivananthan, M.D. Lange and J.P. Faurie, *J. Vac. Sci. Technol. B* 10, 1405 (1992).
2. T.J. deLyon, J.A. Roth, O.K. Wu, S.M. Johnson and C.A. Cockrum, *Appl. Phys. Lett.* 63, 818 (1993).
3. W.S. Wang and I. Bhat, *J. Electron. Mater.* 24, 451 (1995).
4. J.F. Morar, B.S. Meyerson, U.O. Harisseau, F.J. Himpel, F.M. McFeely, D.R. Rieger, A. Taleb-Ibrahimi and J.A. Yarmoff, *Appl. Phys. Lett.* 50, 463 (1987).
5. Y. Takahashi, H. Ishii and K. Fujiuaga, *Appl. Phys. Lett.* 57, 599 (1990).
6. B.A. Joyce and R.R. Bradley, *Phil. Mag.* 15, 1167 (1967).
7. B.A. Joyce, *J. Cryst. Growth* 3-4, 43 (1968).
8. C.H.L. Goodman, ed., *Crystal Growth*, Vol. 1 (New York: Plenum Press, 1980).
9. K. Tamaru, M. Boudart and H. Yaylor, *J. Phys. Chem.* 59, 801 (1955).
10. B. Cunningham, J.O. Chu and S. Akbar, *Appl. Phys. Lett.* 59, 3437 (1991).
11. R. Korenstein, P. Madsian and P. Hallock, *J. Vac. Sci. Technol. B* 10, 1370 (1992).

Thermomigration of Tellurium Precipitates in CdZnTe Crystals Grown by Vertical Bridgman Method

T.S. LEE, J.W. PARK, Y.T. JEOUNG, H.K. KIM, C.H. CHUN, and J.M. KIM

Agency for Defense Development, Youseong P.O. Box 35, Taejeon, Korea

I.H. PARK, J.M. CHANG, S.U. KIM, and M.J. PARK

Korea University, Anamdong 5-1, Seongbugku, Seoul, Korea

Te precipitates in CdZnTe have been characterized by x-ray diffraction at room and higher temperatures. From the x-ray results at room temperature, it has been confirmed that Te precipitates in CdZnTe have the same structural phase as observed in elemental Te under high pressure. The x-ray results at higher temperature indicate that Te precipitates melt around 440°C. CdZnTe samples containing Te precipitates have been annealed at temperatures below and above 440°C with thermal gradient of $\sim 70^\circ\text{C}/\text{cm}$. Results of the observation with infrared microscope before and after the annealings indicate distinct occurrence of thermomigration of Te precipitates in samples annealed at temperature above 440°C compared with ones annealed at temperature below 440°C. Thermomigration velocity obtained from these results is $\sim 50 \mu\text{m}/\text{h}$. The average value for the effective diffusion coefficient of the metallic atoms in Te precipitates calculated by using the thermomigration velocity is $\sim 3 \times 10^{-5} \text{ cm}^2/\text{s}$.

Key words: CdZnTe, effective diffusion coefficient, Te precipitates, thermomigration velocity, x-ray diffraction

INTRODUCTION

CdZnTe is widely preferred as a substrate material for epitaxial growth HgCdTe because it provides the best lattice match to HgCdTe epilayers. CdZnTe is expected to have fewer structural defects than CdTe. Efforts have been ongoing to grow CdZnTe crystal with fewer and fewer structural defects because the crystalline quality of the HgCdTe epilayer is affected by that of the substrate.

Among the various types of defects which could possibly be present in CdZnTe, the special interest is given in the large inclusion of nonmetal particles, namely, Te precipitates. These precipitates have been reported to migrate into HgCdTe epilayer during LPE growth process and to affect the device performance of LWIR HgCdTe arrays.^{1,2} In this paper, an experimental approach is presented to obtain the thermomi-

gration velocity of Te precipitates and then the effective diffusion coefficient of metallic (Cd, Zn) atoms in liquid Te.

EXPERIMENTAL

CdZnTe boule has been grown by the vertical Bridgman method in our laboratory. $\text{Cd}_{0.96}\text{Zn}_{0.04}\text{Te}$ samples of $\sim 1 \times 5 \times 10 \text{ mm}^3$ in approximate sizes are prepared to have the mirror-like surfaces.

The distribution of Te precipitates in as-grown CdZnTe samples has been observed with infrared microscope in the transmission mode. X-ray diffraction experiments at room temperature and at higher temperatures from 410 to 440°C are performed to confirm the presence of Te precipitates and also to determine the melting point of the precipitates. CdZnTe samples are loaded into different quartz ampoules. The quartz ampoules are sealed off in vacuum. The annealing experiments at two different temperatures have been carried out—one at 350°C

(Received November 1, 1994; revised February 10, 1995)

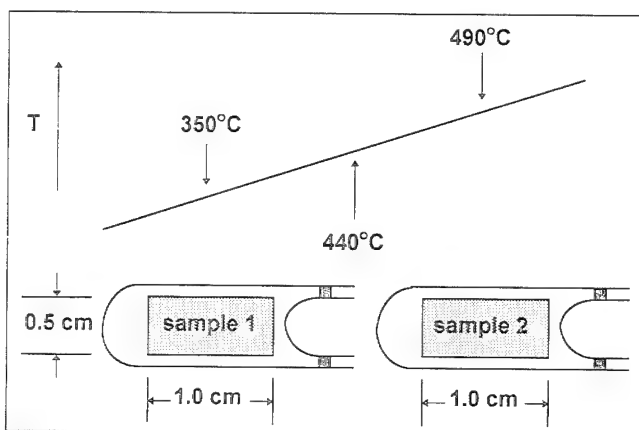


Fig. 1. Annealing temperature profile at the position of the samples.

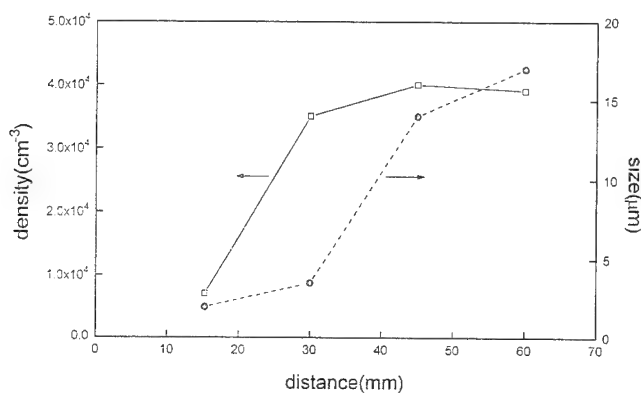


Fig. 2. Density and size of Te precipitates vs distance from the tip of as-grown CdZnTe boule.

with a thermal gradient of 65°C/cm and the other at 490°C with a thermal gradient of 75°C/cm. An annealing time of 3.5 h is used in both experiments. The annealing temperature profile at the position of the ampoules in the furnace is shown in Fig. 1. The position changes of Te precipitates in CdZnTe samples before and after annealings have been examined with infrared microscope to obtain the thermomigration velocity and then the effective diffusion coefficient of (Cd, Zn) atoms in the precipitates.

RESULTS AND DISCUSSION

By the direct observation with infrared microscope, the overall behavior in size and density of Te precipitates in as-grown CdZnTe boule has been investigated (Fig. 2). The size and the density of Te precipitates are in the ranges of 1–20 μm and 10³–10⁴/cm³, respectively, and show an increasing trend in these values toward the upper part of the boule as shown in Fig. 2.

This tendency implies that Te precipitates probably thermally migrate from the lower colder part of the boule to the upper hotter part during growth and also that the upper part becomes more Te rich because of a possible escape of Cd from the upper part to the void space during growth.

Shin and coworkers³ have reported that Te precipitates in CdTe crystal are in the high pressure phase. From the observed angles of the x-ray diffraction peaks, it could be confirmed that the Te precipitate in CdZnTe samples has the same structural phase as observed in elemental Te under high pressure. The

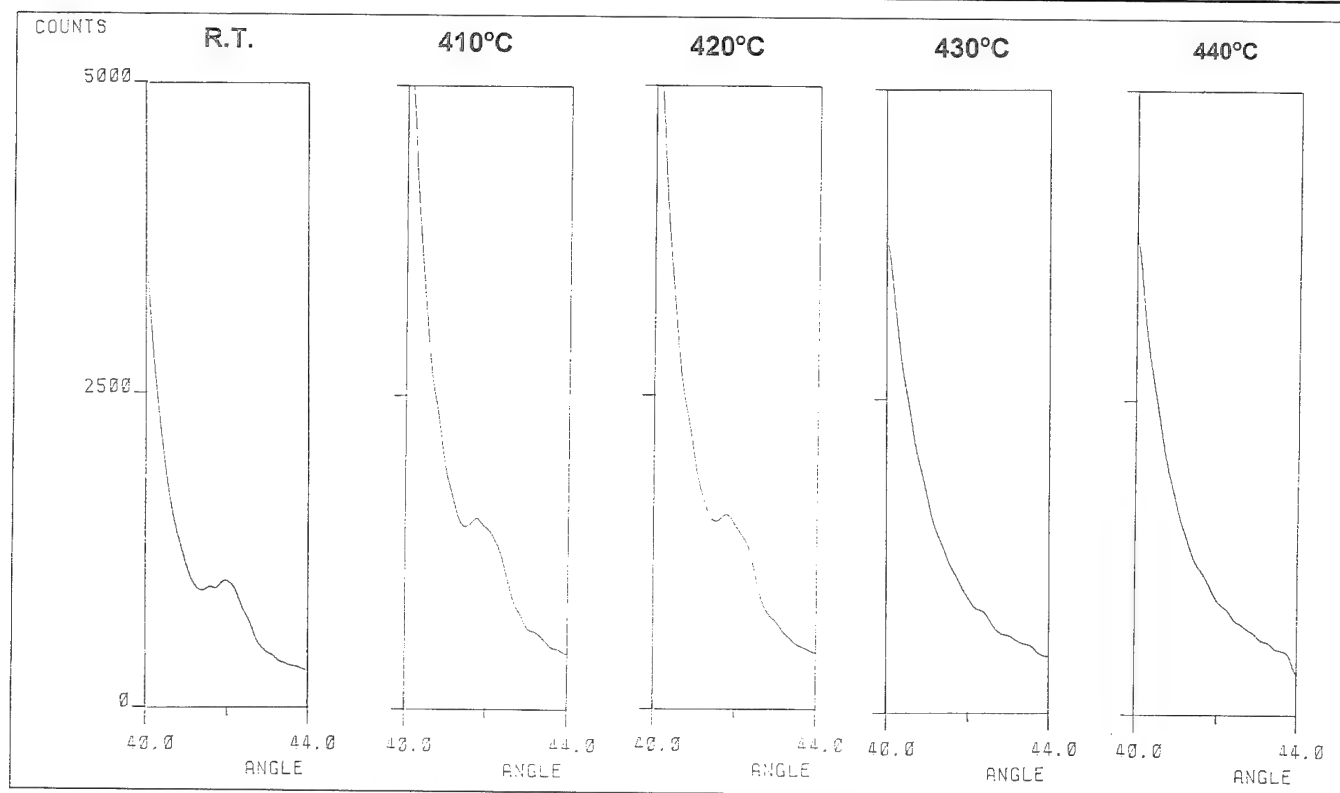


Fig. 3. Gradual change of the intensity of x-ray diffraction peak with measuring temperature.

gradual change of the x-ray diffraction peak at various temperatures is shown in Fig. 3.

The intensity of the peaks changes little from room temperature to 420°C, distinctly decreases, however, around 430°C, and finally disappears at around 440°C. The annihilation of the x-ray peak implies that Te precipitate is not a crystalline solid but is present in a molten state at around 440°C. The x-ray peak annihilation temperature of 440°C is close to the eutectic temperature of 437°C on the Te-rich side in the Cd-Te system.⁴

As can be inferred from the infrared micrographs of CdZnTe samples before and after annealings shown in Fig. 4, Te precipitates have migrated little in sample (#1) annealed at 350°C (Fig. 4a), but have significantly migrated in sample (#2) annealed at 490°C (Fig. 4b). Little thermomigration in sample (#1) means that only solid state diffusion contributes to movement of Te precipitates at temperature below 440°C.

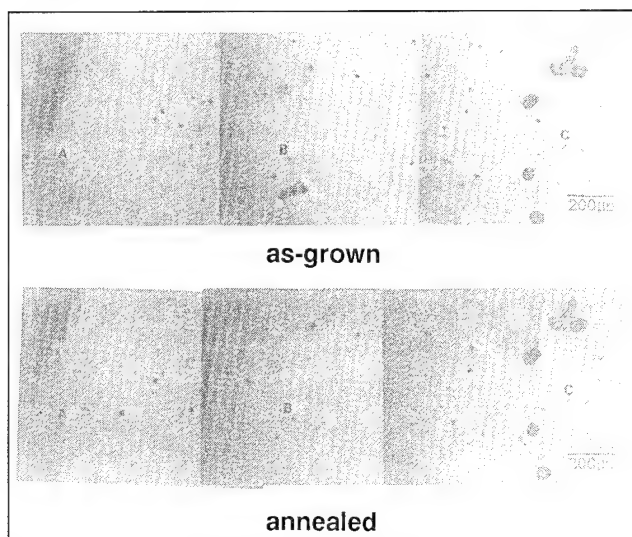
In the case of sample (#2) that showed distinct thermomigration of Te precipitates, the thermomigration velocity is obtained by measuring the distance each Te precipitate thermomigrates in a given annealing period. A plot of the distribution of the computed thermomigration velocity of various Te precipitates looks as a Gaussian behavior (Fig. 5). From this plot, a mean thermomigration velocity of ~50 $\mu\text{m/h}$ is extracted.

Anthony and Cline⁵ have reported the relation of thermomigration velocity and effective diffusion coefficient to be $V = (D^*/C_s)(\partial C/\partial T)_L \nabla T_s$, where the effect of interface kinetics, thermal conductivity, and the Soret effect are incorporated in an approximate effective diffusion coefficient D^* . It is assumed that C_s is the metallic atom concentration of CdZnTe crystal, $(\partial C/\partial T)_L$ the inverse of the slope on liquidus line in the phase diagram of the Cd-Te system, and ∇T_s the thermal gradient in the sample. The effective diffusion coefficient of the metallic (Cd, Zn) atoms in Te precipitate derived from the formula mentioned above is $\sim 3 \times 10^5 \text{ cm}^2/\text{s}$.

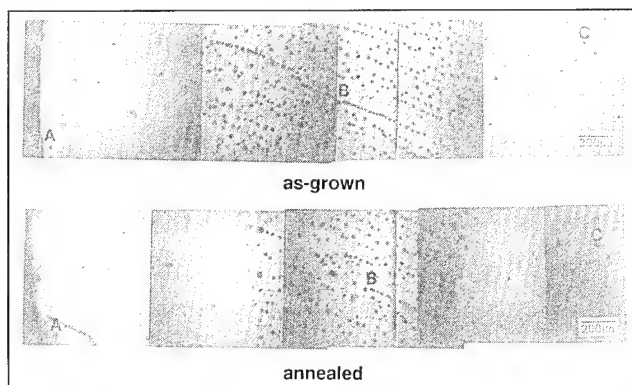
The large values of the thermomigration velocity and the effective diffusion coefficient imply that Te precipitates in CdZnTe substrate most likely migrate into HgCdTe epilayer during a typical LPE growth process, where the growth temperature is around 500°C and the thermal gradient in CdZnTe substrate in the order of 75°C/cm.²

CONCLUSION

The melting point of Te precipitates in CdZnTe crystal, above the temperature of which the thermomigration of Te precipitates becomes active, has been measured by the high temperature x-ray diffraction. The thermomigration of Te precipitates which occurs through thermal gradient annealing above the melting point of Te precipitates has been directly observed by infrared microscopy. The thermomigration velocity and the effective diffusion coefficient have been evaluated from these observations.



a



b

Fig. 4. Infrared micrographs of CdZnTe samples [(a) #1 and (b) #2] before and after annealing (higher temperature at the right hand side of each annealed sample).

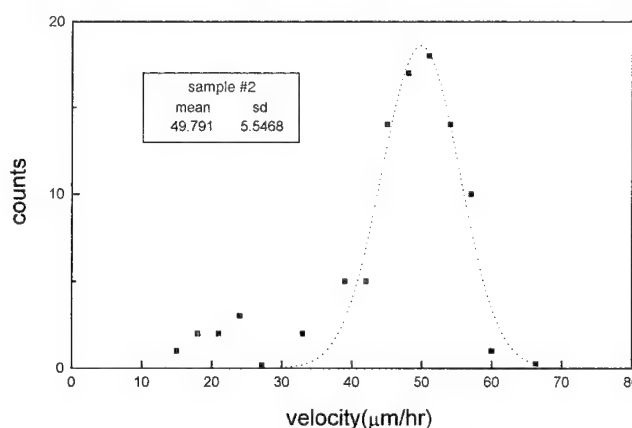


Fig. 5. Gaussian distribution of the thermomigration velocity of Te precipitates in annealed CdZnTe sample #2.

ACKNOWLEDGMENT

The work is partly supported by the SPRC in Chun Buk University and partly by the Basic Science Research Institute Program of the Ministry of Education, 1994.

REFERENCES

1. H.R. Vydyanath, J.A. Ellsworth, J.J. Kennedy, B. Dean, C.J. Johnson, G.T. Neugebauer, J. Sepich and P.K. Liao, *J. Vac. Sci. Technol. B* 10 (4), 1476 (1992).
2. H.R. Vydyanath, J.A. Ellsworth, J.B. Parkinson, J.J. Kennedy, B. Dean, C.J. Johnson, G.T. Neugebauer, J. Sepich and P.K. Liao, *J. Electron. Mater.* 22 (8), 1073 (1993).
3. S.H. Shin, J. Bajaj, L.A. Moudy and D.T. Cheung, *Appl. Phys. Lett.* 43 (1), 68 (1983).
4. P.M. Hansen, *Constitution of Binary Alloy* (New York: McGraw-Hill, 1958), p. 444.
5. T.R. Anthony and H.E. Cline, *J. Appl. Phys.* 43 (5), 2473 (1972).

Vertical Bridgman Techniques to Homogenize Zinc Composition of CdZnTe Substrates

T.S. LEE, S.B. LEE, and J.M. KIM

Agency for Defense Development, Youseong P.O. Box 35, Taejeon, Korea

J.S. KIM and S.H. SUH

Korea Institute of Science and Technology, P.O. Box 131, Cheongryangri, Seoul, Korea

J.H. SONG, I.H. PARK, S.U. KIM, and M.J. PARK

Korea University, Anamdong 5-1, Seongbugku, Seoul, Korea

In order to improve the Zn homogeneity along the axial direction of CdZnTe boule, we have employed a modified Bridgman technique using a (Cd, Zn) alloy source in communication with the melt, whose temperature has been gradually changed from 800 to 840°C during growth. Electron probe microanalysis (EPMA) measurements of Zn composition in the boule shows an excellent homogeneity of Zn along the axis of the CdZnTe boule compared with results in a boule grown by using a fixed source temperature. We have performed a numerical simulation to obtain the approximate temperatures of additional heating and cooling needed to improve the radial Zn homogeneity. CdZnTe boule has been grown by seeded vertical Bridgman furnace with two zones of heater and cooler. Ultraviolet/visible spectroscopic measurements of Zn composition over the length of the boule indicate that the radial distribution of Zn composition is very homogeneous in the body region of the boule, where the radial variation of Zn composition is ± 0.0005 .

Key words: CdZnTe, modified Bridgman technique, numerical simulation, Zn homogeneity

INTRODUCTION

For high density HgCdTe infrared focal plane arrays (IRFPAs), large area and homogeneously lattice-matched substrates of CdZnTe are required. In the case of growing CdZnTe boule by the conventional Bridgman method, however, it is difficult to obtain CdZnTe substrates with both large area and good Zn homogeneity because of two reasons. First, the segregation coefficient of Zn in CdTe is larger than 1 (reportedly 1.16–1.35),^{1,2} that gives rise to an inhomogeneous distribution of Zn along the axial direction in the boule. Second, the shape of the solid/liquid interface during growth, which determines the radial Zn homogeneity in the boule, is difficult to maintain to be nearly flat. In this paper, two tech-

niques are presented to obtain CdZnTe substrates with homogeneous Zn distribution in the lateral direction.

IMPROVEMENT OF AXIAL Zn HOMOGENEITY

In order to improve the axial homogeneity of Zn composition, we have employed a modified Bridgman method, which makes it possible to keep the Zn composition to be constant at the solid/liquid interface during growth. This has been achieved by controlling the temperature of the (Cd, Zn) alloy source, which is in communication with the melt. Figure 1 displays the modified Bridgman furnace system composed of three temperature zones. The upper zone is to control the temperature of (Cd, Zn) alloy source and its vapor pressure, the middle zone is to melt the raw materials of Cd, Zn and Te, and the bottom zone is to

(Received November 1, 1994; revised February 10, 1995)

solidify the melt. The composition of the (Cd, Zn) alloy source and its temperature used in CdZnTe growth by the modified Bridgman technique are $\text{Cd}_{0.96}\text{Zn}_{0.04}$ and 800–840°C, respectively. The growth rate and the thermal gradient at the position of melting point in the furnace have been fixed at 1.8 mm/h and $\sim 10^\circ\text{C}/\text{cm}$, respectively. The CdZnTe samples selected from each of the boules for compositional analysis of Zn via electron probe micro-analysis have been prepared with mirror surface finish.

Figure 2 displays the distribution of Zn along the axis of each boule grown with the conditions summarized in Table I. The distribution of Zn in CdZnTe boule (#1) grown with only Cd source at a constant temperature of 800°C follows the well-known normal freezing curve, from which the segregation coefficient

is calculated to be 1.2 (Fig. 2a). For boule (#2) grown by using (Cd, Zn) alloy source, the temperature of which is fixed at 830°C, the distribution of Zn shows the same tendency as in the boule (#1). As can be inferred from the distribution of Zn in boule (#3) shown in Fig. 2b, however, the axial homogeneity of Zn greatly improves by gradually changing the temperature of (Cd, Zn) alloy source from 800 to 840°C during growth, and the majority of the boule (over 70% in volume fraction) has the Zn composition within 3–4%.

IMPROVEMENT OF RADIAL Zn HOMOGENEITY

It is well known that a flat or slightly convex shape of the solid/liquid interface is necessary to grow a good crystal because the interface shape makes a grain selection possible. In addition, this interface shape improves the radial homogeneity of Zn in CdZnTe boule because the Zn compositional uniformity of the solidified material follows the shape of the interface.

First of all, numerical simulation has been performed by a finite differential method to establish the optimum additional heating and cooling temperatures of the middle and bottom zones (Fig. 1), and to make the solid/liquid interface shape flat, so that a homogeneous distribution of Zn results in the radial direction (Fig. 3). Calculation is made using a two-dimensional axisymmetric model for the boule with both conductive and radiative modes of heat transfer between the furnace wall and the boule. In this calculation, it is neglected the possible convective fluid flow in melt and the thermal effect of the ampoule containing the charge. The boule diameter used is 30 mm and its length 120 mm. The system is considered to be quasi-steady state, i.e., transients are neglected.

Based on the results obtained from the simulation, the temperatures of heater and cooler have been controlled during growth of CdZnTe boule. CdTe crystal has been used as seed for the CdZnTe to grow in the boule with axis of {111}, and it has been found that the axis of the grown boule is oriented $\sim 8^\circ$ off

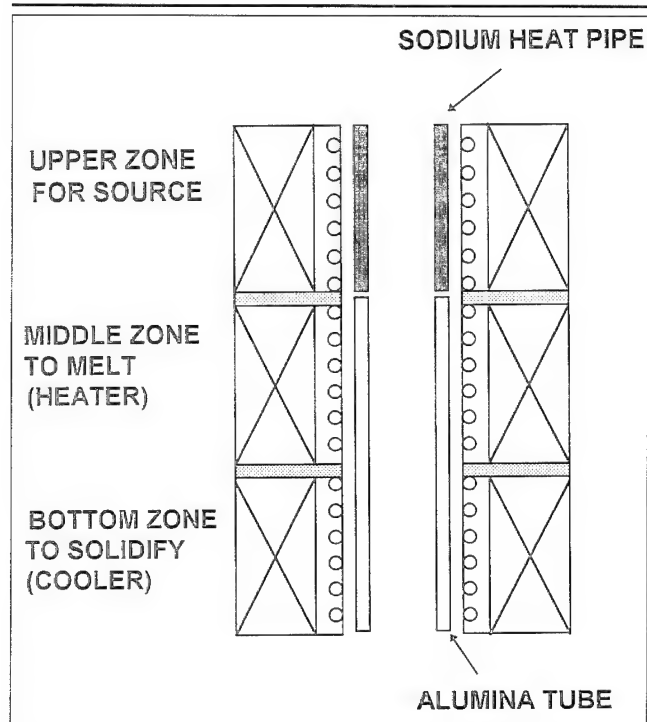


Fig. 1. Schematic diagram of modified Bridgman furnace system.

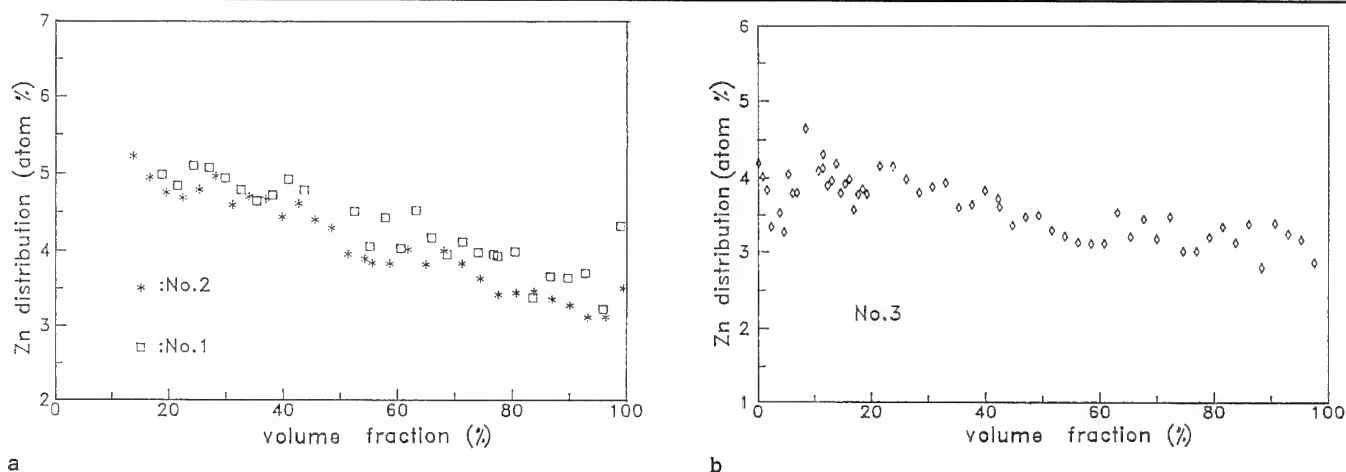


Fig. 2. Distribution of Zn composition vs volume fraction solidified in CdZnTe boule grown with the source temperature (a) at 800°C (\square : only Cd source) and at 830°C ($*$: Cd, Zn source), and (b) gradually changed from 800 to 840°C (\diamond : Cd, Zn source).

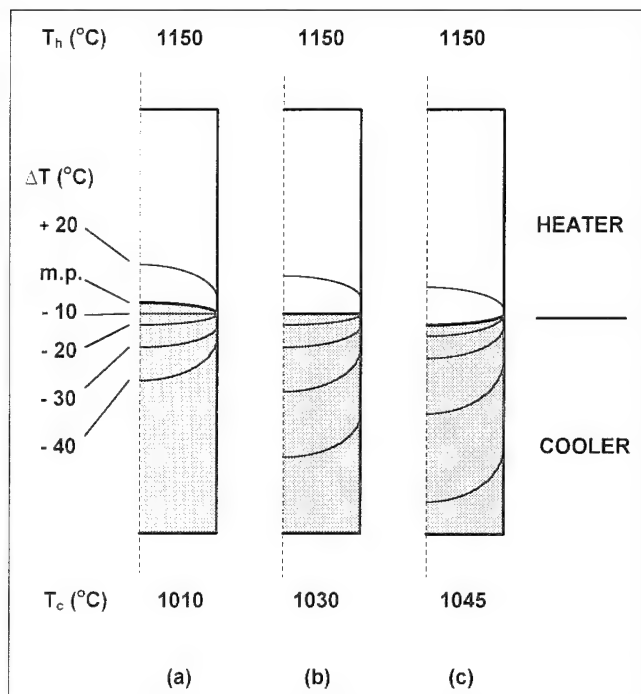


Fig. 3. Solid/liquid interface shape vs cooler temperature at (a) 1010, (b) 1030, and (c) 1045°C.

{111}, using the Laue back reflection x-ray technique. The diameter and the length of the boule are 30 and 120 mm, respectively. The boule is cut perpendicularly to its axis in order to obtain the circular slices with 1 mm thickness, and the wafers with mirror-like surfaces are prepared through polishing. From the cut-on wavelengths measured with ultraviolet/visible spectrometer, the cut-on energies are calculated along the lateral direction of CdZnTe wafers.

The map of Zn composition over the boule is obtained using the relation between Zn composition and cut-on energy.³ The map of Zn composition of CdZnTe boule makes it possible to obtain the contour of Zn composition, in other words, the iso-composition line of Zn shown in Fig. 4. The map indicates that the shoulder region of boule grown at the first stage has a shape of "W" (the shape is convex at center and concave near wall). At the middle stage, however, the concave shape disappears and the interface shape is getting more flat. As a result, the body region (~50% in volume fraction) of the boule has good homogeneity of Zn composition in the radial direction within ± 0.0005 in composition. At the final stage of growth, the interface shape is gradually changed into a concave shape, which is supposed to lead to a few grains in the tail region of the boule.

CONCLUSION

It is found that the axial homogeneity of Zn composition can be improved by the modified Bridgman technique by gradually changing the temperature of a (Cd, Zn) alloy source in communication with the melt. In order to improve the radial homogeneity of Zn within ± 0.0005 in composition, a two-zone furnace with heater and cooler is used and their temperatures

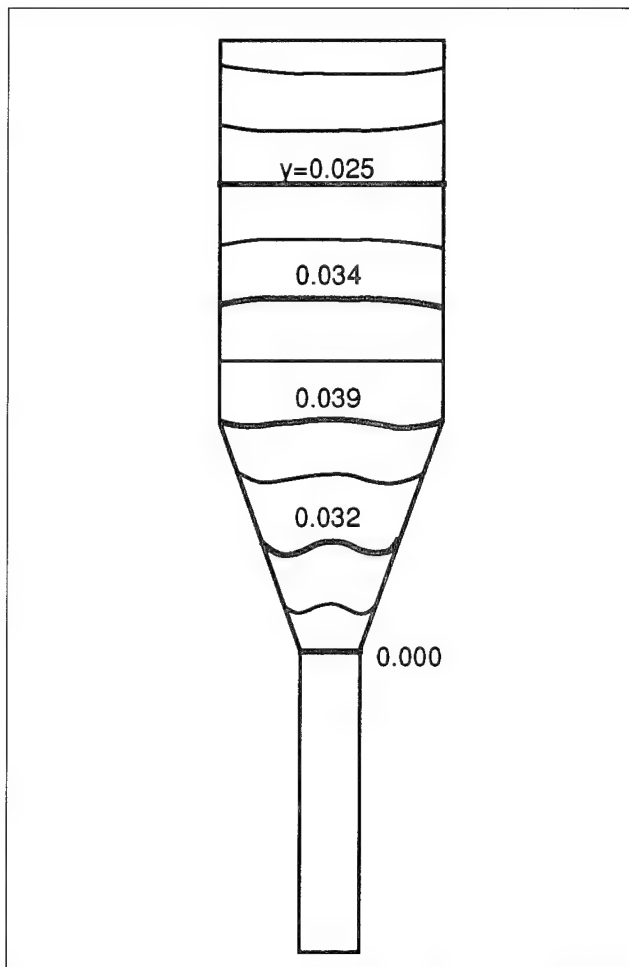


Fig. 4. Contour map of Zn composition in $\text{Cd}_{1-y}\text{Zn}_y\text{Te}$ boule.

are based on those obtained by numerical simulation, which makes the shape of solid/liquid interface flat or slightly convex. As a result, the body region of the grown CdZnTe boule shows a good homogeneity of Zn composition.

The results from the growth experiments indicate that a good homogeneity of Zn composition can be obtained over the majority of CdZnTe boule, making it possible to obtain large area CdZnTe substrates with homogeneous lattice-matching to HgCdTe epilayers grown on them, thus making it possible to eventually improve the yield of high density arrays.

ACKNOWLEDGMENT

The work is partly supported by the SPRC in Chun Buk University and partly by the Basic Science Research Institute Program of the Ministry of Education, 1994.

REFERENCES

1. J. Steininger, A.J. Strauss and R.F. Brebrick, *J. Electrochem. Soc.* 117, 1305 (1970).
2. A. Tanaka, Y. Masa, S. Seto and T. Kawasaki, *J. Cryst. Growth* 94, 166 (1989).
3. S.M. Johnson, S. Sen, W.H. Konkel and M.H. Kalisher, *J. Vac. Sci Technol. B* 9 (3), 1897 (1991).

Assessment of the Purity of Cadmium and Tellurium as Components of the CdTe-Based Substrates

R. TRIBOULET, A. AOUDIA, and A. LUSSON

CNRS, Laboratoire de Physique des Solides de Bellevue, 1, Place Aristide Briand, F 92195 MEUDON Cedex, France

In order to assess the purity of their Cd and Te components, CdTe crystals have been grown by Bridgman using commercial batches of elements of purity ranging from 5N to 6N⁺. The assessment has been achieved through the classical optical and electrical techniques that solid state physics offers, on as-grown and annealed crystals. Some contamination by residual acceptors like Cu, Li, and P is shown to occur during the high temperature growth, mainly if uncoated silica tubes are used, as is emphasized within a comparison between the electrical and optical properties of crystals grown by melt-growth or at lower temperature by solution-growth.

Key words: Bridgman growth, CdTe, impurity incorporation

INTRODUCTION

Impurities in HgCdTe (MCT) can affect material properties such as carrier concentration, mobility and minority carrier lifetime, and impact photodetector performance. The influence of the substrate purity on the electrical properties of epitaxial layers has been stressed in the case of the growth of MCT on commercially available CdTe and CdZnTe substrates by molecular beam epitaxy^{1,2}, organometallic vapor phase epitaxy³ and liquid phase epitaxy.⁴ Impurities have been shown to out-diffuse from the substrate into the layer even at a MBE growth temperature as low as 200°C.¹ It is then of prime importance to estimate the real impact of the purity of the Cd and Te components on the CdTe substrate properties and to try to answer such questions as: How to assess the purity of the elements to be used as substrate components? What purity level for the elements to be used? What is the influence of the growth process on the purity of the crystals? Not only the initial purity of the elements,

but also the technological parameters used at the different steps of the growth process (silica tube, chemical etching, sealing, furnace, growth method) have indeed to be taken into account.

Chemical analysis of Cd and Te by such techniques as glow discharge mass spectrometry (GDMS), spark source mass spectrometry (SSMS), Zeeman corrected graphite furnace atomic absorption (ZCGFAA), flameless atomic absorption spectrometry (FAAS), secondary ion mass spectrometry (SIMS), resonance ionization spectroscopy (RIS), or other methods, is complex and costly, taking much time to cover the whole spectrum of sensitive impurities. Generally, several techniques have to be used in parallel. The results are often disappointing and can be contradictory.

Solid state physics offers a unique means to estimate the purity of the crystals, at a detection level quite lower than chemical analysis does, and precisely for the electrically active impurities to consider for their detrimental behavior in MCT.

Within a comparison between several batches of Cd and Te originating from different companies, classi-

(Received October 4, 1994; revised December 5, 1994)

Table I. Results of Electrical Measurements on CdTe Crystals Grown by Bridgman and THM Using Different Cd and Te Batches

Name	Growth Tech.	Starting Elements Purity, Batch No.	Growth Cond.	N_D (cm ⁻³)	N_A (cm ⁻³)	N_A/N_D	μ_{300K} cm ² /Vs	μ_{max} cm ² /Vs	E_D meV
ER607	THM	6N Cd and Te	$T_G = 780^\circ\text{C}$	1×10^{15}	9.4×10^{14}	0.88	880	21000 (24K)	8.17
0-607-A		6N Te solvent							
CTHM3	THM	CdTe VZM	$T_G = 750^\circ\text{C}$	2.7×10^{14}	9×10^{13}	0.333	1050	20000 (30K)	11
		6N ⁺ Te solvent							
CTHM28	MTHM	CdTe VZM	$T_G = 750^\circ\text{C}$	2.5×10^{14}	1.8×10^{14}	0.72	1130	45500 (30K)	10
		6N ⁺ Te solvent							
CTHM59	CTHM	Cd 6N Te 5N	$T_G = 780^\circ\text{C}$	3.4×10^{14}	1.5×10^{13}	0.04	840	41380 (28K)	15
		6N ⁺ Te solvent							
CTHM54	THM	6N CdTe	$T_G = 1000^\circ\text{C}$	4.85×10^{14}	8.5×10^{13}	0.175	825	13000 (40K)	12
		6N ⁺ Cd solvent							
CT64E1	Bridgman	6N ⁺ -batch 1	GCS	1.75×10^{15}	1.64×10^{15}	0.93	800	12500 (35K)	9.4
CT64E2				2.61×10^{15}	1.65×10^{15}	0.77	800	10000 (39K)	9
CT65	Bridgman	idem CT64	GCC	2.16×10^{15}	9.57×10^{14}	0.44	990	15820 (40K)	9.2
CT69A	Bridgman	idem CT64	GCC	2.25×10^{15}	1.45×10^{15}	0.64	945	16070 (35K)	8.8
CT69B				Highly resistive					
CT72	Bridgman	idem CT64	uncoated silica	Highly resistive					
CT66	Bridgman	6N ⁺ -batch 2	GCS	3×10^{15}	2×10^{15}	0.67	800	23100 (35K)	8
CT67	Bridgman	6N ⁺ -batch 3	GCS	3.35×10^{15}	2.34×10^{15}	0.72	730	13250 (35K)	7.2
CT68	Bridgman	6N ⁺ -batch 4	GCS	2.18×10^{15}	1.08×10^{15}	0.5	770	13650 (35K)	9.3
CT70	Bridgman	6N ⁺ -batch 5	GCS	8.11×10^{14}	4.41×10^{14}	0.54	753	21000 (41K)	11.6
CT71	Bridgman	6N-batch 6	GCS	2.8×10^{15}	2.6×10^{15}	0.94	670	7600 (30K)	7.4
CT73	Bridgman	5N-batch 7	GCS	8.1×10^{15}	8×10^{15}	0.987	323	6707 (31K)	7

Note: MTHM = multipass THM; CTHM = cold THM; VZM = vertical zone melting; T_G = growth temperature. All THM experiments using graphite coated silica. GCS = graphite coated silica; GCC = glassy carbon crucible.

cal electrical measurements (Hall effect and conductivity) performed on annealed CdTe crystals will be shown to be an efficient way to assess the purity of their components, with a further significant advantage of evaluating precisely the purity of the final material used. Following the global estimation of the electrically active residual impurities by electrical measurements, the main acceptor impurities were identified by photoluminescence.

EXPERIMENTAL PROCEDURES

Using batches of cadmium and tellurium of commercial purity 5N, 6N, and 6N⁺, originating from seven different companies, 15 mm diameter CdTe ingots have been grown in a three-zone furnace by the vertical Bridgman technique under controlled Cd vapor pressure⁵ using a single procedure. The 6N⁺ batches we used (batch 1 to 5) cover different high purity products of grades presented commercially by the suppliers as 6N⁺, 6N5, 6N DZR, 6N QZR, 7N⁺, 6N52, and 6N5⁺. The same batch of silica tubes (GE 214) has been used for all the growth experiments. The tubes have been chemically cleaned and backed out at high temperature under the same conditions. The chemical etching of the elements was achieved according to the same process. The same thermal conditions and the same growth rate were used for all

growth experiments. Different environmental conditions have been used for a given 6N⁺ batch (graphite coated silica tubes, uncoated tubes, glassy carbon crucibles) while the comparison between the different batches has been achieved using classical graphite coated silica tubes.

Test samples have been selected from two centimeters from the first-part-to-freeze of every ingot, in order to account for the segregation effects, except for one sample (CT69B) cut from the tail of an ingot (CT69).

The samples dedicated to the electrical measurements have been annealed under saturated Cd vapor pressure at 700°C for 3 h, according to the same protocol for each sample, followed by water quenching. The annealing step is essential for the impurities to out-diffuse from precipitates at which they are included⁶ and to reveal the actual purity of the crystals. Furthermore, it makes the impurities electrically active and allows the conductivity type of the samples to be generally converted from p- to n-type, when achieved under Cd-rich conditions. 700°C, 3 h Cd-saturated annealing has been found adequate to remove Te precipitates. The quenching step has been shown essential to prevent Te precipitation and impurity re-association leading to compensation effects.⁷

The annealed test-samples were then submitted to

electrical measurements, while as-grown and annealed samples were submitted to optical measurements. The electrical properties of the Bridgman samples have been compared to those of some traveling heater method (THM) samples grown according to various THM conditions: classical THM, multipass THM,⁸ and cold THM⁹ using tellurium as the solvent and THM using Cd as the solvent.¹⁰

RESULTS AND DISCUSSION

The results of electrical measurements are gathered in Table I, in which are displayed the names of the ingots; the growth technique used; the purity of the starting elements and the batch number; the growth conditions including growth temperature for THM (all the THM growths were performed in graphite coated silica tubes) and crucible nature for Bridgman; the concentration of electrically active donors and acceptors, respectively N_D and N_A ; the compensation ratio, N_A/N_D ; the room temperature mobility, μ_{300K} ; the maximum mobility at low temperature, μ_{max} , with mention of the low temperature at which mobility peaks; and the ionization energy of donors, E_D .

A typical photoluminescence spectrum measured at liquid helium temperature on an as-grown 6N⁺ sample is pictured in Fig. 1. It displays a dominant A^0X emission, constituted by a majority line at 1.5896 eV, generally identified as the radiative annihilation of excitons bound to neutral substitutional copper Cu_{Cd} ,^{11,12} and two weaker excitonic A^0X lines on its low energy side, at 1.5893 and 1.5889 eV, respectively, attributed to Li_{Cd} and P_{Cd} . At higher energy, a weak D^0X emission, corresponding to the radiative annihilation of excitons on neutral shallow donors, can be seen. It is composed of a dominant line at 1.5928 eV surrounded by weaker lines corresponding to the donors excited states. At lower energy, only two or three very weak DAP bands, generally attributed to residual Li and Na, are visible near 1.53–1.55 eV. No emissions are found in the 1.42 eV region. The spectra of the 5N and 6N samples are similar. The Li A^0X line has been found to dominate over the P and Cu A^0X lines in the spectrum of the THM sample ER607, probably as the result of a segregation coefficient of Cu being smaller than for lithium in the liquid tellurium used as the solvent for the THM growth.¹³

A typical photoluminescence spectrum measured at liquid helium temperature for an annealed 6N⁺ sample is pictured in Fig. 2. It shows qualitatively the same features as for the as-grown samples, but the intensity of D^0X increases, except for the samples from the ingot grown in uncoated silica and in the tail of CT69 for which D^0X remains extremely weak. D^0X even dominates the spectrum of THM sample ER607. As a result of the increase of the intensity of the D^0X line, the intensity of the main A^0X line generally decreases after annealing, except for the samples from the ingot grown in uncoated silica and in the tail of CT69 for which A^0X increases. At lower energy, the trend is also, for all samples, a decrease in intensity of

the deeper DAP bands located around 1.55 eV. The spectra measured on the annealed 5N and 6N samples are qualitatively similar, with a very weak D^0X emission which becomes extremely weak in the crystal grown in an uncoated silica tube (CT72) as well as in those cut from the tail of a 6N⁺ ingot (CT69). Note that the intensity ratios I_{A^0X/D^0X} of as-grown and annealed samples are more to be taken into account than the absolute values of the intensities within a comparison.

In Table II are displayed the emission intensity, in arbitrary units, of the main excitonic A^0X and D^0X lines of the photoluminescence spectra measured at liquid helium temperature, and the ratio of their intensities for both annealed and as-grown samples. For the annealed samples, this ratio is found to follow very roughly the compensation ratio N_A/N_D determined from the electrical measurements.

For the crystals grown using the same batch of Cd and Te (batch 1) and different environmental conditions, the annealing was not able to convert to n-type the conductivity of the crystals either grown in un-

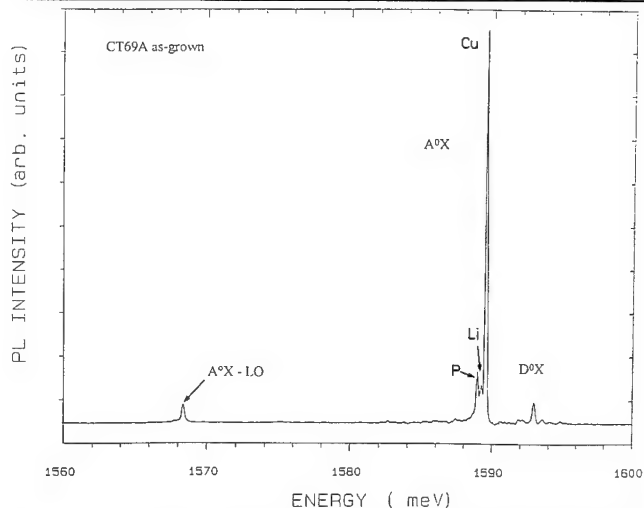


Fig. 1. Typical photoluminescence spectrum measured at 4K of an as-grown Bridgman sample.

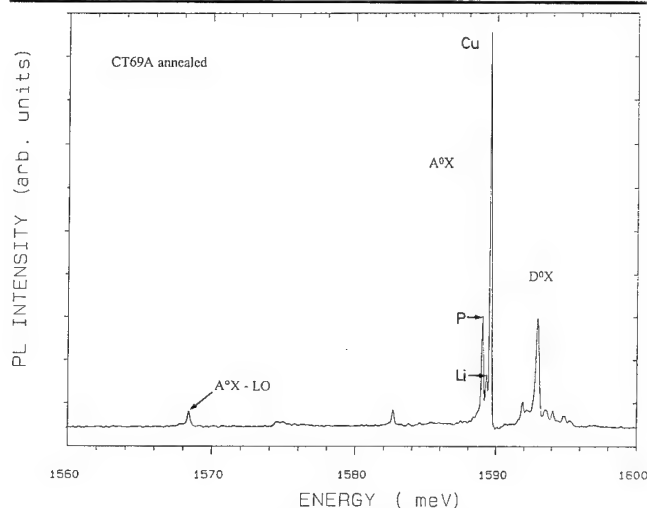


Fig. 2. Typical photoluminescence spectrum measured at 4K of an annealed Bridgman sample.

Table II. Emission Intensity, in Arbitrary Units, of the Main Excitonic Lines A⁰X and D⁰X of the Photoluminescence Spectra Measured at Liquid Helium Temperature

Name	Growth Tech.	Starting Elements Purity, Batch No.	Growth Cond.	N _A /N _D	I _{A⁰X} As-Grown	I _{D⁰X} As-Grown	I _{A⁰X} / I _{D⁰X} As-Grown	I _{A⁰X} An-nealed	I _{D⁰X} An-nealed	I _{A⁰X} / I _{D⁰X} An-nealed
ER607	THM	6N Cd and Te	T _G = 780°C	0.88	4200	280	15	1160	1940	0.6
0-607-A		6N Te solvent								
CT64E1	Bridgman	6N ⁺ -batch 1	GCS*	0.93	11500	150	76	5960	400	15
CT64E2				0.77						
CT65	Bridgman	idem CT64	GCC*	0.44	14300	290	50	830	210	3.9
CT69A	Bridgman	idem CT64	GCC	0.64	9800	650	15	3970	1070	3.7
CT69B					1710	17	100	7600	76	100
CT72	Bridgman	idem CT64	uncoated silica		1270	17	75	1630	30	54
CT66	Bridgman	6N ⁺ -batch 2	GCS	0.67	8800	410	20	4470	690	6.5
CT67	Bridgman	6N ⁺ -batch 3	GCS	0.72	17700	530	33	3470	650	5.3
CT68	Bridgman	6N ⁺ -batch 4	GCS	0.5	20900	840	25	9930	1270	7.9
CT70	Bridgman	6N ⁺ -batch 5	GCS	0.54	9700	130	75	2070	280	7.4
CT71	Bridgman	6N-batch 6	GCS	0.94	17000	340	50	9370	380	24.7
CT73	Bridgman	5N-batch 7	GCS	0.987	2690	70	38	2250	105	21

*GCS = graphite coated silica; GCC = glassy carbon crucible.

coated silica (CT72) or cut from the tail of the ingot (CT69B), as a result of the contamination by acceptors from the silica, for CT72, and of the segregation of acceptors, mainly copper, toward the tail of the ingots, for CT69B. The compensation ratio determined by photoluminescence from the intensity ratio I_{A^0X}/I_{D^0X} remained unchanged before and after annealing. The crystals grown in glassy carbon crucibles show the highest room and low temperature mobilities, as a result of a lower contamination than for those grown in graphite coated or uncoated silica tubes.

Crystals grown in graphite coated silica tubes using different 6N⁺ batches present rather uniform characteristics, with N_D and N_A lying respectively in the ranges 8×10^{14} – 3×10^{15} cm⁻³ and 4×10^{14} – 2×10^{15} cm⁻³ (a factor 4 between minimum and maximum values for both N_A and N_D), with μ_{300K} about 800 cm²/Vs and μ_{max} in the range 10,000–23,000 cm²/Vs. These N_D and N_A values are roughly in agreement with what could be expected for a 6N⁺ purity. The compensation ratio, as determined from I_{A^0X}/I_{D^0X} , is reduced by a factor 3 to 10 after annealing.

The values of N_D and N_A of the crystals grown using 6N elements are very close to those of the 6N⁺ crystals, but are roughly one order of magnitude higher for the "5N" crystals, as expected. The "5N" and "6N" crystals present lower mobilities and a high compensation ratio decreasing only by a factor 2 after annealing, compared to 3 to 10 for the 6N⁺ crystals, as measured from photoluminescence experiments.

By comparison, the crystals grown by THM according to different processes and experimental conditions (except ER607 grown using 6N elements) are shown to present acceptor and donor concentrations, respectively, one order and one to two orders of magnitude lower than the Bridgman ones, as a result of some contamination occurring during the high temperature Bridgman process from, or through, the

silica tubes.

Note that some very rough correlation appears between the compensation state of the crystals and their mobilities. The lower the compensation, the higher the mobilities are. As an example, the 5N sample, with a compensation ratio of ~0.99 presents the lowest room temperature mobility, 323 cm²/Vs, followed by the 6N sample, with a compensation ratio of 0.94 and a room temperature mobility of 670 cm²/Vs.

Note also, that the ionization energies of the donors are all the higher since the compensation is low, as expected from the classical theories of screening of the wave functions of electrons by residual acceptors.

Another observation is that, among all the ingots grown under the same conditions, only the ingot grown in uncoated silica was fully a single crystal. A similar observation has been recently reported by Shetty,¹⁴ who was nevertheless not able to remove such ingots from the uncoated tubes because of a severe sticking on the silica walls together with a great fragility of the material. In our case, the ingot was easily removed, either because of less oxide in the starting elements or because of some difference in the silica tubes. Some computer simulation has been engaged to identify the reasons of this unexpected single crystal growth.

CONCLUSIONS

Owing to the extremely high sensitivity of "solid state physics" measurements to the electrically active residual impurities, some contamination at the 6N⁺ level has been found to occur during the Bridgman growth of CdTe, mainly from acceptors that have been identified from photoluminescence experiments to be mainly copper. Lithium and phosphorous were also found in some cases at a lower level. The contamination is higher toward the tails of the ingots and can be

dramatically high when growth occurs in uncoated silica tubes, clearly indicating silica as the main source of contamination. Contamination can be reduced with graphite coating or by using pure crucibles loaded in the ampoules, or also by using ampoules of larger diameter. When larger diameter ampoules are used, the ratio between the internal "exchange" surface of the tubes and the volume of the ingots decreases. The contamination, occurring as a result of a high temperature melt-growth process such as the Bridgman one, becomes a significant vehicle for impurities when using very pure elements, as is emphasized by the comparison between the electrical and optical characteristics of CdTe crystals grown either at high temperature, or at low temperature by cold traveling heater method and by classical THM.

REFERENCES

1. J.P. Faurie, R. Sporken, Y.P. Chen, M.D. Lange and S. Sivananthan, *Mater. Sci. Eng. B* 16, 51 (1993).
2. T.H. Myers, K.A. Harris, R.W. Yanka, L.M. Mohnkern, R.J. Williams and G.K. Dudoff, *J. Vac. Sci. Technol. B* 10, 1438 (1992).
3. R. Korenstein, R. Olson, D. Lee, P.K. Liao and C.A. Castro, *J. Electron. Mater.*, to be published.
4. A.B. Bollong, G.B. Feldewerth, J.P. Tower, S.P. Tobin, M. Kestigian, P.W. Norton, H.F. Schaake, C.K. Ard, *J. Electron. Mater.*, to be published.
5. R. Triboulet and Y. Marfaing, *J. Electrochem. Soc.* 120, 1260 (1973).
6. J.L. Pautrat, J.M. Francou, N. Magnea, E. Molva and K. Saminadayar, *J. Cryst. Growth* 72, 194 (1985).
7. R. Triboulet, A. Durand, P. Gall, J. Bonnafé, J.P. Fillard and S.K. Krawczyk, *J. Cryst. Growth* 117, 227 (1992).
8. R. Triboulet and Y. Marfaing, *J. Cryst. Growth* 51, 89 (1981).
9. R. Triboulet, Khoan Pham Van and G. Didier, *J. Cryst. Growth* 101, 216 (1990).
10. R. Triboulet, R. Legros, A. Heurtel, B. Sieber, G. Didier and D. Imhoff, *J. Cryst. Growth* 72, 90 (1985).
11. E. Molva, J.P. Chamonand J.L. Pautrat, *Phys. Stat. Sol. (B)* 109, 635 (1982).
12. J.P. Laurenti, G. Bastide, M. Rouzeyre and R. Triboulet, *Solid State Comm.* 67, 1127 (1988).
13. K. Zanio, *Semiconductors and Semimetals, Cadmium Telluride*, Vol. 13, ed R.K. Willardson and A.C. Beer (New York: Academic Press, 1978).
14. R. Shetty, Ph.D. thesis, Clarkson University (1993).

Molecular Beam Epitaxial HgCdTe Material Characteristics and Device Performance: Reproducibility Status

J. BAJAJ, J.M. ARIAS, M. ZANDIAN, J.G. PASKO, L.J. KOZLOWSKI,
R.E. DE WAMES, and W.E. TENNANT

Rockwell International Science Center, Thousand Oaks, CA 91360

Extensive material, device, and focal plane array (FPA) reproducibility data are presented to demonstrate significant advances made in the molecular beam epitaxial (MBE) HgCdTe technology. Excellent control of the composition, growth rate, layer thickness, doping concentration, dislocation density, and transport characteristics has been demonstrated. A change in the bandgap is readily achieved by adjusting the beam fluxes, demonstrating the flexibility of MBE in responding to the needs of infrared detection applications in various spectral bands. High performance of photodiodes fabricated on MBE HgCdTe layers reflects on the overall quality of the grown material. The photodiodes were planar p-on-n junctions fabricated by As ion-implantation into indium doped, n-type, in situ grown double layer heterostructures. At 77K, diodes fabricated on MBE $\text{Hg}_{1-x}\text{Cd}_x\text{Te}$ with $x \approx 0.30$ ($\lambda_{\text{co}} \approx 5.6 \mu\text{m}$), $x \approx 0.26$ ($\lambda_{\text{co}} \approx 7 \mu\text{m}$), $x \approx 0.23$ ($\lambda_{\text{co}} \approx 10 \mu\text{m}$) show R_0A products in excess of $1 \times 10^6 \text{ ohm-cm}^2$, $7 \times 10^5 \text{ ohm-cm}^2$, and $3 \times 10^2 \text{ ohm-cm}^2$, respectively. These devices also show high quantum efficiency. As a means to assess the uniformity of the MBE HgCdTe material, two-dimensional 64×64 and 128×128 mosaic detector arrays were hybridized to Si multiplexers. These focal plane arrays show an operability as high as 97% at 77K for the $x \approx 0.23$ spectral band and 93% at 77K for the $x \approx 0.26$ spectral band. The operability is limited partly by the density of void-type defects that are present in the MBE grown layers and are easily identified under an optical microscope.

Key words: Double layer heterostructures, focal plane array (FPA), HgCdTe, molecular beam epitaxy (MBE), p-n photodiodes

INTRODUCTION

Current and future infrared imaging applications require producible, high performance photovoltaic HgCdTe focal plane arrays (FPAs) operating in the short wavelength (SWIR; 1–3 μm), middle wavelength (MWIR; 3–5 μm), middle-long wavelength (MLWIR; 6–8 μm), long wavelength (LWIR; 8–14 μm) and very-long wavelength (VLWIR; 14–30 μm) infrared regions. A common technological approach that allows flexible manufacturing of all or most HgCdTe IR imaging FPAs is therefore desirable. One such approach being pursued is to develop molecular beam epitaxy (MBE) HgCdTe growth technology for the fabrication of planar p-on-n heterostructure photodiode arrays.

The MBE technology offers flexibility in band gap control, in situ monitoring, simplicity of the process, and adaptability to automation. These attributes are being exploited to improve the manufacturability of conventional HgCdTe FPAs and to develop advanced HgCdTe devices.¹ The MBE growth technology is well suited for in situ multilayer growth for the fabrication of high quality buried planar heterostructure devices. The postulated advantage of a buried planar heterostructure device technology is that it makes the ex situ passivation step less critical compared to the conventional mesa technology because the junction interface is buried.² Indeed, MBE has yielded high performance p-on-n buried planar heterostructure diodes and infrared focal plane arrays (IRFPAs).³ Fabrication of high performance photodiodes and FPAs for infrared detection in the SWIR, MWIR, MLWIR, and LWIR spectral bands, operating under

(Received November 1, 1994; revised April 17, 1995)

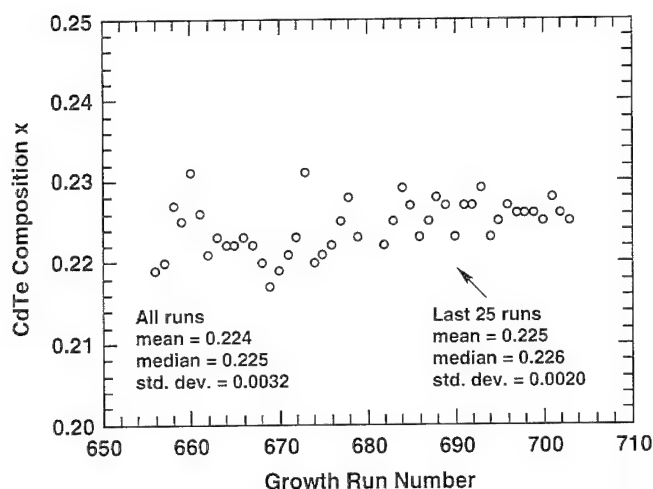


Fig. 1. Reproducibility in composition 'x' of sequentially grown MBE LWIR $\text{Hg}_{1-x}\text{Cd}_x\text{Te}$ epilayers.

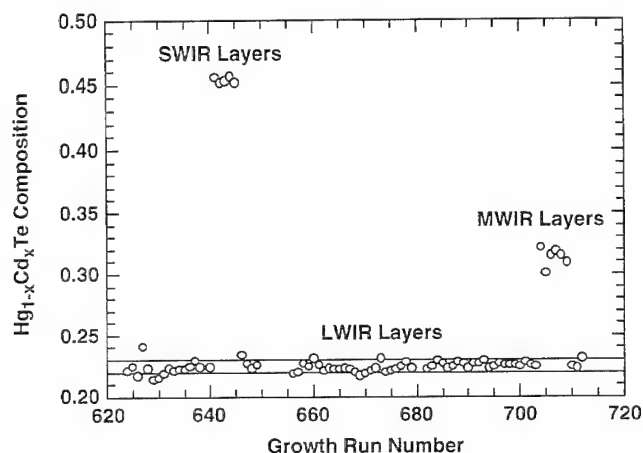


Fig. 2. Cd composition x for a series of SWIR, MWIR, and LWIR HgCdTe MBE layers grown sequentially to demonstrate the composition control flexibility inherent to MBE technology.

high and low background conditions, attests to the flexibility of MBE technology to fulfill the needs of infrared detection applications over a broad spectral range.

The focus of this paper is to demonstrate control of MBE HgCdTe growth conditions, leading to reproducibility of desired materials characteristics and device performance parameters. Extensive material, device, and focal plane array reproducibility data are presented to demonstrate significant advances made in the MBE HgCdTe technology.

MATERIALS GROWTH AND CHARACTERISTICS

All HgCdTe layers were grown in a commercially available MBE system manufactured by Riber (2300 R&D model). All layers were grown directly on near lattice matched (211)B-oriented CdZnTe substrates, purchased from Nimic, Inc. The (211) surface orientation was chosen as it has been demonstrated to yield smooth morphology and high performance photodiodes.^{4,5} The samples were grown at low temperature (185–190°C) to provide epitaxial quality interfaces.

The surface temperature was monitored by an infrared pyrometer. The growth was carried out using effusive sources that contained Hg , Te_2 , and CdTe . The band gap was controlled by the CdTe source temperature, while maintaining the Hg and Te fluxes constant. The beam fluxes (beam equivalent pressure) for Hg and Te_2 sources were 7×10^{-5} Torr and 1×10^{-6} Torr, respectively. The CdTe flux was in the 10^{-7} Torr range and varied depending on the Cd (x) concentration of the $\text{Hg}_{1-x}\text{Cd}_x\text{Te}$ grown epilayer. These fluxes were measured with a nude ion gauge in the growth position and corrected for atomic and molecular weight and ionization efficiency. Under these conditions, growth rates are in the range of 3–4 $\mu\text{m/h}$. The optimum Hg/Te_2 flux ratio necessary to maintain monocrystalline HgCdTe growth was determined by using in situ reflection high-energy electron diffraction (RHEED) analysis.

The in situ grown double layer structure consisted of an indium-doped active narrow bandgap "base" layer and a wider bandgap "cap" layer. This double layer was terminated with a thin (500Å) CdTe layer for surface protection. The choice of this structure was dictated by the device design described in the next section. The n-type base HgCdTe layers were typically 7–10 μm thick and doped with indium at a level of $1\text{--}3 \times 10^{15} \text{ cm}^{-3}$, while the wider band gap cap layer was typically 0.5 μm thick and not intentionally doped.

The characteristics which directly affect the performance of devices fabricated on these materials are the Cd composition x and hence the bandgap, layer thickness, transport characteristics (electron concentration and mobility) of the In-doped base layer, dislocation density, and macroscopic defect density. A statistical database for these properties for LWIR HgCdTe epilayers was generated to assess the reproducibility and control.

Figure 1 shows run-to-run reproducibility of the Cd composition " x " for several consecutively grown LWIR HgCdTe layers. The composition of the epilayers was determined from the room-temperature Fourier transform infrared (FTIR) transmission spectra measured at the center of $2 \times 3 \text{ cm}$ wafers. An average x value of 0.224 was obtained, with a standard deviation of 0.0032. More importantly, the standard deviation for the last 25 layers is 0.002. Spatial uniformity of composition was measured for several wafers. For a typical $2 \times 3 \text{ cm}$ sample, the ratio of the standard deviation to the mean value was measured at $0.002/0.22 = 0.009$.

An important attribute of MBE growth technology is its ability to modify the band gap from run to run. This is illustrated in Fig. 2, where series of LWIR, SWIR, and MWIR layers were sequentially grown to demonstrate the composition control flexibility inherent in this technology.

Run-to-run control of layer thickness is illustrated in Fig. 3. As seen in Fig. 3, the thickness control in MBE growth is excellent. The mean and median thickness values were measured at 8.29 and 8.3 μm ,

respectively. The ratio of the standard deviation to the mean value was calculated to be 0.06.

Control of the n-type doping of the base layer was verified for a set of 45 consecutive growth runs aimed at obtaining a donor concentration ($N_D - N_A$) in the range of $1.5 \times 10^{15} \text{ cm}^{-3}$ to $4 \times 10^{15} \text{ cm}^{-3}$. Hall effect measurements were performed at 2 KG on epilayers subjected to a standard annealing process, carried out under saturated Hg conditions at 250°C for 24 h, to annihilate the Hg-vacancies introduced during growth. The results illustrated in Fig. 4 yielded a mean $N_D - N_A$ value of $2.7 \times 10^{15} \text{ cm}^{-3}$ with a standard deviation to mean value ratio of 0.3. Figure 5 shows 77K electron Hall mobility for the same samples. A mean electron mobility value of $8.3 \times 10^4 \text{ cm}^2/\text{V-s}$ with a standard deviation to mean value ratio of 0.2 was obtained.

Dislocation density (EPD) of the epilayers was measured because it is well-known to be important to the performance of LWIR photodiodes.⁶ The EPD values were obtained using the $\text{HNO}_3/\text{K}_2\text{Cr}_2\text{O}_7/\text{HCl}/\text{H}_2\text{O}$ chemical solution to develop the pits.⁷ Typical EPD values for MBE epilayers grown under opti-

mized conditions are in the 10^4 – 10^6 cm^{-2} range. Figure 6 shows EPD values obtained for successively grown layers. A median EPD value of $2 \times 10^5 \text{ cm}^{-2}$ was determined from these runs. A standard deviation to mean value ratio of 2.9 was obtained. From a device processing standpoint, required EPD values are lower than $5 \times 10^5 \text{ cm}^{-2}$. As can be seen in the figure, 76% of the layers meet this criterion. Even though the variations of EPD reported here are comparable to those values obtained with liquid phase epitaxially (LPE) grown material,⁸ further studies are needed to understand and reduce the sources responsible for the observed variations.

The presence of growth-induced void defects has been reported to be detrimental to HgCdTe photovoltaic devices.⁹ Reducing the concentration of these killer defects in the MBE epilayers is important to improve focal plane array operability.¹⁰ Figure 7 shows a plot of layer void defect concentration as a function of growth run for the last 77 layers grown in the MBE system. The concentration of void defects for the first 47 epilayers was in the 10^2 – 10^4 cm^{-2} range, having a mean value of $2.4 \times 10^3 \text{ cm}^{-2}$ and a standard deviation

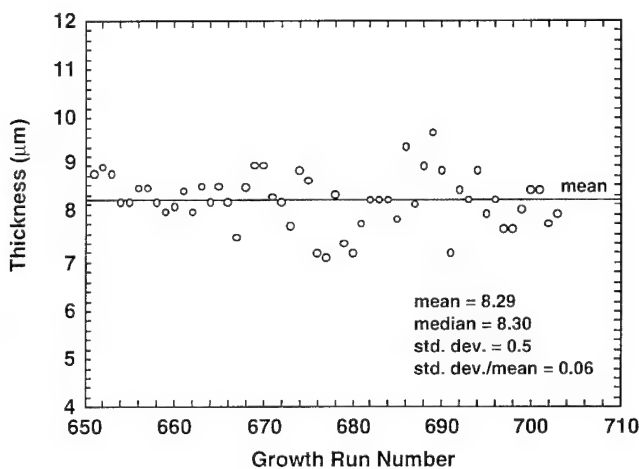


Fig. 3. Layer thickness as a function of growth run number for a series of sequentially grown MBE LWIR HgCdTe.

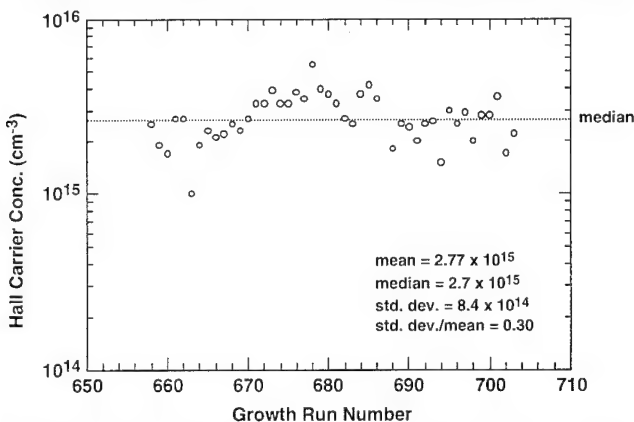


Fig. 4. Carrier concentration at 77K as a function of growth run number for a series of sequentially grown n-type MBE LWIR HgCdTe base layers. The layers were in situ doped using indium atoms.

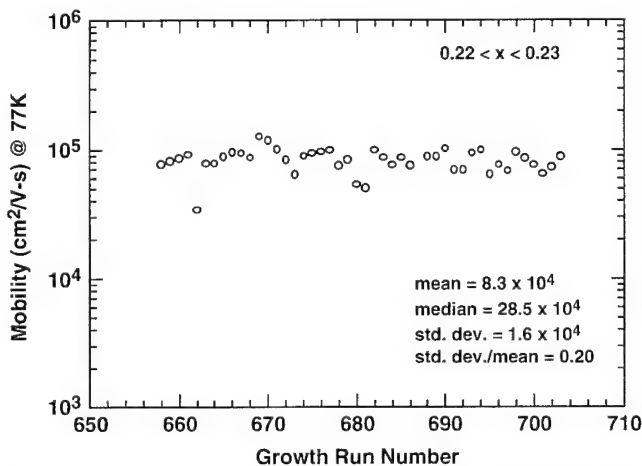


Fig. 5. Electron mobility in n-type MBE LWIR HgCdTe for a series of sequentially grown epilayers.

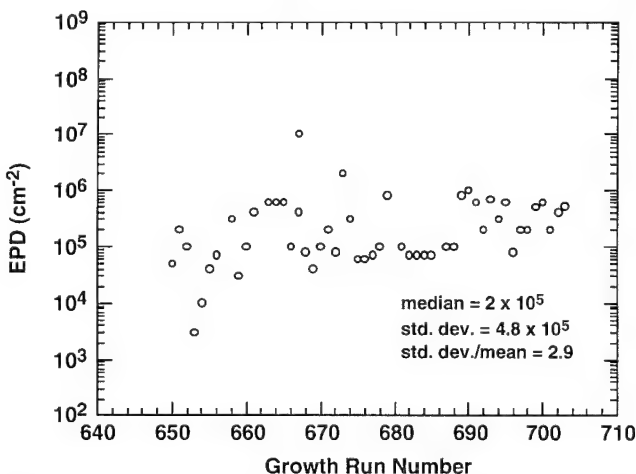


Fig. 6. Etch pit density as a function of growth run number for a series of sequentially grown MBE LWIR HgCdTe epilayers.

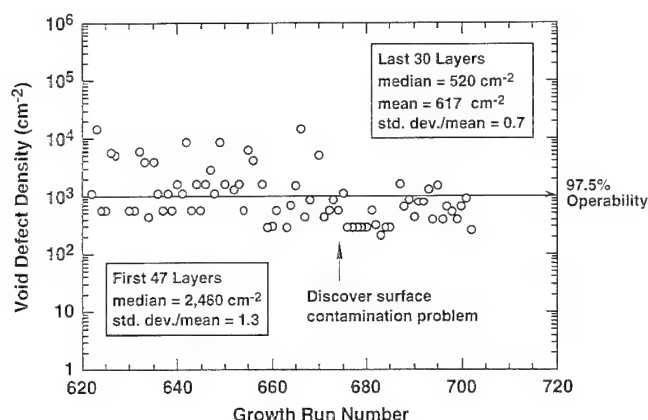


Fig. 7. Growth induced void defect density as a function of growth run number for a series of sequentially grown MBE LWIR HgCdTe epilayers.

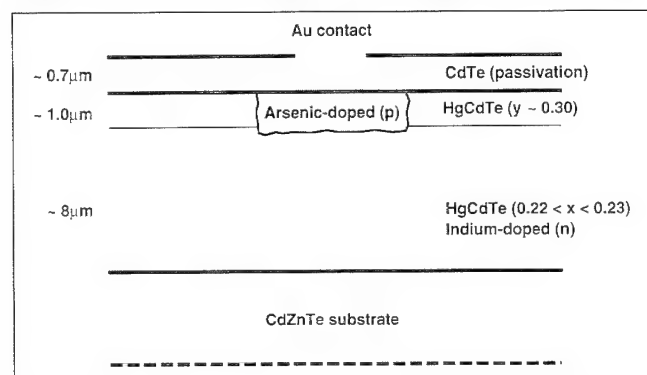


Fig. 8. Schematic cross section of passivated p-on-n planar arsenic-doped HgCdTe heterostructure diode.

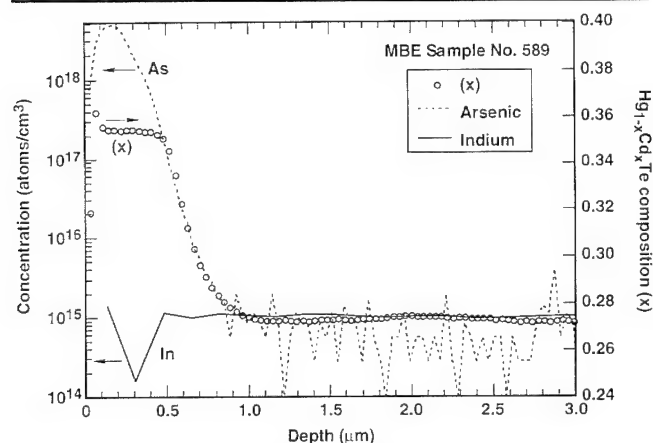


Fig. 9. Typical arsenic and tellurium SIMS profiles for a p-on-n planar $\text{Hg}_{0.73}\text{Cd}_{0.27}\text{Te}/\text{Hg}_{0.65}\text{Cd}_{0.35}\text{Te}$ heterostructure device grown by MBE on a CdZnTe substrate.

to mean ratio of 1.3. A void density of $1 \times 10^3 \text{ cm}^{-2}$ will lead to 128×128 FPAs (50 μm center-to-center spacing) with operabilities greater than 97.5%, assuming each void defect gives one bad pixel.

Several experiments were carried out to understand the formation of void defects. A one-to-one correlation between the presence of surface particles on the CdZnTe substrate and the formation of a void defect on the grown HgCdTe epilayer was established. Once the source of formation of void defects

was tracked to particles present on the surface of the substrate, the next step was to find the nature of such particles. A simple experiment using ultrasonic cleaning was sufficient to demonstrate that the particles were not chemically bound. Finally, the as-received substrates were observed to have particle densities much lower ($<300 \text{ cm}^{-2}$) than the values observed after preparing the substrates for epitaxial growth. The source that was generating the dust particles was determined and reduced. As a result of improvements in sample preparation techniques, for the last 30 growth runs, the yield of layers that met the void defect specification improved to a value of 87%. These results are illustrated in Fig. 7. The median void concentration value for these runs was 520 cm^{-2} ; the standard deviation to mean value ratio was 0.7.

DIODE STRUCTURE AND PERFORMANCE CHARACTERIZATION

Figure 8 is a schematic illustration of the buried planar HgCdTe diode heterostructure. The in situ grown double layer structure consisted of an indium-doped active narrow bandgap "base" layer and a wider bandgap "cap" layer. This double layer was terminated with a thin (500Å) CdTe layer for surface protection. The n-type base HgCdTe layers were typically 7–10 μm thick and doped with indium at a level of $1\text{--}3 \times 10^{15} \text{ cm}^{-3}$, while the wider band gap cap layer was typically 0.5 μm thick and not intentionally doped. The formation of planar p-on-n photodiodes was achieved by selective area arsenic (As) ion-implantation through the cap layer into the narrow gap base layer, using a beam energy of 350 KeV and the ion dose of $1 \times 10^{14} \text{ cm}^{-2}$. The implantation step was followed by a two-step thermal anneal under Hg overpressure.¹¹

The first anneal at $\sim 436^\circ\text{C}$ in Hg vapor activated the dopant by substituting arsenic atoms on the Te sublattice and diffused the arsenic into the base layer to form a homojunction in the active layer. The second anneal at 250°C , performed immediately after the high temperature anneal, annihilated the Hg vacancies formed in the HgCdTe lattice during growth and high temperature annealing step. An approximately 0.7 μm thick polycrystalline CdTe layer deposited at 85°C in the MBE system provided the device passivation.

Figure 9 illustrates the position of the electrical p-n junction with respect to the metallurgical composition junction of the heterostructure. Secondary ion mass spectroscopy (SIMS) measurements were made on samples already subjected to the two-step annealing process. Figure 9 shows the depth profiles of Te, As, and In obtained on a typical MLWIR sample. The Te yield in SIMS reflects the changes in concentration of the matrix elements Hg and Cd so accurately that the Te yield curve can be interpreted as a scaled plot of the energy gap (or Cd (x) composition in the $\text{Hg}_{1-x}\text{Cd}_x\text{Te}$ alloy) as a function of depth.¹² As illustrated in this figure, the arsenic and indium levels come together to form the electrical junction at a

depth of approximately $0.9\text{ }\mu\text{m}$ from the surface. With the depletion width approximately $0.4\text{ }\mu\text{m}$, the edge of the depletion region resides well into the base layer, forming a homojunction in the narrow bandgap active layer.

Figure 10 is a summary of the performance data on devices with varying cut-off wavelengths. The median R_0A product values are plotted against the device cutoff wavelength at 77K for the diode test arrays operating in the LWIR and MLWIR spectral region. All the device R_0A data were measured under zero background, and the area (A) used was the device junction area. The device data were obtained measuring devices with junction areas of $50 \times 50\text{ }\mu\text{m}^2$, which are typical device sizes in HgCdTe photovoltaic focal plane arrays. The number of devices measured per test array was usually 60. The solid curve is the result of a one-dimensional theoretical calculation based on diffusion current from the n-side only, using $N_D - N_A = 3 \times 10^{15}\text{ cm}^{-3}$ and Auger-limited minority carrier lifetime. These MBE diode results match those obtained using devices fabricated by LPE.^{13,14} Details of device performance data in the LWIR, the MLWIR and the MWIR spectral bands are given below.

LWIR HgCdTe Photodiode Performance Characteristics

Table I summarizes some of the recent LWIR device results. Eighteen layers with 77K λ_{co} in the 9.8 to $11.5\text{ }\mu\text{m}$ range were processed into devices and tested. A variable area mask-set was used to fabricate test diodes with areas of 1.3×10^{-5} ($36 \times 36\text{ }\mu\text{m}$), 1.3×10^{-4} ($115 \times 115\text{ }\mu\text{m}$), and 2.0×10^{-3} ($450 \times 450\text{ }\mu\text{m}$) cm^2 . Off-active area contacts were used to exclude the possibility of bonding-damage-induced effects. The spectral response for the devices was measured with a Nicolet Fourier transform infrared spectrometer; the 50% spectral cutoff wavelength (λ_{co}) was used to determine the energy gap of HgCdTe.

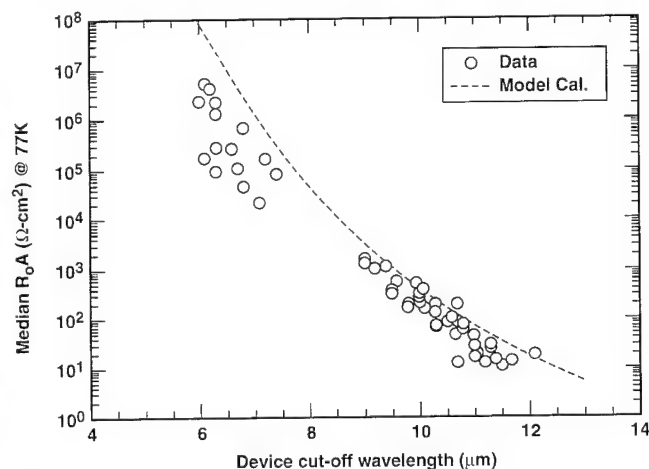


Fig. 10. Median R_0A product plotted against the cutoff wavelength (at zero background) measured at 77K for numerous LWIR and MLWIR p-on-n diode test arrays made by MBE. The number of devices measured per test array was usually 60. The data follow the solid curve which is the result of an R_0A calculation based on the ideal diode equation and Auger-limited minority carrier lifetime.

The 77K spectral response for these devices was broadband. Backside-illuminated quantum efficiency (QE) of these diodes, without antireflection coating, was measured at zero bias on a random sampling of the diodes, using a standard blackbody source, a focused spot, a narrow bandpass filter, and phase sensitive detection techniques. Most devices at 77K had QE values in the 60 to 75% range. Current-voltage (I-V) characteristics were measured at 77K for several diodes of each area and analyzed to determine bulk and surface limitations. Variable temperature measurements ranging from 10 to 280K were performed on a subset of diodes to determine the dominant current limiting mechanisms.

Figure 11 shows 80 and 40K R_0A cumulative distribution functions of an LWIR ($\lambda_{co} = 10.0\text{ }\mu\text{m}$ at 80K) diode array made with layer 685. Mean and median device R_0A values of 186 and $192\text{ }\Omega\text{-cm}^2$ were obtained

Table I. Summary of MBE-LWIR Test Diodes Data At 77K

Sple.	λ_{co} (μm)	QE (%)	Mean R_0A ($\Omega\text{-cm}^2$)	Median R_0A ($\Omega\text{-cm}^2$)
637	10.6	70	108	104
638	10.7	71	84	80
648	10.5	60	80	84
649	10.0	76	176	210
658	9.8	74	172	197
659	10.1	64	139	164
660	10.3	70	73	76
661	10.7	70	72	70
663	11.3	75	9	9
664	10.4	—	17	18
666	10.3	—	19	19
677	10.9	73	16	16
678	10.3	55	62	70
679	11.5	75	11	11
683	11.3	75	33	25
684	10.3	74	76	74
685	10.0	68	493	511
688	10.7	72	12	13

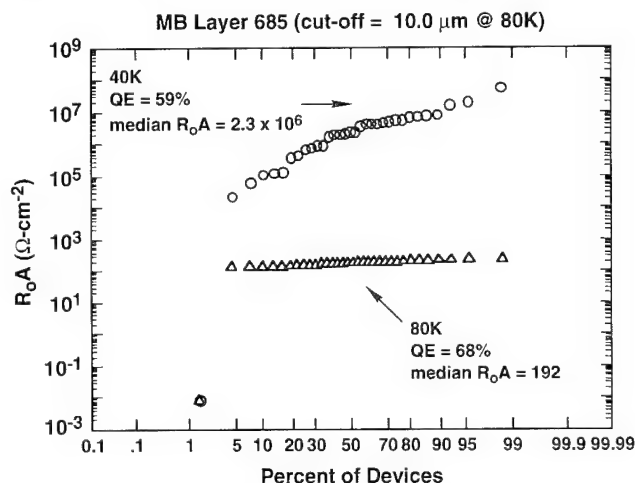


Fig. 11. R_0A cumulative distribution plot for MBE-LWIR ($\lambda_{co} = 10\text{ }\mu\text{m}$ @ 77K) p-on-n HgCdTe diodes at 80 and 40K.

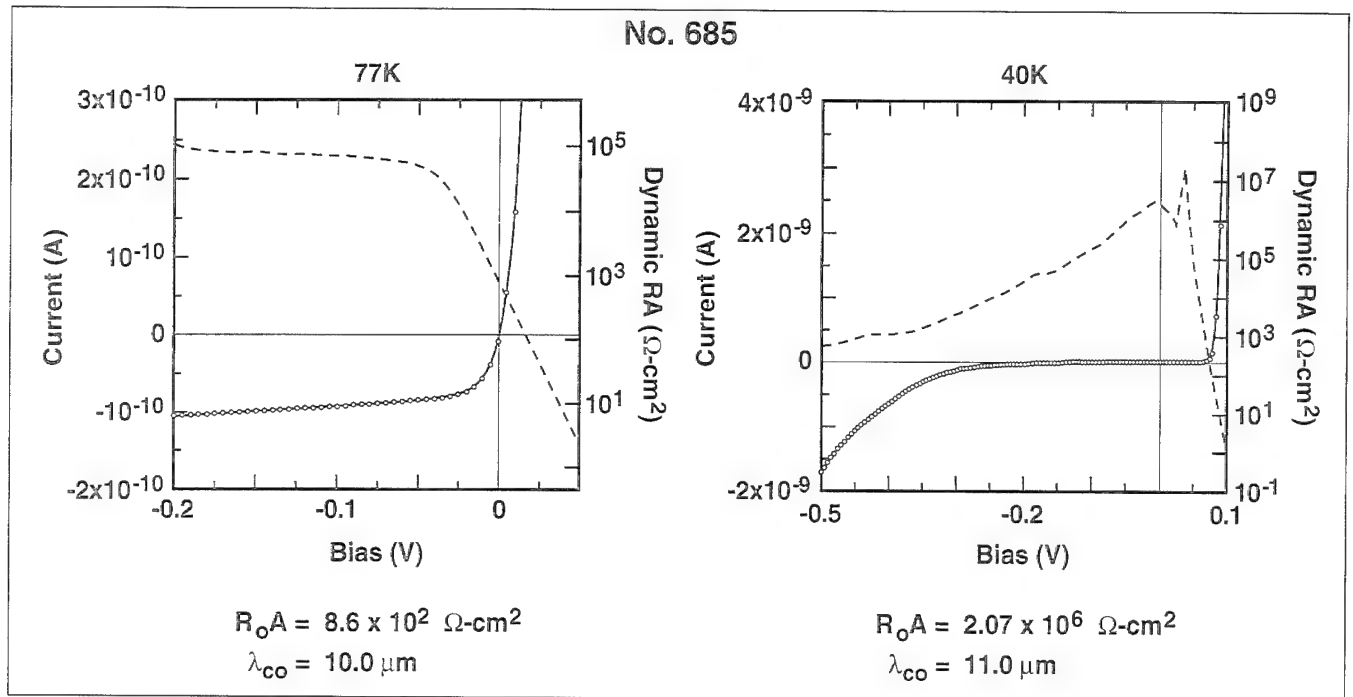


Fig. 12. Detailed I-V and dynamic impedance characteristics under zero background for an MBE-LWIR HgCdTe p-on-n heterostructure diode measured at 77 and 40K.

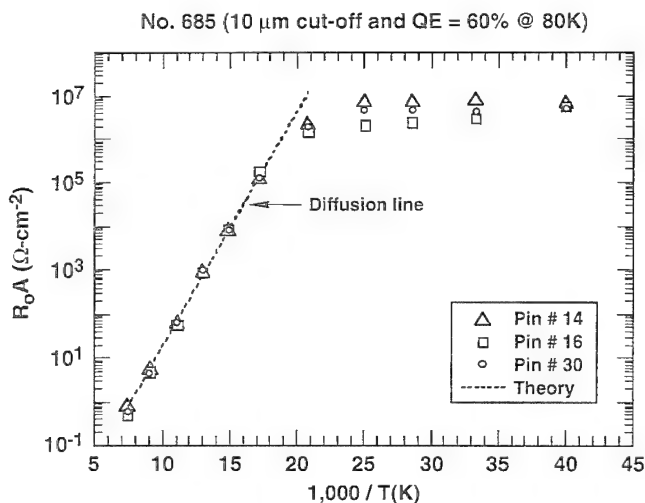


Fig. 13. R_0A dependence on reciprocal temperature for several MBE-LWIR p-on-n photodiodes.

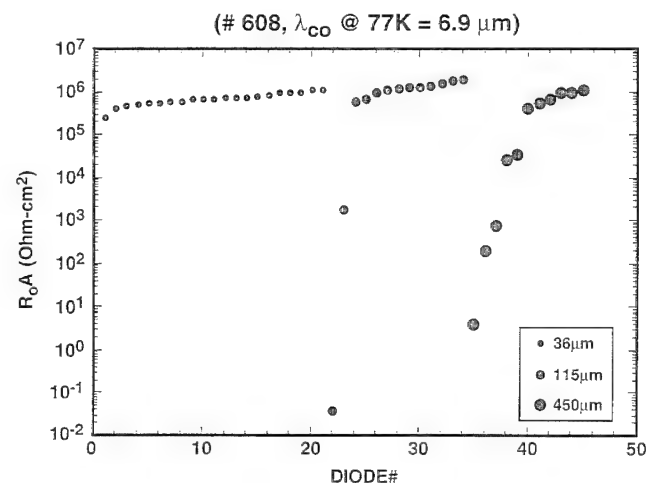


Fig. 14. R_0A cumulative distribution functions plot for MLWIR ($\lambda_{co} = 6.8 \mu\text{m}$) diodes at 77K. Device junction areas are 36×36 , 115×115 , and $450 \times 450 \mu\text{m}^2$.

at 80K. The devices exhibit excellent R_0A uniformity (only one diode was poor). At 40K, even though device uniformity needs further improvement, the overall performance is state-of-the-art. For example, mean R_0A value of $5.2 \times 10^6 \Omega\text{-cm}^2$ was achieved for these LWIR ($\lambda_{co} = 11.2 \mu\text{m}$ at 40K) devices at 40K. The figure also shows 90% of the devices have R_0A values above $1 \times 10^5 \Omega\text{-cm}^2$.

Figure 12 illustrates detailed current-voltage (I-V) and dynamic impedance area-voltage (RA-V) diode characteristics at 77 and 40K for a device made with layer 685. At 77K, the device dark currents are diffusion-limited, and dynamic RA products for the diodes reach values of 10^4 – $10^5 \Omega\text{-cm}^2$ at an applied reverse

bias of 50 mV. To determine the mechanisms controlling the device leakage currents, the I-V characteristics were measured as a function of temperature.

Figure 13 illustrates the temperature dependence of the resistance area (R_0A) product for several LWIR planar devices. For operating temperatures above 58K, the device R_0A products are limited by diffusion dark current processes. For temperatures below 58K, the R_0A products still increase but more gradually, and the observed dependence is less temperature sensitive than expected for generation-recombination currents. At 40K, the detailed analysis of the I-V characteristics over a broad range of voltages suggests that the dark currents consist of a mixture of

diffusion, generation-recombination, and tunneling currents.

MLWIR HgCdTe Photodiode Performance Characteristics

For the MLWIR spectral band too, the variable area mask-set described above was used to fabricate test diodes with off-active area contacts. Current-voltage characteristics were measured at 77K for several diodes of each area and analyzed to determine bulk and surface limitations. Variable temperature measurements ranging from 10 to 280K were performed on a subset of diodes to determine the dominant current limiting mechanisms.

The performance of variable area test diodes fabricated on a representative MLWIR (#608, $\lambda_{co} = 6.8 \mu m$ at 77K) sample is illustrated in Fig. 14. The figure shows a cumulative distribution plot of R_0A values for the three diode areas, measured at 77K under zero background flux conditions. For each area, the diodes are ranked according to increasing R_0A . With increasing area, the R_0A values either show no change, indicating minimal surface limitation; or show a decrease, indicating scattered localized defects. For the smaller, $36 \times 36 \mu m$ devices typically used for focal plane arrays, the mean and median R_0A values of

7.2×10^5 and $7 \times 10^5 \Omega\text{-cm}^2$ were obtained. The quantum efficiency values for these diodes were measured at 72%.

To assess the mechanisms controlling the device leakage currents at a given temperature, I-V characteristics were measured as a function of temperature. Figure 15a illustrates the temperature dependence of the R_0A product for MLWIR (layer #608) planar devices of three junction areas. At temperatures below 80K, tunneling mechanisms dominate the dark current generation. At higher temperatures, the R_0A products are diffusion current limited, as illustrated in Fig. 15b, which shows details of the temperature dependence at higher temperatures. The solid line represents diffusion-limited theoretical R_0A values obtained from one-dimensional calculations based on the ideal diode equation. The current contribution from only the n-side was incorporated using measured $N_D - N_A = 2 \times 10^{15} \text{ cm}^{-3}$, measured layer thickness and Auger-limited minority carrier lifetime. Above 100K, a good agreement between the experimental and theoretical data indicates that the device R_0A products are limited by diffusion dark current processes. At these temperatures ($T > 80K$) of opera-

Table II. Summary of MBE-MLWIR
Test Diodes Data

No.	$\lambda(\mu m)$ @ 65K	QE (%) @ 65K	Mean R_0A @ 77K	Median R_0A @ 77K
586	6.5	72 (77K)	1.1 E5	9.2 E4
589	6.3	72 (77K)	7.9 E6	5.3 E6
604	6.3	51	9.5 E5	1.8 E5
601	6.9	67	3.2 E5	1.1 E5
567	6.49	64	2.0 E6	2.2 E6
567	6.48	63	1.2 E6	1.3 E6
597	7.6	72	7.4 E4	8.2 E4
606	6.4	70	4.2 E6	4.1 E6
607	6.2	65	3.3 E6	2.3 E6
608	6.97	73	7.2 E5	7.0 E5
610	6.87	69	2.7 E5	2.7 E5
615	7.3	55	2.7 E4	2.2 E4
616	6.5	63	2.8 E5	2.8 E5
617	7.0	60	9.0 E4	4.6 E4

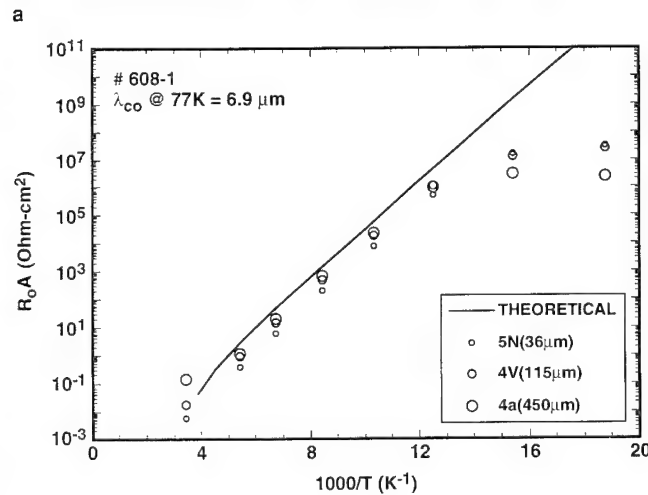
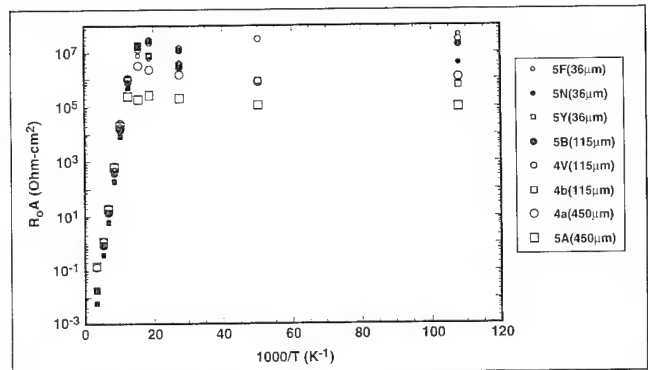


Fig. 15. R_0A dependence on reciprocal temperature for several MLWIR p-on-n planar photodiodes. Device junction areas are 36×36 , 115×115 , and $450 \times 450 \mu m^2$.

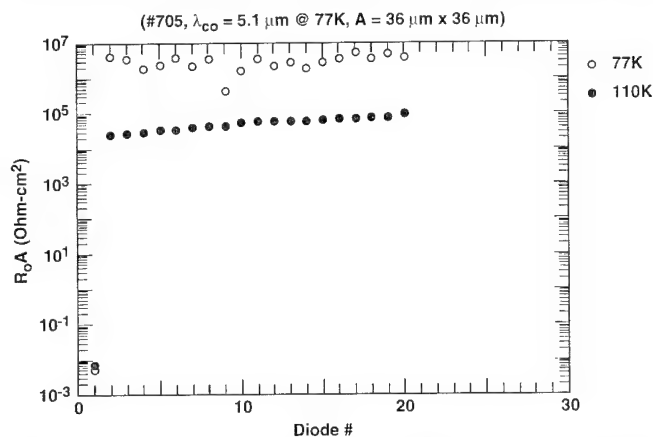


Fig. 16. R_0A cumulative distribution plot for MWIR ($\lambda_{co} = 5.1 \mu m$) diodes at 77 and 110K. Device junction area is $9.0 \times 10^{-6} \text{ cm}^2$.

tion, the data also show no R_0A area dependence, which is a clear indication that the passivated planar devices are not surface limited.

Table II is a summary of the electrical and optical data obtained from test diodes fabricated on 12 different MLWIR layers, illustrating the producibility of MBE MLWIR HgCdTe detectors. This data is included in Fig. 10 which shows median R_0A at 77K plotted against the cutoff wavelength, for both the MLWIR and the LWIR bands. Figure 10 also shows the maximum theoretically expected R_0A value at 77K for each wavelength.

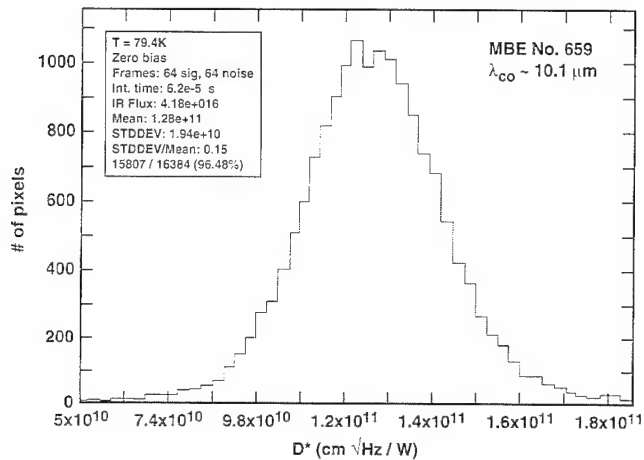


Fig. 17. D^* histogram of a 128×128 LWIR ($\lambda_{co} = 10.1 \mu\text{m}$) MBE HgCdTe hybrid FPA tested under the following conditions: operating temperature of 79K; integration time of 62 μs , and IR background of 4.1×10^{16} photons/ $\text{cm}^2\text{-s}$.

MWIR HgCdTe Photodiode Performance Characteristics

The database for p/n photodiodes operating in the MWIR region is not as extensive as the LWIR or the MLWIR band. However, the early data on MBE MWIR photodiodes show high performance as illustrated in Fig. 16. This figure shows cumulative distribution plots of R_0A values for $36 \times 36 \mu\text{m}$ photodiodes measured at 77 and 110K under zero background flux conditions. The diodes are ranked according to increasing R_0A at 110K. The median R_0A values at 110 and 77K were measured at $5.9 \times 10^4 \Omega\text{-cm}^2$ and $2.9 \times 10^6 \Omega\text{-cm}^2$, respectively. The quantum efficiency for these devices measured at $3.55 \mu\text{m}$ was 72% at 77K.

HYBRID FOCAL PLANE ARRAYS

The planar MBE HgCdTe technology has been further validated with the successful fabrication and operation of hybrid FPAs. Several 128×128 LWIR FPA hybrids have been fabricated and fully tested. The FPAs with devices on $60 \mu\text{m}$ centers were hybridized to a 128×128 complementary metal oxide semiconductor electronically scanned buffered direct injection (ESBDI) multiplexer having low input impedance and low input offset nonuniformity.¹⁵ The hybrids were tested at 78 and 90K using a broadband tactical IR background environment of 4.2×10^{16} ph/ $\text{cm}^2\text{-s}$. Hybrid 659 ($\lambda_{co} = 10.1 \mu\text{m}$) had the highest performance of the devices tested. The mean quantum efficiency value was 59%, and the dynamic-impedance near zero bias was $83 \Omega\text{-cm}^2$. The device was

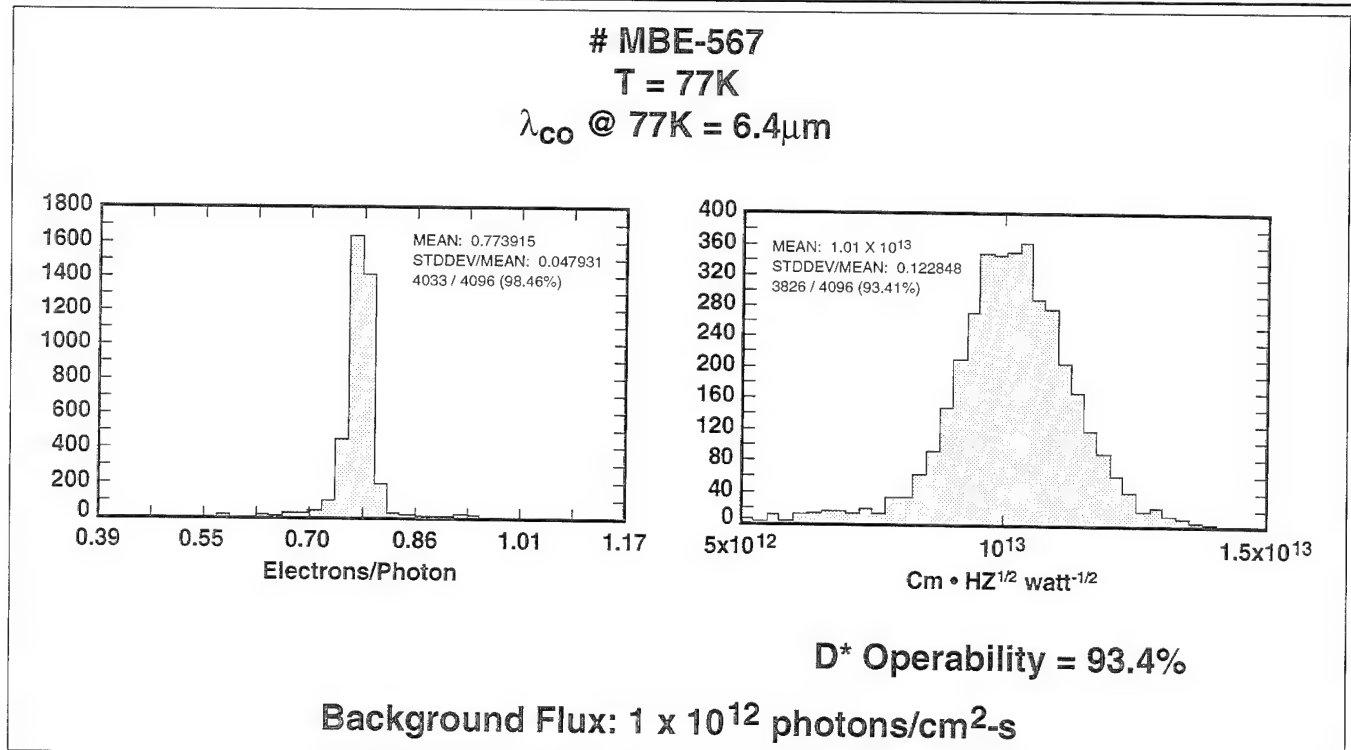


Fig. 18. Histograms of (a) quantum efficiency and (b) D^* for a 64×64 MBE MLWIR ($\lambda_{co} = 6.4 \mu\text{m}$ at 77K) HgCdTe hybrid FPA tested at 77K under a background of 2×10^{12} photons/ $\text{cm}^2\text{-s}$.

BLIP limited at 78K with a mean detectivity (D^*) value of $1.28 \times 10^{11} \text{ cmHz}^{1/2}/\text{W}$ (Fig. 17) when tested at an integration time of 62 μs . The pixel operability, here defined as the yield of pixels having D^* higher than 1/2 of the mean value, was 97.7%. The mean NE ΔT (70% optical transmission) was measured at 5.9 mK when tested at a 60 Hz frame rate. Worst case residual nonuniformity was less than 0.017% with broadband, unfiltered radiation. Use of a cooled spectral filter to eliminate the uncorrectable nonuniformity induced by detector cutoff variation reduced the residual nonuniformity to well below 0.01%.

64×64 focal plane arrays with devices on 36 μm centers were fabricated on several MLWIR samples and hybridized with indium bumps to CMOS multiplexers with CTIA input circuit having low input impedance and low input offset nonuniformity. An example of the performance of the hybrid FPAs is shown in Fig 18. The cut off wavelength of the hybrid fabricated on layer #567 was 6.4 μm at 77K. The mean quantum efficiency at 77K was measured at 77.4% (Fig. 18a) and the mean detectivity (D^*) of this device (Fig. 18b) was measured at $1 \times 10^{13} \text{ cmHz}^{1/2}/\text{W}$ at the tested background of $2 \times 10^{12} \text{ photons/cm}^2\text{-s}$. This mean D^* corresponds to 80% of the BLIP limited value. The pixel D^* operability was measured at 93%. This operability includes all pixels that have the D^* values within the ± 0.5 mean D^* range.

SUMMARY AND CONCLUSIONS

An extensive material and device performance reproducibility database is presented to demonstrate the status of MBE-based HgCdTe growth technology for infrared detection applications. Over 50 LWIR HgCdTe multilayer structures were grown and characterized to generate the database on the reproducibility of band gap, growth rate, thickness, carrier concentration, electron Hall mobility, void defect density, and etch pit density. A summary of the material reproducibility data is given in Table III.

Among the most significant material reproducibility highlights achieved are improvements in composition reproducibility and reduction of growth-induced void defects. Most recent results show that the standard deviation of the LWIR HgCdTe bandgap has been reduced to 0.0020. As a result of this improvement, the yield of layers that meet the composition specifications has increased to 90%. Reproducibility of layer thickness, carrier concentration, and mobility are also excellent. Significant improvements have been made in reducing the concentration of growth-induced void killer defects, from an initial mean reproducibility value of $2.4 \times 10^3 \text{ cm}^{-2}$ down to a mean value of $5.2 \times 10^2 \text{ cm}^{-2}$. Even though the variations of EPD reported in the MBE layers are comparable to those values obtained with LPE grown material, further studies are needed to reduce the observed variations.

The data presented for MBE LWIR p-on-n diode test arrays show median R_0A and QE values at 77K that match those of state-of-the-art p-on-n double heterostructure photodiodes made by LPE. Analysis

of the current-voltage characteristics of LWIR and MLWIR photodiodes as a function of temperature showed that their dark currents are diffusion-limited at temperatures above 60 and 80K, respectively. Under the operating temperatures required for low background applications, however, the device's dark currents are dominated by tunneling currents most likely induced by defects. We must resolve the nature of these currents, identify their origin, and implement appropriate growth and processing changes to minimize their contribution. Due to the special attention given to understanding and reducing epilayer growth-induced void defects, FPA operability has increased from 92 to 98%, by reducing the density of such void defects below $1,000 \text{ cm}^{-2}$. A 128×128 FPA showed D^* background limited performance when operating at 80K in a tactical background environment. Mean D^* was $1.28 \times 10^{11} \text{ cmHz}^{1/2}/\text{W}$, and the corresponding mean NE ΔT was an excellent 5.9 mK. For the more demanding low background imaging applications in the MLWIR (6–8 μm) spectral band, the R_0A device values were high and uniform, as evidenced by both the test diode data and the 64×64 hybrid data. Further progress is needed to achieve higher device operability and yield. The limitations, not unique to the MBE technology, can be addressed by further improvement studies on material quality, substrate quality, and device processing techniques.

A simplistic look at the cumulative distribution of diode performance divides defects into two broad categories of point and extended defects. These two groups of defects address the "common" (higher per-

**Table III. MBE LWIR HgCdTe
Material Reproducibility**

LWIR Uniformity ($2 \times 3 \text{ cm}$ wafer) [Std. Dev. (x)/Mean (x)]	0.002 / 0.22 = 0.009
LWIR (x) Repeatability (Last 25 LWIR runs)	Mean = 0.225 Median = 0.226 Std. Dev. = 0.002 Std. Dev./Mean = 0.009
Film Thickness (μm) (Last 53 layers)	Mean = 8.29 Median = 8.30 Std. Dev./Mean = 0.06
Carrier Conc. (cm^{-3}) (Last 45 runs)	Mean = 2.77×10^{15} Median = 2.7×10^{15} Std. Dev./Mean = 0.30
77K Mobility ($\text{cm}^2/\text{V-s}$) (Last 45 runs)	Mean = 8.3×10^4 Median = 8.5×10^4 Std. Dev./Mean = 0.20
Void Defects (cm^{-2}) (Last 30 runs)	Mean = 617 Median = 520 Std. Dev./Mean = 0.7
Etch Pit Density (cm^{-2}) (Last 50 runs)	Mean = 4.8×10^5 Median = 2×10^5 Std. Dev./Mean = 2.9

formance population with a tight distribution) population and the "sport" (lower performance population with a broad distribution) population, respectively. The extended defects responsible for the "sport" population include dislocations, dislocation clusters, precipitates, impurity clusters, pin-holes, and voids. These defects lend themselves to direct observation using a variety of diagnostic tools. One type of growth-induced defect observed in MBE grown HgCdTe is easily identified under optical Nomarski microscope inspection. This defect has been referred to as a "void-defect", and a one-to-one correlation between the presence of void defect and the performance of LWIR diodes has been reported earlier. The point defects responsible for the "common population" can be intrinsic or extrinsic. While the extrinsic impurities are relatively easily detected using chemical analysis, the intrinsic native defects such as vacancies, antisites, and interstitials do not lend themselves to direct observation. The Hg vacancies have been demonstrated to exist in HgCdTe; however, interstitials and antisite defects have been theoretically predicted in significant quantities.¹⁶ The presence of native point defects is detected inferentially; e.g., by measuring the energy levels in the band gap that are associated with these defects, and comparing them with the levels predicted by theoretical model calculations. An established approach to measuring the energy levels associated with these defects uses deep level transient spectroscopy.¹⁷

In conclusion, extensive material, device and FPA data presented show significant progress achieved by MBE HgCdTe growth technology for infrared applications in the LWIR (8–12 μm), MLWIR (6–8 μm), and MWIR (4–6 μm) spectral regions.

ACKNOWLEDGMENTS

This work was partially supported by the Advanced Research Projects Agency (monitored by the U.S. Army, Night Vision and Electronic Sensors Division) under Contract No. DAAB07-93-C-U505. The authors thank many of their colleagues at Rockwell

Science Center who have contributed to this research, particularly Don Cooper, Lucia Bubulac, and Dennis Stephenson.

REFERENCES

1. J.M. Arias-Cortés, *II-VI Semiconductor Compounds*, ed. M. Pain (Singapore: World Scientific Publishing Co. Pte. Ltd., 1993), p. 509.
2. J.M. Arias, J.G. Pasko, M. Zandian, S.H. Shin, L.O. Bubulac, R.E. DeWames and W.E. Tennant, *J. Electron. Mater.* 22, 1049 (1993).
3. J.M. Arias, J.G. Pasko, M. Zandian, J. Bajaj, L.J. Kozlowski, R.E. DeWames and W.E. Tennant, *Proc. SPIE Symp. on Producibility of II-VI Materials and Devices*, Volume 2228 (1994).
4. J.M. Arias, S.H. Shin, J.G. Pasko, R.E. DeWames and E.R. Gertner, *J. Appl. Phys.* 65, 1747 (1989).
5. J.M. Arias, M. Zandian, J.G. Pasko, S.H. Shin, L.O. Bubulac, R.E. DeWames and W.E. Tennant, *J. Appl. Phys.* 69, 2143 (1991).
6. S.M. Johnson, D.R. Rhiger, J.P. Rosbeck, J.M. Peterson, S.M. Taylor and M.E. Boyd, *J. Vac. Sci. Technol.* B10, 1499 (1992).
7. J.S. Chen, U.S. Patent No. 4, 897,152.
8. L. Colombo, G.H. Westphal, P.K. Liao and H.F. Schaaake, *1994 U.S. Workshop on the Physics and Chemistry of HgCdTe and Other IR Materials*, San Antonio, TX (October 1994), to be published in the *J. Electron. Mater.*
9. J.M. Arias, M. Zandian, J.G. Pasko, L.O. Bubulac, S.H. Shin and R.E. DeWames, *J. Electron. Mater.* 24, 521 (1995).
10. M. Zandian, J.M. Arias, J. Bajaj, J.G. Pasko, L.O. Bubulac, and R.E. DeWames, *J. Electron. Mater.* 24, 1207 (1995).
11. S.H. Shin, J.M. Arias, M. Zandian, J.G. Pasko and R.E. DeWames, *J. Electron. Mater.* 22, 1039 (1993).
12. L.O. Bubulac and C.R. Viswanathan, *Appl. Phys. Lett.* 60, 222 (1992).
13. P.R. Norton, *Optical Eng.* 30, 1649 (1991).
14. P.W. Norton, P. LoVecchio, G.N. Pultz, J. Hughes, T. Robertson, V. Lukach and K. Wong, *Proc. SPIE Symp. on Producibility of II-VI Materials and Devices*, Volume 2228 (1994), p. 73.
15. L.J. Kozlowski, G.M. Williams, G.J. Sullivan, C.W. Farley, R.J. Anderson, J. Chen, D.T. Cheung, W.E. Tennant and R.E. DeWames, *IEEE Trans. on Electron Dev.* 38, 1124 (1991).
16. M.A. Berding, M. Schilfgaarde and A. Sher, *J. Electron. Mater.* 22, 1005 (1993).
17. J.E. Colon, J. Bajaj, J. Arias, M. Zandian and J. Pasko, *1994 U.S. Workshop on the Physics and Chemistry of HgCdTe and Other IR Materials*, San Antonio, TX (October 1994).

Metalorganic Chemical Vapor Deposition of HgCdTe p/n Junctions Using Arsenic and Iodine Doping

P. MITRA, T.R. SCHIMERT, F.C. CASE, and S.L. BARNES

Loral Vought Systems Corporation, P.O. Box 650003, Dallas, TX 75265-0003

M.B. REINE, R. STARR, M.H. WEILER, and M. KESTIGIAN

Loral Infrared & Imaging Systems, Lexington, MA 02173-7393

We report new results on metalorganic chemical vapor deposition (MOCVD) *in situ* growth of long wavelength infrared (LWIR) P-on-n and medium wavelength infrared (MWIR) n-on-P HgCdTe heterojunction photodiodes using the interdiffused multilayer process (IMP). The n-type regions are doped with iodine using the precursor ethyl iodide (EI). I-doped HgCdTe using EI has mobilities higher than that obtained on undoped background annealed films and are comparable to LPE grown In-doped HgCdTe. The p-type layers are doped with arsenic from either tertiarybutylarsine (TBAs) or a new precursor, *tris*-dimethylaminoarsenic (DMAAs). The substrates used in this work are lattice matched CdZnTe oriented (211)B or (100)4°→<110>. Junction quality was assessed by fabricating and characterizing backside-illuminated arrays of variable-area circular mesa photodiodes. This paper presents four new results. First, carrier lifetimes measured at 80K on arsenic doped single HgCdTe layers are generally longer for films doped from the new precursor DMAAs than from TBAs. Second, we present data on the first P-on-n HgCdTe photodiodes grown *in situ* with DMAAs which have R_0A products limited by g-r current at 80K for $\lambda_{co} = 7\text{--}12\text{ }\mu\text{m}$, comparable to the best R_0A products we have achieved with TBAs. Third, we report the first experimental data on a new HgCdTe device architecture, the n-on-P heterojunction, with a wide gap p-type layer which allows radiation incident through the substrate to be absorbed in a narrower gap n-type layer, thereby eliminating interface recombination effects. With the n-on-P architecture, MWIR photodiodes were obtained reproducibly with classical spectral response shapes, high quantum efficiencies (70–75%) and R_0A products above $2 \times 10^5\text{ ohm-cm}^2$ for $\lambda_{co} = 5.0\text{ }\mu\text{m}$ at 80K. Fourth, we report 40K data for LWIR P-on-n HgCdTe heterojunction photodiodes (using TBAs), with R_0A values of $2 \times 10^4\text{ ohm-cm}^2$ for $\lambda_{co} = 11.7\text{ }\mu\text{m}$ and $5 \times 10^5\text{ ohm-cm}^2$ for $\lambda_{co} = 9.4\text{ }\mu\text{m}$. These are the highest R_0A values reported to date for LWIR P-on-n heterojunctions grown *in situ* by MOCVD.

Key words: Doping, heterojunctions, HgCdTe, metalorganic chemical vapor deposition (MOCVD)

INTRODUCTION

The development of metalorganic chemical vapor deposition (MOCVD) for *in situ* growth of high performance HgCdTe p-n junction photodiodes is necessary to realize the benefits of this flexible and production worthy vapor phase growth technology. Due to the low growth temperatures (normally 350–380°C),

MOCVD of HgCdTe is readily amenable to bandgap engineering allowing the growth of multilayer structures which are required for multispectral IR detectors. We have recently demonstrated that alloy compositions and arsenic doping can be controlled precisely and independently to obtain multiple bandgap regions with abrupt dopant profiles.^{1,2} This control in composition and doping was used to demonstrate the first independently accessed p-n-N-P back-to-back dual-band IR detectors by MOCVD *in situ* growth.³

(Received November 1, 1994; revised March 1, 1995)

(In this paper, we use the convention that an upper case P or N denotes the layer of wider energy bandgap.) In these structures, the n-type regions were undoped and relied on the background donors following a low temperature Hg anneal.

For improved performance of p/n junctions, it is necessary that the n-type regions be extrinsically doped with donor impurities which can also be abruptly switched on and off. Using the ethyl iodide (EI) precursor for iodine, we have achieved⁴ controlled donor doping in the range of 7×10^{14} – 2×10^{18} cm⁻³ without the problems of memory effect observed with indium precursors⁵⁻⁷ or isopropyl iodide.⁸ Using the interdiffused multilayer process (IMP) for MOCVD of HgCdTe, we have reported on p-on-n heterojunction photodiodes grown *in situ*, where an arsenic doped layer is grown on an undoped,¹ as well as initial data on iodine doped, long wavelength infrared (LWIR) HgCdTe.² Arsenic doping in these studies was achieved by using the precursor tertiarybutylarsine (TBAs). Our previous diode data¹ showed well behaved characteristics with classical spectral response and high quantum efficiency but also exhibited leakage currents at reverse bias and R₀A products at 80K which are below the theoretically predicted limit due to n-side diffusion current mechanisms alone. Although excellent control in arsenic doping in the range of 2×10^{15} – 5×10^{17} cm⁻³ using TBAs was achieved, it is conceivable that the dissociation chemistry of TBAs at the low MOCVD growth temperature on the HgCdTe surface introduces undesirable byproducts such as As-H and C in addition to the As atoms. Acceptor complexes and unintended impurities have the potential of being recombination centers in the depletion region of the p/n junction and therefore detrimental to diode performance. The use of alternate As precursors with dissociation chemistry which exclude the possibility of formation of such byproducts is thus desirable to explore.

In this paper, we report new results on MOCVD-IMP *in situ* grown HgCdTe photodiodes with arsenic and iodine doping covering the LWIR and medium wavelength infrared (MWIR) spectral bands. The LWIR diodes were grown in the standard P-on-n heterojunction configuration. For p-type doping in the LWIR heterojunctions, TBAs and a new precursor for As-doping of HgCdTe, *tris*-dimethylaminoarsenic⁹ (DMAAs) was used for the first time. DMAAs has several favorable properties for As-doping, which includes the absence of any As-H bonds and a low probability of C incorporation as demonstrated in metalorganic molecular beam epitaxy of GaAs and AlGaAs.¹⁰ DMAAs undergoes unimolecular dissociation at a lower temperature (10% at 350°C)¹¹ and has a conveniently low vapor pressure at ambient temperatures. In their study of homogeneously doped p-type HgCdTe layers using DMAAs, Bevan et al.⁹ have shown that for $x = 0.30$, HgCdTe lifetimes at the radiative limit can be obtained. Here we compare the lifetimes of homogeneously doped single layer p-type films as well as the performance of LWIR hetero-

junctions grown using both precursors at 80K. For TBAs doped LWIR junctions for selected films R₀A products down to temperatures below 40K are also reported.

The MWIR diodes were grown in a new n-on-P heterojunction configuration with I-doping in the n-type and As in the p-type regions using TBAs. This device design was developed to alleviate the problems of low quantum efficiency with sharply peaked spectral response observed previously in the n-on-p MWIR homojunctions which were part of the p-n-N-P dual-band detectors.³ Detailed MWIR diode performance characteristics of the n-on-P detectors are also described.

MOCVD GROWTH

Metalorganic chemical vapor deposition-IMP growth was carried out in a horizontal geometry reactor near atmospheric pressure at 360–370°C. The alternating pairs of HgTe and CdTe were grown with a total period thickness of 0.05–0.1 μm and were subsequently interdiffused to a homogeneous alloy composition. Dimethylcadmium (DMCd) and diisopropyltelluride (DiPTe) were the organometallic precursors used for Cd and Te, respectively, and heated elemental Hg was used as the source for Hg vapor. Additional details of the HgCdTe MOCVD growth system and parameters have been described previously.¹ Lattice matched CdZnTe (4% nominal Zn content) substrates were used in this work with the (100)4–8° → <110> and (211)B orientations. Undoped layers grown on these substrates, following a stoichiometric anneal at 235°C under Hg vapor, are n-type with background carrier concentrations of $(3-8) \times 10^{14}$ cm⁻³ measured at 80K.

For iodine doping, the EI bubbler was operated in a dual dilution flow configuration to achieve precise control of dopant injection in the reactor. In this manner, the partial pressure of EI could be readily controlled from 1×10^{-8} – 1×10^{-5} atm. Since it is necessary for the iodine impurity to substitutionally occupy sites in the tellurium sublattice to be effective as a donor, EI was injected only during the CdTe growth cycle where metal-rich conditions are easily achieved. A Cd/Te ratio of 1.1–1.2 was used in this work. For the low level donor doping used here ($1-2 \times 10^{15}$ cm⁻³) as-grown, the iodine doped HgCdTe was found to be p-type. Following an anneal in saturated Hg vapor at 235°C, the layers converted to n-type with Hall carrier concentrations determined by the EI partial pressure used during growth. Further details of the iodine doping process using EI are described elsewhere.⁴

P-type doping was performed using TBAs or DMAAs as the precursors. A double dilution flow configuration was also used for the TBAs bubbler which allowed precise control of dopant injection with partial pressures in the range 2×10^{-8} – 2×10^{-5} atm. Arsenic doping was also performed under metal-rich conditions in the CdTe growth cycle similar to that used for iodine doping. DMAAs which has a conveniently lower

vapor pressure of 0.96 Torr compared to 101 Torr for TBAs at 15°C was injected in the reactor using standard bubbler conditions. As-doping with DMAAs was also performed under metal-rich conditions during CdTe growth of the IMP cycle.

The LWIR P-on-n and the MWIR n-on-P heterojunctions were grown in most cases with the n-type layer doped with iodine. For the LWIR diodes, the narrow bandgap n-type layers were grown with thicknesses of 10–13 μm at a doping level of $(1-2) \times 10^{15} \text{ cm}^{-3}$. The widegap p-type layers were grown 2–3 μm thick with an arsenic doping level of $(1-3) \times 10^{17} \text{ cm}^{-3}$. For the MWIR diodes an $x \sim 0.40$ layer was grown first with As-doping at $(0.5-2) \times 10^{17} \text{ cm}^{-3}$ to thicknesses with 4–8 μm followed by the n-type layer I-doped at $(0.5-3) \times 10^{15} \text{ cm}^{-3}$ and thicknesses of $\sim 10 \mu\text{m}$. The heterojunctions were annealed under Hg-rich conditions at $\sim 415^\circ\text{C}$ for 5–20 min to ensure complete As activation¹² followed by a standard stoichiometric anneal at $\sim 235^\circ\text{C}$.

FILM CHARACTERIZATION RESULTS

N-Type Doping

By controlling the partial pressure of EI, the donor concentration in HgCdTe can be controlled over the range of 7×10^{14} – $2 \times 10^{18} \text{ cm}^{-3}$. Hall effect measurements at 80K show classical n-type behavior for iodine doped MOCVD HgCdTe.⁴ For example, for LWIR HgCdTe with $x \sim 0.22$ and carrier concentration of $(1-2) \times 10^{15} \text{ cm}^{-3}$, the Hall mobility at 80K is $\geq 1 \times 10^5 \text{ cm}^2 \text{ V}^{-1} \text{ s}^{-1}$ and increases to $\geq 2 \times 10^5 \text{ cm}^2 \text{ V}^{-1} \text{ s}^{-1}$ at 20K. The 80K mobility of several I-doped and undoped HgCdTe layers with carrier concentrations in the ranges of $(1-3) \times 10^{15}$ and $(3-20) \times 10^{14} \text{ cm}^{-3}$, respectively, and x -values in the range of 0.20–0.25 are shown in Fig. 1. The mobility data of the MOCVD grown layers are compared with state-of-the-art liquid phase epitaxy (LPE) HgCdTe shown by the solid line.¹³ The solid line is a polynomial fit to a large number of In-doped LPE HgCdTe films at $(1-2) \times 10^{15} \text{ cm}^{-3}$ grown on CdTe or CdZnTe using a horizontal slider from Te-rich solution. The mobility data for the iodine doped MOCVD-IMP grown HgCdTe are in general higher than the data for undoped layers and are comparable to recent LPE data. By correlating 80K carrier concentrations from Hall measurements with secondary ion mass spectrometry (SIMS) data, we have shown⁴ that the iodine atoms are singly ionized donors with an activation efficiency of 100% over the range of 7×10^{14} – $2 \times 10^{18} \text{ cm}^{-3}$. I-doped LWIR HgCdTe at low 10^{15} cm^{-3} donor concentration exhibit Auger recombination limited lifetimes⁴ of 1 μs at 80K. The lifetime results are comparable to those reported for In-doped LPE HgCdTe with the same carrier concentration and alloy composition.¹⁴ We have also found that EI does not react with DMCD or DiPte in a manner that the HgCdTe alloy composition is affected when it is switched on or off and no memory effect was observed. These data demonstrate the effectiveness of EI as a precursor and the iodine

donor impurity in MOCVD of detector quality HgCdTe.

P-Type Doping

As-doping during MOCVD of HgCdTe films has been achieved in the range of 3×10^{15} – $5 \times 10^{17} \text{ cm}^{-3}$ using both TBAs and the DMAAs precursors. Detailed temperature dependent Hall effect measurements show classical p-type characteristics with the expected freezeout behavior in the Hall carrier concentration as a function of inverse temperature. The mobilities of $x=0.30$ layers are in the range of 160–400 $\text{cm}^2/\text{V-s}$ at 80K depending on the carrier concentration.

For p-type HgCdTe ($x = 0.21$) doped using TBAs, we have previously reported¹⁵ that longer lifetimes were

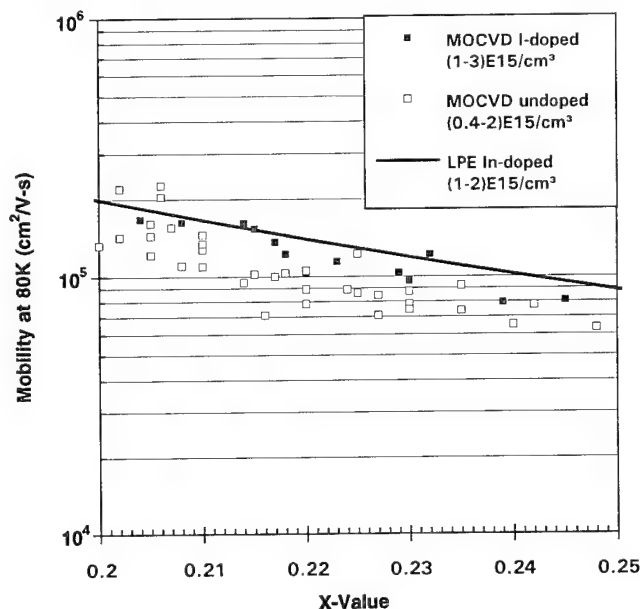


Fig. 1. 80K mobility of I-doped and undoped MOCVD-IMP HgCdTe vs x -value. The solid line is a polynomial fit to 80K mobilities of recent LPE grown In-doped HgCdTe at $(1-2) \times 10^{15} \text{ cm}^{-3}$.

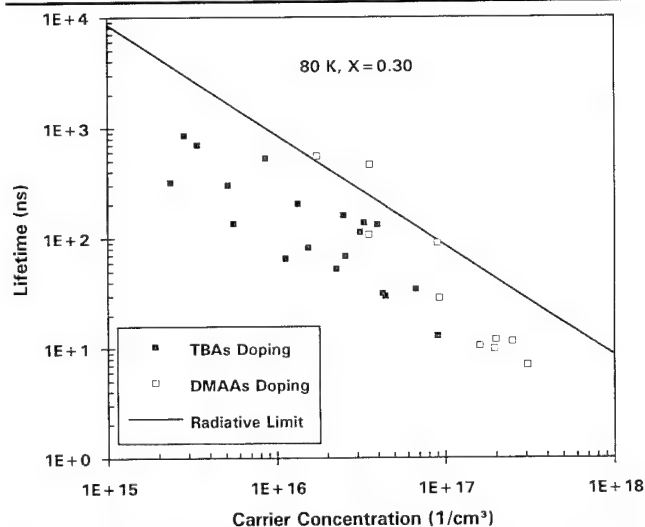


Fig. 2. Transient lifetime data at 80K of MOCVD grown p-type, As-doped HgCdTe ($x = 0.30 \pm 0.01$) using tertiarybutylarsine and tris-dimethylaminoarsenic.

P-on-n MOCVD HgCdTe on 2cm x 1.5cm CdZnTe (100) 4 deg to <110>			
35.6	35.4	36.4	32.8
35.7	37.5	36.8	32.5
36.7	35.7	38.5	37.2

Fig. 3. X-ray double crystal rocking curve map on an LWIR P-on-n heterojunction film grown on a (100) CdZnTe substrate. The film area is 2×1.5 cm.

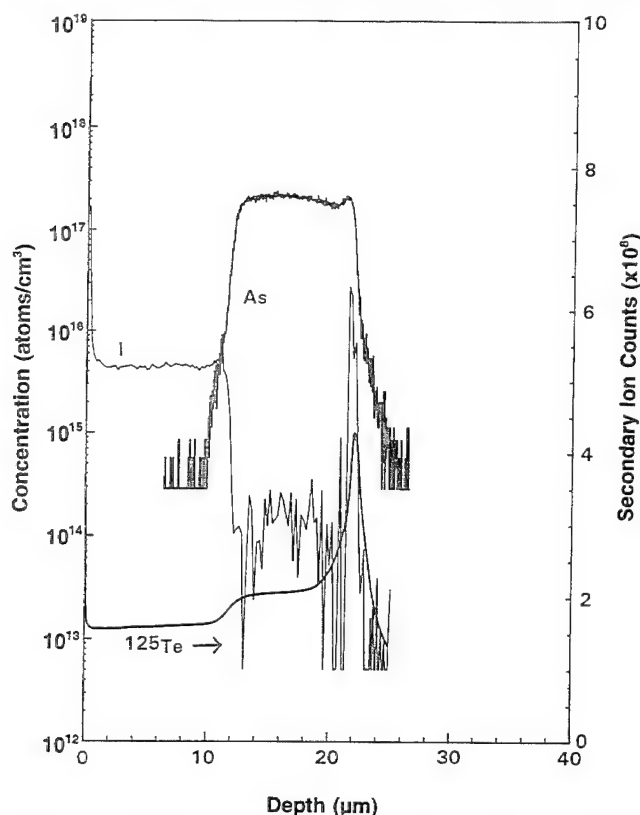


Fig. 4. Secondary ion mass spectroscopy depth profile of composition (^{125}Te), iodine, and arsenic in MOCVD *in situ* grown MWIR n-on-P HgCdTe heterojunction. Data on photodiodes fabricated from this film are shown in Fig. 5.

obtained for As-doped as compared to vacancy-doped HgCdTe for the same carrier concentration and composition. In Fig. 2, the 80K transient lifetimes of several $x = 0.30$ As-doped films and the radiative lifetime calculation are plotted as a function of the 80K Hall concentrations. The data include As-doped films grown with both TBAs and the DMAAs precursors. Lifetime measurements were performed using

the transient millimeter wave reflectance technique.¹⁶ The data show that the lifetimes of the TBAs doped films are always below the calculated radiative limit and in the best cases are lower by a factor of 2–3. Furthermore, in these films with carrier concentrations $>10^{17} \text{ cm}^{-3}$, lifetimes could not be measured reliably within the lower temporal resolution instrument limit of ~ 5 ns. For the films doped using DMAAs with carrier concentrations below 10^{17} cm^{-3} , the lifetimes are significantly longer and are at the radiative limit. For carrier concentrations $>10^{17} \text{ cm}^{-3}$, reliable lifetimes could be measured for the films doped using DMAAs but are below the radiative limit. Our lifetime data of the p-type films doped with DMAAs are similar to that obtained by Bevan et al.⁹ and for concentrations $\leq 10^{17} \text{ cm}^{-3}$ are comparable to that measured in As-doped HgCdTe grown by Hg-rich LPE.¹⁷ These data suggest that DMAAs may be a more promising precursor for p-type doping of HgCdTe than TBAs.

X-Ray Characterization

X-ray double crystal rocking curve (DCRC) measurements have been performed to assess the epitaxial quality of the *in situ* grown heterojunctions. In Fig. 3, a DCRC full width at half maxima map of the an LWIR P-on-n heterojunction grown on a $2 \times 1.5 \text{ cm}^2$ CdZnTe substrate oriented $(100)4^\circ \rightarrow \langle 110 \rangle$ is shown. The DCRC measurements were made using the Cu-K_α line with a beam spot 1 mm wide. The (400) reflection was used. The DCRC map shows that the crystalline quality of this 15 μm thick double layer heterojunction is highly uniform with values in the narrow range of 33–39 arc-sec. It should be noted that the DCRC lineshape has two unresolved components folded in from the two lattice constants of the heterostructure. When the wider bandgap cap layer is etched off, a DCRC width of 30 arc-sec is obtained which approaches the corresponding DCRC width obtained on the substrate of ~ 25 arc-sec.

MWIR n-on-P PHOTODIODES

We have previously reported a new dual-band HgCdTe detector, grown *in situ* by MOCVD, that consisted of an LWIR p-on-n photodiode on top of an MWIR n-on-p photodiode.³ This device was fabricated from a four-layer p-n-N-P HgCdTe film grown *in situ* on a CdZnTe substrate by MOCVD-IMP. Our data for this dual-band device showed that the MWIR n-on-p homojunction photodiodes at 80K had good R_0A products, generally above $1 \times 10^5 \text{ ohm-cm}^2$ for a cutoff wavelength of 4.5 μm . However, the quantum efficiencies were anomalously low, 8–14 %, and in some cases the response spectra were sharply peaked. We attributed these low quantum efficiencies and peaked spectra to interface recombination at the film-substrate interface.

To eliminate the effects of interface recombination and achieve higher quantum efficiencies, the MWIR detector was grown *in situ* in the n-on-P heterojunction configuration. In this structure, the p-type layer is a

wide gap window layer and the n-type absorber layer is well removed from the substrate-film interface. To the best of our knowledge, we report here for the first time the growth and diode characterization for this type of HgCdTe n-on-P heterojunction, although some of its benefits have recently been analyzed theoretically.¹⁸

Secondary ion mass spectrometry depth profiles of the alloy composition, iodine and arsenic dopant levels of one of these films is shown in Fig. 4. Secondary ion mass spectrometry analyses of the ^{125}Te , As, and I profiles were obtained using Cs^+ ion bombardment. The composition profile was determined from the ^{125}Te secondary ion yield¹⁹ and calibrated against the Fourier transform infrared (FTIR) determined alloy composition of the narrower bandgap layer. For the dopants, the data were quantified using relative sensitivity factors determined from ion implant standards of known dosage into HgCdTe and should be accurate to within a factor of 2. The I profile was corrected for the $(^{126}\text{Te}+^1\text{H})^-$ molecular ion interference at nominal mass 127 by monitoring $(^{128}\text{Te}+^1\text{H})^-$ and using natural isotopic abundances ($^{126}\text{Te}/^{128}\text{Te} = 0.589$) to subtract out the molecular contribution.

The n-on-P heterojunctions were processed into backside illuminated variable area circular mesa photodiode arrays that were passivated with ZnS.²⁰ These consisted of 43 elements with radii in the 20–175 μm range. The arrays were bump interconnected to a circuit board and tested in the backside illumi-

nated configuration without any antireflection coating on the substrate surface. The photodiodes were characterized for current-voltage (I-V) curves, zero bias resistance area product R_0A , quantum efficiency, effective lateral optical collection length, and spectral response at 80 K. The one-dimensional quantum efficiency ($\text{QE}(1D)$) and the optical collection length L_{opt} were deduced from the dependence of quantum efficiency on junction area in the variable-area arrays. Figure 5 shows spectral response and I-V data for a photodiode from an array fabricated from an n-on-P heterojunction film. High quantum efficiencies are routinely observed in all the n-on-P heterojunction films. The one-dimensional quantum efficiency for this array was 72%, close to the maximum quantum efficiency that can be achieved with no antireflection coating. The R_0A product for the array with a cutoff wavelength of 4.95 μm is $(1-3) \times 10^5 \text{ ohm-cm}^2$ and is consistent with other arrays processed with the same cutoff wavelength. R_0A data obtained from a large number of test arrays from the n-on-P heterojunction diodes are plotted in Fig. 11 which is discussed in the next section. Very few outages were observed for these test arrays.

The spectral response data in Fig. 5 (upper curve is per watt, lower curve is per photon) show clearly the onset of transmission for the wide gap window layer at 2.4 μm . For wavelengths less than 2.4 μm , most of the photons are absorbed in the window layer, and the resulting photocarriers undergo recombination at the

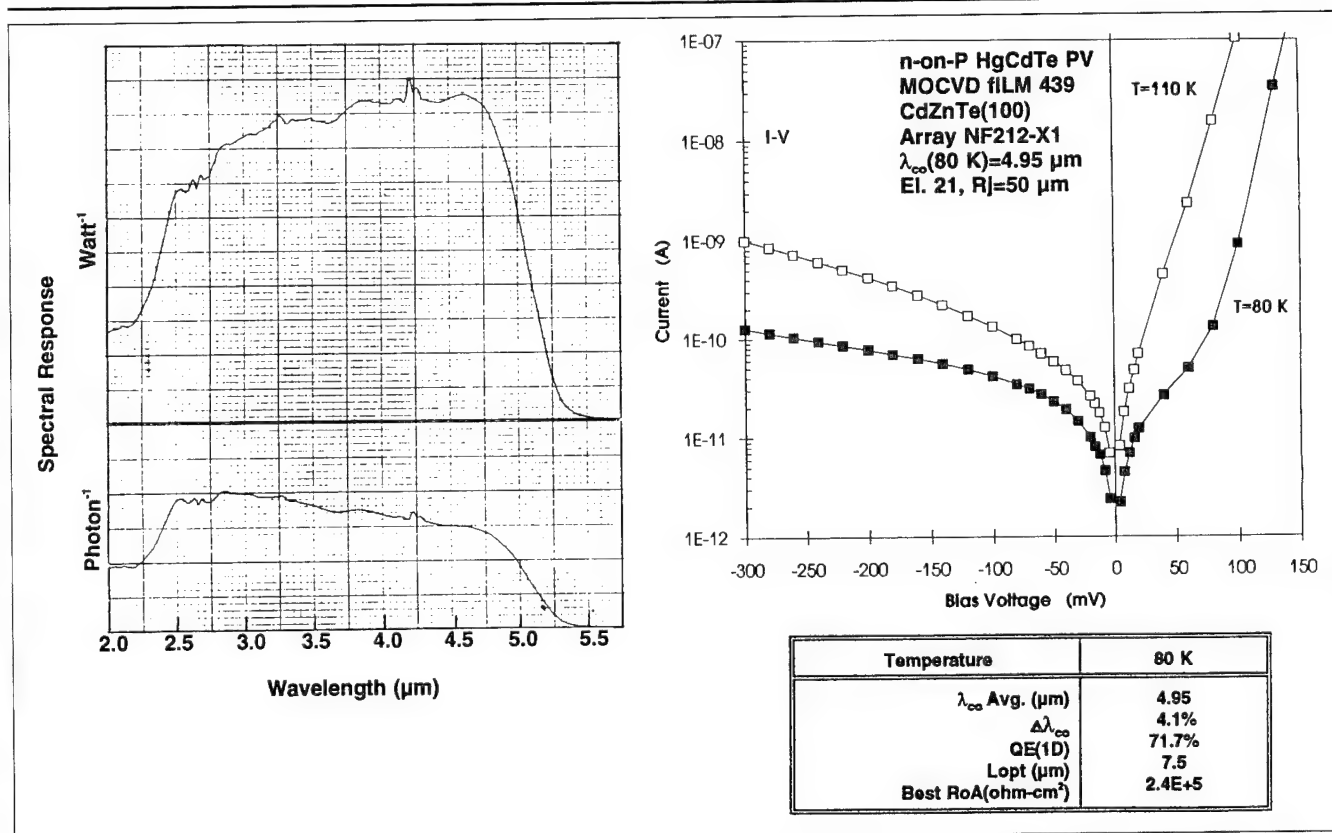


Fig. 5. Spectral response and I-V curves for a MOCVD *in situ* grown n-on-P heterojunction with arsenic and iodine doping and 80 K cutoff wavelength of $\sim 5 \mu\text{m}$.

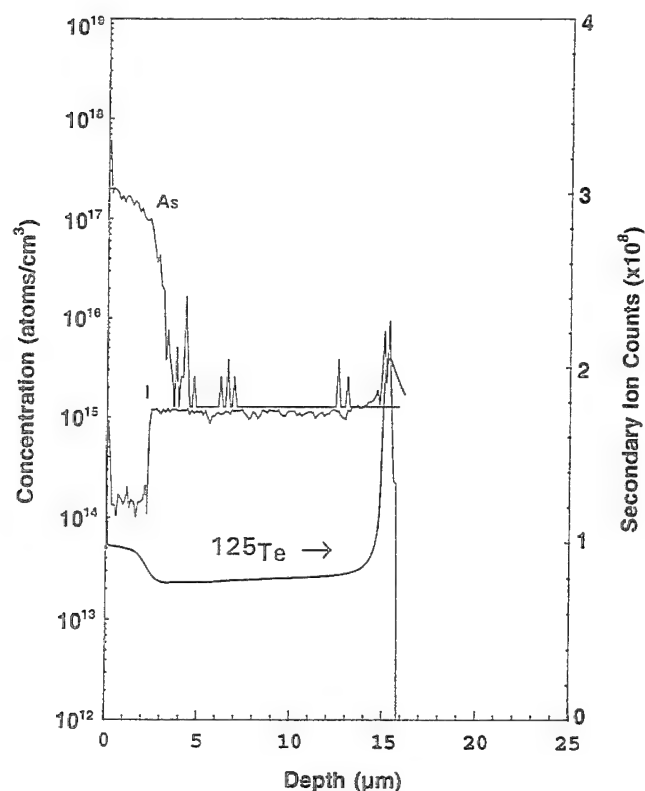


Fig. 6. Secondary ion mass spectroscopy depth profile of composition (^{125}Te), iodine, and arsenic in MOCVD *in situ* grown P-on-n HgCdTe heterojunction.

substrate-film interface and do not contribute to the photocurrent.

LWIR P-on-n PHOTODIODES

A representative SIMS depth profile of an iodine and arsenic doped p-on-n heterojunction grown *in situ* on a CdZnTe (100) substrate is shown in Fig. 6. In the growth of this structure, the iodine doping was switched off when the arsenic doping was switched

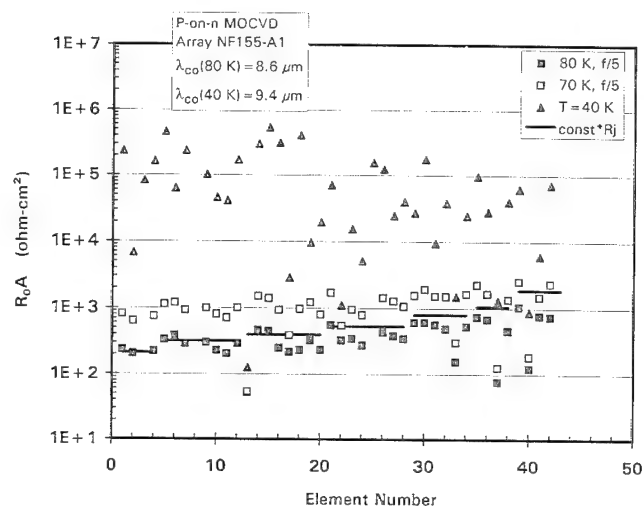
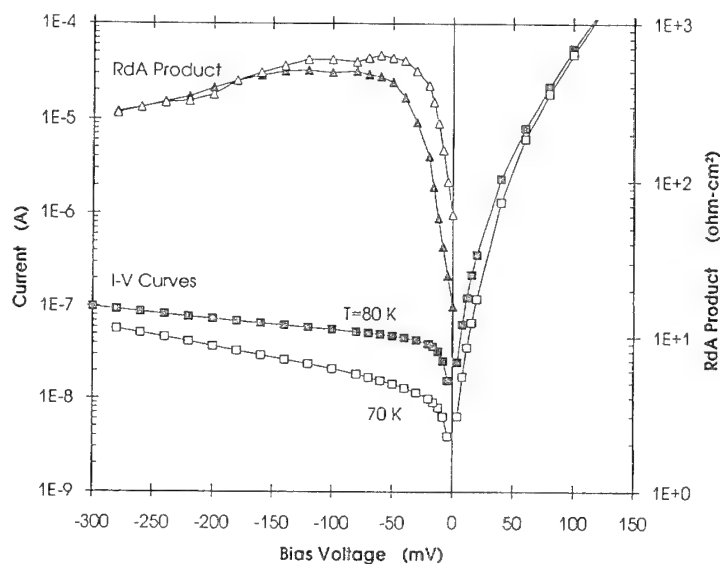
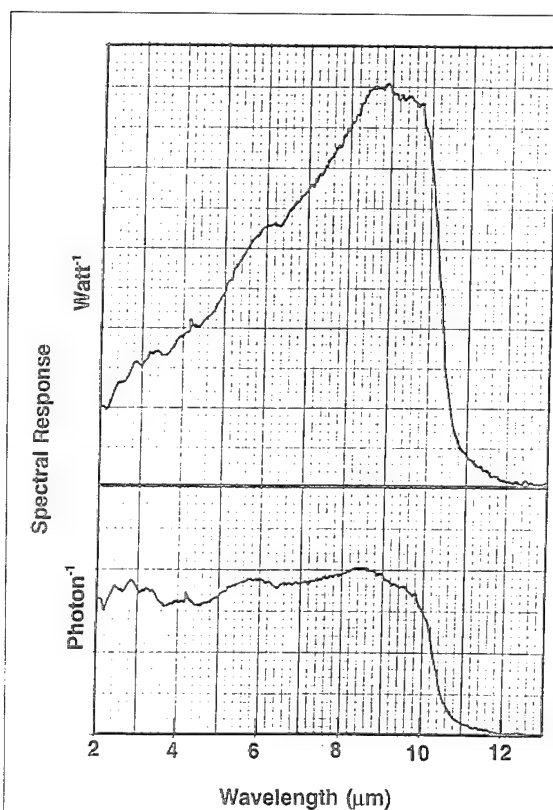


Fig. 7. R_0A data from a 43 element LWIR variable area array at 80, 70, and 40K. The data are plotted with increasing junction radius. $R_j = 20, 30, 38, 50, 75, 100,$ and $175 \mu\text{m}$.



$\lambda_{co} (80 \text{ K}) = 10.4 \mu\text{m}$
Junction Radius = $50 \mu\text{m}$

Temperature	80 K	70 K
QE (1D)	58%	51%
L_{opt}	20 μm	18 μm
Best R_0A	18.9 $\Omega\text{-cm}^2$	66.2 $\Omega\text{-cm}^2$

Fig. 8. Spectral response, I-V and R_0A plots for a MOCVD *in situ* grown P-on-n heterojunction on CdZnTe (100) with arsenic and iodine doping and 80K cutoff wavelength of $10.4 \mu\text{m}$.

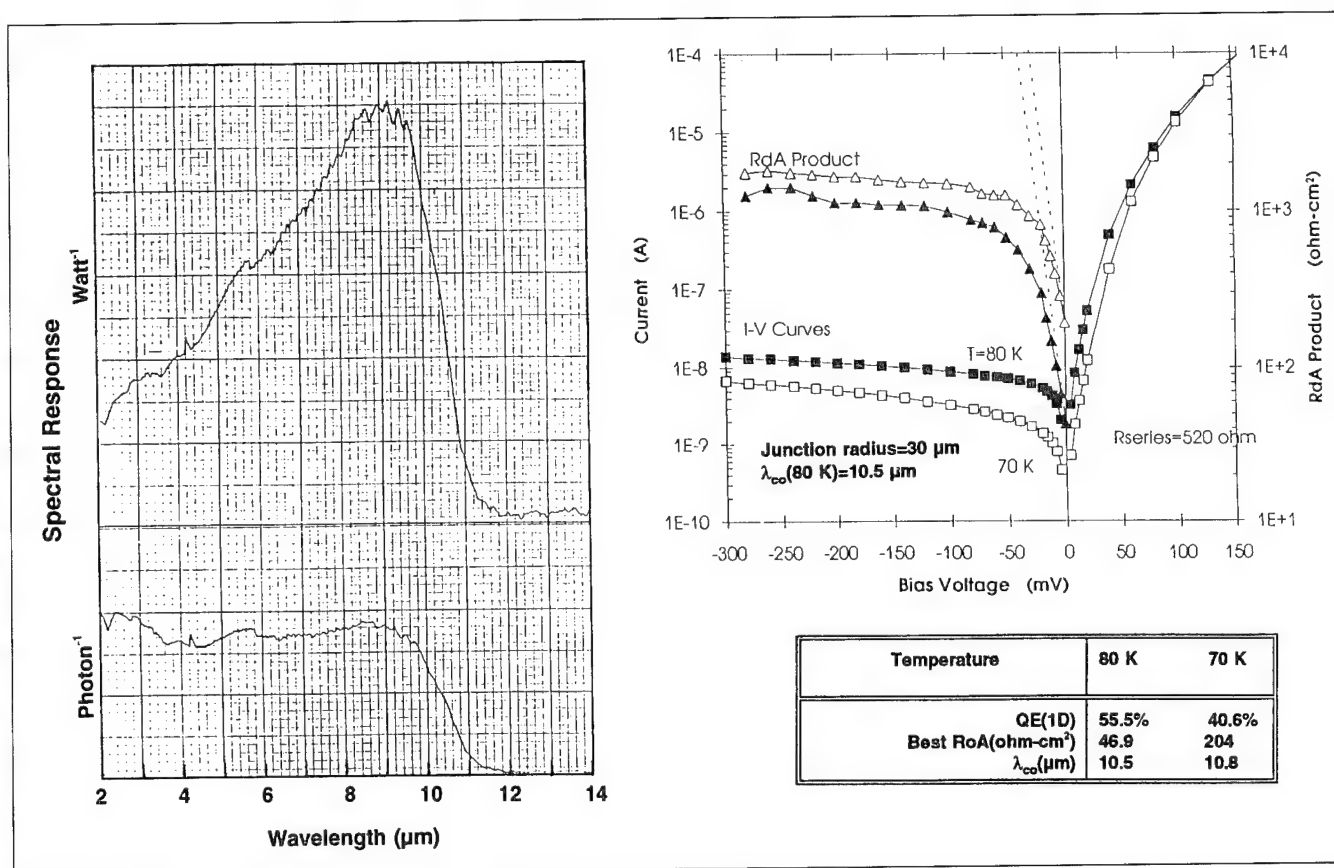


Fig. 9. Spectral response, I-V and R_0A plots for a MOCVD *in situ* grown P-on-n heterojunction on CdZnTe (211)B with 80K cutoff wavelength of 10.5 μm .

on. The iodine doping level falls off abruptly due to the slow diffusion rate at the growth and anneal temperature. The arsenic dopant on the other hand shows significant diffusion of $\sim 1.5 \mu m$ and an approximate Gaussian profile. The composition profile was obtained from the ^{125}Te secondary ion intensity. Some alloy interdiffusion is evident between the narrow gap and wide gap compositions, but not to the extent that the junction overlaps with the graded region. Thus, valence band barriers are not expected to form. Iodine, due to its low diffusivity, acts as an effective marker for determining the location of the prediffused onset of composition change and arsenic doping. This permits the alloy interdiffusion and arsenic diffusion kinetics to be easily evaluated. Dislocations measured on most of the heterojunctions using an etchant described by Hahnert and Schenk²¹ gave etch pit density values in the range of $(1-2) \times 10^6 cm^{-2}$.

Variable-area photodiode arrays were fabricated on the P-on-n heterojunctions in the same manner as the n-on-P diodes described in the previous section. The photodiodes were characterized for I-V curves, zero bias resistance-area product R_0A , the dynamic resistance area product $R_D A$, quantum efficiency, effective lateral optical collection length, and spectral response at 80K. Selected diodes were characterized down to temperatures of 25K.

The R_0A data at 80, 70, and 40K for an entire 43 element array are plotted in Fig. 7, in order of in-

creasing junction radius from 20 to 175 μm . The P-on-n heterojunction was grown on a CdZnTe (100) substrate. The data at 80 and 70K are reasonably uniform within each junction radius group. The R_0A product shows a trend to increase with increasing junction radius, in this ZnS passivated array, which is caused in part by perimeter-only current mechanism such as surface g-r current. This indicates that the R_0A data are partially limited by surface mechanisms and improvement in R_0A is expected with improved passivation. The 80K cutoff wavelength for this array is $8.6 \pm 0.03 \mu m$ and $L_{opt} = 16 \mu m$. The one-dimensional quantum efficiency QE (1D) at 80K is 62%, compared to the maximum of 78% possible for no antireflection coating. Figure 7 shows that the R_0A data at 40K for many elements are orders of magnitude higher than at 80K. The highest R_0A value at 40K is $5 \times 10^5 \Omega \cdot cm^2$. The cutoff wavelength at 40K is 9.4 μm . These are the highest reported R_0A values for HgCdTe heterojunctions grown *in situ* by MOCVD. The 40K R_0A product, however, does not show the same perimeter dependence observed in the 80 and 70K data. This is quite possibly because at 40K the R_0A values are limited by bulk defects rather than surface effects.

Diode data for an element with 50 μm radius from an array grown on a CdZnTe (100) substrate are shown in Fig. 8. The 80K ($\lambda_{co} = 10.4 \mu m$) spectral response per watt (upper curve) and per photon (lower

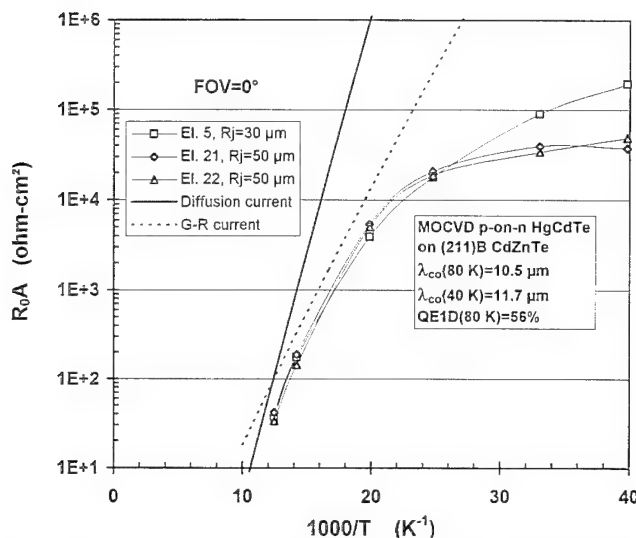


Fig. 10. Temperature dependence of R_0A value from the LWIR P-on-n heterojunction in Fig. 9.

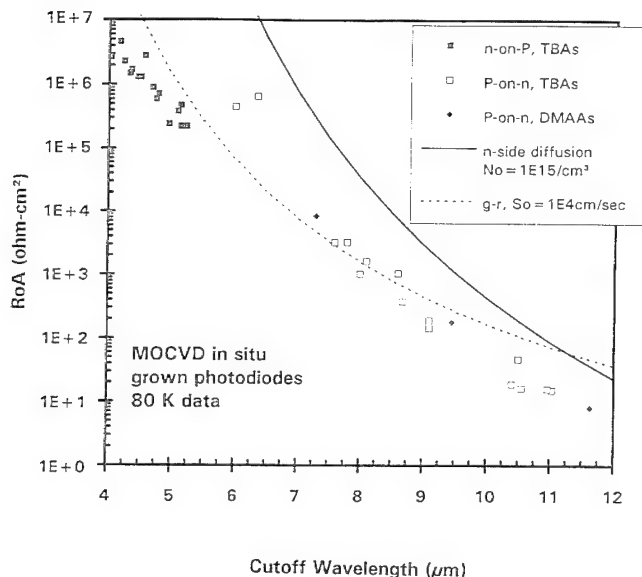


Fig. 11. R_0A vs cutoff wavelengths at 80K for MOCVD *in situ* grown MWIR and LWIR HgCdTe photodiodes using iodine and arsenic doping. The solid and the dotted lines depict calculated R_0A values as described in the text.

curve) are classical in shape, indicative of a long diffusion length in the n-type absorber layer and negligible recombination at the film-substrate interface. The one-dimensional quantum efficiency QE (1D) for this array at 80K is 58%. The I-V curves and R_0A product at 80 and 70K, also shown in Fig. 8, are well behaved. The R_0A product increases from $18.9 \Omega\text{-cm}^2$ at 80K to $66.2 \Omega\text{-cm}^2$ at 70K, about a factor of 3.5, which is slightly greater than the factor of three expected theoretically for pure g-r current with an ideal $n_i(x,T)$ temperature dependence.

The I-V and spectral response data for an element ($\lambda_{co}(80K) = 10.4 \mu\text{m}$) from another array grown on a

CdZnTe (211)B substrate are shown in Fig. 9. Here also spectral response data are classical in shape, with a QE(1D) of 56%. The I-V curves are well-behaved, with no sign of significant tunneling current even out to -300 mV reverse bias. The dynamic resistance R_D at 80K increases by over an order of magnitude from 0 to -50 mV . The R_0A product increases from $46.9 \Omega\text{-cm}^2$ at 80K to $204 \Omega\text{-cm}^2$ at 70K, a factor of 4.35 which is greater than the factor of three expected from pure g-r current, indicating a combination of g-r and diffusion current dominating the R_0A at 80K. These trends can be seen also in the data for R_0A vs $1/T$ in Fig. 10, which shows three elements following a characteristic g-r temperature dependence down to 50K and beginning to follow the characteristic diffusion current temperature dependence at 80K. Note that R_0A has increased to $2 \times 10^4 \Omega\text{-cm}^2$ at 40K, at which temperature the cutoff wavelength is calculated to be $11.7 \mu\text{m}$.

All of the above LWIR photodiodes were grown using TBAs for As-doping. A few LWIR heterojunctions were grown with the DMAAs precursor for As-doping. The photodiode I-V characteristics and QE(1D) in these first P-on-n junctions grown with DMAAs were comparable to the best diodes grown using TBAs. R_0A data vs cutoff wavelengths at 80K are plotted in Fig. 11 for the best elements from variable-area arrays from a large number of P-on-n and n-on-P films grown *in situ* by MOCVD. In all cases, the spectral response data were classical in shape and quantum efficiencies were above 50%. I-V curves were well behaved with g-r current generally the dominant mechanism near zero bias voltage at 80K.

The solid line in Fig. 11 is the calculated R_0A due to diffusion current from the n-layer only for a thickness of $15 \mu\text{m}$ and a lifetime determined by Auger recombination mechanism. The dashed line is the calculated R_0A due to depletion layer g-r current, for doping levels of 1×10^{15} and $1 \times 10^{17} \text{ cm}^{-3}$ on the n-side and p-side, respectively, and for a depleted surface recombination velocity S_0 of $1 \times 10^4 \text{ cm/s}$. From Fig. 11, it is evident that the LWIR diodes grown using the DMAAs precursor and I-doping have 80K R_0A products comparable to the best achieved using TBAs as the As-precursor.

CONCLUSION

This paper has shown that iodine doping performed using the EI precursor improves the mobility of MOCVD grown HgCdTe over the undoped background annealed films, and these mobilities are comparable to state-of-the-art HgCdTe films grown by Te-rich LPE. The use of EI for donor doping was shown to be highly effective in controlling the absorber layer doping for heterojunctions. Medium wavelength infrared photodiodes grown *in situ* in the n-on-P heterojunction configuration show well-behaved performance with classical spectral response, high one-dimensional quantum efficiency (70–75%), and R_0A products of $2 \times 10^5 \text{ ohm-cm}^2$ at 80K for cutoff wavelength of $5.5 \mu\text{m}$. This device configuration solves the problem of

peaked spectral response and low quantum efficiency observed previously.³ Arsenic doping with DMAAs was shown to produce longer lifetimes than with TBAs for the same acceptor concentration in $x = 0.30$ HgCdTe. The improved lifetimes in the As-doped films suggest improved junction performance with this precursor. With better control of alloy composition and doping, the properties of HgCdTe LWIR diodes grown *in situ* by MOCVD in the P-on-n heterojunction configuration have shown significant improvement over that achieved previously.¹ The spectral response is always classical in shape, quantum efficiency high, in the 50–60% range, for these backside illuminated photodiodes. The I-V curves are well-behaved. The photodiodes exhibit large increases in R_D at reverse bias voltage and R_0A products limited by g-r current at 80K. The R_0A data at 40K of $2 \times 10^4 \Omega\text{-cm}^2$ for $\lambda_{co} = 11.7 \mu\text{m}$ and $5 \times 10^5 \Omega\text{-cm}^2$ for $\lambda_{co} = 9.4 \mu\text{m}$ are the highest reported for P-on-n HgCdTe heterojunctions grown *in situ* by MOCVD. The first LWIR photodiodes using the DMAAs precursor for As-doping exhibit performance comparable to the best achieved by using TBAs. These results are most encouraging and provide the motivation for continued development of *in situ* MOCVD growth of HgCdTe junctions with improved uniformity and array reproducibility.

ACKNOWLEDGMENTS

We are grateful to Dr. L.T. Claiborne for his encouragement and support. This work was supported by the U.S. Naval Research Laboratory Contracts N00014-91-C-2357 and N00014-93-C-2114, Dr. J.P. Omaggio C.O.T.R., and by Loral internal research funds.

REFERENCES

1. P. Mitra, T.R. Shimert, F.C. Case, R. Starr, M.H. Weiler, M. Kestigian and M.B. Reine, *J. Electron. Mater.* 24, 661 (1995).
2. P. Mitra, T.R. Shimert, F.C. Case, Y.L. Tyan, M. Kestigian, R. Starr, M.H. Weiler and M.B. Reine, *Proc. SPIE* 2228, 96 (1994).
3. M.B. Reine, P.W. Norton, R. Starr, M.H. Weiler, M. Kestigian, B.L. Musicant, P. Mitra, T. Shimert, F.C. Case, I.B. Bhat, H. Ehsani and V. Rao, *J. Electron. Mater.* 24, 669 (1995).
4. P. Mitra, Y.L. Tyan, T.R. Shimert and F.C. Case, *Appl. Phys. Lett.* 65, 195 (1994).
5. C.D. Maxey, I.G. Gale, J.B. Clegg and P.A.C. Whiffin, *Semicond. Sci. Technol.* 8, S183 (1993).
6. R. Korenstein, P.H. Hallock, D.L. Lee, E. Sullivan, R.W. Gedridge, Jr. and K.T. Higa, *J. Electron. Mater.* 22, 853 (1993).
7. S.J.C. Irvine, J. Bajaj, L.O. Bubulac, W.P. Lin, R.W. Gedridge, Jr. and K.T. Higa, *J. Electron. Mater.* 22, 859 (1993).
8. S. Murakami, T. Okamoto, K. Maruyama and H. Takigawa, *Appl. Phys. Lett.* 63, 899 (1993).
9. M.J. Bevan, M.C. Chen and H.D. Shih, Texas Instruments, Dallas, TX private communication, (1994) to be published.
10. C.R. Abernathy, P.W. Wisk, D.A. Bohling and G.T. Muhr, *Appl. Phys. Lett.* 60, 2421 (1992).
11. D.A. Bohling, C.R. Abernathy and K.F. Jensen, *J. Cryst. Growth* 136, 118 (1994).
12. S.J.C. Irvine, J. Bajaj and L.O. Bubulac, *Mat. Res. Soc. Symp. Proc.* 299 (Pittsburgh, PA: MRS, 1994), p. 99.
13. S.P. Tobin, Loral Infrared & Imaging Systems, Lexington, MA, private communication.
14. V.C. Lopes, A.J. Syllaos and M.C. Chen, *Semicond. Sci. Technol.* 8, 824 (1993).
15. P. Mitra, T.R. Shimert, Y.L. Tyan, A.J. Brouns and F.C. Case, *Mat. Res. Soc. Symp. Proc.* 302 (Pittsburgh, PA: MRS, 1993), p. 403.
16. A.J. Brouns, T.R. Shimert, P. Mitra, F.C. Case, S.L. Barnes and Y.L. Tyan, *Semicond. Sci. Technol.* 8, 928 (1993).
17. T. Tung, M.H. Kalisher, A.P. Stevens and P.E. Herning, *Mat. Res. Soc. Symp. Proc.* 90 (Pittsburgh, PA: MRS, 1987), p. 321.
18. D. Rosenfeld, V. Garber and G. Bahir, *J. Appl. Phys.* 76, 4399 (1994).
19. L.O. Bubulac and C.R. Viswanathan, *Appl. Phys. Lett.* 60, 222 (1992).
20. M.B. Reine, K.R. Maschhoff, S.P. Tobin, P.W. Norton, J.A. Mroczkowski and E.E. Krueger, *Semicond. Sci. Technol.* 8, 788 (1993).
21. I. Hahnert and M. Schenk, *J. Cryst. Growth* 101, 251 (1990).

Real-Time Control of HgCdTe Growth by Organometallic Vapor Phase Epitaxy Using Spectroscopic Ellipsometry

SRIKANTESWARA DAKSHINA MURTHY and ISHWARA BHAT

ECSE Department, Rensselaer Polytechnic Institute, Troy NY 12180

BLAINE JOHS, SHAKIL PITTAL, and PING HE

J.A. Woollam Co., 650 J Street, Suite 39, Lincoln, NE 68508

The use of spectroscopic ellipsometry for monitoring the vapor phase epitaxial growth of mercury cadmium telluride ($\text{Hg}_{1-x}\text{Cd}_x\text{Te}$) in real-time is demonstrated. The ellipsometer is used to perform system identification of the chemical vapor deposition reactor used for the growth of CdTe and to measure the response of the reactor to different growth conditions. The dynamic behavior of the reactor is also studied by evaluating the gas transport delay. The optical constants of $\text{Hg}_{1-x}\text{Cd}_x\text{Te}$ are determined at the growth temperature for different compositions. *In-situ* real-time composition control is performed during the growth of $\text{Hg}_{1-x}\text{Cd}_x\text{Te}$. The required target compositions are attained by the ellipsometer and appropriate corrections are also made by the controller when a noise input in the form of a temperature variation is introduced.

Key words: HgCdTe, *in-situ* monitoring, real-time control, spectroscopic ellipsometry

INTRODUCTION

There is a need for *in-situ*, non-invasive, and real-time monitoring techniques to be developed for use on chemical vapor deposition (CVD) systems in order to achieve reliable control over growth and also to understand the growth process. *In-situ* ellipsometry has shown promise in studying and controlling the growth of various compound semiconductors¹ including $\text{Hg}_{1-x}\text{Cd}_x\text{Te}$ (MCT),^{2,3} where reliable achievement of the desired composition from run to run is found to be difficult.

The determination of suitable operating parameters for the growth of material in the CVD system is also not easily done. Many iterations are required before the proper conditions are established. This can be resolved by using the real-time monitoring capability of ellipsometry to perform "system identification" on the CVD reactor used for growth. This involves studying the growth under different reactor conditions. Both steady state and dynamic response of the growth parameters to changes in reactor conditions such as

reactant flow rates and susceptor temperature can be monitored. This allows the determination of a suitable "operating point" for the reactor within a couple of growth runs. Without the ellipsometer, a trial-and-error technique will take much longer to achieve the same result. The results of the system identification can also be used to design an appropriate control algorithm for controlling the composition and/or the growth rate of the growing material.

HARDWARE AND DATA ANALYSIS

A 44-wavelength spectroscopic ellipsometer (J.A. Woollam Co. NE 68508) was used for the real-time monitoring. The data acquisition and analysis were done using the WVASETM software. The details of the ellipsometer system, *in-situ* mount, modeling techniques^{3,4} and preliminary results on *in-situ* studies of CdTe⁴ and HgCdTe³ have been discussed at length elsewhere, and will not be dealt with here.

EXPERIMENTAL RESULTS

System Identification During Growth of CdTe

The growth of CdTe by organometallic vapor phase

(Received October 4, 1994; revised January 5, 1995)

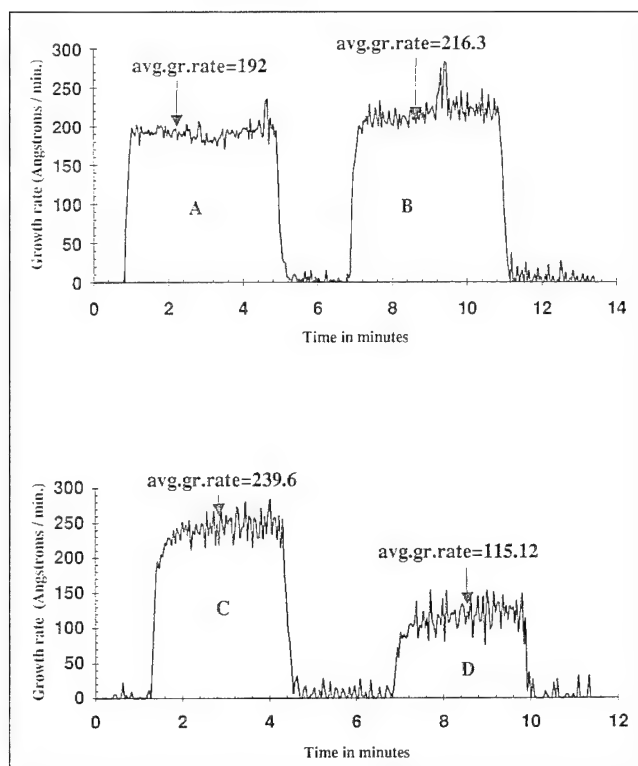


Fig. 1. Instantaneous growth rate of CdTe on GaAs at 350°C for different settings of the dimethylcadmium mass flow controller 30 (A), 45 (B), 60 (C), and 20% (D).

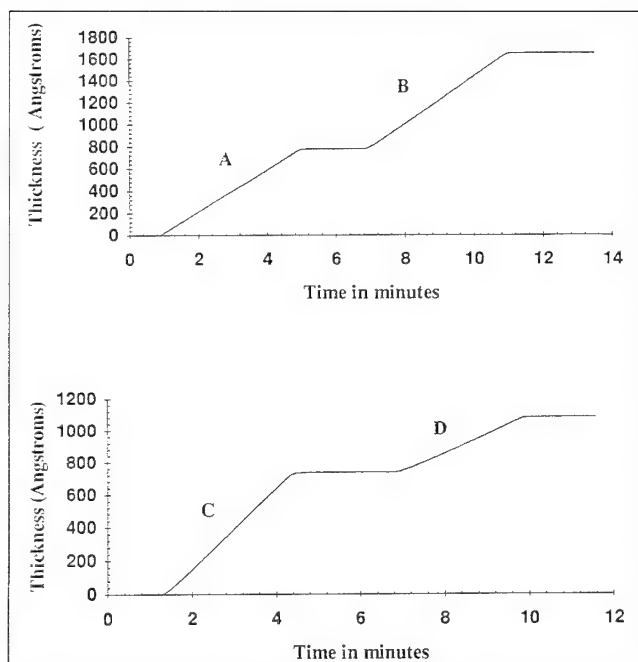


Fig. 2. Variation of CdTe layer thickness with time for different settings of the dimethylcadmium mass flow controller: 30 (A), 45 (B), 60 (C), and 20% (D).

epitaxy was carried out on GaAs (100) substrates, misoriented toward $\langle 110 \rangle$ by 10° . Dimethylcadmium (DMCd) and di-isopropyltelluride (DIPTe) were used as the precursors in a carrier gas of H_2 . Reactant partial pressures were 4.7×10^{-4} atm. (DIPTe) and

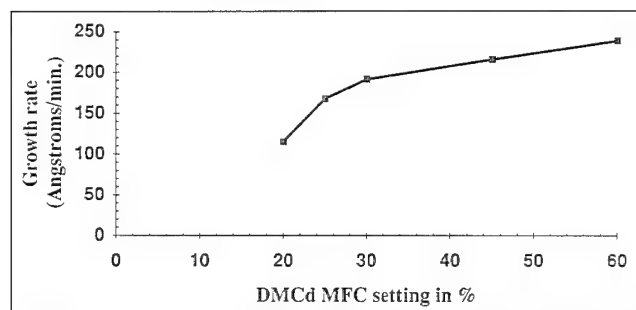


Fig. 3. Variation of CdTe growth rate with setting of the dimethylcadmium mass flow controller.

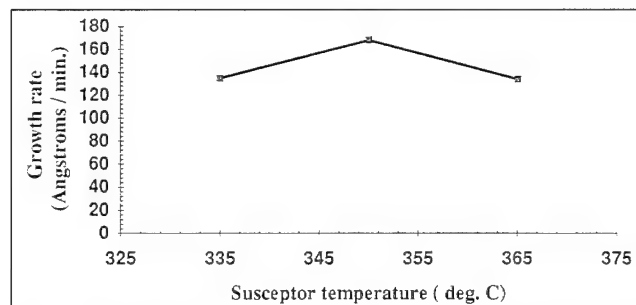


Fig. 4. Variation of CdTe growth rate with susceptor temperature at a fixed flow of H_2 through the dimethylcadmium mass flow controller.

5×10^{-5} atm. (DMCd). This partial pressure of DMCd corresponded to a setting of 30% (15 sccm of H_2) on the DMCd mass flow controller (MFC). The growth was carried out for 15 min and then stopped. Ellipsometric Ψ and Δ data were acquired during this time. The optical constants of CdTe at the growth temperature were determined using this data. These constants were used later on to determine the growth rates of CdTe grown under different conditions.

The first study on the system identification was to determine the growth rates of CdTe obtained at a susceptor temperature of 350°C and reactor pressure of one atmosphere under different partial pressures of dimethyl cadmium (DMCd). The partial pressure of diisopropyltelluride was maintained at 4.7×10^{-4} atm. The initial partial pressure of DMCd used was 5×10^{-5} atm. which corresponded to a DMCd MFC setting of 30%. CdTe was grown for about 4–5 min at various settings above and below this value. The instantaneous growth rates for some of these settings obtained from post-growth analysis are shown in Fig. 1. As we can see, the growth rate at a particular setting is quite constant. There is some noise in the instantaneous growth rate, but this is only of the order of $10 \text{ \AA}/\text{min}$, which corresponds to a variation of a few monolayers of material. As we can see from the thickness vs time data in Fig. 2 for the same cases, the behavior is very steady. The different slopes of the trajectories correspond to the different average growth rates for different settings. Finally, the growth rates at 350°C are plotted vs the corresponding setting of the DMCd mass flow controller in Fig. 3. The growth rate rises sharply for lower flows of DMCd and then flattens out as the flow is increased. This is understandable from a knowledge of the mechanism of the growth.⁵ The

incorporation of tellurium into the layer is caused by a surface-catalyzed pyrolysis of the organometallic tellurium species. The catalyst in this case is cadmium from the dimethylcadmium which readily pyrolyses at this temperature. The amount of cadmium adsorbed on the surface increases as partial pressure of the cadmium species is increased. This brings about a corresponding rise in the growth rate. However, the surface coverage of cadmium adsorbed saturates at higher partial pressures and causes a similar behavior in the growth rate. Note that the II/VI ratio is of the order of 0.1, which ensures that enough of the organometallic tellurium species is available for pyrolysis in all the cases.

The second study was to observe the effect of changing the susceptor temperature on the growth rate of CdTe. The partial pressures of DIPTe used was 4.7×10^{-4} atm. and that of DMCd was 4.16×10^{-5} atm. The susceptor temperature was varied from 350 to 335°C and back up to 365°C. The results of this experiment are shown in Fig 4. At the temperature of 335°C, the surface catalyzed pyrolysis rate of DIPTe is reduced and the growth rate falls appropriately. At the higher temperature of 365°C, the rate of pyrolysis of DIPTe can be expected to be higher, but this merely results in increased depletion of the reactant on the portion of the susceptor upstream of the sample position and a consequently lower growth rate. Thus, 350°C can be taken to be the optimum temperature for the particular configuration.

Information on the system response time is also obtained by taking note of the lag time from the instant at which the gases are diverted from the bypass line into reactor tube to the instant at which the steady growth rate is reached. This has been found to be of the order of 7–8 s. Since the gases travel extremely fast through the 1/4 inch diameter supply tube, we may assume that the major portion of the delay is due to the transit time inside the reactor tube from the gas inlet to the sample. A simple expression for the transit time t_r is given by

$$t_r = l_s / v_g$$

where l_s is the distance from the gas inlet to the sample and v_g is the velocity of the gas stream. Here, v_g is readily obtained from the equation

$$v_g = f_g / (\pi r_t^2)$$

where f_g is the total gas flow rate in standard cubic centimeters/min, and r_t is the inside radius of the reactor tube. Using the particular values for the situation, namely $f_g = 4000$ sccm, $r_t = 3.5$ cm and $l_s = 15$ cm, we obtain a value for the transit time $t_r = 8.7$ s. The observed lag time is slightly smaller but can be explained as a consequence of the reactant diffusing downstream of the flow and reaching the substrate a little faster.

Real-Time Control of HgCdTe Composition

Mercury cadmium telluride ($\text{Hg}_{1-x}\text{Cd}_x\text{Te}$) was grown on (100) GaAs substrates, misoriented 10° toward

$\langle 110 \rangle$, at 350°C and 1 atm. under Te-rich conditions using the direct alloy growth⁶ technique. A CdTe buffer layer was first grown and a multilayer stack of HgCdTe layers of different compositions were grown on this buffer. Ellipsometric data were continuously acquired during growth of HgCdTe of different compositions. The optical constants (at the growth temperature) of the different layers in the stack were

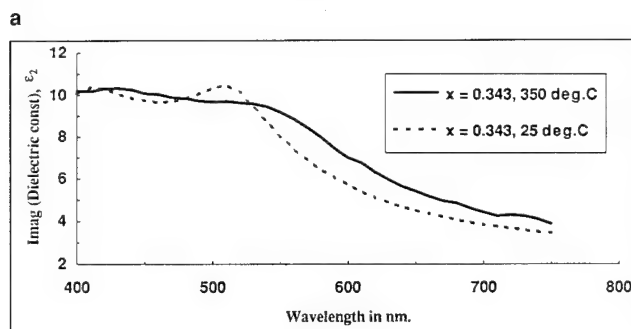
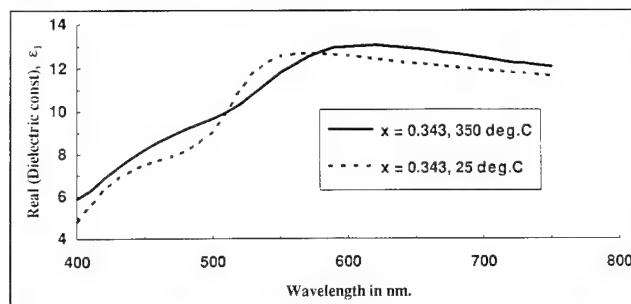


Fig. 5. Real part of the dielectric constant ϵ_1 (A) and imaginary part of the dielectric constant ϵ_2 (B) of $\text{Hg}_{1-x}\text{Cd}_x\text{Te}$ of composition $x = 0.343$ at two different temperatures: 25°C (room temp.) and 350°C.

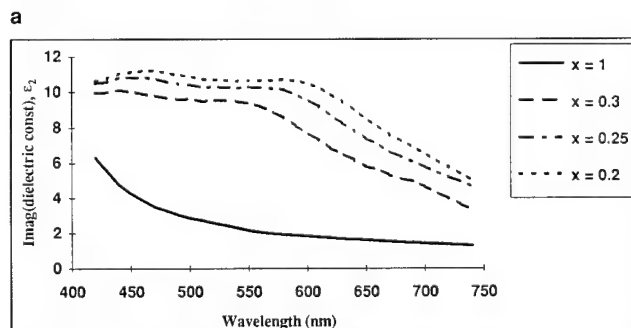
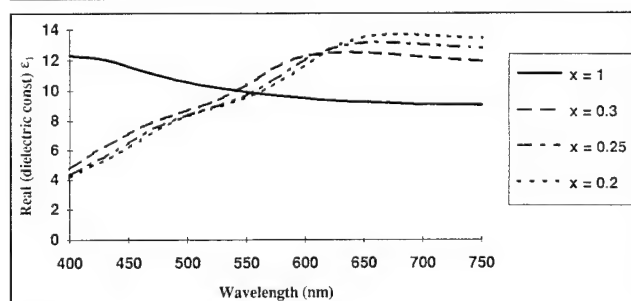


Fig. 6. Real part of the dielectric constant ϵ_1 (A) and imaginary part of the dielectric constant ϵ_2 (B) of $\text{Hg}_{1-x}\text{Cd}_x\text{Te}$ at 350°C for different compositions.

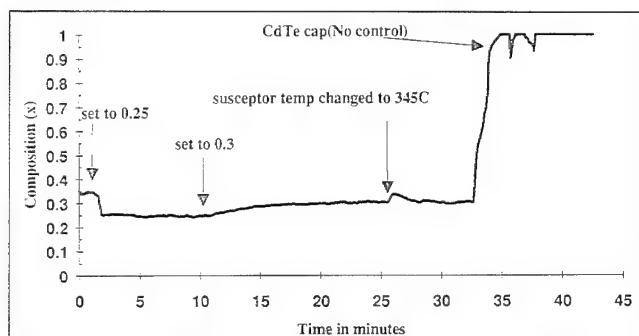


Fig. 7. Real-time monitoring of the composition x of $\text{Hg}_{1-x}\text{Cd}_x\text{Te}$ during a control experiment.

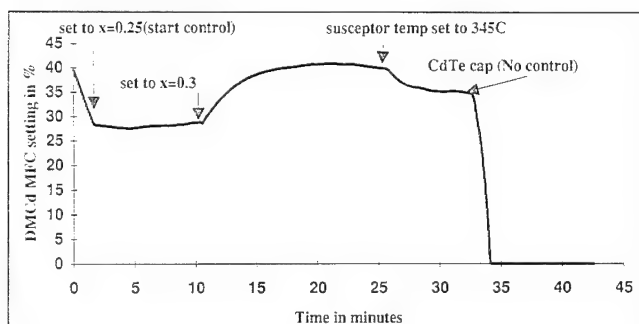


Fig. 8. Instantaneous setting of the dimethylcadmium (DMCd) mass flow controller during the composition control experiment on $\text{Hg}_{1-x}\text{Cd}_x\text{Te}$ growth.

determined using the techniques described previously.³ In order to create a library of optical constants of HgCdTe for different compositions, it was necessary to determine the compositions of the individual layers in the stack. A standard technique like Fourier transform infrared spectroscopy could not be used for this purpose since the resulting spectrum is due to an integrated contribution from all the layers, and it is impossible to resolve them independently. The extensive interdiffusion that occurs between these layers during the growth also prevents the use of this method.

An alternative method was employed to determine the compositions of the layers in the stack. The composition of one of the layers was determined by comparison of its optical constants with the optical constants of a previously grown HgCdTe layer of (known) uniform composition. These constants (Fig. 5) were obtained by heating up the layer to the growth temperature under appropriate Hg overpressure. The composition of a layer is known to be directly related to the energy of the critical point peak⁷ in its dielectric constant spectrum. We assumed that the energy of the critical point peak in the dielectric constant spectrum at the growth temperature varies with composition in a similar manner as it does at room temperature. Thus, knowing the composition of one of the layers in the stack, we could reasonably estimate the composition of the other layers in the stack.

From the results of the above measurements, an alloy file was prepared tabulating the optical constants of the material for different compositions of the material⁸ (Fig. 6). Using the knowledge of these con-

stants, composition control of HgCdTe growth was performed under the same growth conditions. The virtual interface method⁹ was used to obtain the optical constants of incremental layers of HgCdTe grown every few seconds. The critical point-dependent spectrum shifting algorithm¹⁰ was then used to determine the composition in real-time. As can be seen from the optical constant spectra of Fig. 5, the critical point peaks are flattened at higher temperatures, making the precise determination of composition difficult. The composition of the incremental layer thus obtained was then compared with the target and the error was used to correct the setting of the dimethylcadmium mass flow controller using a simple proportional algorithm. The growth rate of the layer was arbitrarily fixed at 3Å/s . This was found to be necessary as the calculated instantaneous growth rate proved to be very noisy since the growth oscillations of a highly absorbing material such as HgCdTe tend to attenuate very rapidly. The assumption of such a constant growth rate is not true, since the growth rate varies with composition. However, it does not affect the composition control because the controller seeks only to minimize the difference between the target and current compositions and is not interested in the growth rate. Figure 7 and Figure 8 show the variation of composition (monitored in real-time) and the setting of the dimethylcadmium mass flow controller during a growth run. The target composition was first set to 0.25 and control handed over to the ellipsometer. After this composition was attained, the target was fixed at 0.3. The controller suitably changed the dimethylcadmium flow to achieve this target. The slow response of the controller was due to the low value of the proportionality constant used for the control, which resulted in small correction changes to the mass flow controller setting. Larger values for this constant were used in subsequent runs, resulting in faster settling times. Later, a disturbance was provided by lowering the growth temperature to 345°C . As expected, the composition immediately increased but was brought down to the required value by the ellipsometer.

CONCLUSION

We have demonstrated the usefulness of *in-situ* spectroscopic ellipsometry as a tool for performing system identification and composition control on chemical vapor deposition systems. The library of optical constants of HgCdTe at the growth temperature needs to be accurately verified for different compositions in order to achieve the precise composition desired by the control algorithm. The ellipsometer is quite capable of distinguishing differences in composition of the order of 0.002 at room temperature. However, due to the flattening of the critical point peaks at higher temperature and the current imprecision in the library of optical constants, the actual resolution of composition at the growth temperature is closer to 0.01. The dynamic response of the system also needs to be incorporated

into the control algorithm in order to achieve a properly damped response.

ACKNOWLEDGMENT

We would like to thank J. Barthel for technical support. This work was partially funded by DARPA Contract No. DAAH01-92-C-R191 and is gratefully acknowledged.

REFERENCES

1. D.E. Aspnes, W.E. Quinn and S. Gregory, *Appl. Phys. Lett.* 57, 2707 (1990).
2. R.H. Hartley, M.A. Folkard, D. Carr, P.J. Orders, D. Rees, I.K. Varga, V. Kumar, G. Shen, T.A. Steele, H. Buskes and J.B. Lee, *J. Vac. Sci. Tech.* 10, 1410 (1992).
3. Dakshina Murthy, I.B. Bhat, B. Johs and S. Pittal, *J. Electron. Mater.* (to be published).
4. B. Johs, S. Pittal, D. Doerr, I. Bhat and S. Dakshina Murthy, *Thin Solid Films* 234, 293 (1993).
5. I.B. Bhat, N.R. Taskar and S.K. Ghandhi, *J. Electrochem. Soc.* 134, 195 (1987).
6. I.B. Bhat, N.R. Taskar and S.K. Ghandhi, *J. Vac. Sci. Tech. A* 4, 2230 (1986).
7. L. Vina, C. Umbach, M. Cardona and L. Vodopyana, *Phys. Rev. B* 29, 6752 (1984).
8. S. Pittal, B. Johs, Ping He, J. A. Woollam, S. Dakshina Murthy and I. Bhat, 21st Intl. Symp. on Compound Semiconductors, San Diego, CA, Sept. 18-24 1994.
9. D.E. Aspnes, *Appl. Phys. Lett.* 62 (4) 343 (1993).
10. P.G. Snyder, J.A. Woollam, S.A. Alterovitz and B. Johs, *J. Appl. Phys.* 68, 5925 (1990).

Low Temperature Growth of (100) HgCdTe Layers with DtBT_e in Metalorganic Vapor Phase Epitaxy

K. YASUDA, H. HATANO, T. FERID, K. KAWAMOTO, T. MAEJIMA,
and M. MINAMIDE

Nagoya Institute of Technology, Gokiso, Showa, Nagoya 466, Japan

Growth characteristics of (100) HgCdTe (MCT) layers by MOVPE at low temperature of 275°C were studied using ditertiarybutyltelluride as a tellurium precursor. Growths were conducted in a vertical narrow-spacing growth cell at atmospheric pressure. Cd composition of MCT layers were controlled from 0 to 0.98 using dimethylcadmium (DMCd) flow. The growth rate was constant for increase of DMCd flow. During the growth, Cd was incorporated preferentially into the MCT layers. Enhancement of Cd incorporation in the presence of Hg was also observed. Crystal quality and electrical properties were also evaluated, which showed that high quality MCT layers can be grown at 275°C. Strain in CdTe layers grown at 425 and 275°C was also evaluated. Lattice parameter of layers grown at 425°C approached bulk value at thickness of 5 μm, while layers grown at 275°C relaxed at 1 μm. The rapid strain relaxation of layers grown at 275°C was considered due to the layer growth on the strain relaxed buffer layer. The effect of the thermal stress on the relaxation of CdTe lattice strain was also discussed.

Key words: CdTe, growth characteristics, HgCdTe, HgTe, lattice strain, metalorganic vapor phase epitaxy (MOVPE)

INTRODUCTION

Low temperature growth of HgCdTe (MCT) layers by MOVPE is expected to have several advantages over usual growth at temperatures around 350 to 425°C. One is a decrease of Hg vacancy formation during growth and another is a decrease of interdiffusion at the growth interface. These effects are important not only for further improvements of infrared detectors but also for application in new electronic devices where the controllability of layer structure and electrical properties by extrinsic dopants are essential. Increase of dopant adsorption on the growth surface and suppression of neutral vacancy-impurity complex are expected at low growth temperature.^{1,2} The lower limit in temperature for MCT growth in

MOVPE is dependent on the stability of Te precursors. To overcome this problem, various growth techniques have been used previously. These are photolysis,³ use of thermally unstable Te precursors⁴⁻⁶ and precracking of precursors.⁷ However, the growth characteristics and electronic properties of layers for a wide range of Cd composition have not been fully studied.

In this paper, we report the growth characteristics of MCT layers at low growth temperature of 275°C using ditertiarybutyltelluride (DtBT_e) over a wide-range of Cd composition in a narrow-spacing growth cell. The growth characteristics were also compared with that at usual growth temperature of 425°C using diethyltelluride (DETe). Crystal quality and electrical properties were also evaluated for layers grown at 275°C. Relaxation of lattice strain was also studied for layers grown at 275 and 425°C.

(Received October 4, 1994; revised February 6, 1995)

EXPERIMENTAL

MCT growths were conducted in a narrow spacing growth cell at atmospheric pressure with rotating susceptor.⁸ The spacing between the substrate and the cell ceiling was set at 10 mm throughout this study. Cell ceiling was heated to 200°C, and Hg supply line was kept at 175°C. Precursors used were DtBTe, DETe, dimethylcadmium (DMCd), and elementary mercury. DtBTe was used for growth at 275°C and DETe was used for growth at 425°C. (100) GaAs substrates were used for the growth of (100) MCT and (100) CdTe. These layers were grown after the growth of CdTe buffer layer at 425°C. During the cooling period of growth temperature from 425 to 275°C, only DETe and hydrogen were supplied continuously. This was necessary to prevent the island growth and to obtain layers with good surface morphology. Several growths were also conducted using CdZnTe substrate to compare the crystal quality of the grown layers. Total hydrogen carrier flow was

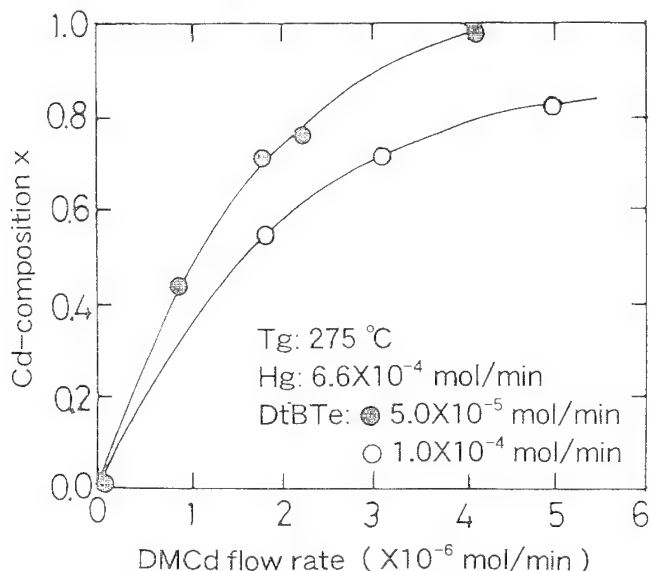


Fig. 1. Dependence of Cd-composition of MCT layers grown at 275°C with DMCd flow.

1500 cm³/min for growth at 275°C, and 1020 cm³/min for growth at 425°C.

Cd-composition of grown layers was examined by electron probe microanalysis (EPMA) with energy dispersive mode, and the compositional uniformity was examined by mapping at interval of 2 mm over the growth surface of 10 × 15 mm². Electrical properties of grown layers were evaluated by van der Pauw Hall measurement. Crystal quality was evaluated by x-ray double crystal rocking curve (DCRC) with Cu-K_α as x-ray source using Si as monochromator crystal. Lattice parameter was evaluated by x-ray diffraction.

RESULTS AND DISCUSSION

Growth Characteristics of MCT Layers

Figure 1 shows variations of Cd-composition x in MCT layers grown at 275°C with the DMCd flow, where the DtBTe flow was set at 5.0×10^{-5} and 1.0×10^{-4} mol/min and the Hg flow was kept constant at 6.6×10^{-4} mol/min. x -value in MCT layers increases very abruptly from 0 to 0.98 with increasing the DMCd flow from 0 to 4.2×10^{-6} mol/min at fixed DtBTe flow of 5.0×10^{-5} mol/min. On the other hand, the dependence of x -value on DMCd flow becomes moderate at high DtBTe flow of 1.0×10^{-4} mol/min. The gradual rise of x -value at high DtBTe flow is caused by the decrease of net Cd species which arrive at the growth surface since slight decrease of the growth rate also occurs here. The decrease of the arrival of Cd species helps Hg species to stick on the growth surface and this results in moderate increase of x -value with DMCd flow. The lower growth rate at high DtBTe flow is caused by the increase of DMCd loss in gas phase by coupling with excess DtBTe, since the incorporation rate of Cd into MCT layer is higher than that of Hg as shown in Fig. 1. The similar dependence of x -value as shown in Fig. 1 was also observed at higher growth temperature of 425°C using DETe as a tellurium precursor.

The growth rates of MCT were independent of the DMCd flow for both of the DtBTe flows. Slight decrease of the growth rate from 5 to 4 $\mu\text{m/h}$ was observed as the DtBTe flow was increased. The growth

Table I. Characteristics of MCT Layers Grown on (100) GaAs and (100) CdZnTe Substrates at 275°C

Cd-Composition x	MCT Thickness μm	CdTe Buffer Thickness μm	FWHM arc-sec	80K Carrier Density cm^{-3}	80K Hall Mobility $\text{cm}^2/\text{V s}$
GaAs Substrates					
1.0	2.1	0.5	338	$*1.2 \times 10^{15}\text{p}$	$*65$
0.93	3.2	8.0	253	—	—
0.87	3.3	5.0	222	$1.5 \times 10^{15}\text{n}$	4.1×10^2
0.44	2.6	5.0	424	$7.4 \times 10^{15}\text{n}$	7.4×10^3
0.00	4.65	8.0	227	$4.6 \times 10^{16}\text{n}^*$	8.0×10^4
CdZnTe Substrates					
0.85	3.0	3.0	94	—	—
0.74	3.0	3.0	100	$3.4 \times 10^{15}\text{n}$	4.2×10^3

*Carrier density and mobility were measured at 300K.

rate of CdTe measured without Hg flow and at DtBTe flow of 5.0×10^{-5} mol/min and DMCd flow of 2.0×10^{-5} mol/min was only $2.3 \mu\text{m/h}$. This indicates that the enhancement of Cd incorporation occurs in the presence of Hg, since the growth rate of MCT ($x = 0.98$) at DMCd flow of 4.0×10^{-6} mol/min is $5 \mu\text{m/h}$ which is higher than that of CdTe grown without Hg flow. The constant growth rate for the increase of DMCd flow indicates that both of the effects, preferential incorporation of Cd and suppression of Hg incorporation, occur in MCT growth at 275°C . For the case of high temperature growth at 425°C with DETe, on the other hand, growth rate remained at constant value or increased for increase of the DMCd flow depending on the carrier flow condition and the cell spacing.

The growth mechanism of MCT at low growth temperature of 275°C is considered as follows. We assume that the surface kinetic reaction is governing the MCT growth as has been observed previously for HgTe growth at 275°C ⁸ and CdTe growth with DETe.^{9,10} The CdTe and HgTe are formed on the growth surface through sticking of Cd and Hg species on Te species covered surface, since Te species have the largest sticking efficiency among the three species.^{11,12} At the same time, Cd precipitation also occurs on the growth surface through alkyl exchange reaction between DMCd and Hg.¹³ This precipitated Cd also attaches to the surface Te species and form CdTe on the growth surface. This CdTe and CdTe formed through sticking of Cd species occupy the large part of surface sites and prevent sticking of Hg species on the growth surface since Cd species have higher sticking efficiency than that of Hg species. This process results in preferential Cd incorporation and constant growth rate which is limited by the surface coverage rate of Te species independent of the DMCd flow.

On the other hand, if there was a wide space above the substrate, Cd precipitation would also occur on the wall of the growth cell where the temperature is usually lower than the substrate. This Cd precipitated on the wall consumes DtBTe by the formation of CdTe on the wall through the similar process as reported by Bhat et al. for DETe pyrolysis.¹⁴ This causes depletion of Cd and Te species in gas phase and results in the decrease of MCT growth rate when the DMCd flow is introduced. This phenomenon has been usually observed in conventional growth cell where wide-space exists upstream or around of the substrate.^{15,16} We have also observed the decrease of the growth rate in horizontal growth cell previously, where the deteriorations of composition and thickness uniformity also occurred if exact adjustment of growth condition was not done for each of the x -value. In contrast to this, the growth characteristics obtained here show that improvement of MCT growth environment is obtained in this narrow-spacing growth cell. Decrease of wall-deposition, efficient precursor transport to the growth surface, and suppression of convection flow over the substrate are contributing to the improvement. Another expected merit of this narrow-spacing cell is a low memory effect for dopant

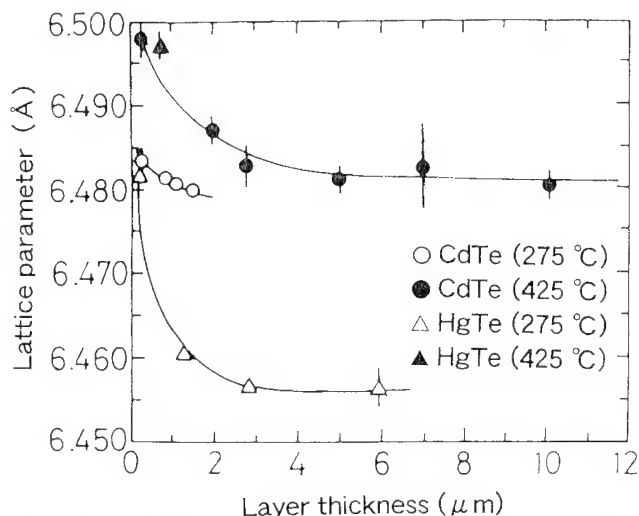


Fig. 2. Variation of the lattice parameter of CdTe and HgTe in the growth direction as a function of thickness, for layers grown at 275 and 425°C .

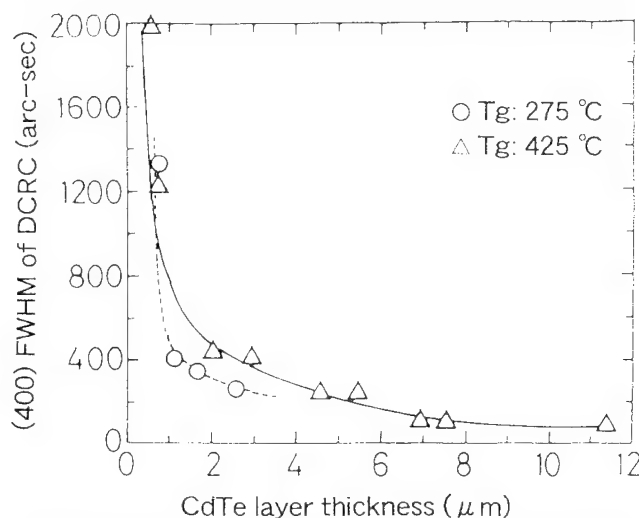


Fig. 3. Dependences of FWHM of DCRC measurement on CdTe layer thickness for layers grown at 275 and 425°C .

introduction.

Compositional uniformity of MCT layers was examined over a substrate area of $10 \times 15 \text{ mm}^2$. The maximum variation in x -value (Δx) was ± 0.01 for layers with mean x -value from 0.44 to 0.93. We think that the uniformity will be improved further since no attempt was made to optimize the growth condition.

Table I shows the full width at half maximum (FWHM) values of DCRC and electrical properties of MCT layers grown at 275°C . Note that the MCT layers were grown at different growth conditions such as Hg flow, DtBTe flow, and buffer layer thickness. When the layers were grown on GaAs substrates, FWHM values of DCRC ranged from 222 to 424 arcs. On the other hand, the layers grown on CdZnTe substrate showed considerable improvement in crystal quality. MCT layers showed n -type properties after annealing at 250°C and 24 h in Hg saturated condition. The annealed layers showed electron den-

sities of 1.5×10^{15} to $7.4 \times 10^{15} \text{ cm}^{-3}$ and mobilities of 4.1×10^2 to $7.4 \times 10^3 \text{ cm}^2/\text{V}\cdot\text{s}$ depending on the Cd composition. The electron densities of MCT layers may be due to Ga contamination rather than impurities in metalorganic sources, since the Ga was detected by secondary ion mass spectroscopy measurement for layers grown on GaAs substrates. The Ga may be incorporated into layers from the substrate through dislocations and also from the Ga-contaminated growth environment since growths were mainly conducted using GaAs substrate. The Ga-contamination is also supposed to occur for layers grown on CdZnTe substrate, since the Ga is known to cause heavy memory effect.² Thus, further decrease in electron density is expected for layers grown on CdZnTe substrates after complete bake-out of the susceptor and the growth cell. Although the layers have high electron densities, the mobilities are comparable to high quality layers.

The above results indicate that the high quality MCT layers can be grown at low growth temperature of 275°C using DtBTc, and the MCT growth environment in MOVPE is improved by employing the narrow space growth cell.

Strain in CdTe and HgTe Layers Grown on GaAs Substrates

Figure 2 shows the variations of lattice parameter in the growth direction with layer thickness for CdTe and HgTe layers grown at 275 and 425°C. Thickness of CdTe layers includes thickness of the buffer CdTe layers (0.5 μm) which was grown at 425°C. Lattice parameter of CdTe layers grown at 275°C approaches bulk value (0.64810 nm) at thickness around 1 μm . For the CdTe layers grown at 425°C, on the other hand, the lattice parameter approaches the bulk value at thickness around 5 μm . HgTe layers grown at 275 and 425°C also show the similar variations of lattice parameter with layer thickness as those of CdTe layers.

Figure 3 shows the dependences of FWHM value of DCRC measurement on CdTe layer thickness for layers grown at 275 and 425°C. Both of the layers show decreases of FWHM value with increase of layer thickness. The FWHM value of layers grown at 275°C decreases more rapidly with increase of layer thickness than that of layers grown at 425°C. This result indicates that the layers with better crystal quality (low dislocation density) were obtained at 275°C even at thin layer thickness. Full width at half maximum value of HgTe layers grown at 275 and 425°C also showed the similar variation with layer thickness as those of CdTe layers.

The above results indicate that the special mechanism works during the growth of CdTe layers at 275°C to relax the lattice strain and to reduce dislocations. The mechanism will be discussed below. The rapid decrease in lattice parameter for layers grown at 275°C is considered due to that these layers grew on strain relaxed buffer layer. The strain in buffer layers relaxes through generating dislocations during the

cooling period from the buffer CdTe growth at 425°C to the layer growth at 275°C, since the buffer layers suffer both compression stresses caused by lattice mismatching and difference of thermal expansion coefficient between CdTe and GaAs substrate (thermal stress). To confirm the strain relaxation in buffer layers during the cooling period to 275°C, we have also evaluated the variations of CdTe lattice parameter with layer thickness for layers grown at 425°C using growth interruption. During the growth interruption, layers were cooled down to 275°C and heated up to 425°C again under a continuous flow of DETe. The lattice parameter of growth interrupted layers showed the similar variation to that grown at 275°C. This result indicates that the strain relaxation occurs on buffer layers during the cooling period. Shin et al. reported that the dislocation density in the CdTe buffer layer increased about two orders of magnitude after the post growth thermal annealing (410–490°C) followed by the n-type annealing (250°C) which was conducted on the (211) MCT/CdTe/GaAs layers grown by molecular beam epitaxy.¹⁷ They also suggested that the thermal stress rather than the lattice mismatching would produce the dislocation generation and movement.¹⁷ Tachikawa et al. also showed that the thermal stress induced dislocation on GaAs/Si in the cooling stage.¹⁸ Although those studies were done on samples of different materials and which were prepared by different growth procedures, those studies support the above proposed mechanism for strain relaxation in CdTe buffer layer.

On the other hand, if the subsequent layers grow on buffer layers with high dislocation density at 275°C, the grown layer would contain high dislocations since threading dislocations develop into the grown layers. In contrast to this, results shown in Fig. 3 show the improvement in the crystal quality. This improvement in the crystal quality indicates that the reduction of dislocations also occurs during the cooling period where growth is interrupted. This was caused by the annihilation and coalescence of dislocations during the movement of dislocations which was induced by the thermal stress. Although the exact mechanism is not clear for the reduction of dislocations yet, the continuous flow of DETe may also contribute to terminate the dislocations at the surface of the buffer layer.

Since the thermal stress was considered as the dominant motive force for the dislocation generation and movement, it is interesting to compare the effect of the thermal stress on the lattice strain for layers grown at different temperatures and on the substrates with different thicknesses. Tatsuoka et al. reported that the strain relaxes with increase of the thickness of CdTe layer up to 10 μm , and that constant residual strain remains up to a thickness of 40 μm .¹⁹ Their results were obtained on (100) CdTe layers grown on (100) GaAs substrates with thickness of 350 μm by hot-wall epitaxy at 300°C. In contrast, the results for CdTe layers grown at 425°C show that the strain relaxes more rapidly than their results and

that the layers become strain free above the thickness of 5 μm . Assuming the bimetal model,²⁰ we have estimated the strain at the surface of CdTe layers due to the thermal stress. The estimated strain is 6.4×10^{-4} which is almost independent of the CdTe thickness from 1.0–10 μm for our substrate thickness of 620 μm . This strain is larger than the reported strain of about 3.5×10^{-4} at the CdTe thickness of 40 μm .¹⁹ The estimated strain is dependent dominantly on the temperature difference between the growth and the measurement, and less dependent on the thickness of substrates down to 100 μm for the growth at 425°C and the thickness of CdTe from 1.0 to 10 μm . Thus, the large thermal stress may relax the lattice strain for layers obtained here. If the relaxation of lattice strain is dependent on the thermal stress and not dependent on the growth procedure, CdTe layers grown at 275°C without the buffer growth at 425°C may show the similar variations of lattice parameter as reported by Tatsuoka et al. since the strain is estimated to be the similar value. This will be confirmed in the future.

CONCLUSION

Growth characteristics of MCT layers in MOVPE at low growth temperature of 275°C were studied using DtBTe as tellurium precursor. Growths were conducted in a vertical narrow spacing growth cell at atmospheric pressure. Cd composition of MCT layers was increased with DMCd flow. The growth rate at 275°C was constant for increase of DMCd flow. During the growth, Cd was incorporated preferentially into MCT layers. Enhancement of Cd incorporation at the presence of Hg was also observed. Crystal quality and electrical properties of layers grown at 275°C were also evaluated.

Strains in CdTe layers grown at 425 and 275°C were also evaluated. Lattice parameter of layers grown at 425°C approached bulk value around the thickness of 5 μm , while layers grown at 275°C approached around 1 μm . The rapid strain relaxation of layers

grown at 275°C was considered due to the layer growth on the strain relaxed buffer layer. The effect of the thermal stress on the relaxation of CdTe lattice strain was also discussed.

REFERENCES

1. M. Ekawa, K. Yasuda, T. Ferid, M. Saji and A. Tanaka, *J. Appl. Phys.* 71, 2669 (1992).
2. M. Ekawa, K. Yasuda, T. Ferid, M. Saji and A. Tanaka, *J. Appl. Phys.* 72, 3406 (1992).
3. S.J.C. Irvine, J.B. Mullin and J. Tunncliffe, *J. Cryst. Growth* 68, 188 (1984).
4. W.E. Hoke and P.J. Lemonias, *Appl. Phys. Lett.* 48, 1669 (1986).
5. R. Korenstein, W.E. Hoke, P.J. Lemonias, K.T. Higa and D.C. Harris, *J. Appl. Phys.* 62, 4927 (1987).
6. J.D. Parsons and L.S. Lichitman, *J. Cryst. Growth* 86, 222 (1988).
7. P.-Y. Lu, C.-H. Wang, L.M. Williams, S.N. Chu and C.M. Stiles, *Appl. Phys. Lett.* 49, 1372 (1986).
8. K. Yasuda, M. Ohno, J. Yamaguchi, T. Onakado, T. Ferid and H. Hatano, *Ex. Abstract. 1993, U.S. Workshop Phys. Chem. MCT*, 27 (1993).
9. K. Yasuda, M. Ekawa, N. Matsui, S. Sone, Y. Sugiura, A. Tanaka and M. Saji, *Jpn. J. Appl. Phys.* 29, 479 (1990).
10. I.B. Bhat, N.R. Taskar and S.K. Ghandhi, *J. Vac. Sci. & Technol. A* 4, 2230 (1986).
11. K. Yasuda, S. Sone, M. Ekawa, Y. Sugiura, N. Matsui, A. Tanaka and M. Saji, *Tech. Digest 1st. Intl. Mtg. on Advanced Process. and Character. Technol. (APCT'89)* (1989) Tokyo, p. 131.
12. S. Sone, M. Ekawa, K. Yasuda, Y. Sugiura, M. Saji and A. Tanaka, *Appl. Phys. Lett.* 56, 539 (1990).
13. A.H. McDaniel, W.G. Xie and R.F. Hicks, *Ex. Abstract. 1993, U.S. Workshop Phys. Chem. MCT*, 25 (1993).
14. I.B. Bhat, N.R. Taskar and S.K. Ghandhi, *J. Electrochem. Soc.* 134, 196 (1987).
15. I.B. Bhat, *J. Cryst. Growth* 117, 1 (1992).
16. H. Takada, T. Murakami, M. Suita, K. Yasumura, Y. Endo, K. Takahashi and M. Nunoshita, *J. Cryst. Growth* 117, 44 (1992).
17. S.H. Shin, J.M. Arias, D.D. Edwall, M. Zandian, J.G. Pasko and R.E. DeWames, *J. Vac. Sci. Technol.* B10, 1492 (1992).
18. M. Tachikawa and H. Mori, *Appl. Phys. Lett.* 56, 2225 (1990).
19. H. Tatsuoka, H. Kuwabara, Y. Nakanishi and H. Fujiyasu, *J. Appl. Phys.* 67, 6860 (1990).
20. S. Timosheuko, *J. Opt. Soc. Am.* 11, 233 (1980).

The Growth and Characterization of (211) and (133) Oriented (Hg,Cd)Te Epilayers (211)B GaAs by Organometallic Vapor Phase Epitaxy

G.J. GOUWS and R.J. MULLER

Mikomtek, CSIR, P.O. Box 395, Pretoria, South Africa

The growth of CdTe buffer layers on (211)B GaAs substrates by organometallic vapor phase epitaxy (OMVPE) was studied, and it was found that, depending on the growth conditions, either the (211) or (133) epitaxial orientation could be formed. In some cases, an epilayer showing a mixed (211) and (133) orientation was also observed. The influence of several growth parameters on the orientation of the CdTe layer was investigated, and it was found that the Te/Cd ratio, together with the growth temperature, have the most significant effect in determining the epilayer orientation. From these results, it was then possible to select nominally optimized growth conditions for CdTe buffer layers of both orientations. (Hg,Cd)Te layers of the same orientations could then be grown and characterized. Although double crystal x-ray diffraction measurements indicated a somewhat better crystalline perfection in the (133) (Hg,Cd)Te layers, these layers showed a poor surface morphology compared to the (211) orientation. Measurement of etch pit densities also indicated defect densities to be typically half an order of magnitude higher in the (133) orientation. Diodes were formed by ion implantation in both orientations and significantly better results were obtained on the (211) (Hg,Cd)Te layers.

Key words: CdTe, HgCdTe, organometallic vapor phase epitaxy (OMVPE), orientation effects

INTRODUCTION

Although CdTe and lattice matched (Cd,Zn)Te have become the favored substrates for the growth of high quality (Hg,Cd)Te (MCT) epilayers, the use of GaAs substrates still offers the possibility of large area, high quality substrates at a reasonable cost. The occurrence of the phenomenon of dual epitaxy in the growth of CdTe on GaAs by nonequilibrium vapor phase techniques such as molecular beam epitaxy (MBE) or organometallic vapor phase epitaxy (OMVPE) is well known for this large mismatch system. If CdTe is grown on the (100) GaAs face, either the (111) or the (100) epilayer orientation can be formed.¹⁻³ Both these orientations are plagued by specific defects which makes them unsuitable for the

growth of good quality MCT layers; in the case of (100) epilayers, the formation of growth hillocks tends to lead to a poor surface morphology,^{4,5} while twinning in the growth of (111) MCT epilayers degrades the electrical characteristics of the layers.^{6,7} This has stimulated work on the (h11) faces of GaAs, where $h = 2, 3, 5$, or 7 .^{8,9} Again, dual epitaxy has been reported for the cases of (211)B and (311)B substrates. In the case of growth on the (211)B face, the formation of the (211) or (133) epilayer orientations have been described,^{10,11} while both the (110) and (311) orientations have been reported on (311)B substrates.^{12,13}

This paper will present the results of an experimental study on the growth of CdTe and (Hg,Cd)Te layers on (211)B GaAs by OMVPE. The purpose of the study was twofold; firstly to investigate the influence of various growth parameters on the orientation of the epilayer in order to select the growth conditions

(Received October 4, 1994; revised May 5, 1995)

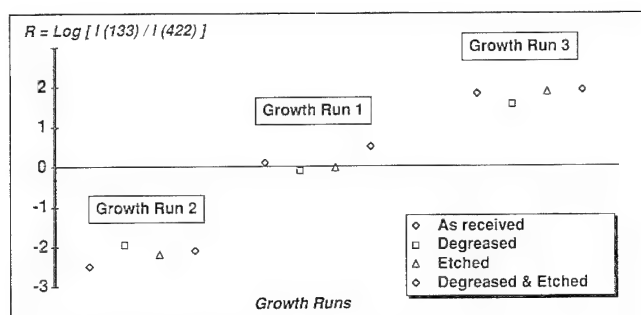


Fig. 1. The influence of various surface preparation procedures on the factor R as measured during three different growth runs.

needed for the growth of good quality layers of either orientation. Secondly, to grow, characterize, and compare (Hg,Cd)Te epilayers of the two orientations in order to decide which is the more suitable for MCT epitaxy and device processing.

EXPERIMENTAL

Epilayers were grown in a horizontal, RF heated OMVPE reactor at atmospheric pressure. Diisopropyltelluride (DIPTe), dimethylcadmium (DMCd), and elemental mercury were used as starting materials. The interdiffused multilayer process (IMP)¹⁴ was used for the growth of (Hg,Cd)Te layers, with typical growth temperatures from 355–375°C. Total gas flow rate through the reactor was 2000 sccm for the growth of the HgTe cycle and 6000 sccm for the growth of CdTe.

The polarity of the GaAs substrates was indicated by the vendor and no further experiments to confirm this were performed. After the substrates were degreased by several rinses in hot xylene and isopropanol, they were etched in a 5:1:1 solution of H_2SO_4 , H_2O_2 , and H_2O , loaded in the reactor and subjected to a pre-growth, high temperature bakeout to desorb the surface oxide.

The orientation and crystalline perfection of the layers were measured by double crystal x-ray diffraction (XRD). These measurements were performed along the direction of maximum tilt between epilayer and substrate and along the direction of zero tilt. The 422 and 133 diffraction peaks were used for the (211) and (133) orientations, respectively, and the signal from each peak was individually optimized at each position. The value of the intensity and the full width at half maximum (FWHM) value for each peak was then averaged over that obtained in the two directions of tilt.

The surface morphology of the epilayers was characterized using optical microscopy and a scanning electron microscope (SEM). Etch pit densities (EPDs) on the (Hg,Cd)Te layers were determined by using the etch of Chen.¹⁵ Hall measurements on the (Hg,Cd)Te layers were performed between 20 and 300K and with magnetic fields up to 7 kG. The composition and thickness of (Hg,Cd)Te layers, as well as the thickness of the CdTe layers were measured by Fourier transform infrared spectroscopy.

RESULTS

Initially, CdTe layers were grown on both the A and B (211) GaAs faces. No dramatic differences were found in the surface morphologies of the CdTe layers on the two different faces, but when HgTe or (Hg,Cd)Te layers were grown, the A face always yielded an epilayer with a very poor morphology. These epilayers showed a high density of elongated pyramids, similar to those described by Bevan et. al.¹⁶ in the growth of (Hg,Cd)Te on (211)A (Cd,Zn)Te. The B face, on the other hand, always showed a much smoother surface morphology, and it was decided to proceed with further work on this face only.

During the first few growth runs, CdTe layers were grown under a wide range of growth conditions on (211)B GaAs substrates and the XRD results on these layers indicated that three possible epitaxial orientations were possible. Both the (211) or the (133) epilayer orientation could be formed, while in several cases, layers were found to show both these orientations, as both the 422 and 133 diffraction peaks were found to be present in the diffraction spectrum. The layers which showed both orientations always had a degraded surface morphology and crystalline structure compared to the single orientations. The growth parameters used in these initial growth runs could later be used as a rough guide to growing one of the three possible orientations. When (Hg,Cd)Te layers were grown on these CdTe buffers, the (Hg,Cd)Te layers were always found to take up the same orientation as the buffer, so that again either the (133) or (211) orientation could be formed. In the cases where the buffer layer showed a mixed orientation, the MCT layers were found to have a poor surface morphology and degraded crystalline perfection.

It was thus decided to perform a systematic study of the influence of various growth conditions on the CdTe orientation. The growth parameters evaluated in the study were the following:

- Substrate surface preparation.
- Pregrowth bakeout temperature.
- Growth temperature.
- Te/Cd ratio.
- Annealing procedures.

Factors Determining the Orientation of CdTe on (211)B GaAs

In order to have a semi-quantitative measure of the orientation of the CdTe layers, the factor R was defined, with

$$R = \text{Log}[I_{331}/I_{422}]$$

where I_{331} and I_{422} are the intensities of the 331 and 422 diffraction peaks obtained from the epilayer. If no presence of a particular reflection could be detected, the intensity of that reflection was set equal to that of the background signal. The larger the value of R , the stronger the (133) component in the layer was thus found to be, while a large negative value for R indicated a strong (211) component. In general, it was

found that an epilayer showed a single epitaxial orientation when $R \geq |2|$.

Effect of Substrate Preparation

CdTe layers were grown in a single growth run on four substrates which had different surface preparations: degreased only, etched only, degreased and etched, and as-received. Using the rough growth parameter guidelines established earlier, an epilayer that was expected to show the mixed orientation was grown on the four differently prepared substrates. No significant difference in the values of R between the four samples were obtained, as can be seen in the results of growth run 1 in Fig. 1. It was thus concluded that the substrate preparation does not appear to determine the epilayer orientation. This experiment was later repeated when the growth conditions were more established by also growing (211) and (133) oriented layers on these four substrates. Again little variation in R was observed between the different substrate preparations. In Fig. 1, the results from all three growth runs are shown.

Effect of the Pregrowth Bakeout Temperature

A series of CdTe layers was grown using growth conditions that had previously been found to yield layers of mixed orientation. The pregrowth bakeout temperature was varied between 500 and 640°C through the series, with all other growth parameters kept constant. Once again, this parameter was found to be not significant in determining the epilayer orientation and hence a pregrowth bakeout at 620°C was used for all further growth runs.

Effect of the Growth Temperature

This parameter was found to have a strong influence on the observed orientation, with lower growth temperatures favoring the formation of the (211) orientation. Figure 2 shows the variation of R with different substrate temperatures, with all other growth parameters kept constant.

Effect of the Te/Cd Ratio

The ratio of DIPTe to DMCd in the gas phase was varied by changing the relative flow through the two bubblers. This parameter was found to be the most critical factor in determining the epilayer orientation. It was found that a high Te/Cd ratio favored the formation of the (211) orientation, with low Te/Cd values leading to a predominantly (133) CdTe epilayer. The value of R could be varied between $R = 1.8$ to $R = -2.5$ by variation of the Te/Cd flow ratio between 4 and 16 at a temperature of 365°C. At other substrate temperatures, similar trends were observed, although the effect is not as dramatic as at this temperature. The variation of R as a function of both growth temperature and Te/Cd flow ratio is illustrated in Fig. 3.

Effect of Post Growth Annealing

The effect of different anneal procedures on the orientation and structure of the layers was studied.

Layers were subjected to a 15 min post growth anneal at the growth temperature and then compared to layers grown without the anneal.

It was found that in the case of 2–3 μm thick CdTe layers, the anneal step had little effect on the orientation or structure of the layer. Annealing a 2.5 μm CdTe layer with a $R = 0.5$ yielded essentially the same value after the anneal. However, in the case of thin layers ($<0.5 \mu\text{m}$), an increase in R was normally observed after the anneal step. This would indicate that some preferential growth of the (133) orientation can take place using these anneal conditions if the layers are thin enough.

Growth Conditions Selected for (211) and (133) Buffer Layers

From the above results, nominally optimized growth conditions could be selected for the growth of either the (211) or (133) CdTe buffer layer. For both of these orientations, the GaAs substrates were similarly prepared by degreasing and etching and both received a pregrowth bakeout at 620°C for 10 min. In order to induce the (211) orientation, epilayer growth was initiated by a short nucleation step at 355°C, using a Te/Cd flow ratio of 16. The substrate temperature was then increased to 365°C and allowed to stabilize for 5 min. At the same time, the Te/Cd flow ratio was decreased to 10. Growth then proceeded for the desired time. This lower Te/Cd flow ratio was found to yield layers with a better surface morphology.

If a (133) oriented CdTe layer was desired, the nucleation step was performed at a temperature of

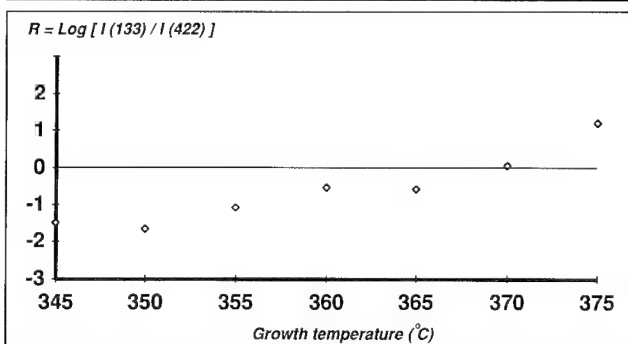


Fig. 2. The variation of R with growth temperature with all other growth parameters kept constant.

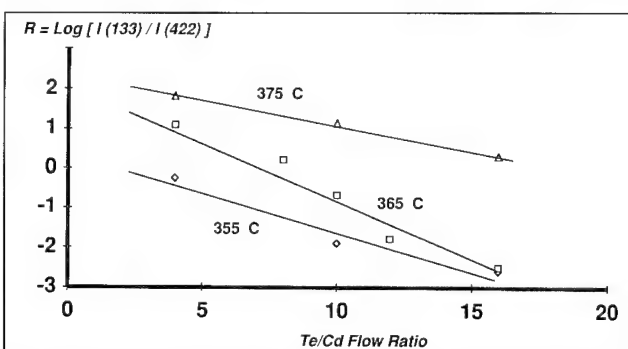


Fig. 3. The variation of R as a function of Te/Cd flow ratio at different growth temperatures.

375°C, using a low Te/Cd flow ratio of 4. The substrate temperature was then adjusted to 365°C and the layer was given a 15 min anneal at this temperature before growth proceeded at a Te/Cd flow ratio of eight for the desired time. In some growth runs of this orientation, growth was also interrupted for short anneal steps. This procedure appeared to yield layers with a slightly improved crystalline structure as indicated by the FWHM XRD values.

The growth conditions used to obtain CdTe buffer layers with either the (211) or (133) orientations are now summarized in Table I.

Using these growth conditions, it was found possible to consistently produce CdTe layers with either the (211) or the (133) orientation. The different char-

acteristics of these two orientations will now be discussed in more detail in the next section.

Characteristics of the (211) and (133) CdTe Buffer Layers

Both orientations showed good morphologies with a specular surface. If the layers were grown thicker than 2 μm , some deterioration of surface quality took place and the layers appeared slightly dull. The (211) layers showed the best surface, with a very smooth morphology. Typically the surface features that are seen on this orientation appear to be dust features from the growth process and not crystallographic growth features. The (133) orientation tends to show some small triangular growth features.

If the FWHM values measured on CdTe layers of approximately 2.5 μm thick of the two orientations are compared, the (133) layers consistently tend to show the narrower half peak widths. Typically, this orientation showed values of 90–100 arc-s, compared to the 140–150 arc-s of the (211) layers. The relative tilt between the GaAs substrate and the epilayer was also measured by XRD, and it was found that the (211) epilayer showed a tilt of approximately 3.2°, while the (133) epilayers showed a tilt of only 0.5°. In both cases, the tilt is in the same direction, with the tilt axis the <311>.

The influence of the CdTe orientation on the crystalline quality as measured by the FWHM of the XRD peaks is illustrated in Fig. 4. In this figure, the FWHM value of both 422 and 133 diffraction peaks is plotted as a function of the value of R. As the FWHM values will also show a significant dependence on the layer thickness, only CdTe layers thicker than 1 μm were plotted. It is clear that a drastic improvement in the crystalline quality of both (211) and (133) oriented layers is observed when $R \geq |2|$, i.e. a single epilayer orientation is achieved. If the mixed orientation is observed, the FWHM values increased to 250 to 500 arc-s, compared to the 100 and 150 arc-s typically observed for the single crystal (133) and (211) orientation, respectively.

Characteristics of (211) and (133) (Hg,Cd)Te Epilayers

(Hg,Cd)Te epilayers of either the (211) or (133) orientation could then be grown by using the procedures described in the section entitled Growth Con-

Table I. A Summary of the Growth Parameters Used to Produce (211) and (133) Oriented CdTe Buffer Layers on (211)B GaAs

Growth Step/ Parameter	(211)CdTe	(133)CdTe
Pregrowth Bakeout	620°C for 10 min	620°C for 10 min
Nucleation Temperature	355°C	355°C
Nucleation Time	3 min	6 min
Nucleation Te/Cd Flow Ratio	16	4
Interrupt Anneal	5 min	15 min
Growth Temperature	365°C	365°C
Growth Te/Cd Flow Ratio	10	8
Further Anneal	None	Interrupt Anneal

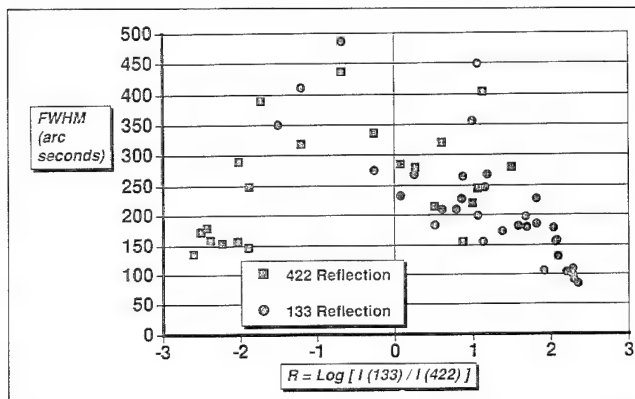


Fig. 4. The FWHM of the 133 and 422 x-ray diffraction peaks plotted as a function of the value of R.

Table II. A Comparison of the Properties of (211) and (133) Oriented (Hg,Cd)Te Epilayers Grown on (211)B GaAs Substrates

Epilayer Property	(211) (Hg,Cd)Te	(133) (Hg,Cd)Te
Surface Morphology	Very smooth—some small (<5 μm) features	Approx. 10 ² /cm ² growth pyramids (up to 15 μm in size)
XRD FWHM	80–90 arc-s	70–75 arc-s
EPD	5–20 $\times 10^6 \text{ cm}^{-3}$	1–7 $\times 10^7 \text{ cm}^{-3}$
Carrier Type, Concentration (77K)	p 2–6 $\times 10^{16} \text{ cm}^{-3}$	p 2–3 $\times 10^{16} \text{ cm}^{-3}$
R ₀ A-Diodes	0.5–0.85 Wcm ²	0.05–0.3 Wcm ²

ditions Selected for (211) and (133) Buffer Layers to select the desired orientation. A CdTe buffer layer of typically 0.5 to 2.5 μm thick was first grown, after which a (Hg,Cd)Te layer of approximately 15 μm was grown continuously using the IMP process. In all cases, the (Hg,Cd)Te epilayer was found to take up the orientation of the CdTe buffer.

Surface Morphology

The two orientations differ markedly in their surface morphology. The (211) epilayer shows a smooth, specular surface with very few features visible. Surface features which are present are also fairly small and appear to be the results of gas phase nucleation rather than a growth related phenomenon. In the case of the (133) orientation, the surface shows an appreciable density ($2\text{--}4 \times 10^2 \text{ cm}^{-2}$) of triangular growth features. These features have dimensions of up to 15 μm in length and seriously interrupt the surface morphology. In Fig. 5, the surface morphologies of the two orientations are contrasted.

Crystalline Structure

Taking the FWHM values of the 422 and 133 diffraction peaks as a measure, the (133) epilayers appear to show a somewhat better crystalline perfection. Typical FWHM values of 70–80 arc-s are obtained on the (133) epilayers, while the (211) epilayers yield somewhat larger values of 80–100 arc-s. These results are in contrast with the results of etch pit densities counted on these layers; densities of $5\text{--}20 \times 10^6 \text{ cm}^{-2}$ were counted on the (211) epilayers, compared to the $1\text{--}7 \times 10^7 \text{ cm}^{-2}$ on the (133) orientation. It was found that the (133) MCT epilayers typically showed half an order of magnitude higher EPDs than the (211) layers grown using the same growth parameters.

A transmission electron microscope (TEM) investigation of the specific defect structure of each epilayer is currently in progress and should yield more information on the specific crystal defects present in these layers.

Electrical Properties

Both (Hg,Cd)Te orientations showed typical p-type behavior in their Hall measurements from 20K to room temperature. However, the (211) orientation consistently showed a somewhat higher 77K hole concentration of mid to high 10^{16} cm^{-3} compared to the low 10^{16} cm^{-3} found in the (133) epilayers.

Device Results

An initial evaluation of the suitability of these two orientations for devices was made when linear arrays of diodes were processed by ion implantation. Both orientations had similar compositions, with cut-off wavelengths of approximately 10.5 μm at 80K. Although both orientations of epilayers showed low R_0A values, those obtained on the (211) were significantly better. This orientation showed R_0A values of 0.5 to 0.85 Ωcm^2 , which were significantly better than the

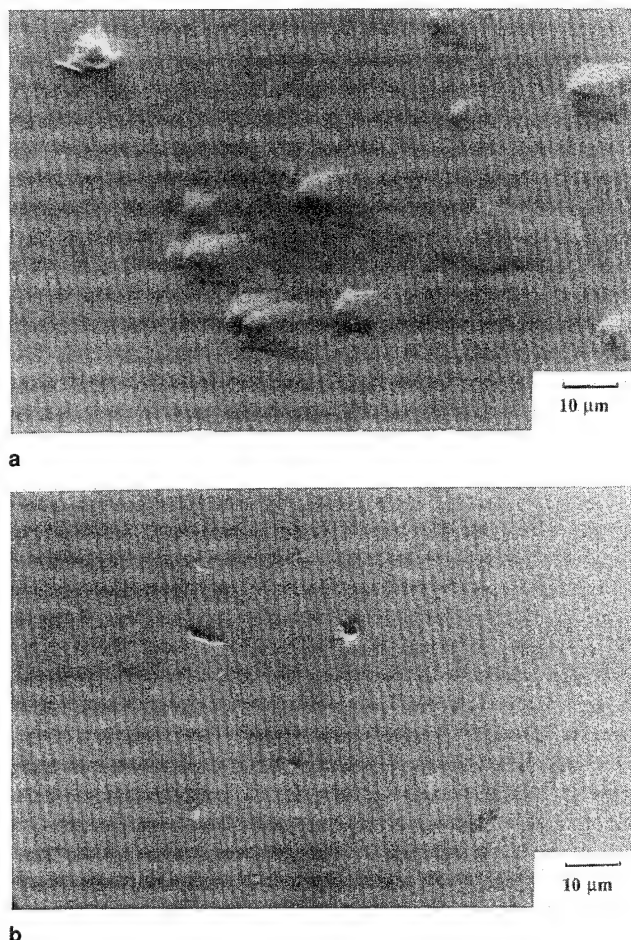


Fig. 5. Two SEM micrographs illustrating the difference in surface morphologies of (133) (a) and (211) (b) (Hg,Cd)Te epilayers.

0.05 to 0.3 Ωcm^2 obtained on the (133) orientation. The (211) orientation thus not only shows higher R_0A values, but also a much better uniformity over the array. Even the best of these R_0A values are still an order of magnitude worse than can be expected from good quality diodes at this wavelength. The reason for this may be twofold; firstly EPD measurements have shown that both epilayers contained high dislocation densities of 2×10^7 and $6 \times 10^7 \text{ cm}^{-2}$ for the (211) and (133) orientation, respectively. Such high values of dislocation densities may well lead to the low R_0A values observed. A second reason may be that the process for diode formation is not yet optimized and optimization of the different process steps will also lead to improved diodes.

The properties of the two different orientations of epilayers are compared in Table II.

SUMMARY

The influence of various OMVPE growth parameters on the orientation of CdTe buffer layers on (211)B GaAs was investigated. The ratio of Te/Cd in gas phase, together with the growth temperature were found to be the most important parameters determining whether the (211) or (133) epilayer or a mixed orientation would be formed. Good control of the Te/

Cd ratio was found to be critical to ensure repeatable results. Different growth procedures were then developed for the repeatable growth of each orientation.

(Hg,Cd)Te layers of these two orientations were grown and evaluated. The (211) (Hg,Cd)Te orientation was found to have a superior surface morphology. Despite the fact that the lower FWHM XRD values of the (133) orientation would seem to indicate a better crystalline perfection, EPD measurements indicate a higher dislocation density in this orientation. This is confirmed by the poor R_0A values observed for diodes fabricated on (133) MCT compared to that on (211) MCT.

Unfortunately, most other published work describing the control of the two epilayer orientations were performed by MBE so that it is difficult to directly compare the results. Lange et. al.¹⁰ found that the epilayer orientation was controlled by the temperature of the pregrowth bakeout; heating to a temperature of 535°C yielded the (133) orientation, while preheating to 550°C yielded the (211). On the basis of x-ray diffraction work as well as transmission electron microscopy, they found the (133) epilayers to be of superior quality.^{10,17} This was ascribed to the fact that the tetrahedral bond network continues from (211) GaAs to (133) CdTe with less distortion than is the case for a (211) epilayer. Sasaki et. al.¹¹ found the orientation to be controlled by the substrate temperature, with all epilayers grown above 290°C having the (133) orientation. At 290°C epilayers were found to contain both orientations, with only the (211) formed below this temperature. They found the XRD FWHM values as well as the surface morphology to improve when epilayers were grown near 290°C.

Our results would seem to indicate that the (211) epilayer orientation is the better for device processing due to both a better surface morphology and a lower

defect density. However, no systematic work on improving the (133) surface morphology or lowering the dislocation density in either of the two orientation has been performed. Only when these issues are addressed can a final conclusion on the suitability of the two orientations be reached.

REFERENCES

1. J.M. Ballingall, M.L. Wroge and D.J. Leopold, *Appl. Phys. Lett.* 48, 1273 (1986).
2. R.D. Feldman, R.F. Austin, D.W. Kisker, K.S. Jeffers and P.M. Bridenbaugh, *Appl. Phys. Lett.* 48, 248 (1986).
3. P.L. Anderson, *J. Vac. Sci. Technol.* A4, 2162 (1986).
4. S.J.C. Irvine, J.S. Gough, J. Giess, M.J. Gibbs, A. Royle, C.A. Taylor, G.T. Brown, A.M. Keir and J.B. Mullin, *J. Vac. Sci. Technol.* A7, 285 (1989).
5. R. Triboulet, A. Tromson-Carli, D. Lorans and T. Nguyen Duy, *J. Electron. Mater.* 22, 827 (1993).
6. R. Druile, F. Desjonquères, A. Katty, A. Tromson-Carli, D. Lorans, L. Svob, A. Heurtel, Y. Marfaing and R. Triboulet, *J. Cryst. Growth* 101, 73 (1990).
7. R. Triboulet, *J. Cryst. Growth* 107, 598 (1991).
8. G.N. Pain, C. Sandford, C.K.G. Smith, A.W. Stevenson, D. Lao, L.S. Wielunski, S.P. Russo, G.K. Reeves and R. Elliman, *J. Cryst. Growth* 107, 610 (1991).
9. A. Tromson-Carli, G. Patriarche, R. Druile, A. Lusson, Y. Marfaing, R. Triboulet, P.D. Brown and A.W. Brinkman, *Mater. Sci. and Eng. B* 16, 145 (1993).
10. M.D. Lange, R. Sporken, K.K. Mahavadi, J.P. Faurie, Y. Nakamura and N. Otsuka, *Appl. Phys. Lett.* 58, 1988 (1991).
11. T. Sasaki, M. Tomono and N. Oda, *J. Vac. Sci. Technol. B* 10, 1399 (1992).
12. L.M. Smith, C.F. Byrne, D. Patel, P. Knowles, J. Thompson, G.T. Jenkin, T. Nguyen Duy, A. Durand and M. Bourdillot, *J. Vac. Sci. and Technol.* A8, 1078 (1990).
13. R. Triboulet, A. Tromson-Carli, G. Patriarche, D. Lorans and T. Nguyen Duy, *Advan. Mater. for Optics and Electronics* 3, 239 (1994).
14. J. Tunncliffe, S.J.C. Irvine, O.D. Dosser and J.B. Mullin, *J. Cryst. Growth* 68, 245 (1984).
15. J.S. Chen, U.S. Patent No. 4,897,152 (1990).
16. M.J. Bevan, N.J. Doyle and T.A. Temafonte, *J. Appl. Phys.* 71, 204 (1992).
17. Y. Nakamura, N. Otsuka, M.D. Lange, R. Sporken and J.P. Faurie, *Appl. Phys. Lett.* 60, 1372 (1992).

Improvement in HgCdTe Diode Characteristics by Low Temperature Post-Implantation Annealing

AKIRA AJISAWA and NAOKI ODA

Material Development Center, NEC Corporation, Kawasaki Kanagawa 216, Japan

Hg_{1-x}Cd_xTe diodes ($x \sim 0.22$) with different carrier concentrations in p type materials have been fabricated by employing an ion-implantation technique. The performances of the diodes, prior to and after low temperature post-implantation annealing, have been investigated in detail by model fitting, taking into account dark current mechanisms. Prior to the annealing process, dark currents for diodes with relatively low carrier concentrations are found to be limited by generation-recombination current and trap-assisted tunneling current, while dark currents for diodes with higher carrier concentrations are limited by band-to-band tunneling current. These dark currents in both diodes have been dramatically decreased by the low temperature annealing at 120~150°C. From the model fitting analyses, it turned out that trap density and the density of the surface recombination center in the vicinity of the pn junction were reduced by one order of magnitude for a diode with lower carrier concentration and that the carrier concentration profile in a pn junction changed for a diode with higher carrier concentration. The improvements are explained by changes in both carrier concentration profile and pn junction position determined by interaction of interstitial Hg with Hg vacancy in the vicinity of the junction during the annealing process.

Key words: HgCdTe, IR photodiodes, low temperature thermal annealing

INTRODUCTION

HgCdTe is the most important material for fabricating infrared focal plane array (IRFPA). High performance HgCdTe FPAs require reducing dark currents in each diode element. The dark currents are mainly composed of diffusion current, which arises in n and p neutral regions, and generation-recombination (GR) current in the depletion layer, trap-assisted tunneling (TAT) current, and band-to-band tunneling (BBT) current, magnitudes of which depend on crystal quality in a pn junction vicinity. Although the p on n type diode structure using an n type substrate with longer minority carrier lifetime seems superior to the n on p type in the long wavelength range,¹⁻³ the n on p type is still in the state of the art for fabricating

IRFPAs with planer structure.⁴⁻⁶ Generally, the pn junction in n on p type diode is created by B ion-implantation in p type material doped with Hg vacancies. Then, the n layer is formed by activating B ions and interstitial Hg atoms yielded by ion-implantation damage.^{7,8} The implantation process introduces lattice damage in a pn junction vicinity and increases dark currents, which can be reduced with post-implantation annealing (PIA). The PIA process can shift the pn junction position from the damaged region to a deeper part of the HgCdTe layer by compensating for Hg vacancies in the layer, due to thermal instability of interstitial Hg atoms.^{9,10} Therefore, the PIA process improves diode characteristics, namely, it reduces dark currents in the depletion layer, by forming a pn junction in the high quality region. The diffused pn junction position is determined not only by the annealing conditions but also by the number of Hg

(Received October 4, 1994; revised January 15, 1995)

Table I. Material Characteristics of HgCdTe Diodes and Annealing Conditions

Sample No.	9D	10A
Carrier Concentration (cm ⁻³)	1.3×10^{16}	4.0×10^{16}
Mobility (cm ² /Vs)	580	450
Epitaxial Layer Thickness (μm)	20	21
Cutoff Wavelength λ_c @82K (μm)	10.21	10.27
Cd Composition x	0.223	0.222
Intrinsic Carrier Concentration n_i (cm ⁻³)	1.37×10^{13}	1.52×10^{13}
PIA1	120°C/1.5H	150°C/0.5H
PIA2	120°C/3H + 150°C/1H	150°C/1.5H

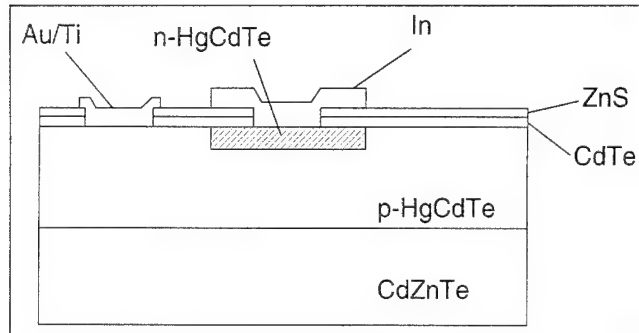


Fig. 1. Cross section view of n on p planar type HgCdTe diode.

vacancies in the p type material, according to the Hg diffusion mechanism.⁹ For designing IRFPAs, the diffused pn junction position has to be accurately controlled, considering the relationship between carrier concentration (Hg vacancies) and annealing conditions. For this purpose, the low temperature PIA process is adequate. Moreover, it is essential to elucidate what physical parameters are influenced by PIA process.

This paper presents fabrication of two kinds of HgCdTe diodes with different carrier concentrations, improvement in diode performances by the PIA process at low temperature and model fitting analyses of the diode performances. To the best of the authors' knowledge, this paper is the first report wherein the improved diode performances achieved by low temperature PIA process are quantitatively related with changes in physical parameters, such as trap densities and carrier concentrations in the pn junction.

DEVICE STRUCTURE AND FABRICATION

The two kinds of materials used, purchased from Fermionics, were undoped p type Hg_{1-x}Cd_xTe (x≈0.22) wafers grown on CdZnTe substrates by liquid phase epitaxy (LPE), with carrier concentrations of 1.3×10^{16} and 4.0×10^{16} cm⁻³, respectively.

Two kinds of diodes were made on each material, as indicated below. After a Br-methanol etch, a 100 nm CdTe layer for the passivating surface¹¹ was deposited in the molecular beam epitaxy (MBE) chamber at 80°C substrate temperature, preventing out-diffusion of Hg atoms during the deposition. The n on p junction was formed with B ion-implantation through the CdTe layer at 160 keV energy and at a 2.5×10^{14} cm⁻² dose. The pn junction is round in shape

with a 20 or 30 μm diameter. After a 300 nm ZnS layer was deposited for electrical isolation using an electron-beam, contact holes were opened through the ZnS and the CdTe layer, and In (1 μm thick) and Au/Ti (300 nm/50 nm thick) were evaporated for n-layer contact and p-layer contact, respectively. Special care was taken to avoid undesired heating (over 80°C) of the samples during the fabrication process. The diode structure is shown in Fig. 1. These diodes were mounted on packages. Table I shows physical parameters such as carrier concentration and hole mobility in the material on which two kinds of diodes were made.

ANNEALING PROCESS AND DIODE PERFORMANCES

Interstitial Hg atoms, which are created in the pn junction vicinity by ion-implantation, are easily diffused at relatively low temperature below 150°C, due to thermal instability of the Hg atoms. Therefore, the improvement in diode performance by low temperature PIA is expected. Moreover, since the PIA process can be carried out for the diodes mounted in packages, improved characteristics of the same sample, before and after the PIA process, are directly observed and compared.

Annealing Process

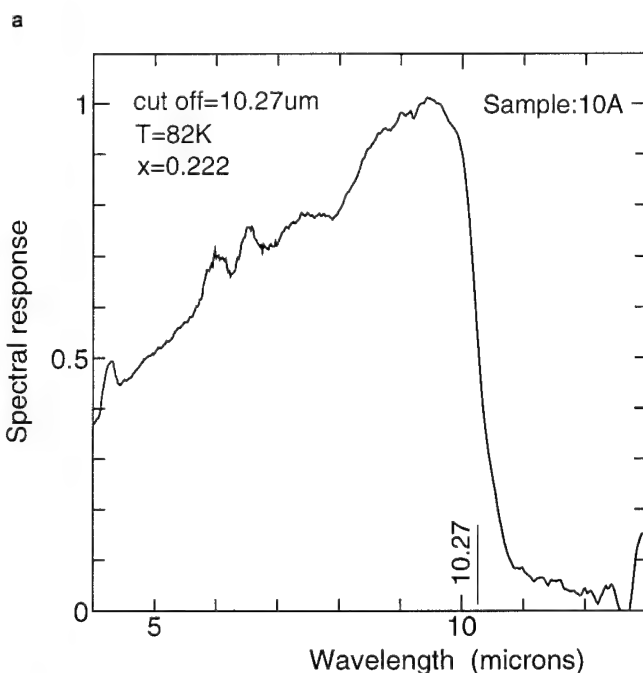
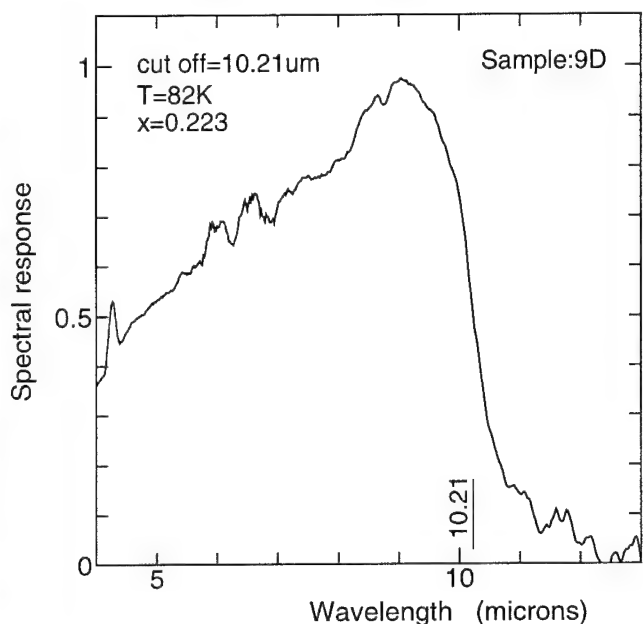
The PIA processings were implemented at 120 and 150°C under N₂ gas atmosphere. Hg out diffusion was neglected because of surface passivation of CdTe and ZnS. The PIA conditions, including annealing time for each diode in this study, are summarized in Table I. These conditions were determined for two types of diode, considering carrier concentrations of p type materials, such that a lower temperature was chosen for the diode with lower carrier concentration. It should be mentioned that, when higher annealing temperature is applied to the diodes with low carrier concentration, pn junction shift becomes uncontrollably large, because the Hg diffusion is too fast.

Diode Performances

Spectral response, current-voltage (I-V) and dynamic resistance-voltage (R-V) characteristics for two diodes were measured at 82K. Figures 2a and 2b show the spectral responses, for sample 9D and for sample 10A, respectively. The cutoff wavelength and the Cd

compositions (x values)¹² are 10.21 μm , $x = 0.223$ and 10.27 μm , $x = 0.222$, respectively. These values, along with intrinsic carrier concentrations calculated from x values,¹² are presented in Table I.

I-V and R-V characteristics, before and after the PIA process, are shown in Fig. 3 for a diode with lower carrier concentration (e.g. sample 9D) and in Fig. 4 for a diode with higher carrier concentration (e.g. sample 10A). It should be mentioned that several other diodes with the low and high carrier concentrations showed characteristics very similar to those in Fig. 3 and Fig. 4, respectively. The dark currents for both diodes at reverse bias voltage are dramatically decreased by



b

Fig. 2. Relative spectral response at 82K for the HgCdTe photodiode: (a) for sample 9D, and (b) for sample 10A.

individual optimal low temperature PIA processes.

Figure 3 confirms that, for a diode treated with PIA1 (120°C/1.5H), dark current is markedly reduced and that dynamic resistance is improved over one order of magnitude in reverse bias region (e.g. maximum value is 30 $\text{M}\Omega$), although the R_0 value for the annealed diode becomes a little bit larger than the R_0 value for an unannealed diode. The drastic improvement is presumably due to reduced TAT current which limits the R-V characteristics at this bias region, as discussed later. On the other hand, R-V characteristics for a diode treated with PIA2 (120°C/3H+150°C/1H) are inferior to those for a PIA1 treated diode. A little flatter slope in the R-V curve at the

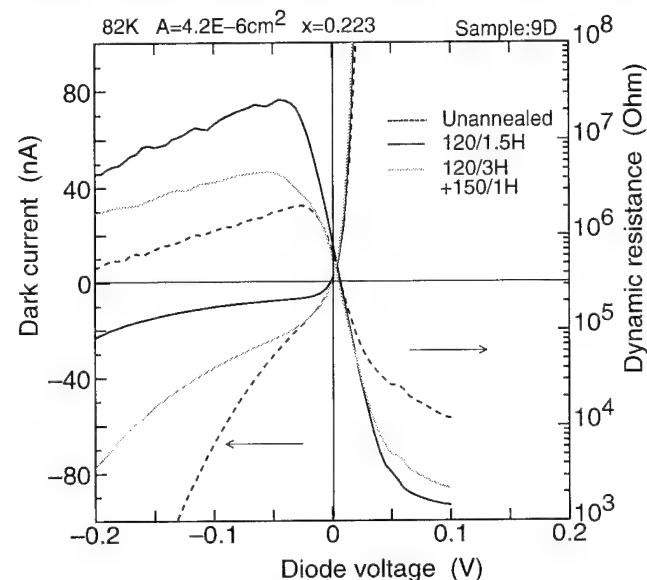


Fig. 3. I-V and R-V characteristics, measured at 82K, for a diode with a lower carrier concentration, $1.3 \times 10^{16} \text{ cm}^{-3}$ (sample 9D). Pn junction area A is $4.2 \times 10^{-6} \text{ cm}^2$ and x is 0.223.

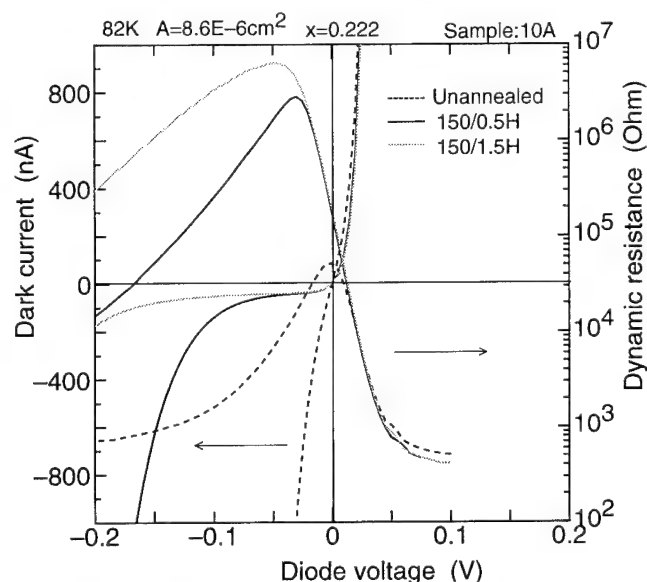


Fig. 4. I-V and R-V characteristics, measured at 82K, for a diode with higher carrier concentration, $4.0 \times 10^{16} \text{ cm}^{-3}$ (sample 10A). Pn junction area A is $8.6 \times 10^{-6} \text{ cm}^2$ and x is 0.222.

reverse bias region indicates that GR current mainly contributes to dark current, rather than TAT current. The inferior characteristics, caused by the excessive PIA for diodes with lower carrier concentration is ascribed to enlargement of the pn junction periphery, resulting from pn junction position shift (see the next section). These experimental results show that the optimal PIA process dramatically increases dynamic resistance at reverse bias for diodes which show diffusion current like the characteristics prior to the PIA, although it hardly changes the R_0 value. Therefore, the PIA process is useful for the device operated at a low reverse bias voltage (~ 50 mV), such as FPAs.

Figure 4 shows I-V and R-V characteristics for diodes with p type carrier concentration as high as $4.0 \times 10^{16} \text{cm}^{-3}$. For an unannealed diode, a dark current at zero bias is dominated by BBT current, because of the higher carrier concentration. The PIA process dramatically improved the diode performance. It is observed that the R-V characteristics for a diode treated with PIA1 ($150^\circ\text{C}/0.5\text{H}$) are dominated by diffusion current around zero bias voltage and by BBT current in reverse bias region. The R-V characteristics were much more improved by a further annealing process ($150^\circ\text{C}/1.5\text{H}$). The improvement can be explained by the change in the carrier concentration profile in the pn junction vicinity, as discussed later in detail.

MODEL FITTING ANALYSES FOR DYNAMIC RESISTANCE

Fitting Model

The measured R-V characteristics can be fitted with a combination of diffusion current, GR current, TAT current, and BBT current. Individual current formulas used in this study are expressed as follows.

Diffusion Current

Diffusion current dominates dark current from around 0 bias to the forward bias region.¹³ A major contribution to the diffusion current for the n on p type diode is a current from the p region (J_{diff}), and, hence,

$$J_{\text{diff}} = J_{\text{odiff}} \left(\exp \frac{qV}{kT} - 1 \right) \quad (1)$$

$$J_{\text{odiff}} = \frac{qn_i^2}{N_A} \left(\frac{kT\mu_e}{q\tau_e} \right)^{\frac{1}{2}} \quad (2)$$

where n_i is the bulk intrinsic carrier concentration,¹² N_A is acceptor concentration in the p type region, that is almost Hg vacancy, and μ_e and τ_e are minority carrier (electron) mobility and lifetime, respectively.

Generation-Recombination Current

Impurities or defects located within the space-charge region can act as generation-recombination

centers, which cause GR current. Generation-recombination current is expressed as follows.¹⁴

$$J_{\text{GR}} = J_{\text{0GR}} \frac{2 \sinh \frac{qV}{2kT}}{\left(1 - \frac{V}{V_{\text{bi}}} \right)^{\frac{1}{2}}} f(b) \quad (3)$$

where V_{bi} is the built in voltage for the pn junction. The function $f(b)$, determined by recombination center energy level, intrinsic Fermi energy level and bias voltage, is expressed in Ref. 14. A coefficient J_{0GR} , which is generated by recombination centers in the space-charge region, is divided into bulk component and surface component and is expressed for a round shaped diode as follows:

$$J_{\text{0GR}} = J_{\text{0GRb}} + J_{\text{0GRs}} = \frac{n_i W_0}{\tau_0} \frac{kT}{V_{\text{bi}}} + \frac{4s_0 n_i W_0}{d} \frac{kT}{V_{\text{bi}}} \quad (4)$$

where τ_0 is effective carrier lifetime in space-charge region, W_0 is depletion layer width at zero bias, s_0 is surface recombination velocity, and d is diode diameter.

Band-to-Band Tunneling Current

Band-to-band tunneling current becomes prominent, as the bandgap of HgCdTe is small. BBT current is expressed as follows.^{15,16}

$$J_{\text{t dir}} = \frac{q^3 (2m^*)^{\frac{1}{2}} E (V_{\text{bi}} - V)}{4\pi^3 (h/2\pi)^2 E_g^{\frac{1}{2}}} \exp \left(- \frac{\pi (m^*/2)^{\frac{1}{2}} E_g^{\frac{3}{2}}}{2qE(h/2\pi)} \right) \quad (5)$$

where m^* is the effective mass characterizing edges of conduction and light-hole bands, h is Planck constant, E is the electric field in the space-charge region, and E_g is bandgap energy.

Trap-Assisted Tunneling Current

Trap-assisted tunneling current results from indirect transition by way of intermediate trap sites in the junction region. Trap-assisted tunneling current is expressed as follows.^{17,18}

$$J_{\text{tSR}} = \frac{\pi^2 q^2 m^* |W_c|^2 N_t (V_{\text{bi}} - V)}{h^3 (E_g - E_t)} \exp \left(- \frac{\sqrt{3} E_g^2}{8\sqrt{2} qP E} \frac{1}{E} f(\alpha) \right) \quad (6)$$

$$f(\alpha) = \frac{\pi}{2} + \sin^{-1}(1 - 2\alpha) + 2(1 - 2\alpha)\sqrt{\alpha(1 - \alpha)}$$

$$\alpha = E_t / E_g \quad (7)$$

where N_t is trap density in the space-charge region, P is Kane matrix element, $|W_c|$ is transition matrix element between trap level and conduction band, and E_t is trap level. It is reasonable to take a relation $E_t = E_g/2$.¹⁷

When model fitting is carried out, several fitting parameters should be determined, such as μ_e/τ_e for diffusion current, s_0 and τ_0 for GR current, N_D for BBT current, and N_t for TAT current [see Eqs. (1–7)], where N_D is donor concentration in n side region. First, the fitting is performed in forward bias region, considering diffusion current, which uniquely determines μ_e/τ_e . Second, BBT current mechanism gives an upper limit for the N_D value, which is obtained by a fitting procedure in the large reverse bias region (~ 0.2 V). Starting with this N_D value, the R-V curve, measured in the small reverse bias region, can be fitted by s_0 , τ_0 , and N_t as well as the N_D value. This whole fitting procedure yields an ambiguity of a factor of three for the free parameters mentioned above.

Performance Improvement for the Diode with Lower Carrier Concentration

The R-V characteristics for the diode with lower carrier concentration $1.3 \times 10^{16} \text{ cm}^{-3}$ (e.g. sample 9D), measured both prior to and after PIA process, are fitted with calculations (see Figs. 5a, 5b, and 5c), using formulae mentioned above. It can be seen in Fig. 5a that the R-V characteristics, measured prior to the PIA process, are fitted with diffusion current and GR current at around 0 bias, while it is fitted with GR current and TAT current in the reverse bias region. The discrepancy between the measurement and the

calculation in the large forward bias region is due to the diode series resistance.

Figure 5b shows both experimentally obtained and theoretical R-V characteristics for a diode treated with $120^\circ\text{C}/1.5\text{H}$ PIA process. At around 0 bias, the R-V characteristics are completely limited by the diffusion current, while in the reverse bias region, they are dominated by GR current and TAT current. Improvement in characteristics is found to be caused by a reduction in surface recombination velocity s_0 and trap density N_t . According to the calculations, N_t decreases from $5 \times 10^{12} \text{ cm}^{-3}$ to $4 \times 10^{11} \text{ cm}^{-3}$ and s_0 decreases from $7 \times 10^4 \text{ cm/s}$ to $5 \times 10^3 \text{ cm/s}$. These parameters are shown in Table II. Since effective carrier lifetime τ_0 hardly contributes to this parameter fitting, it is not discussed here. The improved surface recombination velocity is consistent with values for the CdTe passivation layer.¹⁹ Although these values for trap densities are not exact, because of uncertainties in the calculations and difficulty in directly measuring the value, it is evident that trap density is reduced by the PIA process. The improvement in characteristics or in these parameters can be explained as follows. The PIA process diffuses interstitial Hg atoms into a deeper part of the p type region, so that the pn junction position shifts from the damaged region, which contains many trap densities and recombination centers created by ion-implantation

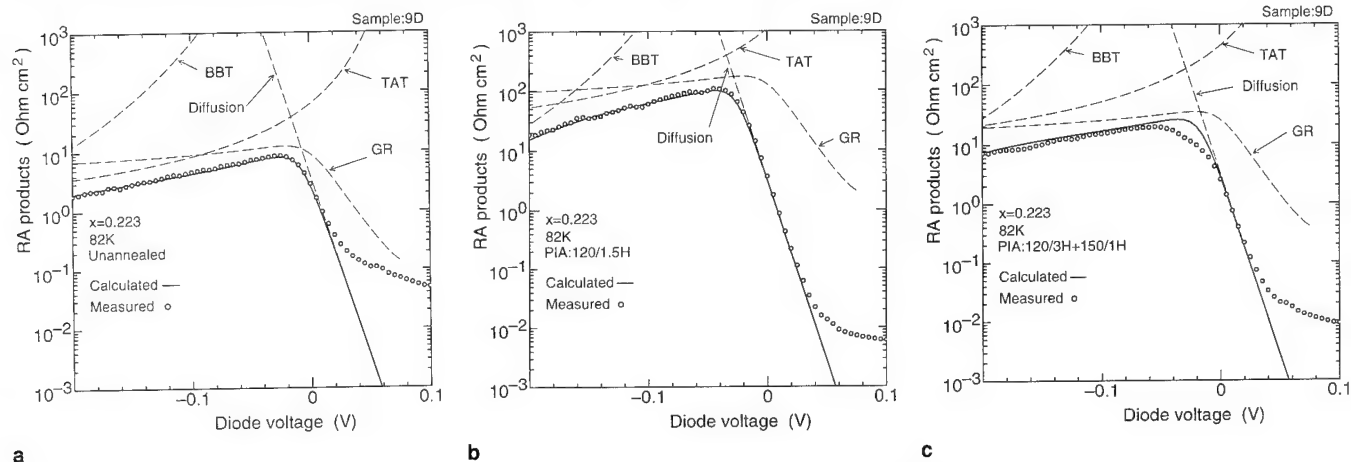


Fig. 5. Measured (dot symbol) and calculated (solid line curve) R-V characteristics for a diode with lower carrier concentration. The characteristics in (a) are for an unannealed diode. Free parameters, with which the characteristics are modeled, are as follows: $\mu_e/\tau_e = 1.7 \times 10^{14} \text{ cm}^2/\text{Vs}^2$, $s_0 = 70000 \text{ cm/s}$, $N_D = 8.0 \times 10^{15} \text{ cm}^{-3}$, $N_t = 5.0 \times 10^{12} \text{ cm}^{-3}$. The characteristics in (b) are for a diode treated with PIA1 ($120^\circ\text{C}/1.5\text{H}$). The parameters are $\mu_e/\tau_e = 2.5 \times 10^{14} \text{ cm}^2/\text{Vs}^2$, $s_0 = 5000 \text{ cm/s}$, $N_D = 7.0 \times 10^{15} \text{ cm}^{-3}$, $N_t = 4.0 \times 10^{11} \text{ cm}^{-3}$. The characteristics in (c) are for a diode treated with PIA2 ($120^\circ\text{C}/3\text{H}+150^\circ\text{C}/1\text{H}$). The parameters are $\mu_e/\tau_e = 2.5 \times 10^{14} \text{ cm}^2/\text{Vs}^2$, $s_0 = 20000 \text{ cm/s}$, $N_D = 7.0 \times 10^{15} \text{ cm}^{-3}$, $N_t = 1.0 \times 10^{12} \text{ cm}^{-3}$.

Table II. Fitting Parameters Adopted in Fitting Models

Sample No.	Anneal ($^\circ\text{C}/\text{h}$)	$\mu_e/\tau_e \times 10^{14}$ (cm^2/Vs^2)	s_0 (cm/s)	$N_A \times 10^{16}$ (cm^{-3})	$N_D \times 10^{16}$ (cm^{-3})	$N_t \times 10^{12}$ (cm^{-3})	Ref.
9D	Unannealed	1.7	70000	1.3	0.80	5.0	Fig. 5a
	120/1.5	2.5	5000	1.3	0.70	0.4	Fig. 5b
	120/3+150/1	2.5	20000	1.3	0.70	1.0	Fig. 5c
10A	Unannealed	50	500000	4.0	3.3	1.0	Fig. 6a
	150/0.5	50	20000	4.0	1.05	0.4	Fig. 6b
	150/1.5	50	15000	4.0	0.65	0.3	Fig. 6c

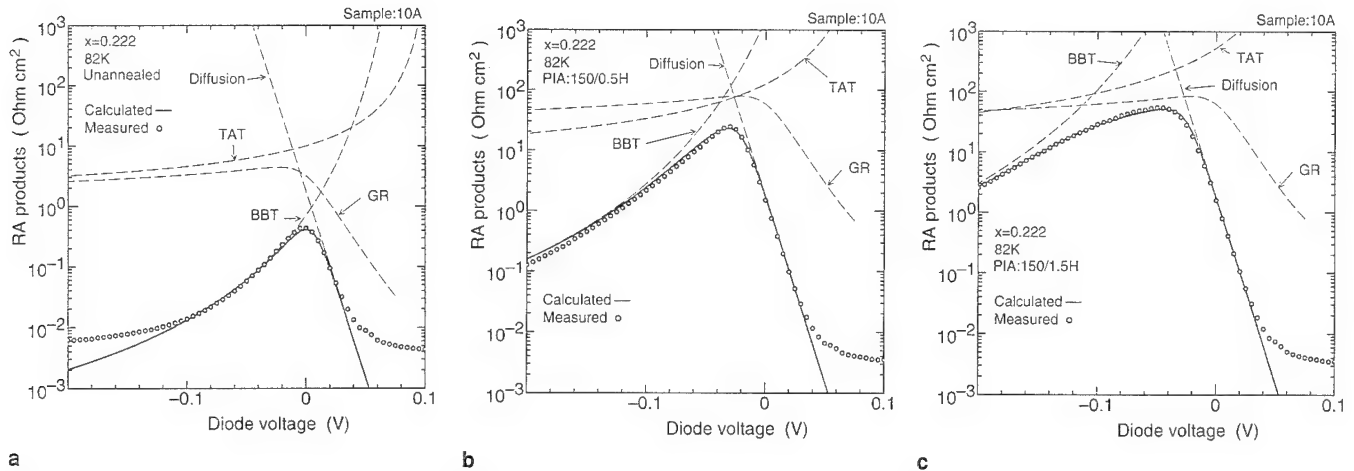


Fig. 6. Measured (dot symbol) and calculated (solid line curve) R-V characteristics for a diode with higher carrier concentration. The characteristics in (a) are for an unannealed diode. Free parameters, with which the characteristics are modeled, are as follows: $\mu_e/\tau_e = 5.0 \times 10^{15} \text{ cm}^2/\text{Vs}^2$, $s_0 = 500000 \text{ cm/s}$, $N_D = 3.3 \times 10^{16} \text{ cm}^{-3}$, $N_A = 1.0 \times 10^{12} \text{ cm}^{-3}$. The characteristics in (b) are for a diode treated with PIA1 (150°C/0.5H). The parameters are $\mu_e/\tau_e = 5.0 \times 10^{15} \text{ cm}^2/\text{Vs}^2$, $s_0 = 20000 \text{ cm/s}$, $N_D = 1.05 \times 10^{16} \text{ cm}^{-3}$, $N_A = 4.0 \times 10^{11} \text{ cm}^{-3}$. The characteristics in (c) are for a diode treated with PIA2 (150°C/1.5H). The parameters are $\mu_e/\tau_e = 5.0 \times 10^{15} \text{ cm}^2/\text{Vs}^2$, $s_0 = 15000 \text{ cm/s}$, $N_D = 6.5 \times 10^{15} \text{ cm}^{-3}$, $N_A = 3.0 \times 10^{11} \text{ cm}^{-3}$.

process, into a less damaged region.

As shown in Fig. 5c, any further PIA process (120°C/3H + 150°C/1H) degrades the R-V characteristics. In other words, the dynamic resistance in the reverse bias region is clearly reduced, as compared with the R-V curve shown in Fig. 5b, and the R-V curve becomes a little flatter, which indicates that GR current becomes more dominant than TAT current. The probable reason for the degradation is expressed as follows. By a further PIA process, pn junction position shifts excessively and reaches a region containing more dislocations in p type material,²⁰ where τ_0 is reduced, due to larger trap density. Therefore, the bulk component of the GR current, rather than the surface component, increases, which suggests that the s_0 value may not be as large as the value presented in Table II.

For a diode with a lower carrier concentration, the PIA process at a temperature as low as 120°C is desired. Then, an appropriate amount of Hg atoms diffuses into a deeper part of the p layer and compensates for a small amount of Hg vacancies. If the diode is treated with a further PIA process at a higher temperature, such as 150°C, the pn junction position shifts beyond the optimal position, which results in degraded characteristics.

Performance Improvement for a Diode with Higher Carrier Concentration

As shown in Fig. 6a, R-V characteristics for unannealed diodes with higher carrier concentrations can be fitted with diffusion current and BBT current, using parameters $\mu_e/\tau_e = 50 \times 10^{14} \text{ cm}^2/\text{Vs}^2$, $N_A = 4.0 \times 10^{16} \text{ cm}^{-3}$ (p type material carrier concentration), and $N_D = 3.3 \times 10^{16} \text{ cm}^{-3}$. The discrepancies between the measurement and the calculation in both the large forward bias region and the large reverse bias region are due to the diode series resistance. The R-V curve looks like a cusp, with a peak near zero bias, and it is dominated by BBT current. Dynamic-resis-

tance voltage characteristics for a diode treated with 150°C/0.5H PIA process is also fitted with diffusion and BBT current (see Fig. 6b). However, the diffusion current becomes dominant at around 0 bias and the bias voltage, which gives the maximum dynamic resistance, is shifted to the reverse bias region by about 30 mV. A value, where $N_D = 1.05 \times 10^{16} \text{ cm}^{-3}$ is used as a fitting parameter, indicative of n⁻ region formation by the PIA process.

Any further PIA process (150°C/1.5H) improved the R-V characteristics, which are fitted with diffusion current, GR current, and BBT current, as shown in Fig. 6c. The RV curve in the reverse bias region changes to a flat shape from a cusp shape. The reason for the improvement is explained as follows. Because the additional PIA process forms a little wider n⁻ region, BBT current is greatly reduced. On the other hand, the wider depletion region contains more recombination centers and, therefore, GR current becomes dominant. The fitting is carried out, using parameters $N_D = 6.5 \times 10^{15} \text{ cm}^{-3}$ and $s_0 = 1.5 \times 10^4 \text{ cm/s}$. Then, the N_D value seems close to the background impurity level, because the n⁻ region is created by compensating for Hg vacancies in the p layer with interstitial Hg atoms. Fitting parameters used in these analyses are summarized in Table II.

In order to improve the characteristics for diodes with higher carrier concentration, the PIA process at a higher temperature, such as about 150°C, is desired. Then, more interstitial Hg atoms diffuse into a deeper part of the p type layer and compensate for Hg vacancies in the layer (n⁻ region formation). The n⁻ region, formed by the PIA process, mainly contributes to an improvement in diode characteristics, because the characteristics prior to the PIA process are dominated by BBT current.

CONCLUSION

Improvement in the diode characteristics for the HgCdTe n on p structure, brought about by the low

temperature PIA process, was studied for two kinds of diodes with low and high carrier concentrations. The improved characteristics were fitted with four dark current mechanisms.

The dark current for a diode with a lower carrier concentration is dominated by GR current and TAT current at reverse bias voltage, both before and after the PIA processes. Improvement in characteristics by the PIA process is found to be caused by a reduction in both surface recombination velocity and trap density, by one order of magnitude. While, before the PIA process, the dark current for a diode with a higher carrier concentration is dominated by the BBT current. After the process, the GR current begins to dominate the dark current. The change in the diode characteristics is explained mainly by formation of the n⁻ region by the PIA process. These improvements for two diodes with different carrier concentrations are explained by changes in both carrier concentration profile and pn junction position, determined by interaction of interstitial Hg atoms with Hg vacancies in the junction vicinity.

In conclusion, the diode performances are improved by the low temperature PIA process, which changes physical parameters in the pn junction, such as trap density, surface recombination velocity, and carrier concentration profile. This process is effective for device fabrication, when an appropriate annealing temperature is chosen, considering the carrier concentration in the p type layer.

REFERENCES

1. A. Rogalski, A. Jozwikowska, K. Jozwikowski and J. Rutkowski, *Infrared Phys.* 33, 463 (1992).
2. J.M. Arias, J.G. Pasko, M. Zandian, S.H. Shin, G.M. Williams, L.O. Bubulac, R.E. DeWames and W.E. Tennant, *J. Electron. Mater.* 22, 1049 (1993).
3. J.M. Arias, J.G. Pasko, M. Zandian, L.J. Kozlowski and R.E. DeWames, *Optical Eng.* 33, 1422 (1994).
4. R.B. Bailey, L.J. Kozlowski, J. Chen, D.Q. Bui, K. Vural, D.D. Edwall, R.V. Gil, A.B. Vanderwyck, E.R. Gertner and M.B. Gubala, *IEEE Trans. Electron Dev.* 38, 1104 (1991).
5. T. Kanno, M. Saga, A. Kawahara, R. Oikawa, A. Ajisawa, Y. Tomioka, N. Oda, T. Yamagata, S. Murashima, T. Shima and N. Yasuda, *SPIE* 2020, 41 (1993).
6. T. Kanno, M. Saga, N. Kajihara, K. Awamoto, G. Sudo, Y. Ito and H. Ishizaki, *SPIE* 2020, 49 (1993).
7. V.A. Cotton and J.A. Wilson, *J. Vac. Sci. Technol. A* 4, 2177, (1986).
8. L.O. Bubulac, W.E. Tennant, R.A. Riedel and T.J. Magee, *J. Vac. Sci. Technol.* 21, 251 (1982).
9. L.O. Bubulac, *J. Cryst. Growth* 86, 723 (1988).
10. S.Y. Wu, W.J. Choyke, W.J. Takei, A.J. Noreika, M.H. Francombe and R.B. Irwin, *J. Vac. Sci. Technol.* 21, 255 (1982).
11. G. Sarusi, G. Cinader, A. Zemel, D. Eger and Y. Shapira, *J. Appl. Phys.* 71, 5070 (1992).
12. G.L. Hansen and J.L. Schmit, *J. Appl. Phys.* 54, 1639 (1983).
13. M.B. Reine, A.K. Sood and T.J. Tredwell, *Semiconductors and Semimetals*, Vol. 18, Chap. 6.
14. C.T. Sah, R.N. Noyce and W. Shockley, *Proc. IRE* 45, 1228 (1957).
15. M.A. Kinch, *J. Vac. Sci. Technol.* 21, 215 (1982).
16. Y. Nemirovsky and I. Bloom, *Infrared Phys.* 27, 143 (1987).
17. W.W. Anderson and H.J. Hoffman, *J. Appl. Phys.* 53, 9130 (1982).
18. Y. Nemirovsky, D. Rosenfeld, R. Adar and A. Kornfeld, *J. Vac. Sci. Technol.* A7, 528 (1989).
19. G. Sarusi, A. Zemel, D. Eger, S. Ron and Y. Shapira, *J. Appl. Phys.* 72, 2312 (1992).
20. D. Chandra, J.T. Tregilgas and M.W. Goodwin, *J. Vac. Sci. Technol.* B9, 1852 (1991).

Effect of Cooling Procedure After Annealing on Electrical Properties of $\text{Cd}_{0.2}\text{Hg}_{0.8}\text{Te}$ Epitaxial Films Grown by Liquid Phase Epitaxy

Z. KAWAZU, S. OCHI, T. SONODA, and S. TAKAMIYA

Optoelectronic and Microwave Devices Laboratory, Mitsubishi Electric Corporation, 4-1, Mizuhara, Itami, Hyogo, 664 Japan

Effect of cooling procedure after annealing on the electrical properties of $\text{Cd}_{0.2}\text{Hg}_{0.8}\text{Te}$ (CMT) epitaxial films grown by liquid phase epitaxy has been investigated to obtain the CMT films with low carrier concentration of 10^{14} cm^{-3} reproducibly. Annealing has been performed at the temperature range from 260 to 350°C for 8 h in a fixed Hg vapor pressure. The quenching and the gradual cooling over a duration of 200 min after annealing have been employed for the cooling procedures. For quenched CMT samples, hole concentration decreases with decreasing anneal temperature and conduction type conversion from p to n is observed at 300°C . For the gradual cooling, all samples show n-type conduction for all annealing temperatures. Electrical properties of annealed layers strongly depend on the cooling procedure. The difference in electrical properties of the annealed CMT between two types of cooling procedure is mainly attributed to the difference in the annihilation of Hg vacancies during cooling procedure. The decrease of Hg vacancies during quenching is negligible, while Hg vacancies are annihilated during gradual cooling by rapid Hg diffusion. The diffusion coefficient of Hg is estimated more than $10^{-9} \text{ cm}^2/\text{s}$ and this value is two orders of magnitude larger than that obtained by radiotracer technique.

Key words: HgCdTe, Hg-rich annealing, Hg vacancies, thermal annealing

INTRODUCTION

For the fabrication of photoconductive infrared (IR) detectors, n-type $\text{Cd}_{0.2}\text{Hg}_{0.8}\text{Te}$ (CMT) with carrier concentration range of low 10^{14} cm^{-3} is needed and the annealing after growth is very important to determine the carrier concentration. In order to obtain such CMT layers, low temperature annealing at less than 300°C has been widely employed.¹⁻⁷ However, it is difficult to control the carrier concentration reproducibly at the low carrier concentration range. The variation of carrier concentration in this range is believed to be caused by the residual impurities and by the variation of annealing condition,⁸ but it has not been clear how the free carrier concentration is actually determined.

Furthermore, few papers have been reported on annealing behavior of CMT for this carrier concentra-

tion range. In order to reproducibly obtain high quality CMT layers with carrier concentration in range of low 10^{14} cm^{-3} , it is important to clarify the mechanism how the free carrier concentration is controlled in such low level.

We have investigated the effect of cooling procedure after annealing at temperatures in the range from 260 to 350°C on the electrical properties of CMT layers grown by liquid phase epitaxy (LPE). The quenching and the temperature controlled gradual cooling for the duration of 200 min after annealing have been employed for the cooling procedure. A constant low carrier concentration of $3 \times 10^{14} \text{ cm}^{-3}$ with mobility more than $2 \times 10^5 \text{ cm}^2/\text{V}\cdot\text{s}$ in the gradually cooled CMT has been obtained at a wide temperature range from 320 to 260°C . The quenched samples show the conduction type conversion from p to n with decreasing anneal temperature.

In this paper, we have concentrated on the annealing behavior, especially the cooling procedure

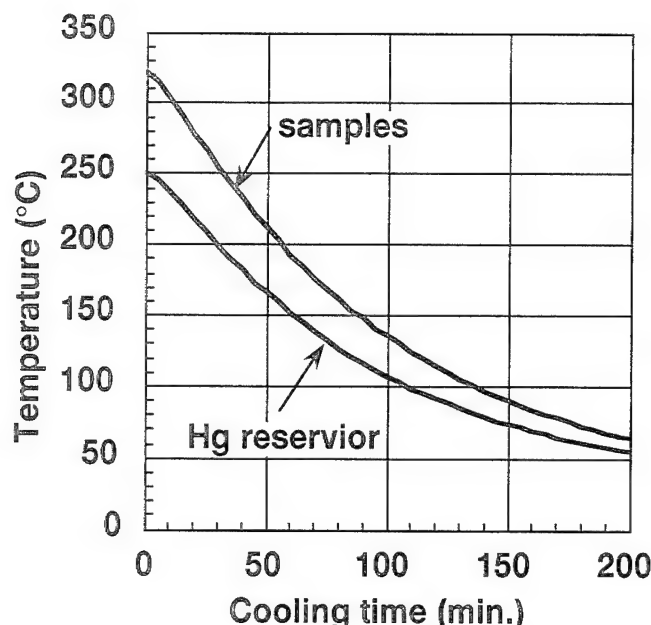


Fig. 1. The temperature of the sample and the Hg reservoir as a function of cooling time after annealing at 320°C.

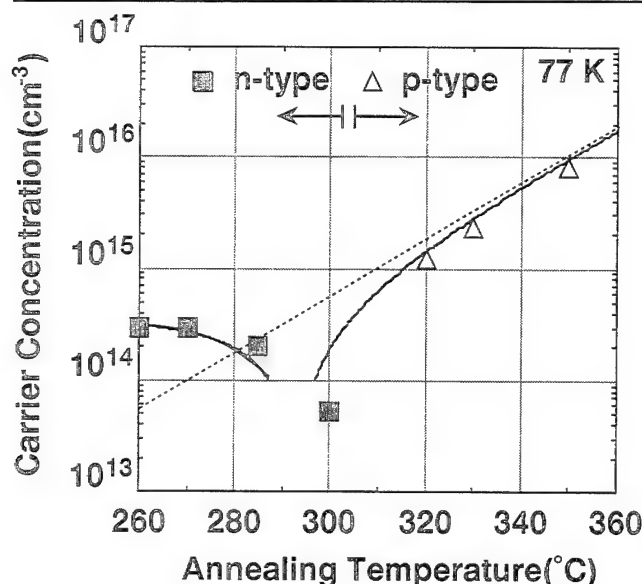


Fig. 2. 77K carrier concentration as a function of annealing temperature for quenched CMT samples. Solid line shows the calculated hole concentration.

after annealing. We compare the electrical properties of CMT between the quenched and the gradually cooled samples, and then discuss how the carrier concentration in these samples are determined. And we have also estimated the diffusion coefficient of Hg during cooling procedure after annealing.

EXPERIMENT

CMT layers were epitaxially grown on (111)B CdTe substrates by LPE using a slider boat in an open tube horizontal system.⁹ Growth started at 480°C and stopped at 465°C. All the as-grown samples had layer thickness of about 25 μm and showed p-type conduction with carrier concentration of 1 to $2 \times 10^{17} \text{ cm}^{-3}$

with Hall mobility about $400 \text{ cm}^2/\text{V}\cdot\text{s}$ at 77K. Annealing was carried out in a closed-tube two-zone system. Before annealing, the samples were cut into six pieces (usually $6 \times 6 \text{ mm}^2$) and were soaked in organic solvents followed by about $1 \mu\text{m}$ etching in Br-methanol. Annealing temperatures for CMT samples were in the range of 260–360 °C and mercury pressure was kept at 0.1 atm (250°C) during the 8 h anneal. After the annealing, the ampoules were rapidly quenched in water, or gradually cooled in the furnace to lower than 50°C in 200 min. The cooling rate of the CMT samples is about $120^\circ\text{C}/\text{h}$ for first 1 h. Figure 1 shows the cooling curves both for the CMT sample and for the Hg reservoir temperatures after 320°C annealing. During gradual cooling, the temperatures of the sample and the Hg reservoir were controlled such that Hg precipitation on CMT layers was avoided and additional Hg vacancies in the layers were also avoided. In order to investigate the dependence of cooling time on the electrical properties, some samples were quenched in water after 15 or 30 min gradual cooling in the furnace.

The composition and thickness of the epitaxial layer were measured by the Fourier transform infrared spectrometer (FTIR) at room temperature. The electrical properties of the annealed samples at 77K were evaluated by using the Van der Pauw method.¹⁰ The Hall measurement data were usually analyzed using one-carrier model. However, because of the extremely lower value of the effective mass of electrons than that of holes in CMT, some of the samples exhibited n-type conduction even when hole is the majority carrier. This is especially true for net hole concentration lower than 10^{16} cm^{-3} . In order to analyze the low carrier concentration samples, simple two-carrier analysis is used to estimate the net carrier concentration more precisely.

In a semiconductor containing free carriers in both the conduction band (electrons) and the valence band (holes), the Hall coefficient R_H is given by

$$R_H = \frac{q(\mu_p^2 p - \mu_n^2 n)}{\sigma_0^2} \quad (1)$$

where n and p are the concentration of electron and hole, respectively, μ_n and μ_p are the corresponding mobilities, q is the absolute value of the electronic charge, and σ_0 is the electrical conductivity given by

$$\sigma_0 = \frac{1}{\rho} = q(\mu_n n + \mu_p p) \quad (2)$$

where ρ is the resistivity.

$$n \cdot p = n_i^2 \quad (3)$$

where n_i is the intrinsic carrier concentration.

The values of n , p , μ_n , μ_p are estimated by fitting self-consistently. The measured values of R_H and ρ are fitted to theoretical values deduced from Eqs (1), (2), and (3). The values of n_i is taken from Hansen et al.¹¹

RESULT AND DISCUSSION

Quenching

Figure 2 shows the carrier concentration and mobility at 77K for quenched samples as a function of annealing temperature. With the decrease of annealing temperature, the hole concentration decreases and conduction type converts from p to n and finally the electron concentration saturates to $3 \times 10^{14} \text{ cm}^{-3}$. The mobility as high as $2 \times 10^5 \text{ cm}^2/\text{V}\cdot\text{s}$ from the sample annealed at lowest temperature (260°C) was obtained. The broken line shows the hole concentration calculated from the concentration of Hg vacancy in annealing temperature, deduced by using the mass action constant reported previously.³ We assumed that the Hg vacancy in the layer was doubly ionized and produced two holes. The solid line shows the difference between the calculated hole concentration and the saturated electron concentration ($3 \times 10^{14} \text{ cm}^{-3}$) determined by residual donor impurities. The calculated carrier concentrations shown by solid line agree well with the measured values.

These results indicate that the free carrier concentration of quenched CMT layers is substantially determined by the difference in concentration between residual donor impurities and holes produced by Hg vacancies. As our annealing experiments were carried out in low temperature, the thermal equilibrium in CMT layers at annealing temperature was frozen in by quenching in water, that is, the concentration change of Hg vacancy in the CMT during quenching is negligible.

Gradual Cooling

Figure 3 shows the carrier concentration and mobility at 77K for gradually cooled samples as a function of annealing temperature. The conduction type of

these samples was always n-type. The electron concentration of $3 \times 10^{14} \text{ cm}^{-3}$ and the Hall mobility as high as $2 \times 10^5 \text{ cm}^2/\text{V}\cdot\text{s}$ are independent of annealing temperature ranging from 260 to 320°C . Uniform electron concentration was obtained up to the interface between the CMT layer and the CdTe substrate in all samples.

These results indicate that the low electron concentration with high mobility for CMT layer is obtained in a wide annealing temperature range by using a gradual cooling method. The electron concentration of the layers gradually increases with the decrease of annealing temperature and approaches to the same saturated value as that for the quenched sample. This agreement of the carrier concentration at low annealing temperature indicates that the carrier concentration in the gradually cooled sample is also determined by the difference in concentration between residual donor impurities and holes produced by Hg vacancies. The Hg vacancies in the CMT layer for the temperature-controlled cooling just prior to cooling procedure have been almost annihilated during the gradual cooling.

Cooling Time Dependence

In the cooled sample, the concentration of Hg vacancy is determined by the difference in concentration between the Hg vacancies at the annealing temperature and the diffused Hg atoms in the layer during cooling. The decrease of Hg vacancy concentration is determined by the surface reaction between Hg and the CMT layer, and by the Hg diffusion in the CMT layer. Assuming that the surface reactions are faster than the Hg diffusion, the decrease of Hg vacancies in the CMT layer was considered to be dominated by the Hg diffusion in CMT layers. Figure 4 shows the dependence of carrier concentration on cooling time compared with calculated hole concen-

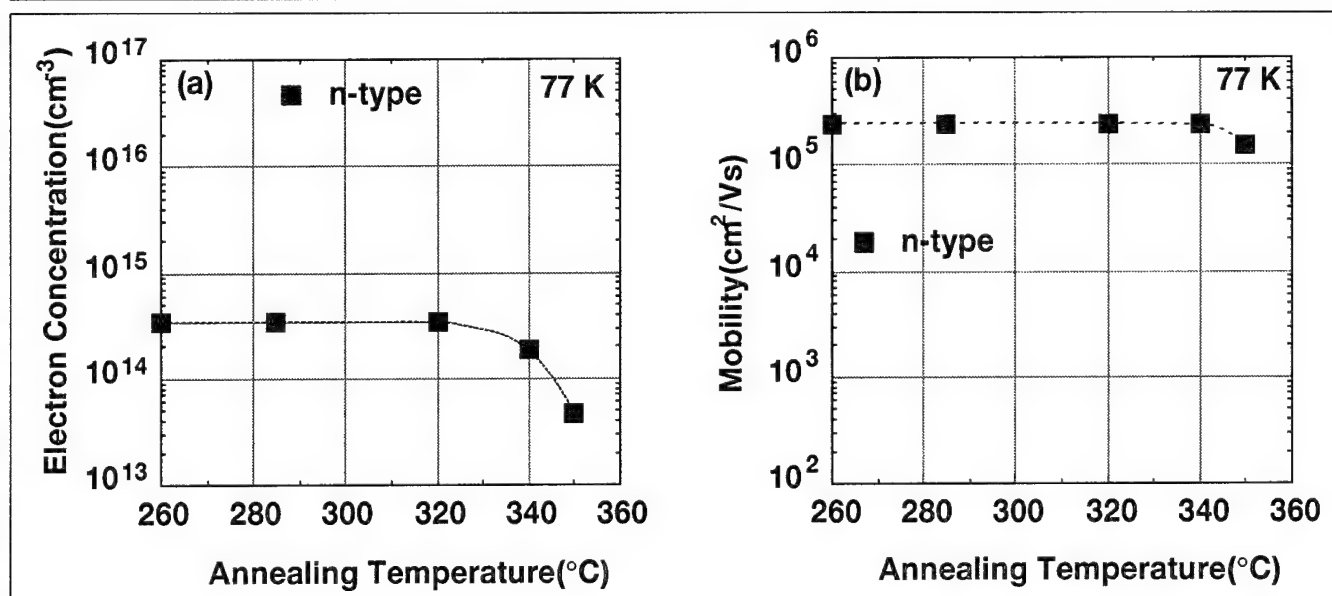


Fig. 3. 77K carrier concentration (a) and Hall mobility (b) as a function of annealing temperature for gradually cooled CMT samples.

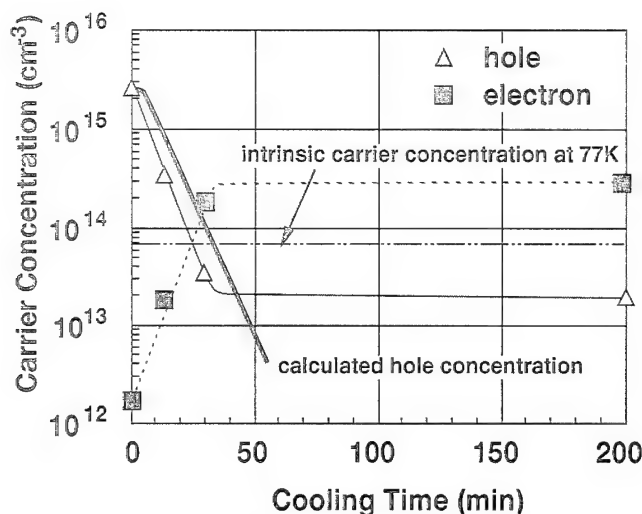


Fig. 4. 77K electron concentration and hole concentration estimated by Hall measurement with two carrier analysis. The solid line shows the calculated hole concentration.

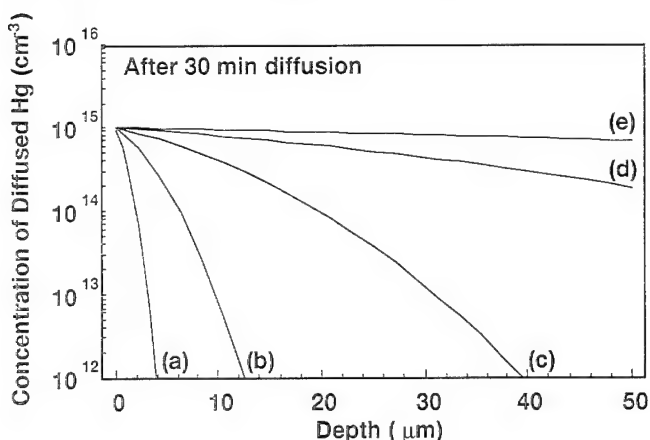


Fig. 5. Calculated diffusion profile of Hg with various diffusion coefficient: (a) 1×10^{-12} cm²/s, (b) 1×10^{-11} cm²/s, (c) 1×10^{-10} cm²/s, (d) 1×10^{-9} cm²/s, and (e) 1×10^{-8} cm²/s.

tration indicated by solid line. All the samples were annealed at 320°C. Uniform carrier concentration was obtained up to the interface between the CMT layer and the CdTe substrate in all samples. The hole concentration is calculated from the concentration of Hg vacancies assuming that at each temperature during cooling the annealing system reaches the thermal equilibrium. The hole concentration decreases as the gradual cooling time becomes longer and it saturates at 2×10^{13} cm⁻³ in about 30 min. The measured hole concentration of the CMT layers quenched after gradual cooling for 15 or 30 min agrees well with the calculated ones. This agreement indicates that Hg atoms diffuse into the CMT layers fast enough to keep the thermal equilibrium during cooling at cooling rate of about 120°C/h.

In order to estimate the diffusion coefficient of Hg atoms in the CMT layer during cooling, the calculation of the Hg concentration profiles as a function of diffusion coefficient was carried out, using following equation

$$C(x, t) = C(0, t) \operatorname{erfc}(x / 2\sqrt{D \cdot t}),$$

where C is the concentration of Hg diffused during cooling process, $C(0, t)$ is the concentration of Hg supplied from vapor phase during cooling at the CMT surface, erfc is the complementary error function, x is the distance from the surface, D is the diffusion coefficient of Hg, and t is the diffusing duration (30 min). We assume that the Hg concentration at the surface is constant and equal to the concentration of Hg vacancy at annealing temperature ($C_{v_{\text{Hg}}}$), and thus there is no mercury vacancy at the surface,

$$C(0, t) = C_0 C_{v_{\text{Hg}}}.$$

We also assume that the diffusion coefficient during cooling is constant to simplify the calculation and the thickness of the CMT layer is infinite. Figure 5 shows the calculated diffused Hg concentration profiles vs distance. The diffusion coefficient as large as 4×10^{-11} cm²/s at 300°C obtained by the radiotracer technique¹² was reported. However, it is not sufficient to entirely annihilate Hg vacancies as much as 1×10^{15} cm⁻³ in the CMT layer in 30 min after annealing. As seen in Fig. 5, diffusion coefficient over 10^{-9} cm²/s is necessary to obtain the n-type CMT layer by gradual cooling in 30 min after annealing. This value is two orders of magnitude larger than that obtained by radiotracer technique. This large difference in diffusion coefficient is considered to be attributed to the difference of the diffusion mechanism. In the case of tracer diffusion experiment, a tracer Hg atom has to exchange with a nonradiative Hg atom in the CMT layer and the tracer atoms diffuse by random walk. On the other hand, in our experiment, Hg concentration gradient makes Hg atoms diffuse into the layer and Hg atoms diffuse via vacancies without exchanging with the Hg atoms in the layer.

CONCLUSION

The carrier concentration of annealed CMT layers is determined by the concentration difference between residual donor impurities and holes produced by the Hg vacancy. The Hg vacancy concentration is determined by annealing temperature and cooling procedure.

High mobility CMT films with electron concentration in the low range of 10^{14} cm⁻³ were obtained by gradual cooling method at wide annealing temperature range. Hg diffusion into the CMT layers via Hg vacancies is fast enough to maintain the thermal equilibrium during cooling at the cooling rate of 120°C/h. It is considered that diffusion coefficient in this experiment is estimated more than 10^{-9} cm²/s and this value is two orders of magnitude larger than that obtained by radiotracer technique. During this cooling, Hg vacancies in the CMT layers are filled with diffused Hg atoms.

The annealing with temperature controlled gradual cooling is one of the most effective methods to obtain

high-quality CMT films reproducibly with low carrier concentration.

REFERENCE

1. J.L. Schmit and E.L. Stelzer, *J. Electron. Mater.* 7, 65 (1978).
2. J. Nishizawa, K. Suto, M. Kitamura, M. Sato, Y. Takese and A. Ito, *J. Phys. Chem. Solids* 37, 33 (1976).
3. H.R. Vidymanath, *J. Electrochem. Soc.* 128, 2609 (1981).
4. H.R. Vidymanath, *J. Electrochem. Soc.* 128, 2619 (1981).
5. H.R. Vidymanath, J.C. Donovan and D.A. Nelson, *J. Electrochem. Soc.* 128, 2625 (1981).
6. C.L. Jones, M.J.T. Quelch, P. Capper and J.J. Gosney, *J. Appl. Phys.* 53, 9080 (1982).
7. H.R. Vidymanath and C.H. Hiner, *J. Appl. Phys.* 65, 3080 (1989).
8. P. Capper, *J. Cryst. Growth* 57, 279 (1982).
9. K. Yasumura, H. Kimura and Y. Komine, *Mat. Res. Soc. Symp. Proc.* 102, 91 (1988).
10. L.J. Van der Pauw, *Philips Res. Rep.* 13, 1 (1958).
11. G.L. Hansen, J.L. Schmit and T.N. Casselman, *J. Appl. Phys.* 53, 7099 (1982).
12. M. Brown and A.F. Willoughby, *J. Vac. Sci. Technol.* A1, 1641 (1983).

Theoretical Evaluation of InTlP, InTlAs, and InTlSb As Long-Wave Infrared Detectors

A. SHER, M. VAN SCHILFGAARDE, S. KRISHNAMURTHY, and
M.A. BERDING

SRI International, Menlo Park, CA 94025

A.-B. CHEN

Physics Department, Auburn University, AL 36849

We have evaluated three III-V semiconductor alloys— $\text{In}_{1-x}\text{Tl}_x\text{P}$ (ITP), $\text{In}_{1-x}\text{Tl}_x\text{As}$ (ITA), and $\text{In}_{1-x}\text{Tl}_x\text{Sb}$ (ITS)—as possible candidates for future long-wave infrared (LWIR) detector materials. The cohesive energies, elastic constants, band structures, electron mobilities, and phase diagrams are calculated and are compared to those of $\text{Hg}_{1-x}\text{Cd}_x\text{Te}$ (MCT) alloys. The band gaps of all three III-V alloys change from negative to positive values as the alloy composition x decreases from 1 to 0. The x values for the 0.1-eV gap are estimated to be 0.67, 0.15, and 0.08, respectively, for ITP, ITA, and ITS. While both ITP and ITA form stable zincblende solid solutions for all alloy compositions, zincblende ITS is stable only for a range of x less than 0.15. The complication of the phase diagram in ITS is caused by the existence of a stable CsCl phase for pure TlSb. The alloy mixing enthalpies for ITP and ITA are comparable to those in MCT, and their phase diagrams should be qualitatively similar, characterized by simple lens-shape liquidus and solidus curves. Both ITP and ITA have considerably larger cohesive energies and elastic constants than those of MCT, indicating that they are structurally robust. At a 0.1-eV gap, the band structures near the gap and the electron mobilities in ITP, ITA, and ITS are also found to be comparable to those of MCT. Since the lattice constants of TlP and TlAs are less than 2% larger than the respective values in InP and InAs, the latter should provide natural substrates for the growth of active LWIR alloys and offer a potential to integrate the detector array and read-out circuit.

Key words: HgCdTe, InTlP, InTlAs, InTlSb, IR detectors

INTRODUCTION

We have proposed that the alloys $\text{In}_{1-x}\text{Tl}_x\text{P}$ and $\text{In}_{1-x}\text{Tl}_x\text{As}$ have properties that distinguish them as outstanding candidates for infrared (IR) electro-optic receiver and emitter devices.¹ Details of the methods used to do the calculations have been published¹ so only the results of importance to this community are extracted for presentation. This paper concentrates on the properties of $\text{In}_{1-x}\text{Tl}_x\text{P}$ in the long-wave infrared (LWIR) because this alloy nearly lattice matches to InP substrates and, therefore, offers the prospect of integrated laser emitters, focal-plane-array (FPA) detectors, and read-out integrated circuits (ROIC) on the same chip. This capability could enable use of device architectures formerly deemed impractical

because currently used LWIR materials are incapable of supporting them.

DISCUSSION

According to our first-principles theory, the following properties of TlP make it an attractive IR material candidate:

- It forms in the zincblende structure.
- Its lattice constant (5.96 Å) closely matches that of InP (5.83 Å) (so the pseudo-binary $\text{In}_{1-x}\text{Tl}_x\text{P}$ liquidus and solidus phase diagrams have simple lens shapes).
- Its cohesive energy per atom (2.56 eV/atom) is 58% greater than that of HgTe (1.62 eV/atom).
- It is a semimetal with a negative gap of -0.27 eV, about the same as that of HgTe (-0.3 eV).

The accompanying table presents the properties of the alloy with a 0.1-eV band gap that are related to

Table I. LWIR MCT ITP and ITA Properties Comparisons

Property	Hg _{0.78} Cd _{0.22} Te		In _{0.33} Tl _{0.67} P	In _{0.85} Tl _{0.15} As
	Theory	Experiment	Theory	Theory
1 \bar{E}_g [eV]	0.1	0.1	0.1	0.1
2 \bar{E}_b [eV/atom]	1.66	1.75	2.75	3.09
3 \bar{a} [Å]	6.45	6.46	5.92	6.08
4 $\hbar\omega_{T_0}$ [meV]	14.5	14.12	34.6	25.8
5 $B[10^{12}\text{erg/cm}^3]$	0.46	0.42	0.61	0.58
6a dE_g/dx [eV]	1.71	1.69 @ 0K	1.42	1.80
6b dE_g/dT [meV/K]	0.36	0.3	~-0.05	—
7 m_e^* @ 0K	0.008	~0.009	0.008	0.007
8 m_h^* @ 0K	0.65	0.38-0.71	0.37	0.375
9 μ_e [cm ² /V-s]				
9a @ 80K	1.07×10^5	0.986×10^5	6×10^4	1.16×10^5
9b @ 200K	2.24×10^4	2.0×10^4	4.5×10^4	6.72×10^4
10 μ_h [cm ² /V-s]				
10a @ 77K	—	600-1400	—	—
10b @ 200K	—	300-600	—	—
11a t_{eA} [ns]	—	10	$t(\text{MCT}) < t(\text{ITP})$	—
11b t_{hA} [ns]	—	40	—	—

LWIR-FPA performance and processing. The salient features are the following:

- The alloy concentration is $x = 0.67$, and the concentration variation of the gap $|dE_g/dx|$ is 1.42 eV, 16% smaller than that of Hg_{0.78}Cd_{0.22}Te (1.69 eV).
- The elastic constants are ~33% larger than those of the LWIR HgCdTe alloy.
- The transverse optical phonon energy is 34.6 meV, 139% larger than that of HgCdTe (14.5), thereby limiting very-long-wave infrared utility to $\lambda_c < 36 \mu\text{m}$ (this is the only negative feature relative to HgCdTe).
- The temperature variation of the band gap² dE_g/dT near 77K is small (~ -0.05 meV/K), about 1/7 as large as that of HgCdTe (0.36 meV/K) (dE_g/dT for Hg_{1-x}Cd_xTe vanishes near $x = 0.5$, while that of In_{1-x}Tl_xP vanishes close to $x = 0.67$, the LWIR concentration, greatly simplifying designs for variable temperature operation and eliminating spatial variation in pixel performance caused by temperature gradients over array areas).
- The electron effective mass is 0.008, almost identical to that of HgCdTe (~ 0.008).
- The hole effective mass is 0.37, 43% smaller than that of HgCdTe (0.65) (which implies higher hole mobilities and substantially longer electron Auger recombination lifetimes for InTlP).
- The electron mobility at 80K (6×10^4 cm²/V-s) is 44% smaller than that of HgCdTe, but it does not die off as rapidly as temperature increases; consequently, electron mobility at 200K is 4.5×10^4 cm²/V-s, while the same for HgCdTe is 2.24×10^4 cm²/V-s, only half as large. (This means the high temperature responsivity should not degrade as rapidly in InTlP.)

ITA also has some virtues as an LWIR detector.

While InAs is not as attractive a substrate as InP (bond energy per atom 3.10 eV), it is still better bound than CdTe (2.20 eV). The gap of TIAs is predicted to be -1.34 eV, so the LWIR concentration of In_{1-x}Tl_xAs is $x = 0.15$. The predicted cohesive energy per atom of this alloy is 3.09 eV, far better than that of LWIR MCT (1.66 eV). Perhaps the most useful property of ITA is that its electron mobility falls very slowly as temperature increases, so at 200°C LWIR ITA has $\mu_e = 0.5 \times 10^4$ cm²/V-s compared to MCT with $\mu_e = 2.24 \times 10^4$ cm²/V-s. At still higher temperatures, the ratio of electron mobilities exceeds a factor of ten. Thus, minority carrier responsivities of p-type material may remain reasonably high at high temperature.

This collection of properties (plus the extra ease of processing, the lower defect densities expected as a consequence of the high cohesive energy, and the superior InP and InAs substrates [for InP there are three inch diameter wafers available with average dislocation densities of $\sim 10^4$ cm⁻²]³) lends support to the contention that In_{1-x}Tl_xP will prove to be a striking LWIR-FPA material, and there may be niches for In_{1-x}Tl_xAs.

ACKNOWLEDGMENTS

Partial support of this work from ONR Contracts N00014-88-C-0096 and N00014-89-K-0132 and from ARPA Contract MDA972-92-C-0053 is gratefully acknowledged.

REFERENCES

1. M. van Schilfgaard, A.-B. Chen, S. Krishnamurthy and A. Sher, *Appl. Phys. Lett.* 65, 2714 (1994).
2. S. Krishnamurthy, A.-B. Chen and A. Sher, *J. Electron. Mater.* 24, 1121 (1995).
3. D.F. Bliss, R.M. Hilton and J.A. Adamski, *J. Cryst. Growth* 128, 451 (1993).

Temperature Dependence of Band Gaps in HgCdTe and Other Semiconductors

SRINIVASAN KRISHNAMURTHY,* A.-B. CHEN,[†] A. SHER,* and M. VAN SCHILFGAARDE*

*SRI International, Menlo Park, CA 94025

[†]Physics Department, Auburn University, Auburn, AL 36849

Band-edge shifts induced by the electron-phonon interaction are calculated for HgCdTe alloys and various semiconductor compounds starting from accurate zero-temperature band structures. The calculated temperature variation of gaps agrees with experiments to better than 10% in all materials except InAs and InSb where the deviation is about 50%. While the simple picture that the intra (inter)-band transitions reduce (increase) the gap still holds, we show that both the conduction band edge E_c and valence band edge E_v move down in energy. These shifts in E_v affect the valence band offsets in heterojunctions at finite temperature. The temperature variations of valence band offset and the electron effective mass are also reported.

Key words: III-V semiconductors, band offset, electron-phonon interactions, HgCdTe and alloys, temperature-dependent band structures

INTRODUCTION

The temperature (T) dependence of energy gaps of semiconductors is of great physical and technological interest. The quantities such as band offset and effective mass depend sensitively on the temperature variation of band edges. Numerous theoretical¹⁻⁹ and experimental¹⁰⁻¹⁹ studies have been undertaken to obtain both qualitative and quantitative variations of various gaps in semiconductors. The gap decreases with increasing temperature in medium-gap and wide-gap semiconductors, and it increases in small-gap materials such as HgCdTe, PbS, PbSe, and PbTe. The thermal expansion of the lattice and electron-phonon interactions are usually considered causes for the temperature variation of the band structures. Thermal expansion always reduces gaps.

In a perturbation-theory treatment of electron-phonon interactions, the intraband transitions reduce the gap whereas interband transitions increase it, and the net shift in the gap can be positive or negative. Here we calculate the gap variation in

Hg_{1-x}Cd_xTe alloys, GaAs, InAs, InSb, InP, and CdTe compounds, starting from accurate band structures, wave functions, proper phonon dispersion relations, and taking account of matrix elements of the electron-phonon interactions. The contributions from each phonon branch to each electron band have been obtained to assist physical understanding of the underlying causes of the variations. We show that *both* conduction and valence band edges move down in energy. When the valence band edge moves more than the conduction band edge, the gap increases with T , as in the case of some Hg_{1-x}Cd_xTe alloys with $x < 0.5$. The reverse occurs for all III-V compounds studied and Hg_{1-x}Cd_xTe with $x > 0.5$. This observation has an important effect on our understanding of the variation of band offsets in semiconductor heterojunctions. In addition to the gap, other features of the band structure change with temperature and will affect the spectral variations of the absorption coefficient and transport properties.

METHOD

Our calculation of the temperature dependence of the band gap starts with accurate band structures.

(Received October 4, 1994; revised January 8, 1995)

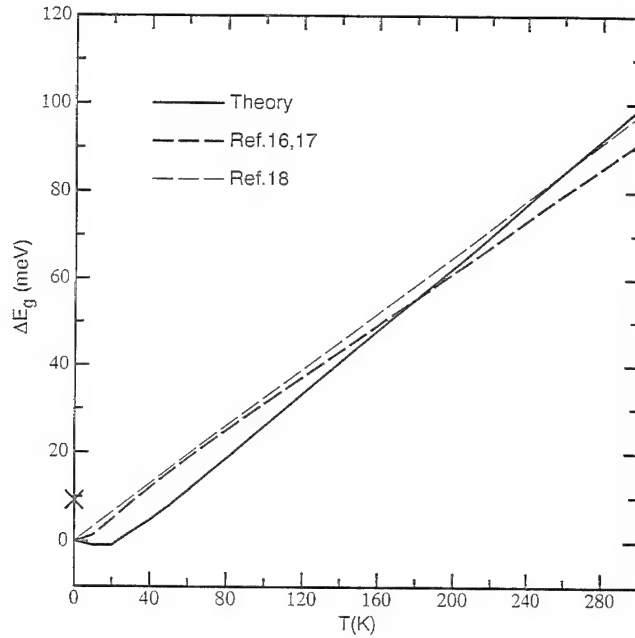


Fig. 1. Change in the band gap of $\text{Hg}_{0.78}\text{Cd}_{0.22}\text{Te}$ with temperature.

Empirical pseudopotential form factors are used to construct a hybrid pseudopotential tight-binding (HPTB) Hamiltonian. The pseudopotential part of the Hamiltonian is universal—it applies to all group IV, III-V, and II-VI compounds. The smaller tight-binding part is expressed in a minimum set of sp^3 Slater orbitals per atom. This Hamiltonian is then transformed into an orthonormal basis. A site-diagonal spin-orbit Hamiltonian is then added. Parameters in the tight-binding perturbation are chosen to fine-tune the band structures to agree well with experiments.^{20,21} Various results obtained using these band structures are found to be quite reliable.^{21–23} The present study subjects the accuracy of the wave functions as well as the energies to a sensitive test.

The dilation contribution to the band gap reduction is given^{5,9} by $3\alpha_T B \partial E_g / \partial P$, where the thermal expansion coefficient of the lattice α_T , the bulk modulus B , and the change in the gap with pressure are obtained from the literature.¹⁹ The electron-phonon interactions with all phonon branches that cause the band structure changes are treated in perturbation theory. The total Hamiltonian is assumed to be a sum of potentials from single atoms. The atomic potential in the solid is traditionally expanded in a Taylor series, with only the leading term retained, and the energy shifts it causes are evaluated in second-order perturbation theory. However, it has been demonstrated by a number of researchers^{3,4,6} that retention of first-order perturbation terms with a second term in the Taylor series expansion is necessary to preserve symmetry. We retain both terms. The change in the energy at a given wave vector k is

$$\Delta E_{nk} = \langle nk | V_2 | nk \rangle + \sum_{n'k'} \frac{\langle n'k' | V_1 | nk \rangle \langle nk | V_2 | n'k' \rangle}{E_{nk} - E_{n'k'}} \quad (1)$$

where V_1 and V_2 are the first two terms in the Taylor expansion of the total electron-phonon potential in powers of atomic displacements ξ . In the TB formalism, Eq. (1) can be written in terms of the matrix elements

$$\langle l'j'\alpha' | V_1 | lj\alpha \rangle = \nabla V_{\alpha\alpha'}(\mathbf{d}_{ll'}^{jj'}) \cdot (\xi_{lj'} - \xi_{lj}), \quad (2)$$

$$\text{and } \langle l'j'\alpha' | V_2 | lj\alpha \rangle = \frac{1}{2} [\xi_{lj'} \cdot (\nabla)^2 V_{\alpha\alpha'}(\mathbf{d}_{ll'}^{jj'}) \cdot \xi_{lj'} + \xi_{lj} \cdot (\nabla)^2 V_{\alpha\alpha'}(\mathbf{d}_{ll'}^{jj'}) \cdot \xi_{lj}], \quad (3)$$

where $\mathbf{d}_{ll'}^{jj'}$ is the position vector connecting atomic sites l , species (anion or cation) j and site l' , species j' , and $V_{\alpha\alpha'}/(\mathbf{d}_{ll'}^{jj'})$ is a HPTB matrix element between the orbitals α and α' located on those atoms. From the quantum theory of harmonic crystals, the atomic displacements ξ can be expressed in terms of normal modes; that is, phonons. We have

$$\xi_{lj} =$$

$$\left[\frac{\hbar}{2NM_j} \right]^{\frac{1}{2}} \sum_{q\lambda} \omega_{\lambda q}^{-\frac{1}{2}} \left[e_{\lambda q}^j a_{\lambda q} e^{iq(1+\tau_j)} + e_{\lambda q}^{*j} a_{\lambda q}^\dagger e^{-iq(1+\tau_j)} \right] \quad (4)$$

where q and ω are phonon wave vector and frequency, λ denotes phonon branch, $a(a^\dagger)$ is a phonon annihilation (creation) operator, M is the atomic mass, and e is an eigenvector in a diamond or zinc-blende structure of the six-dimensional dynamical matrix eigenvalue problem

$$M\omega^2 e = D(q)e \quad (5)$$

Evaluation of the matrix elements given by Eqs. (2) and (3) requires knowledge of spatial variations of the interatomic TB matrix elements $V_{\alpha\alpha'}$. In Harrison's universal TB approach,²⁴ these matrix elements scale as d^{-2} . In our generalization, we assume that $V_{\alpha\alpha'}$ varies as d^{-m} and the repulsive first-neighbor pair energy, following Harrison's overlap argument, as η/d^{2m} . The two unknowns m and η are determined by requiring that the calculated equilibrium bond length and bulk modulus agree well with experiments. This approach, with electrons and phonons treated from the same underlying Hamiltonian, has previously been used successfully to explain hot electron transistor characteristics²³ and is also in fairly good agreement with first-principles calculations.²⁵ The dynamical matrix D is calculated from the valence force field model.²⁶

The calculational procedure is as follows. For a chosen material, m and η are evaluated. Then the first and second derivatives of all interatomic matrix elements are obtained. The dynamical matrix is diagonalized to obtain ω and e as a function of q and λ . The phonon structures and electronic band structures are used [Eqs. (1) through (4)] to obtain the change in the band energy at a given k . The polar coupling terms are

included in the longitudinal optical phonon contributions. When we are interested in studying the change in the direct gap, k is taken to be zero. However, when the temperature variation of the effective masses or indirect gap are studied, nonzero k values must be used and the Brillouin zone summation in Eq. (1) should be carried over the entire zone with reduced, or no, symmetry.

RESULTS

The calculated band-gap change as a function of T in $\text{Hg}_{0.78}\text{Cd}_{0.22}\text{Te}$ is shown in Fig. 1. With increasing T , the direct gap increases in $\text{Hg}_{0.78}\text{Cd}_{0.22}\text{Te}$. Notice that the calculated values are typically within 10 to 15 meV of experimental values.¹⁶⁻¹⁸ The cross (\times) at $T = 0$ represents the calculated zero-point correction to the gap (13.6 meV for $\text{Hg}_{0.78}\text{Cd}_{0.22}\text{Te}$). The zero-temperature band gap calculated without electron-phonon interactions should have this correction subtracted for comparison to experimental values.

The change in the gap is traditionally explained in terms of inter- and intraband interactions. The intravalence (conduction) band interactions push the valence (conduction) band edge up (down), thus reducing the gap. Similarly, the valence-conduction band interactions increase the gap. Hence, one might expect the gap to decrease in wide-gap semiconductors and possibly increase in small-gap semiconductors. In addition, arguments based only on total density of states and ignoring variations in matrix elements will predict the valence band edge E_v move up in energy, because the hole effective mass is one to two orders of magnitude larger than the electron mass. As seen from Fig. 2, our detailed calculations of band edge movements in $\text{Hg}_{0.78}\text{Cd}_{0.22}\text{Te}$ do not support this traditional view. We find that both E_c and E_v (solid lines) move down in energy. This same trend is observed in other semiconductor compounds studied (GaAs, InP, InAs, InSb, and GaSb). The movement of the valence (solid line) and conduction (dashed) band edges due to interaction with other bands is also shown in Fig. 2. The interaction of the band edges

with the conduction bands (CBs) is much stronger than with valence bands (VBs), and consequently both E_v and E_c move down in energy. E_v moves much more than E_c and the gap increases.

We analyze the strength of inter- and intraband electron-phonon interactions by presenting the contributions from each band and from each phonon mode. Table I lists the calculated values for $\text{Hg}_{0.78}\text{Cd}_{0.22}\text{Te}$ at 300K. Although spin is included in our band structure calculations, only spin averaged values are listed. Band indices 1 to 4 correspond to VBs, and the others to CBs. The first two rows show changes in E_v and E_c due to interactions with various bands. Contributions from each phonon mode are listed in the remaining rows. The lowest VB is about 12 eV below E_v and E_c , and hence the interaction does not affect the band edges. We see that the interaction with other VBs tends to push the band edges up in

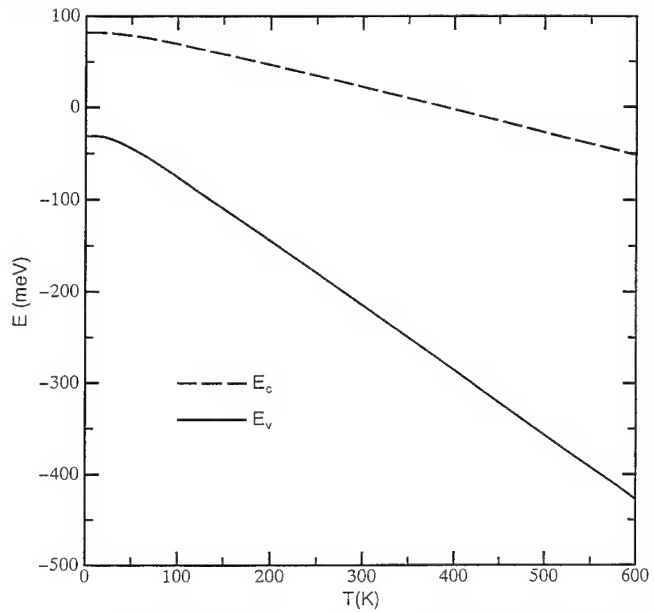


Fig. 2. Variation of conduction (dashed line) and valence (solid line) band edges of $\text{Hg}_{0.78}\text{Cd}_{0.22}\text{Te}$ with temperature.

Table I. Calculated Change in the Valence (v) and Conduction (c) Band Edge Energies (in meV) of $\text{Hg}_{0.78}\text{Cd}_{0.22}\text{Te}$ Alloy

Band		1	2	3	4	5	6	7	8
Total	v	5.90	13.99	56.85	88.51	-80.26	-92.49	-97.45	-102.07
	c	1.04	2.84	17.27	34.07	-23.81	-25.43	-43.96	-42.48
TA	v	4.03	6.21	30.06	41.52	-49.86	-62.17	-61.04	-49.62
	c	0.26	0.65	12.41	27.47	-3.58	-14.81	-24.50	-15.40
LA	v	0.91	3.18	3.14	10.53	-10.63	-5.92	-11.41	-20.59
	c	0.56	1.29	1.27	1.72	-14.94	-3.00	-2.66	-7.17
LO	v	0.33	2.11	6.12	11.22	-9.52	-4.98	-11.80	-17.40
	c	0.13	0.63	0.75	0.44	-3.78	-2.45	-1.18	-7.31
TO	v	0.63	2.48	17.53	25.24	-10.26	-19.42	-13.20	-14.45
	c	0.10	0.27	2.84	4.44	-1.52	-5.16	-15.62	-12.59

Note: Contributions from interaction with various phonon modes are shown in rows 3 to 10.

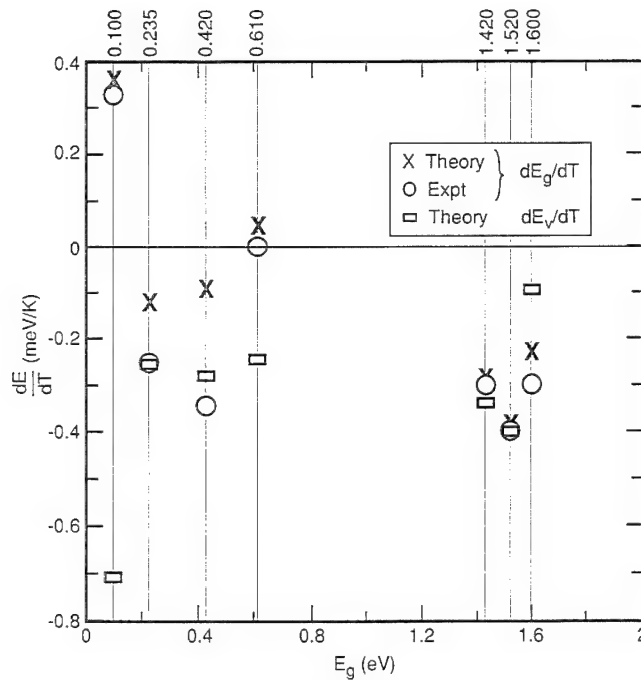


Fig. 3. Derivative of direct gap with temperature for various semiconductor compounds and alloys as a function of zero-temperature gap. The vertical lines represent $\text{Hg}_{0.78}\text{Cd}_{0.22}\text{Te}$, InSb, InAs, $\text{Hg}_{0.5}\text{Cd}_{0.5}\text{Te}$, GaAs, and CdTe, respectively.

Table II. Calculated E_g [meV], γ [eV²], c [eV], and the Effective Mass Ratio of $\text{Hg}_{0.78}\text{Cd}_{0.22}\text{Te}$ Alloy as Functions of Temperature

T	E_g	γ	c	$m^*(T)/m^*(0)$
1.00	113.60	47.7656	0.0588	1.0000
10.00	112.67	47.7553	0.0588	1.0005
20.00	112.56	47.7169	0.0592	1.0072
30.00	114.44	47.6421	0.0598	1.0199
40.00	117.15	47.5582	0.0607	1.0361
50.00	120.42	47.4461	0.0615	1.0532
60.00	123.96	47.3310	0.0624	1.0714
70.00	127.65	47.2091	0.0634	1.0904
80.00	131.44	47.0821	0.0643	1.1095
90.00	135.28	46.9418	0.0653	1.1288
100.00	139.17	46.7964	0.0662	1.1483
150.00	158.85	46.1544	0.0712	1.2529
200.00	178.73	45.5930	0.0767	1.3669
250.00	198.68	45.2441	0.0832	1.4938
300.00	218.66	45.1167	0.0908	1.6342
350.00	238.65	45.3460	0.1000	1.7913
400.00	258.66	46.0193	0.1115	1.9672
450.00	278.67	47.3751	0.1263	2.1657
500.00	298.69	49.8338	0.1468	2.3919
550.00	318.71	54.0581	0.1763	2.6491
600.00	338.74	61.7125	0.2238	2.9445

Note: $m^*(0)$ is 0.008. The zero point correction is 13.6 meV.

energy, as expected. Note that the top two valence bands contribute the most to the fundamental band-edge changes. However, interaction of the band edges with CBs is even stronger and negative. Particularly, the interaction of E_v with all conduction bands is strong. As E_v moves down more than E_c , the gap increases in $\text{Hg}_{0.78}\text{Cd}_{0.22}\text{Te}$. To understand the role of

various phonons, we display the contribution from each mode separately. The phonon-induced changes in the band edges at 300K in $\text{Hg}_{0.78}\text{Cd}_{0.22}\text{Te}$ are listed in the third through tenth rows of Table I. We see that acoustic phonons account for about 75% of the total change in the valence and conduction band-edge energies. The selection rules wipe out interband matrix elements between electrons and polar longitudinal phonons, so in spite of the stronger coupling constant, they do not dominate this phenomenon as they do with mobilities, which depend on intraband matrix elements.

Our calculations for other compounds show a qualitatively similar role for phonons. In addition to $\text{Hg}_{0.78}\text{Cd}_{0.22}\text{Te}$, we studied the band-gap variation with temperature in GaAs, InAs, InP, InSb, GaSb, and CdTe compounds and HgCdTe alloys. The gap changes linearly at high temperatures ($>150\text{K}$). The calculated dE_g/dT values (circle) are compared with experiments (cross) values in Fig. 3. We see that the calculations produced correct trends in all these materials, but compare less favorably with experiments in InAs and InSb. However, it is important to note that the sign of the change is not exclusively determined by the magnitude of the zero-temperature gap. For example, although $\text{Hg}_{0.70}\text{Cd}_{0.30}\text{Te}$ and InSb have the same zero-temperature gap of 0.235 eV, the InSb gap decreases with T, whereas the $\text{Hg}_{0.70}\text{Cd}_{0.30}\text{Te}$ gap increases with T. The combination of gap size, conduction band width, and intervalley separations gives rise to these interesting variations in the gap with T.

The observation that both E_v and E_c move down in energy has an important effect on band offsets in heterojunction-based devices. For example, the zero-temperature valence band offset between $\text{Hg}_{0.78}\text{Cd}_{0.22}\text{Te}$ and CdTe is believed to be around 350 meV. However, we find that at 300K, E_v in $\text{Hg}_{0.78}\text{Cd}_{0.22}\text{Te}$ and in CdTe moves down by 215 and 30 meV, respectively. If the dipole contribution remains the same, the valence band offset decreases to 165 meV at 300K. The contention that the dipole contribution is nearly temperature independent stems from the observation that any shift in the average effective crystal potential should effectively be screened out, since these semiconductors are good dielectrics ($\epsilon \geq 10$). The temperature variation of the bands should be taken with respect to a fixed average potential. For our Hamiltonian, the valence band edge movements in each side of the junction are calculated with reference to a fixed average state. Thus, the calculated temperature dependence of the difference in the VB edge of the constituent heterojunction materials effectively governs the temperature dependence of the band offset. In addition to the electron-phonon interactions discussed above, lattice dilation changes the band edges differently.⁹ This effect is not included here. In any case, this band offset change has important implications for the design of abrupt heterojunction infrared (IR) absorption and confined well laser devices.

In principle, the band structure at any wave vector

k will change with temperature. With the change in the fundamental gap, the band curvature (or effective mass) also changes thus affecting the optical and transport properties of the material. The self-energy calculated in this method will include the effect of scattering due to phonons and the change in the temperature-dependent band structure self-consistently. In the case of a narrow-gap material such as $\text{Hg}_{0.78}\text{Cd}_{0.22}\text{Te}$, the effective mass alone does not explain the low-energy portion of the conduction band structure. The lowest CB energy at any k is best described by a hyperbola,²⁷ $(\gamma k^2 + c^2)^{1/2} - c$. The calculated band gap, effective mass, γ , and c as functions of T are given in Table II. The effective mass and c are directly proportional to the gap and hence monotonically increase with T. This is expected from a k · p theory argument, but the magnitudes predicted by the two theories differ. γ decreases slightly at lower temperatures and then starts to increase with T. In a previous publication,²⁷ we had simulated these temperature variations of γ and c by adjusting the Hg concentration in HgCdTe alloys to produce proper gap at each temperature. Those values are in remarkable agreement with the values reported in Table II. We conclude that γ and c (given in Table II) can be interpolated to considerable accuracy for any positive gap in the HgCdTe alloys.

CONCLUSIONS

Although the calculations produced correct trends in all materials, the calculated changes in the band gap of InAs and InSb were about a factor of two smaller than in the experiments. We find that our calculated TA phonon frequencies away from zone center in these compounds were considerably larger than those found in experiments. As noted from Table I, a substantial contribution comes from acoustic phonons. Consequently, our theoretical values of $E_g(T)$ are smaller than in experiments. Better predictability should result from improvement in the dynamical matrix calculated from the underlying Hamiltonian. In addition, at higher temperatures higher-order perturbation terms must be included along with finite-temperature "renormalized" bands rather than the zero-temperature bands. Such renormalization affects the monotonic change in the gap and introduces nonlinear terms.

In summary, we have calculated the temperature variations of band gaps in various semiconductors. A fairly accurate HPTB Hamiltonian is used in the calculation of electron and phonon structures. The calculations explain the increase in the band gap of $\text{Hg}_{0.78}\text{Cd}_{0.22}\text{Te}$, and the decrease in the band gap of all III-V compounds studied. We show that acoustic phonons make the major contribution. Contrary to traditional thinking based on total density of states arguments, we find that both the valence and the conduction band edges move down in energy. One

important consequence of this observation will be in the band offsets in semiconductor heterojunction devices. Finally, there is a small and usually negligible zero-point motion contribution to low-temperature band gaps arising from electron-phonon interactions.

ACKNOWLEDGMENT

We thank Dr. M. Cardona of the Max Planck Institute, Stuttgart, for pointing us to several references. Funding from ONR (contract N00014-93-C-0091) and ARPA (contract MDA972-92-C-0053) is gratefully acknowledged.

REFERENCES

1. Y.P. Varshini, *Phys.* 34, 149 (1967).
2. V. Heine and J.A. Van Vechten, *Phys. Rev. B* 13, 1622 (1976).
3. P.B. Allen and V. Heine, *J. Phys. C* 9, 2305 (1976).
4. P.B. Allen and M. Cardona, *Phys. Rev. B* 27, 4760 (1983).
5. S. Gopalan, P. Lautenschlager and M. Cardona, *Phys. Rev. B* 35, 5577 (1987).
6. M. Cardona and S. Gopalan, *Progress on Electron Properties of Solids*, eds. R. Girlanda et al. (Amsterdam, The Netherlands: Kluwer Academic Publishers, 1989), p. 52.
7. R.D. King-Smith, R.J. Needs, V. Heine and M.J. Hodgson, *Europhys. Lett.* 10, 569 (1989).
8. S. Zollner, S. Gopalan and M. Cardona, *Sol. State Comm.* 77, 485 (1991).
9. K.J. Malloy and J.A. Van Vechten, *J. Vac. Sci. Technol. B* 9, 2112 (1991).
10. P. Lautenschlager, M. Garriga, S. Logothetidis and M. Cardona, *Phys. Rev. B* 35, 9174 (1987), and references cited therein.
11. Z. Hang, D. Yan, F.H. Pollak, G.D. Pettit and M. Woodall, *Phys. Rev. B* 44, 10546 (1991).
12. L. Pavisi, F. Piazza, A. Rudra, J.F. Carlin and M. Ilegems, *Phys. Rev. B* 44, 9052 (1991).
13. E. Grilli, M. Guzzi, R. Zamboni and L. Pavesi, *Phys. Rev. B* 45, 1638 (1992).
14. P.Y. Liu and J.C. Maan, *Phys. Rev. B* 47, 16274 (1993).
15. M.E. Allali, C.B. Sorenson, E. Veje and P.T. Petersson, *Phys. Rev. B* 48, 4398 (1993).
16. G.L. Hansen, J.L. Schmit and T.N. Casselman, *J. Appl. Phys.* 53, 7099 (1982).
17. D.G. Seiler, J.R. Lowney, C.L. Littler and M.R. Loloee, *J. Vac. Sci. Technol. A* 8, 1237 (1990).
18. J.C. Brice, *Properties of Mercury Cadmium Telluride*, eds. J. Brice and P. Capper (EMIS datareviews series 3, INSPEC publication, 1987), p. 105.
19. *Landolt-Bornstein Numerical Data and Functional Relationships in Science and Technology*, eds., Madelung, Schultz and Weiss, New series, Vol. 17 (1982).
20. A.-B. Chen and A. Sher, *Phys. Rev. B* 23, 5360 (1981).
21. S. Krishnamurthy, A.-B. Chen and A. Sher, *J. Appl. Phys.* 63, 4540 (1988).
22. S. Krishnamurthy, A. Sher and A.-B. Chen, *Phys. Rev. Lett.* 64, 2531 (1990); *Appl. Phys. Lett.* 55, 1002 (1989); *Appl. Phys. Lett.* 52, 468 (1988).
23. S. Krishnamurthy, A. Sher and A.-B. Chen, *Appl. Phys. Lett.* 53, 1853 (1988).
24. W. Harrison, *Electronic Structure and Properties of Solids* (San Francisco, CA: Freeman, 1980).
25. S. Krishnamurthy and M. Cardona, *J. Appl. Phys.* 74, 2117 (1993).
26. R.M. Martin, *Phys. Rev. B* 1, 4005 (1970).
27. S. Krishnamurthy and A. Sher, *J. Electron. Mater.* 24, 641 (1995).

Defect Modeling Studies in HgCdTe and CdTe

M.A. BERDING, A. SHER, and M. VAN SCHILFGAARDE

SRI International, Menlo Park, CA 94025

We have used a quasichemical formalism to calculate the native point defect densities in $x = 0.22$ $\text{Hg}_{1-x}\text{Cd}_x\text{Te}$ and CdTe. The linearized muffin-tin orbital method, based on the local density approximation and including gradient corrections, has been used to calculate the electronic contribution to the defect reaction free energies, and a valence force field model has been used to calculate the changes to the vibration free energy when a defect is created. We find the double acceptor mercury vacancy is the dominant defect, in agreement with previous interpretations of experiments. The tellurium antisite, which is a donor, is also found to be an important defect in this material. The mercury vacancy tellurium antisite pair is predicted to be well bound and is expected to be important for tellurium antisite diffusion. We consider the possibilities that the tellurium antisite is the residual donor and a Shockley-Read recombination center in HgCdTe and suggestions for further experimental work are made. We predict that the cadmium vacancy, a double acceptor, is the dominant defect for low cadmium pressures, while the cadmium interstitial, a double donor, dominates at high cadmium pressures.

Key words: CdTe, defect complexes, defects, HgCdTe

INTRODUCTION

The pseudobinary semiconductor alloy $\text{Hg}_{1-x}\text{Cd}_x\text{Te}$ with $x = 0.22$ is currently the material of choice for high-performance detectors in the long-wavelength infrared (LWIR) (8–14 μm). Unlike most other II-VI systems, both extrinsic p- and n-type doping can be achieved in HgCdTe, although in as-grown material the electrical characteristics are often determined by native point defect concentrations. Understanding the properties of point defects and manipulation of their densities during growth and processing is essential to high-yield manufacturing of focal plane arrays (FPAs). As in other semiconductors, it is difficult to establish the presence and identity of all the important neutral and compensating point defects during growth and processing, much less to determine their concentrations. CdTe is important both as a substrate and passivating material for epitaxial lay-

ers of LWIR HgCdTe. Native point defects are of interest in CdTe in that they relate to its stoichiometry (which in turn has been shown to impact the minority carrier lifetimes¹ in HgCdTe devices), the formation and annihilation of tellurium precipitates,² and the self- and inter-diffusion coefficients that impact materials stability during growth, during subsequent processing, and over the device lifetime.

Our goal in this paper is to theoretically identify the important native defects in HgCdTe and CdTe, to calculate their densities as a function of growth and processing conditions, to validate our predictions by comparison with experimentally deduced properties of the native defects, and to suggest new experiments to begin to unravel the remaining mysteries in these materials. We have included in our analysis of HgCdTe both neutral and ionized states of eight native point defects and one defect pair. Our focus is on $x = 0.2$ (for comparison to annealing data),³ $x = 0.22$ (for LWIR applications), and $x = 1$ (for substrate and passivating layers) $\text{Hg}_{1-x}\text{Cd}_x\text{Te}$. As we will show, we have at-

(Received October 4, 1994; revised January 20, 1995)

tempted to incorporate all of the important contributions to the defect formation free energies and adopt a first-principles approach for most of the quantities we calculate.

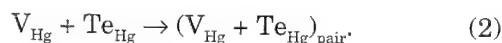
METHODOLOGY

To calculate the concentration of the native point defects in HgCdTe, we employ a quasichemical formalism⁴ in which the formation of independent crystalline defects is expressed as chemical reactions. For example, for the formation of the neutral mercury vacancy in HgTe with the mercury vapor as the reference phase, we have the reaction



Our notation is that of Kröger⁴ in which the primary symbol is the defect species and the subscript indicates the site the defect occupies; V indicates the vacancy, and I the interstitial, and no subscript indicates the species is occupying its normal lattice position; \times indicates the neutral defect species. Although we have chosen the mercury in the vapor phase as our reference and thereby will choose a mercury pressure to determine the chemical potential of mercury in the system, one could have chosen some other reference state for the mercury or tellurium (for example, by specifying a binary solution of $\text{Hg}_{1-y}\text{Te}_y$ at some temperature T in coexistence with the HgTe solid, as is essentially done during liquid phase epitaxy [LPE] growth). For our equilibrium calculations, the limits of mercury pressures within the existence region of $\text{Hg}_{1-x}\text{Cd}_x\text{Te}$ are taken from experiment.⁵

In a similar manner, reactions can be written for the other point defects of the system. In our analysis, we have included eight native point defects (plus their ionized species and the electron and hole): the mercury and tellurium vacancies (V_{Hg} and V_{Te}), the mercury and tellurium antisites (Hg_{Te} and Te_{Hg}), and two types of mercury and tellurium tetrahedral interstitials—one surrounded by four cation near-neighbors ($\text{Hg}_{\text{I}_{\text{Hg}}}$ and $\text{Te}_{\text{I}_{\text{Hg}}}$) and the other surrounded by four anion near-neighbors ($\text{Hg}_{\text{I}_{\text{Te}}}$ and $\text{Te}_{\text{I}_{\text{Te}}}$). We have also included the bound mercury vacancy tellurium antisite pair ($V_{\text{Hg}}-\text{Te}_{\text{Hg}}^{\text{pair}}$), in which the vacancy and antisite occupy near-neighbor cations sites, via the reaction



For low densities of noninteracting defects, the law of mass action can be used to determine the neutral defect concentrations. For the mercury vacancy, this corresponds to

$$K_{V_{\text{Hg}}} \equiv \theta \exp\left(-\frac{F_{V_{\text{Hg}}}}{k_B T}\right) = [V_{\text{Hg}}^{\times}] \quad (3)$$

where $F_{V_{\text{Hg}}}$ is the reaction free energy for the neutral mercury vacancy, k_B is Boltzmann's constant, T is the temperature in kelvin, and θ is the number of unit cells per volume. Thus, once the reaction free energy

is known, it is straightforward to calculate the defect concentrations. Of course, all the work is involved in the calculation of the reaction free energies.

We have attempted to calculate all of the important contributions to the defect reaction free energies. An electronic contribution to the free energy results from the change in the total electron energy of the solid when a neutral defect is created; included in this energy is the electronic energy of free mercury atoms generated or consumed in the defect reaction. To calculate the electronic contribution, we employ the self-consistent first-principles full-potential linearized muffin-tin orbital method⁶ and the local-density approximation (LDA), including gradient corrections of the Langreth-Mehl-Hu type⁷ (which greatly improves the overbinding found in the LDA).^{8,9} The vibrational modes of the system are also changed when a defect is created; we calculate this change to the formation free energy (both the enthalpy and entropy) using a Green's function formalism within a valence force model plus point-charge ionic model. An entropy contribution to the formation free energy also arises from the partial occupation of degenerate levels associated with the defect and from the introduction of a preferred direction via a symmetry-lowering Jahn-Teller distortion.¹⁰ The combination of the electronic, vibrational, degeneracy, and translational (for the calculation of the chemical potential of the mercury atom in the vapor phase) free energies encompasses the primary contributions to the total defect formation free energies when referenced to a mercury vapor. Details of the results for these energies are given in Ref. 9. We have completed only preliminary calculations for the binding energy of the mercury vacancy tellurium antisite pair indicated in Eq. (3), using a 32-atom supercell and with overall lattice constant relaxation only. We expect that this defect may show further relaxation, which could lower the defect pair binding energy and therefore increase their density.

Although we are interested in studying the properties of point defects in HgCdTe, the neutral defect reaction free energies are calculated for HgTe; because we predict that the defects with highest concentrations (the mercury vacancy and the tellurium antisite) reside on the cation sublattice and therefore have four tellurium atoms for first nearest neighbors, we expect that the presence of cadmium will introduce a minor modification to the formation free energies, and of the order of other approximations made in the calculation (for example, using supercells). The presence of cadmium may have a larger impact on interstitial formation free energies, which can occupy sites with cations as near-neighbors. Although we find the density of interstitials to be relatively low,⁹ the cation interstitial in particular is very important in annealing of HgCdTe.¹² For the present, we have included the effects of the cadmium only by adjusting the number of sites available for mercury vacancies and in calculating of the band structure used in predicting the ionized point defect concentrations.

For further discussion and details of the calculation of the reaction free energies, see Ref. 9.

Because the native point defects will in general have localized levels in the band gap, we need to calculate the concentration of the ionized defects in addition to the neutral defects discussed above. Once the density of the neutral defects is determined, the concentration of ionized defects can be calculated from

$$\frac{[X']}{[X^\times]} = \frac{g_{X'}}{g_{X^\times}} \exp\left(\frac{\mu_F - E_a}{k_B T}\right) \quad (4)$$

for an acceptor defect X and

$$\frac{[Y^\bullet]}{[Y^\times]} = \frac{g_{Y^\bullet}}{g_{Y^\times}} \exp\left(\frac{E_d - \mu_F}{k_B T}\right) \quad (5)$$

for a donor defect Y. Once again, we have adopted the notation of Kröger: the bullet superscript indicates a positive charge and a prime, a negative charge. E_a and E_d are the one-electron acceptor and donor levels; μ_F is the Fermi energy, which is determined by demanding charge neutrality; and g_x is the degeneracy of the state, including both spin and Jahn-Teller¹⁰ splitting. Generalizations of these expressions are used for multiple ionized defects. The calculation of the electron and hole populations demands a knowledge of the temperature-dependent band structure and use of Fermi-Dirac statistics. The only significant empirical data we employ in this calculation are those needed to obtain the temperature-dependent band structure, which is extrapolated to high temperatures at which equilibration and annealing take place and for which we are going to predict defect concentrations. Further details are in Ref. 9.

DEFECTS IN HgCdTe

Equilibrium Native Point Defect Concentrations: Annealing Studies

Gibbs' phase rule tells us that for a system of three components (in our case mercury, cadmium, and tellurium) and two phases (zinc-blende solid and vapor), there are three degrees of freedom. In evaluating the equilibrium defect concentrations in $\text{Hg}_{0.8}\text{Cd}_{0.2}\text{Te}$, we have chosen the temperature, the mercury pressure P_{Hg} , and the alloy composition x as these specified variables; the tellurium and cadmium pressures, the crystal stoichiometry, and the density of the various native point defects are determined by these parameters.

In Fig. 1, we show our results for the 77K hole concentrations in $x = 0.2 \text{ Hg}_{1-x}\text{Cd}_x\text{Te}$ as a function of mercury partial pressure for various high-temperature annealing conditions and compare them to the results of Vydyanath.^{3,13} We have assumed that the high-temperature defect structure is frozen in during a quench to 77K. All eight point defects discussed above have been included in our analysis. The agreement with experiment is quite good, given that the

only empirical data used were of the temperature dependence of the band structure used to calculate the intrinsic reaction constant. To demonstrate the sensitivity of our results to the free energies we are calculating from first principles, we have also shown in Fig. 1 the results of a calculation using a mercury vacancy formation energy that has been increased roughly 10%, plus a constant multiplicative constant of the low-temperature hole concentrations at all pressures and temperatures; as one can see, such minor modifications to our calculated parameters yield low-temperature hole concentrations that are in very good agreement with experiment. Certainly, refinements to our theory (for example, including a more accurate high-temperature band structure, more precise incorporation of alloy effects on formation free energies, anharmonic effects in the vibrational free energies, and going beyond the local density approximation) could account for discrepancies of this magnitude. In addition, the experimental data may be impacted by re-equilibration during the quench from high temperature.

At all temperatures, we predicted that equilibrated material will be p-type and that the dominant defect is the doubly ionized mercury vacancy, in agreement with mobility data.³ Our predictions differ from the analysis in Ref. 3 in several ways, though. First, although the data indicate that the material is intrinsic at all annealing temperatures, we predict that the material will be extrinsic for the higher annealing temperatures with $[h^\bullet] \sim P_{\text{Hg}}^{-1/3}$, while at the lower annealing temperatures, the material will be intrinsic.

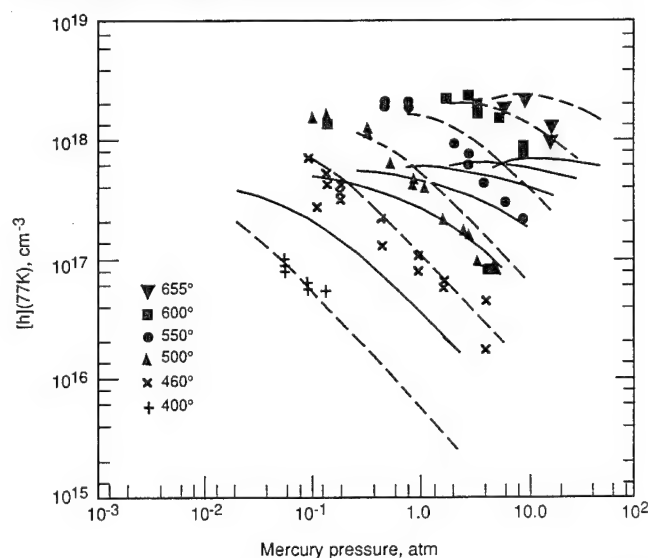


Fig. 1. Hole concentrations at 77K as a function of mercury partial pressure for material annealed at high temperatures, as indicated. Experimental data were taken from Vydyanath.³ Results of our theory are shown as solid lines. To demonstrate the sensitivity of our predictions to small changes in the calculated formation free energies, we show the dashed lines, which are the theoretical results, but with the mercury vacancy formation energy increased by 10% and including a rigid upward shift of the hole concentrations by a factor of 5.5. Note that the results shown here differ from those in Ref. 9 because the inclusion of the additional degeneracy factor for the singly ionized tellurium antisite.¹⁰

sic with $[h^\circ] \sim P_{\text{Hg}}^{-1}$ (for details see Ref. 9). This may be due to either a vacancy formation energy that is too small in our calculation (as demonstrated by the dashed line in Fig. 1) or errors in the high-temperature band structure, which we have extrapolated from the low-temperature formulas.^{14,15} Second, we find at higher temperatures and lower pressures, that the hole concentrations increase with increasing pressure, contrary to what would be expected due to mercury vacancy acceptors alone. In our theoretical predictions, this is due to compensation by tellurium antisites, which we predict are donors, and which are the second most dominant native point

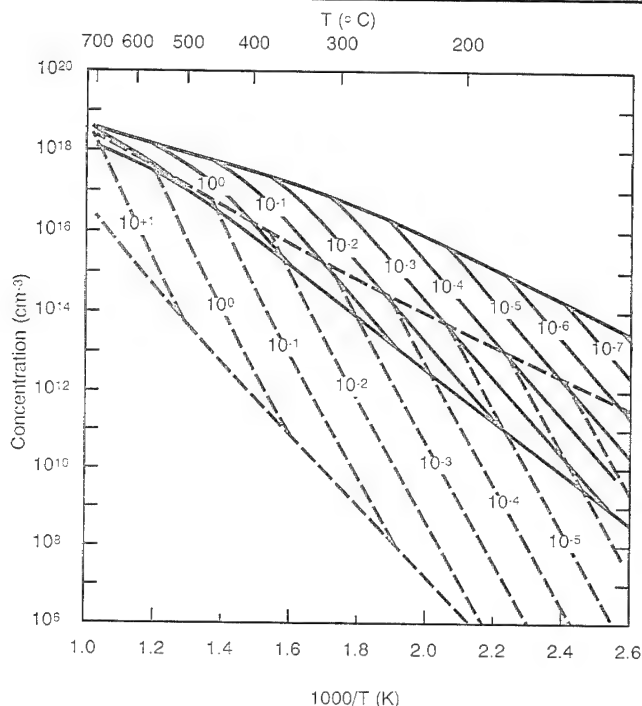


Fig. 2. Total mercury vacancy (solid line) and tellurium antisite (dashed line) densities as a function of mercury partial pressures (atm). Full equilibration of all defects is assumed at all temperatures (see text for further discussion).

defect in $\text{Hg}_{1-x}\text{Cd}_x\text{Te}$. Because the equilibrium antisite density varies roughly as P_{Hg}^{-2} , compared to P_{Hg}^{-1} to $P_{\text{Hg}}^{-1/3}$ for the mercury vacancy, it is most important at low mercury pressures. At the highest temperatures, there does appear to be a corresponding roll-off in the experimental data at the lower pressures, which may be indicative of compensation by tellurium antisites, but it could also be an experimental artifact caused by quenching inefficiencies for the higher temperatures.

Low-temperature mercury-saturated anneals are of technological importance to reducing the as-grown p-type carrier concentrations or to convert the material to n-type in nominally undoped material. In Fig. 2, we have plotted the concentrations of mercury vacancies and tellurium antisites as a function of inverse temperature for constant pressures within the existence region; neither of these concentrations include the defects that are bound into mercury vacancy tellurium antisite pairs. The lower boundaries correspond to the defect densities for mercury-saturated anneals, the upper boundary to tellurium-saturated anneals. As one can see, at a given pressure and temperature, the mercury vacancy concentrations are always in excess of the tellurium antisite population, and in equilibrium the material should always be p-type. As discussed in the following section, we expect that full equilibration of the tellurium antisite density may not take place at lower annealing temperatures, so that the equilibrium concentrations predicted for this defect may not always be realized.

Annealing schedules are also of technological importance in forming p-n junctions in as-grown p-type material via mercury in diffusion.^{16,17} The results of these experiments depend on the mechanism by which mercury diffuses and are related to the identity of the residual donor, both of which will be discussed further below.

The Tellurium Antisite in $\text{Hg}_{0.78}\text{Cd}_{0.22}\text{Te}$

Having predicted that the tellurium antisite will be

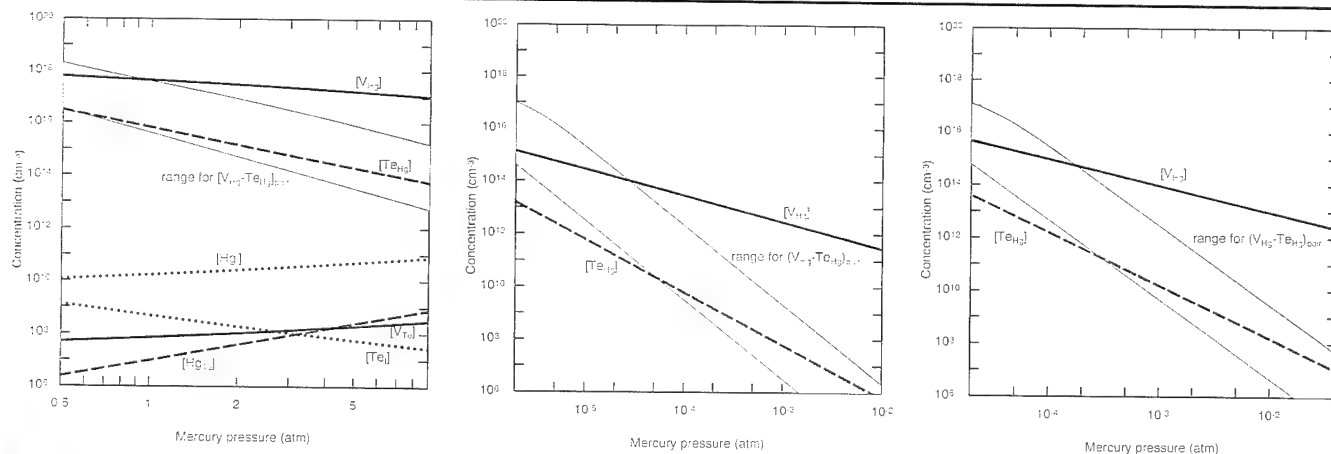


Fig. 3. The concentration of native points as a function of mercury pressure within the phase stability region at (a) 500°C, corresponding to the LPE growth temperature, (b) 185°C, the growth temperature for MBE, and (c) 220°C, a typical temperature for mercury-saturated anneals. A range of concentrations for the mercury vacancy tellurium antisite pair is shown, based on our preliminary results, as discussed in the text.

present in substantial densities, we now address the evidence for their existence in LWIR HgCdTe. We have predicted that the tellurium antisite is a donor, although we have not yet extended our theory to predict whether it is a single or double donor, nor the precise location of the defect levels in the gap. This is perhaps the most difficult part of our calculation because of the LDA band gap errors intrinsic to our method and the dispersion arising from the use of supercells that give defect-level widths larger than the $\text{Hg}_{0.78}\text{Cd}_{0.22}\text{Te}$ band gap. To establish the presence of tellurium antisites without a prediction of the donor level(s) in the gap, we must consider the possibility that there are resonant level(s), shallow level(s), deep level(s), or some combination of these, associated with the tellurium antisite, and look for evidence supporting the presence of the antisite.

One of the outstanding questions in the properties of HgCdTe is the identification and elimination of the residual donor that controls the carrier concentration in material annealed at low temperatures under mercury-saturated conditions. Although purification of starting materials has led to a lowering of the residual donor density, a lower limit of $\sim 10^{14} \text{ cm}^{-3}$ seems to have been reached. To examine the possibility that the tellurium antisite is the residual donor, we have calculated the defect densities at 500°C , roughly the liquid phase epitaxial growth temperature from both the mercury- and tellurium-rich melts, at 185°C , the typical molecular beam epitaxy (MBE) growth temperature, and at 220°C , roughly where low-temperature mercury-rich anneals are done; results are shown in Fig. 3a–3c. It is clear that the material is expected to be p-type for both MBE- and LPE-grown material, and that although postgrowth, mercury-saturated anneals (the right side of Fig. 3c) will lower the vacancy density below the 10^{13} cm^{-3} level, the material is still predicted to be mercury-vacancy-doped p-type. We thus conclude that the residual donor is not due to an equilibrium concentration of native point defects.

The possibility remains that the residual donor is associated with a nonequilibrium defect concentration of tellurium antisites. We expect that the diffusion coefficient of the tellurium antisite is relatively small because the diffusion of an antisite will necessarily involve at least one additional point defect, such as the mercury vacancy or the tellurium interstitial (diffusion via a consorted exchange of a tellurium antisite with a mercury atom on an adjacent cation lattice site is unlikely). As such, the tellurium antisite may not reach equilibrium densities for the times and temperatures corresponding to the low-temperature mercury-saturated anneals typically employed to equilibrate the mercury vacancy density (Fig. 3c). If tellurium antisite densities are in fact equilibrated at a temperature at which the antisite diffusion effectively stops during cooldown from the growth temperature, then the antisites may be frozen in at higher, nonequilibrium concentrations corresponding to the residual donor density.

Addressing the question as to why the antisite density might be frozen in at roughly the same concentration for LPE material grown from both the mercury and tellurium melt, we return to the means by which tellurium antisite diffuses in the material, and assume it diffuses by a mercury vacancy mechanism. This assumption is motivated by several factors. First, this mechanism involves only one point defect in addition to the tellurium antisite and involves a simple migration mechanism between the two defects. Second, it involves the mercury vacancy, whose density is fairly high, and therefore the probability of tellurium antisite mercury vacancy pairs is expected to be fairly high. In addition, the mercury vacancy is an acceptor and the tellurium antisite is a donor so they are expected to form a bound pair based on Coulombic attraction, and the mercury vacancy is too small for the lattice, while the tellurium antisite is too large, so that there is a mechanical attraction between them as well. Finally, the migration mechanism involving an interstitial—for example, via a knockout mechanism whereby a mercury interstitial kicks out the tellurium antisite to form a tellurium interstitial—is unlikely since it involves defects that are all too large for the lattice and are donors and therefore are unlikely to form pairs. The knockout mechanism may be important when mercury interstitials are injected into the material, and is discussed later in this paper. The likelihood of the tellurium antisite diffusion proceeding by the mercury vacancy mechanism is further supported by our preliminary prediction of the mercury vacancy tellurium antisite binding energy of 1.1 eV; the corresponding densities are shown in Fig. 3. We show our predictions for the pair density as a range in which the lower limit corresponds to the defect pair being neutral, as our preliminary predictions indicate, and the upper limit corresponding to the pair having a donor state at the valence band edge and an acceptor level at the conduction band edge. Unlike the native point defects, we expect that these pair defect concentrations may change as we refine the free energy calculations. If tellurium antisite diffusion is via the mercury vacancy, the diffusion coefficient will be proportional to the density of the mercury vacancy tellurium antisite pairs, that is

$$D_{\text{TeHg}} \sim \left[(V_{\text{Hg}} + \text{Te}_{\text{Hg}})_{\text{pair}} \right]. \quad (6)$$

From Fig. 3a for LPE growth, one can see that the density of defect pairs for low mercury pressures, corresponding to material grown from the tellurium-rich melt, is four orders of magnitude higher than for that grown from the mercury-rich melt. This implies that although material grown from the tellurium melt will contain higher densities of tellurium antisites, in the cooldown from the growth temperature the tellurium antisites will re-equilibrate much more rapidly due to the large pair density than will material grown from the mercury-rich melt. In contrast, for material grown from the mercury melt, the

tellurium antisites present at the growth temperature, although lower, may be frozen in because the pair density is also lower.

We now turn to growth by MBE, which takes place at 185°C under mercury-poor conditions, corresponding to the left side of Fig. 3b. At the phase stability boundary, we predict that the material will be mercury-vacancy doped p-type, with a carrier concentration of $\sim 10^{15} \text{ cm}^{-3}$. Experimentally as-grown material is found to be either n- or p-type with carrier concentrations in the 10^{15} cm^{-3} range.¹⁸ Because MBE growth is a nonequilibrium process, it is possible that growth may take place beyond the existence region; for example, if the equivalent pressure were of the order of 10^{-7} atm at 185°C, the materials would be tellurium antisite doped. While this provides a possible explanation of how the material could be n- or p-type as-grown based on equilibrium concentrations of defects, extending this argument, one would expect under some growth conditions to be able to obtain highly compensated material with very low carrier concentrations; this is never seen, to our knowledge. A more likely possibility is that nonequilibrium densities of point defects are frozen into the molecular beam epitaxy material resulting from details of the surface kinetics.

There is substantial experimental evidence of deep levels in LWIR HgCdTe, which have not yet been definitively associated with any particular defect. The minority carrier lifetimes in vacancy-doped material are limited by Shockley-Read recombination; deep-level transient spectroscopy (DLTS) measurements¹⁹⁻²¹ have identified two donor-like defect levels at $0.4E_{\text{gap}}$ and $0.75E_{\text{gap}}$. The densities of these levels roughly track the mercury vacancy concentration, although substantial scatter in the correlation is observed.¹⁹ Neither of these levels is believed to be associated with the mercury vacancy itself, nor do they appear to be associated with the same defect because they do not track one another. In equilibrium, the tellurium antisite density will track with the mercury vacancy concentration, although it will show a sharper dependence on the mercury pressure. In addition, as discussed above, we do not expect that equilibrium concentrations of tellurium antisites will be present except at very high temperatures corresponding to liquid-phase growth, and thus the ratio of tellurium antisites to mercury vacancies expected in equilibrium may not be experimentally realized, leading to substantial deviations from the equilibrium ratio and scattering in their concentrations. Thus, it is plausible that one of the Shockley-Read recombination centers is associated with the tellurium antisite, although to confirm this possibility a more quantitative prediction of the ionization levels of the antisite is needed. Deep levels associated with the tellurium antisite may also be responsible for the 1/f noise, which is found to be roughly proportional to the mercury vacancy concentration²² or they may enhance interband tunneling and thereby contribute to dark currents.

The Role of Native Point Defects in Self-Diffusion

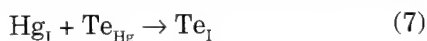
Self-diffusion of mercury is important for the annealing of as-grown mercury-vacancy doped p-type material to n-type, to form p-n junctions,¹⁶ and for understanding junction stability in HgCdTe devices. Although both the mercury vacancies and interstitials are mobile and contribute to mercury diffusion,²³ it is the interstitial diffusion that is found to dominate in the modeling of low-temperature anneals.^{12,17} Thus, although we find equilibrium mercury interstitial concentrations that are negligible in terms of their contribution to the net carrier densities,⁹ they will be important to mercury transport in the material, and therefore their properties are of interest. For both mercury vacancy and interstitial diffusion, more than just defect concentrations enter into the determination of the diffusion coefficients; for the present discussion, we will address only how our defect concentrations relate to the measured diffusion coefficients.

We predict that mercury interstitials are donors and in equilibrium are present in concentrations that are less than 10^6 cm^{-3} at 250°C.⁹ We have compared our results with those of annealing simulations by the Stanford group¹² and find that the concentration of interstitials we have predicted at $\sim 200^\circ\text{C}$ are several orders of magnitude too small to account for their modeling of the formation of p-n junctions. Although a number of approximations in our calculation of the formation energies will affect our interstitial formation free energy (for example, the use of supercells and approximations of the ionization energies), we do not expect these to account for this large a discrepancy. As discussed in the Methodology section above, we have completed the calculation of the electronic contribution to the formation free energies using pure HgTe. For the mercury vacancy and the tellurium antisite that are the major defects in HgCdTe and that occupy the cation sublattice and therefore are surrounded by four tellurium atoms, this is probably not such a bad assumption. Corrections to the electronic energy due to the presence of cadmium may be larger for the interstitials that see four cations as their first nearest neighbors in one tetrahedral site and six cations as near second neighbors in the other tetrahedral site. We are currently calculating the correction to our electronic energies, taking explicit account of cadmium in the lattice to see if it will eliminate the discrepancy with the Stanford model predictions.¹²

There has been a recent investigation²⁴ in $x = 0.22$ and $0.24 \text{ Hg}_{1-x}\text{Cd}_x\text{Te}$ on samples in which high concentrations of nonequilibrium mercury interstitials have been introduced. The observed deep levels near 45 and 60 meV above the valence-band edge were argued to be associated with the mercury interstitials. As discussed above, at this point our calculations are not able to determine the precise positions of the defect levels in the gap, but rather have predicted only that the mercury interstitials will be donor-like. If in fact

there are donor levels associated with the mercury interstitials that are near midgap, we would expect them to exhibit a series of levels corresponding to the different alloy environments about an interstitial. In addition, there are two classes of interstitials that we expect to have relatively high equilibrium densities, both of which occupy tetrahedral sites; the first is surrounded by four cation nearest neighbors, and the second is surrounded by four anion nearest neighbors. Although it is tempting to associate the two defect levels experimentally observed with these two classes of interstitial sites, there is no apparent reason why two levels are seen in the $x = 0.22$ material and only one level in for $x = 0.24$.

Finally, we return to the discussion of the mechanism for tellurium antisite diffusion and re-address the knockout mechanism that proceeds via the reaction



Our calculations predict that this is an exothermic reaction, with an energy of ~ 0.8 eV (the entropy gained in having two point defects rather than just one must also be considered in establishing the equilibrium concentrations of these defects). In non-equilibrium situations in which mercury interstitials are introduced into the material—for example, during ion-beam milling or oxide baking²⁵—this reaction will be pushed to the right, and excess tellurium interstitial will be produced. Thus, in such situations, one might expect tellurium antisite diffusion via the knockout mechanism to be a stronger competitor to the mercury vacancy mechanism, although the barriers to the formation of $\text{Hg}_i\text{-Te}_{\text{Hg}}$ pairs still exist, as discussed above.

In presenting the tellurium antisite as a candidate for the residual donor, we argued why its density might be fixed in the n-type material. On the other hand, when discussing the possibility that it is related to a Shockley-Read recombination center in vacancy-doped p-type material, we argued why its density might vary, depending on the cooldown rate and so forth. These two arguments are somewhat inconsistent. Although the possibility still exists that the tellurium antisite is both the residual donor (via a first ionization level that resonates in the gap) and a Shockley-Read center (via a midgap second ionization level), to be convincing a firmer correlation between the two would have to be established.

The Mercury Vacancy Tellurium Antisite Pair

Several additional consequences of the presence of the mercury vacancy tellurium antisite pairs should be discussed. As one can see from Fig. 3, we are predicting a very large concentration of the defect pairs, which may even exceed the mercury vacancy concentrations for LPE material grown from the tellurium-rich melts. If the pair is electrically inactive, as our preliminary calculations predict, it will not impact the carrier concentrations or mobility. Such a large density of pairs does imply that the nonstoichiometry of the material is larger than that

due to the vacancy concentrations, particularly at lower temperatures where we predict that the equilibrium concentrations of neutral pairs will approach that of the mercury vacancy.

Note that the large binding energy of the mercury vacancy tellurium antisite pair suggests that other bound pairs may be present in the material. For example, a bound Frenkel defect (involving the mercury vacancy-mercury interstitial pair) that involves an acceptor and a donor defect with opposite lattice strains may be important and will impact diffusion of mercury in the lattice. The most likely consequences will be to increase the annihilation capture cross section of mercury interstitials into mercury vacancies and to present a barrier to the formation of free Frenkel defects through a geminate process. These phenomena will be important to understanding diffusion in HgCdTe.¹² Evidence for the mercury vacancy substitutional indium pair has been seen using a nuclear hyperfine technique.²⁶ This defect is similar to the mercury vacancy tellurium antisite pair, and thus we expect it may be well bound. Both of these pairs merit further investigation.

DEFECTS IN CdTe

Like HgCdTe, CdTe has a wide stability region and can be doped both p- and n-type. Its use as both a substrate (along with $\text{Cd}_{1-x}\text{Zn}_x\text{Te}$)²⁷ and a passivant make it an important material in the manufacturing of HgCdTe LWIR FPAs.

We have predicted the density of neutral native point defects in CdTe as a function of temperature and pressure; results for 700°C are shown in Fig. 4. We predict the same electrical type (donor vs acceptor) for the native point defects as in HgCdTe; for example, we find that the cadmium vacancy is an acceptor and

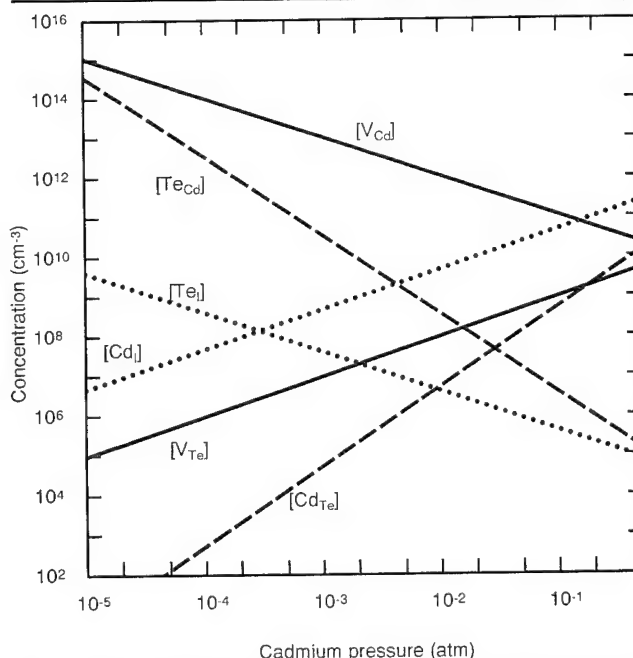


Fig. 4. Neutral native point defect densities of CdTe within the stability region at 700°C.

the cadmium interstitial and tellurium antisite are donors.

Based on the neutral native point defects, we expect that CdTe solid can exist with both excess cadmium and excess tellurium. We find that the cadmium interstitial is the dominant defect for high cadmium pressures, and the cadmium vacancy is most important at mid and low cadmium pressures.

Because the native point defects may have energy levels in the gap associated with them, it is important to include these in the analysis. We have begun to calculate the ionization levels associated with the native point defects but have not yet included the Jahn-Teller distortions,²⁸ which can significantly alter the localized energy levels. For this discussion, we shall assume that the cadmium vacancy has a first ionization level near the valence-band edge and a second level near midgap²⁹ and assume that the cadmium interstitial is a double shallow donor.² In this case, we predict a p- to n-type conversion at 700°C at relatively high cadmium pressures, in agreement with experiment.²

From Fig. 4, we see that the tellurium antisite becomes more important as the cadmium pressure is lowered. Depending on the energies associated with the tellurium antisite donor levels, the material may be highly compensated at the lowest pressures, or another p- to n-type conversion may even occur. Experiments designed to equilibrate on the cadmium-poor side of the stability region can be used to test for the presence of tellurium antisites through both their impact on electrical activities and the presence of localized levels.

CONCLUSIONS AND SUGGESTED EXPERIMENTS

The theory developed here clearly indicates that in $\text{Hg}_{0.8}\text{Cd}_{0.2}\text{Te}$ equilibrated at typical annealing temperatures and pressures (the right side of Fig. 3c), the tellurium antisite and mercury vacancy tellurium antisite pair densities are well below levels that can impact device performance. The primary outstanding question is whether or not tellurium antisite diffusion rates are high enough that normally processed samples fully equilibrate. Experiments are needed to modify these defect populations in a controlled manner so their impact on carrier concentrations, lifetimes, and other device properties can be determined. The basic idea is to modify the tellurium antisite concentration by choosing annealing temperatures, mercury pressures, and times that are long enough to permit a measurable portion of samples to equilibrate.

First, we consider annealing experiments to test for the possibility that the antisite is the residual donor. If tellurium antisite diffusion is so slow that it is not equilibrated during low-temperature mercury-saturated anneals, one must first anneal at higher temperatures and lower mercury pressures to introduce tellurium antisite mercury vacancy pairs (this step could be eliminated for LPE material grown from the tellurium melt), followed by a lower-temperature,

low-mercury-pressure anneal to reduce the antisite density, while still maintaining a relatively high density of pairs, concluded by a low-temperature, mercury-saturated anneal to reduce the mercury vacancy concentration even further. A series of experiments in which the conditions of the first two anneals were varied could be designed to test for the effect they have on the residual donor concentration. A similar experiment could be performed to correlate the Shockley-Read center in mercury-vacancy-doped material with nonequilibrium tellurium antisite densities.

Although we have proposed a series of experiments to establish whether the tellurium antisite is the residual donor or a Shockley-Read recombination center based on nonequilibrium densities, one may be able to design a series of experiments in which equilibrium populations of tellurium antisites are obtained by choosing high enough temperatures, thin enough samples, and long enough annealing times. One could choose annealing conditions to manipulate the mercury vacancy and tellurium antisite populations independently. For example, a 300°C anneal to reduce the hole concentration to $\sim 10^{16}$ will result in an order-of-magnitude more tellurium antisites than an anneal at 400°C to achieve the same hole concentration; Fig. 2 can be used in guiding such a study. The correlation of the tellurium antisite densities with the Shockley-Read center should be possible by doing minority carrier lifetime and/or DLTS measurements on materials with the same mercury vacancy hole concentrations achieved by anneals at different temperatures. Although a study of this type was recently presented,¹ and for a given hole concentration a correlation of lifetimes with the annealing temperature was observed, the effective annealing conditions there were set by the stoichiometry of CdTe cap layers and thus were more complicated than a simple anneal with a controlled mercury overpressure.

Experiments to test the presence of the mercury vacancy tellurium antisite pair are similar to those proposed above for the isolated tellurium antisite. Our preliminary calculations indicate that the pair will be electrically inactive and have no states in the band gap. As such, we do not expect their presence to have a direct impact on the electrical properties, but their presence will be manifested in their impact on tellurium antisite diffusion. Note that these experiments proposed to test for the presence of the tellurium antisite cannot discriminate between the isolated tellurium antisite and the mercury vacancy tellurium antisite pair.

ACKNOWLEDGMENT

The work reported here was supported by NASA Contract No. NAS1-18226, ONR Contract No. N00014-89-K-132, and ARPA Contract No. MDA972-92-C-0053. Use of the Numerical Aerodynamic Simulation supercomputer facilities at NASA Ames Research Center is gratefully acknowledged.

REFERENCES

1. C.F. Wan, M.C. Chen, J.H. Tregilgas, T.W. Orent and J.D. Luttmer, 1993 MCT Workshop.
2. H.R. Vydyanath, J. Ellsworth, J.J. Kennedy, B. Dean, C.J. Johnson, G.T. Neugebauer, J. Sepich and P.-K. Liao, *J. Vac. Sci. Technol. B* 10, 1476 (1992).
3. H.R. Vydyanath, *J. Electrochem. Soc.* 128, 2609 (1981).
4. F.A. Kröger, *The Chemistry of Imperfect Crystals* (New York: J. Wiley & Sons, Inc., 1964).
5. T. Tung, M.H. Kalisher, A.P. Stevens and P.E. Herning, *Mat. Res. Soc. Symp. Proc.* 90, 321 (1987) and references therein.
6. O.K. Andersen, O. Jepsen and D. Glotzel, *Highlights of Condensed Matter Theory*, ed. F. Bassani et al. (Amsterdam, The Netherlands: North Holland, 1985), p. 59.
7. D. Langreth and D. Mehl, *Phys. Rev. B* 28, 1809 (1983).
8. M. van Schilfgaarde, A.T. Paxton, M.A. Berding and M. Methfessel (in preparation).
9. M.A. Berding, M. van Schilfgaarde and A. Sher, *Phys. Rev. B* 50, 1519 (1994).
10. In Ref. 9, we assumed degeneracies of one, two, and one for the neutral, singly, and doubly ionized states of all donor and acceptors in HgCdTe. This is valid if only the α_1 states are occupied and the triply (sixfold including spin) degenerate t_2 states remain unoccupied. (Recall that the point group of an undistorted point defect is T_d .) If the t_2 states are partially occupied, an additional degeneracy will be present that should be included in our calculations; this degeneracy was not included in Ref. 9 but will be added in this paper. For an undistorted defect with the full T_d symmetry, this degeneracy arises from the partial occupation of the sixfold degenerate state (constrained to have a maximal number of spins paired); if the local symmetry is lowered due to a Jahn-Teller distortion (to point group D_{2d} for one or two electrons in the t_2 state, to point group C_{2v} for three, four, or five electrons in the t_2 state),¹¹ this additional degeneracy arises from the extra degree of freedom present in the introduction of a locally preferred direction in space. Going through the counting, we obtain degeneracy factors of (6,3,6,3,6,1) for one to six electrons in the t_2 state, respectively. Results reported here include these full degeneracy factors.
11. See, for example, the discussion of symmetry-lowering distortions in silicon in G.A. Baraff, E.O. Kane and M. Schlüter, *Phys. Rev. B* 21, 5662 (1980).
12. S.L. Holander and C.R. Helms, private communication.
13. H.R. Vydyanath and C.H. Hiner, *J. Appl. Phys.* 65, 3080 (1989).
14. G.L. Hansen and J.L. Schmit, *J. Appl. Phys.* 54, 1639 (1983).
15. G.L. Hansen, J.L. Schmit and T.N. Casselman, *J. Appl. Phys.* 53, 7099 (1982).
16. H.F. Schaake, J.H. Tregilgas, J.D. Beck, M.A. Kinch and B.E. Gnade, *J. Vac. Sci. Technol. A* 3, 143 (1985); H.F. Schaake, *J. Electron. Mater.* 14, 513 (1985).
17. J.L. Meléndez and C.R. Helms, *J. Electron. Mater.* 22, 999 (1989).
18. See, for example, R. Sporcken, M.D. Lange, S. Sivanathan and J.P. Faurie, *Appl. Phys. Lett.* 59, 81 (1991).
19. C.E. Jones, V. Nair and D.L. Polla, *Appl. Phys. Lett.* 39, 248 (1981).
20. C.E. Jones, V. Nair, J. Lindquist and D.L. Polla, *J. Vac. Sci. Technol.* 21, 187 (1982).
21. C.E. Jones, K. James, J. Merz, R. Braunstein, M. Burd, M. Eetemadi, S. Hutton and J. Drumheller, *J. Vac. Sci. Technol. A* 3, 131 (1985).
22. R. Schiebel and D. Bartholomew, *J. Electron. Mater.* 24, 1299 (1995).
23. See, for example, D.A. Stevenson and M.-F.S. Tang, *J. Vac. Sci. Technol. B* 9, 1615 (1991).
24. C.L. Littler, E. Maldonado, X.N. Song, Z. Yu, J.L. Elkind, D.G. Seiler and J.R. Lowney, *J. Vac. Sci. Technol. B* 10, 1466 (1992).
25. J.L. Elkind, *J. Vac. Sci. Technol. B* 10, 1460 (1992).
26. W.C. Hughes, M.L. Swanson and J.C. Austin, *Appl. Phys. Lett.* 59, 938 (1991); *J. Electron. Mater.* 22, 1011 (1993).
27. Because of the low zinc concentrations, our results should be applicable to $x = 0.04$ $\text{Cd}_{1-x}\text{Zn}_x\text{Te}$, which is the more recent substrate of choice for LWIR $\text{Hg}_{0.8}\text{Cd}_{0.2}\text{Te}$ devices.
28. The Jahn-Teller distortion most certainly exists at low temperatures. At high temperatures corresponding to liquid phase growth, these distortions may get washed out by thermal vibrations in the lattice. We are currently examining this issue.
29. P. Höschl, R. Grill, J. Franc, P. Moravec and E. Belas, *Mat. Sci. and Engr.* B16, 215 (1993).

Process Simulation for HgCdTe Infrared Focal Plane Array Flexible Manufacturing

C.R. HELMS, J.L. MELÉNDEZ,* H.G. ROBINSON, S. HOLANDER,
J. HASAN, and S. HALEPETE

Department of Electrical Engineering, Stanford University,
Stanford, CA 94305

The strategy and status of a process simulator for the flexible manufacture of HgCdTe infrared focal plane arrays is described. It has capabilities to simulate Hg vacancy and interstitial effects and cation impurity diffusion, for various boundary conditions in one dimension. Numerical complexity of these problems stems from the necessity of solving diffusion equations for each defect that are coupled to each other via nonlinear interaction terms. The simulator has already led to the prediction of heretofore unexplained experimental data. Current extensions of the one-dimensional simulator planned over the next few years include the addition of Te antisites, antisite-Hg vacancy pairs, and In-Hg vacancy pairs, ion implantation, and various energetic processes (such as ion milling). The sequential effect of various processes will be possible with the input to the simulator looking much like a process run sheet.

Key words: Flexible manufacturing, HgCdTe, infrared focal plane arrays (IRFPAs), process simulations

INTRODUCTION

In the past, semiconductor manufacturing has been characterized by a long, expensive, and tedious process of climbing up the yield curve for the introduction of a new process or device structure. Achieving a low overall cost of ownership (CoO) has required that the initial design/fab/test/redesign costs for both device and process be recovered by high volume production once high yields are achieved. The counter culture to this paradigm has been called flexible manufacturing, where new designs can be implemented rapidly at low cost with a high probability of first pass success through the design/fab/test cycle and mixed in the same production line with existing products.

The application of this new paradigm to Si integrated circuit technology was recently demonstrated successfully in the Microelectronics Manufacturing and Technology program (MMST) carried out by Texas Instruments and funded in part by the Advanced Research Projects Agency (ARPA) and the U.S. Air Force Wright Laboratories.¹⁻³ One of the key accomplishments of this program was the demonstration of a low CoO factory with a 100–2000 wafer/month capacity and 5–15 day cycle times. This compares to the 20,000 wafers/month, 1–3 month cycle times of conventional Si wafer fabs. In addition, a factor of ten reduction of the cost of such a factory (<\$50M vs >\$500M) compared to its conventional counterpart represents a significant reduction in risk for new fab installations.

There are a number of requirements to make flexible manufacturing a reality. The replacement of stand-alone batch tools with modular single wafer

*Current address: Texas Instruments, Inc., P.O. Box 655936, Dallas, TX 75265

(Received December 4, 1994; revised January 28, 1995)

tools is a key technology advancement. Computer integrated manufacturing (CIM), real time process sensing and control, and feed forward are critical. In addition, computed aided design (CAD) tools for equipment, process, device, and circuit design must be available to achieve first pass success and optimization for minimum CoO. In the case of Si integrated circuit technology such tools such as SUPREM, PISCES, SemiCad, SPICE, etc. have provided the key enablers for this implementation.⁴⁻⁶

The application of these concepts to the manufacturing of HgCdTe (MCT) infrared focal plane arrays (IRFPAs) is an obvious extension of the MMST concept. Infrared FPAs are ideally suited due to the small lot sizes imagined, the variety of products to be produced in one factory, and the consistency of the single wafer concept with MCT manufacturing in general. As is the case for Si technology, technology-CAD (TCAD) tools represent a key enabler for MCT IRFPA flexible manufacturing. The purpose of this paper is to describe recent developments in process modeling of MCT VIP IRFPAs.

PROCESS MODELING: GENERAL

Why is the availability of a robust process model so critical for flexible manufacturing? We can make the claim that flexible manufacturing cannot be achieved at all without process modeling! To see this, let us consider a process flow made up of a sequence of unit process steps. A typical flow for MCT VIP IRFPAs is shown in Table I along with some requirements for process simulation. The unit step process parameters such as time, temperature, ambient, etc., effect a large set of materials properties (dopants, defects, extended defects, lifetimes, mobilities, etc.) during that step. In a process flow such as this, each step interacts with the others in subtle ways. The ultimate effect of the process flow on these critical factors cannot be determined in a simple way without numerical computation, keeping track of a number of variables simultaneously. The alternative to process simulation is to perform process design and optimization through extensive design/fab/test cycles. This is an extremely expensive and slow process. Low CoO and fast turnaround through short cycle times

cannot be achieved in this way. A final benefit of a process simulator is its capture of the process cause and effect database and the intuition of design engineers that has been applied in the past. Thus, even years later a process flow can be resurrected and applied even though the designers that developed it have long since moved into other areas.

Let us now define exactly what is meant by process modeling and simulation. The development of a process simulator is a hierarchical process with a number of critical components. It is made up of a number of interacting simulator modules associated with a unit step process such as implantation, annealing, etc. Each module is based on a model for the phenomena of interest which needs to be accurate but also simple enough to be solved in a reasonable time on a workstation class (or slower) machine. These models have as their basis more sophisticated first principles models and calculations⁷ coupled with extensive experimental validation. In the case of implantation, for example, the first principles methods involve quantum molecular dynamics calculations which are typically run on supercomputers. Backing away from this level of complexity, we have Monte Carlo type ion dynamics calculations such as TRIM.⁸ This approach is still not well suited for implementation in a process simulator due to time requirements, even on a workstation class machine. The method we have chosen for the current simulator takes these methods (combined with experimental validation) as a basis and creates a database based on analytical fits, which is embedded in the simulator. The required implantation profiles can therefore be calculated rapidly and accurately without the need to run the more complex calculations time after time. This methodology has proven its worth for both Si and the III-Vs.⁴⁻⁶

MCT PROCESS SIMULATION STRUCTURE

Based on the process flow of Table I, we identify simulator modules for implantation (including point defect generation) and diffusion with submodules for point defects (Hg interstitials, vacancies, and antisites), dopants, and extended defect generation, growth, and dissolution. It is also convenient to define a separate module for boundary conditions, which

Table I. MCT IRFPA VIP Process Flow and Process Simulation Requirements

Process Step	Simulation Requirements
1. MCT Growth	Input Point Defect/Impurity Profiles
2. Defect Reduction Anneal	Diffusion of Point/Extended Defects, Impurities
3. Backside Etch	Reset Back Boundary
4. Backside Passivation	Reset Back Boundary Condition
5. Anneal	Same as 2 with Updated Boundary Condition
6. Bonding/Thinning	Reset Front Boundary
7. Frontside Passivation	Reset Front Boundary Condition
8. Patterning	None
9. Implant	Point/Extended Defect/Impurity Generation/Diffusion
10. Anneal	Same as 5.
11. BEOL Processing/Assy.	None
12. Final Bake	Same as 5.

specifies the properties of the boundaries (Hg flux as a function of pressure for an uncapped surface or a zero flux condition for a capped surface). It is imagined that future device generations will employ energetic processes in the active device regions so a "plasma etch" module is also included.

At this point, the classical functions of a process simulator would be complete, taking the process parameter inputs and providing outputs which would be the dopant, point defect, and extended defect profiles after a sequence of unit process steps. This requires an appropriate IO structure which allows for the proper sequencing of the modules. This is, however, only one piece of the TCAD required for computational prototyping. The other pieces are circuit and device simulators as well equipment models. Given a well integrated set of simulators for circuit, device, process, and equipment modeling, process synthesis can be implemented and the virtual factory achieved.⁹

Our simulator being developed will have the ability to interact with existing device modeling simulators by providing the materials profile information as the necessary inputs to PISCES, SemiCad, etc. In addition the mapping of process parameter variations into the statistical equipment parameter space is possible through the creation of technology-based response surfaces. However, to enhance the utility of the process simulator, device and equipment simulation features will be imbedded to allow rapid estimates of the consequences of process variations on equipment and device electrical properties.

MCT PROCESS SIMULATION STATUS: POINT DEFECTS AND DIFFUSION

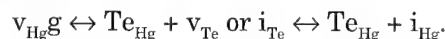
In the remainder of this paper, the status of the current simulation capabilities and on-going efforts to expand these capabilities to span the process flow of Table I will be discussed. The heart of the simulator is the diffusion module which will ultimately track profiles of Hg vacancies (*v*), interstitials (*i*), and excess Te (as a Te antisite) (*a*), and the formation and dissolution of dislocations and Te precipitates, as a function of the process history of the MCT material, including annealing in various ambients, ion implantation, and plasma and reactive ion etching. In addition, impurities can be handled in a similar way.⁹ The basis of this module is a set of continuity equations for the various species of interest, with the initial and boundary conditions and temperature as the inputs for a given process step. For Hg vacancies, interstitials, and Te antisites the equations to be solved

$$\frac{\partial v}{\partial t} = D_v \frac{\partial^2 v}{\partial x^2} + g - k_{iv} vi \quad (1)$$

$$\frac{\partial i}{\partial t} = D_i \frac{\partial^2 i}{\partial x^2} + g - k_{iv} vi \quad (2)$$

$$\frac{\partial a}{\partial t} = \frac{v}{C_o} D_v \frac{\partial^2 a}{\partial x^2} - \frac{a}{C_o} D_v \frac{\partial^2 v}{\partial x^2} \quad (3)$$

The *D*s are the various diffusion coefficients, *g* is the generation rate constant for *v_{Hg}/i_{Hg}* pairs, *k_{iv}* is the recombination rate constant, and *C_o* is the density of possible Hg vacancy sites from hop to hop. The methodology for the Hg vacancies and interstitials has been discussed previously and will not be repeated here.¹⁰⁻¹² For the antisites, it is assumed that they can be grown or diffused in but not created otherwise in the bulk of the MCT. The possible reactions for creation of antisites are (except for implant or other energetic process):



Since both of these reactions require defects that are believed to only occur in extremely small concentrations (*v_{Te}* and *i_{Te}*), the assumption is justified.

The equations appear straightforward except for the two terms on the right hand side in the antisite diffusion equation relating to Hg vacancies. We choose here to implement the physically accurate form for diffusion via a vacancy mechanism instead of using the approximate form where the effective antisite diffusion coefficient is assumed to be proportional to the Hg vacancy concentration. The boundary conditions currently implemented take the form:

$$\frac{dv}{dx} + h_{2v}v = h_{3v} \quad (4)$$

where the equations for interstitials and antisites are similar. For a typical case, the *h₂*s are only functions of temperature and

$$h_{3i} \propto P_{Hg}; h_{3v} \propto P_{Hg}^{-1}; h_{3a} \propto P_{Hg}^{-2}$$

Considering only the vacancy/interstitial problem for the moment, we can see that in order to obtain an accurate solution, the eight (seven independent) materials parameters *D_v*, *g*, *k_{iv}*, *D_i*, *h_{2v}*, *h_{3v}*, *h_{2i}*, and *h_{3i}*, must be known for the specific problem, with the *h*s specific to the actual boundaries (different for a vacuum interface vs an interface with CdTe, etc.). We typically drive the boundary only via the Hg interstitials, leading to six parameters (the surface vacancy concentration equilibrates to the interstitial concentration via the generation and recombination terms).

The relationship between these parameters and those typically measured experimentally will now be given. The most well known value is the Hg vacancy concentration as a function of temperature and pressure. In terms of the above parameters, it is

$$v = \frac{gh_{2i}}{k_{iv}h_{3i}} \quad (5)$$

assuming that the *h₂*s are zero and remembering that *h_{3i}* \propto *P_{Hg}*. Additional information is obtained from previous radiotracer experiments of Hg self-diffusion, leading to the relationship for the radiotracer Hg diffusion coefficient:

$$D_{\text{tracer}} = \left(\frac{D_i h_{3i}}{h_{2i} C_o} + \frac{v D_v}{C_o} \right) \quad (6)$$

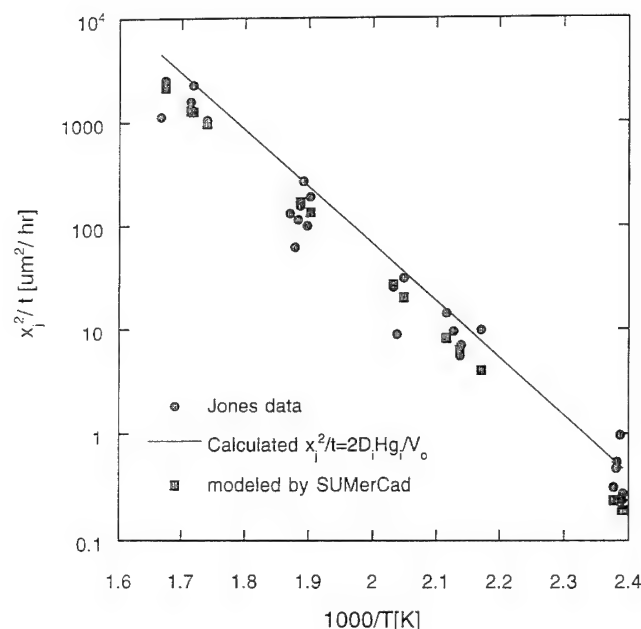


Fig. 1. Plots of the square of the junction depth divided by time vs inverse temperature for an "n on p" process where MCT initially doped with both vacancies and a low level donor is exposed to Hg vapor at the given temperature. The solid circles are from Jones et al.,¹³ line from Eq. (7), and solid squares from the output of the process simulator.

for the "slow" component of diffusion. A final experiment that assists in determining the parameters is "type conversion" where an initially vacancy doped material is converted to n-type by the in-diffusion of Hg. For low temperatures, vacancy diffusion is negligible, leading to a junction depth:

$$x_j^2 = \frac{2D_i h_{3i} t}{v_o h_{2i}} \quad (7)$$

where t is time and v_o is the initial vacancy concentration. With only three measurements and six parameters to determine, the situation may seem hopeless. However, in many cases, the solutions are relatively insensitive to parameter values so long as relationships between the parameters are preserved. The least sensitive is the value for the boundary conditions; so long as the $h_2:h_3$ ratio is fixed (and both values are large enough), the ultimate solutions are little effected. This is easily seen in the above equations, where only the ratio itself appears. The same is true for the $g:k_{iv}$ ratio. For low temperatures and relatively high Hg partial pressures, vacancy diffusion can also be neglected, leading to an additional simplification. Additional information from the literature also provides limits on the various parameters. For example, the type conversion process leading to n on p diodes at lower temperatures, described by the equation above implies that both vacancy diffusion is slow compared to interstitial diffusion and that interstitial diffusion is slow compared to vacancy/interstitial recombination. This leads to the inequalities

$$\frac{D_i h_{3i}}{h_{2i}} \gg D_v v_o \quad \text{and} \quad \frac{2D_i}{v_o k_{iv}} \ll x_j^2$$

good at lower ($< 200^\circ\text{C}$) temperatures. Values for the critical parameters currently implemented are:

$$v = 3.3 \times 10^{28} (\exp(-1.663/kT)) P^{-1} \text{ cm}^{-3}$$

$$D_v = 1.2 \times 10^5 \exp(-1.51/kT) \text{ cm}^2\text{s}^{-1}$$

$$\frac{D_i h_{3i}}{h_{2i}} = 1.43 \times 10^{13} (\exp(-0.457/kT)) P \text{ cm}^{-1}\text{s}^{-1}$$

$$\frac{g}{k_{iv}} = 2.0 \times 10^{44} \exp(-1.97/kT) \text{ cm}^{-6}$$

where the energies are given in eV and Hg pressures in atmospheres. An example of the use of the model is shown in Fig. 1 for fits to type conversion data.¹³ The equation fit refers to Eq. (7); the deviation from this equation is due to Hg vacancy diffusion, especially for the higher temperatures.

A major reason to model the Hg antisites is the claim that they can lead to the formation of Te precipitates (when at supersaturated concentrations) and may be a dominant diffuser in the dissolution of Te precipitates. The key experimental unknowns in the antisite modeling are the equilibrium values as a function of Hg pressure (the effective diffusion coefficient is determined from the vacancy diffusion coefficient given above). Even without these values, we can assess the effect of a particular annealing schedule in reducing the concentration and more accurate values of these concentrations are becoming available from first principles calculations.⁷ An example of two such simulations are shown in Fig. 2. As can be seen, conditions leading to larger diffusive fluxes of antisites are just those leading to high vacancy concentrations.

MCT PROCESS SIMULATION STATUS: IMPLANTATION

The use of implantation for the VIP architecture for MCT IRFPAs differs significantly from its use in other technologies. The principle effect of implantation in MCT VIP technology is to create Hg interstitials which can be released and rapidly diffuse and annihilate vacancies or kick out other impurities. For vacancy doped material this leads to an n on p structure for the photodiode. This mechanism is also one of the most important areas for current research in Si processing, causing transient enhance diffusion (TED) of shallow implants into source and drain regions.

Many researchers employ the "plus-one" model for TED.¹⁴ In this model, each implanted ion displaces a Si atom from its lattice site into an interstitial position, thereby creating an effective dose of Si interstitials equal to the implanted dose. The other model that is used to simulate TED is the "Frenkel" model.^{15,16} In this model, vacancy-interstitial pairs are produced when implanted ions transfer sufficient energy to

lattice atoms to displace them from their lattice sites. Most of these Frenkel pairs recombine during implantation or in the first moments of the anneal, but if the momentum transfer to the recoil is large, separation of the pairs can occur, leading to regions of excess vacancies and interstitials. The vacancy-rich region is nearer the surface, while the interstitial-rich region is deeper into the material because most high momentum transfer events are in the forward direction. The excess surface vacancy concentration can be increased if significant numbers of lattice atoms are sputtered out of the material.¹⁷ The sputtering yield generally increases as the implant energy and temperature decrease.

The dominant source of interstitials, plus-one or Frenkel pairs, is determined by the energetics of the ion-target system. If the momentum transferred from the ion to the recoil is small, (light ions implanted into heavier targets), the separation of the resultant Frenkel pairs will be small and the plus one interstitials will predominate. As the momentum transfer increases (heavier ions implanted into lighter targets), the contribution to the excess interstitial concentration from Frenkel recoils will increase and eventually predominate. The ion-target combinations at which this occurs depend not only on the masses of the ion and lattice atoms, but also on the lattice displacement energy, E_d , and to a lesser extent, the energy of the incident ion.

Modeling of B implantation into MCT builds on the plus-one and Frenkel models described above, but with significant differences. Hg has a smaller displacement energy compared to Cd and Te, and many Hg recoils will be generated per incident ion. Because B is so light compared to Hg (or Te and Cd), however, very little momentum is transferred from the ion to the recoil. Furthermore, much of the B may remain interstitial due to its small size, reducing the number of "plus one" interstitials to an unknown fraction.

As with implantation into Si and GaAs, extended defects formed during implantation of HgCdTe play an important role in regulating the post-implant point defect concentrations. The most easily observed extended defects are extrinsic dislocation loops, which appear in cross-sectional transmission electron microscopy (TEM) images as a band extending from the surface to near R_p , the projected range. These extrinsic loops are believed to coalesce from free interstitials created during the implant. They serve as both sources and sinks for point defects, growing or shrinking in the process. Interstitials captured by the loops are not free to diffuse through the lattice. Observation of changes in the area bound by the loops using TEM is a means of measuring point defect fluxes and/or concentrations.¹⁸⁻²⁰ Other extended defects that might form during implantation are voids and interstitial clusters. Voids coalesce from excess vacancies, while clusters can be viewed as interstitial precipitates. Unlike dislocation loops, both of these defects are three dimensional. They are much more difficult to observe because of their small size and often dilute

concentration. Both can serve as point defect sources and sinks. A comprehensive model of implantation of HgCdTe will need to incorporate the role of dislocations, voids and clusters in regulating point defect concentrations.

Development of an ion implantation module for the HgCdTe process simulator has thus far focused in two areas. The first is to gather data from the literature for both calibration and validation of the implant models. Implanted ion profiles can generally be represented by a four moment (Pearson-IV) distribution. These moments are being extracted from the experimental profiles and placed into a lookup table. Once the table is complete, implant profiles as a function of ion, dose, and energy can be generated. The second area of focus in implant modeling involves defining the initial point defect concentrations prior to the anneal. We have used a Monte Carlo code known as TRIM (TRANSPORT of Ions in Matter)⁸ to predict the number of point defects generated under varying implant conditions. TRIM uses a binary collision approximation (BCA) and therefore does not account for the energy dissipation to neighboring atoms. TRIM also does not calculate channeling tails because it assumes an amorphous target. Despite the limitations of TRIM and other BCA codes, they provide valuable insights into the kinetic processes occurring during implantation. An example of a TRIM simulation of a 150 keV B implant into $\text{Hg}_{0.8}\text{Cd}_{0.2}\text{Te}$, showing both the ion and Hg recoil profiles, is overlaid with the secondary ion mass spectroscopy data in Fig. 3 along with a comparison to experimental data including a Pearson IV fit. Because B is a light ion, most of its stopping is electronic. In spite of this, approximately 1000 Hg recoils are produced per incident ion. Most of these recoils will recombine with vacancies during the implant, but a fraction will remain as free interstitials and diffuse into the lattice or lead to the formation of dislocations. The Hg contained in these

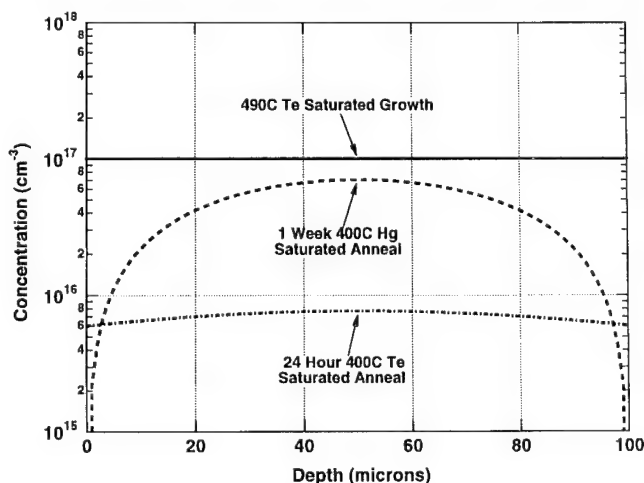


Fig. 2. Plots of the Te antisite profiles for a 100 micron slice of MCT. Solid line is assumed initial concentration equilibrated on the Te-rich side of the phase diagram at 490°C. Dashed line is for a 400°C, Hg saturated anneal for 1 week; dashed-dotted for a Te-saturated anneal for 24 h.

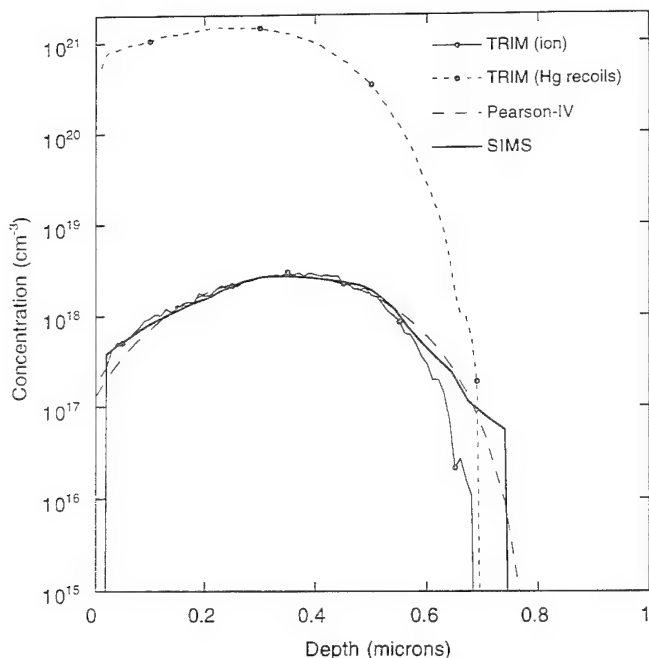


Fig. 3. 150 keV, $1 \times 10^{14} \text{ cm}^{-2}$ B implant into $\text{Hg}_{0.8}\text{Cd}_{0.2}\text{Te}$. Comparison of SIMS and Pearson-IV and TRIM simulations. The as-implanted Hg recoil distribution, as predicted by TRIM, is also shown.

dislocations can be released later during elevated temperature anneals. Knowing the number and distribution of these interstitials provides the initial condition for the post-implant anneal.

MCT PROCESS SIMULATION STATUS: CONCLUSIONS AND FUTURE WORK

We have described the status of the Stanford University Process Simulator for MCT. Currently, we have the capability to model Hg vacancy and interstitial diffusion, Te antisite diffusion, and Au diffusion;⁹ algorithms for ion implantation have been developed and are to be added to the simulator in the near future. An upcoming task is to develop and implement models in the simulator to investigate extended defect (Te precipitate, dislocations, and implant and ion induced damage) nucleation, growth, and dissolution. Methods for this implementation will be based on similar models being applied to Si dislocation problems.^{19,21,22}

ACKNOWLEDGMENTS

Past work at Stanford supported by gift funds from Texas Instruments; current work supported as a subcontract to Texas Instruments (K. Carson; USAF Wright Laboratories, C. Strecker; ARPA, R. Balcerak), and gift funds from Texas Instruments.

REFERENCES

1. R.R. Doering, *Solid State Tech.* 37, 1, 31 (1994).
2. Z. Lemnios, *Solid State Tech.* 37, 2, 25 (1994).
3. M.M. Moslehi, R.A. Chapman, M. Wong, A. Paranjpe, H.N. Najm, J. Kuehne, R.L. Yeakley and C.J. Davis, *IEEE Trans. Elect. Dev.* ED39, 4 (1992).
4. C.P. Ho, J.D. Plummer, S.E. Hansen and R.W. Dutton, *IEEE Trans. on Elec. Dev.* ED30, 1438 (1983).
5. M.E. Law and R.W. Dutton, *Proc. IEEE Trans. Comp. Aided Design* (1987), p. 181.
6. M.R. Pinto, C.S. Rafferty and R.W. Dutton, *Stanford Electronics Laboratory Technical Report* (September, 1984).
7. M.A. Berding, A. Sher and M. Van Schilfgaarde, *J. Electron. Mater.* 24, 1127 (1995).
8. J.F. Ziegler, J.P. Biersack and U. Littmark, *Stopping Powers and Ranges of Ions in Solids* (New York: Pergamon Press, 1985).
9. J.L. Meléndez, J. Tregilgas, J. Dodge and C.R. Helms, *J. Electron. Mater.* 24, 1219 (1995).
10. J.L. Meléndez and C.R. Helms, *J. Electron. Mater.* 24, 565 (1995).
11. J.L. Meléndez and C.R. Helms, *J. Electron. Mater.* 22, 999 (1993).
12. J.L. Meléndez, PhD Dissertation, Stanford University (1993).
13. C.L. Jones, M.J.T. Quelch, P. Capper and J.J. Gosney, *J. Appl. Phys.* 53, 9080 (1982).
14. P.A. Packan and J.D. Plummer, *Appl. Phys. Lett.* 56, 1787 (1990).
15. H.G. Robinson, M.D. Deal, G. Amarantunga, P.B. Griffin, D.A. Stevenson and J.D. Plummer, *J. Appl. Phys.* 71, 2615 (1992).
16. M.D. Giles, *Appl. Phys. Lett.* 62, 1940 (1993).
17. C.C. Lee, M.D. Deal, K.S. Jones, H.G. Robinson and J.C. Bravman, to appear in the *J. of Electrochemical Soc.* (1994).
18. H.L. Meng, S. Prussin, M.E. Law and K.S. Jones, *J. Appl. Phys.* 73, 955 (1993).
19. J.K. Listebarger, K.S. Jones and J.A. Slinkman, *J. Appl. Phys.* 73, 4815 (1993).
20. H.G. Robinson, T.E. Haynes, E.L. Allen, C.C. Lee, M.D. Deal and K.S. Jones, *J. Appl. Phys.* 74, 78 (1994).
21. R.Y.S. Huang and R.W. Dutton, *J. Appl. Phys.* 74, 5821 (1993).
22. H. Park, H.G. Robinson, K.S. Jones and M.E. Law, *Appl. Phys. Lett.* 65, 436 (1994).

Effect of Dislocations on 1/f Noise of Long Wavelength Infrared Photodiodes Fabricated with HgCdTe Layers Grown on GaAs by Metalorganic Vapor Phase Epitaxy

S. MURAKAMI, H. NISHINO, H. EBE, and Y. NISHIJIMA

Fujitsu Laboratories Ltd., 10-1 Morinosato-Wakamiya, Atsugi, 243-01, Japan

We studied the effect of dislocations on the 1/f noise current of long wavelength infrared photodiodes fabricated with HgCdTe layers grown on GaAs by metalorganic vapor phase epitaxy. N-on-p junctions were formed by boron ion implantation into Hg-vacancy doped epilayers. The 1/f noise dominated from 0.5 to 100 Hz, and shot noise caused by photocurrent ($\sqrt{2eI_p}$) dominated at higher frequencies. We observed two types of 1/f noise. One is caused by the leakage current generated at dislocations, and the other is induced by the photocurrent. The 1/f noise current increased with the photon flux in the low-etch pit density (EPD) range independently of EPD. It increased with EPD in the high-EPD range. The 1/f noise current measured at zero field of view increased with EPD. This suggests that the 1/f noise generated by the photocurrent dominated in the low-EPD range, and that the 1/f noise current caused by dislocations dominated in the high-EPD range. In order to obtain a thermal image of a room-temperature object, the 1/f noise current induced by background photon flux is as high as that caused by dislocations of more than 10^7 cm^{-2} . Therefore, the 1/f noise current induced by the photocurrent is dominant in photodiodes fabricated with HgCdTe layers on GaAs, since the EPD is less than $2 \times 10^6 \text{ cm}^{-2}$. We expect the detectivity to be as high as with LPE-layers. We fabricated 64×64 photodiode arrays, and obtained a thermal image.

Key words: 1/f noise, HgCdTe, IR photodiodes, metalorganic vapor phase epitaxy (MOVPE)

INTRODUCTION

Growth of mercury cadmium telluride (HgCdTe) on GaAs by metalorganic vapor phase epitaxy (MOVPE) growth is one of the most promising methods for fabricating large-scale infrared focal plane arrays (IRFPAs). MOVPE is suitable for growing large wafers with uniform composition and thicknesses^{1,2} and GaAs substrates are available in 3 inch sizes or larger. The most serious problem with growing on GaAs is the dislocations caused by lattice mismatch between GaAs and CdTe (14.6%). We reduced the dislocation densities of HgCdTe layers to less than $2 \times 10^6 \text{ cm}^{-2}$ by optimizing the thickness of the CdTe buffer layers.³ This value is the lowest ever reported for as-grown surfaces, but is still one order of magnitude higher than that of LPE-HgCdTe layers on lattice matched CdZnTe substrates.

Dislocations have been known to increase dark current, the 1/f noise at zero field of view FOV, and the

photo-induced 1/f noise in photodiodes.^{4,5} The dependence of R_0A and 1/f noise at zero-FOV has been reported,⁴ but that of photo-induced 1/f noise has not, yet. Photo-induced 1/f noise is assumed to lower the S/N ratio of photodiodes. We must know the dependence of photo-induced 1/f noise on dislocations in order to deduce the upper limit of the dislocation density to obtain a required performance of photodiodes.

We investigated the dependence of the 1/f noise current in n-on-p photodiodes on the amount of incident photons and on the etched pit densities (EPD). Then, we discuss the effect of dislocations on the 1/f noise, and the possibility of using a HgCdTe epilayer on GaAs for LWIR photodiode arrays.

EXPERIMENTS

We grew HgCdTe by the direct alloy growth (DAG) using MOVPE. The details of the growth have been previously reported.¹⁻³ The substrates were GaAs (100), offset by 2° toward (110), and HgCdTe (100) epilayers were grown using 10 to 20 nm ZnTe layers.

(Received October 4, 1994; revised January 20, 1995)

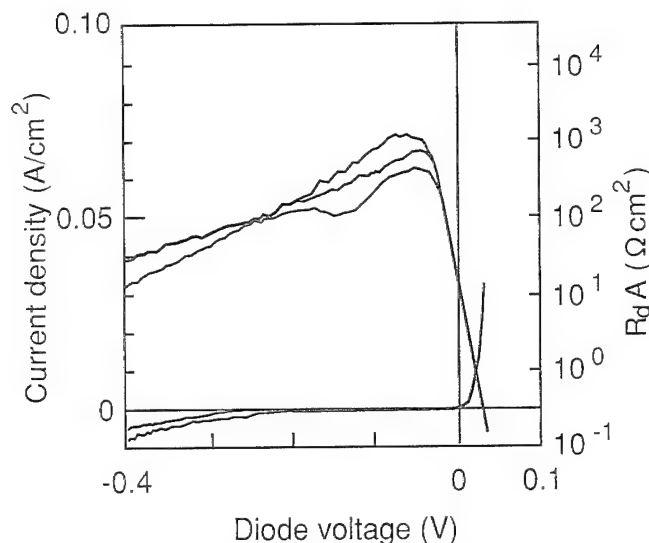


Fig. 1. Current-voltage characteristics of the photodiodes fabricated with HgCdTe grown on GaAs by MOVPE. The dark current is as low as that with LPE-grown HgCdTe on a lattice-matched CdZnTe substrate.

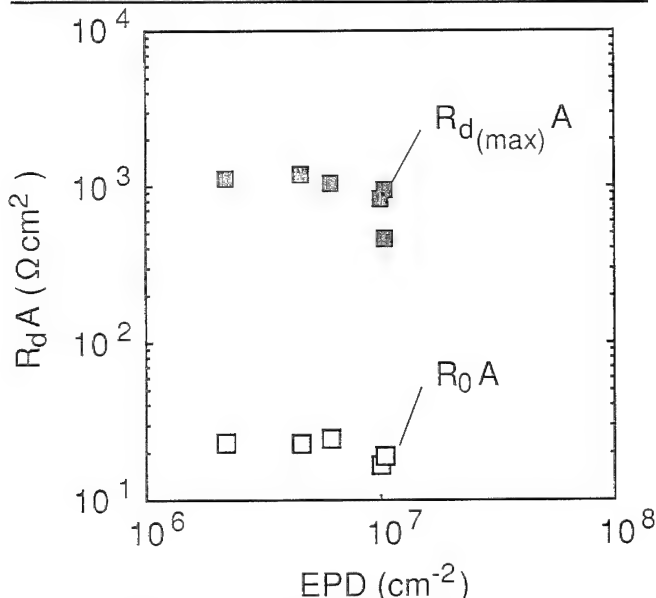


Fig. 2. The dependence of dynamic resistance area product at zero bias and the maximum value on EPD.

The thickness of CdTe buffer layers was 8 μm , and that of HgCdTe layers was 15 μm . The EPD value was 1 to $2 \times 10^6 \text{ cm}^{-2}$,³ and the residual donor concentration was 4 to $5 \times 10^{14} \text{ cm}^{-3}$.⁶

We fabricated 64×64 n-on-p photodiode arrays by boron ion implantation into Hg-vacancy doped HgCdTe layers. We annealed for Hg-vacancy doping after growth, in order to adjust the hole concentration to 1 to $2 \times 10^{16} \text{ cm}^{-3}$. We used ZnS as an insulating layer, and indium as an electrode. The junction area was $1.0 \times 10^{-5} \text{ cm}^2$. The center-to-center spacing of the individual elements was 50 μm .

We measured noise at a detector temperature of 77K, varying the illumination. Illumination was provided by an object at room temperature and varied by changing the slit width of the cold shield. The voltage

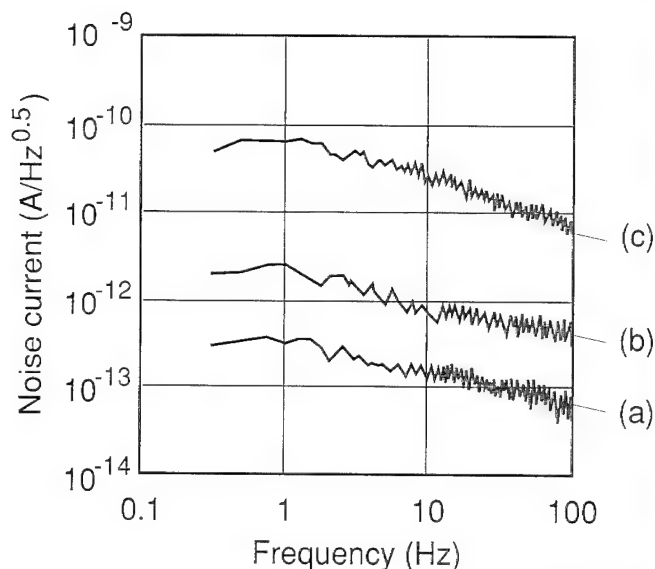


Fig. 3. Noise spectra of the photodiode fabricated with HgCdTe/GaAs. (a) zero FOV, (b) incident photon flux is 4.9×10^{16} photons/cm²s, (c) 4.9×10^{17} photons/cm²s. The $1/f$ noise current dominates and increases with photocurrent.

applied to the photodiodes was -100 mV . This is used as an operating condition in those coupled with Si-CCD.

After measuring noise, we evaluated the EPD for each diode using almost the same technique as Johnson.⁴ The EPD was determined by dividing the number of etched pits in the boron-implanted region by the junction area.

RESULTS AND DISCUSSION

Photodiodes with a low dark current were fabricated with HgCdTe layers grown on GaAs by MOVPE. Figure 1 shows the current-voltage characteristics at 77K in the photodiodes with a cutoff wavelength of 9.7 μm . The dynamic resistance junction area ($R_d A$) was $20 \Omega \cdot \text{cm}^2$ at zero bias and increased exponentially with reverse voltage. The ideality factor was $n = 1.2$, suggesting that the dark current is limited by the diffusion current near zero bias. $R_d A$ reached $10^3 \Omega \cdot \text{cm}^2$ at $V_d = -70 \text{ mV}$. $R_d A$ at zero bias ($R_0 A$) and the maximum value of $R_d A$ ($R_{d(\text{max})} A$) were comparable to those for devices fabricated with LPE-layers or bulk crystal.

Figure 2 shows the dependence of $R_0 A$ and $R_{d(\text{max})} A$ on the EPD between 10^6 and 10^7 cm^{-2} . In this range, the variation of $R_0 A$ and $R_{d(\text{max})} A$ is not seen. This shows that the diffusion current and the band-to-band tunneling current, which is not related to dislocations, is dominant in the dark current.

Figure 3 shows noise spectra of long wavelength infrared (LWIR) photodiodes in a frequency range of 0.25–100 Hz. The diode voltage was -100 mV . The noise current spectral density is proportional to the root of the inverse of the frequency. $1/f$ noise current is dominant in this range. At higher frequencies, the noise current remained almost constant with frequency, and the shot noise was dominant.

The $1/f$ noise current increased with the amount of

illuminated photons, as shown in Fig. 3. Figure 4 shows the dependence of the noise current density at 1 Hz on the photocurrent. The 1/f noise current is not always proportional to the photocurrent. For photocurrents of more than 10^{-6} A, the values of 1/f noise currents in each diode were almost the same. But the noise values at zero FOV were scattered between 10^{-13} and 10^{-11} A. This suggests that the photocurrent causes the 1/f noise and that there are other causes of 1/f noise. Williams reported that the 1/f noise current is proportional to the photocurrent in some diodes, assumed this to be true for all diodes, and deduced several conclusions.⁵ This assumption was not valid

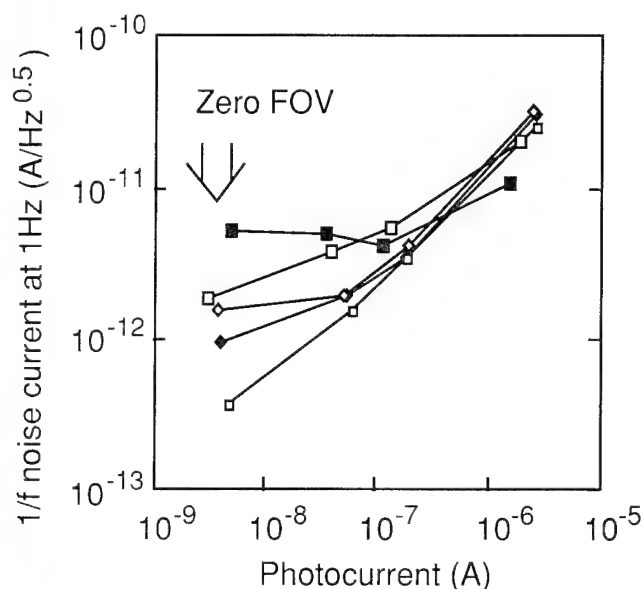


Fig. 4. The relation between 1/f noise current at 1 Hz and photocurrent. 1/f noise current increases with photocurrent, but 1/f noise current does not increase in low photocurrent range in some photodiodes.

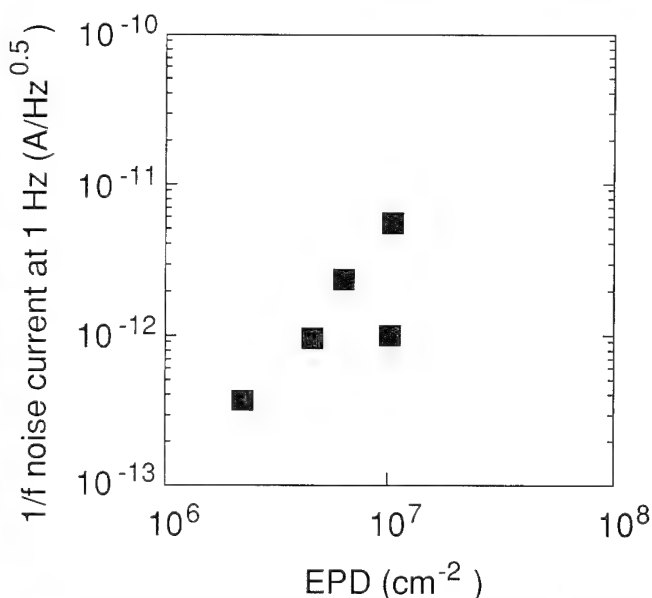


Fig. 5. The dependence of 1/f noise current at 1 Hz on the EPD. Noise currents were measured at zero FOV. 1/f noise current increased with EPD.

in our case.

We investigated the dependence of the 1/f noise current at zero FOV on the EPD (Fig. 5). It increased with the EPD of each diode. As shown in Fig. 6, the total diode current is almost constant with the EPD. As shown in Fig. 7, we defined the leakage current (I_{leak}) as

$$I_{\text{leak}} = I_{\text{total}} - I_{\text{diffusion}}$$

where I_{total} is the total diode current and $I_{\text{diffusion}}$ is the diffusion current. $I_{\text{diffusion}}$ is given by

$$I_{\text{diffusion}} = \frac{kT}{eR_0},$$

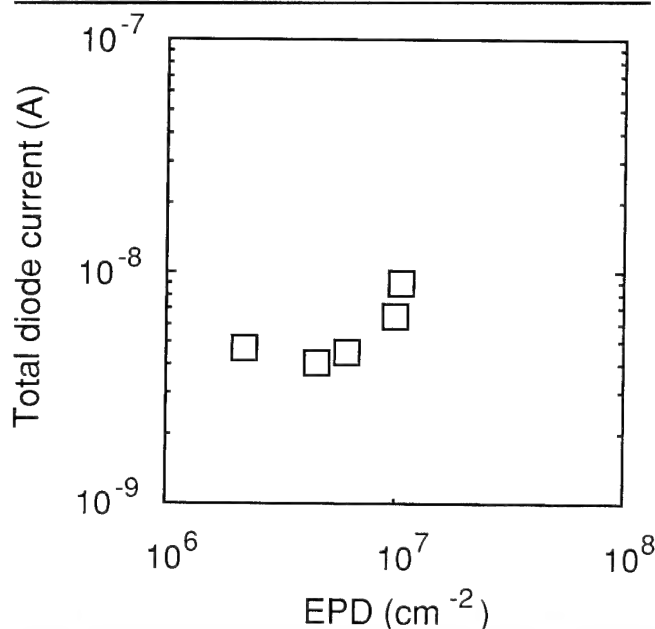


Fig. 6. The dependence of the total diode current on the EPD. The total diode current is almost constant with EPD.

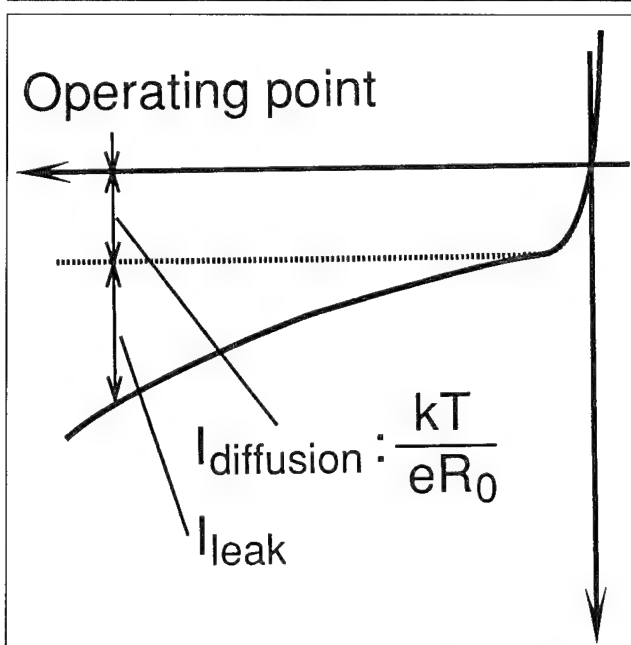


Fig. 7. The schematics of the definition of I_{leak} .

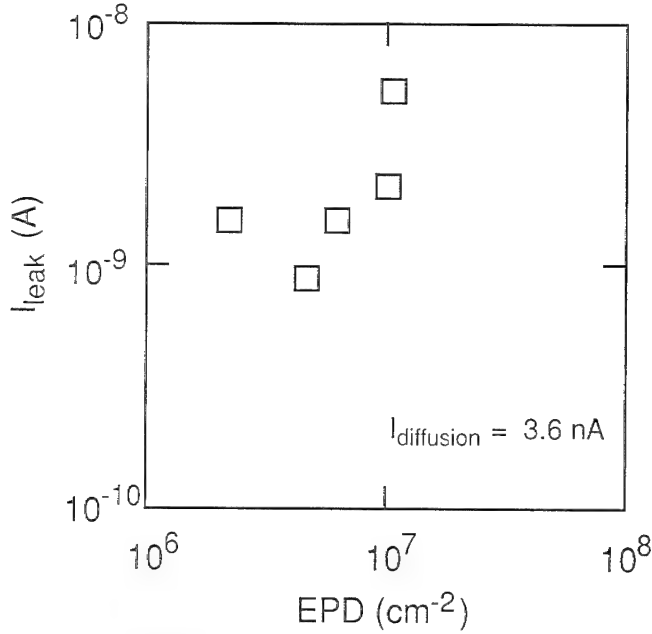


Fig. 8. The dependence of the leak current on EPD. The leak current increased with EPD.

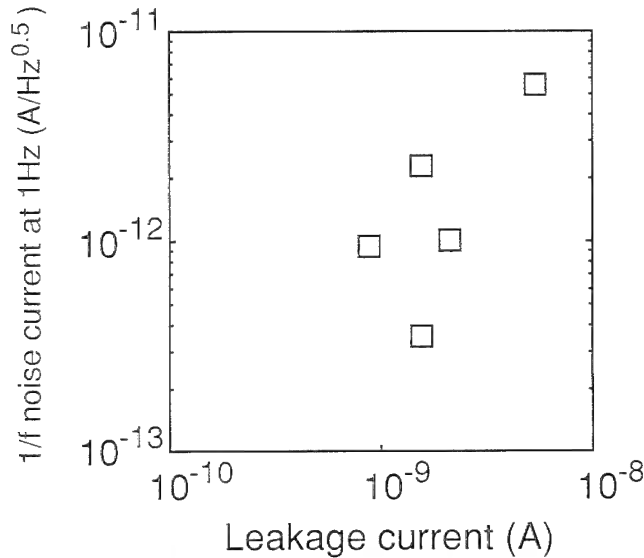


Fig. 9. The relation between 1/f noise current and the leak current. This suggests that the leak current caused by dislocations generates 1/f noise.

where T is operating temperature and R_0 is the dynamic resistance at zero bias.

Figure 8 shows that the leakage current increased with the EPD. It is assumed that the leakage current was generated at dislocations. The 1/f noise current at zero FOV is proportional to the leakage current, as shown in Fig. 9. Based on these results, we speculate that the leakage current generated at dislocations causes the 1/f noise current. Our speculation is consistent with reported results. Johnson reported that the 1/f noise current depends on the total diode current.⁴ The diffusion current in their heterodiodes was less than that in ours, and therefore the total diode current was assumed to be limited by the leakage current

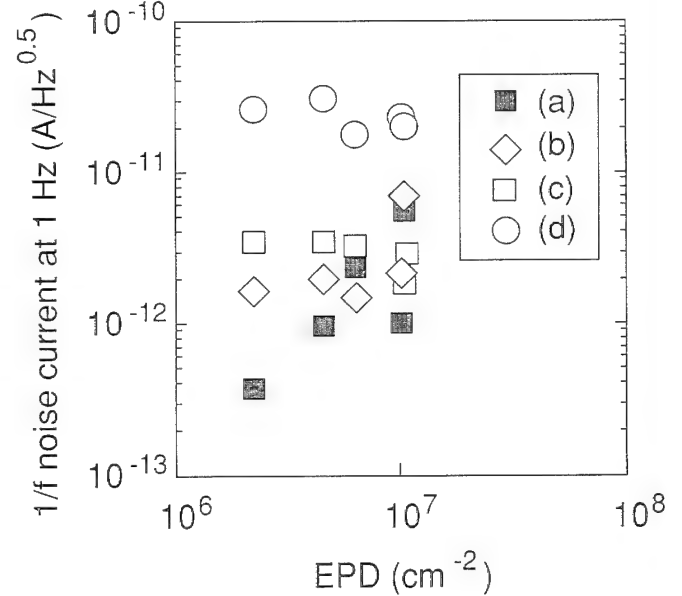


Fig. 10. The dependence of 1/f noise current at 1 Hz on EPD. (a) zero FOV, (b) incident photon flux is 2.9×10^{16} photons/cm²s, (c) 4.9×10^{16} photons/cm²s, (d) 4.9×10^{17} photons/cm²s. At zero FOV, 1/f noise current increased with EPD. But in low-EPD range, 1/f noise current increased with photocurrent and is independent of EPD. Therefore, two mechanism of 1/f noise exists.

in the EPD range of 10^6 to 10^8 cm⁻².

Figure 10 shows the dependence of the photo-induced 1/f noise current on the EPD. Photo-induced 1/f noise is almost constant with the EPD. This shows that the mechanism of photo-induced 1/f noise generation is independent of dislocations. In the thermal imaging of a room temperature object at $f/1.5$ FOV, the incident photon flux is more than 4.9×10^{16} /cm²s, and the photo-induced 1/f noise is dominant, since the EPD of HgCdTe epilayers on GaAs is 1 to 2×10^6 cm⁻². In a low photon flux of less than 10^{16} /cm²s, such dislocations could be a serious problem.

The noise current density I_n of the 1/f noise is given by

$$I_n = \alpha (I_d)(f)^{-1/2},$$

where I_d is the diode current, f is the frequency, and α is the coefficient deduced from the measurement.⁷ In our cases, α is about 10^{-5} when I_d is the photocurrent. It is about 10^{-3} when I_d is the leakage current generated at dislocations. This difference in α value indicates that two different mechanisms of 1/f noise generation exists.

We estimated the mean-square noise current (\bar{I}_n^2) using,

$$\bar{I}_n^2 = \int I_n^2 df,$$

where I_n is the noise current density. We summed the noise current density from 0.5 to 10^5 Hz. The detectivity (D^*) is expressed by

$$D^* = \frac{\lambda}{hc} \eta e \frac{\sqrt{A_c} \sqrt{\Delta f}}{\sqrt{\bar{I}_n^2}},$$

where λ is wavelength, η is the quantum efficiency, A_c

Table I. Detectivity Estimation

	I_{photo} (A)	EPD (cm ⁻²)	$I_{1/f}$ at 1 Hz (A/√Hz)	$\bar{I}_{1/f}^2$ (A ²)	\bar{I}_{shot}^2 (A ²)	D^* (cm√Hz/W)
f/1.5, 300K, η = 50%	1 × 10 ⁻⁷	2 × 10 ⁶	3 × 10 ⁻¹²	1 × 10 ⁻²²	3 × 10 ⁻²¹	1 × 10 ¹¹
	1 × 10 ⁻⁷	5 × 10 ⁶	3 × 10 ⁻¹²	1 × 10 ⁻²²	3 × 10 ⁻²¹	1 × 10 ¹¹
	1 × 10 ⁻⁷	1 × 10 ⁷	5 × 10 ⁻¹²	2 × 10 ⁻²²	3 × 10 ⁻²¹	1 × 10 ¹¹
	1 × 10 ⁻⁷	2 × 10 ⁷	2 × 10 ⁻¹¹	5 × 10 ⁻²¹	3 × 10 ⁻²¹	7 × 10 ¹⁰
f/1.5, 230K, η = 50%	1 × 10 ⁻⁶	2 × 10 ⁶	1 × 10 ⁻¹²	1 × 10 ⁻²³	6 × 10 ⁻²²	3 × 10 ¹¹
	1 × 10 ⁻⁶	5 × 10 ⁶	2 × 10 ⁻¹²	4 × 10 ⁻²³	6 × 10 ⁻²²	3 × 10 ¹¹
	1 × 10 ⁻⁶	1 × 10 ⁷	5 × 10 ⁻¹²	3 × 10 ⁻²²	8 × 10 ⁻²²	2 × 10 ¹¹
	1 × 10 ⁻⁶	2 × 10 ⁷	5 × 10 ⁻¹¹	5 × 10 ⁻²¹	1 × 10 ⁻²¹	8 × 10 ¹⁰

is the effective area of detection, and Δf is the width of frequency.⁷

The estimated results are summarized in Table I. When obtaining a thermal image of a 300K object in the field of view of f/1.5, the 1/f noise current induced by the photocurrent is larger than that caused by dislocations. Therefore, dislocations of less than 1 × 10⁷ cm⁻² do not degrade the photodiode performance. Shot noise dominates in the photodiode fabricated with HgCdTe layers on GaAs, and a D* value of 1 × 10¹¹ cm√Hz/W is anticipated, since the EPD is less than 2 × 10⁶ cm⁻². For a 230K object, the photocurrent is ten times less, and the 1/f noise current caused by dislocations is larger than that caused by the photocurrent in the EPD-range of more than 2 × 10⁶ cm⁻². We need to reduce the EPD to less than 2 × 10⁶ cm⁻² in order not to degrade the performance.

We fabricated 64 × 64 photodiode arrays. The thermal image of a face is shown in Fig. 11. The squared noise current in photodiodes was 4.6 × 10⁻²¹ A². This is almost the same as the calculated shot noise. D* was 9.1 × 10¹⁰ cm√Hz/W and is comparable to LPE-grown layers. The rate of defective pixels was 2%. A few clusters of several defective pixels were observed. We confirmed that these clusters were caused by macro defects which are the origin of hillock. We assumed that these can be eliminated, since the HgCdTe epilayer on GaAs (100) with regions larger than 1 cm⁻² free of hillocks was reported.⁸

SUMMARY

We studied the effect of dislocations on the 1/f noise current in long wavelength infrared photodiodes. The photodiodes were fabricated using HgCdTe(100) layers grown on GaAs(100) by MOVPE.

We observed two types of 1/f noise. One was caused by the leakage current generated at dislocations. The other was induced by photocurrent and was independent of dislocations. When carrying out thermal imaging of a room temperature object, the photo-induced 1/f noise current was dominant in the EPD range of 1–2 × 10⁶ cm⁻². Therefore, the S/N ratio of the

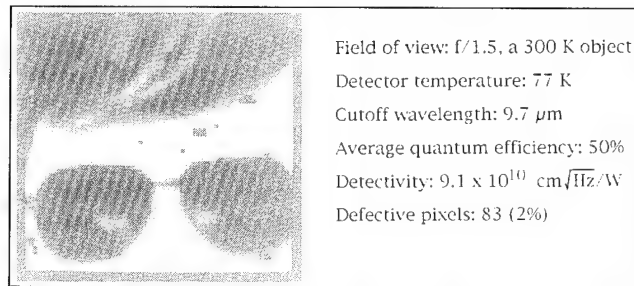


Fig. 11. Thermal image of a human face composed by our 64 × 64 photodiode array fabricated with HgCdTe/GaAs layer.

photodiode fabricated with HgCdTe layers on GaAs was expected to be as high as with LPE-grown layers on lattice matched CdZnTe. We fabricated 64 × 64 photodiode arrays and obtained a thermal image. The detectivity was 9.1 × 10¹⁰ cm√Hz/W. These results show that high-performance photodiodes can be fabricated using MOVPE-grown HgCdTe layers on GaAs.

ACKNOWLEDGMENTS

We thank Dr. Y. Ishizaki, Dr. H. Takigawa and Dr. Yamakoshi for useful discussions, also Mr. Awamoto and Mr. Watanabe for evaluating the photodiode arrays.

REFERENCES

1. S. Murakami, Y. Sakachi, H. Nishino, T. Saito, K. Shinohara and H. Takigawa, *J. Cryst. Growth* 117, 33 (1992).
2. S. Murakami, Y. Sakachi, H. Nishino, T. Saito, K. Shinohara and H. Takigawa, *J. Vac. Sci. Technol. B* 10, 1380 (1992).
3. H. Nishino, S. Murakami, T. Saito and H. Takigawa, *J. Electron. Mater.* 24, 533 (1995).
4. S.M. Johnson, D.R. Rhiger, J.P. Rosbeck, J.M. Peterson, S.M. Taylor and M.E. Boyd, *J. Vac. Sci. Technol. B* 10, 1499 (1992).
5. G.M. Williams, R.E. DeWames, J. Bajaj and E.R. Blaziejewski, *J. Electron. Mater.* 22, 931 (1993).
6. H. Nishino, S. Murakami, H. Ebe and Y. Nishijima, *J. Cryst. Growth* 146, 619 (1995).
7. M.B. Reine, A.K. Sood and T.J. Treadwell, *Semiconductors and Semimetals*, Vol. 18, ed. R.K. Willardson and A.C. Beer (New York: Academic Press, 1981), p. 297.
8. S.J.C. Irvine, J.S. Gough, J. Giess, M.J. Gibbs, A. Royle, C.A. Taylor, G.T. Brown, A.M. Keir and J.B. Mullin, *J. Vac. Sci. Technol. A* 7, 285 (1989).

The Role of Surface Adsorbates in the Metalorganic Vapor Phase Epitaxial Growth of (Hg,Cd)Te onto (100) GaAs Substrates

J. GIESS, J.E. HAILS, A. GRAHAM, G. BLACKMORE, M.R. HOULTON,
J. NEWHEY, M.L. YOUNG, and M.G. ASTLES

Defence Research Agency, St. Andrews Road, Malvern, Worcestershire,
WR14 3PS, UK

W. BELL and D.J. COLE-HAMILTON

School of Chemistry, University of St. Andrews, St. Andrews, Fife,
KY16 9ST, UK

It has been established that a compound present as an impurity in the propan-2-ol used in the preparation of GaAs (100) substrates for the metalorganic vapor phase epitaxy growth of (Hg,Cd)Te has a marked effect on the crystalline perfection and surface morphology of the resulting layers. In particular, the presence of this species, which contains Na, ensures that (i) the epitaxial overgrowth is of (100) orientation without the need for ZnTe nucleation layers, and (ii) the density of pyramidal hillocks on the surface can be reproducibly $< 10 \text{ cm}^{-2}$.

Key words: HgCdTe, metalorganic vapor phase epitaxy (MOVPE), surface adsorption

INTRODUCTION

Historically, one of the major problems with epitaxial (Hg,Cd)Te (MCT) grown by metalorganic vapor phase epitaxy (MOVPE) has been the presence of surface morphological defects either faceted (hillocks), polycrystalline lumps or a combination of the two, often with a density of $> 10^4 \text{ cm}^{-2}$. Photographs of these defects can be seen in, for example, Refs. 1 to 7. Although the origin of hillocks has not yet been uniquely identified, considerable work has been done to elucidate their nature. Indeed, there are probably several possible causes of the surface morphological defects and more than one type may exist on a given layer. In extreme growth conditions, there may be a large density of polycrystalline lumps and faceted hillocks with a range of different sizes. These features are due to dust formation during growth of the epi-

taxial layer and may be virtually eliminated by careful control of the growth conditions. The more persistent type of morphological defect shows a characteristic of having identical sized faceted features for a given epitaxial layer. These faceted features have all originated at the substrate/layer interface, their lateral dimensions are directly proportional to the layer thickness and they are invariably crystallographically aligned with the substrate. The faceted hillock is usually submicron in height, but it is often decorated with a polycrystalline lump up to $50 \mu\text{m}$ high which can cause severe problems in device fabrication. Layers containing a variable density of such hillocks have been assessed by double crystal x-ray diffractometry.^{7,8} The full width half maximum (FWHM) of double crystal rocking curves was shown to increase significantly in areas of poor surface morphology. Further assessment⁹ showed that the anisotropy in FWHM measurements, when the sample is rotated 90° about its surface normal, is most pronounced in and close to

(Received October 4, 1994; revised December 6, 1994)

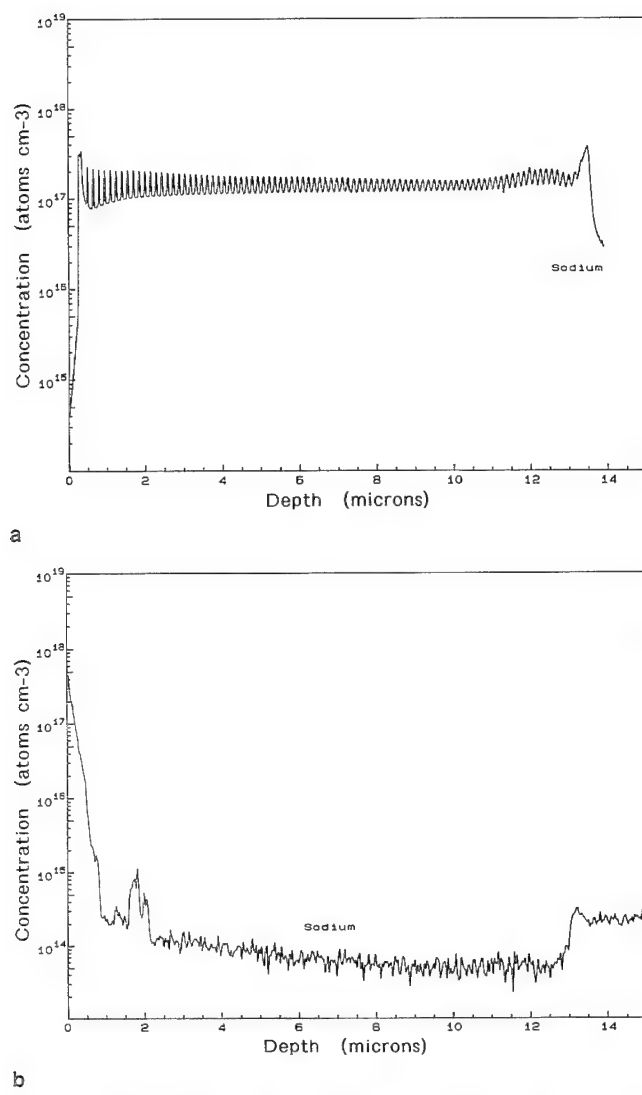


Fig. 1. Secondary ion mass spectroscopy depth profiles for Na obtained from layers of (Hg,Cd)Te grown by MOVPE onto (100) GaAs at 370°C. Final substrate rinses were (a) Na-contaminated propanol from supplier 2, and (b) Na-free propanol from supplier 1.

regions of high hillock density. Texture camera analysis of these regions has revealed the presence of twinning. Both the $\langle 122 \rangle$ surface normal and $\langle 447 \rangle$ surface normal (twinning within the twin) were seen. The twin density was also measured to be an order of magnitude higher in the direction of high FWHM. This very poor structural quality in regions close to high hillock density can be extremely detrimental to the quality of devices fabricated.

Methods of reducing the numbers of surface features on the (100) orientation have been proposed, such as the use of buffer layers consisting of combinations of discrete HgTe and CdTe layers or graded from ZnTe to CdTe.¹⁰ The lowest achievable hillock densities quoted in the literature are of the order of 10 cm^{-2} , 1 cm^2 free of hillocks was also reported but this was not reproducible.⁷ In addition to surface quality, the morphology between the hillocks has often been found to be variable and nonreproducible and we have found that this variation in background morphology also

reflects variation in crystallinity and hence crystal quality. This paper details a way, discovered in our laboratories, of overcoming many of these problems for growth onto (100) GaAs substrates through the control of trace quantities of sodium salts in the final stages of substrate preparation.

EXPERIMENTAL

GaAs (100) substrates were prepared by degreasing in trichloroethylene, etching in 5:1:1 $\text{H}_2\text{SO}_4:\text{H}_2\text{O}:\text{H}_2\text{O}_2$ for 5 min, washing in water and boiling in propan-2-ol before drying and loading into the MOVPE growth reactor. The substrates were heated to 385°C and baked for 20 min before cooling to 320°C. Di-*iso*-propyl telluride (Pr_2Te) was flushed into the reactor to maintain the (100) orientation¹¹ and growth was initiated by switching in di-methyl cadmium (Me_2Cd). After a fraction of a micron of CdTe had been deposited, the temperature was raised to 370°C and the rest of the $6 \mu\text{m}$ CdTe buffer grown. $12 \mu\text{m}$ of (Hg,Cd)Te were grown onto this at 370°C using the interdiffused multilayer process (IMP).⁶ All layers were grown on a Thomas Swan MOVPE system with hydrogen carrier gas being passed through a palladium diffuser before use. The metalorganics were purchased from Epichem Ltd. and the Hg was supplied by Attenborough and Peacock (Birmingham) Ltd.

Gas chromatography-mass spectrometry (GC-MS) analysis of propan-2-ol samples was carried out on a Hewlett Packard 5890 Series II gas chromatograph fitted with a 5970 mass selective detector and a 7673 autosampler. Secondary ion mass spectroscopy (SIMS) analyses were performed on a Cameca IMS 3f machine using an O_2 primary beam at 8.0 KeV energy and 1 μA current.

RESULTS AND DISCUSSION

It came to our attention that using the procedures outlined above, it was possible to grow MCT layers with dramatically different surface morphologies while using apparently identical growth conditions. By a careful process of elimination, this difference was eventually tracked down to the chemical cleaning of the GaAs and to the source of the propan-2-ol (propanol) used for the final substrate rinse. Propanol from one source, supplier 1, gave rise to layers which were mainly matt with pyramid densities $>10^5 \text{ cm}^{-2}$. Using propanol from supplier 2 always resulted in very shiny layers with a uniform background and hillock densities $\approx 10 \text{ cm}^{-2}$ and frequently approaching zero. As many different batches of propanol as possible from the two suppliers were examined by GC-MS to determine if there were any volatile impurities consistently present. That from supplier 1, which had given the matt layers, was found to contain none except for traces of other organic solvents such as hexane in some batches. The propanol which gave the good surfaces did contain another species which was eventually identified as the $(\text{C}_3\text{H}_7\text{O})_3\text{B}$ compound tri-*iso*-propylborate $[(\text{Pr}^i\text{O})_3\text{B}]$ by comparison of the chro-

matographic retention time and mass spectrum with those from an authentic sample. The GC-MS was calibrated for various levels of $(\text{Pr}^{\text{i}}\text{O})_3\text{B}$ in propanol and using toluene as an internal standard for the analysis, concentrations of $(\text{Pr}^{\text{i}}\text{O})_3\text{B}$ were determined for the different batches of propanol and found to vary between 0.1 and 1.5 ml/litre. According to the manufacturers, the final stage in the preparation of the propanol from supplier 2 was the distillation from NaBH_4 to reduce residual traces of acetone to propan-2-ol. It would appear that this process also contaminates the propanol with $(\text{Pr}^{\text{i}}\text{O})_3\text{B}$.

To determine if the tri-*iso*-propylborate was the reason for the good surfaces being produced, it was added to the propanol from supplier 1 at the concentration of 1 ml/litre. Layers grown on GaAs substrates prepared with this contaminated propanol were indistinguishable from those prepared from the original uncontaminated propanol, i.e. they were matt, while the control samples in the same growth run, prepared using propanol from supplier 2, were of good morphology with a low hillock density. It was concluded, therefore, that $(\text{Pr}^{\text{i}}\text{O})_3\text{B}$ was not the active ingredient.

Secondary ion mass spectroscopy analysis had revealed the presence of sodium in MCT layers grown on substrates prepared from propanol obtained from supplier 2 whereas those prepared with propanol from supplier 1 did not (Figs. 1a and 1b). Over a series of layers, the following was established as a pattern. The best morphology layers were grown when propanol from supplier 2 was used. This propanol contained $(\text{Pr}^{\text{i}}\text{O})_3\text{B}$ and the resulting layers contained Na at the 10^{17} atoms cm^{-3} level. Using propanol from supplier 1 in the substrate preparation resulted in significantly poorer morphology but the layers did not contain Na (5×10^{13} atoms cm^{-3}) and the propanol did not contain

$(\text{Pr}^{\text{i}}\text{O})_3\text{B}$. It appeared that the presence of sodium and $(\text{Pr}^{\text{i}}\text{O})_3\text{B}$ were probably connected and if $(\text{Pr}^{\text{i}}\text{O})_3\text{B}$ was not the source of the improvement, then the presence of Na could be governing the crystallinity.

To test this hypothesis, two experiments were undertaken. Firstly, propanol from supplier 1 was redistilled from NaBH_4 to replicate the final stage in the manufacture of supplier 2. Layers grown on substrates prepared using the resulting distillate contained Na (10^{17} atoms cm^{-3}) and had significantly better surfaces than those prepared with propanol as received from supplier 1 and were comparable to those using propanol from supplier 2. Secondly, the propanol from supplier 2 was purified by distillation; GC-MS analysis of the distillate showed that it contained no volatile impurities. Using this distillate in the GaAs substrate preparation had the effect of reducing the Na level in the as-grown MCT from 10^{17} to 10^{13} atoms cm^{-3} . The layer surfaces were also considerably worse with hillock densities of 3×10^3 cm^{-2} . This confirmed that the presence of Na in the final stages of substrate preparation had a beneficial effect on the morphology and crystallinity of the resulting MCT layer.

At this stage, it seemed likely that the beneficial species present in the propanol were either sodium *iso*-propoxide (NaOPr^{i}) or $\text{Na}[\text{B}(\text{Pr}^{\text{i}}\text{O})_4]$ which was decomposing to NaOPr^{i} and $(\text{Pr}^{\text{i}}\text{O})_3\text{B}$ on standing or on heating to above the boiling point of propanol (82°C) e.g. in the GC-MS injection port. All of these compounds are volatile enough to distill over in trace amounts.

Alternative Additives

Water, methanol and ethanol have all been tried as a final substrate rinse instead of propan-2-ol and in conjunction with the growth procedure outlined in the

Table I. Summary of the Alternative Final GaAs Substrate Rinses

Layer	Additive Species	Concentration g/l	Solvent	Surface Quality	Hillock Density (cm^{-2})
F323	NaOH	0.16	cold water	part shiny/part matt	>2000
F340	NaOH	0.24	cold water	matt	
F341	NaOH	0.12	cold water	matt	
F345	NaOH	0.16	methanol	part patchy/part matt	>300
F346	NaOH	0.16	hot water	shiny with matt lines/ drying stains	3×10^4
F386	NaOH new bottle	0.16	propanol	very shiny	10
F422	NaOH	0.16	propanol-same solution as F386	matt	10^5
F427	NaOH	0.16	propanol	matt	$>2 \times 10^4$
F428	NaOH	0.16	propanol	matt	5×10^4
	KBH_4	distilled	propanol	shiny	
F339	KOH	0.23	cold water	very shiny	10
F343	KOH	0.11	cold water	very patchy	$>10^4$
F347	KOH	0.22	hot water	shiny with fern-like drying stains	50
F349	KCl	0.30	hot water	part shiny/part matt	9×10^3
F338	$\text{Ca}(\text{OH})_2$	0.29	cold water	matt	polycrystalline
F348	$\text{Ba}(\text{OH})_2$	0.68	hot water	very matt	polycrystalline
F422	$(\text{NH}_4)_2\text{SO}_4$	0.26	cold water	matt	8×10^4

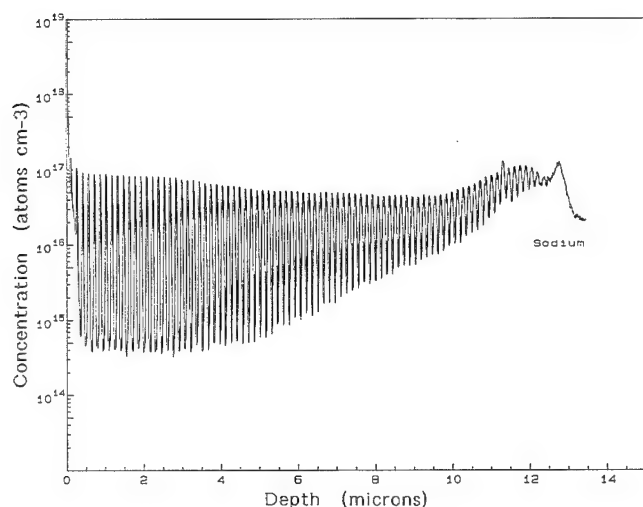


Fig. 2. Secondary ion mass spectroscopy depth profile for Na obtained after layer in Fig. 1a was given a Hg-rich isothermal anneal at 200°C for 67 h.

experimental section all consistently produced surfaces with considerably higher hillock densities, a poorer surface morphology and which were generally less reproducible than those produced from substrates prepared using the propanol from supplier 2. Secondary ion mass spectroscopy analysis, however, showed that the layers did not contain high Na concentrations (5×10^{15} atoms cm^{-3}).

To confirm that Na was the active species, we tried adding various Na containing compounds to the final solvent rinse and then growing an MCT layer on top in the usual manner. The results are summarized in Table I. A control specimen which had been treated with either the propanol from supplier 2 or that from supplier 1 which had been distilled from NaBH_4 was included in each growth run to confirm that the growth had been successfully carried out.

It was assumed that for every molecule of $(\text{Pr}^i\text{O})_3\text{B}$ detected in the propanol, there would be an equivalent Na atom. Hence NaOH was dissolved in water to give a similar concentration of Na to that assumed to be in the contaminated propanol. This is considerably higher than the level of 0.2 ppm quoted by supplier 2 to be present in their propanol. The use of the cold solution as the final rinse for GaAs combined with the growth procedure outlined in the experimental gave layers of MCT with some matt areas and some shiny areas. These were not comparable with the contaminated propanol from supplier 2 but were an improvement on the pure water final rinse. Higher and lower concentrations of NaOH were not as successful (layers F340 and F341). The use of hot NaOH solution in water produced an improved shiny surface compared with the cold solution but drying stains became a problem. NaOH dissolved in water/methanol gave a layer (F345) with significant shiny areas but some matt regions. Hillock densities of $3 \times 10^3 \text{ cm}^{-2}$ were achieved. At its best fresh NaOH pellets from a previously unopened bottle dissolved readily in propanol and gave an excellent layer (F386) with a

hillock density of $\approx 10 \text{ cm}^{-2}$ and a sodium level of 5×10^{17} . It is expected that both NaOH and NaOPr^i species are present in a propanol solution of NaOH. In conclusion, although the addition of NaOH to the final solvent rinse could give a significant improvement, the treatment was not found to be reproducible and unless the NaOH was really fresh and the solution freshly prepared the layers grown on the resulting substrates were not acceptable.

To establish if this phenomenon was a unique property of Na, other elements were tried. As a first step, propanol from supplier 1 was distilled from KBH_4 and the distillate used for the final rinse of the GaAs substrate prior to the MCT growth. The resulting surfaces were shiny but with a hillock density of 10^4 cm^{-2} . In short, they were not as good as from propanol distilled from NaBH_4 but a considerable improvement on propanol as received from supplier 1. Secondary ion mass spectroscopy showed low Na (2×10^{15} atoms cm^{-3}) and a raised level of 10^{16} K atoms cm^{-3} . The distillate from the KBH_4 /propanol was used again after storage for two months after the original experiments and produced layers with poor surfaces. It was concluded that the species in the propanol were not as stable as the Na equivalent. The potassium concentration is also likely to be lower in the distillate than that of sodium from the NaBH_4 . The K containing species will have a higher molecular weight and therefore a lower vapor pressure and hence will distill over in lower concentrations than the Na analogues making this a less efficient way of introducing the K impurity.

KOH (0.227g/l) dissolved in cold water used as a final substrate rinse produced a layer (F339) with a mirror-like surface and with a hillock density of 10 cm^{-2} . The experiment was repeated using hot (92°C) KOH solution at the same concentration. The resulting layer with 50 hillocks cm^{-2} was almost as good as that from cold KOH except that drying stains became a problem during the blow dry.

The experiment with KOH in cold water was repeated with a KOH concentration of 0.11g/l i.e. half the previous level. While the layer surface (F343) was still a significant improvement over using clean water as the final rinse, the layer was not as good as when using the higher concentration. The layer was shiny but had a higher hillock density of $3 \times 10^4 \text{ cm}^{-2}$.

From the above experiments, it was concluded that Group I elements were having a beneficial effect on the surface of the final layer. As a check that it is the K or Na that is effective and not a basic solution, a final rinse of KCl in hot (86°C) water was employed (F349). The concentration of KCl was 0.30g/l. The resulting MCT layer was largely shiny with a few matt areas but a relatively high hillock density of $9 \times 10^3 \text{ cm}^{-2}$. This, however, is still an improvement on the use of water alone.

Because the presence of Group I elements could cause problems with the electrical properties of the MCT layers, it was decided to try Group II compounds to see if their presence in the final solvent rinse would

be similarly beneficial and hence eliminate any deleterious effect on the electrical properties. $\text{Ca}(\text{OH})_2$ was insufficiently soluble in water to give a Ca concentration equivalent to that of Na previously used. Nonetheless, the resulting solution was used as the final rinse. It gave a matt layer. $\text{Mg}(\text{OH})_2$ was dismissed on the grounds of insolubility. $\text{Ba}(\text{OH})_2$ dissolved readily in hot water (0.68g/l). The resulting solution was used as the final rinse and produced one of the mattest MCT layers (F348) ever seen in our laboratories!

As an alternative to Group I elements, amine/ NH_4^+ compounds were tried. $(\text{NH}_4)_2\text{SO}_4$ in water, NH_3 in water and propanol distilled from $\text{NMe}_3\cdot\text{BH}_3$ produced variable results, none of which were as good as propanol distilled from NaBH_4 .

Sodium Incorporation into (Hg,Cd)Te Layers

As has already been indicated, SIMS analysis has shown that when a Na compound is present in the final substrate rinse, Na is incorporated in the subsequently grown MCT layer. A typical Na concentration within the MCT layer is measured to be approximately 10^{17} atoms cm^{-3} with lower Na concentrations incorporated in the CdTe buffer and cap (Fig. 1). It is believed that the Na diffuses during layer growth from the GaAs substrate/buffer interface into the MCT. Approximately one monolayer of Na would need to be adsorbed onto the GaAs surface from the propanol to produce a concentration of 10^{17} atoms cm^{-3} throughout the 10 μm MCT layer after diffusion. Detailed SIMS analysis has shown that the Na concentration oscillates within the MCT layer. The periodicity of this oscillation is identical to the IMP cycle thickness and has been proved not to be an artifact of the SIMS measurement technique by deliberately altering the IMP period.

A SIMS plot of a typical layer after a Hg-rich isothermal anneal to remove Hg vacancies is shown in Fig. 2. Anneal conditions were 200°C for 67 h. After this long anneal, the Na concentration is still high and still shows strong oscillations within the layer. This behavior contrasts to that of Na during the Hg-rich annealing of liquid-phase epitaxial MCT layers where the Na level drops dramatically to $< 10^{14}$ atoms cm^{-3} .¹²

This apparent dilemma can only be explained if it is assumed that during layer growth the Na diffuses rapidly from the GaAs substrate surface to be incorporated within the MCT layer. But the Na must then become pinned within the residual IMP structure; and once pinned, it is only very slowly released during subsequent annealing. This pinning produces the

apparent slow diffusion rate out of the layer. The annealed layers are typically measured to be p-type with $p_{77} \approx 10^{16} \text{ cm}^{-3}$ and this is believed to be related to the presence of the pinned Na suggesting that this species can be an active acceptor.

CONCLUSIONS

In conclusion, the presence of a Group I element on the surface of a GaAs wafer significantly improved the surface morphology of the resulting MCT layer when combined with the specific growth conditions outlined in the experimental section. The presence of a Group II element does not have this effect. In addition, the form in which the element is put onto the surface is of importance as is the manner in which it is dried otherwise the presence of a dissolved impurity can lead to drying stains in the resulting material. The most successful final substrate rinses have been the propanol/ NaBH_4 distillate and KOH in cold water. At this stage, it is premature to speculate on why the presence of a Group I element should have such a beneficial effect on the morphology of MCT layers grown onto (100) GaAs or indeed what the mechanism for this process is.

ACKNOWLEDGMENTS

Published with the permission of the Controller of Her Majesty's Stationary Office.

REFERENCES

1. L.M. Smith and J. Thompson, *Mater. Lett.* 7, 461 (1989).
2. J.E. Hails, G.J. Russell, A.W. Brinkman and J. Woods, *J. Cryst. Growth* 79, 940 (1986).
3. P. Capper, C.D. Maxey, P.A.C. Whiffin and B.C. Easton, *J. Cryst. Growth* 96, 519 (1989).
4. D.D. Edwall, J. Bajaj and E.R. Gertner, *J. Vac. Sci. Technol.* A 8, 1045 (1990).
5. J. Giess, J.S. Gough, S.J.C. Irvine, G.W. Blackmore, J.B. Mullin and A. Royle, *J. Cryst. Growth* 72, 120 (1985).
6. J. Tunnicliffe, S.J.C. Irvine, O.D. Dosser and J.B. Mullin, *J. Cryst. Growth* 68, 245 (1984).
7. S.J.C. Irvine, J.S. Gough, J. Giess, M.J. Gibbs, A. Royle, C.A. Taylor, G.T. Brown, A.M. Keir and J.B. Mullin, *J. Vac. Sci. Technol.* A 7, 285 (1989).
8. G.T. Brown, A.M. Keir, M.J. Gibbs, J. Giess, S.J.C. Irvine and M.G. Astles, *Proc. Electrochem. Soc. Symp. on Heteroepitaxial Approaches in Semiconductors*, Electrochem. Soc. Fall Mtg., Chicago, Oct. 1988.
9. G.T. Brown, A.M. Keir, J. Giess, J.S. Gough and S.J.C. Irvine, *Inst. Phys. Conf. Ser. Vol. 100*, Microsc. Semicond. Mater. 457 (1989).
10. R. Triboulet, A. Tromson-Carli, D. Lorans and T. Nguyen Duy, *J. Electron. Mater.* 22, 827 (1993).
11. R.D. Feldman, D.W. Kisker, R.F. Austin, K.S. Jeffers and P.M. Bridenbaugh, *J. Vac. Sci. Technol.* A 4(4), 2234 (1986).
12. M.G. Astles, H. Hill, G. Blackmore, S. Courtney and N. Shaw, *J. Cryst. Growth* 91, 1 (1988).

Reaction Chemistry and Resulting Surface Structure of HgCdTe Etched in CH₄/H₂ and H₂ ECR Plasmas

ROBERT C. KELLER, M. SEELMANN-EGGEBERT, and H.J. RICHTER

Fraunhofer Institut für Angewandte Festkörperphysik, 79108 Freiburg, Germany

We report on several new aspects of etching of Hg_{1-x}Cd_xTe ($x = 0.22$), HgTe, and CdTe in CH₄/H₂/Ar plasmas generated by an electron cyclotron resonance plasma source. Using a residual gas analyzer, we have identified elemental Hg, TeH₂, Te(CH₃)₂, and Cd(CH₃)₂ as the primary reaction products escaping from a HgCdTe surface during the plasma exposure. We have also demonstrated that a bias is not needed to etch HgCdTe at moderate temperatures (30–40°C), as previously suggested by other researchers. We have also developed a technique that avoids the formation of hydrocarbon polymer films on a HgCdTe sample during etching. Moreover, we have examined by x-ray photoelectron spectroscopy analysis and ellipsometry the surface condition of HgCdTe resulting from etching with this technique at zero bias. After exposure to the CH₄/H₂/Ar plasma (or to a H₂/Ar plasma only), the HgCdTe samples exhibited a depletion of the HgTe component in the near surface region (increase of the x -value). The depletion covered a range from virtually $x = 1$ after H₂/Ar (10:2 in sccm) etching to values $0.4 < x < 0.5$ after CH₄/H₂/Ar (7:7:2 in sccm) etching. Exposures to the plasmas were found to result in surface roughening of HgCdTe, however, plasmas rich in H₂ were observed to cause significantly rougher surfaces than plasmas with small H₂/CH₄ ratios. This difference in the resulting surface condition is attributed solely to chemical effects since the respective ion energies are considered to be below the damage threshold for HgCdTe in both cases. We also investigated the etching of HgTe and CdTe single crystals. The etch rate of HgTe was found to be over one order of magnitude higher than that of CdTe under similar conditions. This large difference in etch rates is assumed to be responsible for the observed preferential etching of the HgTe component indicated by the HgTe depletion of the HgCdTe surface region.

Key words: Electron cyclotron resonance (ECR) plasma, ellipsometry, HgCdTe, plasma etching, x-ray photoelectron spectroscopy (XPS)

INTRODUCTION

Mercury cadmium telluride (HgCdTe) is the standard detector material used in the fabrication of high-performance infrared focal plane arrays (IRFPAs). In the lithography of mesa structures for IRFPAs, the need for anisotropic etching increases as the size of the detector elements decreases. Recent interest in developing nanoscale structures in HgCdTe places even higher demands on etching. Plasma etching of HgCdTe offers an alternative to wet etching with the possible advantages of higher anisotropy, lower con-

sumption of materials, cleanliness, and compatibility with an all-vacuum process.

One challenge in the development of a successful plasma etching process for HgCdTe is the low damage threshold of HgCdTe to energetic ions. Ion bombardment of HgCdTe by ions in the range of 100–1000 eV, such as in an ion milling process, has been shown to cause type conversion of p-type material to n-type extending tens of microns into the substrate.^{1–4} To avoid the damage associated with the removal of substrate atoms by inert-ion sputtering, an etching process is needed which relies on solely chemical reactions to form volatile compounds with the substrate.

(Received October 4, 1994; revised January 29, 1995)

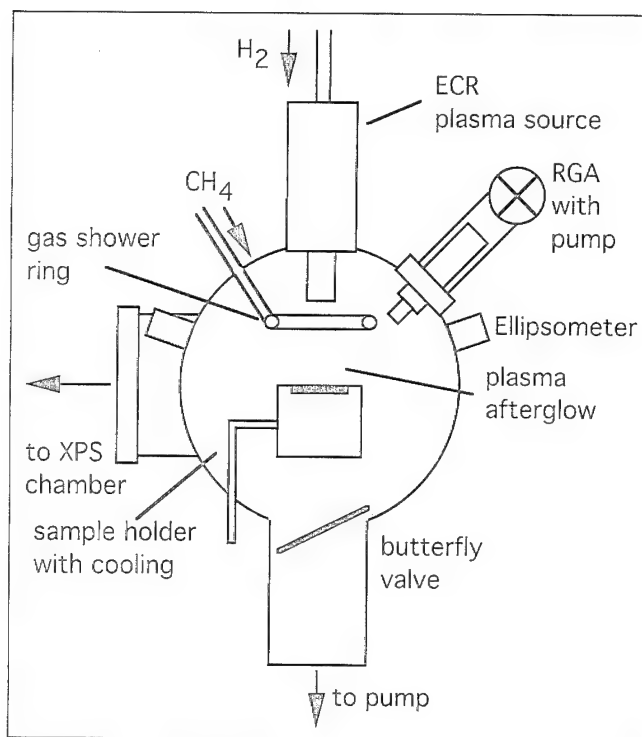


Fig. 1. Schematic diagram of plasma chamber and diagnostic equipment.

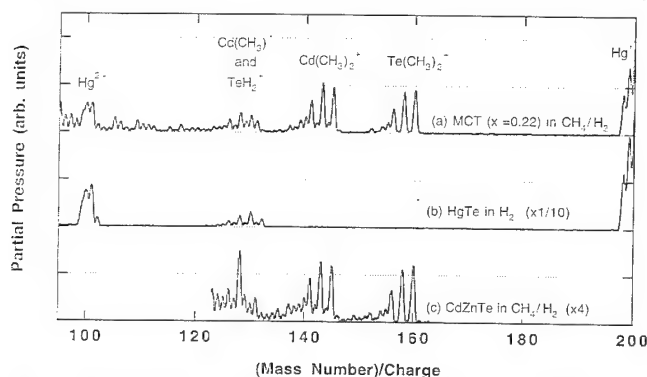


Fig. 2. Mass spectrum of the reaction products of (a) HgCdTe ($x = 0.22$), (b) HgTe and (c) CdTe. The spectrum for HgTe (b) has been divided by ten and the spectrum for CdTe (c) has been multiplied by four, indicating the much larger flux of etch products for HgTe. The different peaks within each group are due to the various isotopes of Hg, Cd, and Te.

Unlike in the cases of Si and most III-V compounds, fluorine and chlorine etching chemistries are not viable for HgCdTe due to the low vapor pressure of the cadmium halides and chlorides.⁵ Recently, methane (CH_4) and hydrogen (H_2) plasmas, which allow for dry etching of compound semiconductors by the formation of volatile methyl and hydride compounds, have been investigated as a possible etching system for both III-V⁶⁻⁹ and II-VI¹⁰⁻¹⁸ compounds. Previous studies of CH_4/H_2 plasma etching of HgCdTe have used radio frequency (rf) parallel plate reactors,^{11,12} a microwave resonant cavity discharge,^{5,10} a microwave barrel reactor,¹⁸ and electron cyclotron resonance (ECR) plasma reactors.¹³⁻¹⁷ Radio frequency parallel plate reactors suffer from the disadvantage that at

the low pressures needed for increased anisotropy, the ion energy can exceed several hundred volts, which may lead to significant damage near the surface. Previous work on microwave barrel reactors and microwave cavity reactors suggests that the low ion energies offered by those methods lack the anisotropy needed for etching nanometer size structures.^{5,10,18}

Recent work on HgCdTe etching has focused on ECR plasmas.¹³⁻¹⁷ The main advantages of ECR plasmas are a high density of excited species (up to 10%) and low ion energies (10–20 eV) at the pressures needed for anisotropic etching.¹⁹ Sidewall angles of better than 88° and aspect ratios of 5:1 have been shown possible in HgCdTe using CH_4/H_2 ECR plasmas.¹⁶ The low ion energies for ECR plasmas has the potential to minimize the adverse effects of ion bombardment such as type conversion, changes of the stoichiometric composition or other damage phenomena caused by the absorption of ion energy in the near surface region. Previous work on CH_4/H_2 etching using a rf parallel plate reactor¹² has suggested a preferential loss of Hg, with the Cd forming a film which hindered the etching with time. On the other hand, electrobeam electroreflectance (EBER) measurements of HgCdTe etched in a gentler microwave cavity reactor,⁵ where the ion energy is negligibly small, showed no measurable change in stoichiometry for the top 4000 Å or so at the surface. However, to date no previous investigations of the effect of CH_4/H_2 ECR plasma etching on the stoichiometric composition of HgCdTe surfaces have been published.

In this paper, we report on an investigation on the effects of $\text{CH}_4/\text{H}_2/\text{Ar}$ ECR plasmas on the surface condition of HgCdTe. We have identified the etch products during plasma exposure of $\text{Hg}_{1-x}\text{Cd}_x\text{Te}$ ($x = 0.22$), CdTe, and HgTe and were able to correlate the relative abundances of the various etch products to the resulting surface condition. We found that etching of HgCdTe, CdTe, and HgTe at no applied substrate bias is possible without formation of a hydrocarbon polymer film on the substrate. However, HgCdTe etching at even no applied bias results inevitably in a region at the surface depleted of the HgTe component (rich in CdTe). This region seems to be formed not by ion bombardment of the substrate but mainly by chemical reactions at the substrate, which preferentially etch the HgTe component over the CdTe component.

EXPERIMENTAL DETAILS

To provide *in vacuo* characterization of the samples after plasma exposure, we attached to an existing surface analysis facility an UHV chamber (Fig. 1) equipped with a commercially available compact ECR plasma source (ASTEX, operating at 875 Gauss and 2.45 GHz), a differentially pumped residual gas analyzer (RGA) and a single-wavelength ellipsometer (SENTECH). The plasma chamber was pumped with a 500 l/s turbomolecular pump, with a throttle valve between the pump and the chamber to control pumping speed and chamber pressure. The base pressure of

the chamber was typically $<5 \times 10^{-9}$ Torr. The flows of up to four gases ($>99.995\%$ purity) could be simultaneously controlled by a MKS multigas controller and passed either through the ECR plasma source or bypassed into the plasma afterglow (effluence) through a quartz shower ring shown in Fig. 1. In general, Ar was introduced into the ECR in addition to H₂ and/or CH₄ to ease ignition of the plasma. Samples were mounted on a stainless steel probe holder which was tightly held against a copper block during the plasma exposure. The temperature of the copper block was regulated between 5–90°C using a Lauda RM6 thermostat.

The differentially pumped RGA was used during the etch process for monitoring the reaction products escaping from the surface. The pressure difference between the RGA and the plasma chamber was three orders of magnitude, allowing use of a secondary electron multiplier in the RGA. The single wavelength ellipsometer (6328Å, 70°) was used to examine the surface roughness and composition of the substrate during the etching process. The subsequent compositional and structural surface analyses were based on x-ray photoelectron spectroscopy (XPS) and x-ray photoelectron diffraction (XPD), using MgK α x-rays. Rough estimates of etch rates were made by placing a thin metal mask over a part of the sample during the etching and measuring the resulting etch steps by a surface profilometer.

The samples used in this work were HgCdTe grown by solid state recrystallization (SSR), and Bridgman-grown HgTe and CdTe single crystals (the later with a small mole-fraction of ZnTe which we disregard for the purpose of this paper). All substrates were etch-polished with 0.5% Br/methanol prior to plasma etching, thus causing an etching residue of elemental Te (approx. 1 monolayer) at the surface.

RESULTS AND DISCUSSION

The result of a RGA analysis during exposure of a HgCdTe ($x = 0.22$) sample at a sample temperature of 60°C and no added bias to a CH₄/H₂/Ar (7:6:6 in sccm) plasma with a total chamber pressure of 2 mTorr is shown in Fig. 2 [spectrum (a)]. Hg, TeH₂, Te(CH₃)₂, and Cd(CH₃)₂ were clearly visible as the main reaction products. The occurrence of different peaks in each group is due (largely) to the different isotopes of Hg, Cd, and Te. Comparison of the isotopic abundances with the observed peak heights confirmed the identification of the chemical species. Due to the limited mass range of the RGA ($m/z < 200$), it was not possible to detect Hg compounds such as Hg(CH₃)₂. It has been speculated that CH₄/H₂ etching works through a reverse MOCVD process by formation of group II-methyl compounds and group VI-hydrides.²⁰ This is supported by our results, with the exception of Te, which was found to form di-methyl compounds as well as hydrides. However, the formation of Te(CH₃)₂ is not surprising as Te(CH₃)₂ can be used as a Te source in MOCVD growth of HgCdTe.²¹ The etching of HgCdTe in a H₂/Ar (10:2 in sccm) plasma produced Hg and

TeH₂ as etch products, but no respective Cd species were observed. This confirms previous findings that the etching of Cd requires a supply of CH₃ radicals.

In contrast to previously published results on CH₄/H₂ plasma etching of HgCdTe,^{15–17} we found that a bias was not necessary to accomplish HgCdTe etching at moderate temperatures (30–40°C) as indicated by RGA analysis and surface profilometry. The bias had been presumed to be necessary by other researchers to overcome the alleged low volatility of the Cd etch product. We believe the problem actually lies in polymer formation on the substrate. As in the previous work, introducing the CH₄ into the ECR plasma source with the sample at no applied bias resulted in the formation of a thick hydrocarbon polymer film on the etched sample for CH₄/H₂ > 0.1 . Formation of hydrocarbon polymer films from CH₄/H₂ plasmas is a well-known phenomenon and is related to the production of polymer forming radicals such as CH and CH₂ in the plasma.²² The occurrence and rate of polymer deposition also appears to depend on the surface composition. For example, even if HgCdTe was etched under conditions which did not produce a deposit on HgCdTe, a hydrocarbon polymer film was found to develop on the stainless steel holder of the respective sample. Therefore, it seems likely that etching of a particular surface can locally suppress the formation of these polymers. As an applied bias can result in an increased etch rate during the plasma etching, we believe this increase in the etch rate suppresses the polymer formation on the surface.

Of course the disadvantage of applying such a bias to the substrate is the possible increase in extended damage to the HgCdTe. For example, Bahir and Finkman⁴ have found that 100–150 eV Ar ions can convert over 10 μm of p-type HgCdTe to n-type in 2–3 min. Therefore, applying 100 volts to the substrate

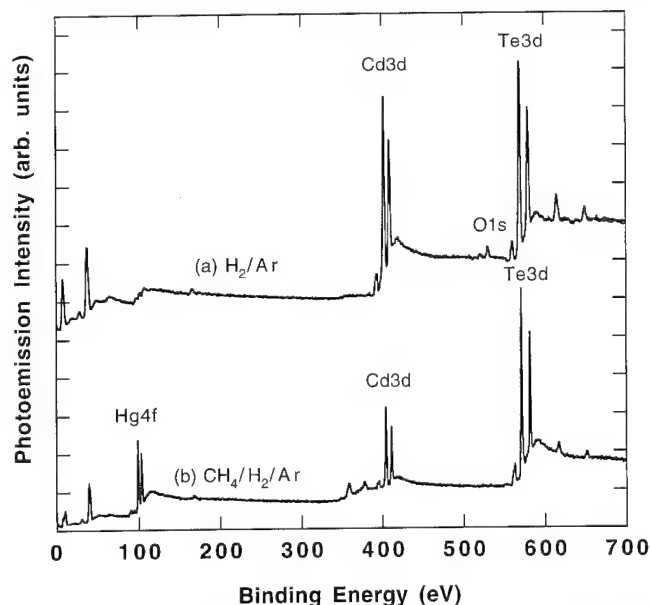


Fig. 3. X-ray photoelectron spectroscopy survey spectrum of HgCdTe ($x = 0.22$) after etching (a) with H₂/Ar (10:2 in sccm) and (b) with CH₄/H₂/Ar (7:3:3 in sccm).

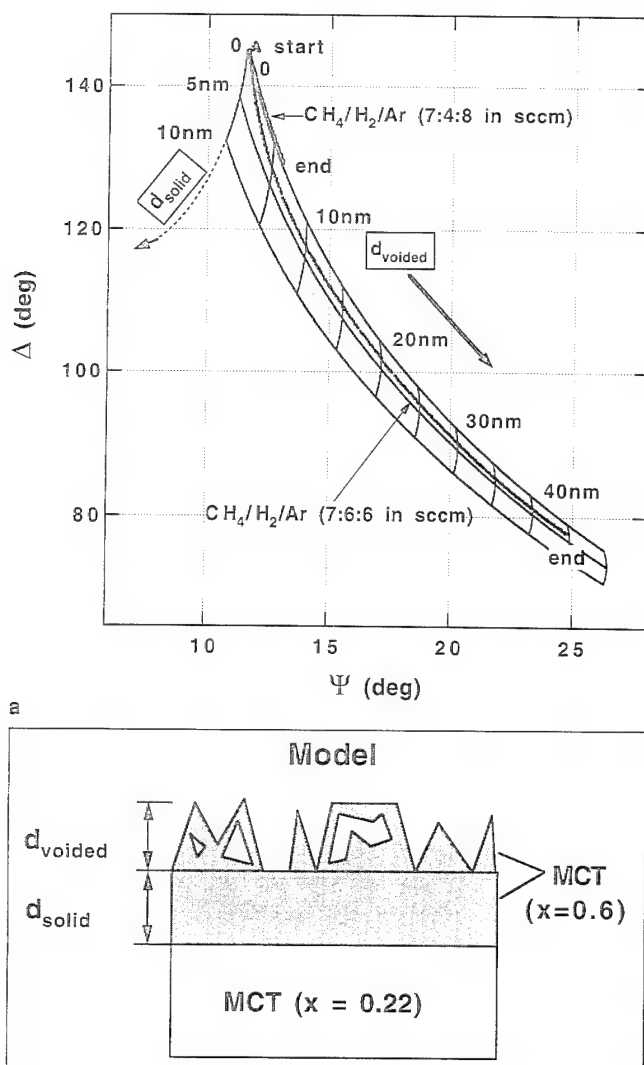


Fig. 4. (a) Ellipsometry parameters Ψ and Δ for two samples of HgCdTe ($x = 0.22$) etched for 15 min with $\text{CH}_4/\text{H}_2/\text{Ar}$ (7:4:8 in sccm) and (7:6:6 in sccm) mapped onto a grid representing the model shown schematically in (b). The model included a voided top layer of HgCdTe ($x = 0.6$), a middle layer of solid HgCdTe ($x = 0.6$), and a substrate of HgCdTe ($x = 0.22$). Note that the $\text{CH}_4/\text{H}_2/\text{Ar}$ (7:4:8 in sccm) etch resulted in much less surface roughness than the $\text{CH}_4/\text{H}_2/\text{Ar}$ (7:6:6 in sccm) etch.

may also result in such type conversion, although it has been shown for GaAs that the damage caused by reactive etching is less than for inert ion etching at comparable energies.²³ Problems with the formation of polymers in CH_4/H_2 plasmas has also placed a limitation on the ratio of CH_4/H_2 used by previous workers to generally less than 25% even with an applied bias, since higher CH_4/H_2 ratios result in considerable co-deposition of polymers. As described below, the CH_4/H_2 ratio is important in determining the condition of the resulting surface, and therefore it is important to develop an etching process which avoids the complications of polymer formation altogether.

To prevent the formation of polymers in our work, we fed only H_2 and Ar into the ECR source itself, while CH_4 was added to the H_2/Ar plasma in the afterglow region. Provided there existed a sufficient flow of gas

exiting the ECR (H_2 and/or Ar) to prevent backflowing of CH_4 into the ECR source, we found that polymer formation was suppressed and etching of HgCdTe at zero bias was accomplished without the concurrent deposition of hydrocarbon polymers on the sample. Seemingly, this gentler method for the breaking of the CH_4 molecule allows for formation of CH_3 radicals under conditions in which the generation of polymer forming radicals is less probable. Using this method, we were able to etch HgCdTe using only CH_4 and Ar (2:10 in sccm) without any hydrocarbon appearing on the etched surface.

Having basically solved the problem of polymer formation on the etched HgCdTe, we proceeded to characterize the condition of the samples during and after plasma exposure. By XPS analysis of the respective surfaces after exposure to H_2/Ar and $\text{CH}_4/\text{H}_2/\text{Ar}$ plasmas, we found that etching of HgCdTe ($x = 0.22$) resulted inevitably in a depletion of the HgTe component near the surface, even for etching with no applied bias. The composition of the depleted region covered a range from virtually pure CdTe after 15 min etching in a H_2/Ar (10:2 in sccm) plasma [Fig. 3, spectrum (a)] to $\text{Hg}_{1-x}\text{Cd}_x\text{Te}$ with $0.4 < x < 0.5$ for $\text{CH}_4/\text{H}_2/\text{Ar}$ (7:3:3 in sccm) etching [Fig. 3, spectrum (b)]. The ratio of Hg and Cd to Te in each case clearly indicates that this Cd-rich layer is CdTe and not elemental Cd. In addition, hemispheric diffraction patterns of the Cd3d and Te3d photoelectrons for the H_2 plasma etched surface revealed that the surface region fully depleted of HgTe still retains the crystal structure of the underlying HgCdTe bulk. This suggests that the inherent problem does not lie in the lack of sufficient volatility of the Cd etch products, which would lead to an excess of Cd at the surface, but rather in the breaking of the stronger CdTe bonds. X-ray photoelectron spectroscopy analyses also indicated that native oxides and/or elemental Te commonly found on Br/methanol etch-polished HgCdTe are quickly and completely removed from the sample by plasma etching.

Ellipsometry was used to observe changes in the surface condition during the plasma exposure. Ellipsometry is a useful tool for monitoring changes in surface conditions with respective coverages, roughness, and compositions (Rhiger²⁴ has written an excellent review of the application of ellipsometry to HgCdTe and related materials). The usefulness of ellipsometry is enhanced in combination with *in vacuo* XPS measurements, since the identification of the surface composition eases the preselection of a model which will eventually agree with the ellipsometry data. Of additional interest is the ability of ellipsometry to detect surface roughness, which is not possible by XPS measurements alone. The ellipsometry parameters Ψ vs Δ as measured during a 15 min exposure to a $\text{CH}_4/\text{H}_2/\text{Ar}$ (7:4:8 in sccm) plasma and to a $\text{CH}_4/\text{H}_2/\text{Ar}$ (7:6:6 in sccm) plasma are shown in Fig. 4a, along with a mesh generated from the model shown in Fig. 4b. A model which is consistent with the measured data requires the assumption of both the existence of a

layer depleted of HgTe and considerable surface roughening or voiding. The model is based on two layers on the HgCdTe substrate. The top layer of thickness d_{rough} consists of 65% voided HgCdTe (35% HgCdTe and 65% void) with $x = 0.6$. The void can be either due to roughness or to cavities. The optical constants for the film were estimated by the effective medium approximation of Bruggemann.²⁵ In the Bruggemann approximation, the change in the optical constants n and k is actually much more affected by voids than by the x -value for HgCdTe. For example, for a rough film, it is difficult to differentiate between a 60% CdTe layer and a 65% voided Hg_{0.5}Cd_{0.5}Te layer, as the optical constant n is similar for both. We have chosen a composition of $x = 0.6$ in the model based on our XPS results. Below the rough layer in our model, we have included a solid layer of HgCdTe of thickness d_{solid} and composition $x = 0.6$. Using this model, the surface of the HgCdTe after exposure to a CH₄/H₂/Ar (7:4:8 in sccm) plasma for 15 min agrees with $d_{\text{rough}} = 6$ nm and $d_{\text{solid}} = 0$, while etching in the CH₄/H₂/Ar (7:6:6 in sccm) plasma results in a much thicker rough layer ($d_{\text{rough}} = 45$ nm) on top of a depleted, solid layer ($d_{\text{solid}} = 3$ nm). The inclusion of the solid layer in a model which agrees with the data does not necessarily imply the actual presence of such a layer, but it may also suggested a more graded roughening region of higher density near the bulk. A more detailed discussion of monitoring the process by ellipsometric and mass spectroscopic measurements during CH₄/H₂ plasma etching of HgCdTe will be published in a later paper.

To gain more insight into the different etching behavior of the HgTe and CdTe component of HgCdTe under plasma exposure, we also investigated the ECR plasma etching of HgTe and CdTe single crystals. For HgTe etching, RGA analysis showed Hg and TeH₂ as the etch products in a H₂/Ar (10:2 in sccm) plasma [Fig. 2, spectrum (b)], while in CH₄/H₂/Ar (7:6:6 in sccm) plasmas Hg and Te(CH₃)₂ were mainly released from the HgTe surface. Exposure of CdTe to H₂/Ar plasmas produced no detectable amounts of etch products, although ellipsometry measurements indicated a roughening of the surface during exposure. Etching of CdTe in CH₄/H₂/Ar (7:6:6 in sccm) plasmas produced Cd(CH₃)₂ and Te(CH₃)₂ [Fig. 2, spectrum (c)]. As shown in Fig. 2, the flux of etch products measured during etching HgTe is more than an order of magnitude higher than that for CdTe obtained under similar conditions (the HgTe spectrum has been reduced by ten and the CdTe spectrum has been increased by four). The flux of etch products observed during HgCdTe etching falls in between these extremes, indicating an intermediate etch rate. We measured using surface profilometry etch rates of roughly 2000 Å/min for the HgTe, 100 Å/min for the HgCdTe ($x = 0.22$), and an etch rate below detectable limits for the CdTe. This observed difference in etch rates can account for the formation of the surface layer depleted of HgTe during the etching of HgCdTe, if the HgTe and CdTe components of HgCdTe etch largely independently. The depleted layer would likely

grow until the etch rate of the HgTe component, reduced because it is covered by a CdTe surface layer, equals the etch rate of the CdTe component, resulting in a steady state surface composition.

CONCLUSIONS

In this paper, we report on several new aspects of etching of HgCdTe, HgTe, and CdTe in CH₄/H₂/Ar plasmas generated by an ECR plasma source. First, using a residual gas analyzer, we have identified elemental Hg, TeH₂, Te(CH₃)₂, and Cd(CH₃)₂ as the primary reaction products escaping from a HgCdTe surface during the plasma exposure, thus confirming the interpretation of the CH₄/H₂/Ar etching process for HgCdTe as a "reverse" MOCVD process. Second, we have demonstrated by a modification of this etching technique (i.e. without channelling of the CH₄ gas through the ECR plasma source) that a bias is not needed to avoid the formation of hydrocarbon polymer films on a HgCdTe sample during etching at moderate temperatures (30–40°C). Moreover, we have examined by XPS analysis and ellipsometry the surface condition of HgCdTe resulting from this etching at zero bias. After exposure to the CH₄/H₂/Ar plasma (or to a H₂/Ar plasma only) the HgCdTe samples exhibited a depletion of the HgTe component in the near surface region (increase of the x -value). The depletion covered a range from virtually $x = 1$ after H₂/Ar (10:2 in sccm) etching to values $0.4 < x < 0.5$ after CH₄/H₂/Ar (7:3:3 in sccm) etching. Exposures to either one of the plasmas were found to result in surface roughening of HgCdTe, however, plasmas rich in H₂ were observed to cause significantly rougher surfaces than plasmas with small H₂/CH₄ ratios. This difference in the resulting surface condition is attributed solely to chemical effects since the respective ion energies are considered to be below the damage threshold for HgCdTe in both cases. In addition, we also investigated the etching of HgTe and CdTe single crystals. The etch rate of HgTe was found to be over one order of magnitude higher than that of CdTe under similar conditions. This large difference in etch rates is assumed to be responsible for the observed preferential etching of the HgTe component indicated by the HgTe depletion of the HgCdTe surface region.

Further investigations are needed to minimize the effects of roughening and/or compositional changes at HgCdTe surfaces and to fully assess the potential of ECR plasma etching for IR device technology.

ACKNOWLEDGMENTS

Expert help by P. Meisen (this institute) in the design and execution of these experiments is gratefully acknowledged. We appreciate the helpful advice of John Coburn, formerly at this institute. The samples used for this study were kindly provided by J. Ziegler, L. Palm, and M. Bruder (AEG, Heilbronn).

REFERENCES

1. U. Solzbach and H.J. Richter, *Surf. Sci.* 97, 191 (1980).
2. M.V. Blackman, D.E. Charlton, M.D. Jenner, D.R. Purdy,

- J.T.M. Wotherspoon, C.T. Elliot and A.M. White, *Elect. Lett.* 23, 978 (1987).
3. P. Brogowski, H. Mucha and J. Piotrowski, *Phys. Stat. Sol. A* 114, K37 (1989).
4. G. Bahir and E. Finkman, *J. Vac. Sci. Technol. A* 7 (2), 348 (1989).
5. J.E. Spencer, J.H. Dinan, P.R. Boyd, H. Wilson and S.E. Buttrill, *J. Vac. Sci. Technol. A* 7 (3), 676 (1989).
6. R. Cheung, S. Thoms, S.P. Beamont, G. Doughty, V. Law and C.D.W. Wilkinson, *Electron. Lett.* 23 (16), 857 (1987).
7. T.R. Hayes, M.A. Dreisbach, P.M. Thomas, W.C. Dautremont-Smith and L.A. Heimbrook, *J. Vac. Sci. Technol. B* 7 (5), 1130 (1989).
8. C. Constantine, D. Johnson, S.J. Pearton, U.K. Chakrabarti, A.B. Emerson, W.S. Hobson and A.P. Kinsella, *J. Vac. Sci. Technol. B* 8 (4), 596 (1990).
9. A. Semu and P. Silverberg, *Semicond. Sci. Technol.* 6, 287 (1991).
10. J.E. Spencer, T.R. Schimert, J.H. Dihan, Darrel Endres and T.R. Hayes, *J. Vac. Sci. Technol. A* 8 (3), 1690 (1990).
11. A. Semu, L. Montelius, P. Leech, D. Jamieson and P. Silverberg, *Appl. Phys. Lett.* 59 (14), 1752 (1991).
12. J.L. Elkind and Glennis J. Orloff, *J. Vac. Sci. Technol. A* 10 (4), 1106 (1992).
13. S.J. Pearton and F. Ren, *J. Vac. Sci. Technol. B* 11 (1), 15 (1993).
14. G.J. Orloff, John A. Wollam, Ping He, William A. McGahan, J.R. McNeil, R.D. Jacobson and B. Johs, *Thin Solid Films* 233, 46 (1993).
15. C.R. Eddy, E.A. Dobisz, C.A. Hoffmann and J.R. Meyer, *Appl. Phys. Lett.* 62 (19), 2362 (1993).
16. C.R. Eddy, C.A. Hoffmann, J.R. Meyer and E.A. Bobisz, *J. Electron. Mater.* 22 (8), 1055 (1993).
17. C.R. Eddy, E.A. Dobisz, J.R. Meyer and C.A. Hoffmann, *J. Vac. Sci. Technol. A* 11 (4), 1763 (1993).
18. M. Neswal, K.H. Gresslehner, K. Lischka and K. Lübke, *J. Vac. Sci. Technol. B* 11 (3), 551 (1993).
19. J. Asmusss, *J. Vac. Sci. Technol. A* 7 (3), 883 (1989).
20. L. Henry, C. Vaudry and P. Granjoux, *Electron. Lett.* 23, 1253 (1987).
21. A.H. McDaniel, B. Liu and R.F. Hicks, *J. Cryst. Growth* 124, 676 (1992).
22. H.V. Boenig, *Plasma Science and Technology*, (München, Germany: Carl Hanser Verlag, 1982).
23. O.J. Glembocki, B.E. Taylor and E.A. Dobisz, *J. Vac. Sci. Technol. B* 9 (6), 3546 (1991).
24. D.R. Rhiger, *J. Electron. Mater.* 22 (8), 1993.
25. D.E. Aspnes, *Thin Solid Films* 89, 249 (1982).

The Interface of Metalorganic Chemical Vapor Deposition-CdTe/HgCdTe

Y. NEMIROVSKY, N. AMIR, D. GOREN, and G. ASA

Kidron Microelectronics Research Center, Department of Electrical Engineering, Technion, Haifa 32000, Israel

N. MAINZER and E. WEISS

SCD Semi-conductor Devices, Dept. 99, P.O. Box 2250, Haifa 31021 Israel

The metalorganic chemical vapor deposition (MOCVD) growth of CdTe on bulk n-type HgCdTe is reported and the resulting interfaces are investigated. Metal-insulator-semiconductor test structures are processed and their electrical properties are measured by capacitance-voltage and current-voltage characteristics. The MOCVD CdTe which was developed in this study, exhibits excellent dielectric, insulating, and mechano-chemical properties as well as interface properties, as exhibited by MIS devices where the MOCVD CdTe is the single insulator. Interfaces characterized by slight accumulation and a small or negligible hysteresis, are demonstrated. The passivation properties of CdTe/HgCdTe heterostructures are predicted by modeling the band diagram of abrupt and graded P-CdTe/n-HgCdTe heterostructures. The analysis includes the effect of valence band offset and interface charges on the surface potentials at abrupt hetero-interface, for typical doping levels of the n-type layers and the MOCVD grown CdTe. In the case of graded heterojunctions, the effect of grading on the band diagram for various doping levels is studied, while taking into consideration a generally accepted valence band offset. The MOCVD CdTe with additional pre and post treatments and anneal form the basis of a photodiode with a new design. The new device architecture is based on a combination of a p-on-n homojunction in a single layer of n-type HgCdTe and the CdTe/HgCdTe heterostructure for passivation.

Key words: Band bending, CdTe, HgCdTe, metalorganic chemical vapor deposition (MOCVD), metal-insulator semiconductor (MIS) devices, surface passivation

INTRODUCTION

Significant advances in the performance of long wavelength infrared focal plane arrays (LWIR FPAs) have been demonstrated in P-on-n HgCdTe double layer heterojunctions employing CdTe as a passivation. Mesa devices as well as planar devices, based on a variety of growth technologies, have been reported.¹⁻⁴

Although CdTe has become the preferred passivation of HgCdTe photodiodes, the published work in the open literature addressing this passivation, is rather limited [Ref. 5 and references therein]. Recent studies include preliminary investigations of the interfaces between in-situ grown MOCVD CdTe and

MOCVD HgCdTe and ex-situ grown MOCVD CdTe on bulk p-type HgCdTe.⁶⁻¹⁰ The requirements of a good passivation for HgCdTe photodiodes vis-a-vis the passivation features of CdTe/HgCdTe heterostructures are discussed in Ref. 10.

In this study, we report the MOCVD growth of CdTe on bulk n-type HgCdTe and investigate the resulting interfaces. Metal-insulator-semiconductor (MIS) test structures are processed and their electrical properties are measured by capacitance-voltage (C-V) and current-voltage (I-V) characteristics. The heterostructures are also characterized by Auger depth profiles and double crystal rocking curves (DCRC).

In order to investigate the passivation properties of CdTe/HgCdTe heterostructures, we have modeled the band diagram of abrupt and graded P-CdTe/n-

(Received October 4, 1994; revised January 25, 1995)

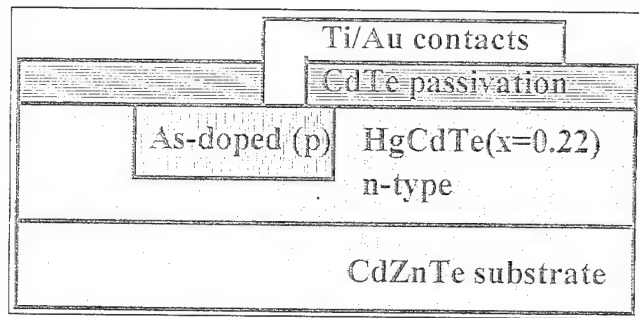


Fig. 1. Schematic cross section of a new device architecture (for backside illumination) based on a single layer of HgCdTe, a p-on-n, implanted homojunction, and a CdTe(CdZnTe)/HgCdTe heterostructure for passivation.

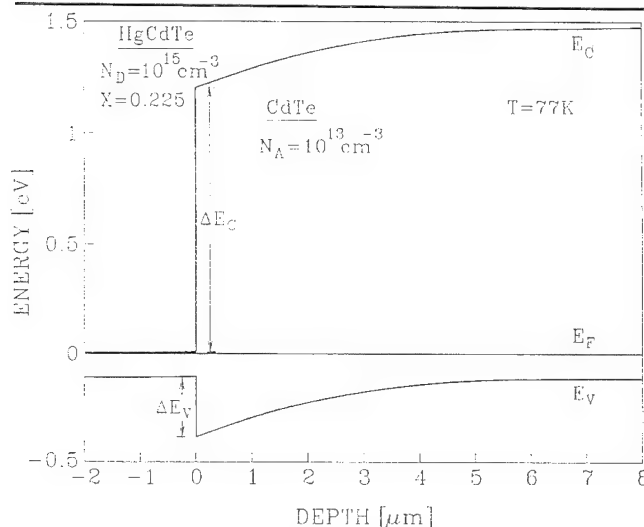


Fig. 2. Calculated band diagram and surface potentials at 77K, of P-CdTe/n-HgCdTe with the following parameters: valence band offset of 0.27 eV and zero interface charge density. The doping level of the CdTe is $N_A = 10^{13} \text{ cm}^{-3}$ at 300K, and the acceptor level is 0.15 eV. The doping level of the HgCdTe is $N_D = 10^{15} \text{ cm}^{-3}$, at 77K.

HgCdTe heterojunctions. We present the effect of valence band offset and interface charges on the surface potentials at abrupt hetero-interface, for typical doping levels of the n-type layers and the MOCVD grown CdTe. In the case of graded heterojunctions, we study the effect of grading on the band diagram for various doping levels, while taking into consideration a generally accepted, rather large, valence band offset.¹¹⁻¹³ The modeling of the CdTe/HgCdTe heterostructures forms the basis for the design of a new photodiode based on a single layer of n-type HgCdTe, with MOCVD-CdTe as the passivation, in a new device architecture discussed below.

A NEW DEVICE ARCHITECTURE AND MOCVD CdTe PASSIVATION

State-of-the-art photodiode arrays are based on double layer HgCdTe heterostructures, either in planar or mesa configuration.^{1-4, 14, 15} We propose a simplified planar device architecture based on a single layer of HgCdTe, a p-on-n implanted homojunction for sensing the infrared radiation, and a CdTe(CdZnTe)/HgCdTe heterostructure for passivation, as shown in Fig. 1.¹⁶ The MOCVD CdTe passivation (with appro-

prate pretreatments and activation and annealing steps) is a key technology in this device design and architecture. The implanted homojunction is at least partially activated during the MOCVD CdTe passivation, which also provides the capping for the surface during the subsequent anneal.

The main processing steps, required to fabricate the design shown in Fig. 1, include:

- Starting with an n-type HgCdTe layer with a predetermined composition and predesigned electrical properties.
- Performing ion implantation of arsenic to form an arsenic-rich layer in regions that will become the p-side of the homojunction.
- Growing an MOCVD CdTe passivation layer (with appropriate pre treatments) on the n-type HgCdTe layer and implanted arsenic-rich regions.
- Annealing the capped n-HgCdTe and capped implanted regions.
- Providing contacts, metallization and anti-reflection coatings.

The proposed structure is not only a major simplification in device architecture, in that it is based on a single n-type layer in contrast to known, double layer heterostructures, but in addition, it is based on the use of homojunctions for sensing the infrared radiation and heterostructures for passivation. This combination best integrates the benefits of each structure.

Furthermore, the new design allows application of different growth technologies for the sensing material and the passivation layer. This allows the sensing material to be supplied via the best available production techniques. An additional feature and advantage is a reduction in the number of required processing steps. Therefore, the production process can be simplified and the yield may be increased.

BAND DIAGRAM OF A P-CdTe/n-HgCdTe ABRUPT HETEROJUNCTION

A major requirement for a good passivation for HgCdTe photodiodes, is a well controlled and close to flat band surface potential. We, therefore, model the band diagram of a P-CdTe/n-HgCdTe abrupt heterojunction, at equilibrium, and calculate the surface potentials, taking into consideration the effect of the valence band offset, interface charges, and the doping levels of CdTe and HgCdTe. The model and the methodology of the calculations are briefly given in Ref. 10 where the modeling of isotype P-CdTe/p-HgCdTe heterostructures was presented.

The energy band diagram and the calculated surface potentials of a representative heterojunction, are given in Fig. 2, which exhibits the major passivation features of the CdTe/HgCdTe heterostructure. The surface potential of HgCdTe is close to flat band and barriers are formed for both electrons (majority carriers) and holes (minority carriers). In addition, the depletion region extends well into the low-doped CdTe (this issue will be further discussed in the Summary section). The doping levels assumed in Fig. 2 represent

typical doping levels of n-type HgCdTe and the low doped MOCVD CdTe actually obtained in our growth experiments. A zero interface charge density is also assumed in Fig. 2. The barrier for holes is determined by the valence band offset while the large barrier for electrons, the conduction band offset, is mainly determined by the large difference in band gap energies across the heterojunction (since $\Delta E_v + \Delta E_c = \Delta E_g$). The generally accepted value of 0.35 eV for HgTe/CdTe¹² is used in Fig. 2 and the actual offset of the heterostructure is taken as 0.27 (see below).

Below, we investigate the effect of the valence band offset, the effect of the interface charge density (taken as a parameter) as well as the effect of varying the doping levels of CdTe and HgCdTe, upon the band diagram, surface potentials, and passivation properties of P-CdTe/n-HgCdTe heterojunction.

The Effect of Valence Band Offset

The value of the valence band offset between HgTe and CdTe has been a controversial subject for several years. Recently, experimental observations have resolved the controversy in favor of a large offset value (>300 meV). Theoretical and experimental results indicate that it is possible that the actual valence band offset may be even larger than 400 meV,¹¹ but a valence band offset of 0.35 eV is currently the generally accepted value for HgTe/CdTe.¹² A linear variation of the valence band maximum with alloy composition x between the values for the binary compounds HgTe and CdTe is assumed. This is supported by the experimental data and theoretical model of Shih and Spicer.¹³ Hence, if we denote by ΔE_v the valence band offset between HgTe and CdTe, i.e. $\Delta E_v = E_v(\text{HgTe}) - E_v(\text{CdTe})$ and let $\Delta X = X_1 - X_2$ to be the difference between the alloy compositions of the two sides of the heterostructure, we obtain for the actual band offset:

$$\Delta E_v = \Delta x \cdot \Delta E_{v_0}$$

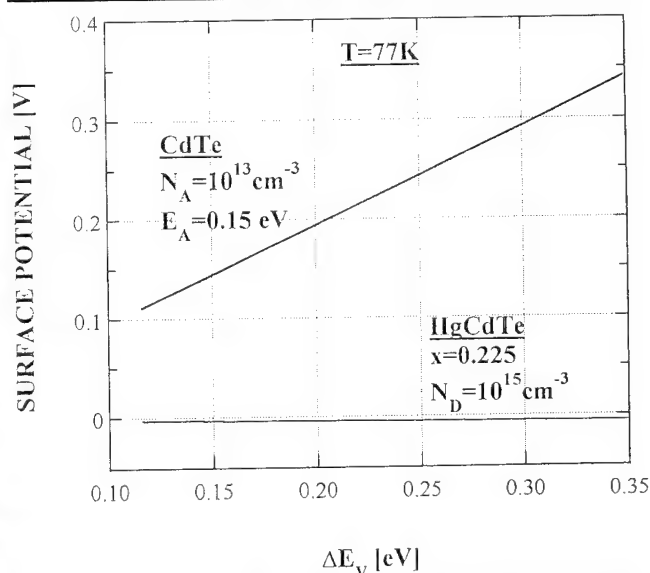
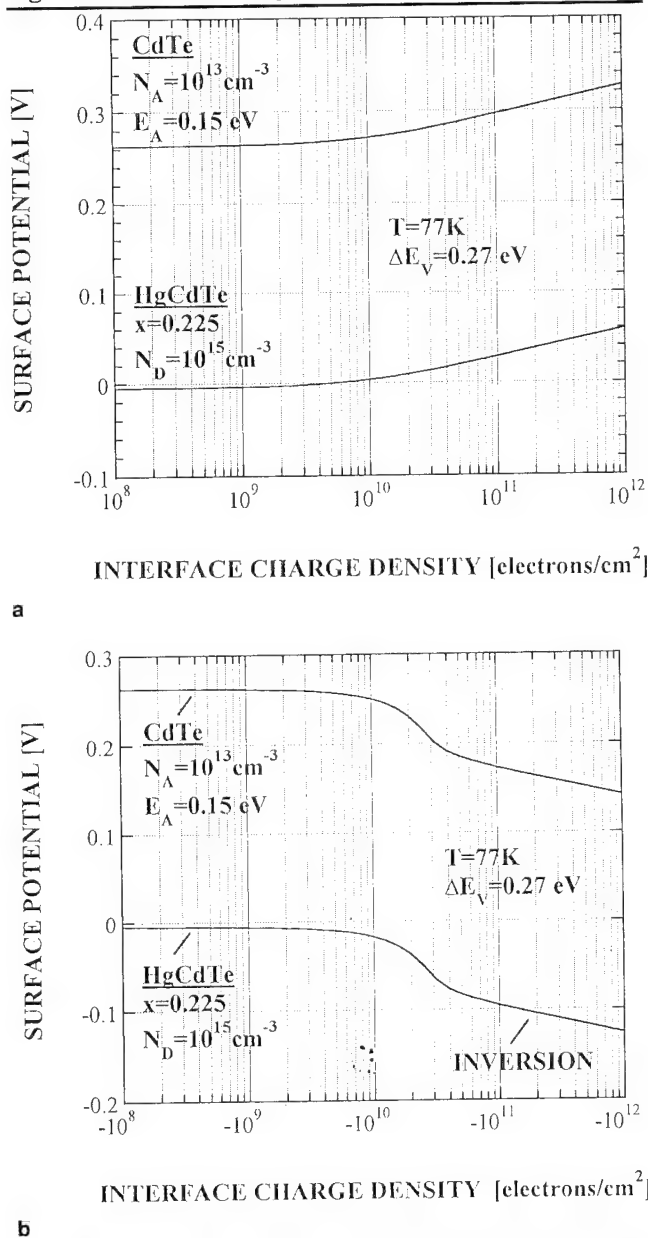


Fig. 3. The dependence of the calculated surface potentials of HgCdTe and CdTe, at 77K, upon the actual valence band offset. The interface charge density is taken as zero.

The dependence of the calculated surface potentials of HgCdTe and CdTe, at 77K, upon the valence band offset, assuming a zero interface charge density, is shown in Fig. 3. In the wide range of the assumed valence band offset values (0.15–0.45 eV), the HgCdTe surface is practically at flat band. Hence, it can be concluded that although the exact value of the valence band offset determines the exact values of barriers for electrons and holes, it hardly affects the surface potential.

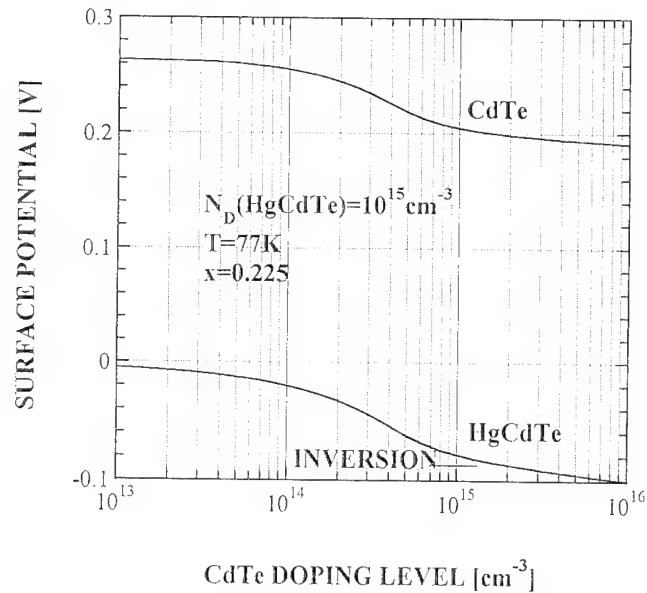
The Effect of Interface Charge Density

The drastic effect of interface charges upon the band diagram and surface potentials of CdTe and HgCdTe is shown in Fig. 4. Negative interface charges

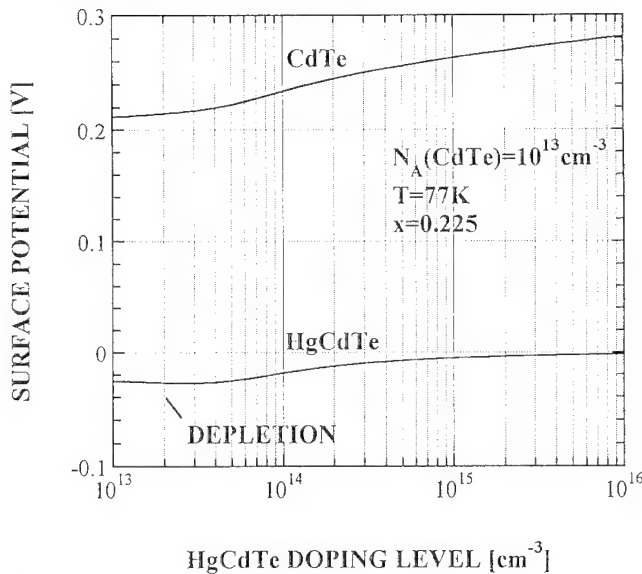


b

Fig. 4. The dependence of the calculated surface potentials of HgCdTe and CdTe, at 77K, upon the interface charge density. The actual valence band offset is taken as 0.27 eV. (a) positive interface charges, and (b) negative interface charges.



a



b

Fig. 5. The dependence of the calculated surface potentials of HgCdTe and CdTe, at 77K, upon the doping level of (a) CdTe, and (b) HgCdTe. The interface charge density is taken as zero. The actual valence band offset is taken as 0.27 eV.

induce inversion in the n-HgCdTe side while positive interface charges induce accumulation. Figure 4 exhibits that interface charge density of the order of $\pm 2 \cdot 10^{10} \text{ cm}^{-2}$ is sufficient to cause significant deviations from flat band conditions, in the case of n-type HgCdTe, doped to 10^{15} cm^{-3} and assuming a valence band offset of 0.27 eV (i.e. $\Delta E_v = 0.35 \text{ eV}$).

The Effect of the Doping Levels of CdTe and HgCdTe

The doping level of the CdTe passivation, in comparison to the doping level of the HgCdTe layer, also exhibits a significant effect on the band diagram and the surface potentials, as shown in Fig. 5. For $N_D = 10^{15} \text{ cm}^{-3}$, a low doped CdTe ($N_A = 10^{13} \text{ cm}^{-3}$) is required

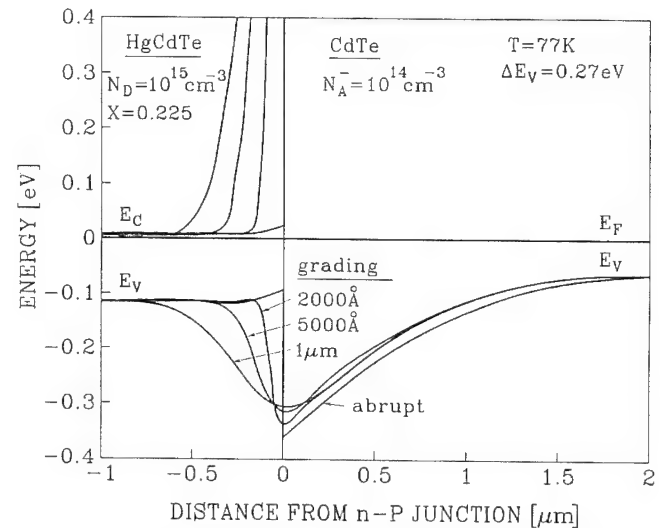


Fig. 6. Calculated band diagram and surface potentials at 77K, of P-CdTe/n-HgCdTe graded heterojunction, for different grading: (a) abrupt and 1000 Å, (b) 2000 Å, (c) 5000 Å, and (d) 1 μm. The calculations are done with the following parameters: valence band offset of 0.27 eV and zero interface charge density. The doping level of the CdTe is $N_A = 10^{13} \text{ cm}^{-3}$. The doping level of the HgCdTe is $N_D = 10^{15} \text{ cm}^{-3}$, at 77K.

to obtain a close to flat band surface potential at the HgCdTe side. CdTe layers with higher doping ($N_A/N_D = 1/10$) induce depletion. For $N_A = N_D$, strong inversion is observed. A lower doped HgCdTe layer, of the order of $N_D = 10^{14} \text{ cm}^{-3}$, imposes even more demanding requirements for a low doped CdTe, since more or less the same surface potentials are calculated for a given ratio of N_A/N_D . Obviously, in order to design a device according to Fig. 1, a higher doped n-type HgCdTe layer is preferred.

The calculations take into account the freezeout in the CdTe as determined by the energy of the acceptor level. We assume that the acceptor level of the MOCVD CdTe is 0.15 eV, corresponding to a shallow level due to residual impurities such as copper.¹⁷ We have also calculated the band diagram with the acceptor level as a parameter and found that this parameter has a negligible effect on the surface potential of HgCdTe. This results from the fact that for the CdTe doping levels under study, the CdTe is easily depleted. Since the acceptor level follows the bended valence band, it remains below the Fermi level. As long as the acceptor level is below the Fermi level, the acceptors are ionized.

BAND DIAGRAM OF A P-CdTe/n-HgCdTe GRADED HETEROJUNCTION

We have calculated the energy band diagram for graded CdTe/HgCdTe heterostructures at equilibrium conditions by solving Poisson's equation in one dimension (z) using standard relaxation methods.¹⁸ In the physical assumptions and the numerical calculations, we have extended the work of Migliorato and White,¹⁹ Bratt and Casselman,²⁰ Oda²¹ and Madarasz and Szmulowicz (Ref. 22 and references therein). The complete and quantitative details of our model and calculations as well as a detailed comparison with the previous models, will be reported elsewhere.²³

The most pronounced effect of the graded heterojunction, with grading in composition and doping, is to smooth out the band bending in n-HgCdTe in cases where the doping level of the CdTe is high enough to impose depletion or even inversion. An example which illustrates the possible benefits of a graded heterojunction is shown in Fig. 6. In this example, $N_d = 10^{15} \text{ cm}^{-3}$ and $N_a = 10^{14} \text{ cm}^{-3}$. In the case of an abrupt heterojunction, the HgCdTe surface is clearly depleted. A grading of 1000Å hardly affects the band diagram, whereas a grading of 2000Å slightly reduces the band bending in the HgCdTe and the well for holes (minority carriers) is now separated from the hetero-interface where $n = p$. The effect becomes more pronounced with a grading of 5000Å. The barrier for holes is also reduced as the grading increases. However, for a grading of 5000Å and with the assumed actual valence band offset, an effective barrier that

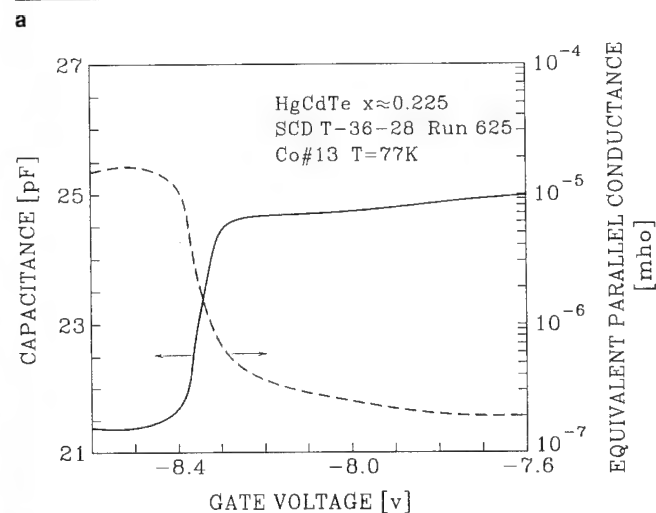
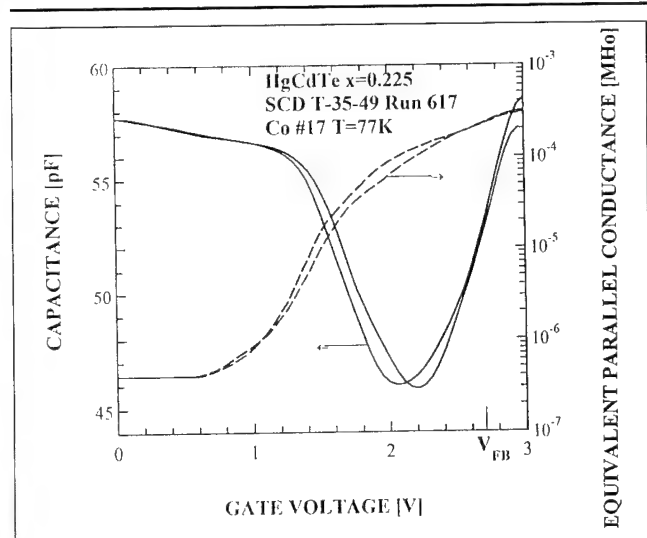


Fig. 7. Measured (solid line) capacitance-voltage and equivalent parallel conductance (dashed line) characteristics of MIS devices. The measurement temperature is 77K and the measurement frequency is 100 kHz. Gate area is 0.002 cm². (a) the MOCVD-CdTe was grown at 430°C with DETe, and (b) the MOCVD-CdTe was grown at 350°C with DIPT.

exceeds 200 mV is calculated, which is still large compared to the thermal voltage of 6.5 mV at 77K. A grading of 1 micron further reduces both the barrier for holes and the band bending in HgCdTe (close to flat band conditions are observed). It is evident from the calculations that some degree of grading actually improves the passivation properties of the heterojunction. The grading that starts to exhibit a pronounced effect on the band diagram is of the order of the depletion width in the HgCdTe. This is determined by N_d/N_a and is typically of the order of several thousands angstroms or less. In addition, the effect of interface charges, that drastically affect abrupt heterostructures can be modified in graded heterojunctions.²³

EXPERIMENTAL

The MOCVD growth of CdTe epilayers on HgCdTe substrates, to be used as passivation of photodiodes, is a technological challenge since several demanding requirements must be achieved simultaneously:

- The electrical properties of the CdTe epilayer must be controlled and should correspond to pre-designed values indicated by the model calculations presented in the two previous sections. A mirror-like morphology is also required for further processing of the photodiodes.
- The electrical properties of the HgCdTe substrates must be preserved, whether bulk HgCdTe wafers or HgCdTe epilayers are used as substrates.
- The interface properties between the HgCdTe and the CdTe passivation must be controlled, including a close to flat band surface potential of

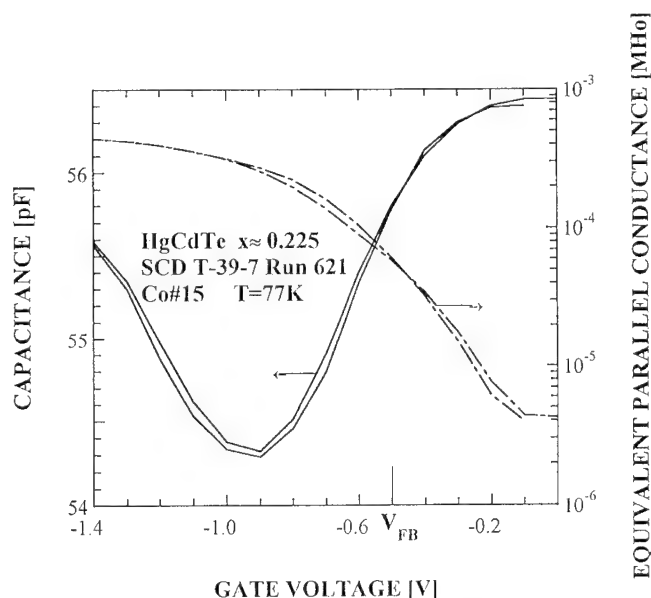


Fig. 8. Measured (solid line) capacitance-voltage and equivalent parallel conductance (dashed line) characteristic of an MIS device. The measurement temperature is 77K and the measurement frequency is 100 kHz. Gate area is 0.002 cm². The MOCVD-CdTe was grown at 350°C with DIPT. The MIS device was annealed at 350°C for one hour in the MOCVD system in the presence of flowing hydrogen.

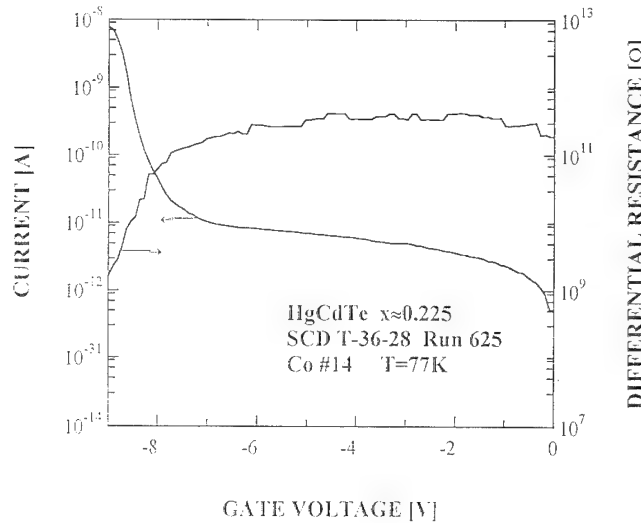


Fig. 9. Measured, at 77K, DC gate current-voltage and differential resistance-voltage characteristics of the MIS device of Fig. 7b.

HgCdTe and a low density of fixed and fast surface states as well as trapping centers.

Our MOCVD system and the growth of CdTe on CdTe substrates was previously reported.²⁴⁻²⁷ The modifications tailored to the growth of CdTe on HgCdTe substrates are briefly reported in Ref. 10. The grading of the MOCVD-CdTe/HgCdTe heterostructures was estimated by Auger electron spectroscopy. It was found that the graded region is less than 1000Å for heterostructures grown at 350°C and less than 2000Å if grown at 430°C.

CHARACTERIZATION

Metal-insulator-semiconductor devices were fabricated and were used to electrically characterize the heterostructures. The insulator of the MIS device consisted of the MOCVD grown CdTe epilayer. The combination of evaporated titanium (500Å) and gold (0.5–1 μm) was used for bulk and gate metallization. The gate electrodes of approximately 500 μm diameter were evaporated through a metal mask and the bulk contact was evaporated on the rear side of the HgCdTe substrate. The devices were bonded and sealed with a cold shield at 77K, in a dewar. Capacitance and equivalent parallel conductance were measured as a function of gate voltage with an HP 4192A impedance analyzer. The DC gate current was measured as a function of gate voltage with an HP 4145A semiconductor parameter analyzer. Simple MIS theory, neglecting modifications due to the non-parabolicity of the HgCdTe conduction band and the grading of the heterostructure, was applied for the analysis. We assume that the depleted wide band gap CdTe can be approximately described as an ideal insulator at 77K. Measured capacitance-voltage and equivalent parallel conductance-voltage characteristics of MIS devices are shown in Fig. 7. Figure 7a corresponds to growth at 430°C (with DETe) while Fig. 7b corresponds to growth at 350°C (with DIPT). The C-V characteristic of Fig. 7a is analyzed with the

following inputs:

$C_{\text{insulator}}$ (from Fig. 7a) = 60pF

C_{minimum} (from Fig. 7a) = 45pF

Gate area (measured) = $2 \cdot 10^{-3} \text{cm}^2$

Relative dielectric constant of CdTe = 10.6

Relative dielectric constant of HgCdTe = 18

The following MIS parameters are derived from simple MOS theory:

HgCdTe effective doping concentration = $4 \cdot 10^{15} \text{cm}^{-3}$

CdTe thickness = 3100 Å

Flat band capacitance = 56pF

Flat band voltage, V_{FB} = 2.8V

We assume that the metal-semiconductor (titanium-HgCdTe) work function difference is $\psi_{\text{MS}} = 0.28,^{29}$ From $V_{\text{FB}} = \psi_{\text{MS}} - Q_{\text{ss}}/C_{\text{ox}}$ we obtain $Q_{\text{ss}} = -5 \cdot 10^{11} \text{electrons/cm}^2$. Hence, it is seen that in the case of the experiment of Fig. 7a, the HgCdTe surface is inverted and negative fixed interface charges are observed. This result may be explained with the modeling of the section on the effect of the doping levels of CdTe and HgCdTe since the HgCdTe substrate of Fig. 7a was a low doped n-type material and the n-type doping was based on Hg interstitials introduced by a low temperature prolonged Hg anneal. The overall growth conditions at 430°C could cause a skin interface layer deficient in Hg, which may account for the observed negative interface charges.

The MIS results obtained with MOCVD CdTe growth experiments at 430°C indicates the following trends: in growth experiments with a UV pretreatment at 50°C and UV photons during steps I and II of the temperature cycle, but without a Hg boat, the HgCdTe surface became a low doped p-type material and high frequency C-V curves were measured even at 100 kHz, with a negligible hysteresis. At zero gate bias the p-type like surface was inverted and the corresponding Q_{ss} was positive. In experiments employing similar UV pretreatments and in addition incorporating a Hg boat at 250°C, the surface retained the n-type conductivity but was inverted as shown in Fig. 7b.

The C-V characteristic of Fig. 7b, corresponding to growth at 350°C, is analyzed in a similar manner with the following inputs:

$C_{\text{insulator}}$ (from Fig. 7b) = 25pF

C_{minimum} (from Fig. 7b) = 21.5pF

The following MIS parameters are derived from simple MOS theory:

HgCdTe effective doping concentration = $2.5 \cdot 10^{15} \text{cm}^{-3}$

CdTe thickness = 7500 Å

Flat band capacitance = 24pF

Flat band voltage, V_{FB} = -8.35 V

From $V_{\text{FB}} = \psi_{\text{MS}} - Q_{\text{ss}}/C_{\text{ox}}$, we obtain $Q_{\text{ss}} = 6.5 \cdot 10^{11} \text{electrons/cm}^2$. Hence, it is seen that in the case of the experiment of Fig. 7b, the HgCdTe surface is strongly accumulated and positive fixed interface charges are observed. The MIS results obtained with MOCVD CdTe growth experiments at 350°C have indicated the following trends: in growth experiments with UV

pretreatments and with a Hg boat at 250°C, the HgCdTe surface retained its n-type conductivity but became strongly accumulated at zero gate bias and the corresponding Q_{ss} was positive.

The accumulation was significantly reduced by adding an annealing phase at 350°C. Metal-insulator-semiconductor devices similar to those of Fig. 7b were annealed in the MOCVD system for one hour, at 350°C, in the presence of flowing hydrogen. With this post treatment anneal, C-V characteristics corresponding to the requirements of photodiodes were measured, as shown in Fig. 8. The C-V characteristics, which were measured at 100 kHz, exhibit slightly accumulated surfaces and a small hysteresis (within the resolution of the measurement). From the MOS analysis, we obtain HgCdTe effective doping concentration = $3 \cdot 10^{16} \text{ cm}^{-3}$, CdTe thickness = 3300Å, flat band capacitance = 55pF and the flat band voltage is -0.5 V. The corresponding positive interface charges are $Q_{ss} \approx 8.8 \cdot 10^{10} \text{ electrons/cm}^2$.

The DC gate current-voltage and differential resistance-voltage characteristics of the MIS device adjacent to the device of Fig. 7b, is shown in Fig. 9. These curves demonstrate the insulation properties of the MOCVD CdTe at 77K as determined from capacitance measurements. The DC leakage current of the MOCVD CdTe which was grown at 350°C, was less than 10 pA in a wide range of gate voltages exceeding 10 V (we also measured the leakage current in positive gate voltages, not shown in Fig. 9). The corresponding dynamic resistance was over $10^{11} \Omega$. This corresponds to an approximately 7500Å thick CdTe, as determined from the capacitance measurements. The I-V and C-V characteristics were stable during repeated measurements and electrical stresses imposed by a wide range of gate voltages. It was observed that the ac conductivity (the equivalent parallel conductance) corresponded to the DC conductivity and is probably an indication of the dielectric strength of the CdTe rather than surface states.

SUMMARY

A controlled growth process as well as pre and post treatments and anneals have been developed to obtain an MOCVD CdTe/n-HgCdTe heterostructure for passivation of photodiodes. This passivation plays an important role in a new device architecture based on a combination of a p-on-n homojunction in a single layer of n-type HgCdTe and the CdTe/HgCdTe heterostructure for passivation.¹⁶ The MOCVD CdTe exhibits excellent dielectric, insulating, and mechanochemical properties as well as interface properties, as exhibited by MIS devices where the MOCVD CdTe is the single insulator. We have obtained interfaces characterized by slight accumulation and a small hysteresis in the C-V characteristics.

The fine details of the MOCVD CdTe growth process must be tailored to the HgCdTe material (bulk or epilayer, undoped or intentionally doped and orientation). From the modeling of the heterostructure, it is evident that close to flat band conditions are achieved

more easily on higher doped n-HgCdTe which is also less sensitive to fixed surface states. Hence, it can be concluded that intentionally doped, n-type epilayers with $N_d = 10^{15} \text{ cm}^{-3}$ or higher, are the preferred starting material for the single layer p-on-n photodiodes of Fig. 1, although bulk material can be also used.

For the present study, we have used unintentionally doped, bulk n-type HgCdTe which is a well characterized, reproducible and available material. The (111) orientation corresponds to LPE HgCdTe epilayers.

The growth temperature as well as the pre and post treatments, drastically affect the electrical properties of the interface. The UV photons are an important ingredient in the overall process. The Hg atoms in the vapor phase efficiently absorb the UV photons. In the presence of excited Hg atoms, hydrogen radicals are formed via direct collisions in the vapor phase. The hydrogen radicals form volatile hydrides with Te atoms and possibly with additional impurity atoms that may reside on the HgCdTe surface. The hydrogen radicals also reduce native oxides and remove water molecules that are easily adsorbed on the polar surface of (111) HgCdTe. In addition, it is quite possible that hydrogen radicals passivate the HgCdTe surface, but this has not been proven so far. Furthermore, it seems that the excited Hg atoms in the vapor phase are more effective in controlling the n-type conductivity of HgCdTe substrates, but this issue should be further studied.

From the modeling, it is evident that some degree of grading is actually beneficial for passivation. This is corroborated by the experimental results. The MIS device that was exposed to post treatment and anneal at the elevated temperature of 350°C for one hour, exhibited the lowest density of fixed surface states. It is quite possible that in the graded heterostructure, a damaged layer of several hundreds of angstroms is consumed by interdiffusing with the CdTe. The sur-

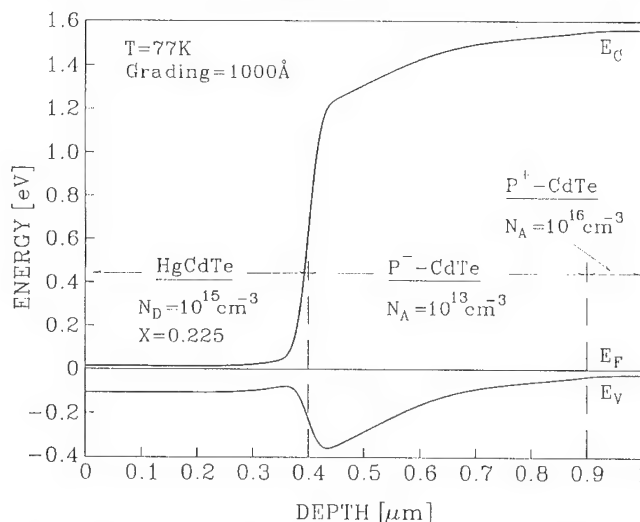


Fig. 10. Calculated band diagram of a $P^+ - P^-$ MOCVD CdTe/n-HgCdTe graded heterostructure, at 77K. The doping level of the HgCdTe is $N_d = 10^{15} \text{ cm}^{-3}$, the doping level of the P^- CdTe is $N_A = 10^{13} \text{ cm}^{-3}$ and the doping level of the P^+ CdTe is $N_A = 10^{16} \text{ cm}^{-3}$. The grading is 1000Å.

face charges that drastically affect the narrow band gap HgCdTe hardly affect the wider band gap HgCdTe.

Finally, it should be noted that the low doped MOCVD CdTe is easily depleted and the depletion width may extend to several microns. In practice, the MOCVD passivation which is less than 1 micron, is fully depleted. For the passivation of photodiodes, it is not advisable to have a CdTe with a charged outer surface which may affect the CdTe/HgCdTe interface. There are three possible technological solutions: the first is to cover the CdTe passivation with a metallic layer, similar to the gate of the MIS devices presented in this study. The second is to evaporate thick CdTe or ZnS layers. This solution is not ideal since the new interface which is now formed (between the CdTe and the evaporated insulator) is not well defined and there is ample experimental evidence that a double layer insulator introduces additional difficulties.²⁸ The third and most elegant solution is to terminate the MOCVD CdTe growth by growing arsenic doped CdTe. The band diagram of the proposed $P^+ - P^- - \text{CdTe}/n\text{-HgCdTe}$ graded heterostructure is shown in Fig. 10. Approximately 0.5 microns of the low doped CdTe are now depleted while the bending of the $P^+ \text{CdTe}$ with $N_A = 10^{16} \text{ cm}^{-3}$ is less than several tenth of micron. The proposed $P^+ - P^- - \text{CdTe}$ can be grown in a single run and hence there is no concern for the formation of a new interface.

ACKNOWLEDGMENT

This research was performed in the laboratories donated by Etia and Miguel Meilichson. The research was partially supported by the fund for the promotion of research at Technion-Israel Institute of Technology. We are much indebted to E. Khanin for the DCRC measurements. We are grateful to A. Shai and D. Schoenmann for the maintenance of the MOCVD system and assembling the MIS devices.

REFERENCES

1. W.E. Tennant, C.A. Cockrum, J.B. Gilpin, M.A. Kinch, M.B. Reine and R.P. Ruth, *J. Vac. Sci. Technol. B* 10, 1359 (1992).
2. L.O. Bubulac, R.E. DeWames and W.E. Tennant, *J. Electron. Mater.* 22, 1049 (1993).
3. J.M. Arias, G. Pasko, M. Zandian, S.H. Shin, G.M. Williams, L.O. Bubulac, R.E. DeWames and W.E. Tennant, *Appl. Phys. Lett.* 62, 976 (1993).
4. S.M. Johnson, D.R. Rhiger, J.P. Rosebeck, J.M. Peterson, S.M. Taylor and M.E. Boyd, *J. Vac. Sci. Technol. B* 10, 1499 (1992).
5. Y. Nemirovsky, N. Mainzer and E. Weiss, *Narrow-Gap Cadmium-Based Components*, ed. P. Capper, (EMIS/IEEE, 1994).
6. G. Sarusi, G. Cinader, A. Zemel, D. Eger and Y. Shapira, *J. Appl. Phys.* 71, 5050 (1992).
7. G. Sarusi, A. Zemel, D. Eger, S. Ron and Y. Shapira, *J. Appl. Phys. Lett.* 72, 2312 (1992).
8. V. Ariel, V. Garber, G. Bahir and A. Sher, *J. Electron. Mater.* 24, 655 (1985).
9. G. Bahir, V. Ariel, V. Garber, D. Rosenfeld and A. Sher, to be published in *Appl. Phys. Lett.*
10. Y. Nemirovsky, N. Amir and L. Djaloshinsky, *J. Electron. Mater.* 24, 647 (1995).
11. K.A. Harris, et al., *J. Vac. Sci. Technol. B* 10, 1574 (1992).
12. R. Sporken, et al., *J. Vac. Sci. Technol. A* 7, 427 (1989).
13. C.K. Shih and W.E. Spicer, *Phys. Rev. Lett.* 58, 2594 (1987).
14. G.N. Pultz, P.W. Norton, E.E. Kruger and M.B. Reine, *J. Vac. Sci. Technol. B* 9, 1724 (1991).
15. C.C. Wang, *J. Vac. Sci. Technol. B* 9, 1740 (1991).
16. A patent application has been filed on this subject matter by Technion Research & Development Foundation Ltd. (Y. Nemirovsky, inventor).
17. J.L. Pautrat and N. Magnea, *Properties of Narrow Gap Cadmium-Based Compounds*, ed. P. Capper, data reviews series, No. 10, (London: INSPEC publication, 1994).
18. W.H. Press, *Numerical Recipes* (New York: Cambridge University Press, 1987).
19. P. Migliorato and A.M. White, *Solid State Electron.* 26, 65 (1983).
20. P.R. Bratt and T.N. Casselman, *J. Vac. Sci. Technol. A* 3, 238 (1985).
21. N. Oda, *Infrared Phys.* 27, 49 (1987).
22. F.L. Madarasz and F. Szmulowicz, *SPIE* Vol. 1106, 117 (1989).
23. D. Goren, G. Asa and Y. Nemirovsky, to be submitted to *J. Appl. Phys.* 1994.
24. E. Khanin, N. Amir, Y. Nemirovsky and E. Gartstein, submitted to *Appl. Phys. Lett.* (1994).
25. N. Amir, D. Goren, D. Fekete and Y. Nemirovsky, *J. Electron. Mater.* 20, 227 (1990).
26. Y. Nemirovsky, D. Goren and A. Ruzin, *J. Electron. Mater.* 20, 609 (1991).
27. Y. Nemirovsky, A. Ruzin and A. Bezinger, *J. Electron. Mater.* 22, 977 (1993).
28. R. Strong, *J. Vac. Sci. Technol. B* 10, 1530 (1992).
29. Y. Nemirovsky, R. Adar, A. Korenfeld and I. Kidron, *J. Vac. Sci. Technol. A* 4, 1986 (1986).

Electrical and Structural Properties of Epitaxial CdTe/HgCdTe Interfaces

V. ARIEL, V. GARBER, D. ROSENFELD, and G. BAHIR

Department of Electrical Engineering, Technion, Haifa 32000, Israel

V. RICHTER

Solid State Institute, Technion, Haifa 32000, Israel

N. MAINZER

SCD, P.O. Box 2250, Haifa 31021, Israel

A. SHER

Soreq NRC, Yavne 70600, Israel

In this study, CdTe epilayers were grown by metalorganic chemical vapor deposition on epitaxial HgCdTe with the purpose of developing suitable passivation for HgCdTe photodiodes. Two types of CdTe layers were investigated. One was grown directly, *in situ*, immediately following the growth of HgCdTe. The second type of CdTe was grown indirectly, on top of previously grown epitaxial HgCdTe samples. In this case, the surface of the HgCdTe was exposed to ambient atmosphere, and a surface cleaning procedure was applied. The material and structural properties of the CdTe/HgCdTe interfaces were investigated using secondary ion mass spectroscopy, Auger electron spectroscopy, Rutherford back scattering, and x-ray double crystal diffractometry techniques. Electrical properties of the CdTe/HgCdTe heterostructure were determined by capacitance-voltage (C-V) characterization of Schottky barrier devices and metal insulator semiconductor devices. Also, a preliminary current-voltage characterization of n⁺p photodiodes was performed. A theoretical model suitable for analysis of graded heterojunction devices was used for interpretation of C-V measurements.

Key words: HgCdTe, metalorganic chemical vapor deposition (MOCVD), metal insulator semiconductor (MIS) devices, passivation

INTRODUCTION

High performance infrared imaging systems are currently based on a two-dimensional matrix of photovoltaic detectors, cooled to 77K and coupled with a Si processor in the focal plane.¹ The photovoltaic detectors suitable for sensing thermal radiation in the 8–12 μm range are usually made of either one or two HgCdTe layers.^{2,3} The passivation of HgCdTe is a critical step, especially for the small area devices typically used for imaging applications. During the

previous decade, the dominant surface passivation process for photodiodes was based on ZnS. A comprehensive review of the requirements for HgCdTe surface passivation, as well as a review of the passivation techniques, was given by Nemirovsky and Bahir.⁴

Recently, deposition of CdTe on HgCdTe surfaces emerged as a standard method for passivation of HgCdTe photodetectors.^{1–3,5–12} CdTe appears attractive for passivation of HgCdTe because it is a wide gap semiconductor which is nearly lattice matched and is chemically compatible with HgCdTe. In addition, CdTe is transparent to infrared radiation, not hygroscopic (like ZnS), and mechanically harder than

(Received November 1, 1994; revised February 20, 1995)

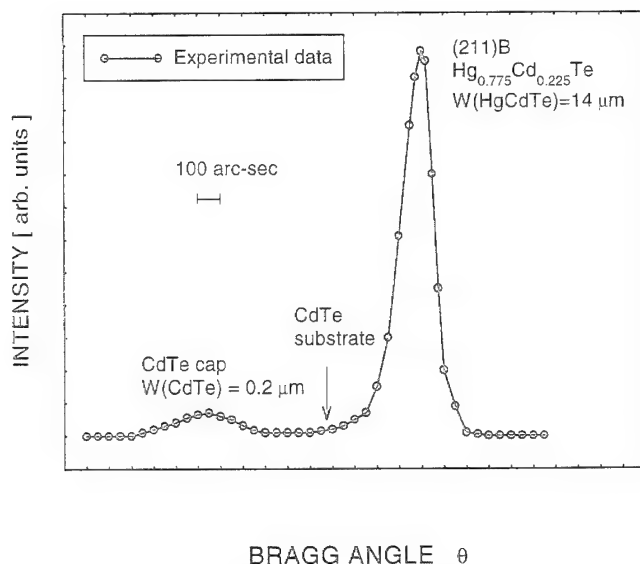


Fig. 1. Double crystal rocking curve for the CdTe/HgCdTe heterojunction indicating the CdTe cap layer peak and the HgCdTe peak. Note that the CdTe cap layer peak is shifted from the expected position because of the elastic strain at the interface caused by the lattice mismatch.

HgCdTe. Epitaxially grown CdTe on HgCdTe reduces the number of dangling bonds, leading to reduction of generation centers, recombination centers, and traps at the interface. Thus, the presence of CdTe layers can reduce surface leakage and improve diode performance. Furthermore, a graded CdTe/HgCdTe heterojunction produces an electric field in HgCdTe that pushes minority carriers away from the interface and consequently reduces the surface recombination velocity of minority carriers.

The CdTe layer can be deposited using various techniques.⁸ Practical realization of epitaxially grown CdTe/HgCdTe heterojunctions became feasible due to recent progress in molecular beam epitaxy (MBE) and metalorganic chemical vapor deposition (MOCVD). These techniques enable direct growth of high quality CdTe on top of HgCdTe in a single run. Such a procedure avoids contamination of the CdTe/HgCdTe interface by exposure to the ambient atmosphere. However, such direct, *in situ*, growth of CdTe is not always possible because additional technological steps are sometimes required before the growth of the passivation layer; for example, etching of mesa,^{2,3} or passivation of buried implanted junction in planar process¹. In such cases, the indirect CdTe passivation must be used and the HgCdTe surface preparation procedure must be taken into account.^{11,13}

Understanding the electrical properties of CdTe/HgCdTe heterostructures is essential for development of suitable photodetector passivation. Either an inversion or accumulation layer at the interface can degrade diode performance by inducing leakage currents. Therefore, it is desirable to achieve a near flat-band condition at the surface of HgCdTe. Parasitic interface charges cause energy band bending as well as increase of recombination and tunneling currents

at the surface. Consequently, a low parasitic charge density is needed at the interface. The work of Zimmermann et al.⁶ described the fundamental differences between classical dielectric passivation and semiconductor heterostructure passivation. The effect of CdTe doping on abrupt CdTe/HgCdTe heterojunctions was discussed by Sarusi et al.⁷ The effects of interface grading and valence band offset were previously analyzed,¹⁴⁻¹⁶ while the influence of the interface charges was considered by Nemirovsky et al.¹¹ The effects of metal contact to CdTe were briefly mentioned.^{6,7} Numerical modeling of CdTe/HgCdTe heterojunctions is essential for proper device design,¹⁴⁻¹⁶ in particular, the effects of carrier degeneracy, and conduction band nonparabolicity must be addressed.¹⁷⁻¹⁹ Still, the existing publications on CdTe passivation and properties of CdTe/HgCdTe interface are very limited.

In this work, we consider the electrical and structural properties of the epitaxial CdTe/HgCdTe interface from the point of view of infrared photodiode passivation. First, we discuss the material growth and device preparation procedure, followed by the experimental investigation of structural and electrical properties.

CRYSTAL GROWTH AND DEVICE PREPARATION

In this work, two types of MOCVD CdTe growth were used. In the first case, CdTe was grown directly, *in situ*, immediately following the HgCdTe growth. In the second, the MOCVD CdTe layer was grown on top of a previously grown HgCdTe layer whose surface was exposed to ambient atmosphere and subsequently subjected to a surface cleaning procedure.

In the direct process, the CdTe/HgCdTe heterostructures were grown on (211)B CdTe substrate in a horizontal reactor using the interdiffused multilayer process^{20,21} (IMP). The source materials were diisopropyltelluride (DiPTe), dimethylcadmium (DMCd), and metallic mercury. The growth temperature was 360°C and the growth rates were 3.6 and 3 μm/h for the CdTe and HgTe, respectively. Normally, a heat treatment was carried out for an additional 30 min at growth temperature in order to complete the homogenization of the HgCdTe. The p-type samples were undoped, but we cannot reject the possibility of unintentional background doping with p-type impurities. The n-type samples were obtained by a low temperature anneal of the undoped material.

In the indirect process, MOCVD (211)B or liquid phase epitaxy (LPE) (111)B HgCdTe epitaxial layers were used. Following an appropriate surface cleaning procedure, the CdTe layer was grown in the MOCVD chamber with the same growth conditions as for the direct process. Several samples of each type were prepared, with more than 20 devices on each sample.

The structure of the sample was 10 μm of either p- or n-type $\text{Hg}_{1-x}\text{Cd}_x\text{Te}$ ($x \approx 0.22$), covered by a (1000–15000) Å layer of CdTe. The surface morphology of the CdTe cap layer was mirror-like with no hillock-type

defects of any kind.

In this study, we used Schottky barrier devices, MIS capacitors, and p-n diodes to study the electrical properties of the CdTe/HgCdTe interface. Schottky barrier was formed on top of the CdTe layer by the deposition of Ti/Au. Metal insulator semiconductor capacitors were fabricated by the deposition of 3500–4000 Å of ZnS on top of CdTe, with Ti/Au used for gate metallization. Ohmic contacts were obtained by etching the CdTe layer followed by Au deposition.

Planar photodiodes used in this study were fabricated by implantation of 300 KeV boron ions through the CdTe cap layer into p-type HgCdTe active layer. This procedure was applied to devices with the directly, *in situ*, grown CdTe passivation. Consequently, the n-type implanted region, the p-type substrate, and the junction depletion region were all passivated by the CdTe cap. An additional 1 μm layer of ZnS was deposited on top of the CdTe at room temperature in order to improve the dielectric properties of the passivation.¹⁹

STRUCTURAL PROPERTIES

A number of complementary techniques were used to analyze the crystal quality and chemical composition of the samples.

The crystal quality was investigated using double crystal x-ray diffractometry (DCD). The double crystal x-ray rocking curve of a CdTe/HgCdTe (211)B structure is shown on Fig. 1. The diffraction peak of the CdTe thin film clearly demonstrates the single crystal nature of the CdTe cap layer. The diffraction peak of the substrate CdTe is missing (its approximate location is indicated by an arrow) because the HgCdTe epitaxial layer is thicker than the penetration depth of the x-rays. The angular shift of the CdTe cap layer, in respect to the CdTe substrate, reflects elastic deformation due to the lattice mismatch at the CdTe/HgCdTe interface. The grading of the CdTe/HgCdTe heterojunction causes a very broad peak corresponding to the CdTe cap layer, as can be seen in Fig. 1. Because of the strong influence of strain on DCD measurements, it was difficult to determine the difference between directly and indirectly grown samples. We found that for the growth in the (211) direction and for thickness larger than 5000 Å, the strain is relaxed, probably by misfit dislocations that relieve the stress between the cap and the HgCdTe substrate. The relationship between the CdTe thickness, strain effects, and electrical properties of MIS devices is currently being studied.

Rutherford back scattering (RBS) was used for analysis of the crystal quality of the interface between the CdTe cap layer and the HgCdTe base layer. The analyzing beam consisted of 320 KeV H^+ ions in a 165° back scattering configuration. Figure 2 shows the random and channeled spectra of 1000 Å CdTe grown on the epitaxial HgCdTe layer. The good crystallinity of the CdTe is seen by the low ratio between channeled and random spectra. Nearly the same ratio is kept in the HgCdTe area, which demonstrates the quality of

the interface. Note that there is a clear difference between the channeled spectra for LPE HgCdTe (111) and for MOCVD HgCdTe (211). A larger dechanneling rate is observed for the LPE grown samples which is evidence of a larger defect concentration at the CdTe/HgCdTe interface with LPE HgCdTe. Presently, we cannot measure differences between direct and indirect growth of CdTe because of insufficient sensitivity of the RBS technique.

The element distribution and interface grading were determined by Auger electron spectroscopy (AES). The measurements were performed in the first derivative mode by a Perkin-Elmer PHI 590A spectrometer using a primary beam of 3.0 KeV, 1 μm electrons. Depth profiles were obtained by 1.1 KeV, Ar^+ ion sputter etching with simultaneous monitoring

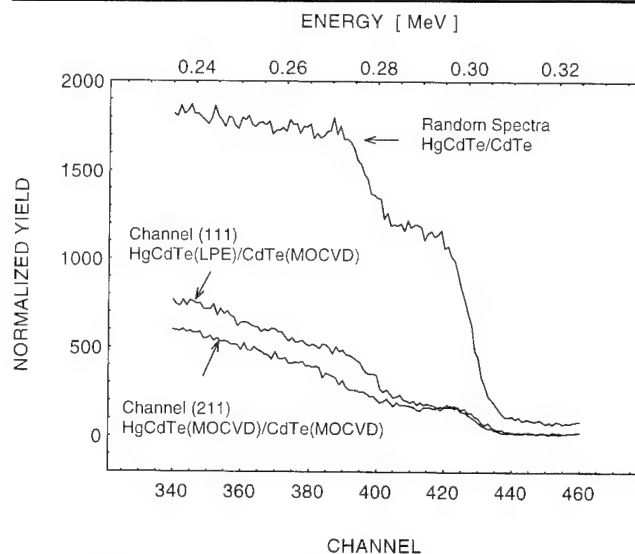


Fig. 2. Aligned and random spectra of 320 KeV of H^+ ions back scattered from CdTe/HgCdTe interface. The 1000 Å CdTe cap layer was grown by MOCVD on top of LPE or MOCVD grown HgCdTe.

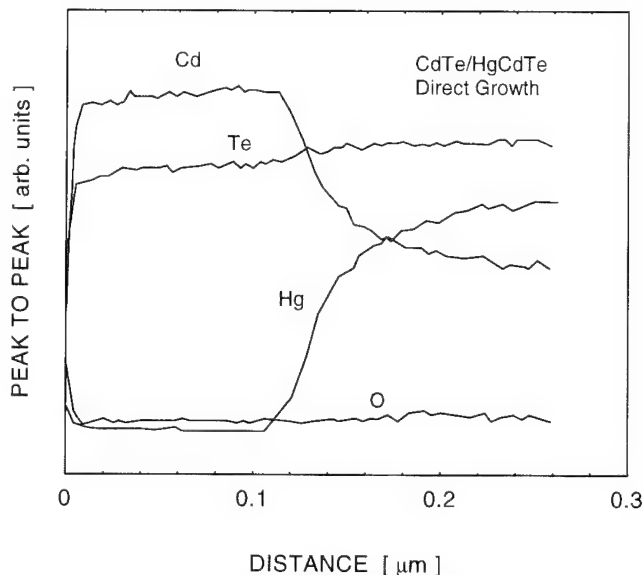


Fig. 3. Auger electron spectroscopy measurements which allow estimation of the CdTe cap layer width and the CdTe/HgCdTe interface grading.

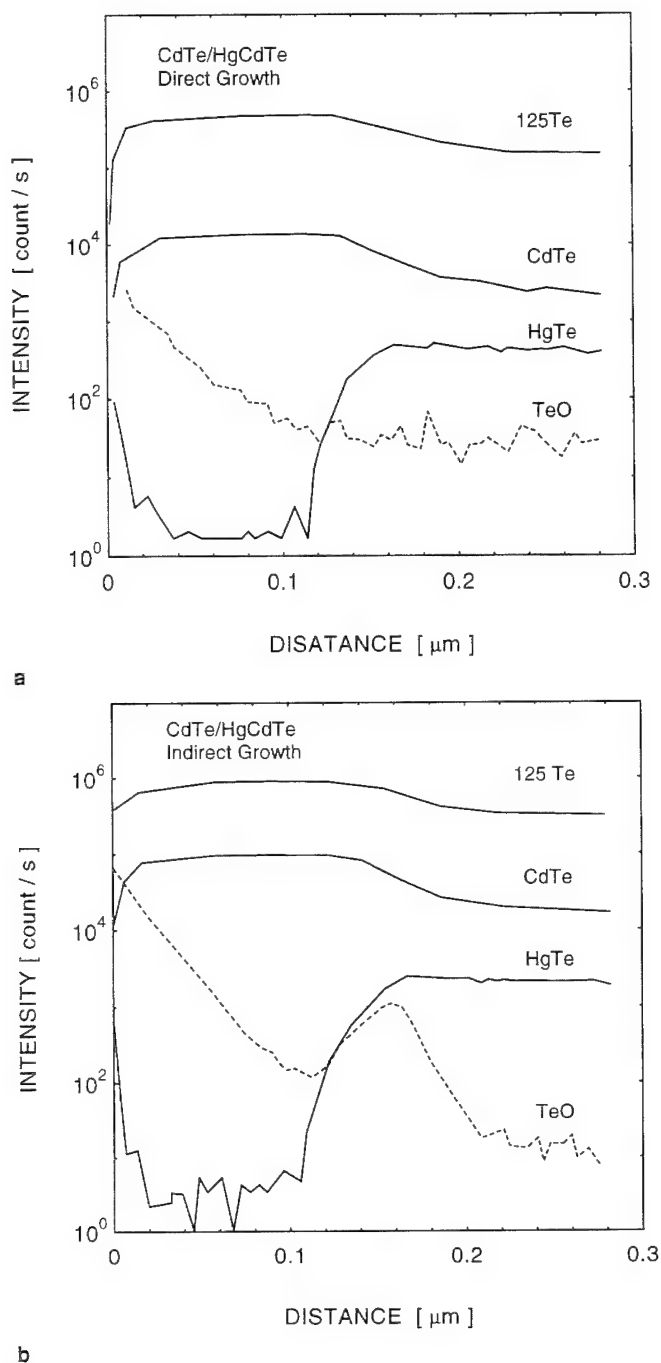


Fig. 4. Secondary ion mass spectroscopy measurements for the (a) directly and (b) indirectly grown CdTe layer. Note the oxide peak present in the indirectly grown samples which appears to be the result of the HgCdTe surface exposure to the atmosphere and subsequent surface treatment procedure.

of the peak-to-peak intensities of the corresponding Auger transitions. Figure 3 shows the composition depth profile of a characteristic CdTe/HgCdTe layer measured by AES. As can be seen in the figure, the thickness of the pure CdTe is about 1200Å while the graded region is about 800Å thick.

Secondary ion mass spectroscopy (SIMS) data were used to investigate the chemical properties of the interfaces for the different CdTe/HgCdTe growth

methods. The SIMS depth profiles were measured in a Cameca IMS4f ion microscope, using a Cs^+ primary beam with an impact energy of 14.5 KeV. The diameter of the analyzed area was 33 μm , while the primary beam was rastered over an area of $200 \times 200 \mu\text{m}^2$. Both SIMS and AES measurements were used to determine the thickness of the CdTe layer, which was around 1200Å. The width of the CdTe/HgCdTe graded region was in the 500–1000Å range, depending on the heat treatment following the crystal growth. Figure 4 shows SIMS depth profiles of directly and indirectly grown CdTe layers. An oxide peak is clearly present at the CdTe/HgCdTe interface for the indirectly grown structure, while no oxide peak was observed in samples grown by the direct method. It appears that the thin oxide layer is the result of the surface cleaning procedure prior to the CdTe growth process.¹³ The effect of this interface layer on the electrical properties of the heterostructure will be discussed later.

ELECTRICAL PROPERTIES

The effective doping and mobility were obtained from Hall measurements. The electrical characteristics of typical wafers at 77K are: $N_D = (1-5) \times 10^{15} \text{ cm}^{-3}$, $\mu_n = 6 \times 10^4 \text{ cm}^2/(\text{V}\cdot\text{s})$ for n-type, and $N_A = (1-2) \times 10^{16} \text{ cm}^{-3}$, $\mu_p = (400-600) \text{ cm}^2/(\text{V}\cdot\text{s})$ for p-type.

The impurity distribution in the immediate vicinity of the CdTe/HgCdTe interface was studied with C-V profiling of Schottky barriers.¹² This procedure also allowed us to determine the valence band offset of the heterojunction. The energy band bending at the CdTe/HgCdTe was investigated with C-V measurements of the ZnS/CdTe/HgCdTe MIS capacitors. The MIS capacitors were mounted in a dewar with a cold shield and measured at a temperature of 77K. Capacitance and conductance were measured as a function of the gate voltage using an HP4280A C-V Plotter at a frequency of 1 MHz.

The simulation of the C-V measurements was accomplished with the help of a numerical solution of the one-dimensional Poisson's equation.¹⁴⁻¹⁶ The simulation used the device and material parameters as inputs, with the fixed interface charge density assumed to be the only unknown parameter. The underlying physical model includes effects of carrier degeneracy and conduction band nonparabolicity which are necessary for a proper description of HgCdTe devices.^{12,17,18} These effects were implemented with the help of an approximation for the nonparabolic carrier concentration^{12,18} which eliminated the need for numerical evaluation of the nonparabolic Fermi-Dirac integral. The model can account for position-dependent doping, material composition, dielectric constant, electron affinity (band offsets), and interface charges. The model was used to calculate the band structure and the quasi-static small-signal capacitance of the device, assuming negligible currents and neglecting fast surface states.

The typical results of C-V measurements for the directly, *in situ*, grown CdTe layer are presented in Fig. 5. The main feature of these measurements is a

near flat-band condition, as determined from a comparison to the theoretical calculation, which implies a low density of fixed charges. We cannot be certain about the spatial distribution of the interface fixed charges; therefore, it is assumed that they are located at CdTe/HgCdTe interface. Note that the difference between the theoretical and experimental MIS C-V curves is due to the fact that the model is suitable for low frequency C-V while the measurements were performed at MHz which can be considered a high

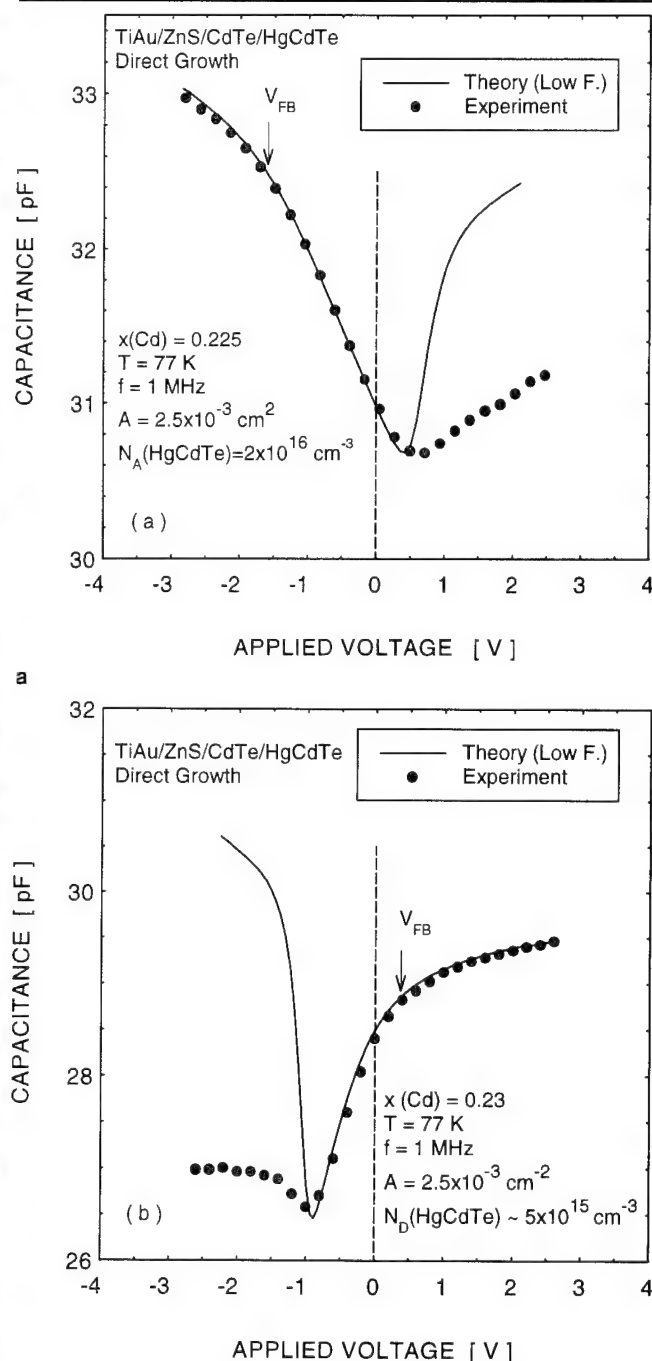


Fig. 5. The measured C-V characteristic of an MIS device with directly grown CdTe cap layer for (a) p-type and (b) n-type HgCdTe substrates. Note a near flat band position of the C-V curve.

frequency. The p-type samples, Fig. 5a, were slightly depleted with a flat-band voltage of -1.5 V. This indicates that the fixed charge density is $\sigma_i = (5 \pm 2) \times 10^{10} \text{ cm}^{-2}$, assuming the work function difference^{11,12} $\phi_{ms} \approx 0$ V between Ti and HgCdTe ($x = 0.22$). The error resulted from the flat-band voltage fluctuations for different devices. The n-type samples, Fig. 5b, indicated the fixed interface charge density of $\sigma_i = -(2 \pm 1) \times 10^{10} \text{ cm}^{-2}$. Both interfaces are characterized by a small hysteresis loop of about 0.1 V (not shown in the figure), for applied voltages between -5 to 5 V. The devices were stable with respect to temperature cycles from 77 to 370 K.

Samples with indirectly grown CdTe and n-type HgCdTe also demonstrated a nearly flat-band condition, as can be seen in Fig. 6. However, they were characterized by a significant hysteresis loop which can be explained by the presence of a large density of slow traps at the CdTe/HgCdTe interface. The surface of indirectly grown p-type samples (not presented here) was found to be slightly inverted, probably due to fixed interface charges. It appears that the observed large densities of interface traps and fixed charges are the consequence of the interruption in the growth process. This can be related to the SIMS measurements which demonstrated an oxide presence at the CdTe/HgCdTe interface for the indirectly grown samples. Consequently, it appears that the oxide at the interface causes a large density of slow interface traps which in turn causes a significant hysteresis in MIS C-V measurements. Therefore, an appropriate surface treatment procedure must be used in order to reduce the surface oxidation for indirectly grown CdTe/HgCdTe samples. This is the subject of continuing research.

The preliminary current-voltage measurements

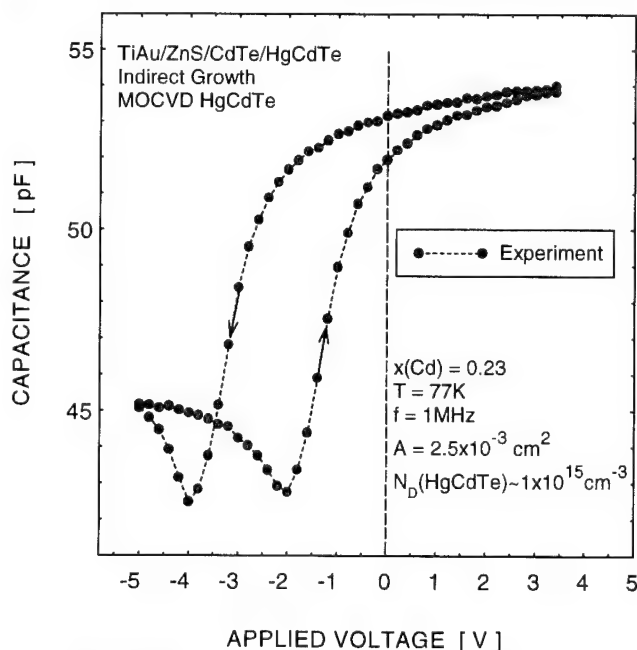


Fig. 6. Metal insulator semiconductor C-V measurements for the indirectly grown CdTe passivation on top of MOCVD HgCdTe.

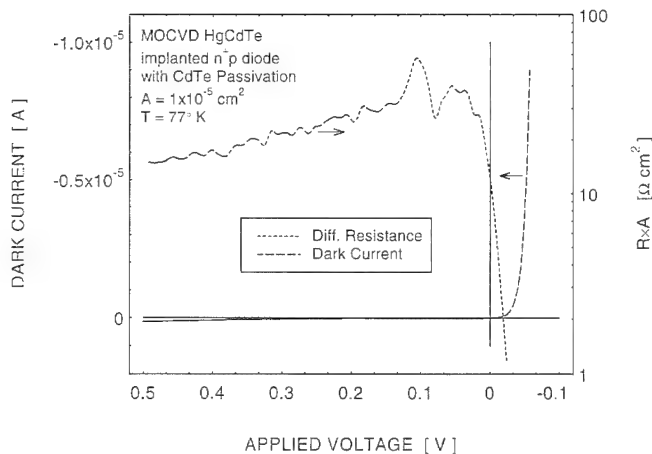


Fig. 7. The current-voltage characteristic and the dynamic resistance of an ion implanted n+p photodiode with a directly grown CdTe passivation.

were performed for photodiodes with direct CdTe passivation. In Fig. 7, we present the current-voltage and dynamic resistance characteristics of such a photodiode. Typical values of R_0A were in the range 10–20 Ωcm^2 for photodiodes with the cut-off wavelength 9.8 μm at 77K. The detailed properties of the photodiodes are currently being investigated.

CONCLUSIONS

In this study, we investigated electrical and structural properties of epitaxial CdTe layers grown as passivation on top of epitaxial HgCdTe. The DCD and RBS measurements showed good crystalline properties of the HgCdTe substrate and CdTe cap layer. Chemical properties were investigated with AES and SIMS measurements which allowed us to determine the width of the CdTe cap layer and the grading of the interface. Also, SIMS measurements showed an oxide peak at the CdTe/HgCdTe interface for indirectly grown CdTe layers. This oxide can be attributed to the HgCdTe surface exposure to ambient atmosphere and the surface preparation procedure. The C-V characteristics were measured for the TiAu/ZnS/CdTe/HgCdTe MIS heterostructure with both directly and indirectly grown CdTe layers. The test structures with directly grown CdTe demonstrated a nearly flat-band condition and a very small hysteresis. Samples with indirectly grown CdTe showed hysteresis which can be attributed to the slow interface traps caused by the oxide at the interface. The current-voltage characteristics of photodiodes with directly grown CdTe passivation were measured. We conclude that directly grown epitaxial CdTe is suitable for passiva-

tion of HgCdTe while indirectly grown CdTe on n-type HgCdTe is still acceptable, though less desirable than directly grown CdTe. It might be possible to reduce the density of the interface charges by applying an appropriate surface preparation procedure.

ACKNOWLEDGMENTS

We would like to thank A. Zohar, D. Schoenmann, S. Dolev, and N. Steinbrecher for superb technical assistance. We also thank R. Brenner and C. Cytermann for help with SIMS and Auger measurements. P. Bejerano of Soreq NRC is acknowledged for his assistance with MOCVD growth.

REFERENCES

1. J.M. Arias, J.G. Pasko, M. Zandian, J. Bajaj, L. Kozolowsky, R.E. DeWames and W.E. Tenant, *SPIE* 2228, 210 (1994).
2. P.W. Norton, P.L. LoVecchio, G.N. Pultz, J. Hughes, T. Robertson, V. Lukach and K. Wong, *SPIE* 2228, 73 (1994).
3. T. Tung, L.V. DeArmond, R.F. Herald, P.E. Herning, M.H. Kalisher, D.A. Olson, R.F. Risser, A.P. Stevens and S.J. Tighe, *SPIE* 1735, 109 (1992).
4. Y. Nemirowsky and G. Bahir, *J. Vac. Sci. Technol. A* 7, 450 (1989).
5. W.E. Tennant, C.A. Cockrum, J.B. Gilpin, M.A. Kinch, M.B. Reine and R.P. Ruth, *J. Vac. Sci. Technol. B* 10 (4), 1359 (1992).
6. P.H. Zimmermann, M.B. Reine, K. Spignese, K. Maschhoff and J. Schirripa, *J. Vac. Sci. Technol. A* 8 (2), 1182 (1990).
7. G. Sarusi, G. Cinander, A. Zemel, D. Eger and Y. Shapira, *J. Appl. Phys.* 71, 5070 (1992).
8. Y. Nemirowsky, N. Mainzer and E. Wieww, *Narrow-Gap Cadmium Based Component*, ed. P. Copper, (EMIS/IEEE, 1994).
9. Yuan, L. He, J. Yu, M. Yu, Y. Qiao and J. Zhu, *Appl. Phys. Lett.* 58, 914 (1991).
10. H. Tregilgas, C.-F. Wan and H.-Y. Liu, *J. Electron. Mater.* 22, 821 (1993).
11. Y. Nemirowsky, N. Amir and L. Djaloshinski, *J. Electron. Mater.* 24, 647 (1995).
12. V. Ariel, V. Garber, G. Bahir and A. Sher, *J. Electron. Mater.* 24, 655 (1995).
13. M. Seelmann-Eggebert, G. Carey, V. Krishnamurthy and C.R. Helms, *J. Vac. Sci. Technol. B* 10 (4), 1297 (1992).
14. P.R. Bratt and T.N. Casselman, *J. Vac. Sci. Technol. A* 3 (1), 238 (1985).
15. P. LoVecchio, M.B. Reine and M.N. Grimbergen, *J. Vac. Sci. Technol. A* 3 (1), 247 (1985).
16. F.L. Madarasz and F. Szmulowicz, *J. Appl. Phys.* 62 (8), 3267 (1987).
17. R. Dornhaus and G. Nimtz, *Springer Tracts in Modern Physics* (Berlin: Springer, 1983).
18. V. Ariel-Altschul, E. Finkman and G. Bahir, *IEEE Trans. Electron Dev.* ED-39, 1312, (1992).
19. G. Bahir, V. Ariel, V. Garber and A. Sher, *Appl. Phys. Lett.* 58, 828 (1991).
20. K. Ghandi, K.K. Parat, H. Ehsani and I. Bhat, *Appl. Phys. Lett.* 58, 828 (1991).
21. G. Cinader, A. Raizman and A. Sher, *J. Vac. Sci. Technol. B* 9, 1634 (1991).
22. R.L. Strong, *J. Vac. Sci. Technol. B* 10 (4), 1530 (1992).

Characterization of CdTe for HgCdTe Surface Passivation

L.O. BUBULAC,* W.E. TENNANT,* J. BAJAJ,* J. SHENG,† R. BRIGHAM,†
A.H.B. VANDERWYCK,* M. ZANDIAN,* and W.V. MC LEVIG*

*Rockwell Science Center, Thousand Oaks, CA

†Charles Evans & Associates, Redwood City, CA

The objectives of this work are to study the physical and chemical structure of CdTe films using secondary ion mass spectrometry (SIMS) and atomic force microscopy (AFM) and to demonstrate the usefulness of these analytical techniques in determining the characteristics of CdTe-passivation films deposited by different techniques on HgCdTe material. Three key aspects of CdTe passivation of HgCdTe are addressed by different analytical tools: a) morphological microstructure of CdTe films examined by atomic force microscopy; b) compositional profile across the interface determined by Matrix (Te)—SIMS technique; c) concentration of various impurities across the CdTe/HgCdTe structure profiled by secondary ion-mass spectrometry.

Key words: Atomic force microscopy, CdTe passivation, HgCdTe, molecular beam epitaxy (MBE), secondary ion mass spectrometry (SIMS)

INTRODUCTION

CdTe passivation of HgCdTe infrared detectors has become the standard approach in the infrared industry.¹ Various techniques are being used to deposit CdTe films on mesa or planar device structures.²⁻⁴ Studies addressing some aspects of CdTe passivation have been published.⁵⁻⁸ More work is needed to fully understand and control the passivation process. While this approach yields excellent results, surface passivation appears to limit diode operability to some degree for all device architectures and at all wavelengths.

Structurally, the thin passivation film should be a high density, stoichiometric, conformal coating with minimal (zero) pin hole type defects. It should adhere

well to the HgCdTe material and should have a surface suitable for stable metallization. The film should have minimal stress to ensure its stability after several thermal cycles. It should be bakeable at $>150^{\circ}\text{C}$ and should withstand the subsequent steps of device processing. Electrically, the passivation procedure should provide a low density of fixed charges at the interface. The goal is to reduce the interface fixed charge density below $10^{11}/\text{cm}^2$ and obtain near flatband surface potential conditions.

Another key requirement is that, both structurally and electrically, the passivation layer be spatially uniform. One of the more exacting tests of a good passivation is in device performance at low temperature and low background, and in the device tolerance to ionizing radiation environment.

Texas Instruments group⁸ has observed that thermal annealing removes the passivation problem due

(Received February 10, 1995)

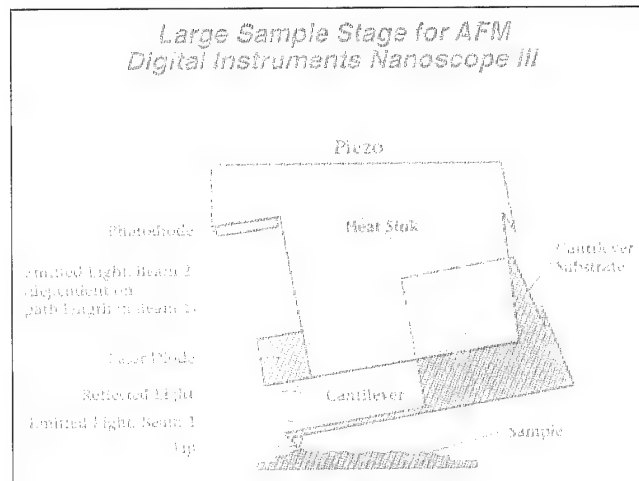


a

to the interdiffusion that occurs in the CdTe/HgCdTe interface. The assumption is that the thermally induced compositional grading near the interface occurs such that the HgCdTe 'electrical' surface is shifted away from the initial defective interface in a relatively benign wider gap region. This interdiffusion should then lead to devices that are thermally stable and do not degrade with time. The conclusion of this work was that a thermally interdiffused HgCdTe/CdTe interface leads to a reproducible improvement in passivation, irrespective of the growth method used for CdTe.

The objectives of this work are to examine the physical and chemical structure of a variety of CdTe passivation films using secondary ion mass spectrometry (SIMS) and atomic force microscopy (AFM). Three key aspects of CdTe passivation of HgCdTe are addressed:

- morphology of CdTe film;
- compositional profile across the interface; and



b

Fig. 1. Atomic force microscopy provides new insight to CdTe surfaces: (a) Si-tip and (b) large sample stage for AFM Digital Instruments NanoScope III.

- impurities at the interface and in CdTe films.

We present the comparative results of passivation of LPE—HgCdTe with CdTe films deposited by electron-beam deposited at room temperature and molecular beam epitaxy (MBE) at 90°C.

ANALYTICAL METHODS

Different analytical tools have been used to address three key aspects of CdTe passivation of HgCdTe:

- Atomic force microscopy to examine the morphological microstructure of CdTe films;⁹
- Matrix (Te)—SIMS to determine the compositional profile across the interface;¹⁰
- Secondary ion-mass spectrometry to profile the concentration of various impurities across the CdTe/HgCdTe structure.^{11,12}

New insight into CdTe surfaces is gained by applying the AFM technique to CdTe/HgCdTe structures. This technique allows microstructure assessment of very fine spatial features. The magnitude of roughness becomes graphically evident on a few tenths of angstroms scale in the vertical direction, and a few tens of angstroms in the x-y plane.

The AFM analyses were performed by using a Digital Instruments NanoScope III in Tapping Mode. The configuration of the Tapping Mode tip assembly used to sense the sample surface is shown in Fig. 1. By this method, a 3D image of the surface of a sample is compiled by scanning an etched silicon tip (Fig. 1a) across the surface while the tip and its supporting cantilever (Fig. 1b) are oscillated at their resonant frequency (which is on the order of a few hundred kilohertz). The cantilever substrate is vibrated to a frequency set by the user to coincide with the resonant frequency of the cantilever. The position of the tip is detected by the beam (beam 1) emitted by the laser diode. A portion of this beam is reflected by the cantilever back into the laser. The resulting interference causes laser output fluctuations that are dependent on the tip position. These fluctuations are

As Deposited CdTe Films

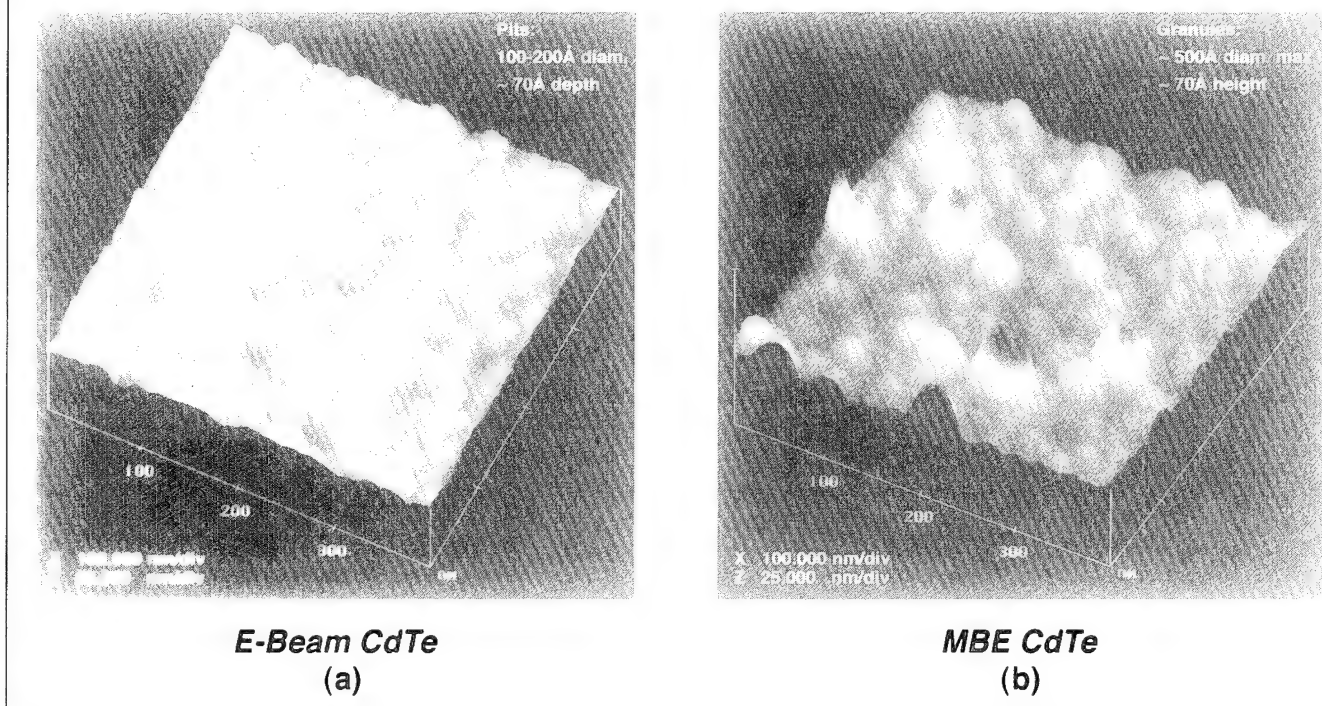


Fig. 2. Morphological microstructure of CdTe depends on the deposition technique: (a) AFM perspective view (3D) for e-beam CdTe, and (b) same for MBE CdTe.

detected by a photodiode monitoring the back side emission (beam 2) of the laser. The signal from the photodiode is used in a feedback loop for a vertical adjustment of the tip position.

The tip is scanned in the x-y plane as it oscillates in z direction. When the tip touches the sample surface, a damping of the oscillation of the tip occurs. A 3D image of the surface is constructed by recording the feedback signal from the photodiode to the tip to maintain a small and constant degree of damping during the surface scan.

The resolution of the surface features in AFM techniques is high. Vertical resolution is controlled by instrument design and is on the order of a few tenths of an angstrom. Lateral resolution is determined by the sharpness of the tip, and it can be less than 50Å. The tips are about 7 μm long and can render slopes as steep as 75° from the horizontal. The resolution of pits on the surface depends on the shape of Si tip and on the diameter of the pit. Typically, the depth measurement of a pit with 70–100Å in diameter will be limited to ~100Å. Because only very slight damping of the tip oscillation is required, tip pressure of only a few tenths of a nanonewton (with almost no lateral component) is imparted to the sample, which is compatible with soft materials like CdTe and HgCdTe.

MATERIALS, SAMPLE PREPARATION, AND CdTe DEPOSITION

Sample preparation conditions represent a range of current deposition technique. The material used

throughout this work was a single layer LPE $\text{Hg}_{1-x}\text{Cd}_x\text{Te}$ grown on CdZnTe substrate. Single layer HgCdTe material was chosen to avoid the complication of the double layer interface. The x-value for this work was ~0.26; however, the findings apply to HgCdTe material with any composition. The passivation film was CdTe. We have used two different techniques to deposit CdTe; the electron-beam deposition at room temperature with a deposition rate of 1.5–2Å/s and MBE deposition at higher temperature (80–90°C) with a growth rate of 2.8Å/s. The thickness of the e-beam deposited CdTe was ~0.8 μm and of MBE deposited CdTe was ~1.2 μm .

Two different samples of each deposition were characterized, one of each more extensively. The HgCdTe samples were prepared by a chemical etch process in 0.2% Br-methanol solution. Samples from each CdTe deposition (e-beam and MBE) were analyzed in various conditions: as-deposited as well as heat treated in a low-temperature anneal (250°C/10 h) and in a high-temperature anneal (430°C/15 min). The anneal was performed in an open-tube apparatus with saturated partial pressure of Hg and with a partial pressure of H_2 .

ANALYSIS RESULTS

Atomic Force Microscopy

This technique⁶ is used to determine the film morphology and density and to detect cracks, hillocks, pits, and other microscopic defects. Atomic force

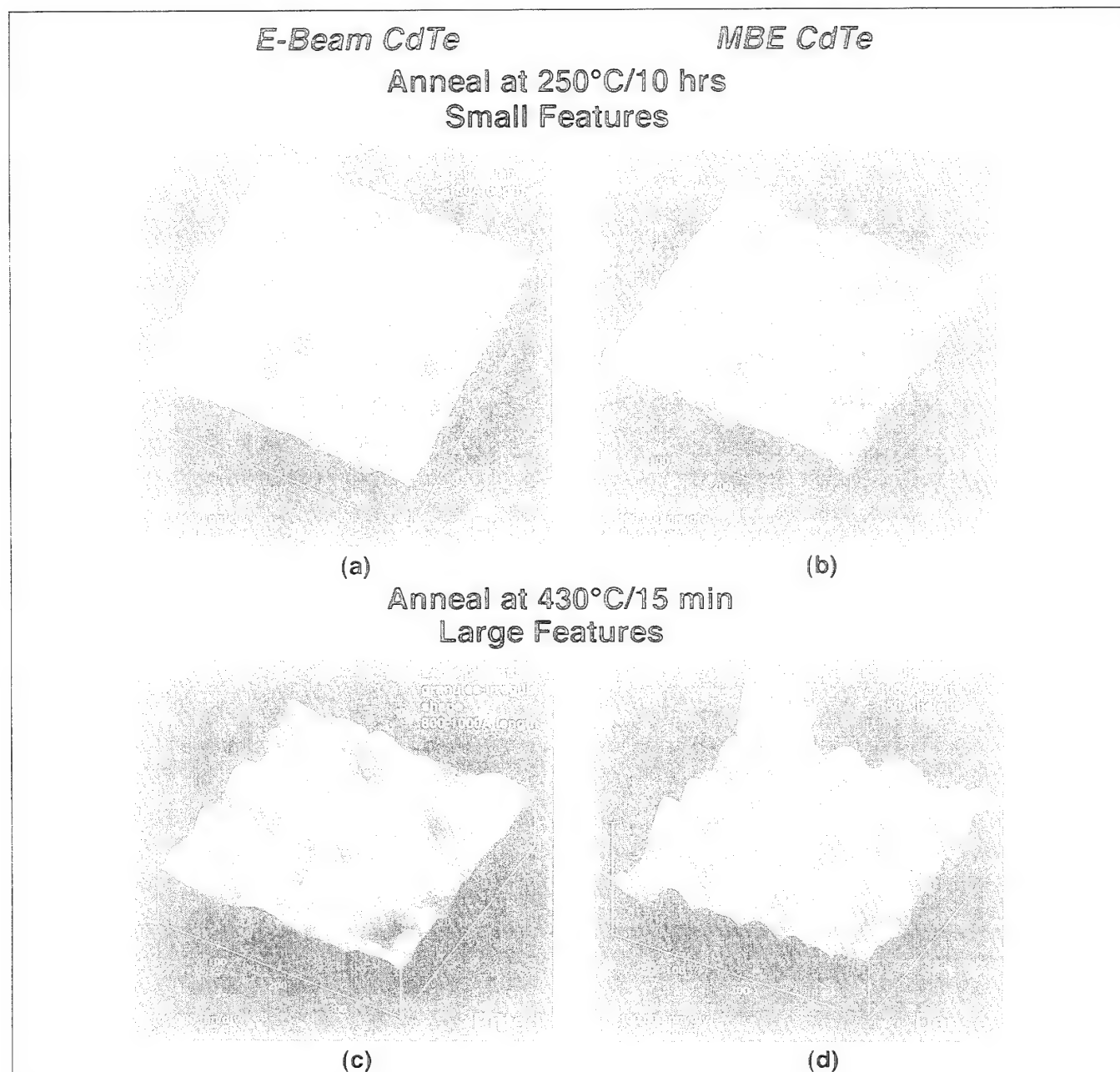


Fig. 3. Post deposition annealing significantly changes the structure in both e-beam and MBE CdTe: (a), (b) AFM perspective view (3D) for e-beam, and (c), (d) same for MBE CdTe.

microscopy of CdTe/HgCdTe passivation shows large variations in morphology for various films.

Typical perspective 3D images are shown in Fig. 2, for e-beam deposited CdTe (Fig. 2a) and for MBE deposited CdTe (Fig. 2b). From the image section analysis⁹ of these AFM images, we have obtained information about the type of features present on the surface and about their size. Morphological structure of CdTe film was observed to depend on the deposition method, e-beam at room temperature vs MBE at 90°C. The data shows features mostly of pit type in e-beam CdTe films (Fig. 3a) and of hillocks type in MBE (90°C) CdTe films. The e-beam CdTe film (Fig. 2a) appears to be relatively smoother but less dense.

The typical size of the pits in e-beam CdTe was 100–200Å in diameter with a depth of ~70Å. Relatively larger granules were observed in MBE CdTe (Fig. 2b), ~500Å in height and ~60Å in diameter.

Post deposition anneal significantly changes the structure of the CdTe film in both e-beam and MBE CdTe. The surface AFM results, from the annealed samples with CdTe deposited by both techniques, are shown by perspective (3D) views and by the data of the section analysis in Fig. 3. Low temperature (250°C) annealing results are shown in Fig. 3a for e-beam CdTe and in Fig. 3b for MBE CdTe. It becomes evident that even the low temperature annealing caused significant modification in the surface structure. In e-

beam CdTe the formation of pit-type defects is enhanced; the film becomes more pitted. Section analysis showed relatively deeper pits, of $\sim 1500\text{\AA}$ diameter, compared to as-deposited sample in Fig. 2a. In contrast, the MBE CdTe appears reproducibly a higher density film. High temperature annealing, shown in Fig. 3c for e-beam CdTe and in Fig. 3d for MBE CdTe, changes the microstructure more drastically by increasing the feature size in both types of CdTe; pits or irregularly shaped granular features of $\sim 1000\text{\AA}$ in length in the x-y plane are typical. E-beam CdTe (Fig. 3c) becomes even more pitted, while MBE CdTe (Fig. 3b) remains a much denser film. In the last case, the recrystallization that occurs increases the size of the crystallites without inducing pitting.

Surface preparation of HgCdTe samples induces changes in the microstructure of CdTe films deposited by both techniques. In the example of e-beam CdTe, shown in Fig. 4, all the deposition conditions were nominally the same as for e-beam sample in Fig. 2a, except for relatively longer ambient exposure to air (3 vs 0.5 h). The data show increase in feature size and relatively deeper pits compared to the relatively shorter time (Fig. 2a). Elongated pits of $\sim 1500\text{\AA}$ long and $\sim 200\text{\AA}$ deep (perhaps due to coalescence of small pits during deposition) were observed. The decrease in the film structural quality was confirmed by electrically short MIS devices built on sample shown in Fig. 4 vs MIS built on samples shown in Fig. 2 which were electrically good.

Atomic force microscopy analysis revealed that from the two types of CdTe films that were investigated, CdTe deposited by MBE at $\sim 90^\circ\text{C}$ appears to be a better film in terms of density and annealing

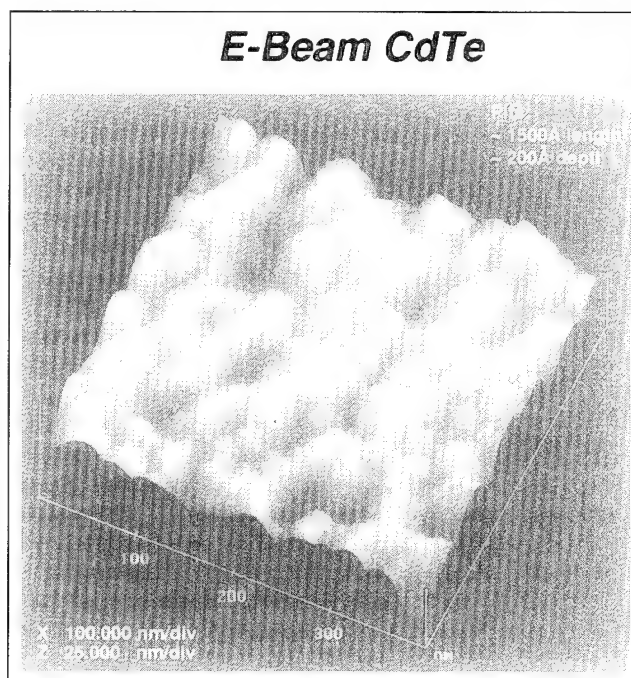


Fig. 4. E-beam CdTe microstructure depends on surface preparation: AFM perspective view (3D) for relatively longer ambient exposure.

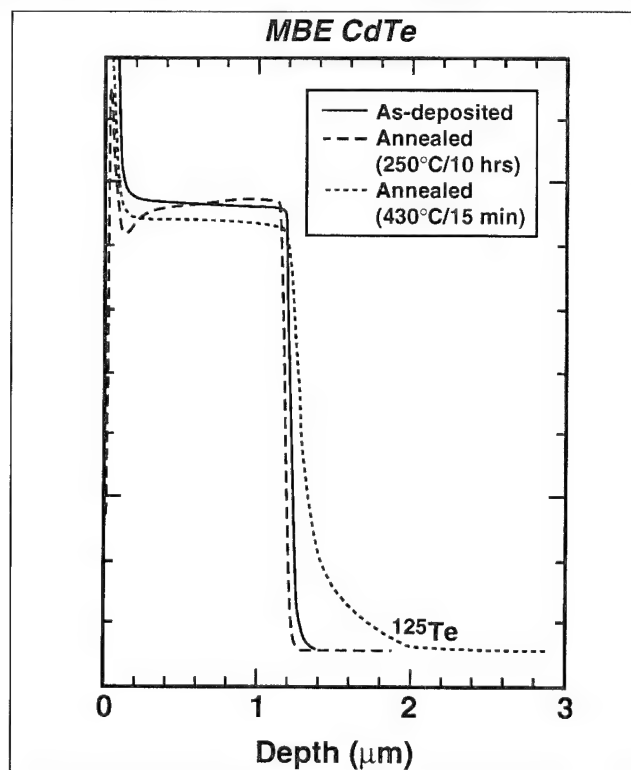
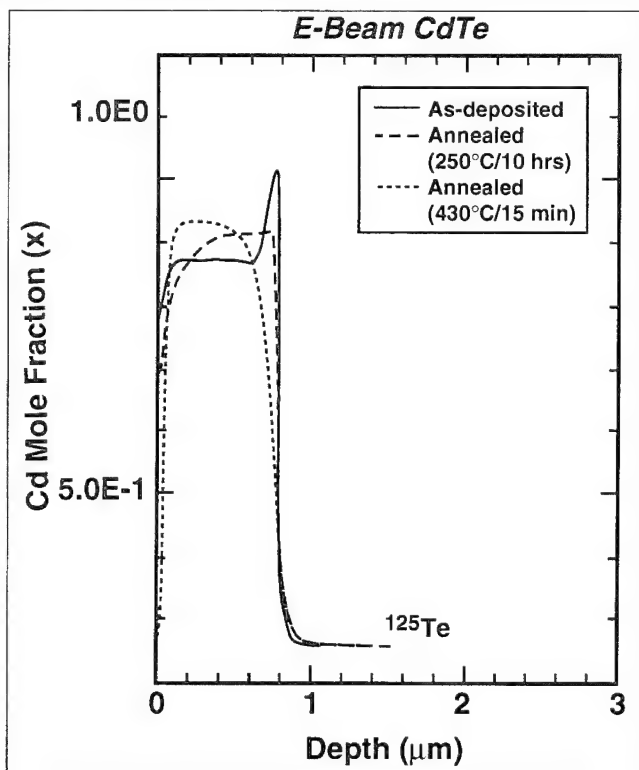


Fig. 5. Compositional depth profiles from SIMS-Matrix (Te) reveal the dependence of the interface on CdTe characteristics: (a) SIMS compositional profile across the interface for e-beam CdTe (solid line—as deposited, dashed line— 250°C anneal, dotted line— 430°C anneal), and (b) same for MBE CdTe.

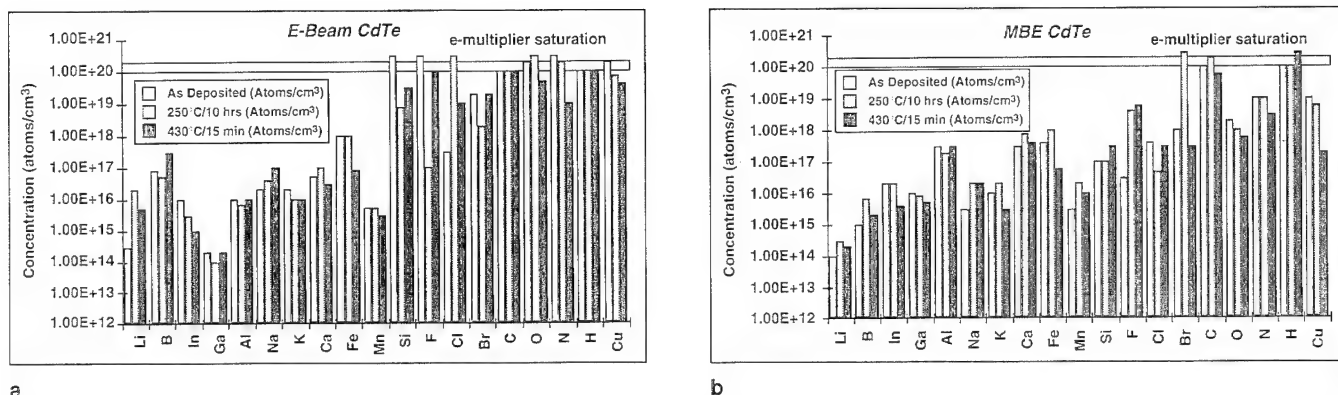


Fig. 6. Impurity gettering at the interface was observed regardless of CdTe-deposition techniques and annealing conditions: (a) spikes of various elements determined by SIMS for e-beam CdTe (open columns—as deposited, grey columns—250°C anneal, dark columns—430°C anneal), (b) same for MBE CdTe.

capability.

Matrix (Te)-SIMS

Compositional depth profiles across the CdTe/HgCdTe interface are determined from ^{125}Te -SIMS analytical technique.⁶ In this technique, the ion yield of ^{125}Te -matrix element, taken with Cs-primary ion beam, is in a linear relationship with Cd mole fraction. The data shown in Fig. 5 reveal the dependence of the interface on the CdTe thin film characteristics. In the as-deposited CdTe/HgCdTe samples, a significant difference is noticed: a Te^{125} peak occurs at the interface in e-beam deposited CdTe case (Fig. 5a—solid line), as opposed to MBE CdTe (Fig. 5b—solid line), which is flat. This feature suggests more defects in the e-beam CdTe/HgCdTe interface, possibly Cd deficiency. The low temperature anneal (250°C/10 h) seems to remove ^{125}Te -peak from the e-beam CdTe case (Fig. 5a—dashed line). In the case of MBE CdTe, no significant changes are observed (Fig. 5b—dashed line). High temperature anneal (430°C/15 min) causes a significant change in the interface for both cases. In the e-beam CdTe samples (Fig. 5a—dotted line), changes occur mainly in the thin CdTe layer, and no significant band gap change in HgCdTe is observed. Pitted e-beam CdTe and a more defective interface cause Hg diffusion into CdTe, but no Cd diffusion into HgCdTe occurs to change the material bandgap. In the MBE CdTe samples (Fig. 5b—dotted line), a classical interdiffusion profile was observed in the HgCdTe layer. The results of this analysis show that the diffusion of matrix components depends on deposition method; CdTe deposited by MBE technique at 90°C appears to be more predictable in terms of interdiffusion behavior, and therefore it can be designed to shift the “electrical” interface deeper than the initial defective interface.

SIMS-Impurity Profiling

Secondary ion mass spectrometry was used to determine the impurity content at the CdTe/HgCdTe interface and in the CdTe layer. Several elements were depth-profiled across the interface by using both O—primary ion beam (Li, B, In, Ga, Al, Na, K, Ca, Fe,

Mn) and Cs-primary ion beam (Si, F, Cl, Br, C, O, N, H, Cu).

Comparative results are shown in Fig. 6 for e-beam (Fig. 6a) and MBE (Fig. 6b) CdTe for all three conditions: as-deposited (open columns), low temperature anneal (250°C) (grey columns), and high temperature anneal (430°C) (black columns). All the analyzed elements exhibit spikes at the interface in both cases. Some spikes were very high and saturated the electron-multiplier, which implies a concentration level in the range of $(1-3) \times 10^{20}/\text{cm}^3$. The estimation takes into account the calibration errors of high levels due to electron multiplier saturation and matrix effects at the interface. Although the SIMS detection limit is different for every element,¹³ as well as the machine background at the time of the experiment, each mentioned spike rose well above the background level, and therefore the shown spike concentration is real. Basically, the spike concentrations are similar in both types of samples for all the sample conditions. The layer coverage can be calculated either by integrating under the peak, or by considering an average thickness of the peak of 200–300 Å (the sampling period for one element). In the later case, concentrations in the range higher than $10^{19}/\text{cm}^3$ translate into a full monolayer coverage. Lower concentrations correspond to submonolayer coverage. Additional data (not shown in the figure) taken from samples with variation in surface preparation indicate lower levels of some elements (e.g., C, O, H, N) in MBE CdTe films by ~2–3 orders of magnitude vs e-beam CdTe. The results from SIMS analysis indicate, therefore, that regardless of the deposition technique of CdTe and of the post-deposition anneal, the impurity spikes at the interface occur and that the levels depend on how the surface is prepared.

The ex situ surface preparation involves handling, chemical etching, and ambient exposure of the sample, which are potential sources for the impurities gettering at the interface. Higher concentration in e-beam CdTe in some cases can also occur after the anneal; the interface can getter impurities from the background impurities in HgCdTe layer, and from the CdTe thin layer (which can come from the evaporation process).

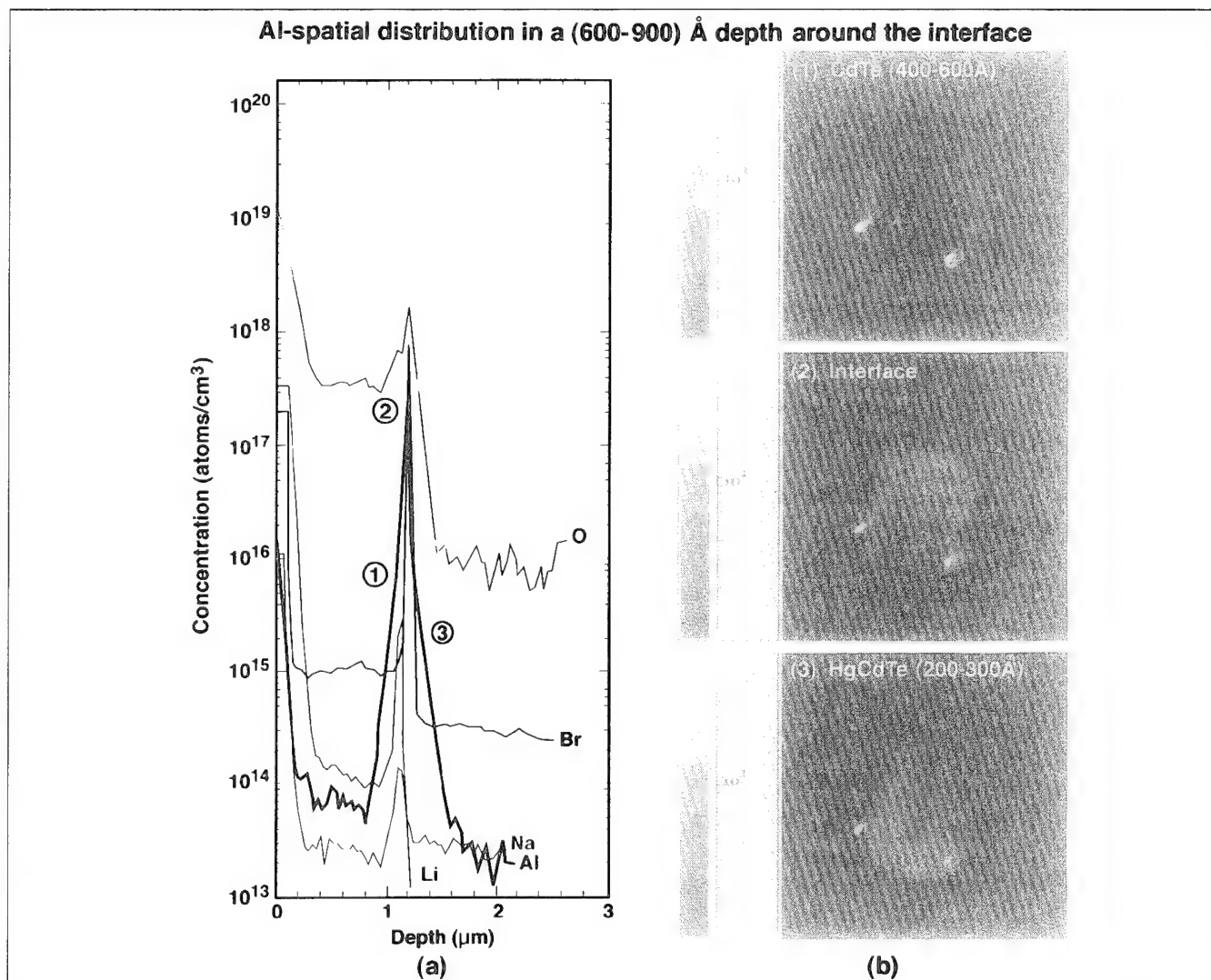


Fig. 7. Spatial distribution of impurity spikes at the interface is nonuniform as revealed by SIMS for e-beam CdTe: (a) Al-depth profile—SIMS, (b) Al-imaging—SIMS.

The impurity spikes should be correlated in further experiments with the density of the fixed charges at the interface.

The spatial distribution of impurity spikes at the interface appears to be spatially nonuniform as revealed by SIMS imaging technique. The example of Al is shown in Fig. 7 by SIMS depth profiling (Fig. 7a) and by SIMS imaging (Fig. 7b) taken in a depth range of 600–900Å around the interface: (1) into CdTe before the interface (400–600Å); (2) in the interface, and (3) beyond the interface (200–300Å) toward the HgCdTe layer.

The regions at the interface with high concentrations of impurities may act as sources for diffusion of impurities into the HgCdTe layer. The consequences of impurity penetration into HgCdTe may be very important. When band gap widening, as shown in the MBE-CdTe case (Fig. 5b), is deeper than the impurity penetration, then the interdiffusion obtained in annealing may shift the HgCdTe “electrical” surface in a more benign region. This may alleviate problems

associated with the variability in chemical etching and surface exposure to the ambient. However, in some cases, impurity penetration is deeper than compositional interdiffusion, as in e-beam CdTe in Fig. 7a, causing defects in HgCdTe layers. An example is shown by Al which penetrates into HgCdTe to a depth of $\sim 0.2 \mu\text{m}$ at a concentration of $\sim 10^{15}/\text{cm}^3$.

The interaction of impurity spikes with the defects deserves further investigation. From the high concentration regions at the interface, “short circuit” diffusion of impurities can occur relatively deeper through channels provided by structural defects in the material and eventually reach the junction region. In this case, not only the passivation is affected by the impurities at the interface, but the bulk junction as well.

It is possible to obtain a clean interface in a double layer structure. The results from an LPE double layer in situ growth, with a difference in x-value from ~ 0.34 in the cap layer to ~ 0.225 in the base layer, are presented in Fig. 8. This example shows no gettering of impurities at the interface.

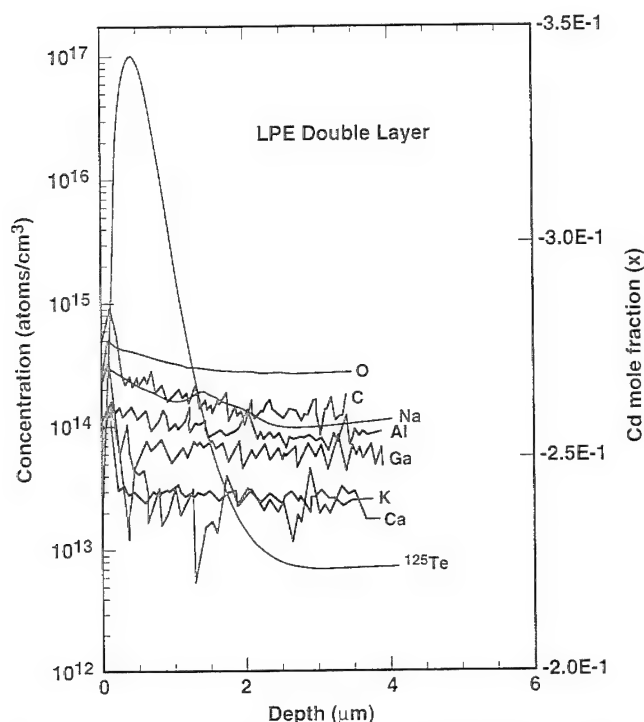


Fig. 8. In situ grown double layer structures show no impurity gettering—as revealed by SIMS impurity depth profiling.

SUMMARY AND CONCLUSIONS

Atomic force microscopy reveals differences in CdTe microstructure due to deposition technique (MBE at 90°C vs E-Beam at room temperature), surface preparation, and post-deposition annealing conditions. Deposition method appears to affect the interdiffusion characteristics of the matrix components. Interfaces exhibit impurity spikes regardless of deposition technique and post deposition annealing. Spatial distribution of impurities at the interface is nonuniform.

The initial surface condition appears to affect the CdTe characteristics. Molecular beam epitaxy CdTe deposited at 90°C appears to be a relatively denser film, more thermally stable, and to have a predictable interdiffusion behavior in the post deposition anneals.

ACKNOWLEDGMENTS

We thank Dr. K. Vural for technical support.

REFERENCES

1. W.E. Tennant, C.A. Cockrum, J.B. Gilpin, M.A. Kinch, M.B. Reine and R.P. Ruth, *J. Vac. Sci. Technol. B* 10, 1359 (1992).
2. S.M. Johnson, D.R. Rhiger, J.P. Rosbeck, J.M. Peterson, S.M. Taylor and M.E. Boyd, *J. Vac. Sci. Technol. B* 10, 1499 (1992).
3. J.M. Arias, J.G. Pasko, M. Zandian, S.H. Shin, L.O. Bubulac, R.E. DeWames and W.E. Tennant, *J. Electron. Mater.* 22, 1049 (1993).
4. J. Bajaj, J.M. Arias, M. Zandian, J.G. Pasko, L.J. Kozlowski, R.E. DeWames and W.E. Tennant, *J. Electron. Mater.* 22, 1067 (1995).
5. Y. Nemirovsky, N. Mainzer and E. Weiss, *Narrow-Gap Cadmium-Based Components*, ed. P. Copper, (EMIS/IEEE).
6. G. Sarusi, G. Cinadar, A. Zemel, D. Eger and Y. Shapira, *J. Appl. Phys.* 71, 5070 (1992).
7. Y. Nemirovsky, N. Amir and L. Djaloshinski, to be published in *J. Cryst. Growth*, 1994.
8. J.H. Tregilgas, C.-F. Wan, A.M. Turner, P.B. Smith, R.L. Strong, R.S. List, H.-D. Shih, T.W. Orent, H.F. Schaaake, M. Bevan and D.U. Bartholomew, unpublished.
9. Rama L. Hdy, Mark A. Chonko and Philip J. Tobin, The Electrochem. Soc. Spring Meeting, Honolulu, Hawaii, May 16–21, 1993, *Ext. Abs.* 383, Vol. 93-1.
10. L.O. Bubulac, D.D. Edwall, J.T. Cheung and C.R. Viswanathan, *J. Vac. Sci. Technol B* 10 (4), 1633 (1992).
11. R.J. Blattner and C.A. Evans, Jr., *Scanning Electron Microscopy/1990/IV-Sem. Inc.*, (AMF O'Hare, Chicago, 1990), p. 200.
12. R.G. Wilson, F.A. Stevie and C.W. Magee, *Secondary Ion Mass Spectroscopy* (New York: Wiley, 1989).
13. Robert G. Wilson, Fred A. Steve and Charles W. Magee, *Secondary Ion Mass Spectrometry*, (New York: John Wiley & Sons, 1989).

Bake Stability of Long-Wavelength Infrared HgCdTe Photodiodes

A. MESTECHKIN, D.L. LEE, B.T. CUNNINGHAM, and B.D. MAC LEOD

Raytheon Company, Research Division, Lexington, MA 02173

The bake stability was examined for HgCdTe wafers and photodiodes with CdTe surface passivation deposited by thermal evaporation. Electrical and electro-optical measurements were performed on various long-wavelength infrared HgCdTe photodiodes prior to and after a ten-day vacuum bakeout at 80°C, similar to conditions used for preparation of tactical dewar assemblies. It was found that the bakeout process generated additional defects at the CdTe/HgCdTe interface and degraded photodiode parameters such as zero bias impedance, dark current, and photocurrent. Annealing at 220°C under a Hg vapor pressure following the CdTe deposition suppressed the interface defect generation process during bakeout and stabilized HgCdTe photodiode performance.

Key words: HgCdTe photodiodes, long-wavelength infrared (LWIR) detectors, thermal annealing

INTRODUCTION

Surface passivation of HgCdTe p/n heterojunction photodiodes by thermal evaporation of CdTe has the advantages of simple operation, excellent run-to-run reproducibility, and low capital equipment requirement. The developed and implemented passivation process provides bulk defect limited photodiode performance with an excellent R_0A product at 77K close to the diffusion limit.¹⁻³ However, devices passivated by this technique have a tendency to degrade after an 80°C, 240 h vacuum bakeout. Analysis shows that defects, possibly electrically active Hg vacancies, generated by the bakeout process at the CdTe/HgCdTe interface are responsible for this degradation. This effect has been eliminated by the use of a post-passivation anneal at 220°C under Hg vapor pressure which, it is believed, inhibits the generation of Hg vacancies.

DEVICE FABRICATION AND TESTING

LPE Grown Photovoltaic HgCdTe Devices

Heterojunction photodiode test structures were fabricated on a liquid phase epitaxy (LPE) grown wafer

following the standard process, included CdTe passivation deposition with substrate at room temperature. A second portion of this wafer was processed with an additional Hg anneal after passivation step with substrate at 155°C. This wafer consisted of an LPE grown In-doped n-type HgCdTe layer ($1 \times 10^{15} \text{ cm}^{-3}$ donor concentration) capped by a 1 μm thick p-type layer of wider bandgap ($x = 0.300$) and with an acceptor concentration of $5 \times 10^{17} \text{ cm}^{-3}$. The cutoff wavelength of the diodes was $\lambda_c = 10.1 \mu\text{m}$. One type of test die consisted of variable area square photodiodes with mesa side lengths varying from 22 to 250 μm . Another die contained a mini-array of identical diodes (22 μm mesa-side). A metal insulator semiconductor (MIS) capacitor, formed by a $500 \times 200 \mu\text{m}$ field plate over the n-layer with the CdTe passivation as the insulator, was also used in the characterization.

For the photodiodes, DC dark current measurements were performed with an HP 4141B DC source/monitor. AC photo-response measurements were performed using an Electro-Optical Industries, Inc., black-body radiation source (Model WS143) operated at a temperature of 500K and chopped at a frequency of 41.5 Hz. The signal was amplified by an EG&G 114 Signal Conditioning Amplifier and stored with a Tektronix 7854 digitizing oscilloscope. Spectral response was performed with an Optronics Laborato-

(Received October 4, 1994; revised April 29, 1995)

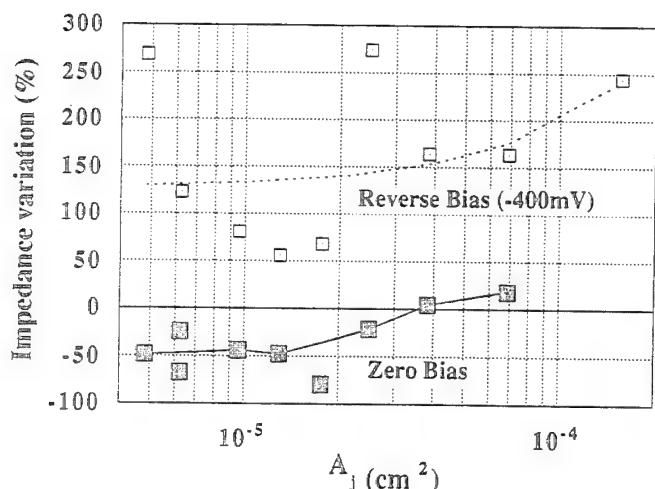


Fig. 1. Standard process sequence. Impedance variation after bakeout 240 h at 80°C.

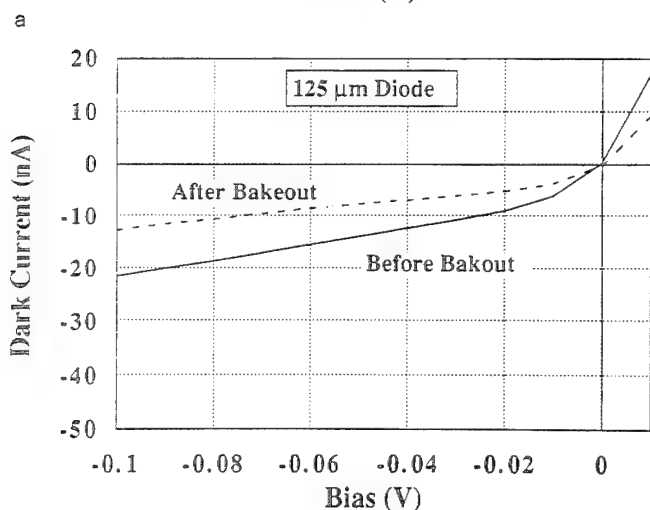
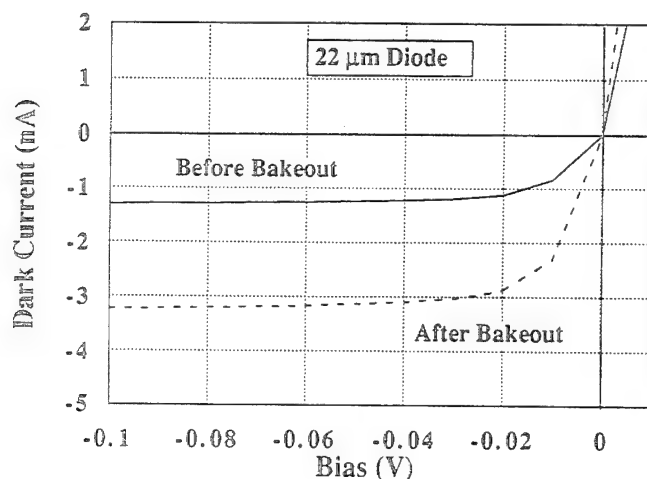


Fig. 2. (a) Standard process sequence. Dark current I-V curves before and after 240 h bakeout for 22 µm (mesa-size) diode, and (b) dark current I-V curves before and after 240 h bakeout for 125 µm (mesa-size) diode.

ries Inc., infrared spectroradiometer (Model 746-D). Capacitance-voltage (C-V) measurements of the MIS devices were made with an HP 4275 multi-frequency

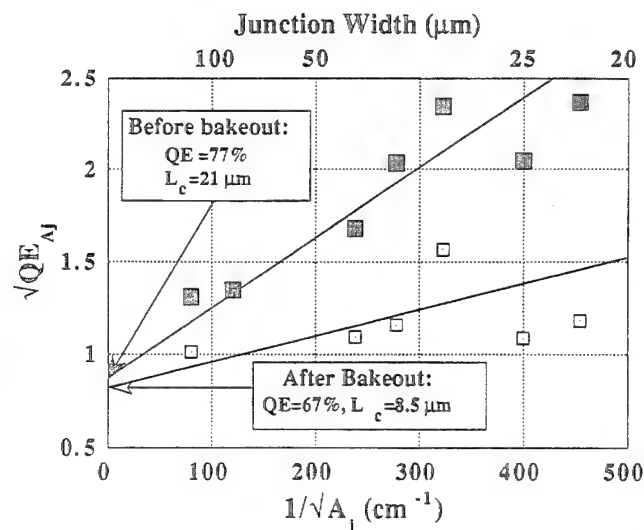


Fig. 3. Standard process sequence. Quantum efficiency and collection distance before and after 240 h bakeout.

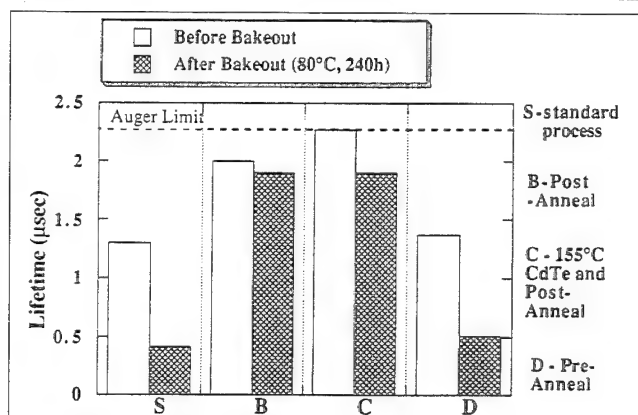


Fig. 4. Minority carrier lifetime of $n = 1 \times 10^{15} \lambda_c = 10.1 \mu\text{m}$ LPE grown HgCdTe layers passivated with thermally evaporated CdTe before and after bakeout at 80°C for 240 h.

LCR meter.

LPE Grown HgCdTe N-Layer

An LPE-grown n-type HgCdTe layer on CdTe substrate was cleaved into four pieces. The n-layer was 20 µm thick, had a carrier concentration of $1 \times 10^{15} \text{ cm}^{-3}$, a calculated Auger lifetime (τ_{Auger}) of 2.2 µs, and $x = 0.215$ ($\text{Hg}_{1-x}\text{Cd}_x\text{Te}$). The piece, part "S" (standard), was passivated with 5000 Å of CdTe deposited at room temperature,² and then prepared for bakeout and measurement. Part "B" underwent the same passivation as "S" and was then annealed at 220°C under Hg vapor after the CdTe deposition.² Part "C" was annealed after the CdTe deposition at a substrate temperature of 155°C ("Hot" CdTe). Part "D" was annealed before passivation.

The minority carrier lifetime was measured by the photoconductive decay technique at a wavelength of 850 nm using Model 6020 Light Pulse Generator (Berkeley Nucleonics Corporation) as a radiation source. The lifetime values reported represent the average of several measurements at different locations on each sample.

Bakeout was performed in a vacuum oven at 80°C and 0.01 Torr for a total time of 240 h. A full set of characterization measurements was performed before and after completion of the bakeout. All measurements were performed at device temperatures from 77 to 80K.

EXPERIMENTAL RESULTS AND DISCUSSION

Devices Fabricated Without Anneal

The zero-bias impedance under dark (0° field of view [FOV]) conditions—one of the most important photodiode parameters—decreased after bakeout for small area diodes but increased slightly for large diodes (Fig. 1). Under strong reverse bias (−400 mV), the impedance increased after bakeout for all sizes of diodes, the largest increase being for large diodes. The impedance variation is defined as the percentage change in impedance from its initial value before bakeout to its final value after bakeout.

Figure 2 shows typical results for 0° FOV current-voltage (I-V) measurements of 22 and 125 μm diodes before and after bakeout. The dark current is observed to increase for small diodes (Fig. 2a) mostly because the saturation current increased. Both I-V

curves have almost the same slope before and after bakeout for biases greater than 3 to 5 kT/q (35–40 mV). This indicates that recombination current due to bulk defects did not increase after bakeout. Meanwhile, the 125 μm diode shows defect-limited behavior, and the dark current after bakeout did not change significantly (Fig. 2b). There is no sign of increased saturation current in this case.

Analysis of the chopped blackbody photodiode response measurements for variable area diodes yields values for quantum efficiency and the lateral collection distance.³ These results are shown in Fig. 3 where QE_{A_j} is the apparent quantum efficiency, assuming the optical and junction area are equal, and is determined by equation:

$$\sqrt{QE_{A_j}} = \sqrt{QE} + \sqrt{QE} \frac{2L_c}{\sqrt{A_j}}$$

where A_j is the junction area, L_c is the lateral collection distance, which is the distance beyond the junction edge from which photo-generated carriers

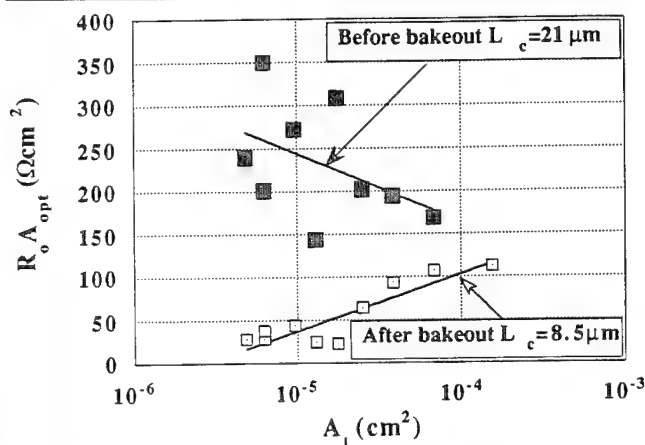


Fig. 5. Standard process sequence. $R_o A_{opt}$ performance as a function of detector junction area before and after bakeout for 240 h at 80°C.

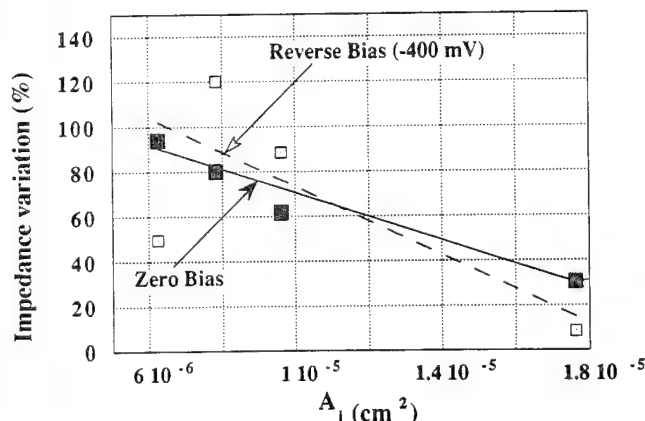


Fig. 6. CdTe deposited at 155°C followed by a Hg anneal. Impedance variation after bakeout for 240 h at 80°C.

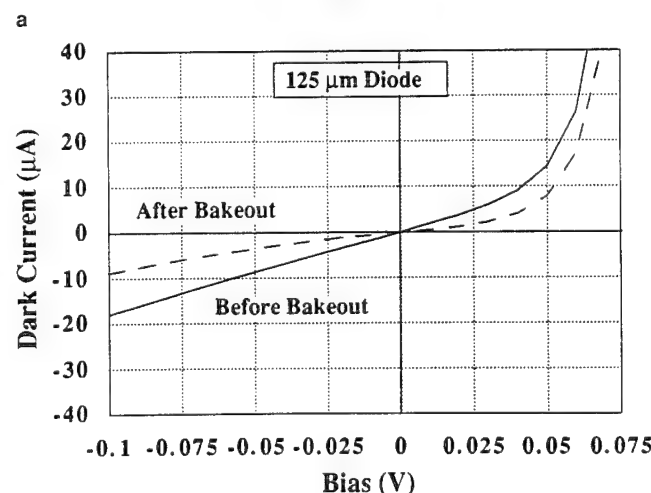
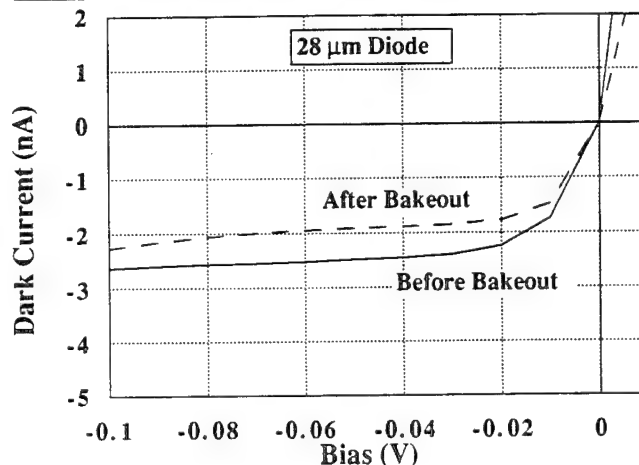


Fig. 7. (a) CdTe deposited at 155°C followed by a Hg anneal. Dark current I-V curves before and after 240 h bakeout for 28 μm (mesa-size) diode, and (b) CdTe deposited at 155°C followed by a Hg anneal. Dark current I-V curves before and after 240 h bakeout for 125 μm (mesa-size) diode.

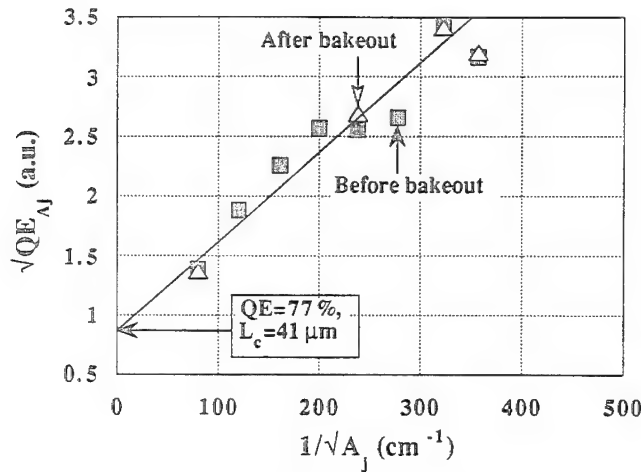


Fig. 8. CdTe deposited at 155°C followed by a Hg anneal. Quantum efficiency and collection distance before and after 240 h bakeout.

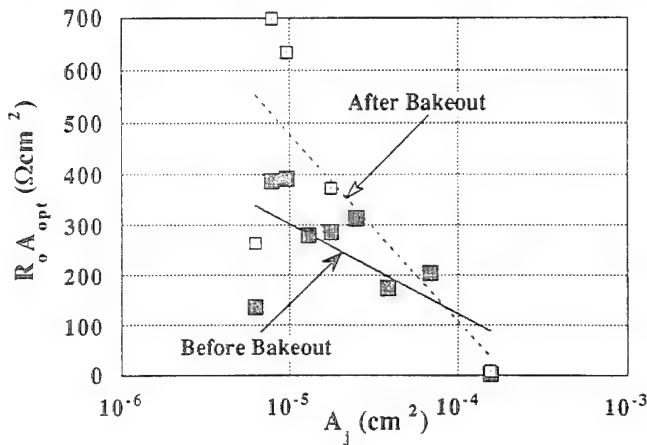


Fig. 9. CdTe deposited at 155°C followed by a Hg anneal. $R_0 A_{opt}$ performance as a function of detector junction area before and after bakeout for 240 h at 80°C.

are collected. This equation has the form of a straight line with the y-intercept equal to the actual quantum efficiency and the slope proportional to the lateral collection distance. Both the quantum efficiency and the lateral collection distance decreased after bakeout, as seen in Fig. 3, but the lateral collection distance (which is proportional to the minority carrier lifetime) decreased by a greater amount (more than a factor of two).

To confirm that a lifetime variation is responsible for parameter degradation after bakeout, direct lifetime measurements were performed on the four quarters of the single n-layer wafer, before and after vacuum bakeout for 240 h at 80°C. The measurement results shown in Fig. 4 show a significant lifetime degradation (more than a factor of three) after bakeout for the sample "S" (standard process sequence), a result which is consistent with the above mentioned parameter degradation.

Because dark current and impedance degradation were sufficient only for small area devices where the perimeter-to-area ratio is very high, meaning the diodes are highly sensitive to surface quality, surface

defect generation was presumed to be the cause of this degradation.

Analysis of the $R_0 A_{opt}$ product as a function of photodiode junction area has been performed to determine if surface or bulk effects are responsible for bakeout degradation.^{4,5} As seen in Fig. 5, for devices fabricated using the standard process, diodes which showed bulk defect limited performance before the bakeout became surface limited after bakeout.

Devices Fabricated with Post-Passivation Anneal

It is thought that some kind of defect, possibly Hg vacancies, is being generated at the CdTe/HgCdTe interface during the long-term elevated temperature bakeout. To prevent the incorporation of electrically active Hg vacancies, a post-passivation anneal under high Hg pressure was performed for both the single n-layer and photodiode test structures. Fabricated devices were then subjected to the 240 h vacuum bake at 80°C and measured.

The measurement results on Hg annealed samples are summarized as follows:

- For the photodiode test structures, zero and reverse bias impedance (Fig. 6) and dark current (Fig. 7) did not degrade for all size diodes. In this case, both small and large diodes showed the same kind of performance.
- Quantum efficiency and lateral collection distance (Fig. 8) were the same before and after bakeout.
- For the n-layer samples annealed after CdTe passivation ("B" and "C"), the minority carrier lifetime did not change after bakeout (Fig. 4). However, the part of the wafer annealed before passivation ("D") showed the same lifetime degradation as the standard process part.
- For the photodiode test structures, analysis of the $R_0 A_{opt}$ product vs photodiode junction area (Fig. 9) confirmed bulk defect limited photodiode performance both before and after bakeout.

Thus, it was confirmed that annealing at 220°C under Hg vapor, after CdTe passivation deposition, suppressed surface defect generation and significantly improved the bake stability performance.

CONCLUSION

It was found that defects are created at the CdTe/HgCdTe (LPE-grown with n-layer doping of 1×10^{15}) interface during a 240 h bakeout at 80°C under vacuum for wafers with LWIR photodiodes passivated by a technique based upon thermal evaporation of CdTe. These defects (which are believed to be electrically active Hg vacancies) degrade the minority carrier lifetime, as well as photodiode zero bias impedance, dark current and photo response. A Hg anneal treatment after CdTe passivation has been shown to prevent the incorporation of electrically active Hg vacancies and significantly improve photodiode stability for bakeout similar to conditions used for preparation of tactical dewar assemblies.

ACKNOWLEDGMENTS

The authors wish to acknowledge Julie Cook and Patricia Richard for their most valuable contributions to diode fabrication and measurements which helped to define the defect mechanism nature. Authors acknowledge valuable discussions with Eugene Sullivan.

REFERENCES

1. A. Van der Ziel, *Solid State Physical Electronics*, (Prentice Hall, 1968), Chap. 15.
2. D.L. Lee, A. Mestechkin, B.T. Cunningham and B.D. MacLeod, Mtg. IRIS Specialty Group on Infrared Detectors (Aug. 1994).
3. C.A. Cockrum, F.I. Gesswein, J.P. Rosbeck and S.M. Taylor, *Proc. IRIS Detector*, Vol. 1 (1991), p. 241.
4. D.R. Rhiger, R.D. Rodrigues and J.M. Peterson, *Proc. IRIS Detector*, Vol. 1 (1991), p. 191.
5. S.M. Johnson, D.R. Rhiger, J.P. Rosbeck, J.M. Peterson, S.M. Taylor and M.E. Boyd, *J. Vac. Sci. B* 10, 1499 (1992).

The Relationship Between Lattice Matching and Crosshatch in Liquid Phase Epitaxy HgCdTe on CdZnTe Substrates

S.P. TOBIN, F.T.J. SMITH, and P.W. NORTON

Loral Infrared & Imaging Systems, Two Forbes Road, Lexington, MA 02173

J. WU* and M. DUDLEY

State University of New York at Stony Brook, Department of Materials Science and Engineering, Stony Brook, NY 11794

D. DI MARZIO and L.G. CASAGRANDE

Northrop-Grumman Advanced Development Center, Stewart Avenue, Bethpage, NY 11714

X-ray topography provides a very sensitive map of lattice mismatch between a HgCdTe LPE epitaxial layer and its (111) CdZnTe substrate. A well-defined crosshatch pattern in the three $\langle 110 \rangle$ directions indicates a positive room-temperature lattice mismatch. For conditions of near-perfect lattice matching ($\pm 0.003\%$ mismatch), the crosshatch pattern disappears, presumably because there are few or no misfit dislocations present near the interface, and a region free of topographic contrast is observed. The crosshatch-free region occurs for a small positive room-temperature mismatch (about 0.02%); this is attributed to differences in the lattice matching condition at room temperature and the growth temperature. For negative mismatches, where the film is in tension, a mosaic pattern, rather than a crystallographically oriented crosshatch, is observed in the topograph. Rocking curve full width at half maximum of the epitaxial layer is minimized in the crosshatch-free zone at a value nearly equal to that of the substrate. Etch pit density of the HgCdTe layer shows a strong minimum for perfect room temperature lattice matching, with values as low as $1 \times 10^4 \text{ cm}^{-2}$. For nearly lattice matched layers, crosshatch is present throughout the thickness of the epitaxial layer except for a narrow graded-composition region near the substrate interface. Crosshatch contrast appears to result from long-range strain fields associated with a misfit dislocation network near the substrate interface. Spatial variations in topographic features and mismatch across relatively small lateral distances are caused by variations in substrate alloy composition. For truly lattice-matched substrates, better control over the substrate lattice parameter is required.

Key words: Lattice matching, mercury cadmium telluride, x-ray diffraction

INTRODUCTION

X-ray diffraction topographs of liquid phase epitaxy (LPE) $\text{Hg}_{0.78}\text{Cd}_{0.22}\text{Te}$ epitaxial layers on nominally lattice-matched $\text{Cd}_{0.96}\text{Zn}_{0.04}\text{Te}$ substrates typically show a strong threefold symmetric crosshatch pattern which is quite different from the mosaic pattern seen for the same films grown on CdTe substrates.

The crosshatch is not visible by Nomarski contrast optical microscopy and does not correspond to any x-ray topographic features of the substrate. In addition, bands completely free of diffraction contrast sometimes appear in films on CdZnTe substrates. The objective of this work was to understand how these different features relate to lattice matching between the epilayer and substrate. The approach was to directly measure lattice mismatch by x-ray rocking curves and relate it to features in x-ray topographs. In addition, epilayer quality as measured by rocking

*Presently at General Instruments Corp., Westbury, NY
(Received October 4, 1994; revised April 10, 1995)

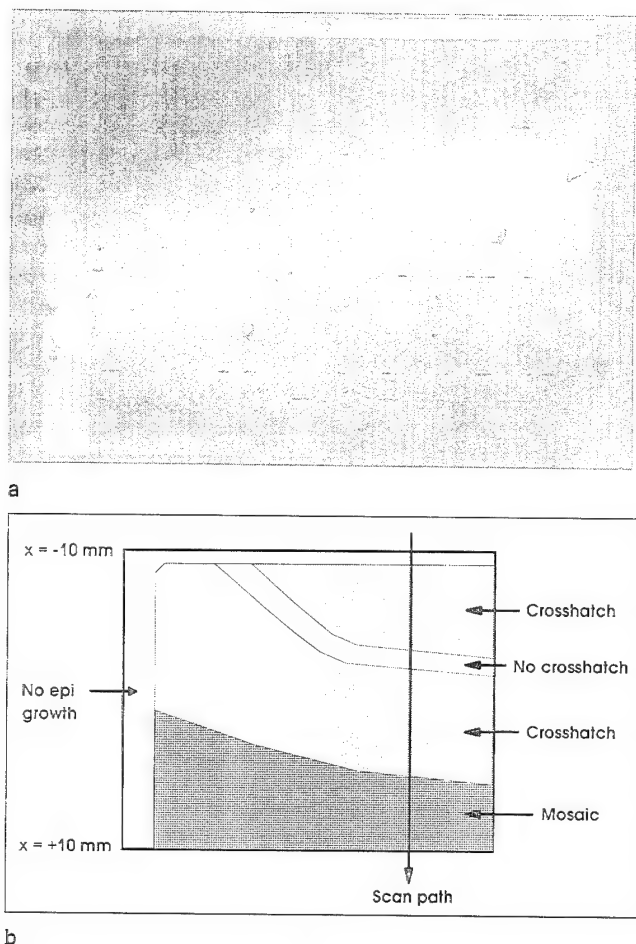


Fig. 1. (a) X-ray topograph of double layer heterojunction film LD312F (246 reflection, Lang camera, negative contrast). Full wafer image, 2.0×2.5 cm. (b) Schematic diagram showing the various regions and the location of the rocking curve measurements.

curve width and etch pit density has been related to the amount of mismatch.

EXPERIMENTAL

The samples reported here were $\text{Hg}_{0.78}\text{Cd}_{0.22}\text{Te}$ epitaxial layers about $18 \mu\text{m}$ thick grown on the Te face of (111) oriented single crystal substrates of nominal composition $\text{Cd}_{0.96}\text{Zn}_{0.04}\text{Te}$. The HgCdTe layers were grown by Te-rich liquid phase epitaxy in a horizontal slider system at approximately 500°C . In one case, a heterojunction sample was used in which a higher bandgap layer, $1 \mu\text{m}$ thick, was grown by LPE in a Hg-rich vertical dipping system. The substrates were from different vendors, grown by both horizontal and vertical Bridgman techniques, and were $2 \text{ cm} \times 3 \text{ cm} \times 1 \text{ mm}$ in size.

X-ray topography measurements were made on two different systems. A Lang camera from Bede Scientific was used with a conventional 1.5 kW Cu x-ray source at Loral. Reflection mode topographs using a (246) reflection were recorded on Agfa D7 x-ray film. Prints made directly from the negatives (negative contrast; white = highest intensity) are reproduced here. Synchrotron white beam topographs were re-

corded at the Stony Brook Topography Station of the National Synchrotron Light Source at Brookhaven National Laboratory. The technique is described in Ref. 1. Multiple Laue reflection topographs were recorded on Kodak SR5 film. Positive prints (black = highest intensity) are reproduced here.

X-ray rocking curve measurements of lattice mismatch were made at Loral on a high-resolution diffractometer from Bede Scientific (Model 200) equipped with a Si(022) channel-cut collimator (CCC), a Si(111) monochromator crystal on the first axis, and a 100 mm XY sample translation stage incorporating 360° rotation about the specimen surface normal. The CCC and monochromator were set to the maximum of the $\text{Cu K}\alpha_1$ Bragg peak. The x-ray beam size in cross section was $2.6 \times 0.4 \text{ mm}$ at the sample. For samples with relatively large mismatches, the (333) reflection was used. For more closely spaced peaks, reflections with larger Bragg angles [(444), (246), (535)] were used for better resolution. The HgCdTe epitaxial layers were too thick to directly measure a substrate diffraction peak for mismatch measurements. This difficulty was overcome by etching off the epitaxial layer on part of the sample and overlapping the x-ray beam with the epilayer and substrate at the etched edge.

Lattice parameter measurements were made at Northrop-Grumman using the Bond method on an automated Bartels system from Blake Industries using the $\text{Cu K}\alpha_1$ (333) reflection. The error of the measurements was $\pm 0.0003 \text{ \AA}$. Absolute lattice parameters were calibrated with various bulk single crystal materials including CdTe , HgTe , and $\text{Hg}_{0.8}\text{Cd}_{0.2}\text{Te}$.

Dislocation etch pits were created using the Hähnert and Schenk etch² for the HgCdTe layers and the Nakagawa etch³ for the CdZnTe substrate.

RESULTS

Correlation of Topographic Crosshatching with Lattice Mismatch

X-ray topographs of our HgCdTe epitaxial layers on (111) CdZnTe substrates typically show a strong threefold symmetric crosshatch pattern with crosshatch lines running in the three equivalent $\langle 110 \rangle$ directions. This is consistent with other published results.⁴⁻⁷ However, on some layers there is a clear band across the wafer with no crosshatch, while on others the crosshatch degrades into a fine scale mosaic appearance with no crystallographic orientation. We have postulated that these differences in topographic features result from differences in lattice parameter matching between the epilayer and substrate. Under this hypothesis, the clear regions are almost exactly matched, the crosshatched regions are slightly mismatched, and the mosaic regions are more strongly mismatched. Supporting evidence comes from topographs of layers on CdTe substrates, where the mismatch is large (0.3%) and a mosaic appearance is always observed.

In this experiment, two epitaxial samples were chosen with topographic features ranging from no crosshatch to strong crosshatch to a mosaic structure in different parts of the wafers. X-ray rocking curves were used to directly measure the lattice mismatch between the substrate and epilayer in the various regions.

The first sample was a double layer heterojunction LPE HgCdTe wafer. Figure 1 shows its x-ray topograph and a schematic diagram illustrating the different contrast features. Topographs of this sample were measured three times: as an n-type base layer at Loral and at the Brookhaven synchrotron, and as a double layer heterojunction at Loral. All three showed the same features; there were no significant differences between the single and double layer topographs. A narrow, crosshatch-free band was bordered on either side by crosshatch regions. At one edge of the wafer, the crosshatch graded into a mosaic structure with no obvious orientation features. A trench, 5 mm wide, was etched down to the substrate to allow rocking curves of the substrate to be measured. The trench passed through the different topographic regions parallel to the 2 cm direction of the substrate. Rocking curves were measured at the edge of the trench with the x-ray beam overlapping both the substrate and epilayers, perpendicular to the edge. The location of the measurements is shown in Fig. 1. This allowed the mismatch between the epilayer and substrate to be measured. Rocking curves were measured every 1 mm across the sample to look at changes in mismatch. We used an asymmetric (246) reflection which gives increased sensitivity to small values of lattice mismatch relative to a standard (333) reflection. The in-plane orientation of the wafer was such that the beam was nearly perpendicular to the etched edge.

Figure 2 shows selected rocking curves measured at five locations across the wafer. The distance in mm (x) is indicated for each curve, with the center of the wafer at zero. There are generally three peaks in each curve: the substrate (marked S), the base layer (marked B), and the cap layer (marked C). The identities of the peaks were verified by moving the beam slightly in the y direction (into or out of the trench) and observing the relative change in intensity of the peaks. The substrate peak is to the right of the base peak for negative x coordinates, and to the left of the base for positive x , with overlapping peaks near the center of the wafer.

In Fig. 3, the peak separation is shown as a function of position. There is a smooth variation across the wafer. A linear least squares line indicates that zero peak splitting occurs at $x = +1$ mm. The location of the no crosshatch region is also indicated in the figure. Unexpectedly, it does not correspond to the zero peak splitting location.

Assuming that the epilayer is relaxed (probably a good assumption for a film 18 μm thick), we can determine the lattice mismatch from the peak splitting. From the relationship $m = -\Delta\theta/\tan \theta$, where the

mismatch m is defined as $m = (a_L - a_S)/a_S$, $\Delta\theta$ is the peak splitting, θ is the Bragg angle, and a_L and a_S are the lattice parameters of the layer and substrate, we find that $m/\Delta\theta = -2.46\text{E-}6/\text{s}$ for the (246) reflection.

Figure 3 also shows the calculated lattice mismatch as a function of position. The mismatch varies by

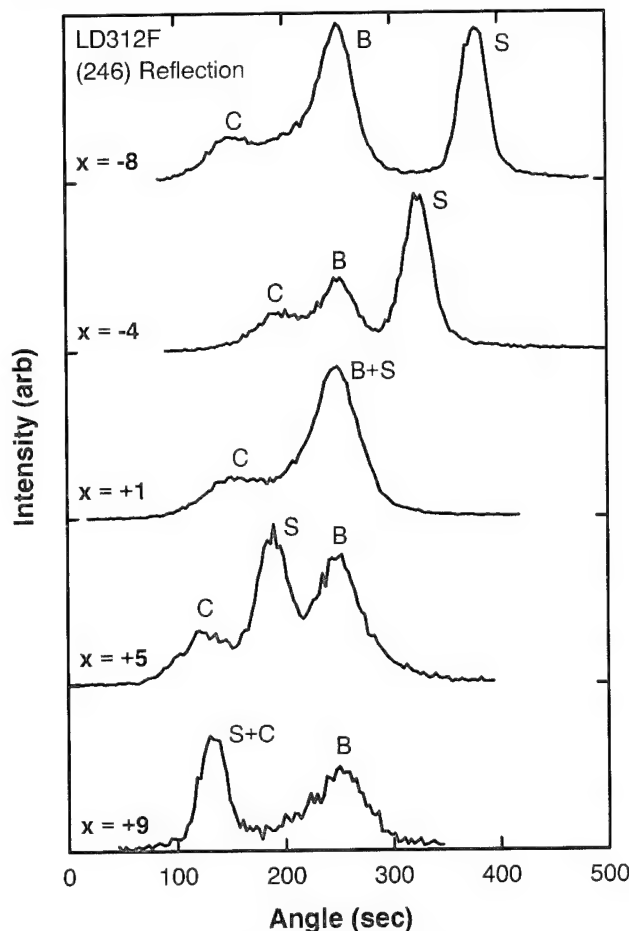


Fig. 2. Rocking curves measured at selected locations across wafer LD312F (246 reflection). B = base layer peak, C = cap layer peak, and S = substrate peak.

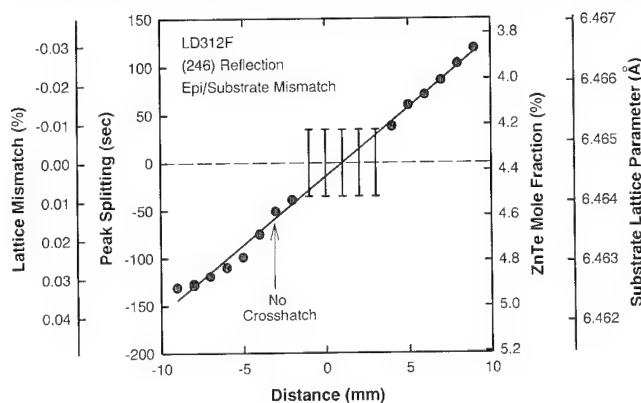


Fig. 3. Separation between base layer and substrate rocking curve peaks as a function of position across wafer LD312F. Error bars indicate overlapping peaks. Additional axes show the corresponding lattice mismatch between layer and substrate, the inferred substrate lattice parameter, and substrate alloy composition.

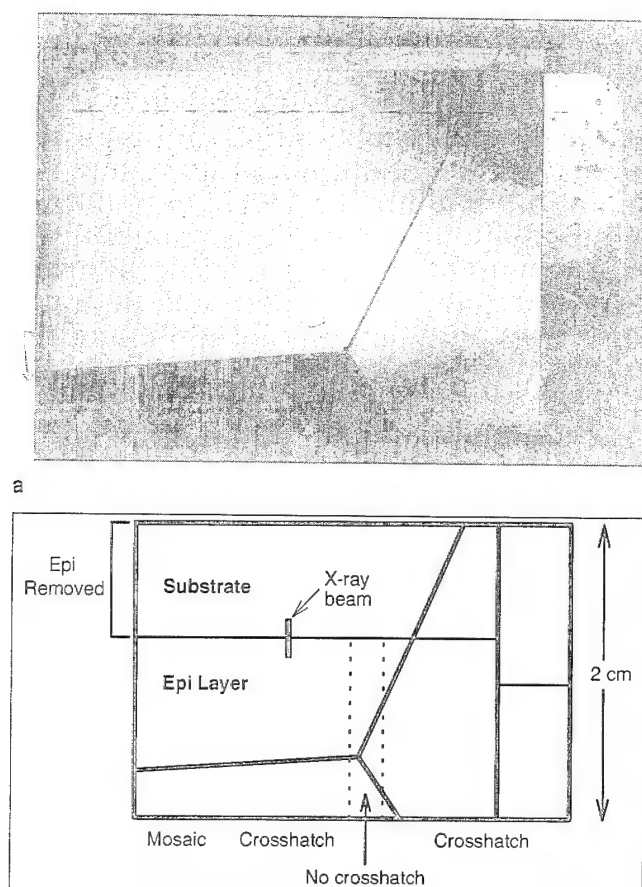


Fig. 4. (a) X-ray topograph of single layer epitaxial sample LI576L prior to etching to reveal the substrate (246 reflection, Lang camera, negative contrast). The sample was broken into four pieces, one of which, at bottom left, was tilted slightly on the sample holder and did not diffract. Dark spots in the upper right corner are residual LPE melt. The interrupted dark horizontal line near the top of the wafer is a mechanical scratch. (b) Schematic diagram of the wafer after etching to remove part of the epilayer. The size of the x-ray beam is to scale.

0.06% across the 2 cm wafer. This is caused almost entirely by variations in Zn composition of the substrate; we know from Fourier transform infrared (FTIR) transmission measurements that the HgCdTe composition is quite uniform laterally ($x = 0.220 \pm 0.0004$, corresponding to a lattice parameter variation of $2.6 \times 10^{-4}\%$).

Assuming that the base layer composition near the P/n junction is the same as that measured by FTIR for the base layer prior to growth of the P-type cap layer, and knowing the lattice parameters of CdTe (6.4812 Å) and HgTe (6.460 Å), we calculate the lattice parameter of the HgCdTe base layer to be 6.46466 Å. (We neglect the change in composition caused by meltback during the cap layer growth, estimated to be 0.002 in x , because it gives a negligible change in lattice constant of 0.00004 Å.)

From the measured mismatch, we then calculate the lattice parameter of the CdZnTe substrate as a function of position (Fig. 3). From the known lattice parameters of CdTe and ZnTe (6.1026 Å), we then calculate the composition of the substrate as a func-

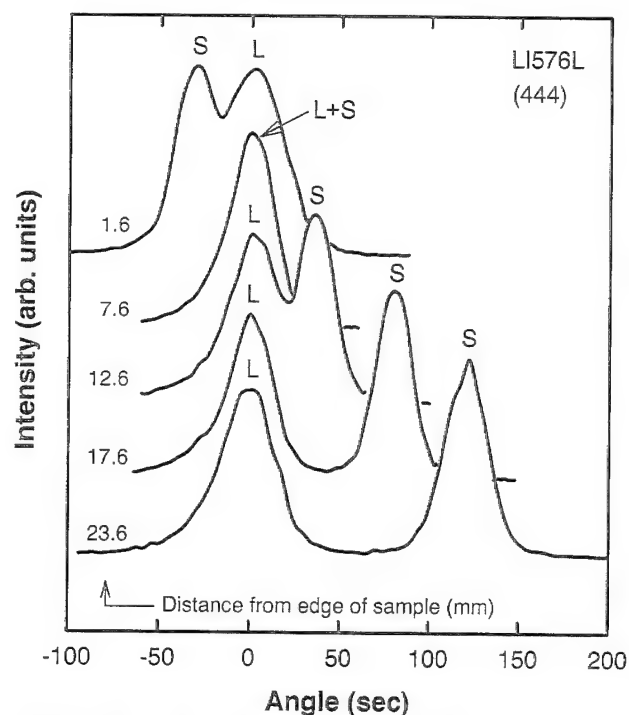


Fig. 5. Rocking curves measured at selected locations across wafer LI576L (444 reflection). L indicates the layer peak and S indicates the substrate peak.

tion of position (Fig. 3). The substrate composition variation is relatively large, 1% absolute, across the 2 cm dimension of the substrate. The range of substrate compositions corresponding to the crosshatch-free zone, on the other hand, is less than 0.1 %.

These results have been confirmed for a second sample on a CdZnTe substrate from another vendor. This sample was a single epitaxial layer, 18 μm thick, with $x = 0.217 \pm 0.0005$ as measured by Fourier transform infrared transmission. Figure 4a shows a (246) reflection topograph of the sample, which was broken into four pieces. Fig. 4b is a schematic diagram of the sample. A no-crosshatch band runs vertically through the sample just to the right of center. Crosshatch is observed on both sides of the clear region, but it grades into a mosaic structure near the left edge of the sample. The epilayer was removed in the top part of the sample by wet chemical etching to reveal the substrate. The x-ray beam was positioned to overlap the epilayer and substrate normal to the etched edge as shown in Figure 4b and stepped across the sample left to right to measure the mismatch profile.

Figure 5 shows (444) rocking curves measured at several positions across the sample. Similar to the first sample, the splitting changed smoothly from positive to negative with position. Figure 6 plots the peak splitting as a function of position across the sample. Two sets of data are shown, differing by a 180 degree rotation of the sample. This was done to check for the presence of tilt between the (111) planes of the epilayer and substrate; within experimental accuracy, none was observed. The results of Fig. 6 are very similar to those of Fig. 3 for the previous sample. Namely, the crosshatch-free zone occurs for a small

negative peak splitting, there are crosshatch regions on both sides of it, and a mosaic structure is observed for positive peak splittings.

To directly check our assumption that variations in the substrate composition cause differences in mismatch, lattice parameter measurements were made at several positions across the sample in both the substrate and epilayer. The results in Fig. 7 confirm that the major variation is in the substrate lattice parameter, that there is a positive mismatch at the no-crosshatch location, and that the mismatch becomes more positive in moving from left to right across the sample. One unexpected result is that the epilayer lattice parameter is larger than the predicted value based on Vegard's law, by 0.0011 Å. The difference is more than the accuracy of the measurement and thus appears to be real.

Figure 6 shows the measured lattice mismatch across the sample. There is good agreement between the rocking curve splittings and direct lattice parameter measurements. These results are again in good agreement with the previous sample of Fig. 3; in particular, the lattice mismatch in the no-crosshatch zone is again about +0.02%.

Figure 8 shows the results in terms of substrate lattice parameter and ZnTe mole fraction across the sample. The rocking curve mismatch measurements were converted to substrate lattice parameters using the average measured lattice parameter of the epilayer, shown in the figure. Again, there is good agreement in substrate lattice parameters between the rocking curve splitting and direct lattice parameter measurements. Similar to the first sample, there is about a 1% absolute composition variation across the substrate. Figure 8 shows that the no-crosshatch zone in the x-ray topograph occurs for a very narrow range of substrate compositions, less than 0.1%.

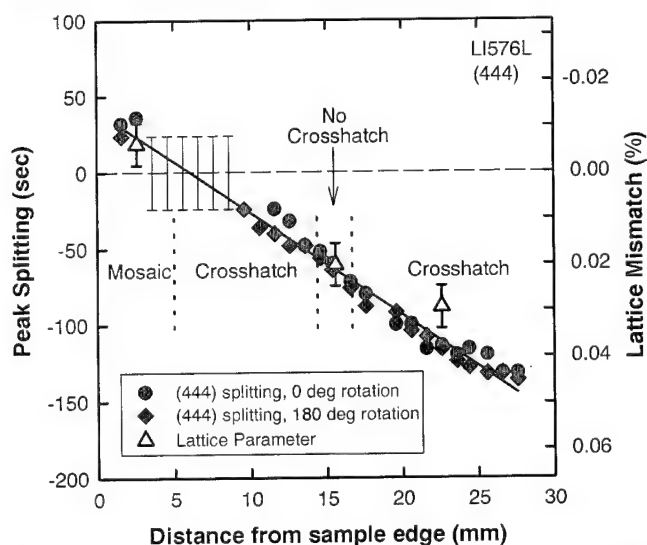


Fig. 6. Separation between epilayer and substrate rocking curve peaks as a function of position across wafer LI576L. Error bars indicate the region of overlapping peaks. Lattice mismatch is shown on the right axis, both calculated from (444) rocking curve splitting and measured directly from epilayer and substrate lattice parameters.

Effect of Lattice Mismatch on Epilayer Quality

In addition to topographic contrast differences, we observed significant variations of the epilayer rocking curve full width at half maximum (FWHM) and etch pit density across the samples. Figure 9 shows that the epilayer FWHM reached a minimum in the no-crosshatch zone, close to the FWHM of the substrate. The substrate FWHM, on the other hand, did not vary significantly across the sample. It is interesting to note that the FWHM appears to saturate for large mismatch values. The FWHM values are about the same for large positive or negative mismatch, despite the difference in topographic features (crosshatch in

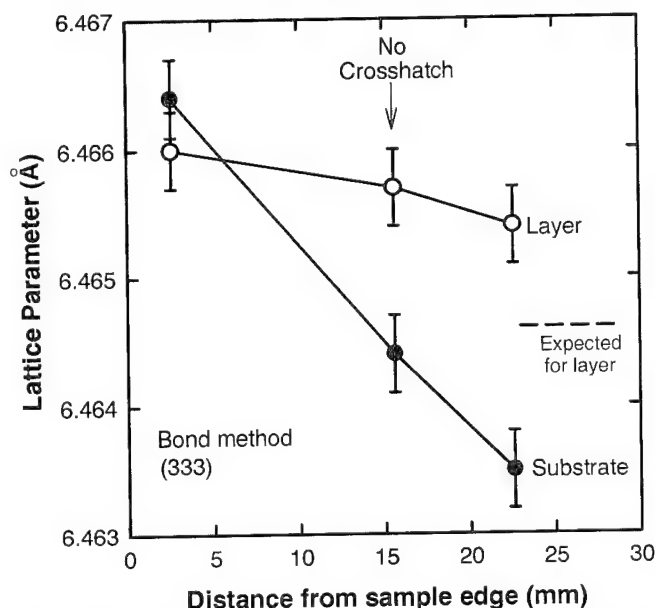


Fig. 7. Direct lattice parameter measurements of the substrate and epilayer of wafer LI576L using the Bond method. The measured points were about 2 mm on either side of the etch line.

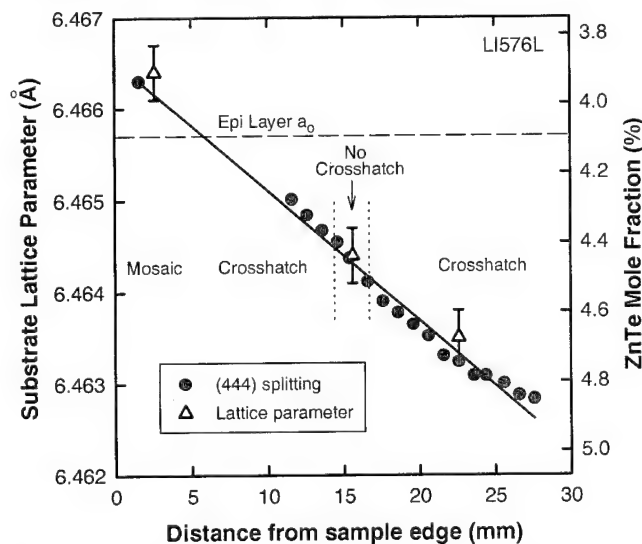


Fig. 8. Substrate lattice parameter as a function of position across sample LI576L. ZnTe mole fractions are inferred from the lattice parameter.

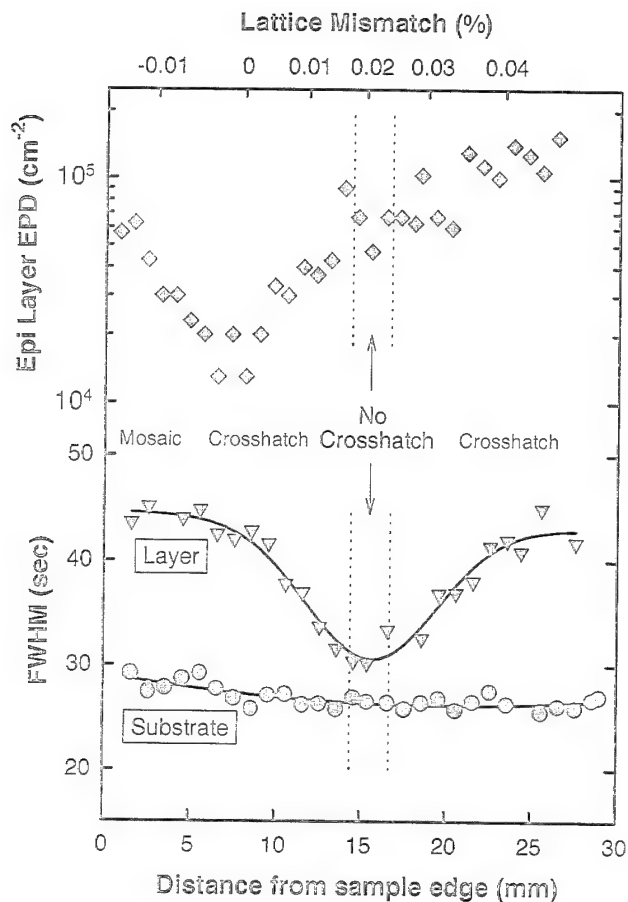


Fig. 9. Variation of rocking curve FWHM and etch pit density across sample LI576R. FWHM measurements were made 3 mm above and below the etched edge; EPD was measured just below the etched edge.

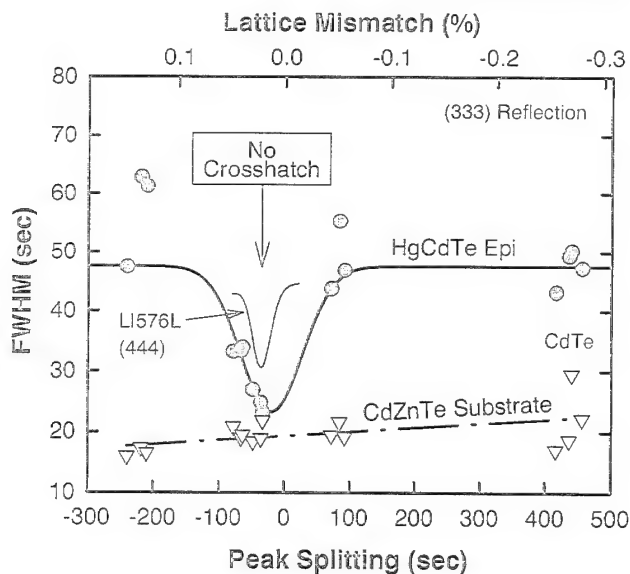


Fig. 10. Correlation between HgCdTe epilayer rocking curve FWHM and degree of lattice matching with the CdZnTe substrate for a range of samples. The epilayers all have $x \approx 0.22$ but were grown on substrates with different compositions, including CdTe. Lines through the data points are intended only to guide the eye.

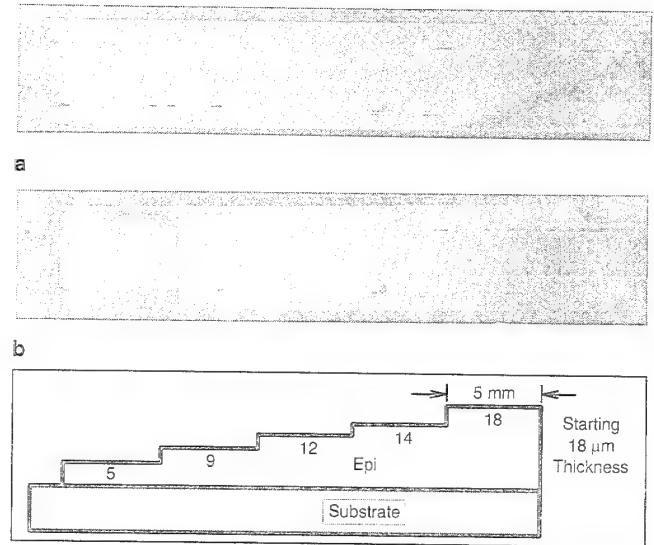


Fig. 11. (a) X-ray topograph of HgCdTe epilayer before etching, (b) x-ray topograph of step-etched epilayer, and (c) schematic of structure showing epi thickness profile. (246 reflection, Lang camera, negative contrast).

one case, mosaic in the other). It is also interesting that the region of improved FWHM is considerably wider ($\pm 0.02\%$ mismatch) than the region of no visible contrast ($\pm 0.003\%$ mismatch). This is consistent with an observed gradual increase in the density and intensity of crosshatch contrast outside the no-crosshatch zone, rather than an abrupt transition.

We note that the FWHM values in Fig. 9 were sensitive to the beam size, the chosen reflection, and instrument resolution, and therefore should not be used as an absolute measure of material quality. Using a smaller beam (0.4×1.3 mm) and the (333) reflection, FWHM values of 17 s were measured for the substrate in the same apparatus. This is close to the instrument resolution of 13 s imposed by beam divergence with a two-bounce channel cut collimator. In the Northrop-Grumman diffractometer with a smaller beam (0.3×1.0 mm) and a four-bounce Bartels monochromator, (333) FWHM values of 10 s for the substrate and 17 s for the HgCdTe layer were measured in the no-crosshatch zone. These are equivalent to the best values reported in the literature.

To correlate dislocation density with the topographic features, etch pit density (EPD) measurements of the epilayer were made using the Hähnert and Schenk etch. Figure 9 shows the correlation of EPD with lattice mismatch and topographic features. The epilayer EPD reached a minimum of $(1-2) \times 10^4 \text{ cm}^{-2}$ near the zero mismatch condition, five to ten times lower than for a positive mismatch of 0.04%. Interestingly, the crosshatch-free zone did not correspond to the region of minimum EPD.

To explore the effects of lattice mismatch for a wider range of substrate compositions, rocking curve mismatch measurements were made on a set of epilayers on different CdZnTe substrates with different alloy compositions. The x-ray beam overlapped both sub-

strate and epilayer at an etched step, and the same (333) rocking curve was used to measure mismatch and FWHM of the peaks. Figure 10 shows a strong correlation between epilayer quality, as measured by the rocking curve FWHM, and lattice matching. A minimum in epilayer FWHM was observed near the lattice matched condition. This agrees with the previous results for sample LI576L, also shown in Fig. 10. Also in agreement with earlier results, the epilayer FWHM is nearly constant away from the lattice-matched condition, whether the mismatch is positive or negative, even for CdTe substrates. The most closely matched sample in Fig. 10 had an epilayer FWHM of 24 s, very close to that of its substrate (22 s). It can be seen that the substrates all had a FWHM of about 20 s, so substrate quality is high and substrate variations are not responsible for the differences in epilayer quality. (Again recall that x-ray beam divergence in our setup limits the minimum measurable FWHM to 13 arc-s even for a perfect Si wafer).

X-ray topographs were also measured on these samples. The features were consistent with the results of the section on correlation of topographic crosshatching with lattice mismatch above. Namely, samples with a negative mismatch had a mosaic structure, those with a positive mismatch were strongly crosshatched, and the most closely lattice matched sample had weak or no crosshatch. Etch pit density measurements of the epilayers on CdZnTe substrates ranged from 1 to $2 \times 10^5 \text{ cm}^{-2}$ with no apparent dependence on mismatch or substrate EPD. Substrate EPD values were lower than those of the epilayers, ranging from 1 to $7 \times 10^4 \text{ cm}^{-2}$. None of the samples from this group were exactly lattice matched (zero peak splitting), so the sharp minimum in EPD of Fig. 9 was not observed.

Depth Distribution of Crosshatch

Two experiments were conducted to understand the origin of the crosshatch pattern. In the first, an epilayer with known crosshatch was step-etched to leave regions with epi thicknesses ranging from 5 to 18 microns. Figure 11 shows topographs of the sample before and after etching and a schematic diagram of the sample. It can be seen that the crosshatch extends throughout the thickness of the layer, to within five microns from the substrate. For the thinnest region in Fig. 11, the diffracted intensity is reduced relative to the other regions (darker image). One reason is because the epi rocking curve is broader in the region closest to the substrate. Figure 12 shows the rocking curve FWHM as a function of the remaining epi thickness. Figure 12 also shows etch pit density as a function of thickness; one possible cause of broadened rocking curves is a higher dislocation density near the interface. However, the data indicate that the dislocation density is relatively constant with depth. Another reason for reduced diffracted intensity of the crosshatch in the thinnest region is that the crosshatch does not extend all the way to the interface; as

described below, crosshatch is absent in the graded composition region near the interface. In agreement with that finding, a subsequent etch of this sample to reduce the epi thickness resulted in thin epi islands with no crosshatch.

It was also found that the crosshatch pattern could be observed with a Nomarski optical microscope in the most deeply etched region, but not in the thicker epilayers. This is possibly due to a slight preferential etching of the strained crosshatch lines. Etch pits produced by the Hähnert and Schenk etch did *not* line up preferentially on the visible crosshatch lines, even close to the interface, but appeared to be randomly distributed. This agrees with our observation that etch pits at the surface of full-thickness films are randomly distributed and do not line up with the $\langle 110 \rangle$ directions of the crosshatch lines. It shows that the x-ray diffraction contrast is *not* due primarily to the presence of threading dislocations in the crosshatch lines.

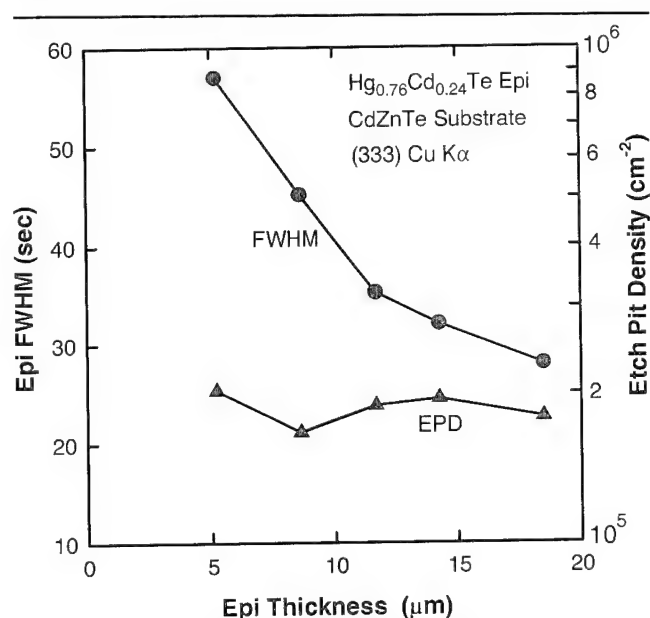


Fig. 12. Epilayer FWHM and EPD as a function of remaining epi thickness for the step-etched sample.

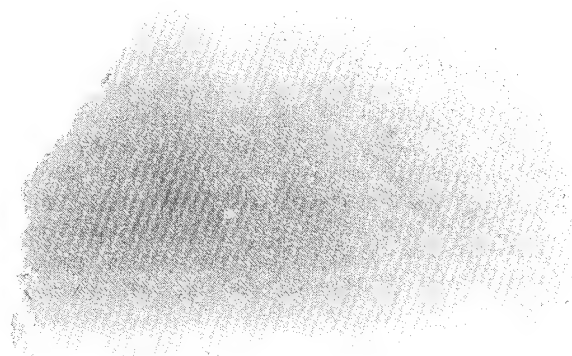


Fig. 13. Synchrotron reflection topograph of an angle lapped HgCdTe epilayer on a CdZnTe substrate (422 reflection, positive contrast).

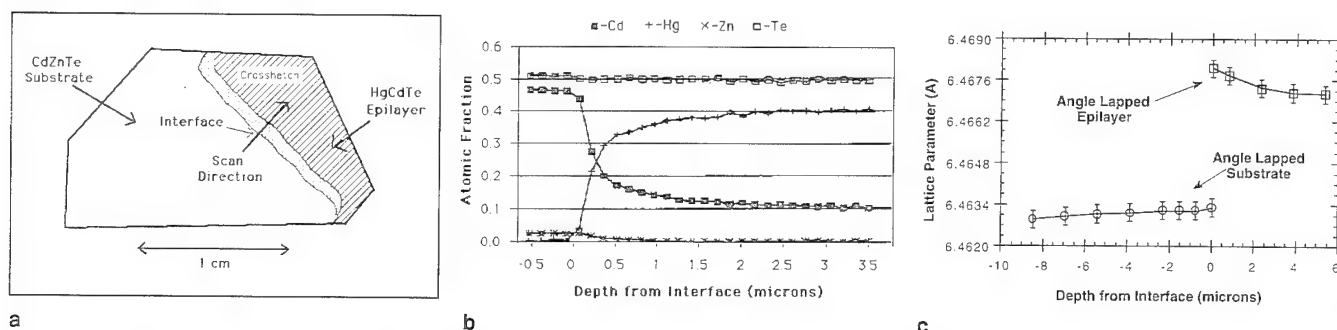


Fig. 14. (a) Diagram of angle lapped HgCdTe/CdZnTe sample showing analysis area, (b) composition profile of angle lapped sample from x-ray microprobe analysis, and (c) precision lattice parameter profile.

Table I. Summary of Lattice-Matching Conditions at Room Temperature and the Growth Temperature for $x = 0.22$ HgCdTe on CdZnTe

Parameter	Value at 27°C	Value at 490°C
CdTe a_0 (Å)	6.4812	6.4969
HgTe a_0 (Å)	6.4600	6.4756
ZnTe a_0 (Å)	6.1026	6.1280
Hg _{0.78} Cd _{0.22} Te a_0 (Å)	6.4647	6.4803
y in lattice-matched Cd _{1-y} Zn _y Te	4.37%	4.49%

Note: Assumed thermal expansion coefficients are 5.23×10^{-6} for CdTe⁹ and HgTe and 9.0×10^{-6} for ZnTe.¹⁰

To investigate the near-interface region in more detail, synchrotron topography of angle lapped epilayers deposited on CdZnTe as well as CdTe substrates was employed. Figure 13 shows a (422) reflection topograph of an angle lapped $x = 0.228$ HgCdTe epilayer on a CdZnTe (111)B substrate. The lower left-hand portion of the image reveals the underlying substrate. A wavy band of darker contrast (higher diffracted intensity) with *no* crosshatching marks the beginning of the HgCdTe epilayer. The crosshatching is seen to begin 1.3 mm from the beginning (interface) of the layer, corresponding to a film thickness of 2 μm at this lapping angle. The crosshatching then persists to the upper right hand corner of the film where it reaches a thickness of 15.4 μm . Grazing x-ray incident angle topographs with sub-micrometer surface penetration also show this crosshatching, which indicates that this feature extends to the epilayer surface. The border of the HgCdTe was confirmed optically as well as with FTIR microscopy and x-ray microprobe measurements. Figure 14b shows wavelength dispersive spectrometry measurements on the angle lapped sample. Compositional measurements as a function of position across the interface show a graded region with a sharp rise in Hg content beginning at the HgCdTe border and extending 2 μm into the epilayer. The crosshatching begins as the composition levels off toward the nominal layer value. We obtained similar results with a HgCdTe epilayer grown on a lattice unmatched CdTe substrate. What was a threefold crosshatching for the lattice matched substrate appeared random for the epilayer on CdTe, but a con-

trast-free region in the epilayer appeared again at the interface.

Figure 14c shows precision lattice parameter measurements of the angle lapped sample. The difference in lattice parameter at the interface is +0.07%. This substrate/epilayer combination is clearly not lattice matched at the interface. Moreover, the lattice parameter for the lapped sample at its maximum thickness (16 μm) is higher than expected for $x = 0.22$ HgCdTe. This higher than expected lattice parameter of the HgCdTe layer was confirmed on another sample of similar thickness which had not been angle lapped and also on the second sample of the section on correlation of topographic crosshatching with lattice mismatch. The reason for this is not fully understood and requires further work.

DISCUSSION

These results support the hypothesis that the presence or absence of crosshatch is related to lattice mismatch between the CdZnTe substrate and HgCdTe epilayer. Crosshatch is observed for positive lattice mismatch (epilayer lattice parameter larger than that of the substrate, causing in-plane compression of the epilayer). When the epilayer lattice parameter is smaller than that of the substrate (negative mismatch, or in-plane tension of the epilayer), the crosshatch changes into a mosaic structure similar to that seen for epilayers on CdTe substrates (even larger negative mismatch). One intriguing feature is that the narrow band free of topographic contrast does not correspond to the case of zero mismatch, as had been expected, but rather to a small positive mismatch of about 0.02%. Several possible explanations have been considered for this discrepancy. The first is that the critical mismatch is between the substrate and the *bottom* of the epilayer, not between the substrate and the *surface* of the epilayer, as we have measured here. There is a Cd/Hg composition gradient in the film, particularly near the interface, so the lattice matching condition could be different at different depths. Misfit dislocation networks, the probable source of crosshatch, are created during the initial stages of epilayer growth when the layer thickness exceeds a critical value, so that the interface composition may be more relevant than the surface composition. However, this argument goes the wrong way to explain the data.

Referring to Fig. 7, we would need a *smaller* epilayer lattice parameter to match the substrate in the region of no crosshatch. However, the Cd composition gradient gives a higher x near the interface, and therefore a *larger* lattice parameter. There is also some interdiffusion of Zn into the film which would *reduce* the lattice parameter near the interface. However, this explanation is inconsistent with the lattice parameter profile of Fig. 14c, which shows an increased lattice parameter near the interface. An alternate explanation is that misfit dislocation generation is determined by the lattice mismatch *at the growth temperature*, and not at room temperature, as we have measured. This explanation requires different thermal expansion coefficients for the layer and substrate. In particular, a larger thermal expansion coefficient for the substrate would give results qualitatively in agreement with the observed data. Although the thermal expansion coefficients of HgCdTe and CdZnTe, particularly near the growth temperature, are not known well enough to rigorously test this idea, we can make a rough calculation based on reasonable assumptions.

Table I summarizes a calculation of lattice matching conditions at room and growth temperatures using thermal expansion coefficients for CdTe and ZnTe measured at 200°C, an assumption of equal expansion coefficients for CdTe and HgTe (based on room temperature results), and linear interpolations of lattice parameters and expansion coefficients for the ternary alloys. The larger expansion coefficient for ZnTe relative to CdTe and HgTe does lead to a slightly larger ZnTe mole fraction for lattice matching at higher temperatures, which goes in the right direction to explain the data. The calculated result explains only about half of the measured discrepancy, but there is considerable uncertainty in the expansion coefficients, especially at the growth temperature. We note that Basson and Booyens⁸ predicted this effect in 1983; their calculations *overestimate* the discrepancy because different thermal expansion coefficients were used.

If the crosshatch-free band represents the lattice-matched condition at the growth temperature, why doesn't it also coincide with the minimum in etch pit density? Etch pits reveal threading dislocations passing through the epilayer, as opposed to misfit dislocations which are in the plane of the film near the interface. The two are different and may have different origins. (We have never observed etch pits preferentially lining up with crosshatch lines.) It is possible that threading dislocations are generated or redirected by strains in the layer as it cools from the growth temperature. If the net strain is minimized where the epilayer and substrate are lattice matched at a given temperature, and the lattice matching condition changes as a function of temperature because of thermal expansion differences, then the region of minimum EPD could be different than the region of no misfit dislocations. The coincidence of the minimum EPD with zero room temperature lattice

mismatch would be consistent with this picture if dislocations are mobile at temperatures approaching room temperature.

If we assume that the crosshatch-free band represents the lattice matched condition at the growth temperature, it is clear that only a very small region of the film meets this condition. In the two samples examined in detail here, the crosshatch-free band was only 1 to 2 mm wide. The relatively large variation in Zn composition across the substrate is the problem. From the width of the crosshatch-free band, we can estimate that the substrate composition must be within $\pm 0.04\%$ (absolute) of the lattice-matched composition to show no crosshatch. Substrates fabricated by present processes are not able to meet this condition over large areas because of Zn segregation during bulk CdZnTe crystal growth. "Lattice-matched" CdZnTe substrates are a misnomer except over very small areas.

Insight into the nature of the crosshatch contrast has been gained from the depth distribution study. The fact that the crosshatch-free region near the interface corresponds to the compositionally graded region between substrate and epilayer is in good agreement with earlier transmission electron microscopy (TEM) results showing that misfit dislocations in MCT on CZT occur *after* most of the compositional grading in the epilayer.¹¹ It is also in good agreement with published etch pit studies of HgCdTe epilayer cross sections,^{7,12,13} verified in our laboratory, which show high etch pit densities in the epilayer starting some distance from the interface. This is evidence that the crosshatch is associated with misfit dislocations, since it occurs only above the band of misfit dislocations.

The conventional view of misfit dislocations at heterojunctions is usually predicated on the assumption of binary layer components with negligible intermixing at the interface. The fact that we have Hg-Cd interdiffusion and Zn outdiffusion into the epilayer at relatively high growth temperatures ($\approx 500^\circ\text{C}$) results in ternary and quaternary composition components at a graded interface. The lattice parameter does not necessarily follow a simple increasing or decreasing trend as the interface is crossed. Utke et al.⁷ have shown that a variety of strain distributions can occur in HgCdTe deposited on CdTe and CdZnTe substrates. Strain maxima, and consequently regions of high dislocation density, can occur away from the interface depending on atomic sizes and atomic diffusion coefficients. For the case of HgCdTe on CdZnTe, Utke et al.⁷ demonstrated that the stress maximum moved away from the interface and into the layer, in agreement with our observations.

For conventional epitaxial growth with negligible intermixing, misfit dislocations are formed when a critical thickness is exceeded, the critical thickness depending on the amount of mismatch. Cohen-Solal et al.¹⁴ recently presented a simple universal model of critical thickness, wherein the critical thickness t_c is given by $t_c = 0.15 m^{-3/2}$, where m is the mismatch. This

model was shown to fit experimental data for CdTe on CdZnTe in particular, as well as other materials systems, and so may be relevant here. This model predicts that the critical thickness would equal our LPE layer thickness for a mismatch of 0.02%. In other words, the layer should be free of misfit dislocations for a mismatch range of $\pm 0.02\%$. As seen in Fig. 9, the region showing no crosshatch in x-ray topographs is narrower than this ($\pm 0.003\%$), although the width of the region with improved FWHM is comparable.

What causes the crosshatch contrast? The misfit dislocation network near the substrate interface is too far below the epilayer surface to be directly imaged by x-ray topography. Penetration depths of the x-rays are much less than the film thickness. Etch pit studies have shown that threading dislocations do not preferentially line up on the crosshatch lines, so that threading dislocations are not the cause of the crosshatch contrast. It appears that x-ray crosshatch is rather caused by long-range strain fields associated with misfit dislocations near the interface running in the three $\langle 110 \rangle$ directions. The fact that these strain fields can be observed so far from their point of origin is somewhat surprising. This may indicate a clumping of the misfit dislocations to enhance the strain field, or a strain field interference effect between the many closely spaced, parallel misfit dislocations.

One anomalous result of this work is the higher than expected lattice parameter of the $\text{Hg}_{0.78}\text{Cd}_{0.22}\text{Te}$ epitaxial layers. The measurements appear reliable because single crystal reference standards gave the expected lattice parameters. In particular, a (111) bulk HgCdTe sample from Cominco with $x = 0.206$ by FTIR cutoff had a measured lattice parameter of 6.4640\AA , close to 6.4644\AA calculated by Vegard's law. The expected error of the measurement (0.0003\AA) is considerably smaller than the apparent discrepancies of 0.0011\AA in Fig. 7 and 0.0024\AA in Fig. 14c. One explanation is that films grown under Te-rich conditions may have larger lattice parameters due to nonstoichiometry. There is some data to support a variation of lattice parameter with stoichiometry.¹⁵ However, Carlson et al.¹⁶ reported $x = 0.24$ and $x = 0.31$ HgCdTe layers grown by Te-rich LPE under conditions similar to ours with lattice parameters in excellent agreement with our assumed linear interpolation between the bulk values of CdTe and HgTe. Their measurements were also made by the Bond method. A second explanation is that the epitaxial layer is strained, with a larger lattice parameter normal to the film than in the plane of the film. (The lattice parameter normal to the film is measured with a symmetrical (333) or (444) rocking curve.) Normally, one would expect very thick films such as ours to be relaxed by the formation of misfit dislocations, but this may not relieve all of the mismatch strain. If the strain were caused by mismatch differences, then a positive mismatch would lead to a lattice expansion normal to the film, at least qualitatively in agreement with the measured data. On the other hand, a negative mismatch should result in epilayer lattice param-

eters lower than the expected value. This is not seen in Fig. 7, where the mismatch changes from negative to positive across the sample yet the epilayer lattice parameter is essentially constant and always larger than expected. Mismatch strain in the layer is, therefore, not responsible for the lattice parameter discrepancy. Further work is planned to understand the source of this anomaly in epilayer lattice parameters.

A question remaining for the future is if the differences in crystal quality related to lattice mismatch have any measurable effect on device performance. The observed variation of EPD with lattice matching would be expected to have a negligible effect on LWIR photodiode quantum efficiency and R_0A at 77K, based on prior correlations of device performance with etch pits.¹⁷ However, there may be measurable effects on diode reverse I-V characteristics and noise at 77K, and on R_0A at lower temperatures; these parameters can be limited by dislocation effects. Since the requirements for exact lattice matching are so stringent, it will require careful screening of substrate composition or epilayer mismatch to make devices for such a study.

CONCLUSIONS

X-ray topography provides a very sensitive map of lattice mismatch between a (111) CdZnTe substrate and HgCdTe epitaxial layer. A well-defined crosshatch pattern in the three $\langle 110 \rangle$ directions indicates a positive room-temperature lattice mismatch. For conditions of near-perfect lattice matching ($\pm 0.003\%$ mismatch), the crosshatch pattern disappears, presumably because there are few or no misfit dislocations present near the interface, and a region free of topographic contrast is observed. The crosshatch-free region occurs for a small positive room-temperature mismatch (about 0.02%); this is attributed to differences in the lattice matching condition at room temperature and the growth temperature. For negative mismatches, where the film is in tension, a mosaic pattern, rather than a crystallographically oriented crosshatch, is observed in the topograph. Rocking curve FWHM of the epitaxial layer is minimized in the crosshatch-free zone at a value nearly equal to that of the substrate. Etch pit density of the HgCdTe layer shows a strong minimum for perfect room temperature lattice matching, with values as low as $1 \times 10^4 \text{ cm}^{-2}$. Achieving EPD below 10^5 cm^{-2} in our HgCdTe epilayers requires *both* a low substrate EPD and near-perfect lattice matching. For nearly lattice matched layers, crosshatch is present throughout the thickness of the epitaxial layer except for a narrow graded-composition region near the substrate interface. Crosshatch contrast appears to result from long-range strain fields associated with a misfit dislocation network near the substrate interface. Spatial variations in topographic features and mismatch across relatively small lateral distances are caused by variations in substrate alloy composition. For truly lattice-matched substrates, better control over the substrate lattice parameter is required.

ACKNOWLEDGMENT

This work was sponsored by ARPA under the Infrared Materials Producibility Program (Johnson Matthey Electronics, prime contractor), monitored by Mr. Ray Balcerak (Contract No. MDA972-91-C-0046).

REFERENCES

1. M. Dudley, *Mater. Res. Soc. Symp. Proc.* 307, 213 (1993).
2. I. Hähnert and M. Schenk, *J. Cryst. Growth* 101, 251 (1990).
3. K. Nakagawa, K. Maeda and S. Takeuchi, *Appl. Phys. Lett.* 34, 574 (1979).
4. S.L. Bell and S. Sen, *J. Vac. Sci. Technol. A* 3, 112 (1985).
5. B. Pellicari, G.L. Destefanis and L. Di Cioccio, *J. Vac. Sci. Technol. A* 7, 314 (1989).
6. S. Bernardi, C. Bocchi, C. Ferrari, P. Franzosi and L. Lazzarini, *J. Cryst. Growth* 113, 53 (1991).
7. I. Utke, L. Parthier and M. Schenk, *J. Cryst. Growth* 123, 269 (1992).
8. J.H. Basson and H. Booyens, *Phys. Stat. Solidi. (A)* 80, 663 (1983).
9. M.G. Williams, R.D. Tomlinson and M.J. Hampshire, *Solid State Comm.* 7, 1831 (1969).
10. H.J. Holland and K. Beck, *J. Appl. Phys.* 39, 3498 (1968).
11. A. Nouruzi-Khorasani, I.P. Jones, P.S. Dobson, D.J. Williams and M.G. Astles, *J. Cryst. Growth* 96, 348 (1989).
12. D. Chandra, J.H. Tregilgas and M.W. Goodwin, *J. Vac. Sci. Technol. B* 9, 1852 (1991).
13. M. Yoshikawa, *J. Appl. Phys.* 63, 1533 (1988).
14. G. Cohen-Solal, F. Bailly and M. Barbé, *J. Cryst. Growth* 138, 68 (1994).
15. J.C. Brice, *Properties of Mercury Cadmium Telluride*, EMIS Datareviews Series No. 3 (London: INSPEC, The Institution of Electrical Engineers, 1987), p. 4.
16. R.A. Carlson, R.J. Hager and R.A. Wood, *J. Vac. Sci. Technol. A* 5, 3048 (1987).
17. S.M. Johnson, D.R. Rhiger, J.P. Rosbeck, J.M. Peterson, S.M. Taylor and M.E. Boyd, *J. Vac. Sci. Technol. B* 10, 1499 (1992).

Electron Cyclotron Resonance Plasma Etching of HgTe-CdTe Superlattices Grown by Photo-Assisted Molecular Beam Epitaxy

K.A. HARRIS,* D.W. ENDRES, R.W. YANKA, L.M. MOHNKERN, and A.R. REISINGER

Martin Marietta Laboratories-Syracuse, P.O. Box 4840, Syracuse, NY 13221

T.H. MYERS,† A.N. KLYMACHYOV,‡ C.M. VITRUS,‡ and N.S. DALAL‡

West Virginia University, †Department of Physics, ‡Department of Chemistry, Morgantown, WV 26506

In order to form HgTe-CdTe superlattice diode arrays, a well-controlled etch process must be developed to form mesa structures on HgTe-CdTe superlattice layers. Wet etch processes result in nonuniform, isotropic etch profiles, making it difficult to control etch depth and diode size. In addition, surface films such as a Te-rich layer may result after wet etching, degrading diode performance. Recently, a dry etch process for HgTe-CdTe superlattice materials has been developed at Martin Marietta using an electron cyclotron resonance plasma reactor to form mesa diode structures. This process results in uniform, anisotropic etch characteristics, and therefore may be a better choice for etching superlattice materials than standard wet etch processes. In this paper, we will present a comparison of etch processes for HgTe-CdTe superlattice materials using electron microscopy, scanning tunneling microscopy, surface profilometry, and infrared photoluminescence spectroscopy to characterize both wet and dry etch processes.

Key words: Electron cyclotron resonance (ECR), HgTe-CdTe superlattices, infrared

INTRODUCTION

Development of II-VI infrared detector materials sensitive to very long wavelength infrared (VLWIR) radiation will require the use of exotic materials such as HgTe-CdTe superlattice (SL) devices, in which the band-gap of the material can be precisely controlled.¹ This is because HgTe-CdTe SLs offer the potential for better cutoff wavelength control and improved transport perpendicular to the epilayer for applications in the LWIR and VLWIR regions of the electromagnetic spectrum. The development of fabrication processes for HgTe-CdTe SL materials grown by photon-assisted molecular beam epitaxy (PAMBE) has been our subject of study over the past few years. Superlattice materials have been grown and processed to evaluate device characteristics, as well as the effects of pro-

cesses on device performance. This paper compares bromine-based wet-etching with plasma dry etching for HgTe-CdTe superlattice materials.

The HgTe-CdTe superlattice materials used in this study were constructed of alternating layers of HgTe and CdTe, typically 20 to 50 angstroms thick, grown on <211> oriented CdTe substrates. Layers were doped with arsenic and indium to form p-type and n-type doped layers, grown in a homojunction configuration. The device material was then processed to fabricate test devices (mesa diodes) which can be evaluated to determine material and device characteristics.

There is, however, great concern that processes used to fabricate the HgTe-CdTe superlattice will cause device degradation. Because the HgTe-CdTe superlattice layers are so thin, care must be used in processing the material to avoid heating, which could cause interdiffusion of the layers and change the effective band-gap of the material.

Much attention in this work has been focused on the

*Present address: II-VI Incorporated, 375 Saxonburg Boulevard, Saxonburg, PA 16056

(Received October 4, 1994; revised May 3, 1995)

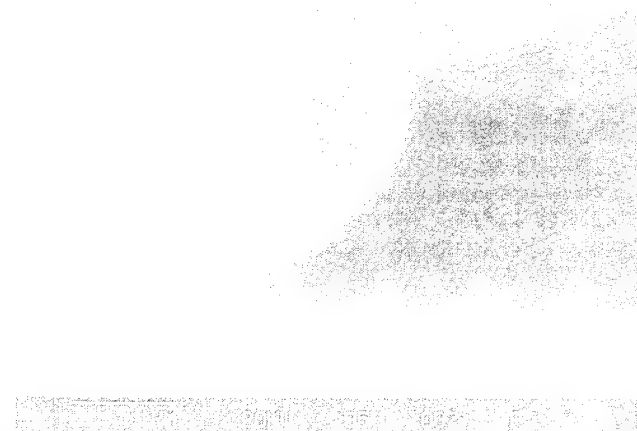


Fig. 1. Scanning electron microscopy photo of a wet-etched HgTe-CdTe superlattice mesa structure. The superlattice was etched in 5% bromine/ethylene glycol. The etch process is isotropic, undercutting the etch mask (not shown) with an aspect ratio of 1:1. There is no visible evidence of selective etching of the superlattice.

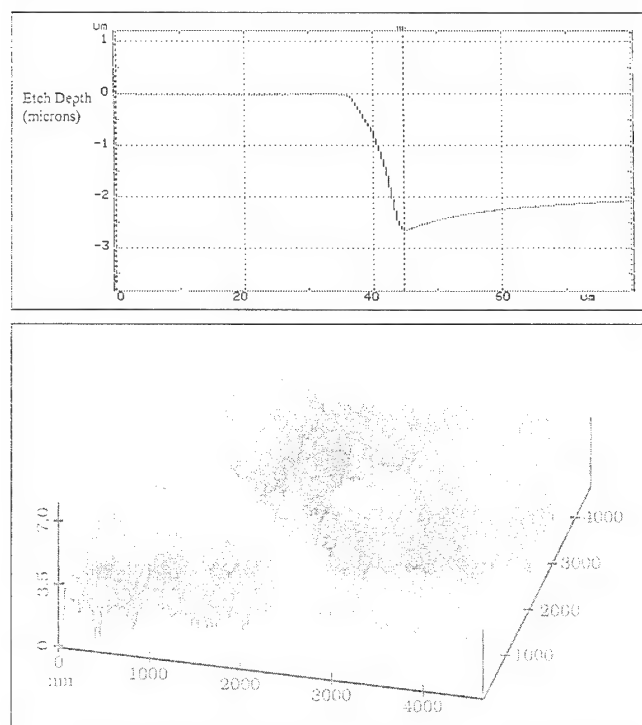


Fig. 2. Surface profile of wet-etched HgTe-CdTe superlattice mesa structure (top) shows nonuniform etching of the material. Etch depth is greatest near the edge of the mesa. Scanning tunneling microscopy image of the wet-etched superlattice (bottom) reveals the surface roughness is about 4 nm.

mesa etch process. Wet-etch processes commonly used for HgCdTe alloys may not have equal etch rates for the individual HgTe and CdTe layers in the superlattice material. Thus, wet-etches may result in a scalloped edge on the mesa diode walls. Wet etchants such as bromine/methanol are inherently difficult to control and result in nonuniform etch rates. Wet-etches may also leave a tellurium-rich surface layer, because the individual constituents are etched at

different rates, with tellurium being the slowest. These effects may lead to increased surface leakage across the p-n junction and degrade the diode characteristics.

Dry-etch processes for HgCdTe based on methane/hydrogen plasma chemistry offer an alternative to wet-etch processes.² An effective approach is to use an electron cyclotron resonance (ECR) plasma reactor to produce a low ion-energy plasma which uses mixtures of methane and hydrogen to etch HgCdTe materials. Recent work with ECR technology has successfully fabricated nanometer-scale structures in HgCdTe materials.³ Electron cyclotron resonance can also be used to deposit CdTe passivating layers which offers the potential for in situ device processing.

Wet-etch and ECR plasma characteristics of HgTe-CdTe superlattice materials were evaluated by scanning electron microscopy (SEM) and profilometry to determine etch rates and surface characteristics after etching. Scanning tunneling microscopy (STM) was also used to provide additional information on the etched surface characteristics.⁴ Infrared photoluminescence (IRPL) spectra from superlattice materials was used to determine if processing caused changes in the band-gap of the material.⁵ Diode characteristics of wet etched and dry etched HgTe-CdTe superlattice devices were compared to discern whether wet etch or dry etch processes have a greater impact on devices from the same superlattice substrate.

EXPERIMENTAL DETAILS

HgTe-CdTe superlattice epilayer growth was performed in one of two custom MBE machines modified for PAMBE growth. These systems have been described in an earlier publication.⁶ All of the epilayers were grown on <211>B CdTe substrates at a deposition temperature of 170°C. The substrates were prepared using standard wet-etch techniques followed by thermal processing prior to growth.⁷ Typical beam equivalent pressures used for the source ovens were $3-5 \times 10^{-4}$ Torr for Hg, $1-3 \times 10^{-6}$ Torr for Te, and $5-10 \times 10^{-7}$ Torr for CdTe. Overall growth rates employed were in the range of 0.5 to 1.0 $\mu\text{m/h}$. The Te and Cd sources were shuttered, resulting in a constant Hg overpressure throughout the growth. This produced barrier layers consisting of $\text{Hg}_{1-x}\text{Cd}_x\text{Te}$, where $x = 0.90$. Superlattices investigated for this study utilized CdTe and HgTe layers with thicknesses in the range of 20–50 angstroms with cutoff wavelengths between 8 and 10 μm .

N-type doping of epilayers was achieved by the introduction of an indium flux during film growth. Indium was chosen because of its ease of incorporation, thermal stability, and high level of dopant activation.^{8,9} A constant indium flux was maintained throughout n-type superlattice growth allowing indium to incorporate into both the CdTe and HgTe layers.

Arsenic was utilized to produce p-type material because of its thermal stability and high activation

rate.⁸ During superlattice growth, however, arsenic is incorporated only into the CdTe layers, to avoid compensation problems associated with Hg-based materials such as HgTe.¹⁰ When these techniques are combined, controlled doping of HgTe-CdTe superlattice materials has resulted in p on n device structures.⁸

As grown, the p layer is typically about 2 μm thick, which means that the mesa etch process must remove HgTe-CdTe superlattice material to a depth greater than 2 μm to achieve diode isolation. To pattern and etch the superlattice material, the following process was used. First, a low temperature silicon dioxide (SiO_2) masking layer was deposited (2–3000 angstroms thick) on the material by ECR chemical vapor deposition. A pattern was then defined on the SiO_2 film by photolithography, using a variable-area pattern with squares and circles with dimensions from 50–100 μm . The SiO_2 film was dry etched using a CF_4/O_2 plasma in a parallel plate plasma reactor. After the photoresist was stripped, the surface was cleaned with dilute bromine/methanol prior to mesa etching.

The mesa etch process was performed using either bromine in solvent (methanol, ethylene glycol, or HBr) for wet-etch samples, or an ECR plasma for dry-etch samples. A SEM photo of a superlattice sample, after static etch in a solution of 5% bromine/ethylene glycol, is shown in Fig. 1. The surface of the superlattice is very smooth. No selective etching of the superlattice material severe enough to cause scalloped edges was observed for any of the other wet-etch solutions. Scanning tunneling microscopy (STM) imaging reveals that the etched superlattice surface has structure on a scale of about 4 nm.⁴ Independent etch rate determination for MBE grown HgTe and CdTe layers confirms that the etch rates are equivalent. The mesa profile is isotropic (i.e., mask undercut = etch depth), and the etch depth is nonuniform across the surface. Figure 2 shows a typical wet-etch profile, in which the etch depth varies by 30% or more across the sample. A STM image is also shown in which a surface roughness of about 4 nm can be resolved. Smooth surfaces are generally required for effective, reproducible surface passivation during device processing. All wet-etch processes evaluated resulted in similar profiles on HgTe-CdTe superlattice materials.

Dry etch processes for HgTe-CdTe superlattice materials were developed in a PlasmaQuest Model 877D system, which is equipped with an ASTeX ECR plasma source. A cross-section diagram of the ECR reactor is depicted in Fig. 3. The etch chamber is 12 inches in diameter and is pumped by a 1200 l/s turbomolecular pump. The ECR system has a base pressure of about 1×10^{-7} Torr. During etching, a hydrogen/argon gas mixture (4% H_2) is introduced upstream into the ECR plasma discharge tube, and a methane/argon gas mixture (10% CH_4) is injected downstream from the ECR source. Pressure during ECR etching is typically 2–5 milliTorr, depending on gas flow. Microwave energy (2.45 GHz) generates a plasma, which occurs at around 875 gauss in the ECR discharge tube, and ions are carried by the gas flow

into the downstream chamber where they react with methane. Methane ions and hydrogen ions are probably the dominant etch species for Hg, Cd, and Te, forming volatile chemical compounds such as dimethylmercury, dimethylcadmium, and tellurium hydride. The HgTe-CdTe superlattice sample is loaded onto RF biased chuck, which is cooled by a recirculating bath. The magnetic field generated in the ECR source helps prevent loss of ions from collisions with the chamber wall, and the magnetic field assists in control of the etch profile (anisotropy).

Etch rates for HgTe and CdTe were measured in the ECR reactor, so that the ratio of etch rates could be determined. Typically, HgTe films etch about four times faster than CdTe under the same reactor conditions. This result suggests that the ECR etch rate is dependent on the ratio of Hg to Cd on the Group II site, which implies that selective etching of the HgTe-CdTe superlattice might occur.

However, we found no evidence of differential etching in the superlattices used for this study. Figure 4 shows a superlattice mesa test pattern after ECR etching. A high magnification view of the mesa edge

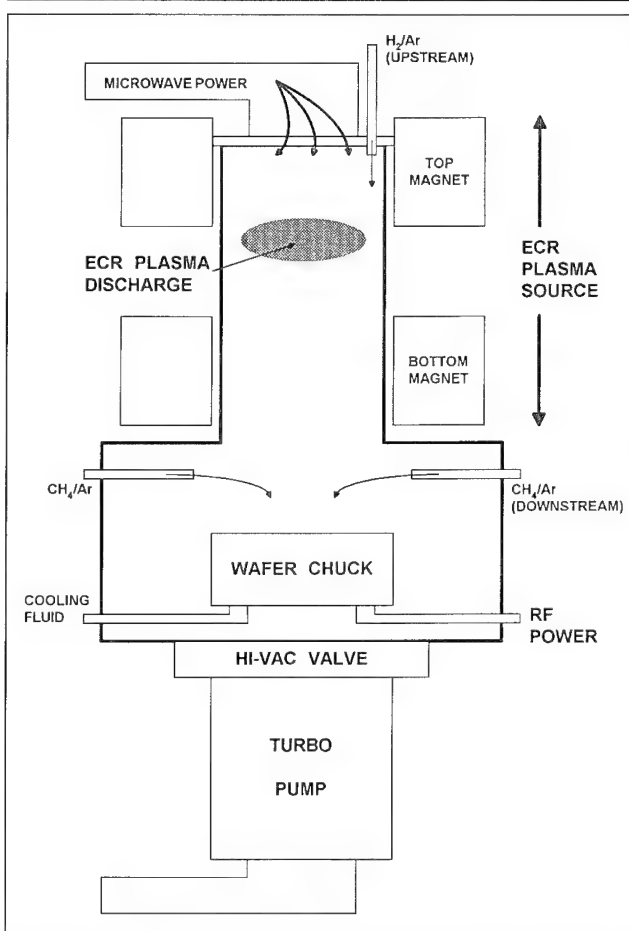


Fig. 3. Schematic diagram of the Martin Marietta ECR reactor used to develop etch processes for HgTe-CdTe superlattice devices. A plasma discharge is created when microwave energy couples with the magnetic field at about 875 gauss in the ECR plasma source. The plasma creates ions from hydrogen and methane, which react with and etch the HgTe-CdTe superlattice materials.

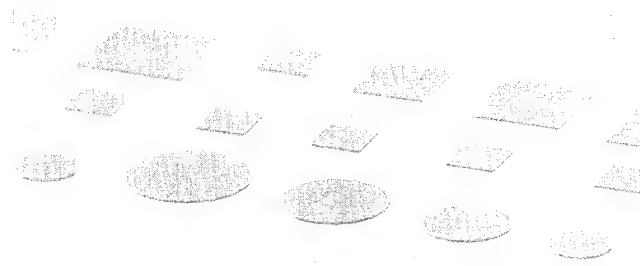


Fig. 4. Scanning electron microscopy photo of an ECR etched HgTe-CdTe superlattice substrate, showing the mesa diode test pattern.

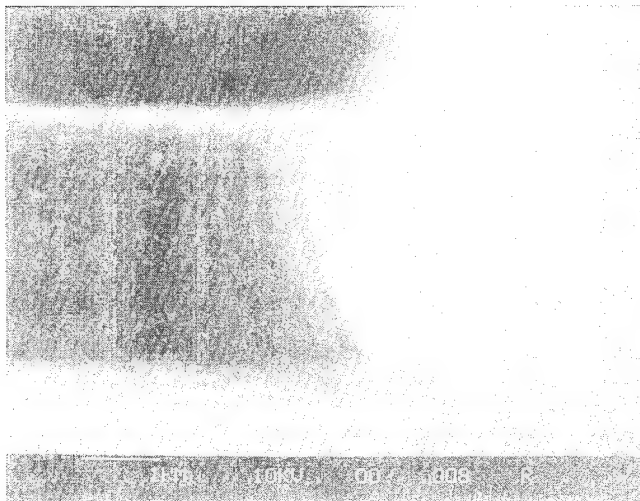


Fig. 5. Scanning electron microscopy photo showing the mesa edge profile of a HgTe-CdTe superlattice after ECR etching. There is only slight undercut of the etch mask (shown), with an aspect ratio of about 5:1. There is no visible evidence of selective etching of the superlattice layers.

(Fig. 5), shows that the dry-etched superlattice surface is almost as smooth as typical wet-etched surfaces. There is no visible evidence of selective etching of the superlattice layers. There is also much less mask undercut (the aspect ratio is about 5:1), compared with wet-etch processes. This suggests that the ECR etching of superlattices is controlled by the surface potential which depends on the thickness of the constituent layers. This implies that differential etch effects will occur only when the constituent layers of the SL are of a sufficient thickness to etch independently.

Process conditions were adjusted to give an anisotropic etch profile, shown in Fig. 6. Conditions used for achieving the anisotropic profile are listed in Table I. There is no visible evidence of selective etching of the superlattice layers, and there is no undercut of the etch mask. The most important factors for controlling

Table I. Anisotropic Etch Conditions

Hydrogen/Argon Flow	100 sccm
Methane/Argone Flow	20 sccm
Chamber Pressure	4 milliTorr
Microwave Power	750 watts
RF Power	50 watts
RF Bias	-3 volts
Magnet Current (top)	185 amps
Magnet Current (bottom)	125 amps
Etch Time	20 min

Note: These are the ECR system parameters used for dry etching the HgTe-CdTe superlattices in this study.



Fig. 6. Scanning electron microscopy photo of HgTe-CdTe superlattice mesa structure after ECR etching with a process optimized for anisotropy. There is no undercut of the etch mask, and there is no evidence of selective etching of the superlattice layers. The line feature at the midpoint of the mesa wall was caused by a process interruption to check etch progress midway through the process.

anisotropy are the addition of RF bias on the wafer (about 50 watts), and control of temperature during etching. RF bias increases ion energy (developed self bias is about -3 volts on the RF chuck), and there is a corresponding increase in the superlattice etch rate, typically from about 500 angstroms/min without RF bias, to about 1500 angstroms per min with RF bias, depending on ECR reactor conditions.

As the ion energy is increased with RF bias, the heat load also increases. Superlattice temperature must be maintained below about 100°C, maximum, to

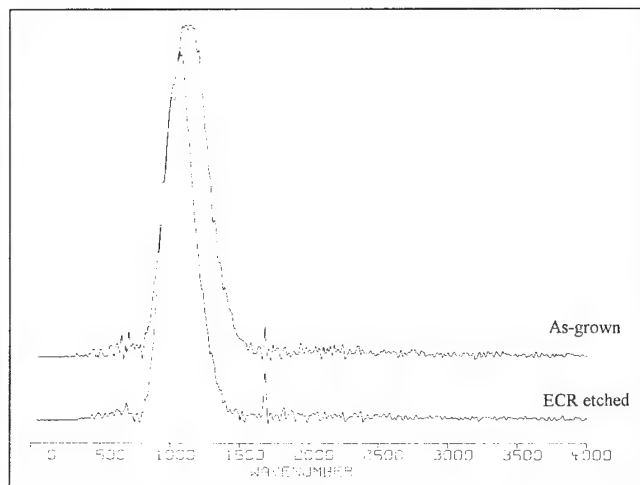


Fig. 7. Infrared photoluminescence spectra for HgTe-CdTe superlattice device sample as-grown (top), and after ECR mesa etch (bottom). The IRPL peak energy and intensity are the same for both samples, within the limits of the experiment. This indicates that ECR etch conditions do not cause interdiffusion of the superlattice and do not damage the surface.

prevent damage to the material. To control the surface temperature during etching, the duration of the etch step was limited to about 1.0 min, followed by a cooling cycle. HgTe-CdTe superlattice materials were then evaluated by IRPL spectroscopy to determine if there were any changes in the IRPL characteristics due to interdiffusion of the HgTe-CdTe superlattice, caused by ECR etching.

Infrared photoluminescence spectroscopy has been shown to resolve surface damage and features attributed to monolayer material structure in superlattices,^{11,12} and therefore it should be sensitive to even slight interdiffusion of the superlattice layers. Surface damage will diminish the IRPL signal. If interdiffusion occurs, the IRPL peak will be broadened and shifted significantly to higher energy. Figure 7 shows a comparison of superlattice IRPL characteristics before and after ECR etching. The IRPL peak from the ECR etched superlattice is within the range expected from IRPL data taken from the as-grown sample. The slight differences in peak energy and location are within the limits of the measurement. This result indicates that no significant interdiffusion has occurred. Furthermore, the peak intensity after etching is not diminished, which indicates minimal near-surface etch damage.

Figure 8 shows a typical profile of a HgTe-CdTe superlattice after ECR etch. A smooth, flat surface profile is produced because the low pressure of the ECR process improves etch uniformity over wet-etch processes. Although ECR etching results in a more uniform etch profile than wet-etching, the ECR etched surface is rougher than a wet-etched superlattice surface. The STM imagery of an ECR etched superlattice surface reveals a roughness of about 40 nm.⁴ The ECR etched surfaces are not quite as smooth as the wet-etched surfaces. They are, however, nearly an order of magnitude smoother than that typically

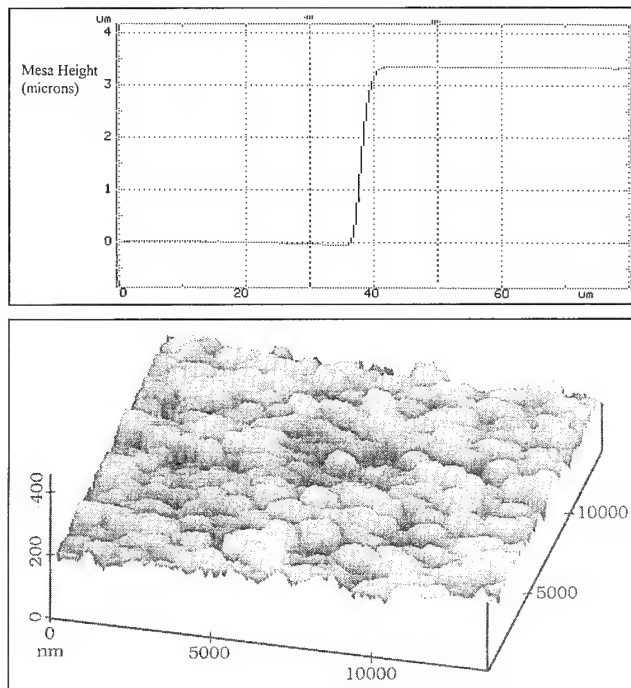


Fig. 8. Surface profile of ECR etched HgTe-CdTe superlattice mesa structure (top) shows uniform etching of the material. Etched surface is flat. Scanning tunneling microscopy image of the ECR etched superlattice (bottom) reveals the surface roughness is about 40 nm, roughly an order of magnitude smoother than etched LPE layers.

observed for HgCdTe layers grown by LPE, indicating that the surfaces are more than sufficiently smooth for device passivation and fabrication.

CONCLUSIONS

Wet-etch and dry-etch processes have been developed for HgTe-CdTe superlattice materials. The etch processes have been characterized, and the effects of the etch processes on superlattice materials have been evaluated. The wet-etch processes based on bromine etch solutions, are characterized by smooth surfaces with surface feature heights only about 4 nm. Wet etch processes resulted in rounded etch profiles typical of isotropic etching with no clear evidence of selective etching of the superlattice. Etch depths were found to vary by >30% in the same sample indicating difficulty in etch control.

Dry-etch processes based on methane/hydrogen etch chemistry have been developed for HgTe-CdTe superlattices. Control of process parameters in the ECR reactor enable anisotropic etching of superlattice materials, resulting in sharp etch profiles with good uniformity and little or no mask undercut. Differential etching was not observed presumably due to a single surface potential formed by the thin constituent layers of the SL. Dry etched surfaces exhibited surface feature heights of about 40 nm, roughly an order of magnitude better than that commonly observed in LPE-grown layers. Heating of the superlattice during ECR etching can be limited, and no change in IRPL characteristics was observed for well controlled ECR etch processes.

ACKNOWLEDGMENT

This work was supported by the Air Force Wright Laboratory Materials Directorate under contract number F33615-90-C-5922, contract monitor Ms. L.E. Brown.

REFERENCES

1. J.N. Shulman and T.C. Magill, *Appl. Phys. Lett.* 34, 663 (1985).
2. J.E. Spencer, T.R. Schimert, J.H. Dinan, D.W. Endres and T.R. Hayes, *J. Vac. Sci. Technol. A* 8, 1690 (1990).
3. C.R. Eddy, E.A. Dobisz, C.A. Hoffman and J.R. Meyer, *Appl. Phys. Lett.* 62, 2362 (1993).
4. T.H. Myers, A.N. Klymachyov, C.M. Vitus, N.S. Dalal, D.W. Endres, K.A. Harris, R.W. Yanka and L.M. Mohnkern, *Appl. Phys. Lett.* 66, 224 (1995).
5. A.R. Reisinger, R.N. Roberts, S.R. Chin and T.H. Myers, *Rev. Sci. Instrum.* 60, 82 (1989).
6. K.A. Harris, S. Hwang, D.K. Blanks, J.W. Cook, Jr., J.F. Schetzina and N. Otsuka, *J. Vac. Sci. Technol. A* 4, 2061 (1986).
7. T.H. Myers, R.W. Yanka, J.P. Karins, K.A. Harris, J.W. Cook, Jr., and J.F. Schetzina, *Mater. Res. Soc. Symp. Proc.* 90, 295 (1987).
8. K.A. Harris, T.H. Myers, R.W. Yanka, L.M. Mohnkern and N. Otsuka, *J. Vac. Sci. Technol. B* 9, 1752 (1991).
9. M. Boukerche, P.S. Wijewarnasuriya, S. Sivananthan, I.K. Sou, Y.J. Kim, K.K. Mahavadi and J.P. Faurie, *J. Vac. Sci. Technol. A* 6, 2830 (1988).
10. R.L. Harper, Jr., S. Hwang, N.C. Giles, J.F. Schetzina, D.L. Dreifus and T.H. Myers, *Appl. Phys. Lett.* 54, 170 (1989).
11. C.A. Warwick, W.Y. Jan and A. Ourmazd, *Appl. Phys. Lett.* 56 (26), 2666 (25 June 1990).
12. R.F. Kopf, E.F. Schubert, T.D. Harris and R.S. Becker, *Appl. Phys. Lett.* 58 (6), 631 (11 Feb. 1991).

Origin of Void Defects in $\text{Hg}_{1-x}\text{Cd}_x\text{Te}$ Grown by Molecular Beam Epitaxy

M. ZANDIAN, J.M. ARIAS, J. BAJAJ, J.G. PASKO, L.O. BUBULAC,
and R.E. DEWAMES

Rockwell Science Center, Thousand Oaks, CA 91360

Characterization of defects in $\text{Hg}_{1-x}\text{Cd}_x\text{Te}$ compound semiconductor is essential to reduce intrinsic and the growth-induced extended defects which adversely affect the performance of devices fabricated in this material system. It is shown here that particulates at the substrate surface act as sites where void defects nucleate during $\text{Hg}_{1-x}\text{Cd}_x\text{Te}$ epitaxial growth by molecular beam epitaxy. In this study, we have investigated the effect of substrate surface preparation on formation of void defects and established a one-to-one correlation. A wafer cleaning procedure was developed to reduce the density of such defects to values below 200 cm^{-2} . Focal plane arrays fabricated on low void density materials grown using this new substrate etching and cleaning procedure were found to have pixel operability above 98.0%.

Key words: Atomic force microscopy, HgCdTe , molecular beam epitaxy (MBE), void defects

INTRODUCTION

Currently, $\text{Hg}_{1-x}\text{Cd}_x\text{Te}$ is the most important material system for fabrication of focal plane arrays (FPAs) for use in infrared imagery applications.^{1,2} However this technology requires strict control of surface conditions for growth of high quality material.³ Molecular beam epitaxial (MBE) growth of $\text{Hg}_{1-x}\text{Cd}_x\text{Te}$ on CdZnTe offers the great control over bandgap engineering, composition and dopant profiles, crystalline quality, thicknesses, interfaces, and specifically, surface preparations.⁴⁻⁶ The primary issue associated with void defects in MBE grown $\text{Hg}_{1-x}\text{Cd}_x\text{Te}/\text{CdZnTe}$ materials is the adverse electrical effect of such defects on device performance. A device correlation study which clearly demonstrated that growth-in-

duced void defects are detrimental to photovoltaic devices indicated that epilayers with low void density are needed to obtain high pixel operability in FPAs.⁵ In this paper, we present our results on characterization of void defects. We have investigated the effect of substrate surface preparation on formation of void defects and established a one-to-one correlation which indicates particulates at the substrate surface act as sites where voids nucleate during epitaxial growth by MBE. A wafer cleaning procedure was developed to reduce the density of such defects to values below 200 cm^{-2} ; focal plane arrays fabricated on low void density materials grown using this new substrate etching and cleaning procedure had high pixel operability. The substrate surface preparation used in this study did not affect the dislocation density, optical, and electrical properties of the HgCdTe epilayers.

Characterization of epilayer voids and substrate

(Received November 1, 1994; revised February 15, 1995)

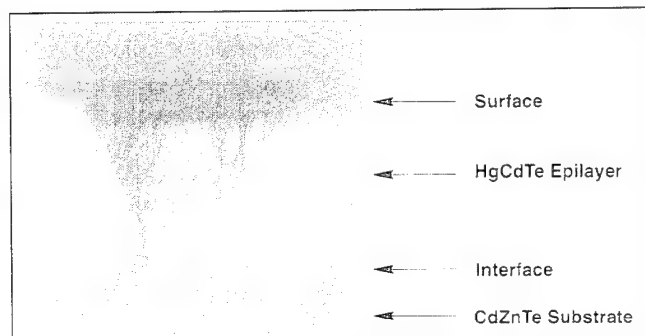
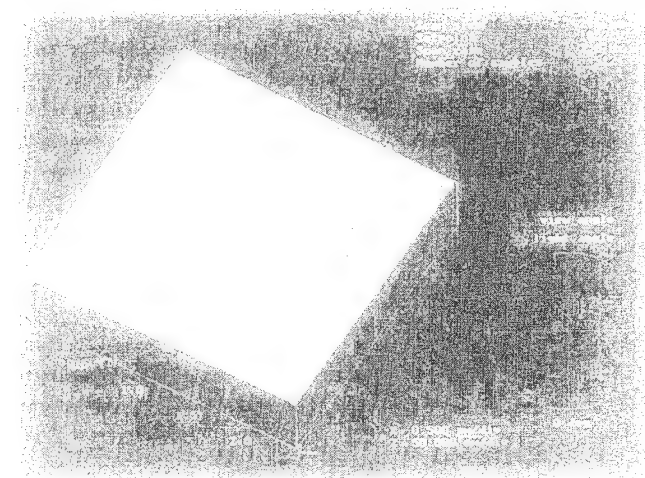
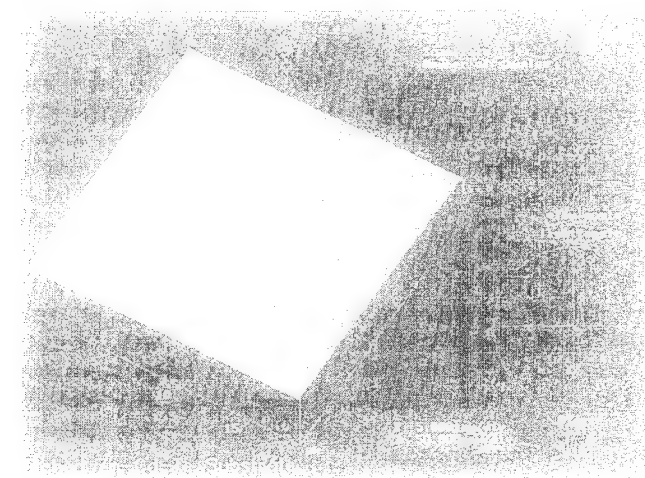


Fig. 1. Cross section SEM photograph of a void defect induced during the MBE growth of HgCdTe.



a



b

Fig. 2. Atomic force microscopy photograph of CdZnTe substrate surface prior to etching (a) and after etching and removal of 5 μm (b). Note the presence of high density of particulates and polishing damage prior to Br/methanol etch.

surface defects were carried out using atomic force microscopy (AFM), optical microscopy, and scanning electron microscopy (SEM). In the next section, we discuss our experiment. Results on pixel operability of long wavelength infrared (LWIR) focal plane arrays will be discussed in the Results and Discussion section. Concluding remarks are also presented.

EXPERIMENT

The heterostructures were grown in a RIBER 2300 MBE system. A detailed discussion of MBE HgCdTe growth procedures and device fabrication used here can be found in Refs. 5 and 6. The epilayers were grown on near lattice-matched CdZnTe to minimize the dislocation density in the HgCdTe. The (211)B orientation was chosen since we have obtained excellent surface morphology and high performance photodiodes on epitaxial layers grown on this orientation.⁴⁻⁶ CdZnTe substrates were etched in 1% chemical solution of bromine methanol to remove approximately 5 μm from the surface region followed by rinse in methanol bath and nitrogen dry immediately after rinse. Samples were then loaded into the MBE chamber to avoid any contamination of the surface. The substrates were first outgassed and prepared for growth. Molecular beam epitaxially grown heterostructures consist of a 12 μm thick indium-doped ($2 \times 10^{15} \text{ cm}^{-3}$) $\text{Hg}_{1-x}\text{Cd}_x\text{Te}$ LWIR absorbing layer followed by growth of a 1 μm thick undoped $\text{Hg}_{1-y}\text{Cd}_y\text{Te}$ ($y = x + 0.075$) layer and a final 1000Å thick CdTe layer. P-on-n planar photodiodes were fabricated using these heterostructures. The formation of planar photodiodes was achieved by first selectively implanting arsenic through windows made on a mask of photoresist/ZnS and then diffusing the arsenic by annealing through the cap layer into the narrow gap base layer. A schematic of the device structure can be found in Ref. 5.

RESULTS AND DISCUSSION

A cross section SEM photograph of a void defect (Fig. 1) shows that the void defects nucleate at the onset of growth on the substrate surface and propagate to the epilayer surface during the growth of HgCdTe. The size of void defects at the surface increases as growth continues, and for epitaxial layers of 10–15 μm in thickness, a void defect size of 5 μm is frequently observed. Inside these void defects, the HgCdTe growth is polycrystalline.

Figure 2a is an atomic force microscopy picture of the as-received CdZnTe substrate surface prior to etching and cleaning. These substrates are epi-ready polished by vender. A high density ($>10^8 \text{ cm}^{-2}$) of particulates and polishing damage lines is evident in this picture, and an etching step is required to remove the surface damage region in these substrates. Figure 2b shows the reduction in density of particulates after 5 μm of surface region is removed in 1% chemical solution of bromine methanol. Note the polishing damage lines are also removed using this etching step. The density of remaining particulates (for clarity picture is shown for area where there is a particulate at this magnification) at the substrate surface after this step is in the range of 100–200 cm^{-2} . Epitaxial layers grown on these substrates have routinely resulted in high quality HgCdTe epilayers with low void density also in the range of 100–200 cm^{-2} . These dust particulates on CdZnTe are not chemi-

cally bonded to the surface, and application of ultrasonic cleaning in methanol results in movement of particulates on surface. Hence, one would expect that these particulates would all be removed in the etching step and that the density should drop to approximately zero rather than $100\text{--}200\text{ cm}^{-2}$ range. The

origin of particulates that give rise to the $100\text{--}200\text{ cm}^{-2}$ void density in HgCdTe is most likely due to particulates in methanol, additional particulates from N_2 blow dry, dust in air from spin drying, and from the air during transfer of the wafer to the MBE chamber. An optical picture of $\text{Cd}_{0.96}\text{Zn}_{0.04}\text{Te}$ substrate surface, il-

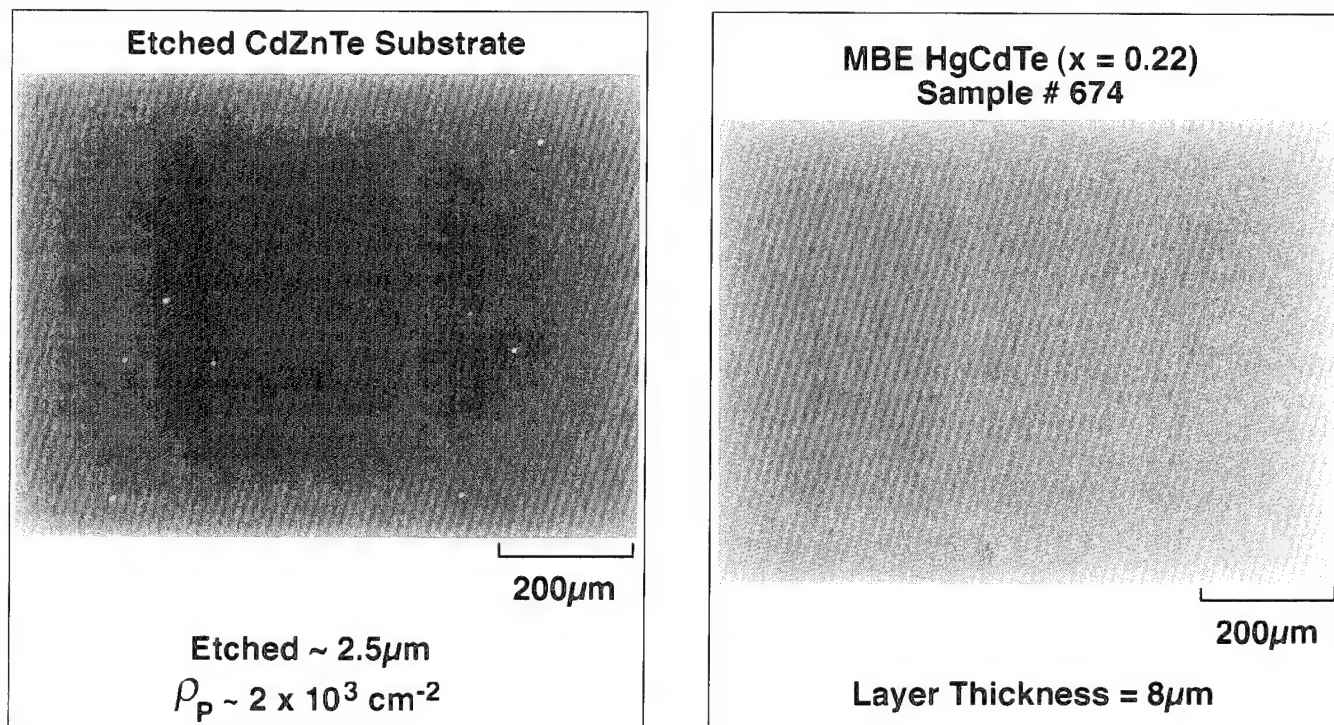


Fig. 3. (a) An optical dark field picture of (211)B CdZnTe substrate prior to growth showing the presence of the particulates on the substrate surface. (b) Optical picture of the same area after growth of $8\text{ }\mu\text{m}$ $\text{Hg}_{0.78}\text{Cd}_{0.22}\text{Te}$. Note void defects are only formed at the same sites where the particulates are present at the substrate surface.

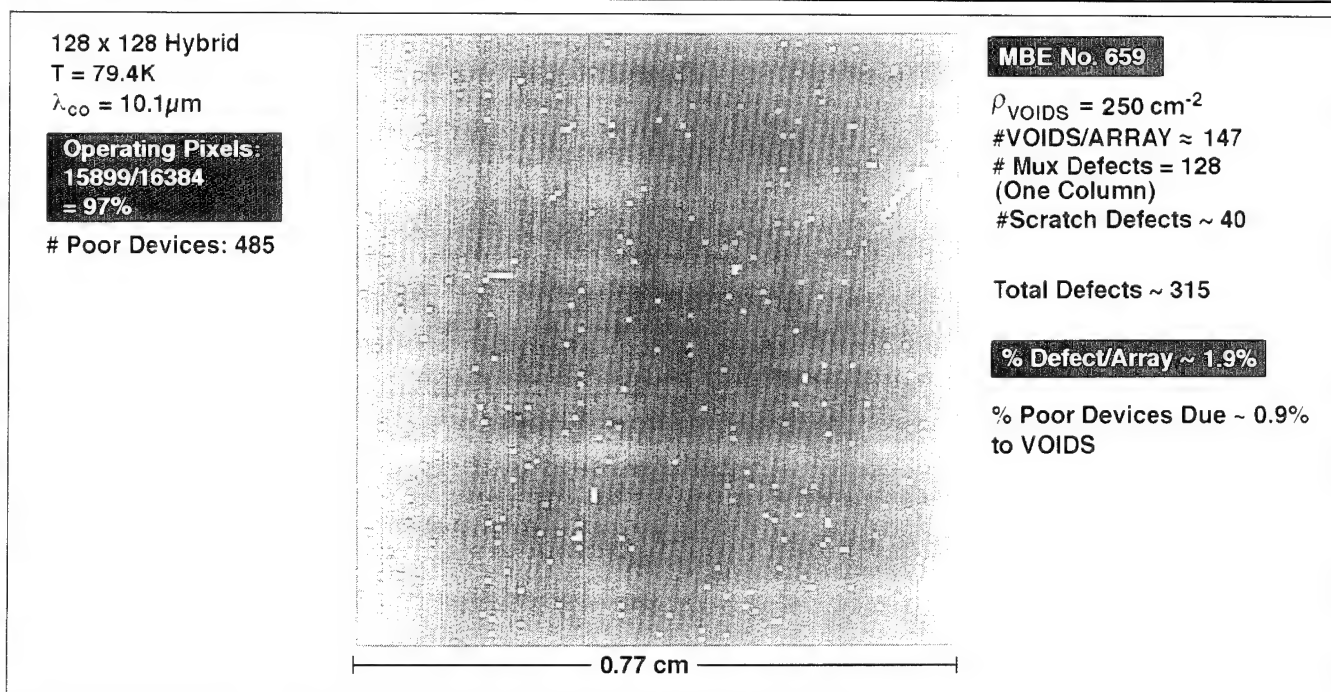


Fig. 4. Pixel operability map of a MBE HgCdTe LWIR 128×128 hybrid focal plane array. The pixel operability measured at the hybrid level is 97%. Defective pixels in this map are indicated by light color.

lustrated in Fig. 3a taken prior to growth shows the presence of different particulates at the surface. In Fig. 3b, an optical picture of the HgCdTe surface is taken at the same position after 8 μm thick epitaxial $\text{Hg}_{0.78}\text{Cd}_{0.22}\text{Te}$ was grown on this surface clearly demonstrates that formation of void defects occurs only where the particulates are present on substrate surface. The density of void defects in the epilayer may be reduced even further by improvement in substrate etching and preparation steps to clean the surface.

We have used void density value to estimate number of defective pixels in FPAs and observed a strong correlation with array pixel operability. A pixel operability map of a typical MBE HgCdTe LWIR 128×128 hybrid FPA is shown in Fig. 4. The total number of defects in this hybrid including the void defects for the area of the array, scratch defects, and multiplexer defects, corresponds to approximately 1.9% poor devices. This value is estimated based on void density of 250 cm^{-2} for this layer, defective pixels in the multiplexer, and defective pixels due to scratch during processing. The pixel operability value of 97% (pixel having $D^* > 1/2$ [mean D^*]) measured for this hybrid agrees well with the 98.1% estimate. Similar results have been observed for several hybrid arrays for both MLWIR and LWIR FPAs. We have demonstrated array pixel operability above 98.0% for a MBE HgCdTe LWIR 256×256 hybrid FPA by reducing void defect density in our epitaxial layers to values below 200 cm^{-2} .

SUMMARY

Formation of void defects in $\text{Hg}_{1-x}\text{Cd}_x\text{Te}$ grown by MBE and CdZnTe (211)B substrate surface defects were investigated using optical microscopy, atomic force microscopy, and secondary electron microscopy.

Void defect formation was found to be caused primarily by polycrystalline nucleation of HgCdTe on the dust particulates at the CdZnTe substrate surface. The density of these void defects can be reduced to values below 200 cm^{-2} using a chemical solution of bromine methanol to etch CdZnTe and dust-free dry nitrogen or spin drying. MLWIR and LWIR focal plane arrays fabricated on low void density materials grown using this new substrate etching and cleaning procedure had pixel operability above 98.0%. Density of void defects in the epilayers may be reduced even further by improvement in substrate preparation.

ACKNOWLEDGMENTS

The authors thank Dr. W.E. Tennant for many helpful discussions. This work was supported by Advanced Research Projects Agency (monitored by U.S. Army, Night Vision and Electronic Sensor Division) under Contract No. DAAB07-93-C-U505.

REFERENCES

1. R.E. DeWames, J.M. Arias, L.J. Kozlowski and G.M. Williams, *Infrared Detectors State of the Art*, SPIE Conf. Proc. 1735, 2 (1992).
2. R. Balcerak and L. Brown, *J. Vac. Sci. Technol. B* 10, 1353 (1992).
3. M. Seelmann-Eggebert, G. Carey, V. Krishnamurthy and C.R. Helms, *J. Vac. Sci. Technol. B* 1 (4) 1297 (1992).
4. J.M. Arias, *II-VI Semiconductor Compounds*, ed. M. Pain (Singapore: World Scientific Publishing Co. Pty. Ltd., 1992).
5. J.M. Arias, M. Zandian, J. Bajaj, J.G. Pasko, L.O. Bubulac, S.H. Shin and R.E. DeWames, to be published in *J. Electron. Mater.*
6. J.M. Arias, J.G. Pasko, M. Zandian, S.H. Shin, G.M. Williams, L.O. Bubulac, R.E. DeWames and W.E. Tennant, *J. Electron. Mater.* 22 (8), 1049 (1993).

Analysis of Low Doping Limitation in Molecular Beam Epitaxially Grown HgCdTe(211)B Epitaxial Layers

P.S. WIJEWARNASURIYA,* M.D. LANGE,[†] S. SIVANANTHAN,* and J.P. FAURIE*

*University of Illinois at Chicago, Microphysics Laboratory, Physics Department, 845 W. Taylor St., Room 2236, Chicago, IL 60607-7059

[†]EPIR Ltd., P.O. Box 803827-P2E, Chicago, IL 60680-3827 and Physics Branch, Research and Technology Division, Naval Air Warfare Center Weapons Division, China Lake, CA 93555

We report the results of the transport properties and the recombination mechanisms of indium-doped HgCdTe(211)B ($x \approx 23.0\% \pm 2.0\%$) layers grown by molecular beam epitaxy. We have investigated the origin(s) of the background doping limitation in these layers. Molecular beam epitaxially grown layers exhibit excellent Hall characteristics down to indium levels of $2 \times 10^{15} \text{ cm}^{-3}$. Electron mobilities ranging from $(2-3) \times 10^5 \text{ cm}^2/\text{v-s}$ at 23K were obtained. Measured lifetime data fits very well with the intrinsic band-to-band recombinations. However, below $2 \times 10^{15} \text{ cm}^{-3}$ doping levels, mobility vs temperature curves starts to reflect nonuniformity in carrier distribution. Also, when we reduced the Hg vacancy concentration down to 10^{12} cm^{-3} range, by annealing at 150°C, Hall characteristics shows an increase in the nonuniformity in the epilayers. It was found that after annealed at 150°C, the obtained SR defect level has a different origin than the previously obtain Hg-vacancy related defect level.

Key words: HgCdTe, lifetimes, molecular beam epitaxy, n-type doping, transport properties

INTRODUCTION

Minority carrier lifetime (τ) of the excess photogenerated carriers and the behavior of extrinsic dopants in HgCdTe are of great importance for the performance of infrared detectors. Small concentrations of unintentionally added elements can, if electrically active, affect the transport properties of the material and influence the performance of devices.

In molecular beam epitaxy (MBE) material, several factors such as substrate orientation, substrate supplier, growth temperature, and Hg flux appeared to influence the electrical properties.¹ In the non-intentionally doped layers, it is difficult to determine what controls electronic properties, namely; native defects (Hg vacancy, interstitial Te, etc.) or back-

ground impurities introduced during the growth and/or diffusing from the substrates. The outdiffusion of impurities had been previously reported in the literature for liquid phase epitaxial (LPE) growth² as well as for MBE^{1,3} growth of HgCdTe. Hence, selecting a suitable substrate is a very critical factor for the growth of HgCdTe by MBE. In order to determine the residual impurity background, we have analyzed as-grown and annealed layers. Indium has been used as a n-type dopant in MBE-HgCdTe epilayers at EPIR and at the University of Illinois at Chicago. From our previous studies,^{4,5} we have shown that the incorporation of indium during the growth by MBE of HgCdTe is under control down to a doping level of $\approx 2.0 \times 10^{15} \text{ cm}^{-3}$. This is supported by the measured lifetime and transport data, which attests for the high quality of MBE-grown HgCdTe layers and their suitability for IR photodiodes. However, it is extremely important to

(Received October 15, 1994; revised February 6, 1995)

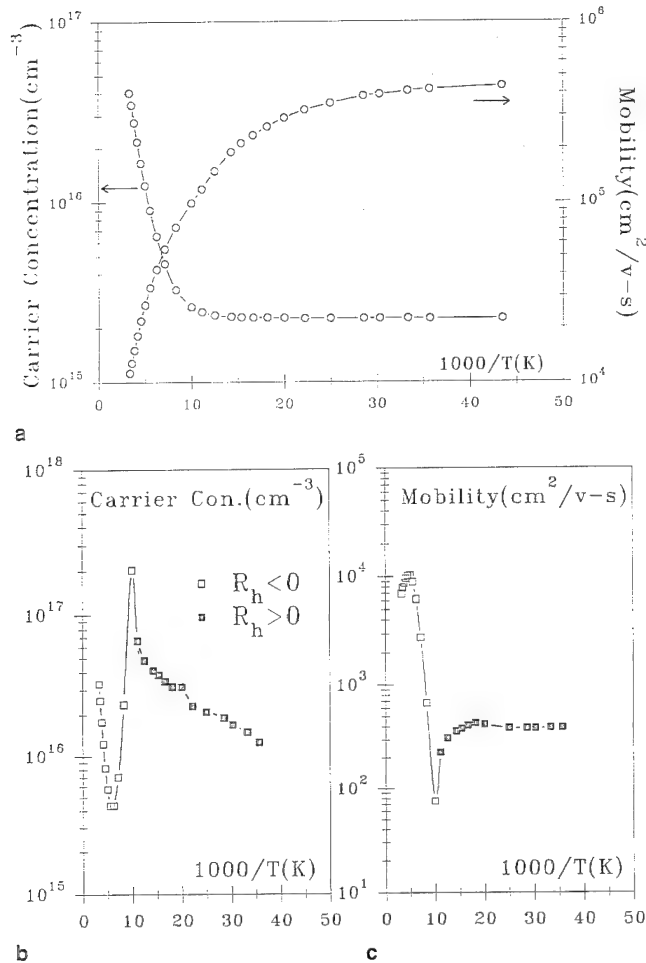


Fig. 1. Hall characterization of indium-doped MBE-Hg_{0.79}Cd_{0.21}Te grown on a selected substrate supplier at magnetic field strength of 0.2 Tesla; (a) carrier concentration and mobility of after n-type isothermal anneal (b), (c) carrier concentration and mobility of after p-type anneal vs reciprocal temperature, respectively.

investigate the origin(s) of this limit in order to control, if possible, the background doping in the 10¹⁴ cm⁻³ range or even lower.

In this work, we present an analysis of electrical properties and recombination mechanisms of indium-doped MBE-grown epilayers which will shed some light on the current limitation on the background doping in MBE-grown Hg_{1-x}Cd_xTe (x = 0.22 to 0.23) layers.

EXPERIMENT

Molecular beam epitaxy-HgCdTe layers were grown at EPIR Ltd. Details on the growth have been previously reported (for example see Ref. 1). Investigated layers were doped in-situ during MBE growth with indium. The Cd composition and the layer thickness were determined at room temperature by infrared transmission measurements. All of the layers investigated were annealed in a sealed quartz ampoule. Two types of annealing were performed. In the n-type case, layers were annealed at 250°C for 24 h, and at 250°C for 24 h followed by at 150°C for 30 days. In both cases, annealing was done under Hg-saturated atmo-

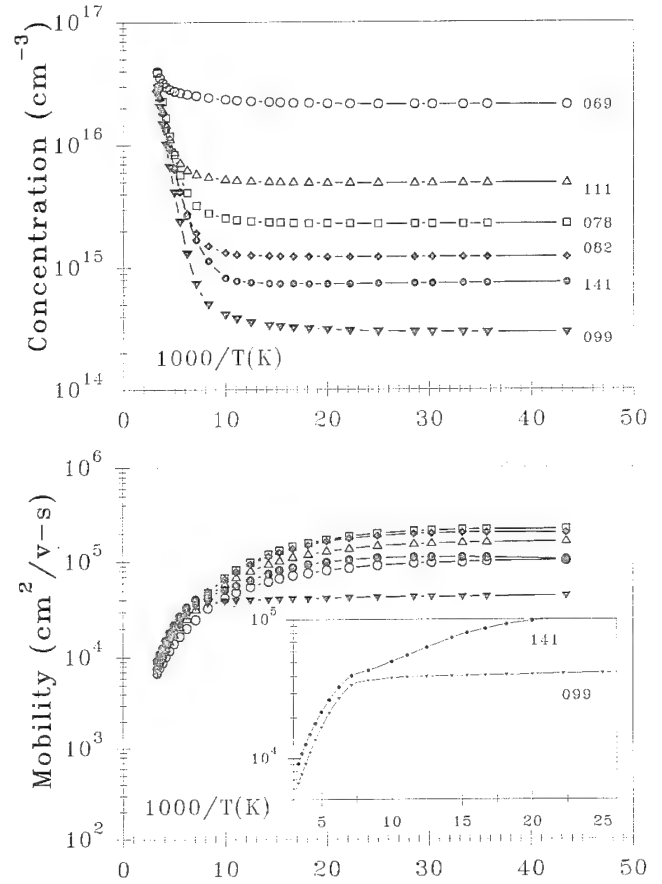


Fig. 2. (a) Carrier concentration and (b) mobility vs reciprocal temperature of (211)B indium-doped MBE grown Hg_{0.78}Cd_{0.22}Te layers grown on selected CdZnTe substrates. Insert shows the mobility vs reciprocal temperature in an expanded temperature scale.

sphere. This type of annealing will reduce the Hg-vacancy concentration created during the MBE growth at 185°C. In the p-type case, layers were annealed by keeping the sample temperature higher than the Hg source temperature. The carrier concentration [extracted from the Hall coefficient $R_h(T)$] and the mobility [extracted from $R_h(T)/\rho(B=0, T)$] of the layers were measured by the van der Pauw technique⁶ for temperatures ranging from 300 to 20 K and magnetic fields up to 1.0 Tesla. The lifetime measurements (typical sample dimensions are $\approx 3 \times 3$ mm²) were carried out using the photoconductive decay technique. Since, we do not passivate our samples after annealing, all the samples were etched in Br-methanol solution prior to both measurements.

The measured lifetime data vs temperature were analyzed, using different recombination mechanisms; namely Auger, radiative, and Shockley-Read (SR) processes. These have been discussed extensively in the literature^{4,7} and therefore we will not repeat here again. The effective lifetime τ is calculated from,

$$\frac{1}{\tau} = \frac{1}{\tau_A} + \frac{1}{\tau_R} + \frac{1}{\tau_{SR}}$$

where τ_A , τ_R , and τ_{SR} are Auger, radiative, and SR lifetime, respectively.

RESULTS AND DISCUSSION

We have previously studied¹ the dependence of Hall characteristics (carrier concentration and mobility) vs temperature of $\text{Hg}_{1-x}\text{Cd}_x\text{Te}$ layers grown under similar conditions on (211)B CdZnTe substrates bought from various suppliers. Measured data displayed striking differences in the carrier concentration and as well as the mobility vs temperature. All of the layers were non-intentionally doped and Cd composition ranges between 0.22 to 0.23. When doping was low, Hall characteristics showed mixed conduction⁸ and these were related to the presence of nonuniform impurity distribution in the layers. The influence of the mixed conduction to the transport properties varies with the substrate suppliers or sometimes even from lot to lot of the same supplier. After isothermal anneal at 250°C some layers showed degraded Hall characteristics. Layers grown on some substrates, show even p-type characteristics after n-type anneal at 250°C. These differences in the transport properties could be explained satisfactorily by the diffusion of impurities originating from the substrates. These background impurities are competing with the native defects to govern the electrical properties in the 10^{14} cm^{-3} to 10^{15} cm^{-3} range. The impurity level varies from supplier to supplier and even from lot to lot. Secondary ion mass spectroscopy (SIMS) analysis have been performed and impurities such as Li, Na, Ag, and Cu have been found¹ and are distributed nonuniformly throughout the layer. This explains the observed anomalous Hall characteristics vs temperature on some of the layers. Impurities diffusing from the substrate are nonuniformly distributed along the growth axis and are very likely to be nonuniform across the epilayer plane.

This mixed conduction behavior prevents the determination of the true background doping level in the MBE-grown HgCdTe layers. Hence, substrate screening is one of the critical steps regarding the growth of HgCdTe by MBE.

It appears that, layers grown on one of the supplier's substrates (obtained from Nippon Mining Corporation) show less mixed conduction effects in transport properties at low temperatures. We have studied the incorporation of indium in HgCdTe when these substrates are used. This has been carried out not only to control mid to high donor levels but also to establish a background doping level which is important in the infrared detection technology especially in the photo conduction (PC) mode.⁹ Layers grown on these substrates show excellent electrical properties and they do convert completely as n-type and p-type after suitable respective anneals. Figure 1 shows the carrier concentration and the mobility vs reciprocal temperature of a typical layer grown on this selected substrate under different annealing conditions. As can be seen, this In-doped layer after n-type anneal exhibit excellent electrical properties. The Cd composition of this layer is 0.21. Electron mobility exceeds $4 \times 10^5 \text{ cm}^2/\text{v-s}$ at 23K and compares well with the best

mobilities reported so far. These layers do convert to p-type after a suitable p-type anneal. As an example, the carrier concentration and mobility vs reciprocal temperature for the same layer are shown in Fig. 1b and Fig. 1c, respectively, after a suitable p-type anneal.

To establish the lowest n-type background level controlled by indium, HgCdTe layers were grown under different indium fluxes. Figure 2 shows the carrier concentration (Fig. 2a) and the mobility (Fig. 2b) vs reciprocal temperature of indium-doped n-type layers which have been annealed at 250°C. Cd composition on these layers were between 0.22 and 0.23. Electron mobilities ranging from $2-3 \times 10^5 \text{ cm}^2/\text{v-s}$ at 23K were obtained with doping levels down to $\approx 2 \times 10^{15} \text{ cm}^{-3}$. These values are comparable with the best mobilities reported for HgCdTe for this Cd composition and for this doping level.

Figure 3 shows the mobility vs doping measured at 23K after annealed at 250°C. The expected behavior of increase in mobility with decreasing doping levels can be clearly seen down to $2.0 \times 10^{15} \text{ cm}^{-3}$. When the doping level decreases below $2.0 \times 10^{15} \text{ cm}^{-3}$, the measured Hall mobility started to decrease instead of an increase. From Table I and Fig. 3, it appears that these annealed layers can be classified into two different categories.

Region I: $N_d - N_a \geq 2.0 \times 10^{15} \text{ cm}^{-3}$

Layers which fall into this category always show well behaved Hall characteristics (see Fig. 2). Carrier concentration and mobility vs reciprocal temperature curves show no visible mixed conduction effects.⁸ Electrical properties are fully explained by the intrinsic material properties. Measured mobility decreases

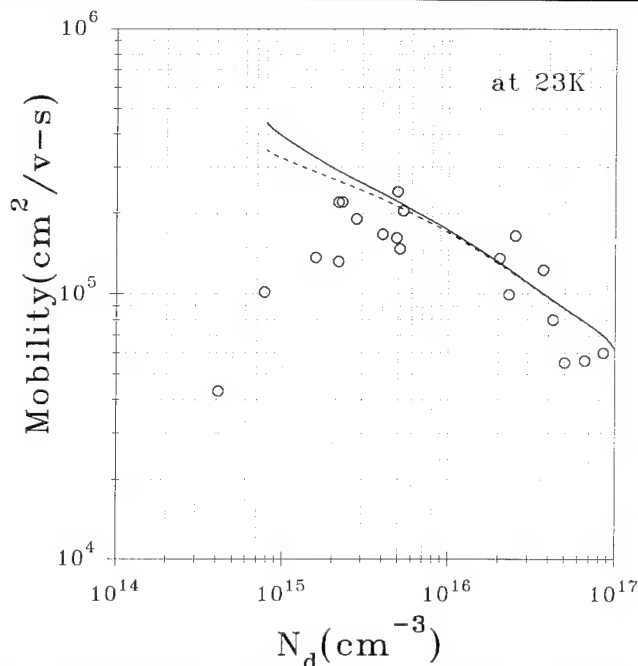


Fig. 3. Dependence of mobility vs doping concentration at 23K. The solid line is the theoretical calculation assuming no compensation and the dash line takes into account compensation as described in the text.

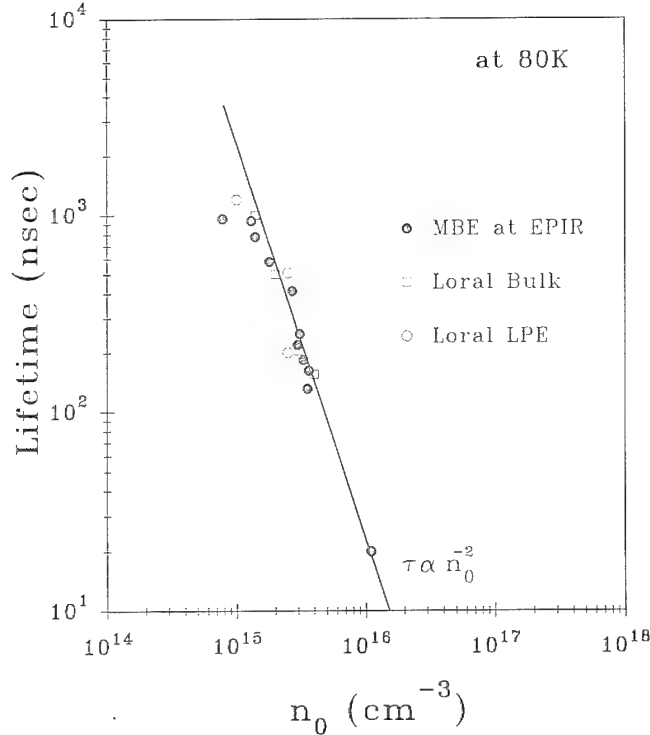


Fig. 4. Measured minority carrier lifetime on electron density (solid symbols) at 80K on indium-doped MBE-grown HgCdTe layers. Data also included Loral LPE-grown (O) and bulk-grown (□) HgCdTe layers obtained from Ref. 14. The solid line shows the calculated Auger lifetime at 80K with $|F_1 F_2| = 0.22$.

when doping level increases. This is an indication of the scattering due to ionized impurities.¹⁰ The solid line in Fig. 3 shows the overall mobility calculated at 23K as a function of the doping concentration by reciprocally combining the mobility due to ionized impurity and that due to lattice scattering:

$$\frac{1}{\mu} = \frac{1}{\mu_{\text{Lattice}}} + \frac{1}{\mu_{\text{Ionized}}}$$

where μ_{Ionized} is the ionized impurity scattering mobility (assuming no compensation) given by,¹¹

$$\mu_{\text{Ionized}} = \frac{0.20 \epsilon}{(m_0^*/m)^2 g(b)} \frac{E_g}{(2E_F + E_g)^2}$$

where ϵ is the dielectric constant,¹² $m_0^* = 3 \hbar^2 E_g / 4P^2$, $P = 8 \times 10^{-8}$ eV cm,¹² and E_F is the Fermi energy.

The screening factor $g(b)$ is given by,

$$g(b) = \ln(1+b) - \frac{b}{1+b}$$

$$b = \frac{0.85 \epsilon}{(m_0^*/m)^{1/2}} \frac{\sqrt{E_F E_g} (E_F + E_g)^{1/2}}{(2E_F + E_g)}$$

We have assumed¹³ $\mu_{\text{Lattice}} = 1 \times 10^7$ cm²/v-s.

According to the HgCdTe P-T phase diagram, an-

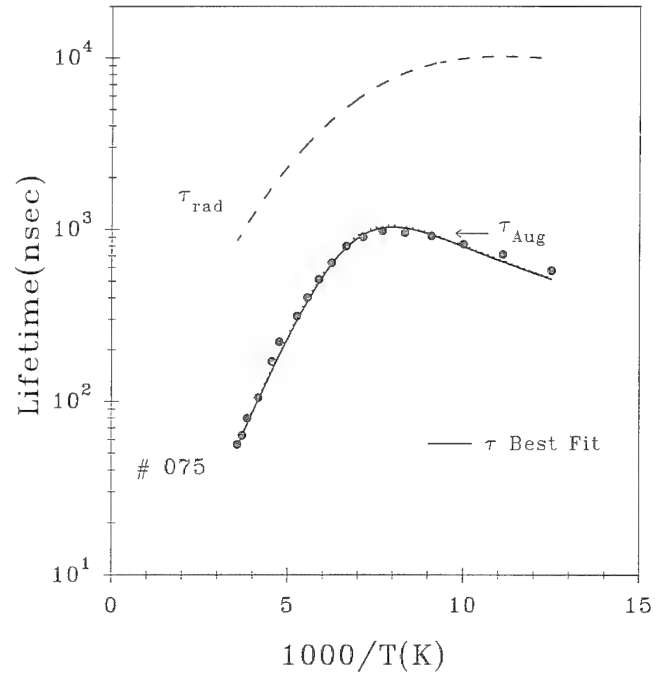


Fig. 5. Measured (●) and theoretical minority carrier lifetime on a indium-doped HgCdTe layer #075 vs reciprocal temperature after anneal at 250°C. Lines show various contributions from radiative (---), Auger (···), and combined Auger plus radiative (—) recombination processes.

nealing at 250°C under Hg saturated conditions should reduce the Hg vacancies to low 10^{14} cm⁻³ range. Hence, when N_d is above 2×10^{15} cm⁻³, layers can be considered not to be compensated by these Hg vacancies, which is in very good agreement with the theory. The dash line in Fig. 3 was obtained by assuming compensating acceptor concentration of 1.0×10^{14} cm⁻³. These compensating acceptors start to play a significant role when $N_d < 2-3 \times 10^{15}$ cm⁻³ as seen by the dash line in Fig. 3.

Figure 4 shows the relation between lifetime and electron concentration of indium-doped Hg_{1-x}Cd_xTe ($x \approx 23.0\% \pm 2.0\%$) layers at 80K. Lifetime decreased from ≈ 1 μsec to ≈ 20 nsec when doping increased from $\approx 2 \times 10^{15}$ cm⁻³ to 1×10^{16} cm⁻³. The solid symbols represent layers grown by MBE at EPIR Ltd. The measured lifetime data can be explained satisfactorily by the intrinsic limited band-to-band recombination processes throughout the temperature region down to 80K (see also in Refs. 4 and 5). For comparison purposes, we have also included in Fig. 4 lifetime data at ≈ 80 K of Loral LPE- and bulk-grown layers.¹⁴ As can be seen, our MBE-grown layers compare very well with the Loral layers with comparable doping densities. Figure 5 shows the behavior of lifetime of layer #075 vs temperature as measured by the photoconductive decay method. Solid circles represent measured experimental data points after anneal at 250°C. The peak lifetime reaches ≈ 1.0 μs at 130K; and at lower temperatures, it decreases exponentially. The solid line represents the theoretical curve, which include only intrinsic band-to-band (namely, Auger and radiative) processes. As can be seen, there is an

Table I. Hall Characteristics and Lifetime Behavior of Some of the Selected Layers

Name	t (μm)	FWHM (arc-s)	Doping $N_d - N_a$ (cm ⁻³)	μ at 23K (cm ² /v-s)	Hall Data	Lifetime Data (SR Visible or Not)
069	09.5	53	2.0×10^{16}	1.1×10^5	Classical	No
111	12.2	—	4.9×10^{15}	1.6×10^5	Classical	No
078	10.8	33	2.2×10^{15}	2.3×10^5	Classical	No
139	11.2	97	1.4×10^{15}	1.6×10^5	Classical	No
082	10.4	41	1.2×10^{15}	2.0×10^5	Classical	Yes
141	11.4	90	7.8×10^{14}	1.1×10^5	Slightly Mixed	Yes
099	19.9	60	2.9×10^{14}	4.4×10^4	Mixed	—

excellent agreement between the experimental data and the intrinsic material properties of MBE-grown HgCdTe layers. This layer has a doping level of $2.2 \times 10^{15} \text{ cm}^{-3}$. Similar behavior is obtained for higher doping levels. The Auger lifetime dominates throughout the entire temperature region from 300 to 80K. The solid line in Fig. 4 shows n_0^{-2} dependence as expected and this further confirms that the measured lifetime is limited by the Auger recombination at 80K.

Region II: $N_d - N_a < 2.0 \times 10^{15} \text{ cm}^{-3}$

In this range, layers are compensated due to Hg vacancies. As can be seen from Fig. 3, there is a substantial discrepancy between the calculated mobility and the measured mobility at 23K assuming 10^{14} cm^{-3} of compensating acceptors. Hence, this drastic reduction in mobility cannot be due to the compensating acceptors. For the lowest doping of $\approx 3.0 \times 10^{14} \text{ cm}^{-3}$, this decrease in mobility is clearly visible.

Layers, falling between $1 \times 10^{15} \text{ cm}^{-3}$ to $2 \times 10^{15} \text{ cm}^{-3}$, show no mixed conduction effects (see Table I). Measured lifetimes on these layers could be explained by intrinsic band-to-band processes without SR recombination, similar to the high doped layers. Figure 6a shows lifetime data on layer #139 which has a doping level of $1.3 \times 10^{15} \text{ cm}^{-3}$ after 250°C anneal.

Measured lifetime on most of the layers (doping between $(1-2) \times 10^{15} \text{ cm}^{-3}$), could be explained by assuming SR recombination centers in addition to the band-to-band recombination processes. Figure 7a shows measured lifetime on layer #082. This layer has a doping level of $1.4 \times 10^{15} \text{ cm}^{-3}$. The behavior of lifetime vs temperature data are similar to the ones obtained for higher doping levels. The combined Auger and radiative lifetime is in good agreement with the experimental data in the intrinsic region. But, in the extrinsic temperature region, the data is lower than the theoretical value by a factor of ≈ 1.2 . In order to obtain a good fit throughout the entire temperature range, we had to assume SR recombination level of 45 meV below the conduction band. This defect level is located $\approx (3/4)E_g$ with respect to the valence band edge.

When the doping falls below $2.0 \times 10^{15} \text{ cm}^{-3}$, compensation should indeed occur after n-type annealed at 250°C. However, as can be seen from Table I, mixed conduction effects started to be visible in the mobility vs temperature curve in the extrinsic temperature region (see Fig. 2). This mixed conduction can only be

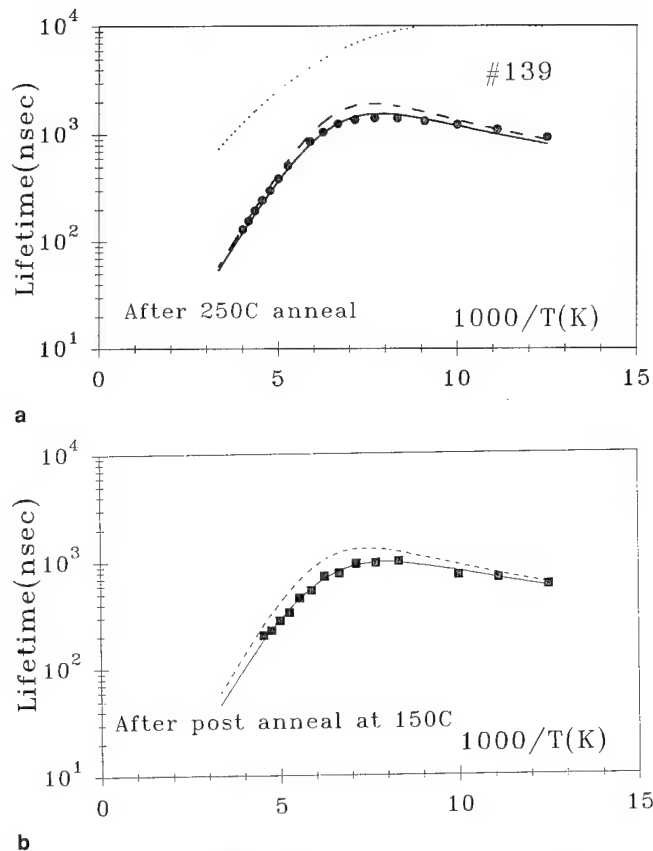


Fig. 6. (a) Measured (●) and theoretical minority carrier lifetime on a indium-doped HgCdTe layer #139 vs reciprocal temperature after annealed at 250°C. Lines show various contributions from Auger (---), radiative (···), and combined Auger plus radiative (—) recombination processes. (b) Measured (■) and theoretical minority carrier lifetime vs reciprocal temperature of the same layer after post annealed at 150°C. Lines show various contributions from Auger plus radiative (---), and combined Auger, radiative and SR (—) recombination processes.

explained by nonuniform distribution of carriers. There is no evidence that this mixed conduction, only slightly visible, is due to nonuniformity in Hg vacancy distribution. This point will be discussed later.

Measured minority carrier lifetime data requires recombinations from SR centers in order to get a good fit throughout the entire extrinsic temperature region. Figure 7b shows the measured lifetime data, on layer #141 which has a doping of $7.8 \times 10^{14} \text{ cm}^{-3}$. At 80K, measured lifetime is lower than the value calculated from the recombination by Auger plus radiative processes. The same SR defect level which is located

Table II. Summary of the Measured and Fitted Parameters of MBE-Grown $\text{Hg}_{1-x}\text{Cd}_x\text{Te}$ Layers that were Annealed at 250°C and Post Annealed at 150°C

Name	Anneal at 250°C			Post Anneal at 150°C		
	N_d (cm^{-3})	$N_d - N_a$ (cm^{-3})	μ at 80K ($\text{cm}^2/\text{v}\cdot\text{s}$)	N_d (cm^{-3})	$N_d - N_a$ (cm^{-3})	μ at 80K ($\text{cm}^2/\text{v}\cdot\text{s}$)
069	2.2×10^{16}	2.2×10^{16}	5.1×10^4	2.2×10^{16}	2.2×10^{16}	5.3×10^4
078	3.0×10^{15}	2.3×10^{15}	9.7×10^4	2.9×10^{15}	2.8×10^{15}	8.8×10^4
075	2.3×10^{15}	2.2×10^{15}	9.5×10^4	2.7×10^{15}	2.7×10^{15}	8.6×10^4
077	2.4×10^{15}	1.9×10^{15}	7.6×10^4	3.1×10^{15}	3.1×10^{15}	5.4×10^4
139	1.9×10^{15}	1.4×10^{15}	7.0×10^4	2.1×10^{15}	2.1×10^{15}	4.5×10^4
082	1.4×10^{15}	1.2×10^{15}	9.4×10^4	—	—	1.6×10^4

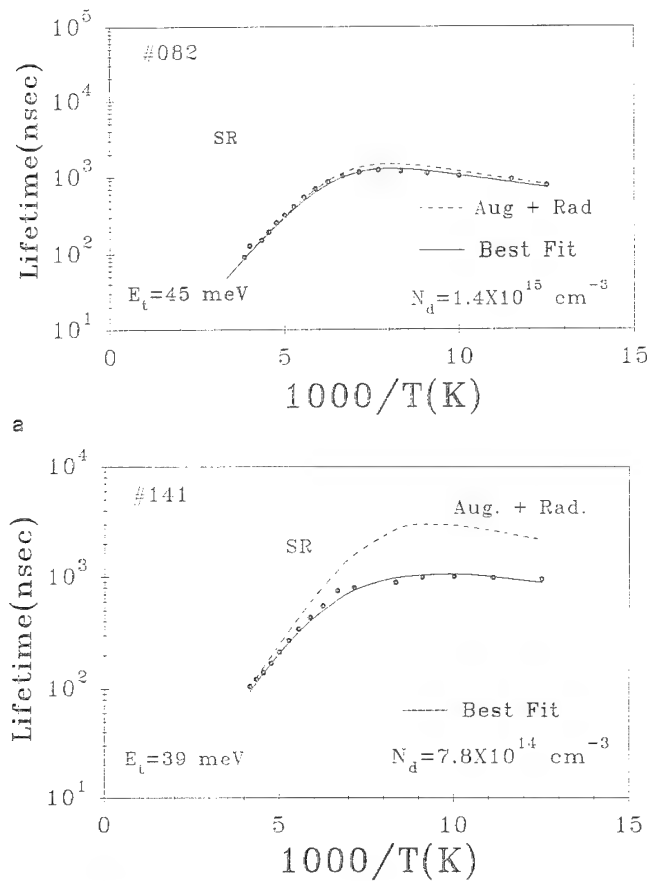


Fig. 7. Measured of minority carrier lifetime vs reciprocal temperature on (a) layer #082 and (b) layer #141. Lines show various contributions; SR recombination (\cdots), combined Auger and radiative recombination ($-\cdots$), and combined Auger, radiative, and SR recombination ($—$).

$\approx (3/4)E_g$ with respect to the valence band has to be used. This indicates that it has the same origin compared to the layers which have doping levels between $1 \times 10^{15} \text{ cm}^{-3}$ and $2 \times 10^{15} \text{ cm}^{-3}$. As we have concluded from our previous article,⁴ we believe that these SR levels are somehow related to the Hg vacancies.

It should be pointed out that this Hg vacancy related SR defect level exists in all the In-doped layers since Hg-annealing conditions are the same. However, the correction factor (for layer #082 it is about 1.2) should decrease when N_d increases (lifetime de-

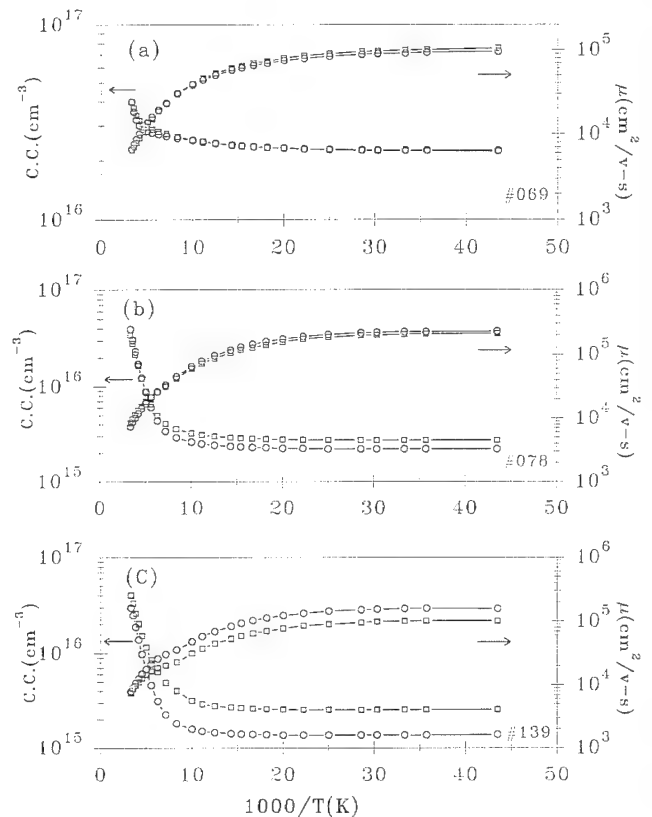


Fig. 8. Hall characteristics of layer #069, #078, and #139 at magnetic field strength of 0.4 Tesla after 250°C (\circ) and post 150°C (\square) anneals.

creases) and therefore it can be neglected and this explains why this SR level "is not seen" in layers with higher doping levels.

As pointed out earlier, compensation from Hg-vacancies does show up for low-doped as-grown layers as well as for low-doped annealed layers at 250°C. Also, the observed SR defect level is somehow related to the Hg vacancies. Hence, in order to reduce the Hg vacancy concentration further down, these layers were annealed at 150°C. This study was carried out in order to understand the limitation of the current lower limit of $\approx 2.0 \times 10^{15} \text{ cm}^{-3}$. We concentrated more on the low-doped layers which mostly show SR recombination in the extrinsic temperature region. Table II shows the measured electrical data for epilayers annealed at 250°C and post annealed at 150°C. As can be seen for all the layers, the doping level $N_d - N_a$

increased after the 150°C anneal. The increase in $N_d - N_a$ after 150°C anneal is more visible as the doping decreases. This is expected since N_a decreased after anneal at 150°C. As expected, at higher doping levels, this reduction in Hg vacancy concentration is not noticeable. This indicates that compensation should decrease and therefore, both electron mobility and minority carrier lifetime should increase. But from Table II, it is clear that a decrease in electron mobility for all the layers is visible except for layer #069 which has the highest doping in this study. Figure 8 shows Hall curves vs reciprocal temperature of three selected layers which falls in the two regions that we discussed in the Fig. 3. Data on Fig. 8 compares after 250°C (○) and post 150°C (●) anneals. For layer #139, mobility curve shows mixed conduction effects indicating the presence of nonuniformity in carrier distribution in the layer after annealed at 150°C, where as no nonuniformity was visible after the 250°C anneal. Also, minority carrier lifetime is reduced after a post anneal at 150°C as illustrated in Fig. 6b for layer #139. In addition, the fitting of the lifetime data vs temperature requires recombination from SR centers in addition to the band-to-band recombinations. The obtained SR energy level is very different than that of Hg vacancy related SR centers. We obtained $E_t = 97$ meV which is deep below the conduction band edge and is about $(1/4)E_g$ with respect to the valence band edge.

Similar behavior is observed for layer #077 after post anneal at 150°C. Figure 9 shows the measured lifetime data vs reciprocal temperature. Lifetime data cannot be explained by intrinsic band-to-band recombinations alone. As seen in the Fig. 9, this layer shows very complicated recombination mechanism at low temperatures.

As the Hg vacancy concentration falls down to 10^{12} cm⁻³ range, defect level associated with Hg vacancies reduces. But, another defect level which has a different origin other than the Hg vacancy becomes important. In addition, the nonuniformity in carrier distribution is much more pronounced after the post anneal at 150°C rather than in layers annealed at 250°C. Hence, this nonuniformity is neither due to indium nor due to Hg vacancy but very likely due to nonuniformly distributed impurities (i.e. brought from diffusion). Diffusion of impurities from the substrates appear to be the best hypothesis which can explain the observed results. However, it is not very clear why these impurity associated defect levels do not show up after 250°C annealing. After 150°C annealing, the Hg vacancy related defect level diminishes and an impurity related defect level starts to appear. It seems that these impurities are more electrically active when both indium and Hg vacancy concentrations are low. In this case, these nonuniformly distributed electrically active impurities give mixed conduction which will dominate the transport properties. Therefore, even after careful screening, it seems that CdZnTe substrates are the source of contamination for low doped HgCdTe epilayers grown by MBE. Hence, the

doping level $N_d - N_a = 2.0 \times 10^{15}$ cm⁻³ is certainly not the lower limit achievable in terms of doping in HgCdTe grown by MBE.

CONCLUSION

In this work, we have studied the transport properties and the minority carrier lifetime on Hg_{1-x}Cd_xTe layers with Cd composition $\approx 23.0\% \pm 2.0\%$. From a previous study,¹ we have selected a substrate which gave the lowest contamination possible in terms of diffusion of impurities. On these substrates, we have been able to control the doping level down to $\approx 10^{15}$ cm⁻³ level. In order to determine the origin of the residual doping, we have studied the transport properties of annealed In-doped HgCdTe MBE layers grown on these selected substrate. When the doping level is above $\approx 2.0 \times 10^{15}$ cm⁻³, MBE-grown layers exhibit excellent electrical properties. Measured lifetime data fits very well with the intrinsic band-to-band recombination mechanisms above 2×10^{15} cm⁻³ of doping levels. Hence, the incorporation of indium during the growth of MBE HgCdTe is under control down to the doping levels of 2×10^{15} cm⁻³, and the excellent electrical data are supported by the measured lifetime data, indicating the high quality of MBE-HgCdTe layers.

Layers annealed at 250°C show compensation by Hg vacancies when the doping level is less than 2×10^{15} cm⁻³. In some layers, mobility vs reciprocal temperature curves start to reflect nonuniformity in carrier distribution. Minority carrier lifetime vs reciprocal data require SR recombination centers to be included. A single level located $\approx (3/4)E_g$ with respect to the valence band was necessary to explain the measured data. This level appeared to be related to

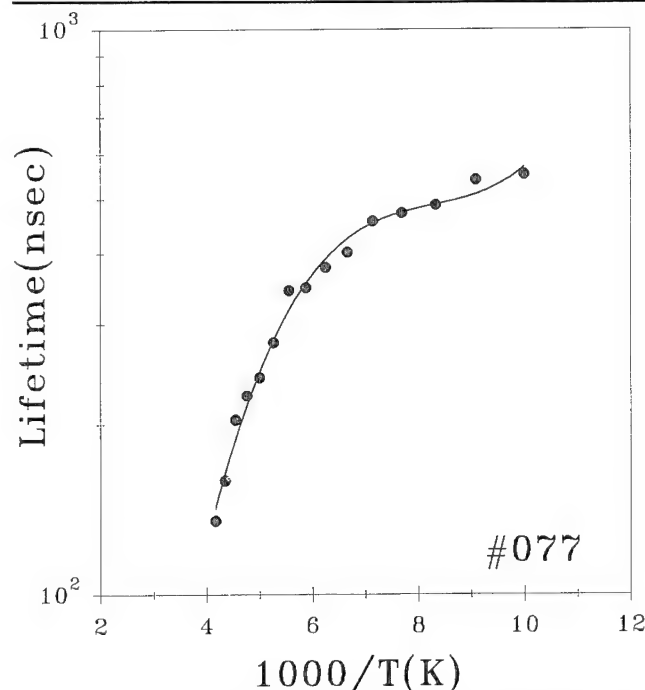


Fig. 9. Dependence of minority carrier life time on layer #077 after post anneal at 150°C.

the Hg vacancies. In order to reduce the Hg vacancy concentration down to 10^{12} cm^{-3} range, we have annealed these layers at 150°C . Such layers had lower mobility and minority carrier lifetime values compared to layers annealed at 250°C . This shows an increase in the nonuniformity of the carrier distribution after the anneal at 150°C . The obtained SR defect level has a different origin than the previously obtained Hg-vacancy related defect level. This defect level is located approximately $(1/4)E_g$ with respect to the valence band. It seems that these impurities are more electrically active when both indium and Hg vacancy concentration are low. Diffusion of impurities from the substrate is still a problem which limits the lowest doping level achievable by MBE. Hence, the current lower doping $\approx 2.0 \times 10^{15} \text{ cm}^{-3}$ is certainly not the lower limit achievable by MBE.

ACKNOWLEDGMENTS

This work was funded by the Advanced Research Projects Agency and monitored by the U.S. Air Force Office for Scientific Research under contract #F49620-91-C-0007.

REFERENCES

1. J.P. Faurie, S. Sivananthan and P.S. Wijewarnasuriya, *SPIE Proc.* 1735, 141 (1992).
2. T.H. Myers, K.A. Harris, R.W. Yanks, C.M. Mohnkan, R.J. Williams and E.K. Dudoff, *J. Vac. Sci. Technol. B* 10, 1438 (1992).
3. P. Rudolph, M. Muhlberg, M. Neubert, T. Boeck, P. Mack, L. Parthier and K. Jacobs, *J. Cryst. Growth* 118, 202 (1992).
4. P.S. Wijewarnasuriya, M.D. Lange, S. Sivananthan and J.P. Faurie, *J. Appl. Phys.* 75, 1005 (1994).
5. P.S. Wijewarnasuriya, M.D. Lange, S. Sivananthan and J.P. Faurie, *J. Eletron. Mater.* 24, 545 (1995).
6. L.J. van der Pauw, *Philips Tech. Rev.* 20, 220 (1958).
7. M.A. Kinch, M.J. Brau and A. Simmons, *J. Appl. Phys.* 44, 1649 (1973).
8. L.F. Lou and W.H. Frye, *J. Appl. Phys.* 56, 2253 (1984).
9. M.A. Kinch and S.R. Borrello, *Infrared Phys.* 15, 111 (1975).
10. J.J. Dubowski, T. Dietl, W. Szymanska and R.R. Galazka, *J. Phys. Chem. Solids* 42, 351 (1981).
11. D. Long, *Phys. Rev.* 176, 923 (1968).
12. R. Finkman, *J. Appl. Phys.* 54, 1883 (1983).
13. J.R. Meyer, C.A. Hoffman, F.J. Bartoli, D.A. Arnold, S. Sivananthan and J.P. Faurie, *Semicond. Sci. Technol.* 8, 805 (1993).
14. M.B. Reine, K.R. Maschhoff, S.P. Tobin, P.W. Norton, J.A. Mroczkowski and E.E. Krueger, *Semicond. Sci. Technol.* 8, 788 (1993).

Compositional Dependence of Cation Impurity Gettering in $\text{Hg}_{1-x}\text{Cd}_x\text{Te}$

JOSÉ L. MELÉNDEZ, JOHN TREGILGAS, and JOHN DODGE

Corporate Research, Texas Instruments Inc., Dallas, TX 75265

C.R. HELMS

Department of Electrical Engineering, Stanford University, Stanford, CA 94305

Cation impurity gettering in $\text{Hg}_{1-x}\text{Cd}_x\text{Te}$ is described in the context of process models which include the interactions of the impurities and the dominant native point defects. Experimental results are presented using secondary ion mass spectroscopy (SIMS) profiles of Au redistribution in $\text{Hg}_{1-x}\text{Cd}_x\text{Te}$ ($x = 0.2, 0.3, 0.4$) following Hg anneals and ion mills, which are processes known to inject excess Hg interstitials. In either process, the IB impurity distributes preferentially to high vacancy regions. The junction depth of the low to high impurity transition is determined by SIMS. For Hg-rich anneals of Au-doped high vacancy concentration material, the impurity junction behavior with respect to anneal time and temperature is compared to that expected for type converted electrical junctions in vacancy-only material. For milled Au-doped $\text{Hg}_{0.7}\text{Cd}_{0.3}\text{Te}$ with a high vacancy concentration, the impurity junction depths are approximately proportional to the amount of material removed, as was the case with $x = 0.2$ material. Hg anneal type-conversion rates are found to have a strong compositional dependence which compares favorably with the strong self-diffusion coefficient dependence on x -value. In contrast, the mill conversion rate has a weak x -value dependence. Effects of trace vs dominant Au levels compared to the background vacancy concentration are quantified. True decoration of intrinsic defect processes requires $[\text{Au}] \ll [\text{Cation Vacancies}]$.

Key words: Defect interactions, HgCdTe, impurity gettering, native point defects

INTRODUCTION

Diffusion experiments in $\text{Hg}_{1-x}\text{Cd}_x\text{Te}$ have traditionally focused upon $x = 0.2$ material for long wavelength infrared (LWIR) imaging applications. Investigation of the existence region and of fundamental diffusion phenomena such as Hg self-diffusion and type-conversion of vacancy doped material are well documented for LWIR material.¹⁻¹¹ Indeed, this relatively complete information set has been instrumental in the development of comprehensive point defect models to describe diffusion in $\text{Hg}_{0.8}\text{Cd}_{0.2}\text{Te}$.¹²⁻¹⁵ However, these models do not quantitatively treat mid-wave (MWIR, $x = 0.3$) nor short-wave (SWIR, $x = 0.4$) $\text{Hg}_{1-x}\text{Cd}_x\text{Te}$.¹² This limitation is due in large part to the incomplete diffusion characterization of the $x \neq$

0.2 compositions available in the literature. In addition to the native point defect physics, interaction mechanisms of impurities such as Au and Cu have not been extensively investigated for these shorter wavelength materials. By comparison, group IB cation impurity redistribution in $\text{Hg}_{0.8}\text{Cd}_{0.2}\text{Te}$ has been studied in detail for Hg anneals and ion etching.^{14,16} Group IB doped LWIR material has demonstrated promise as the base material for high performance, stable ion implanted homojunctions. In this report, we will present experimental and modeling results for the redistribution of IB cation impurities in MWIR and SWIR $\text{Hg}_{1-x}\text{Cd}_x\text{Te}$. These results will be contrasted to what is observed experimentally in LWIR material. In addition, the differences observed will be discussed in the context of anticipated variable x dependencies based upon Hg self-diffusion data.³

(Received October 4, 1994; revised January 15, 1995)

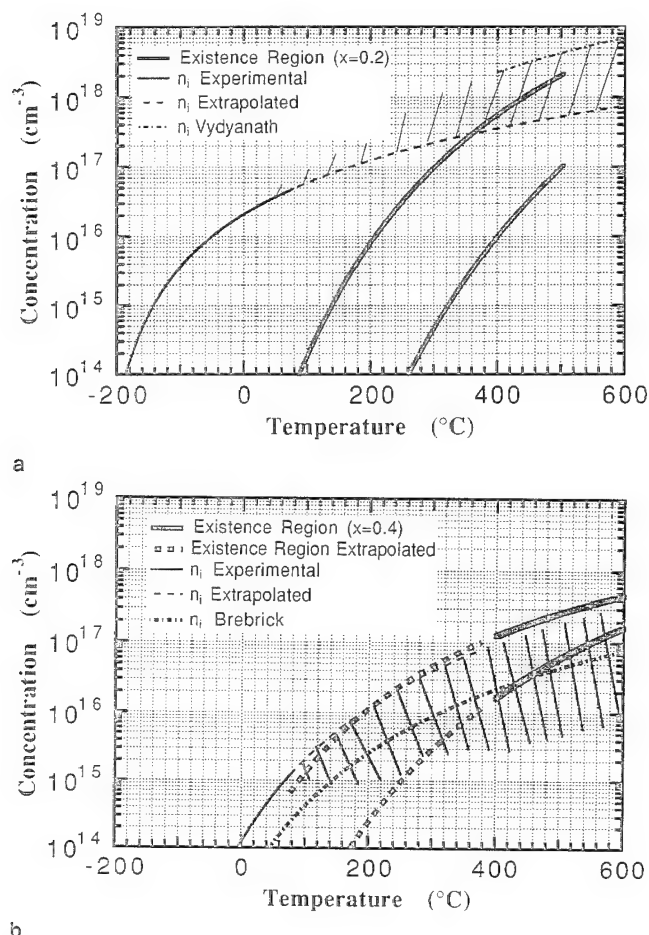


Fig. 1. Comparison of intrinsic carrier concentrations and phase limits at processing temperatures for compositions of (a) $x = 0.2$ and (b) $x = 0.4$.^{1,17,18} The existence region is bound by the Hg and Te-saturated conditions from low to high vacancy concentration, respectively.

REVIEW OF POINT DEFECT KINETICS MODELING

Process models which define point defect interactions and quantify macroscopic diffusion phenomenon in LWIR material have previously been presented and discussed in detail.¹²⁻¹⁴ These models are based on continuity equations which track the motion of each point defect by diffusion or drift, and terms which define the generation and recombination (G-R) processes. The G-R terms are based upon first order reaction kinetic descriptions of the dominant quasi-chemical reactions between the important point defects. In describing group IB impurities, the four-point defect species of interest are the Hg interstitials, cation vacancies, impurity interstitials, and substitutional impurities. The interactions of interest are the Frenkel, Frank-Turnbol, and kickout. The Frenkel reaction involves the recombination of Hg interstitials and cation vacancies or the generation of these in the reverse direction by having a Hg on a cation site move into an interstitial position. The Frank-Turnbol interaction is similar to the Frenkel, except it involves Au instead of Hg. The kickout mechanism drives substitutional Au off of its site through a "kickout"

interaction with a Hg interstitial. In the reverse direction, Au interstitials "kickout" substitutional Hg. In LWIR material, drift terms are typically neglected since the relatively small bandgap (0.12 eV) results in intrinsic material under most process conditions.

Discussions in Refs. 13 and 14 have begun to outline the kinetic formalisms for variable composition systems. The key differences in the models necessary for shorter wavelength material regard the need to quantify the compositional dependence of the interaction parameters and the point defect diffusion coefficients, since the specific kinetics and thermodynamics are undoubtedly functions of composition. Drift terms to provide for ionized point defect motion and corresponding built-in electric fields are necessary since the material may not be intrinsic at typical process temperatures. In addition, the kinetic description and solution is complicated by gradients in composition, though these are neglected in the present discussion since the materials under investigation are homogeneous. A modeling approach for the general x -value system has been described in Ref. 14, where we developed a set of continuity equations for the interdiffusion problem. Perhaps the most significant barrier is the lack of a complete experimental database in the literature for $x \neq 0.2$ material, though several investigators have provided some of the necessary information.^{1,3,17,18}

The present understanding of the intrinsic carrier concentrations and phase limits is summarized for $x = 0.2$ and 0.4 material in Figs. 1a and 1b, respectively. The thick lines are the phase limits plotted as two times the respective vacancy concentrations (assuming doubly ionized vacancies). The thin lines are various determinations of the intrinsic carrier concentrations. The measured intrinsic carrier concentrations are given by the thin solid lines below 80°C .¹⁹ The dashed extensions are extrapolations of an empirical fit to the lower temperature data. As discussed in Ref. 14, the pressure dependence near the Te-saturated limit may be used to determine the intrinsic carrier concentration based on equilibrium point defect relationships. The upper dot-dashed curve in Fig. 1a was determined by Vydyanath utilizing such an analysis.¹ It is not clear why Vydyanath's intrinsic carrier concentrations are much higher than the extrapolation of the low temperature experimental data. The uncertainty is indicated in the figure by the shaded region. Based on a similar study of the $x = 0.4$ phase limits above 400°C , Vydyanath determined that the material was extrinsic in all cases.¹⁷ This restricts the intrinsic carrier concentrations to values below the lower dot-dashed curve calculated by Brebrick and shown in Fig. 1b.¹⁸ However, there is some question as to the accuracy of Brebrick's calculations, since they do not match the measured intrinsic carrier concentrations at room temperature. Vydyanath's intrinsic carrier concentrations also fall far below the extrapolated low temperature experimental results. The uncertainty is roughly indicated by the shaded area. The intrinsic carrier concentra-

tions at process temperatures will need to be better defined in order to quantify electric field effects during processing.

In addition to establishing the phase limits for other x -values, type-conversion analyses in these materials will also be required in order to resolve the Hg interstitial and vacancy diffusion components. The Au gettering results presented in this paper for Hg-rich anneals indicate that the type-conversion rate in $x = 0.4$ material is substantially reduced. This is consistent with the much smaller Hg-rich self-diffusion coefficients reported by Archer et al. for $x = 0.4$ material.³

RESULTS AND DISCUSSION

In this section, we will present and discuss the experimental results of Au gettering experiments in $\text{Hg}_{1-x}\text{Cd}_x\text{Te}$ ($x = 0.2, 0.3, 0.4$). The samples are liquid phase epitaxy (LPE) films grown from an indium counterdoped melt on Au-doped, CdZnTe lattice matched substrates. Extrinsic P-type doping of the LPE layer was achieved through a post-growth annealing schedule which ultimately results in a low background vacancy concentration ($\approx 10^{13} \text{ cm}^{-3}$). The high background vacancy levels are set through subsequent Hg poor anneals using a Te-rich capping layer. The capping layer and several microns of $\text{Hg}_{1-x}\text{Cd}_x\text{Te}$ are then stripped by wet etching, prior to the Hg interstitial injection process.

The Au profiles are measured by secondary ion mass spectroscopy (SIMS) using 14.5 keV Cs ions with a resulting material etch rate of roughly 30 Å/s. While it has been established that ion milling can significantly alter the point defect densities in $\text{Hg}_{1-x}\text{Cd}_x\text{Te}$, this process typically utilizes Ar ions at a much lower energy of 0.5 keV. The validity of the SIMS technique in measuring the actual Au distributions in high concentration regions has previously been established.¹⁶ However, the low levels observed in near surface regions depleted of Au, are believed to be an artifact resulting from kinetic gettering to the surface of some Au during the SIMS etch.¹⁶

Gettering Dependence on Au Concentration ($x = 0.2$)

The use of extrinsic impurity gettering to decorate underlying point defect processes and distributions is not new. In 1983, Bubulac et al. reported gettering of Li to implant damage, inclusions, and cation vacancies in LWIR and MWIR material.²⁰ Indeed, these authors suggested the use of Li as an analytical tool for understanding junction formation processes, which is the subject of the present investigation using Au, though Au itself is of interest for device applications, since it has important implications for extrinsically doped photodiodes. Schaake et al. used Cu in LWIR material to quantify type conversion rates as well as the Hg-rich phase limits at low temperature (200°C) through equilibrium point defect relationships.^{2,21} More recently we have used Au to study Hg annealing, ion milling, and ion implantation in LWIR material.^{14,16}

For the temperatures used in our experiments, the vacancy diffusion contribution to the junction profile is likely negligible.¹²⁻¹⁴ The intrinsic point defect parameter values may be calculated using the SUMerCad simulator or the relationships presented in Ref. 12. Neglecting vacancy diffusion, in the steady state limit of the kinetic formulation,^{14,21}

$$\frac{x_j^2}{t} = \frac{2 D_i i_R}{f v_o} \quad (1)$$

where x_j is the junction depth, t is the Hg anneal time, D_i is the Hg interstitial diffusivity, i_R is the Hg-rich interstitial concentration, v_o is the initial vacancy concentration, and f is the interstitial sink factor. If only vacancies consume interstitials, then $f = 1$. If extended defects consume Au interstitials without liberating Hg interstitials, then the incoming Hg interstitials must fill the original vacancies plus vacated Au sites for the junction to progress. In addition, if extended defects consume Hg interstitials, then f is given by,

$$f v_o = v_o + [\text{Net Au interstitials consumed by non-Hg interstitial liberating defects}] + [\text{Net H interstitials consumed by nonvacancy defects}], \quad (2)$$

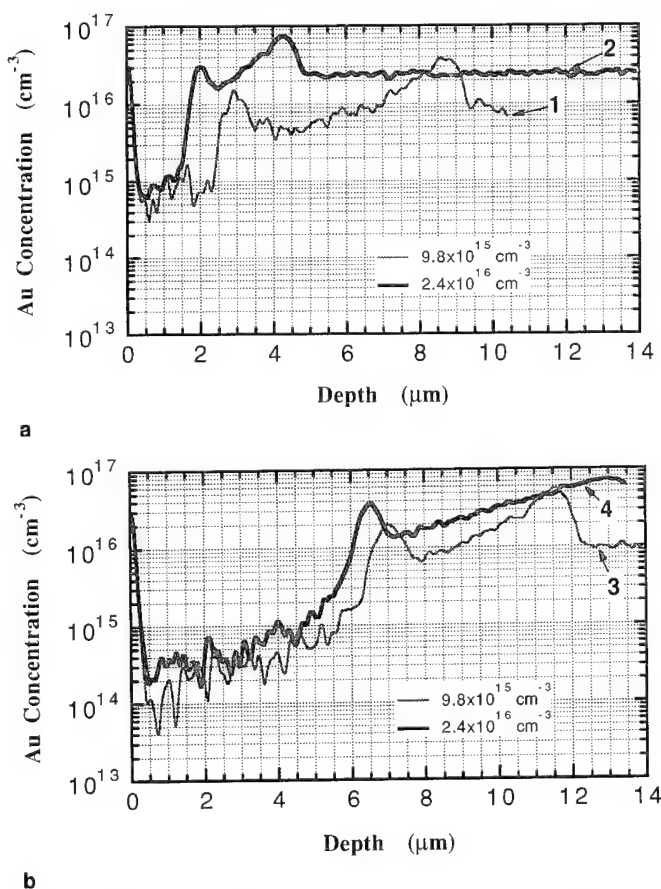


Fig. 2. Effect of Au concentration on redistributed Au profiles for (a) 175°C for 1h and (b) 205°C for 1h Hg anneals of 300°C Te equilibrated $\text{Hg}_{0.8}\text{Cd}_{0.2}\text{Te}$. The sample numbers are identified in the figure and can be referenced in Table I.

Table I. Summary of Initial Te-Rich Equilibration, Hg Anneal Conditions, and Junction Depths Determined from Au SIMS Profiles for all Samples

Sple.	x-value	Au Conc. (cm ⁻³)	Estimated Vacancy Conc. (cm ⁻³)	Te Equilibrium Temp. (°C)	Hg Anneal Temp. (°C)	Hg Anneal Time (h)	1/2 Max Junction Depth (μm)	$x_j^2 v/2t$ (cm ⁻¹ /s)	f
1	0.2	9.8×10^{15}	4.8×10^{16}	300	175	1	2.5	4.2×10^5	2.79
2	0.2	2.4×10^{16}	4.8×10^{16}	300	175	1	1.75	2.0×10^5	5.85
3	0.2	9.8×10^{15}	4.8×10^{16}	300	205	1	6.8	3.1×10^6	2.65
4	0.2	2.4×10^{16}	4.8×10^{16}	300	205	1	5.95	2.4×10^6	3.43
5	0.2	1.8×10^{16}	4.8×10^{16}	300	175	1	2.55	4.3×10^5	2.72
6	0.2	1.8×10^{16}	4.8×10^{16}	300	205	1	6.4	2.7×10^6	3.05
7	0.2	2×10^{16}	1.2×10^{17}	350	205	1	4.4	3.2×10^6	2.57
8	0.3	3×10^{16}	8×10^{16}	350	205	4	5.5	8.8×10^5	—
9	0.3	3×10^{16}	8×10^{16}	350	205	16	12.0	1.0×10^6	—
10	0.3	3×10^{16}	8×10^{16}	350	225	4	9.0	2.2×10^6	—
11	0.4	9×10^{17}	4×10^{16}	350	205	4	1.0	1.4×10^4	—
12	0.4	9×10^{17}	4×10^{16}	350	205	16	2.05	1.5×10^4	—

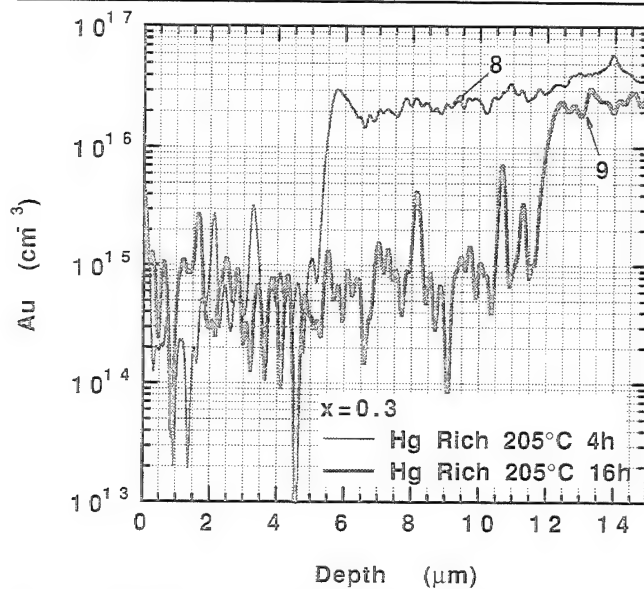


Fig. 3. Redistributed Au profiles for 205°C Hg anneals of 350°C Te equilibrated $\text{Hg}_{0.7}\text{Cd}_{0.3}\text{Te}$ for anneal times of 4 and 16 h. The sample numbers are identified in the figure and can be referenced in Table I.

where the second term may always be neglected if $\text{Au} \ll v_0$, but is not necessarily important when $\text{Au} > v_0$. Recall that if vacancies below the junction are the only net consumers of Au interstitials from the converted side, net Hg interstitials will come from the p-side to take part in the vacancy annihilation process. This occurs because recombination of Au interstitials through the Frank-Turnbol interaction lowers the vacancy concentration, which in turn drives the Frenkel reaction to generate additional vacancies and Hg interstitials to maintain equilibrium.

In using extrinsic impurities for understanding and quantifying formation processes, care must be exercised to ensure that the presence of the decorating impurity does not affect the interactions and resulting distributions of the intrinsic defects under study. An example of such an effect in $\text{Hg}_{0.8}\text{Cd}_{0.2}\text{Te}$ is demonstrated by Au SIMS profiles in Fig. 2a for a

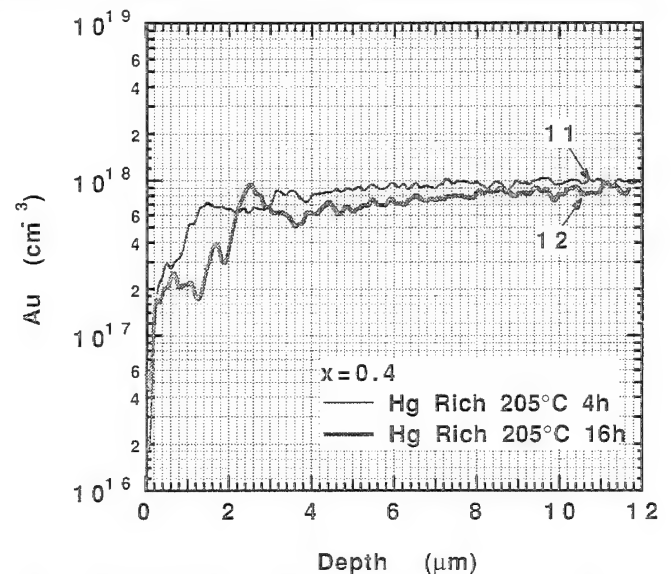


Fig. 4. Redistributed Au profiles for 205°C Hg anneals of 350°C Te equilibrated $\text{Hg}_{0.6}\text{Cd}_{0.4}\text{Te}$ for anneal times of 4 and 16 h. The Au/v_0 ratio in this material is 22.5. The sample numbers are identified in the figure and can be referenced in Table I.

175°C 1h Hg anneal and Fig. 2b for a 205°C 1h Hg anneal, as a function of the concentration of the decorating impurity. The initial background vacancy concentration was set by a Te-rich anneal at 300°C which results in a background vacancy concentration of roughly $4.8 \times 10^{16} \text{ cm}^{-3}$.² The Au levels used for decoration were $9.8 \times 10^{15} \text{ cm}^{-3}$ and $2.4 \times 10^{16} \text{ cm}^{-3}$. The Au to vacancy ratio (Au/v_0) is 0.2 and 0.5, respectively. Clearly, the junctions are shallower for the higher Au content indicating a $\text{Au}/v_0 < 0.5$ is required. Whether 0.2 is sufficient is still a question, though a look at the interstitial sink factor, f , yields further insight. The f values for all $x = 0.2$ samples are summarized in Table I, where the (D, i_R) product was determined by using the SUMerCad simulator. For samples 1, 3, and 7, $\text{Au}/v_0 \leq 0.2$ yielding an average f of 2.67. This is an indication that net Hg interstitials are being consumed by nonvacancy defects. For twice as much Au,

or $\text{Au}/v_0 = 0.4$, the average f was 2.89; and for $\text{Au}/v_0 = 0.5$, the average f was 4.64 for two samples. The saturation observed from 0.5 down to 0.2 indicates $\text{Au}/v_0 \leq 0.2$ may be adequate for decoration. However, note that the apparent strong dependence of f on Au/v_0 may be exaggerated by sample #2 which has an f seemingly inconsistently higher than the other samples. Neglecting this sample, a slope of 1 for f vs Au/v_0 fits most of the data adequately. However, the limited data set is insufficient to determine whether or not f increases at a rate higher than a simple contribution from the additional Au lattice sites.

A more comprehensive set of experiments is necessary to understand the effect of Au/v_0 on f , as well as to quantify what material properties (such as which extended defects) give rise to an f which is significantly greater than 1 for $\text{Au}/v_0 \ll 1$.

Ambient Anneal Au Gettering ($x = 0.3, 0.4$)

In this section, we will study the dependence of the Au redistribution in an initially uniform high vacancy background for MWIR and SWIR material following Hg-rich anneals; as a function of anneal time and temperature. As was found for the LWIR material in a previous study, the observed behavior of the low to high Au transition is consistent with that expected for type converted electrical junctions in vacancy-only material.¹⁶

We have studied the time dependence of Hg anneal induced Au redistribution in high vacancy uniformly Au-doped MWIR by comparing 4 and 16 h 205°C Hg-rich anneals of 350°C Te equilibrated material. The resulting Au distributions are shown in Fig. 3, and the experiment is summarized in Table I for samples 8 and 9. From Eq. (1), we expect the vacancy junction to go roughly as the square root of time for Hg anneals. Based on the kinetic models, we expect the vacancy junction to correspond approximately to the position of the steep Au rise. From Fig. 4, we estimate junction depths of 5.5 and 12.0 μm for the 4 and 16 h anneals, respectively. The depth ratio is 2.2, which compares well to two for square root [consistent with Eq. (1)], rather than four for linear. The f of these samples could not be determined since unlike $\text{Hg}_{0.8}\text{Cd}_{0.2}\text{Te}$, the D_i and i_R product has not been well established for $\text{Hg}_{0.7}\text{Cd}_{0.3}\text{Te}$. From interpolation of the phase limits in Fig. 1 between $x = 0.2$ and $x = 0.4$, we estimate the vacancy concentration following a 350°C Te equilibration anneal to be $8 \times 10^{16} \text{ cm}^{-3}$. This yields a Au/v_0 ratio of roughly 0.4 for all of the $x = 0.3$ samples. If we assume f is independent of composition and neglect electric field effects, then $(D_i i_R)$ is approximately $2.7 \times 10^6 \text{ cm}^{-1}/\text{s}$ using $f = 2.89$. In contrast, at 205°C $(D_i i_R)$ is $8.2 \times 10^6 \text{ cm}^{-1}/\text{s}$ in $\text{Hg}_{0.8}\text{Cd}_{0.2}\text{Te}$.

$\text{Hg}_{0.6}\text{Cd}_{0.4}\text{Te}$ samples were processed in the same manner as the two MWIR samples discussed above. The resulting Au distributions are shown in Fig. 4, and the experiment is summarized in Table I for samples 11 and 12. From Fig. 4, we determine junction depths of 1.0 and 2.05 μm for the 4 and 16 h anneals, respectively. The depth ratio is 2.05, which

again compares favorably with the behavior predicted by Eq. (1). The f of these samples could not be determined since the D_i and i_R product has not been established for $\text{Hg}_{0.6}\text{Cd}_{0.4}\text{Te}$. From the phase limits in Fig. 1b, we estimate the vacancy concentration following a 350°C Te equilibration anneal to be $4 \times 10^{16} \text{ cm}^{-3}$. This yields a Au/v_0 ratio of roughly 22.5 for these samples. Based on extension of the dependence of f in LWIR material on the Au/v_0 ratio, we would expect f to be quite large. If $(D_i i_R)$ for $\text{Hg}_{0.6}\text{Cd}_{0.4}\text{Te}$ at 205°C drops by the same factor in going from $x = 0.3$ to $x = 0.4$ as was observed from $x = 0.2$ to $x = 0.3$, $(D_i i_R)$ would equal $8.9 \times 10^5 \text{ cm}^{-1}/\text{s}$ and f would be 61, again neglecting electric field effects. However, for a firm determination of $(D_i i_R)$, the experiment will need to be repeated using a much lower Au concentration.

The temperature dependence of Hg anneal induced Au redistribution in high vacancy uniformly Au-doped $\text{Hg}_{0.7}\text{Cd}_{0.3}\text{Te}$ is shown in Fig. 5 comparing 205 and 225°C 4 h Hg-rich anneals of 350°C Te-equilibrated material. The experiment is summarized in Table I for samples 8 and 10. From Eq. (1), we can determine the ratio of $(D_i i_R)$ at the two temperatures. Using a junction depth ratio of 1.64, $(D_i i_R)$ at 225°C is found to be $7.2 \times 10^6 \text{ cm}^{-1}/\text{s}$ (again assuming $f = 2.89$ and neglecting electric field effects). We can determine an activation energy, and write,

$$D_i i_R(x = 0.3) = 9.3 \times 10^{16} \exp\left(\frac{-1.0 \text{ eV}}{kT}\right). \quad (3)$$

Recall that the Hg self-diffusion coefficient is given by,

$$D_{\text{Hg}} = \left(\frac{D_i i_R}{C_o}\right), \quad (4)$$

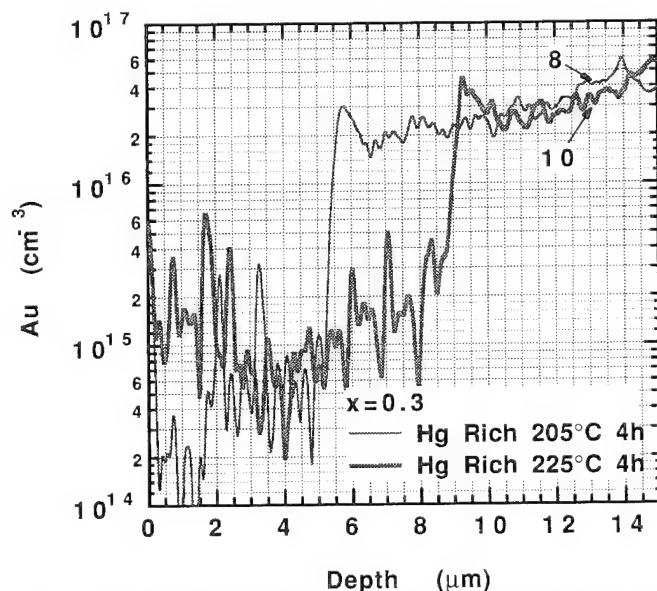


Fig. 5. Redistributed Au profiles for 4 h 205°C vs 225°C Hg anneals of 350°C Te equilibrated $\text{Hg}_{0.7}\text{Cd}_{0.3}\text{Te}$. The sample numbers are identified in the figure and can be referenced in Table I.

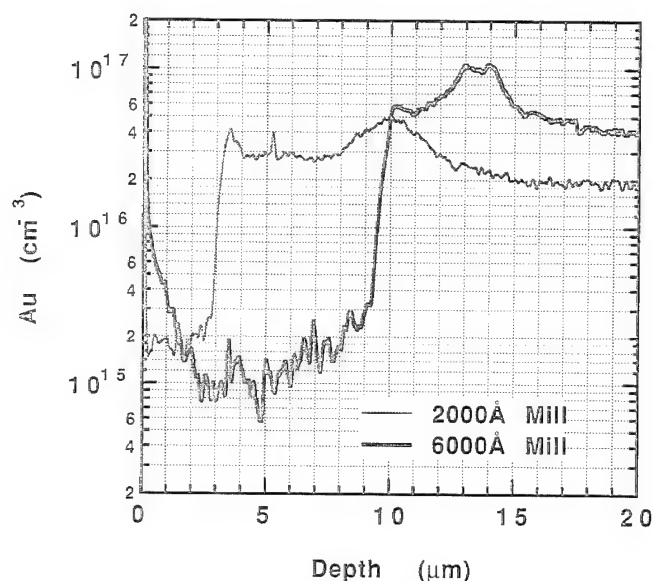


Fig. 6. Redistributed Au profiles for 2000 and 6000 Å Ar mills of 350°C Te equilibrated $\text{Hg}_{0.7}\text{Cd}_{0.3}\text{Te}$.

where C_0 is the density of Hg lattice sites.¹³ The Hg self-diffusion coefficient for $\text{Hg}_{0.7}\text{Cd}_{0.3}\text{Te}$ is then given by,

$$D_{\text{Hg}}(x = 0.3) = 8.9 \times 10^{-6} \exp\left(\frac{-1.0\text{eV}}{kT}\right), \quad (5)$$

compared to,

$$D_{\text{Hg}}(x = 0.2) = 3 \times 10^{-3} \exp\left(\frac{-1.2\text{eV}}{kT}\right), \quad (6)$$

for $\text{Hg}_{0.8}\text{Cd}_{0.2}\text{Te}$.³

For $\text{Hg}_{0.7}\text{Cd}_{0.3}\text{Te}$, we determine $D_{\text{Hg}} = 1.9 \times 10^{-14} \text{ cm}^2/\text{s}$ at 307°C and $7.8 \times 10^{-14} \text{ cm}^2/\text{s}$ at 352°C. The values for $x = 0.2$ material are $1.1 \times 10^{-13} \text{ cm}^2/\text{s}$ and $6.4 \times 10^{-13} \text{ cm}^2/\text{s}$, respectively. This strong dependence of the Hg self-diffusion coefficient on composition compares favorably with that reported by Archer et al. in Fig. 5 of Ref. 3 for these two temperatures.

Ion Mill Au Gettering ($x = 0.3$)

In our previous work, we reported on the gettering of Au from low to high vacancy regions by an ion milling process.¹⁶ For 300°C Te equilibrated $\text{Hg}_{0.8}\text{Cd}_{0.2}\text{Te}$, the type conversion observed was roughly 9.3 times the amount of material removed. Since the mill technique is a "kinetic" injection process vs the "thermodynamic" interstitial injection from a Hg ambient anneal, the compositional dependence of the type conversion rate by milling is not expected to be a strong function of composition. Secondary ion mass spectroscopy profiles are shown in Fig. 6 for 2000 and 6000 Å mills of 350°C Te equilibrated $\text{Hg}_{0.7}\text{Cd}_{0.3}\text{Te}$. The junction depths are 3.2 and 9.8 μm, respectively, yielding a conversion rate of approximately 16 times the amount of material removed. This high conversion rate is an indication that the estimate of $8 \times 10^{16} \text{ cm}^{-3}$ for the vacancy concentration established by interpolation from the phase limits shown in Fig. 1 may be too high. Assuming the Hg interstitial injection rate

is independent of composition implies a vacancy concentration of $2.8 \times 10^{16} \text{ cm}^{-3}$ for the 350°C $x = 0.3$ Te-rich anneal, which is closer to the $x = 0.4$ phase limits.

SUMMARY AND CONCLUSIONS

We have presented a number of experimental results aimed at increasing our understanding of cation impurity and native point defect diffusion and gettering mechanisms in $\text{Hg}_{1-x}\text{Cd}_x\text{Te}$. By studying Au gettering in $\text{Hg}_{0.8}\text{Cd}_{0.2}\text{Te}$ as a function of the Au/ v_0 ratio, it was established that trace amounts of the impurity are required to ensure that the "decorating" impurity does not in fact alter the apparent underlying intrinsic point defect distributions for a given type-conversion process. For both the MWIR and SWIR material, the Hg annealed gettering junction depth followed a square root of time dependence as predicted by the steady state model formalism. However, the Au/ v_0 ratios in these materials were dramatically different with estimates of 0.4 for the MWIR and 22.5 for the SWIR. The junction depths in the SWIR material were almost certainly governed by the high Au concentration. Finally, since the mill technique is a "kinetic" injection process vs the "thermodynamic" interstitial injection from a Hg ambient anneal, a weak compositional dependence of the mill Hg interstitial injection rate was found.

REFERENCES

1. H.R. Vidyantath, *J. Electrochem. Soc.* 128, 2609 (1981).
2. H.F. Schaake, *J. Electron. Mater.* 14, 513 (1985).
3. N.A. Archer, H.D. Palfrey and A.F.W. Willoughby, *J. Electron. Mater.* 22, 967 (1993).
4. N.A. Archer, H.D. Palfrey and A.F.W. Willoughby, *J. Cryst. Growth* 117, 177 (1992).
5. N. Archer and H. Palfrey, *J. Electron. Mater.* 20, 419 (1991).
6. Mei-Fan Sung Tang, Ph.D. Thesis, Stanford University (1987).
7. D.A. Stevenson and M-F.S. Tang, *J. Vac. Sci. Technol. B* 9, 1615 (1991).
8. M. Brown and A.F.W. Willoughby, *J. Cryst. Growth* 59, 27 (1982).
9. C.L. Jones, M.J.T. Quelch, P. Capper and J.J. Gosney, *J. Appl. Phys.* 53, (1982).
10. John-Sea Chen, Ph.D. Thesis, University of Southern California (1985).
11. D.T. Dutton, E. O'Keefe, P. Capper, C.L. Jones, S. Mugford and C. Ard, *Semicond. Sci. Technol.* 8, S266 (1993).
12. J.L. Meléndez and C.R. Helms, *J. Electron. Mater.* 24, 565 (1995).
13. J.L. Meléndez and C.R. Helms, *J. Electron. Mater.* 24, 573 (1995).
14. J.L. Meléndez, Ph.D. Thesis, Stanford University (1993).
15. S. Holander, V. Sabnis, J. Hasan, J. Meléndez and C.R. Helms, *SUMerCad Process Simulator Software*, Stanford University (1994).
16. J.L. Meléndez, C.R. Helms, J. Tregilas and J. Elkind, *SPIE* 228, 106 (1994).
17. H.R. Vidyantath and C.H. Hiner, *J. Appl. Phys.* 65, 3080 (1989).
18. R.F. Brebrick and J.P. Schwartz, *J. Electron. Mater.* 9, 771 (1980).
19. G.L. Hansen and J.L. Schmit, *J. Appl. Phys.* 54, 1639 (1983).
20. L.O. Bubulac, W.E. Tennant, R.A. Riedel, J. Bajaj and D.D. Edwall, *J. Vac. Sci. Technol. A* 1, 1646 (1983).
21. H.F. Schaake, J.H. Tregilas, J.D. Beck, M.A. Kinch and B.E. Gnade, *J. Vac. Sci. Technol. A* 3, 143 (1985).

A Comparison of the Diffusion of Iodine into CdTe, $\text{Hg}_{0.8}\text{Cd}_{0.2}\text{Te}$ and $\text{Zn}_{0.05}\text{Cd}_{0.95}\text{Te}$

E.D. JONES and J. MALZBENDER

School of Natural and Environmental Sciences, Coventry University,
Coventry, CV1 5FB, UK

N. SHAW

DRA Electronics Division, RSRE, St. Andrews Road, Great Malvern,
Worcester, WR14 3PS, UK

P. CAPPER

GEC Marconi Infra-Red, P.O.Box 217, Millbrook, Southampton,
SO15 0EG, UK

J.B. MULLIN

Electronic Materials Consultant, The Hoo, Brockhill Road, West Malvern,
Worcester, WR14 4DL, UK

Studies on the diffusion of iodine into CdTe, mercury cadmium telluride ($\text{Hg}_{0.8}\text{Cd}_{0.2}\text{Te}$, referred to as MCT) and zinc cadmium telluride ($\text{Zn}_{0.05}\text{Cd}_{0.95}\text{Te}$, referred to as ZCT) in the temperature range of 20 to 600°C are compared and discussed. The concentration profiles were measured using a radiotracer sectioning technique. As with the diffusion studies using the halogens into CdTe, the profiles were composed of four parts to which a computer package consisting of the sum of four complementary error functions (erfc) gave satisfactory fits. The diffusivity for the diffusion of iodine into MCT was faster than for the diffusion into CdTe, which was faster than for the diffusion into ZCT. The high diffusivity for the fastest profile part at 20°C indicates that when iodine is diffused from the vapor into these materials, it is not a suitable long term stable dopant in devices where sharp junctions are required.

Key words: CdTe, HgCdTe , iodine diffusion, ZnCdTe

INTRODUCTION

Despite recent advances in materials technology, it remains a difficult task to control the conductivity and to maintain a stable junction in p-n junction devices manufactured from II-VI semiconducting materials. Consequently, it is vital that the rates of diffusion of appropriate dopants through the host material are known so that the most suitable one can be selected for a particular device.¹

Indium has been the most widely used n-type dopant in CdTe and $(\text{Hg}_x\text{Cd}_{1-x})\text{Te}$, but as it has proved to be a fairly fast diffusant² attention has been directed to the halogens, which are expected to reside on anion sites. In this case, different diffusion mechanisms will

operate which may be much slower. The halogens are now used on a regular basis as n-type dopants in devices which are grown epitaxially.¹ However, measurements on the diffusion of iodine into CdTe from the vapor produced complex diffusion profiles which could be fitted empirically by a function composed of the sum of four complementary error functions giving four values for the diffusivity D_1 to D_4 . The results can be summarized by the following Arrhenius parameters:³

$$\begin{aligned} Q_1 &= (0.21 \pm 0.05) \text{ eV}, D_{01} = (7 \pm 3) \cdot 10^{-11} \text{ cm}^2 \text{ s}^{-1}, \\ Q_2 &= (0.29 \pm 0.04) \text{ eV}, D_{02} = (2.1 \pm 0.8) \cdot 10^{-13} \text{ cm}^2 \text{ s}^{-1}, \\ Q_3 &= (0.28 \pm 0.03) \text{ eV}, D_{03} = (3.8 \pm 1.2) \cdot 10^{-14} \text{ cm}^2 \text{ s}^{-1}, \\ Q_4 &= (0.28 \pm 0.05) \text{ eV}, D_{04} = (2.1 \pm 1.6) \cdot 10^{-15} \text{ cm}^2 \text{ s}^{-1}. \end{aligned}$$

These Arrhenius parameters indicate that iodine is a fairly fast diffusant if diffused from an external source,

(Received October 4, 1994; revised December 15, 1994)

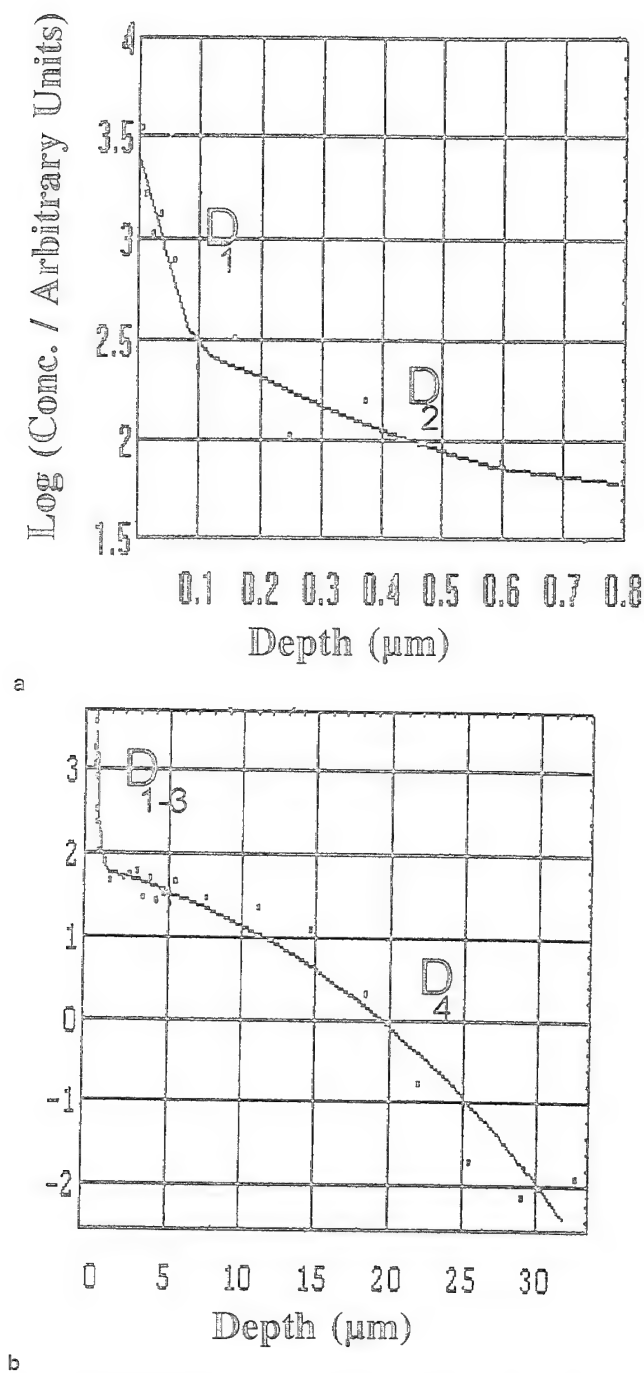


Fig. 1. A concentration profile for the diffusion of CdI_2 into $\text{Zn}_{0.05}\text{Cd}_{0.95}\text{Te}$ (ZCT) for a diffusion carried out at 600°C for 2.7 days. The four parts of the profile (labeled D_1 – D_4) can be seen clearly. The two components which occur near the surface of the slice (D_1 and D_2) are shown under high resolution in (a) and the whole profile is shown in (b).

producing diffusivities of $10^{-14} \text{ cm}^2 \text{ s}^{-1}$ for the fastest diffusing component at 20°C . In addition, surface concentrations of up to 10^{23} cm^{-3} at 200°C were observed for the slowest diffusing component D_1 .³

It must be emphasized that the erfc relationship and the resulting diffusivity applies only when well-defined boundary conditions are specified.⁴ In the case of the diffusion of group II impurities into CdTe, two component diffusion profiles are common and

their occurrence is well documented.⁵ In spite of using well-defined boundary conditions for the diffusion of iodine into CdTe, profiles with four distinct components were obtained, resulting in four empirical values of the diffusivity. All four diffusivities were independent of time and gave, when plotted as a function of inverse temperature, reproducible results,^{3,6} which agreed with previously published data.

Chlorine diffusion into CdTe has been reported by Shaw and Watson² and more recently by Jones et al.⁷ In both cases, complex profiles were observed, but recent advances in the sectioning techniques developed by the authors have enabled better resolved profiles to be obtained. The diffusion profiles thereby revealed were found to be even more complex but were fitted mathematically by a function composed of the sum of four complementary error functions in a way similar to that used for the diffusion of iodine into CdTe.³ The projected room temperature diffusivity for the fastest profile part of the chlorine diffusion profiles ($6 \cdot 10^{-25} \text{ cm}^2 \text{ s}^{-1}$)⁷ was much lower than the corresponding one of the iodine profiles. Again surface concentrations of up to 10^{23} cm^{-3} at 200°C were observed for the slowest diffusing component, D_1 .

More recently measurements on the diffusion of bromine into CdTe have been reported⁸ and again four component profiles were obtained. The value of the activation energies for all four components were similar to those for the iodine diffusion, but the surface concentrations were independent of temperature, giving a value of 10^{19} cm^{-3} for the slowest diffusing component.

A model was proposed^{3,6,7} to account for these four component profiles. The first component, D_1 , was due to the formation of an eutectic layer involving CdTe and a compound of the form Cd_nX_m (X is either I, Cl or Br, n and m are integers) formed by a chemical reaction between CdX_2 and CdTe and the subsequent diffusion of the halogen in the form of the defect complex $(\text{V}_{\text{Cd}}\text{X}_{\text{Te}})_x$ accounted for the second component, D_2 . The formation of precipitates within the CdTe slice and the subsequent diffusion from these precipitates through dislocations were responsible for the third and fourth components, D_3 and D_4 , respectively. Different values of the activation energies for the diffusion of chlorine into CdTe as compared with iodine were possibly due to the different electro-negativities of those elements and their related binding strength to a Cd vacancy.

EXPERIMENTAL TECHNIQUES

Both the MCT slices, supplied by GEC Marconi Infrared, Southampton, and the ZCT slices, supplied by the University of Durham, were in a polished state when received and so no further pre-diffusion surface preparation was necessary. The epitaxial layers of MCT, which were grown by metalorganic vapor phase epitaxy (MOVPE), were also supplied by GEC Marconi Infrared, Southampton, and were grown as described by Maxey et al.¹

In the diffusions, the slices were sealed in evacu-

ated silica capsules with sufficient tracer material, CdI_2 containing radioactive iodine, to maintain the vapor pressure due to CdI_2 at saturation values throughout the anneals. The anneals were carried out under isothermal conditions in horizontal tube furnaces.

The temperature ranges used were 200–600°C for the diffusion of iodine into ZCT, and 20–310°C for MCT. To prevent deterioration of the surfaces of the MCT slices during the diffusion anneal due to the out-diffusion of mercury from the slices, elemental mercury was added to the diffusion source. The high saturation vapor pressure of mercury, which exceeds one atmosphere at temperatures above 360°C, imposed an upper limit for the MCT anneals on safety grounds.

The concentration profiles for the iodine diffused CdTe slices were measured using RTS⁹ at Coventry University. A combination of anodic oxidation⁹ (section thickness 0.006–0.2 μm to a depth of 2 μm) and bromine etching (section thickness: 0.3–5 μm to a depth of 30 μm) was used on mesa shaped slices of CdTe.⁹ The iodine concentration was measured directly using a liquid scintillation counter.

RESULTS AND DISCUSSION

The diffusion profiles which were obtained in all experiments showed four distinct regions and a function composed of the sum of four complementary error functions gave satisfactory fits to the experimental data. This phenomena as well as the results obtained

for the diffusion of CdI_2 into CdTe have been discussed elsewhere.^{3,6} Consequently, these results will not be discussed here but, for completeness, the results will be given for comparison purposes only.

Typical profiles for the diffusion of CdI_2 into ZCT and MCT are shown in the Fig. 1 and Fig. 2, respectively, and the diffusivities for the diffusion of iodine into ZCT and MCT are compared with that of iodine into CdTe on an Arrhenius plot in Fig. 3. Because of the high resistivity of the epitaxially grown MCT layer, anodic oxidation could not be used as a sectioning technique, and so the whole profile was measured using bromine etching. Consequently, it was not possible to observe the slowest profile part, D_1 , but it can be seen in Fig. 3 that the measured diffusivities for D_2 , D_3 , and D_4 agree in the case of epitaxially and bulk grown MCT.

The whole set of results for the diffusion of iodine into MCT is slightly higher than for the corresponding measurements into CdTe. From the diffusion profiles of iodine into MCT values of the Arrhenius parameters, D_0 and the activation energy Q , were calculated, and are listed as follows:

$$\begin{aligned} Q_1 &= (0.20 \pm 0.04) \text{ eV}, D_{01} = (2.5 \pm 1.5) \cdot 10^{-10} \text{ cm}^2 \text{ s}^{-1}, \\ Q_2 &= (0.29 \pm 0.04) \text{ eV}, D_{02} = (2.1 \pm 1.0) \cdot 10^{-11} \text{ cm}^2 \text{ s}^{-1}, \\ Q_3 &= (0.25 \pm 0.06) \text{ eV}, D_{03} = (7.7 \pm 3) \cdot 10^{-14} \text{ cm}^2 \text{ s}^{-1}, \\ Q_4 &= (0.30 \pm 0.08) \text{ eV}, D_{04} = (5.1 \pm 4) \cdot 10^{-15} \text{ cm}^2 \text{ s}^{-1}, \end{aligned}$$

In the case of the diffusion of iodine into ZCT the diffusivities are slightly lower than the corresponding measurements in CdTe, but because of the limited

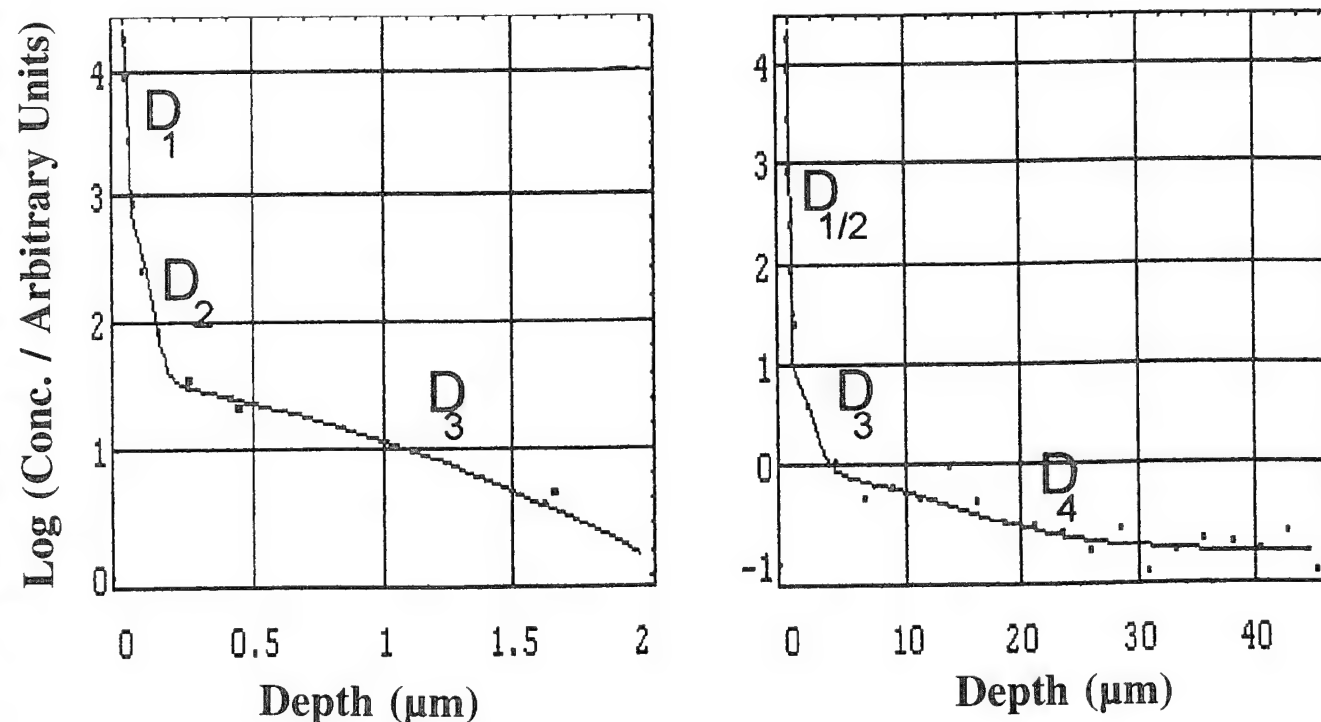


Fig. 2. A concentration profile for the diffusion of CdI_2 into $\text{Hg}_{0.8}\text{Cd}_{0.2}\text{Te}$ (MCT) for a diffusion anneal carried at 173°C for 5 days. The four parts of the profile (labeled D_1 – D_4) can be seen clearly. The three components which occur near the surface of the slice (D_1 – D_3) are shown under high resolution in (a) and the two deeper components are shown in (b).

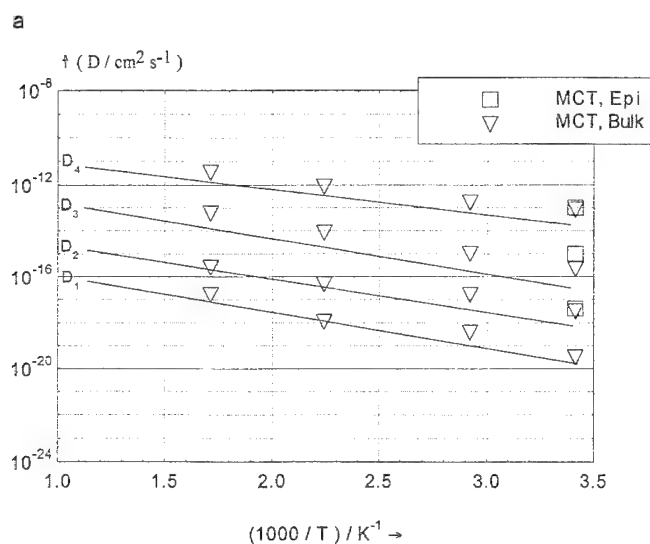
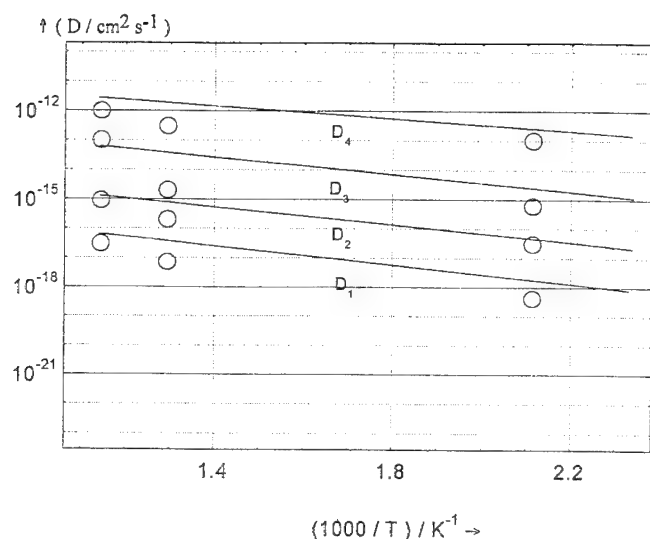


Fig. 3. Arrhenius plots showing a comparison of the diffusivities for the diffusion of CdI_2 into $\text{Zn}_{0.05}\text{Cd}_{0.95}\text{Te}$ (ZCT) (a) and $\text{Hg}_{0.8}\text{Cd}_{0.2}\text{Te}$ (MCT) (b). The best fits for the diffusion of CdI_2 into CdTe are shown by straight lines.

number of measurements, it was not possible to calculate the diffusion parameters accurately.

It is possible that these results are related to the ionic radii of zinc and mercury, which are in the case of zinc lower than that of cadmium and for mercury higher. Consequently, the introduction of these materials into CdTe causes a slight change in the lattice constant.

The values of the surface concentration, C_0 , are shown in Fig. 4, where a comparison with the corresponding results for the diffusion of iodine into CdTe is made. It can be seen that the C_0 values for the diffusion of iodine into ZCT show a slight variation when compared with the corresponding results for the diffusion of iodine into CdTe, particularly at high temperatures; whereas in the case of MCT, the values agree for the slower profile parts (D_1 and D_2), but show systematically lower values (approximately one decade) for the faster profile parts (D_3 and D_4) at tem-

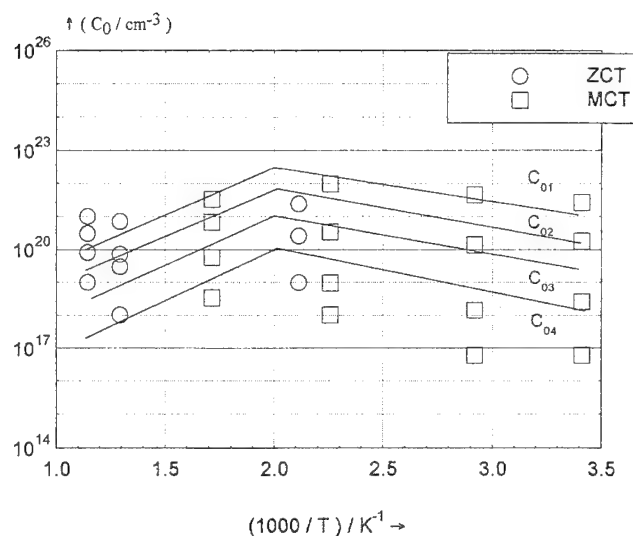


Fig. 4. Arrhenius plots showing a comparison of the C_0 values for the diffusion of CdI_2 into $\text{Zn}_{0.05}\text{Cd}_{0.95}\text{Te}$ (ZCT) and $\text{Hg}_{0.8}\text{Cd}_{0.2}\text{Te}$ (MCT) with the diffusion of CdI_2 into CdTe (straight lines).

peratures lower than 200°C.

Reasons for the occurrence of the four component profiles reported here, similar to those obtained for the diffusion of iodine, chlorine, and bromine into CdTe, have been explained in the literature³⁻⁵ and have been summarized in the introduction. The results presented here are not as extensive as for the diffusion of iodine into CdTe, but sufficient measurements have been carried out to propose that the diffusion mechanism for the diffusion of iodine into MCT and ZCT is similar to that for the diffusion of iodine into CdTe.

The diffusion of iodine into CdTe and MCT has shown similar diffusivities. This agreement with the stated theory suggests that the number of defects created by the diffusion of iodine into these materials is by far higher than native point defects, or point defects created by the presence of the Hg vapor in the capsule.

A room temperature diffusivity of $\sim 10^{-14} \text{ cm}^2 \text{ s}^{-1}$ implies that iodine is not a very stable dopant in either of these materials, when it is diffused into the slice from the vapor, and questions the use of iodine as a long term stable dopant in devices where sharp junctions are required. Iodine is used as a dopant in epitaxially grown MCT and was reported to give sharp junctions¹ possessing good long term stability. This suggests that iodine diffused from the vapor source may occupy a different lattice site to that which it occupies when it is introduced into the lattice using epitaxial growth, or it may exist in different defect forms in the two cases.

CONCLUSIONS

It is possible to draw the following conclusions from the work reported in this paper:

- The diffusivities for the diffusion of iodine into MCT are slightly higher than the corresponding values for the diffusion of iodine into CdTe;

whereas in the case of the diffusion of iodine into ZCT, the diffusivities are slightly lower than the corresponding measurements in CdTe.

- The surface concentrations, C_0 , for the diffusion of iodine into both MCT and ZCT show slight variations to the corresponding ones for the diffusion of iodine into CdTe
- The diffusivity of iodine into CdTe, MCT, and ZCT at 20°C is approximately $10^{-14} \text{ cm}^2 \text{ s}^{-1}$ and this questions the use of iodine as a dopant in CdTe, MCT, and ZCT in devices where sharp junctions are formed by diffusion doping.

ACKNOWLEDGMENTS

The authors wish to thank Dr. C.D. Maxey and Dr. E.S. O'Keefe, GEC Marconi Infrared, Southampton, for supplying the MCT slices, Dr. A.W. Brinkman, University of Durham, for supplying the ZCT slices,

and Dr. M.G. Astles, DRA Electronic Division, Malvern, who suggested the project.

REFERENCES

1. C.D. Maxey, P.A.C. Whiffin and B.C. Easton, *Semicond. Sci. Technol.* 6, C26 (1991).
2. D. Shaw, *J. Cryst. Growth* 86, 788 (1988).
3. E.D. Jones, J.C. Clark, J. Malzbender, J.B. Mullin, N. Shaw and A. W. Brinkman, *J. Electron. Mater.* 24, 581 (1995).
4. J. Crank, *The Mathematics of Diffusion* (New York: Oxford University Press, 1986).
5. H.H. Woodbury, *Physics and Chemistry of II-VI Compounds* (Amsterdam, North-Holland Publ. Co., 1967), p. 223.
6. J. Malzbender, Ph.D. Thesis, Coventry University, 1994.
7. E.D. Jones, J. Malzbender, J.B. Mullin and N. Shaw, *J. Phys. C* 6, 7499 (1994).
8. J. Malzbender, E.D. Jones, J.B. Mullin and N. Shaw, *Mat. Science Forum*, Vol. 182-184, (Switzerland: Trans. Tech. Publ., 1995), p. 57.
9. E.D. Jones, N.M. Stewart and J.B. Mullin, *J. Cryst. Growth* 117, 244 (1992).

HgCdTe and Other Infrared Material Status in the Ukraine

V.K. MALYUTENKO

Institute of Semiconductor Physics, National Academy of Sciences, Kyiv,
Ukraine

This is the first article to explain and illustrate the HgCdTe and other infrared (IR) material status in the Ukraine. It develops the background needed to understand the what and where of IR physics, devices, and materials, but does not pretend to be a comprehensive treatment of the subject as some data still remain classified.

Key words: HgCdTe, infrared (IR) materials, thermoelectric coolers

INTRODUCTION

Now that the Cold War is over, some of the resources of the former Soviet Union (SU) National Institutions that have played a major role in assuring the SU security, are increasingly available for nondefense high-technology research and development. They face the challenge of redefining their role as a result of the significantly diminished demand for their weapons-related capability. The knowledge developed in these labs and plants may offer an opportunity for international cooperation. Such technology development and transfer would be clearly of mutual interest and dual benefit to both scientists and developers in the Commonwealth of Independent States (CIS) and international scientific community.

By participating in SU large scale defense and civilian programs, Ukrainian scientists and engineers have successfully developed various types of efficient optoelectronic devices for the infrared (IR) which are known in the West only as "made in Russia." Now after SU's collapse, this large European country looks like a blank white spot on the world "photonic devices

and materials" map. This is the first article to explain and illustrate the HgCdTe and other IR material status in the Ukraine. It develops the background needed to understand the what and where of IR physics, devices, and materials, but does not pretend to be a comprehensive treatment of the subject as some data still remain classified.

STATE OF DEVELOPMENT

Science

The Institute of Semiconductor Physics (Kyiv)¹ is generally believed to be a leader in this area. Although the institute's interest is primarily in the fundamental interaction of light with matter, the radical shift was made in recent years toward practical applications of the light emitting and detection in a new generation of photonic devices. Contrary to the traditional approach exploiting low temperature IR detectors, the main thrust in this section deals with new research to raise the operating temperature of narrow gap semiconductor (NGS) devices and to demonstrate the physical principles and parameters of related nonorthodox IR light emitting diodes (LEDs).

It is difficult to obtain a high injection level in NGS

(Received October 4, 1994; revised January 3, 1995)

(for example, by contact injection or by photoexcitation) because of a small lifetime ($\tau < 10^{-8}$ s), a high efficiency of nonlinear Auger recombination and a high value of intrinsic carrier density ($n_i \geq 10^{16} \text{ cm}^{-3}$). For these reasons NGS IR devices are cooled either thermoelectrically or by small Stirling-cycle devices which keep temperatures between 70 and 200K. In most cases, these cooling devices drive up the system cost beyond a commercially viable price, particularly in the civilian field. The requirement for cooling does not appear to be fundamentally necessary. Auger recombination-generation processes can be suppressed and the need for cryogenic operation reduced or even eliminated by operating the devices in the non-

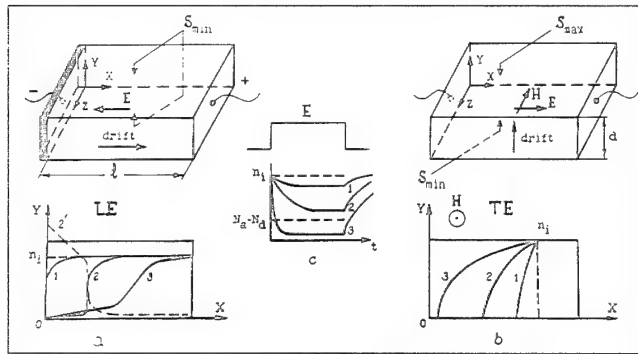


Fig. 1. (a) Longitudinal (p+-p junction from the left), and (b) transverse carrier exclusion in the slab with near-intrinsic conductivity and lateral contacts. Below: (a) 1-3, carrier distribution along the crystal at $V_3 > V_2 > V_1$; 2'-E distribution along the crystal; (b) carrier distribution across the crystal at $E_3 > E_2 > E_1$; and (c) time dependence of nonequilibrium carrier concentration in the excluded region.

equilibrium mode where the carrier densities are below their thermal equilibrium values.

There are two simple ways to decrease carrier densities in NGS with intrinsic conductivity.² The first approach is the contact exclusion occurring when reverse voltage bias is applied to an antiblocking contact (n^+-n or p^+-p junction). As a result of longitudinal minority carrier drift along the current lines to an opposing contact, an extended region of bipolar exclusion appears. If the opposite contact is ohmic, the minority carrier density may be reduced below the equilibrium density over much of the sample volume. The second way is realized if a crystal with ohmic contacts is exposed to crossed electric (E) and magnetic (H) fields (magnetoconcentration effect, MCE). In this case, the Lorentz force causes transverse carrier drift toward the lateral face of the crystal slab, and the whole volume of the crystal becomes the region of exclusion, except for a narrow surface layer near the face to which the carriers drift (Fig. 1). In InSb and HgCdTe (MCT) the longitudinal exclusion region may be as large as 100 μm at room temperature wherein the carrier density is decreased almost a hundredfold becoming less than the density of uncompensated impurities. As a result, exclusion effects dramatically change optical, electric, and photoelectric properties of the crystals.

First of all, the decrease in electron and hole density ($n, p < n_i$) is accompanied by a decrease in the power of spontaneous radiation, $P < P_0$ (P_0 is equilibrium thermal radiation value), in the range of band-to-band transitions $\omega > E_{g/h}$ (E_g -bandgap)—negative lumines-

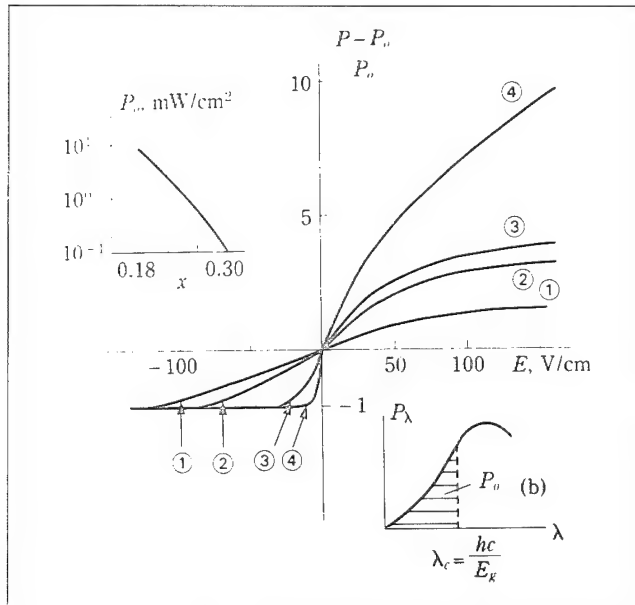


Fig. 2. (a) Field dependences of the fractional change in integral emissive power of MCE MCT emitters at $T = 300\text{K}$. $H = 10 \text{ kOe}$, x : 1-1'-0.20; 2-2'-0.22; 3-3'-0.28; 4-4'-0.30. 1-4—positive luminescence, 1'-4'—negative luminescence. Insertions show: left: maximal negative luminescence power (P_n) vs x at 300K; right: spectral distribution of black body emission; cross-hatched part corresponds to the negative luminescence power in the spectral range of interband transitions. Note: an essential qualitative aspect of negative luminescence is that it cannot exceed the magnitude of equilibrium emission, since the absolute radiant emission cannot be reduced below zero. (b) Spectral characteristics of luminescence of varying gap MCT at room temperature and $H = \pm 10 \text{ kOe}$. E , V/cm; 1.6-20; 2-40; 3.7-80; 4-160; 5-240. Positive luminescence: 1-5, negative luminescence: 6-7. Inset: diagram of MCE transverse carrier exclusion experiment.

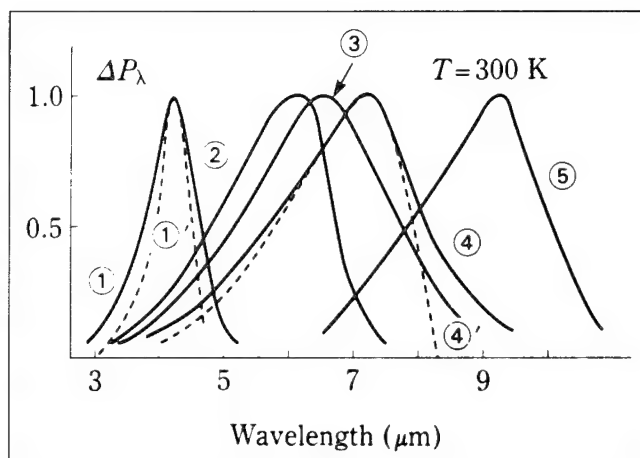


Fig. 3. Difference emission spectra of MCE MCT emitters at $T = 300\text{K}$. $H = 10\text{ kOe}$, $E = 1\text{ V/cm}$; x : 1-0.30, 2-0.22, 3-0.215, 4-0.20, 5-0.18. 1', 4'-theory.

cence.³ In the limiting case of large-signal exclusion, the recombination radiation is fully suppressed: the radiation deficit equals the equilibrium value P_0 ($\Delta P = P - P_0 \approx -P_0$). The maximal power of negative luminescence is determined by integrating the formula for the Planck spectral distribution over the interval $E_g \leq \hbar\omega \leq \infty$ (Fig. 2). Because of this, the negative luminescence power in $\text{Hg}_{0.8}\text{Cd}_{0.2}\text{Te}$ at 300K is estimated to be 10 mW cm^{-2} whereas it does not exceed 1 mW cm^{-2} for InSb. The negative luminescence has been investigated in detail for InSb and MCT crystals and films as well as for MCT epitaxial structures.⁴⁻⁶ As a result, the most important features of this phenomenon are established and unorthodox high-temperature InSb and MCT IR sources (Fig. 3) for those applications requiring stable, reliable sources of low power IR energy have been developed.⁷

The radiative cooling effect⁸ induced by the exclusion region (when the crystal pumps thermal energy from its surroundings and does not radiate back) is also under study. A maximal temperature differential as high as $\Delta T = 3\text{K}$ at room temperature has been achieved using excluded MCT thin film as a cooling body.

The Auger generation suppression results in the appearance of a region of negative differential conductivity (N-type) in I-V characteristics.⁹ Experimentally, this region is detected as the appearance of oscillations at the flat tops of current pulses through the material. The oscillation frequency depends on E , and the amplitude attains 50% of the current mean value. The latter corresponds to a pulse power up to 100 W.

The exclusion effects occurring in photogenerated electron-hole plasmas cause a significant decrease of the photoresponse time which is not accompanied by a decrease in the responsivity because the crystal resistivity in the dark is increased.¹⁰

An alternative way to suppress the Auger processes in NGS and to improve the performance of IR devices is to employ pressure. Auger (τ_A) and radiative (τ_R) carrier lifetime calculations within the Kane model,

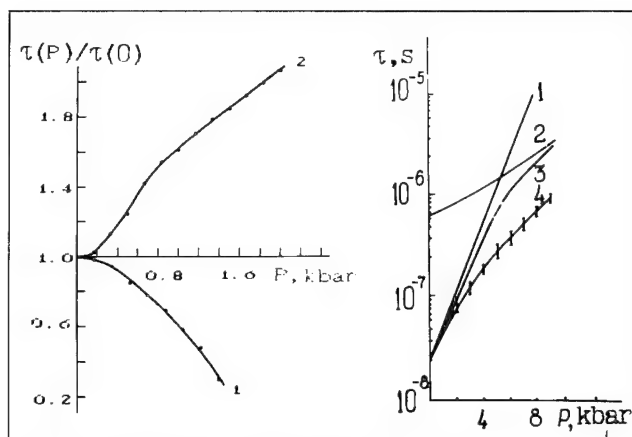


Fig. 4. Relative carrier lifetime vs pressure. Left—uniaxial pressure, 1- τ_R for MCT ($x = 0.29$) at $T = 150\text{K}$, 2- τ_A for MCT ($x = 0.2$) at $T = 100\text{K}$. Right—hydrostatic pressure, 1- τ_A , 2- τ_R , 3- $\tau^{-1} = \tau_A^{-1} + \tau_R^{-1}$, 4—experiment for InSb at $T = 300\text{K}$.

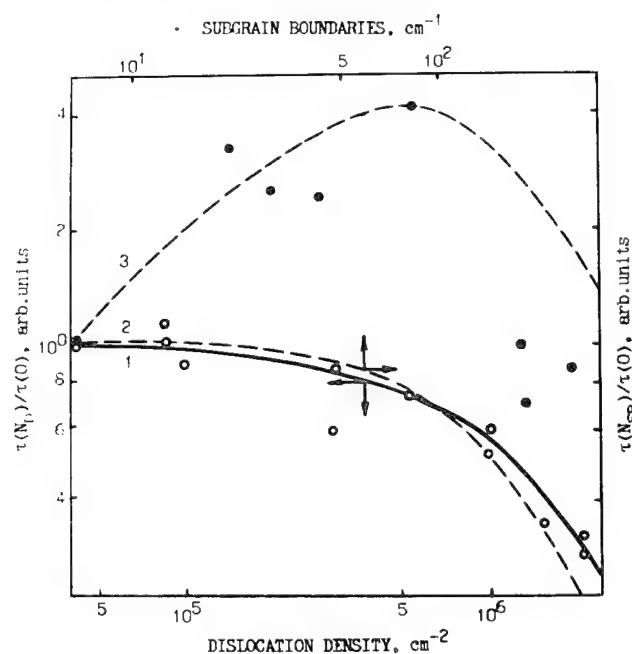


Fig. 5. Relative carrier lifetime vs dislocation density N_d (1-calculation, open circles—experiment) and subgrain boundary value N_{sb} (2- $[V_{Hg}] = 10^{15}\text{ cm}^{-3}$, 3- $[V_{Hg}] = 10^{13}\text{ cm}^{-3}$) for MCT ($x = 0.2$) at $T = 77\text{K}$.

with allowance for uniaxial pressure along $\langle 100 \rangle$ of HgCdTe, shows that the hole effective mass in the upper of two valence subbands decreases (E_g is not affected by uniaxial pressure practically).¹¹ As a result, τ_A increases and τ_R decreases, as it is shown in Fig. 4. Such a redistribution between radiative and nonradiative channels could result in increases of both the quantum efficiency of radiative recombination ($x \geq 0.2$, $T \geq 150\text{K}$) and responsivity of the IR detectors ($x \leq 0.2$, $T \leq 100\text{K}$). On the contrary, hydrostatic pressure induces a marked increase of E_g followed by an increase in τ_A and τ_R . Calculation and experiments show¹² that for InSb crystals ($T = 300\text{K}$) radiative recombination increases from 6 to 25%, whereas, the response time of photodetectors increases by 30 times

when the 8 kbar pressure is applied (Fig. 4). Also hydrostatic pressure impact at negative and positive luminescence parameters in MCT heterostructures seems to be attractive for practical applications.¹³ Naturally, a shift of emission and photosensitivity toward short wavelengths occurs.

Finally, the impact of structural and point defects on the electronic and optical properties of MCT as well as NGS material characterization are typical examples of the work permanently conducted by institute scientists at Kyiv. Figure 5 demonstrates the MCT carrier lifetime dependence on the dislocation density and subgrain boundary value. It shows that dislocations provoke a lifetime decrease, whereas the subgrain boundaries, acting as point defect getters, promote the photosensitivity rise of materials.¹⁴

IR MATERIALS

Presently, there are two Ukrainian enterprises which have been significant SU-wide suppliers of electronic and photonic materials for 20 years, the titanium and

magnesium plant at Zaporozhye¹⁵ and the pure metals plant at Svitlovodsk.¹⁶

The titanium and magnesium plant at Zaporozhye delivers large quantities of low-cost Si (bulk material and wafers) and Ge (doped and undoped crystals) as well as the Ge-based optic accessories for IR applications. It has the capabilities to manufacture, by various crystal-growth techniques, Si and Ge mono- and polycrystals which satisfy the different needs of the semiconductor and optoelectronic industry.

As-grown Czochralski, dislocation-free, Si monocrystals (ingots) with different doping levels ($\rho = 0.01\text{--}40\ \Omega\ \text{cm}$ for n-type and $\rho = 0.005\text{--}40\ \Omega\ \text{cm}$ for p-type) can be delivered with a diameter up to 150 mm. Carbon concentration does not exceed $3 \cdot 10^{16}\ \text{cm}^{-3}$, and the spatial nonuniformity of dopants is less than 5%. Floating zone technique-grown Si monocrystals ($\rho = 0.1\text{--}2 \cdot 10^4\ \Omega\ \text{cm}$ for n-type and $\rho = 0.1\text{--}4 \cdot 10^4\ \Omega\ \text{cm}$ for p-type) with a diameter up to 105 mm and carbon or oxygen concentrations less than $1 \cdot 10^{16}\ \text{cm}^{-3}$ are also available. Also, there are polycrystalline Si cylindrical ingots available ($d = 800\ \text{mm}$, $h = 70\ \text{mm}$).

The present production ability of dislocation-free zone-refined Ge polycrystals ($\rho = 48\ \Omega\ \text{cm}$) as well as Ge crystals for optical accessories ($\rho = 5\text{--}40\ \Omega\ \text{cm}$, n-type) with diameters from 10 to 420 mm is estimated as 5 ton/year. In addition, GeCl_4 and GeO_2 are also available.

The pure metals plant at Svitlovodsk supplies with high uniformity, low carrier concentration single crystal HgCdTe as well as liquid phase epitaxially (LPE) grown p-HgCdTe/CdTe structures ($0.185 < x < 0.300$,

Table I. HgCdTe Wafers (Polished)

Molar content, x	0.190–0.240 0.240–0.320
Conductivity	n,p
Carrier concentration at 77K, cm^{-3}	n-type– $7 \cdot 10^{13}$ – $1 \cdot 10^{15}$ p-type– $1 \cdot 10^{15}$ – $1 \cdot 10^{17}$
Carrier mobility at 77K $\text{cm}^2/\text{V}\cdot\text{s}$	n-type– $3 \cdot 10^4$ – $2.5 \cdot 10^5$ p-type– ≥ 200
Surface, cm^2	0.25–4.0
Thickness, mm	0.7–1.0

Table II. Gallium Arsenide Ingots

Method: LEC	Semi-Insulating (i-GaAs)	Conductive (n/p-GaAs)		
Ingot diameter, mm	52±0.5 78.2±0.5	52±0.5	78.2±0.5	
Crystal orientation	<100>, <111>	<100>, n Te	<111> n Si	p Zn
Conductivity type dopant	None or Cr			
Crystal annealing	As atmosphere, 950°C, 2.5 h			
Car. concentration, $10^{17}\ \text{cm}^{-3}$		1–5	1–8	5–200
Resistivity, $10^7\ \Omega\cdot\text{cm}$	1–10			
Carrier mobility	>4000 $\text{cm}^2\ \text{V}^{-1}\ \text{s}^{-1}$			
Disl. density, cm^{-2}	< $8 \cdot 10^4$ < $1.5 \cdot 10^5$	8·10 ⁴	< $1.5 \cdot 10^5$	

Table III. Si-Doped GaAs EPI-Wafers

Method: Liquid Phase Epitaxy	Application: Infrared Light Emitting Diodes		
Diameter, mm		35–40	
Orientation		<100>	
Structure type	p-GaAs:Si	n-GaAs:Si	n-GaAs
Dopant	Si	Si	Sn
Carrier concentration, cm^{-3}	$1 \cdot 10^{16}$ – $1 \cdot 10^{18}$	$1 \cdot 10^{16}$ – $5 \cdot 10^{17}$	($0.5\text{--}1.5$)· 10^{17}
Layer thick, μm	50–70	5–35	360–380
Emiss. max. λ , μm		0.9–0.98	p-GaAs (Si) n-GaAs (Si) n-GaAs(Sn)
Emiss. pow. of 1 mm dia. mesa-str., I = 100 mA		>4.5 mW	
Voltage drop at I = 100 mA		<1.5 V	

$p_0 = 5 \cdot 10^{15}$ to $2 \cdot 10^{16} \text{ cm}^{-3}$, $\mu_p \geq 300 \text{ cm}^2/\text{V} \cdot \text{s}$ at $T = 77\text{K}$). Most standard wavelengths are available (Table I). Ultrahigh purity Cd, Te, Hg starting materials are also available.

GaAs (polycrystalline, semi-insulating, conductive, Si-doped EPI-wafers, multilayer GaAs/AlGaAs EPI-wafers)¹⁷ and InAs single crystals with diameters ranging from 25 to 81 mm, both n- and p-type, and CdTe ($\rho = 10^8 \Omega \cdot \text{cm}$, dislocation density $\leq 10^5 \text{ cm}^{-2}$) are available for immediate shipment (see Tables II–IV). Monocrystalline Si (Sn, As, P, B-doped) dislocation-free ingots of diameters 78, 100, 125 mm with parameters similar to that of SEMI standard can be also delivered.

Also, researchers and technologists at the Institute for Single Crystals at Kharkiv¹⁸ have succeeded in developing the technology of A^2B^6 , alkali halide and sapphire crystal growth. As an example, bulk ZnSe single crystals ($d \leftarrow 63 \text{ mm}$, $h = 50 \text{ mm}$, $\rho = 10^{10} \Omega \cdot \text{cm}$) and wafers are practically transparent within the 1–15 μm spectral range ($k = 0.002 \text{ cm}^{-1}$). This material's laser beam damage threshold exceeds 15 kW/cm^2 for a 0.5 mm diameter beam, and the value of half-wave voltage at 10.6 μm is 160 kV. The wafers can be covered with antireflecting, reflecting, or highly protective (diamond films) coatings. KCl, NaCl, KBr, and KCl-KBr single crystals can be grown with $d = 60$ –500 mm and maximal bubble size $\leq 0.2 \text{ mm}$. MgF_2 , CaF_2 , BaF_2 , LiF ceramics of various forms and sized are also available.

New materials for IR devices are also under development by researchers at the University of Chernivtsy.¹⁹ They have been developing the technology of $\text{Cd}_x\text{Mn}_{1-x}\text{Te}$ and $\text{Cd}_x\text{Mn}_y\text{Hg}_{1-x-y}\text{Te}$ crystal growth

for several years, and now have a production facility for it. The technologies developed (zone-melting, LPE, and vapor phase epitaxy [VPE]) provide high cross-sectional homogeneity and low structural defect concentrations both in 12–30 mm diameter ingots and epitaxial structures. These materials' resistance to degradation over time seem to be superior to those achieved for HgCdTe.²⁰ The parameters of interest at 80K are $\mu_n \geq 2 \cdot 10^6 \text{ cm}^2/\text{V} \cdot \text{s}$ ($x = 0.16$), $\mu_p \geq 6 \cdot 10^5 \text{ cm}^2/\text{V} \cdot \text{s}$ ($y = 0.07$), $n_0 = 10^{15}$ – 10^{16} cm^{-3} , spectral range $\lambda = 9$ –14 μm . Photoresistors, photodiodes, and photoelectromagnetic (FEM) detectors based on these materials are at the experimental stage. This group also believes they have demonstrated the first InSb-InBi superlattices (10–1000Å) grown with laser induced technology.

DEVICES

To date, Rythm Optoelectronics (RO)²¹ at Chernivtsy is probably the major supplier of photodetectors with total wavelength coverage from ultraviolet (UV) to near IR. The company has more than 20 years' experience in the design and manufacture of silicon (p-n, p-i-n, avalanche photodiodes, 0.20–1.1 μm , ordinary, UV enhanced, built-in interference filters, transimpedance amplifier modules), germanium (p-n and avalanche photodiodes, 0.5–1.7 μm) as well as lead chalcogenides (PbS, PbSe photoresistors operating at room temperature or thermoelectrically cooled, 0.8–5.0 μm) single and multi-element (1 . . . 256) devices with the highest detector performance. Full in-house capabilities for design, fabrication, and test of customized devices are available. As an example, Tables V and VI provide a more detailed look at the lead

Table IV. Multilayer GaAs/AlGaAs EPI-Wafers

Method: Liquid Phase Epitaxy	Application: "Red" Light Emitting Diodes			
Diameter, mm	35–40			
Orientation	<100>			
Structure type	n ⁺ -AlGaAs	n-AlGaAs	p-AlGaAs	p ⁺ -GaAs
Dopant	Te	Te	Zn	Zn
Carrier Concentration 10^{17} cm^{-3}	5–20	1–3	8–20	50–200
Layer Thickness, μm	15–25	15–25	10–25	350–450
Emiss. max., λ , μm	0.65–0.68			
Light power of $0.35 \times 0.35 \text{ mm}$ chip at $I = 100 \text{ mA}$	type A: > 300 cd type B: > 600 cd		n ⁺ -AlGaAs(Te) n-AlGaAs(Te) p-AlGaAs(Zn) p ⁺ -GaAs(Zn)	

Table V. Lead Chalcogenide Photodetectors

Device Parameters	PbS		PbSe	
	T = 293K	T = 195K	T = 293K	T = 195K
Spectral range, μm	0.8–3.0	0.8–3.5	1.0–4.5	1.0–5.0
λ_{max} , μm	2.5 ± 0.2	2.8 ± 0.2	3.5 ± 0.3	4.0 ± 0.3
Time constant, μs	~200	~2000	~5	~30
Dark resistance, $\text{M}\Omega$	~0.5	~5	~1	~10
Responsivity, V/W	$(3\text{--}8) \cdot 10^4$	$(1\text{--}5) \cdot 10^5$	$(2\text{--}7) \cdot 10^4$	$(2\text{--}7) \cdot 10^5$
$D_{\lambda\text{max}}^*$, $10^{10} \text{ cm Hz}^{1/2} \text{ W}^{-1}$	3–10	50	0.3–1.2	2–8
at mod. frequency, Hz	1000	70	1000	1000

Table VI. Silicon Photodiodes ($T = 20^\circ\text{C}$)

PD Type	Spectral Range, μm	Dark Current pA/mm^2	Capacitance at V_p , pF/mm^2	Responsivity at λ , A/W
UV enhanced	0.2–1.1	≤ 10 at 10 mV	≤ 12 at 10 mV	≥ 0.08 at $0.62 \mu\text{m}$ 0.62 at $0.63 \mu\text{m}$
Low Noise	0.4–1.1	≤ 100 at 10V	≤ 1.8 at 10 V	≥ 0.3 at $0.63 \mu\text{m}$
Threshold	0.4–1.1	≤ 20 at 10 V	≤ 1.5 at 10 V	≥ 0.32 at $0.63 \mu\text{m}$
responsivity enhanced				
Common-use	0.4–1.1	≤ 1 at 10 mV	≤ 12 at 10 mV	≥ 0.4 at $0.63 \mu\text{m}$

Table VII. Thermoelectric Module Parameters

Module Type	ΔT_{max} , $^\circ\text{C}$	Q_{max} , W	I_{max} , A	V_{max} , V	Base $\text{mm} \times \text{mm}$	Height mm	Cooled Surface $\text{mm} \times \text{mm}$
TE02-1	95	0.48	0.3	5.0	6.0×9.0	9.0	2.48×4.2
TE02-3	80	55.0	7.5	12.0	40.0×40.0	7.0	40.0×40.0
TE02-4	80	32.0	4.8	12.0	40.0×40.0	7.0	40.0×40.0
TE02-5	98	1.5	5.0	0.9	8.0×12.0	6.8	5.0×6.0
TE02-6	95	0.3	4.6	0.2	6.0×8.0	5.5	2.0×4.0
TE02-7	98	0.48	2.0	0.7	12.0×12.0	6.8	2.0×4.0
TE02-8	98	2.2	2.5	2.8	12.0×15.0	6.8	5.0×8.0
TE03-2	109	0.3	3.0	5.0	15.0×20.0	12.5	2.0×10.0
TE03-3	110	0.52	1.2	3.0	8.5×5.0	10.0	3.0×3.0
TE03-4	109	1.6	7.5	1.1	12.0×1.0	12.5	2.0×2.0
TE03-5	110	1.6	2.5	3.2	14.0×14.0	12.5	2.0×6.0
TE03-6	108	1.7	0.06	1.7	4.0×4.0	12.5	0.8×0.8
TE04-1	118	1.45	2.0	6.0	21.0×20.0	22.0	8.0×12.0
TE04-2	118	4.9	5.0	7.0	18.0×20.0	20.0	5.0×20.0
TE04-3	119	6.7	3.7	12.0	27.4×41.0	21.3	9.5×14.5
TE04-4	110	0.68	0.9	0.7	12.4×16.3	11.65	4.1×8.0
TE04-7	115	0.81	1.0	7.5	12.5×16.4	13.7	3.0×7.3
TE05-1	125	0.8	1.0	8.0	16.0×25.0	15.0	4.0×10.0
TE04-9	120	1.1	1.2	6.5	15.4×19.0	16.6	2.6×8.5
TE06-1	133	0.3	1.1	4.6	12.4×10.0	12.5	5.5×5.5

ΔT_{max} —max. temperature differential between base ($T = 300\text{K}$) and cooled surface (vacuum, no thermal load).

Q_{max} —cooled surface thermal load at $\Delta T = 0$. I_{max} and V_{max} —current voltage supply.

chalcogenide and silicon detector parameters.

The RO's near-term goal is to become the major "eyes" supplier for the unmanned satellite program started by the National Space Agency. RO is also considering expanding its activity toward longer wavelength devices based on MCT, Ge(Hg), and Pt-PtSi.

The Research and Production Corporation Termoprylad²² at Lviv has nearly 40 years of extensive experience in the development and production of efficient devices for remote and contact temperature (-35°C to $+5000^\circ\text{C}$) measurements. To date, manufacturing capability exists for the production of analog and digital resistor thermometers, thermoelectric temperature transducers (thermocouples), as well as IR-pyrometers based on PbS, PbSe, Si, Ge, LiNb, and operating within the $0.5\text{--}14 \mu\text{m}$ spectral range.

Also, a multilayer thin film ($100\text{--}200\text{\AA}$) superconducting tunnel junction IR-bolometer operating as $0.3\text{--}5\text{K}$ has been developed at the institute for low temperature physics and engineering²³ at Kharkiv. The device is equipped with a compact cryogenic system (no external pumping, remote control) and is ready for use in zero-gravity conditions. Basic device

parameters (spectral range $2.0\text{--}30 \mu\text{m}$, $\text{NEP} = 1.4 \cdot 10^{-15} \text{ W/Hz}^{1/2}$, $\tau = 3 \cdot 10^{-3} \text{ s}$) allow its use in satellite photometers and radiometers as well as at low background radiation metrological facilities (background emission power $\geq 10^{-12} \text{ W cm}^{-2}$) operating in this institute. In addition, a three-range ($3\text{--}5 \mu\text{m}$, $8\text{--}10.5 \mu\text{m}$, $5\text{--}13 \mu\text{m}$) space radiometer (satellite orbit height $\approx 70 \text{ km}$) based on cooled MCT 3×128 array detector modules is now at the experimental stage.

High sensitive and fast response pyroelectric detectors (TGS, LiTaO_3) can be delivered from the Institute of Physics at Kyiv.²⁴ This broadband ($1\text{--}50 \mu\text{m}$) detector series combines both low-noise performance ($3 \cdot 10^{-10} \text{ W/Hz}^{1/2}$) and high bandwidth (50 MHz) at room temperature. These detectors can be optimized for radiometry, IR gas analysis, Fourier transform infrared (FTIR) spectroscopy as well as for measuring laser power and energy (minimal energy $\sim 10^{-10} \text{ J}$ and pulse duration $\sim 10^{-9} \text{ s}$).²⁵ Reportedly, these devices have been in use on "meteor"-type satellites, the interplanetary station "Phobos," and on the orbital station "Mir."

A family of efficient single and multistage (up to

nine) thermoelectric coolers for commercial and scientific applications have been developed by researchers from the Institute of Thermoelectricity at Chernivtsy.²⁶ Made with bismuth telluride materials, these devices can be used in IR focal plane detector arrays. Maximum current ratings range from 0.06 to 7.5 A and a maximum temperature differential of 70 to 133°C is possible.²⁷ Table VII provides a more detailed look at these device parameters. Custom designs are also available upon request.

Ukranalyt R&D Company in Kyiv²⁸ produces both efficient multilayer IR interface filters and multipath optical cells for two wavelength coverages (2–8 and 8–14 μm). The filters can be delivered with $T_{\text{max}} \geq 50\%$ transmittance at λ_0 for 2–8 μm and $T \geq 40\%$ for 8–14 μm spectral ranges. The relative halfwidth $\frac{\Delta\lambda_{0.5}}{\lambda_0}$ does not exceed 2.2–4%. When illuminated with IR noncoherent light the multipath cells provide up to a 25 m long beam traveling length and more than a 70 m path when illuminated with an IR laser. Based on these optical components, the company has developed the IR gas analyzers for air monitoring and vehicle exhaust gas analysis.

GOVERNMENT GUARDIANSHIP

Government support in this area is growing and helping. In its declared overall strategy, the government plans to balance spending on civilian and defense programs. However, the switch from defense to a civilian focus is happening slower than anticipated for several reasons. First, private companies have exhibited little interest in the electronic and optoelectronic business. Secondly, the times seem to favor small science, not big physical projects, and thirdly, the national roadmap aimed to remedy the situation and to improve the worldwide competitiveness of the Ukrainian optoelectronics industry has not been developed yet.

All in all, the State Committee on Science and Technology is permanently funding as many as 30 scientific projects to develop efficient semiconductor lasers, IR LEDs and two-dimensional focal plane area detectors. Some of these projects are concerned with fiberoptics and optical storage components.

The National Academy of Sciences assistance in financing practically all aspects of fundamental studies such as new materials (primarily narrow-gap semiconductors and semimetals), new generations of photonic devices, fundamental aspects of radiation-substance interaction, should be mentioned also. The number of grants dealing with different aspects of IR physics and devices reportedly exceeds a hundred. Finally, after the government decision to fix civilian R&D funding for FY 1995 at 1.7% of gross domestic product, the future of Ukrainian IR science is not seen as being in doubt.

The National Space Agency follows more application-oriented goals. Their task is clearly formulated: the family of Ukrainian satellites (the first one is to be launched by 1996) have to be equipped with domestic-made IR-systems.

The Department of Conversion concern is to focus on the IR optoelectronic technologies as key dual-use technologies with important enabling applications in both the defense and civilian areas and to turn many of the fundamental laboratory developments into manufacturable products. The strategic and commercial forces at work are similar to those that grew the optoelectronics industry in North America, Europe, and Japan—defense, scientific research, medicine, ecology, and industrial modernization. Naturally, economic factors and a shift away from defence contracts raise more questions than answers.

CONCLUSIONS

The results presented indicate that the IR photonics status in the Ukraine is quite comparable to that achieved in other countries. On the contrary, the cost of acquiring, processing, and producing the IR photons in this country is now so cheap as to be almost free. These two circumstances appear to provide the basis for understanding both the scientific and commercial opportunities of cooperation with Ukrainian scientists and developers.

In the author's opinion, the top high-growth economy in Europe at the turn of the century will be the Ukraine, this European China. Clearly, the status of Ukrainian IR photonics constitutes a promising opportunity for the international community. Ukrainian semiconductor materials and optoelectronic devices could capture a significant portion of the semiconductor market in the near future, but the serious doubt exists that any Ukrainian group will jump to international market alone (no domestic high-technology expertise exists, only a few of this products are suitable for export market). The question is who will be that entrepreneur to join Ukrainian developers and producers in this jump. It is costly and risky, but the potential rewards are alluring.

What is envisioned now is a series of long-term, large-scale international programs that would be difficult for others to tackle because of their size, complexity, and long-term nature as well as "work for others" in small science application-oriented and dedicated projects. While this may seem dire, the picture is not as bad as it may look at first. Isn't it nice to have a choice? The stakes are high. In conclusion, the author's goal is not simply to ride the crest of this wave, but to be one of the forces driving this process forward.

REFERENCES

1. 45 Nauki Prospect, Kyiv, 252028 Ukraine, Fax: (044) 265-8342.
2. V.K. Malyutenko, *Semicond. Sci. Technol.* 8, 393 (1993).
3. S.S. Bolgov, V.K. Malyutenko and V.I. Pipa, *Sov. Phys. Semiconductors* 17, 134 (1983).
4. V.K. Malyutenko, E.I. Yablonovsky, S.S. Bolgov, G.V. Beketov and O.Yu. Salyuk, *Fiz. Tekh. Poluprovodn.* 18, 340 (1984).
5. V. Malyutenko, E. Yablonovsky, V. Igumenov and V. Konstantinov, *Optoelectronics—Devices and Technologies* 4, 83 (1989).
6. S.S. Bolgov, V.K. Malyutenko, V.I. Pipa and A.P. Savchenko, *Infrared Phys.* 33, 409 (1992).

7. V. Malyutenko, A. Pigida and E. Yablonovsky, *Optoelectronics—Devices and Technologies* 7, 321 (1992).
8. P. Berdhal, V. Malyutenko and T. Morimoto, *Infrared Phys.* 26, 667 (1989).
9. A.A. Akopyan, S.S. Bolgov, V.K. Malyutenko and A.P. Savchenko, *Phys. B* 162, 243 (1990).
10. V.K. Malyutenko, G.I. Teslenko and I.I. Boiko, *Infrared Phys.* 14, 351 (1974).
11. F.T. Vas'ko, S.G. Gasan-zade, M.I. Strikha and G.A. Shepel'skii, *JETP Lett.* 50, 318 (1989).
12. V.K. Malyutenko, K.Yu. Guga, V.P. Kislyi and A.M. Shirokov, *Fiz. Tekh. Poluprovodn.* 20, 1536 (1986).
13. S.S. Bolgov, V.P. Kislyi, V.K. Malyutenko and A.P. Savchenko, *Sov. Phys.—Semiconductors* 27, 93 (1993).
14. N.N. Grigoriev, L.A. Karachevtseva and A.V. Lyubchenko, *Fiz. Tekh. Poluprovodn.* 25, 1649 (1991).
15. 330085 Zaporozhye, Ukraine, Fax: (0612) 35-41-74.
16. 317000 Svitlovodsk, Ukraine, Fax (05236) 23710.
17. Remark for users. GaAs optics is to be used instead of Ge optics for IR imaging systems because of negligible losses at $T \leq 400\text{K}$, high index of refraction and two times less than Ge index of refraction change with temperature.
18. 60 Lenin Ave., 300001 Kharkiv, Ukraine, Fax: (0572) 320273.
19. 2 Kotsyubinskii Str., 274012 Chernivtsy, Ukraine, Fax: (03722) 53838.
20. O.A. Bodnaruk, I.N. Gorbatyuk and I.M. Rarenko, *Neorgan. Mater.* 28, 335 (1992).
21. 246 Golovna Str., 274032 Chernivtsy, Ukraine, Fax: (03722) 42633.
22. 3 Naukova Str., 290053 Lviv, Ukraine, Fax: (0322) 353043.
23. 27 Lenina Prospect, 310164 Kharkiv, Ukraine, Fax: (0572) 32-23-70.
24. 46 Nauki Prospect, 252650 Kyiv-22, Ukraine, Fax: (044) 2651589.
25. V.F. Kosorotov, L.S. Kremenchugsky, V.B. Samoilov and L.V. Shchedrina, *Pyroelectric Effects and its Practical Applications*, Kyiv, Naukova Dumka (in Russian) (1989).
26. General Post Office, Box 86, Chernivtsy, Ukraine, Fax: (03722) 35118.
27. L.I. Anatychuk, *J. Thermoelectricity* 1, 5 (1993).
28. 6 Tverskaya Str., 252006 Kyiv, Ukraine, Fax: (044) 2695268.

Numerical Simulation of HgCdTe Detector Characteristics

G.M. WILLIAMS and R.E. DE WAMES

Rockwell Science Center, 1049 Camino Dos Rios, Thousand Oaks, CA 91358

We discuss analytic and numerical models for HgCdTe photodiodes and present examples of their application. Analytic models can account for the performance obtained by many device architectures. Numerical and analytic models agree in predicting several aspects of device performance, such as diffusion limited dark current, confirming the approximations used in deriving the analytic models. Areas are noted where improvement in the numerical models would allow application to a wider range of device simulations. Useful results are obtained from the numerical simulators that cannot be obtained from our analytic model. Flux dependent R_0A products are shown to be a direct result of bias dependent quantum efficiency, a mechanism that is much more evident in heterojunction device architectures. Material compositional grading is demonstrated to lead to lower signal to noise ratio in devices designed to detect a particular infrared wavelength. We also show, particularly for high temperature operation, that heterojunction detectors can at best equal the performance of well-designed homojunction detectors; so, for photodetector design, heterojunctions do not offer any inherent performance advantages over homojunctions. Nevertheless, heterostructures, though ideally not required, may be helpful in achieving high performance in practice.

Key words: Heterojunctions, HgCdTe, infrared detectors

INTRODUCTION

HgCdTe photovoltaic detector technology for second generation focal plane arrays (FPAs) has transitioned from feasibility demonstrations to initial phases of product insertion. However, the cost of FPAs is still too high for many applications. Low cost high performance FPAs can only be achieved by increasing manufacturing yield through process control and variance reduction. Since process control is demonstrated through prediction and achievement of array performance based on design parameters, sufficiently accurate detector modeling is a necessity. Modeling HgCdTe detectors, using both analytic and numerical methods, is the subject of this paper.

Generally, the differences between designed characteristics and measured performance of HgCdTe FPAs must be quantified. Although particular aspects of detector performance often agree with their respective models, less perfect agreement is usually obtained with a self-consistent model that simultaneously accounts for multiple aspects of device performance such as, dark current, optical response, and their respective dependence on temperature and bias voltage. Nevertheless, individual detectors with performance that agrees with basic self-consistent models can be found. This indicates that the technology may be capable of achieving a level of maturity that makes modeling an especially worthwhile activity, since it can lead to an understanding of the limitations on current detector array performance and provide information needed for further improvement.

(Received October 4, 1994; revised February 10, 1995)

The models we discuss are based on standard semiconductor device equations and HgCdTe specific material parameters. Photovoltaic detector performance models are basically derived from the physics of current flow mechanisms in semiconductor p/n junctions. The current mechanisms considered in this paper are fundamental in the sense that they apply to photodiodes in any semiconductor and are described in terms of a small number of device design parameters. A HgCdTe specific material library and independently measured device parameters are all that are needed to test these models against experiment. Consequently, the models discussed address homogeneous aspects of device performance; that is, mechanisms which yield uniform device characteristics, as opposed to those related to localized flaws.

We have investigated both analytic and numerical models and discuss their applicability and limitations. We begin with a description of a one-dimensional analytic model, which provides confidence in our selection of a HgCdTe material library. The material library and device models are documented, and examples of the application to HgCdTe detectors are presented. Next, numerical models are discussed. Numerical models provide a validation of the approximations used in the analytical expressions and allow better simulation of advanced device architectures which employ heterojunctions, multiple junctions, and layers with graded band gaps. We compare results obtained with HET III (provided by SBRC) and two commercially available numerical device simulators, Semicad Device by Dawn Technologies, Inc., and Atlas/Blaze/Luminous by Silvaco International. Areas where the numerical models are applicable are noted. Finally, we present examples which demonstrate the usefulness of the numerical techniques.

ANALYTIC MODEL

Analytic models can provide insight and efficiency that is beyond the capability of purely numerical techniques. The analytic model we have adopted can account for a large fraction of the experimental results obtained on the best HgCdTe photovoltaic detectors, whether they be homojunctions or heterojunctions. This has been achieved by aggressive application of conventional models. Our approach is consistent with results obtained from more complete numerical calculations, presumably justifying our assumptions. The adopted one-dimensional analytic model considers current from the space charge neutral regions on both sides of the p/n junction (diffusion current), the depletion region of the junction, and band-to-band tunneling across the junction.

Optically generated currents are taken from Hovel.¹ Contributions from the p-side and n-side neutral regions and depletion region of the junction are included in this calculation. Optionally, a reflection from the back optical interface may be included to allow for a second pass of light through the detector.

The diffusion current model² for dark current includes the effect of neutral region thicknesses and

associated boundary surface recombination velocities on both sides of the junction. Although specification of a low surface recombination velocity (for example, zero) can lead to a violation of current conservation for this model, in practice the benefits of low recombination velocity interfaces can be obtained by employing high/low junctions³ (carrier concentration variation), and/or isotype heterojunctions. So, even though this simple model does not strictly include the effects of nearby junctions, we can proceed as if it does by choosing appropriate interface recombination velocities. This consideration is important for analytically modeling heterojunction p on n HgCdTe diodes, which can be modeled as p/n homojunction devices with very thin p-type regions bounded on the p-side with a low recombination velocity interface. For a p/n homojunction device, diffusion current from the thin p-side will dominate total diffusion leakage current because of the high electron mobility and the proximity of the p-side ohmic contact, which is by definition a high recombination velocity interface. An interposed isotype p/p heterojunction can eliminate this problem, allowing diffusion current from the n-side of the junction to dominate leakage current; in fact, an isotype heterojunction, a high/low junction, or very heavily doped high quality p-type material is required to achieve competitive performance from this device architecture in the diffusion limited temperature regime. Also, the side of the junction connected to the substrate is often modeled as if the interface recombination velocity is zero. In a real device, current continuity is achieved by lateral current flow; consequently, the one-dimensional model will underestimate this current component unless an appropriate effective recombination velocity is used. Remarkably, we find that for the best HgCdTe diodes fabricated in our laboratory, and the best diodes reported by others in the literature, assumptions which limit dominant current generation to the substrate side of the junction, assume zero recombination velocity for the active layer/substrate interface, and use only intrinsic recombination mechanisms that are within a factor of two of accounting for experimental data.

Depletion region (g-r) currents are usually associated with Shockley-Read centers. We adopt the formulation⁴ which applies to asymmetrical junctions and uses computed limits to evaluate the associated integrals. Because radiative and Auger lifetime limiting mechanisms can dominate recombination in the neutral regions, we also include their contribution in the depletion region.⁵ For the device architectures, we typically fabricate, these contributions to leakage current are small, except at low temperatures with Shockley-Read recombination enabled.

The functional dependence of the band to band tunneling current model is taken from Moll.⁶ The electric field is calculated from the depletion approximation, and half of the maximum value is used as the relevant field in the tunneling current expression. The reduced mass ($m_r = 2 \cdot m_e \cdot m_h / (m_e + m_h)$) is used for the tunneling effective mass, where m_e is the

electron effective mass, and m_h is the hole effective mass. A choice is still required for the shape of the potential barrier. We use an empirical constant, fit to experimental data, for the value associated with barrier shape; this constant is between the theoretical values derived for parabolic and triangular shaped barriers. Although this model is extremely sensitive to parameter variation, we find this fitting constant is independent of material composition, within the limits of experimental error, for the mid wave infrared (MWIR) and long wave infrared (LWIR) devices we measured.

Finally, a HgCdTe material library must be selected to provide model parameters. The required parameters, and the sources we use, are as follows: electron effective mass,⁷ high frequency and static dielectric constants,⁸ bandgap,⁹ intrinsic carrier con-

centration,¹⁰ Auger lifetime,¹¹ radiative lifetime,¹² Shockley-Read lifetime,¹³ electron and hole mobility,¹⁴ and optical absorption coefficient.¹⁵ The overlap integral for Auger recombination is taken to be 0.2. The hole effective mass is 0.5, independent of material composition. The majority and minority carrier mobilities are assumed equal.

APPLICATION OF THE ANALYTIC MODEL

Two examples of application of the analytic model are presented. The first example models devices from a very long wavelength infrared (VLWIR) array fabricated in HgCdTe grown by molecular beam epitaxy, and the second example models MWIR detectors fabricated in material grown by liquid phase epitaxy. Both are planar p/n heterostructure detectors.

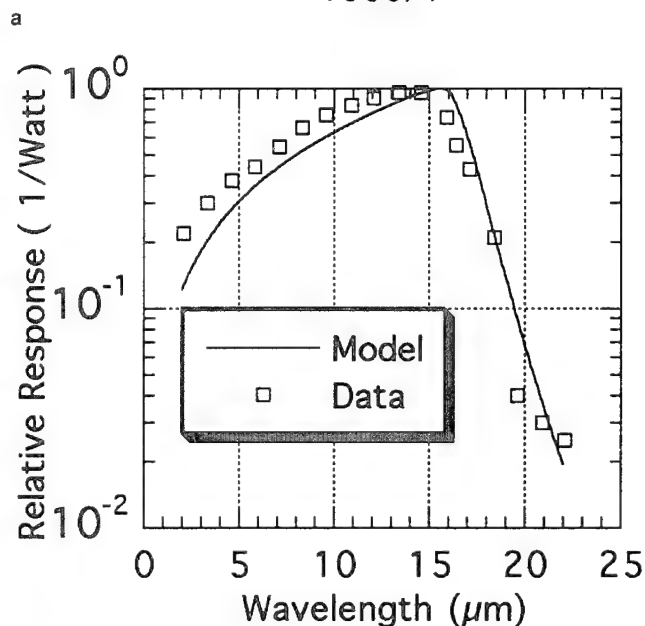
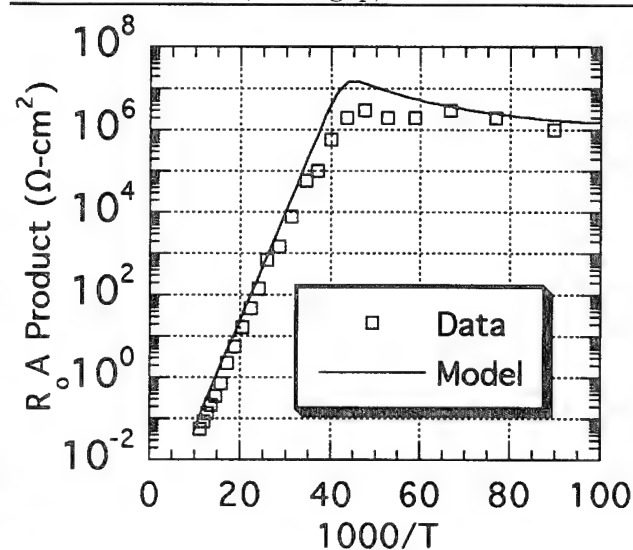


Fig. 1. Experimental data and model calculations of R_0A product as a function of temperature and spectral response at 78K for a HgCdTe diode with a cutoff wavelength of 16.4 microns at 78K.

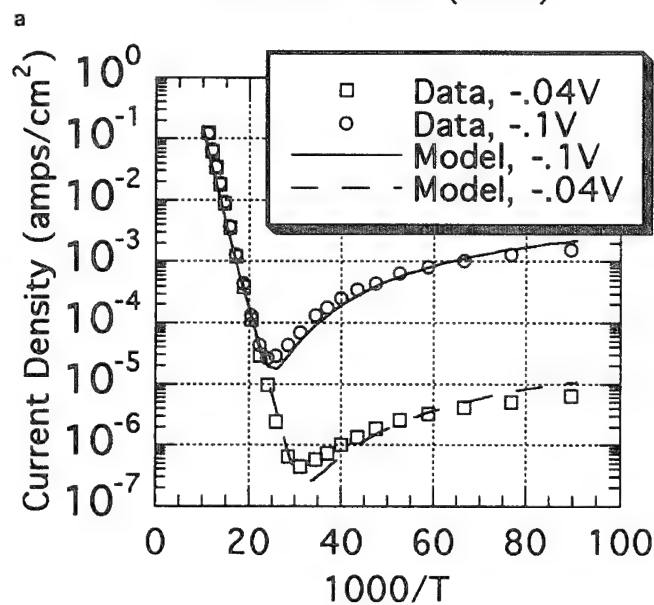
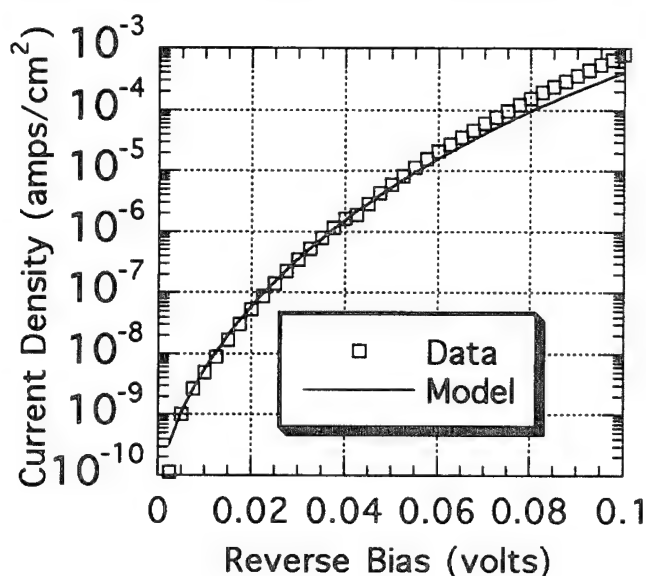


Fig. 2. Calculated and measured reverse bias I-V curve at 21K, and calculated and measured current density vs inverse temperature at two different reverse bias voltages for the detector from Fig. 1.

Figure 1 shows experimental data and model calculations of R_0A product as a function of temperature and spectral response at 78K for a HgCdTe diode with a cutoff wavelength of 16.4 μm at 78K. Based on independent measurement, the model input parameters are junction depth (1 μm), layer thickness (11 μm), and n-side carrier concentration of $2 \times 10^{15} \text{ cm}^{-3}$ obtained from Hall measurements. The material composition ($x = 0.194$) is selected to match the cutoff wavelength. Zero surface recombination velocity was assumed for both the back and front interfaces, and only radiative and Auger recombination mechanisms were considered. The fit to the data over the entire temperature range is remarkably good. In light of the demanding assumptions made by the model, which amounts to defect-free material and ideally functioning interfaces, the experimental result repre-

sents a considerable technological achievement. At high temperature, the device is limited by diffusion current from the n-side of the junction, while at low temperature band-to-band tunneling current dominates.

Good agreement is also obtained between calculated and measured current-voltage (I-V) characteristics. Figure 2 shows calculated and measured reverse bias I-V curve at 21K, and calculated and measured current density vs inverse temperature at two different reverse bias voltages. The dominance of diffusion current at high temperature and the smooth transition to band-to-band tunneling current at low temperatures is again noted. Figure 3 shows measured and calculated forward bias I-V curves, including the effect of series resistance. Good agreement is observed at 30K and above, but at lower temperatures significant deviations from the model are obtained. Current larger than predicted observed at low forward bias is likely due to band-to-band tunneling, which was not included in this calculation, and trap-assisted tunneling at somewhat larger bias; but, the lower than predicted current at intermediate forward bias is unexplained. Carrier freezeout in p-type material might provide some answers.

Figure 4 shows experimental data and model calculations of R_0A product as a function of temperature, spectral response at 78K, and quantum efficiency vs temperature for a HgCdTe diode with a cutoff wavelength of 5.3 μm at 78K. The model input parameters are junction depth (2 μm), layer thickness (15 μm), and n-side carrier concentration of $5 \times 10^{15} \text{ cm}^{-3}$ obtained from Hall measurements. The material composition ($x = 0.2996$) is selected to match the cutoff wavelength. Zero surface recombination velocity was assumed for both the back and front interfaces, and only radiative and Auger recombination mechanisms were considered. At temperatures below 100K, the

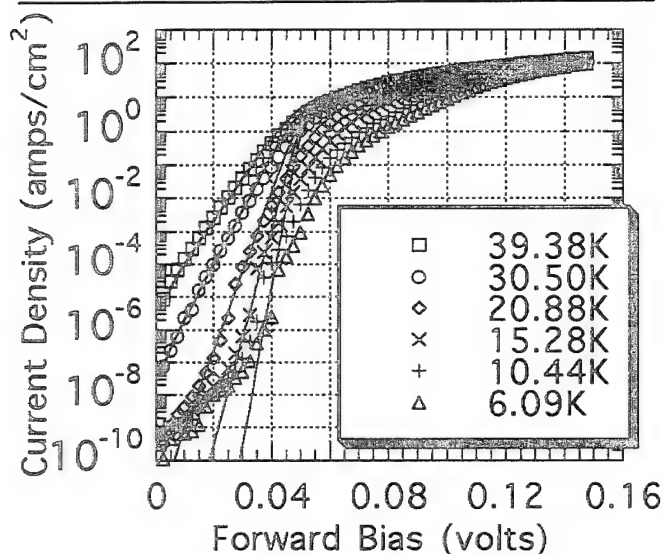


Fig. 3. Measured and calculated forward bias I-V curves, including the effect of series resistance, for the detector from Fig. 1.

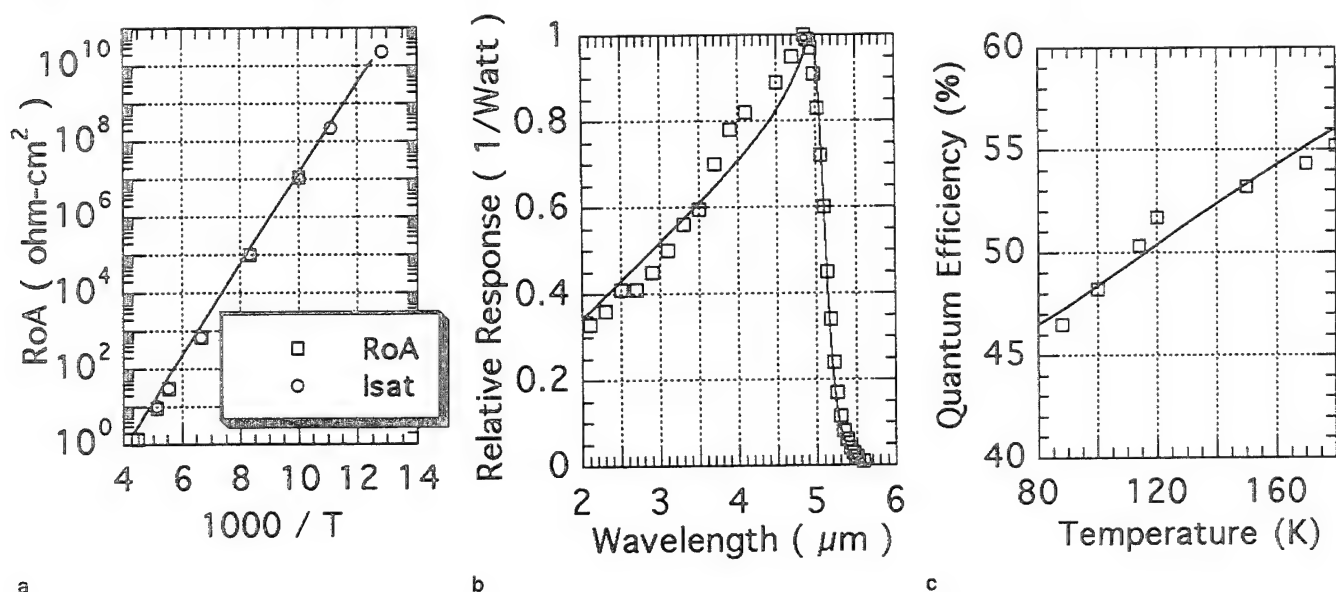


Fig. 4. Experimental data and model calculations of R_0A product as a function of temperature, spectral response at 78K, and quantum efficiency vs temperature for a HgCdTe diode with a cutoff wavelength of 5.3 microns at 78K.

R_0A product could not be directly measured because of equipment limitations and the low currents involved; so was calculated based on the measured saturation current at reverse bias. Again, the fit to the data over the entire temperature range is remarkably good, in spite of the demanding assumptions made by the model. The device is limited by diffusion current from the n-side of the junction, over the entire temperature range.

These examples demonstrate that the analytic model accounts for experimental detector data, and its dependence on temperature and voltage is self-consistent. The relatively small number of input parameters in each case was taken from independently supplied data and the material library, and not by adjusting parameters to provide a fit to the model. These results are significant for three reasons. First, the material library, which is also needed for numerical modeling, must be fairly good. Second, the assumptions used to derive the analytic models are reasonable, so design trades based on consideration of the equations have practical value. Third, the technology is capable of achieving performance which follows from device design.

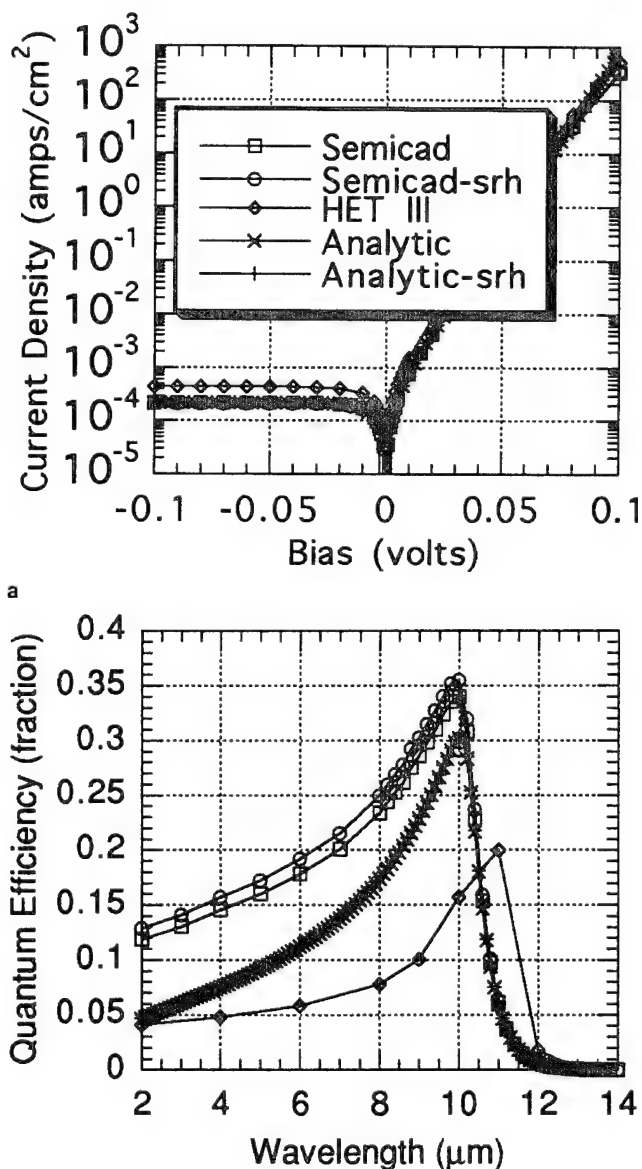
NUMERICAL SIMULATORS

Numerical simulation allows investigation of more complex device architectures; such as those which simulate real device structures, and may employ heterojunctions and graded band gap regions. Also, two- and three-dimensional effects can be explored. We have used HET III, a version of SEDAN III from Stanford University modified by Santa Barbara Research Center (SBRC), and two commercial semiconductor device simulators, Semicad Device by Dawn Technologies, Inc., and Atlas/Blaze/Luminous by Silvaco International. These are compared, along with results of the above analytical model.

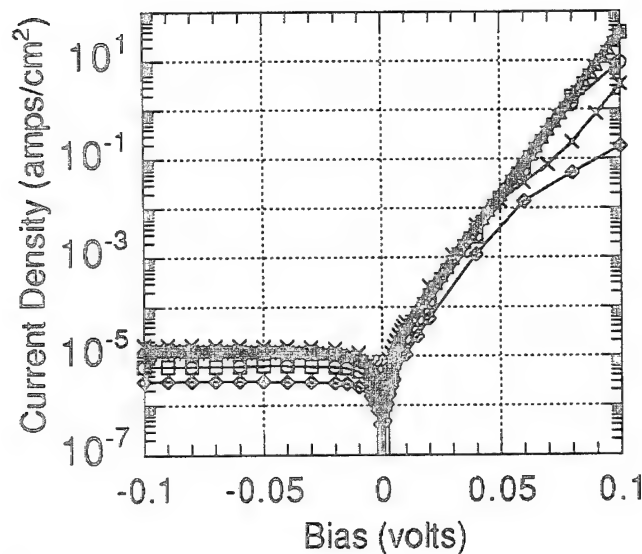
Our material library was implemented for both commercial device simulators. We used the library supplied with HET III for its simulations, since implementation of our library would require more work than we were prepared to do. Also, only HET III does not support the radiative and Auger recombination mechanisms; so, an effective Shockley-Read lifetime must be generated for comparison. Although HET III claims to support Auger recombination, it will not include the effect for calculation of reverse bias dark currents, leading to nonphysical results in the calculation of current-voltage characteristics. We ran cases with Semicad using just Shockley-Read recombination compared to the results obtained using intrinsic mechanisms to estimate the effect of this limitation. The procedure will not always lead to an equivalent R_0A product unless an unrealistically long (longer than radiative) lifetime is chosen for one side of the junction and will not correctly predict R_0A product temperature dependence or current-voltage characteristics.

Initially, we checked calculations for a homojunction device with ohmic contacts at both boundaries against

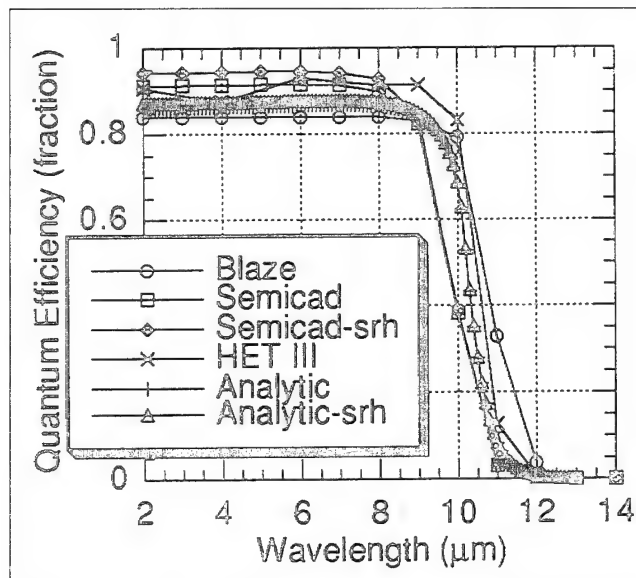
the analytic model, since this structure can be accurately represented by all models. Current-voltage curves and quantum efficiencies vs wavelength are shown in Fig. 5. Excellent agreement for all models was obtained in calculation of diffusion limited current-voltage characteristics. HET III yielded slightly larger (by about a factor of two) dark current, presumably due to slight differences in the material libraries. We also noted somewhat lower current at large forward bias for the numerical models (current density greater than 100 amps/cm²), which probably indicates the onset of high injection. HET III predicts a longer cutoff wavelength, likely a result of absorption coefficient model differences. The quantum efficiencies at shorter wavelength are not in agreement, with the highest predictions coming from the Semicad, and the lowest from HET III. Also, note that different



b
Fig. 5. Calculation of I-V curves and quantum efficiency vs wavelength for a homojunction HgCdTe diode bounded by ohmic contacts.



a



b

Fig. 6. Calculation of I-V curves and quantum efficiency vs wavelength for a p/n heterojunction detector in graded bandgap material.

quantum efficiency is obtained by Semicad if a Shockley-Read lifetime replaces the equivalent intrinsic lifetime, although this replacement had no effect on calculated dark current. The overall agreement between analytic and numerical simulation results at high temperature is encouraging; but, at low temperatures where g-r currents or band-to-band tunneling dominate, significant deviations were obtained. The numerical packages predict much larger tunneling current than the analytic model. Also, while HET III terminates calculation of tunneling current at some reverse bias threshold, the commercial packages will predict nonzero tunnel current at zero bias and negative current at small forward bias. Furthermore, numerical problems prevent the commercial packages from predicting I-V curves at low current, where g-r currents are important.

Next, we compare simulations of a p/n heterojunction detector in graded bandgap material, as shown in Fig. 6. The structure modeled is the same as that modeled by Kosai and Radford,¹⁶ (cap composition of 0.3, heterojunction width of 0.2 μm , and base carrier concentration of $2 \times 10^{15} \text{ cm}^{-3}$). The analytic model assumes boundaries with zero recombination velocities and uses a constant material composition representing an average of the narrow band gap material (0.223) with thickness (10 μm) corresponding to the narrow bandgap region of the structure. Both commercial simulators provide identical results in the I-V calculation, except at the largest forward bias. HET III predicts somewhat larger dark current and is consistent with the difference in homojunction results which was ascribed to library differences. Also, Semicad indicates different dark current depending on the recombination mechanism, predicting slightly lower dark currents when a Shockley-Read lifetime mechanism is used in place of the intrinsic mechanisms. The analytic model is in good agreement with the numerical models. Some differences in quantum efficiency are noted; the commercial simulators differ in spite of their agreement for dark current. Some variation in calculated cutoff wavelength is also observed. Calculated quantum efficiency of 82% and cutoff wavelength of 10.5 microns from Ref. 16 are in fair agreement with our results, considering library differences. The R_0A product was not mentioned in Ref. 16, but we calculate 1100 ohm-cm² with the commercial simulators and our library; this value is likely higher than what they measured.

A summary of our experience with these simulators is found in Table I. Diffusion currents are well predicted by all models. The commercial numerical simulators both have numerical problems at low temperatures (meaning low current) which prevent meaningful comparison of g-r limited currents; while HET III and, of course, the analytic model do not. The analytic model and HET III are in good agreement in calculating g-r currents; for example, at 20 mV reverse bias for a LWIR homojunction device, the analytic model predicts $5 \times 10^{-10} \text{ amps/cm}^2$ dark current, while HET III predicts $9 \times 10^{-10} \text{ amps/cm}^2$. We note that a heterojunction implementation of the device only reduces this g-r current to $6 \times 10^{-10} \text{ amps/cm}^2$, as calculated by HET III. All of the numerical simulators predict larger band-to-band tunneling current than we observe experimentally. Differences in quantum efficiency calculations are noted, but experimental uncertainties in device parameters and measurement accuracy make discrimination between models on this basis uncertain. Cutoff wavelength differences are ascribed to library differences (HET III) and an addressable programming issue (Blaze). In spite of the problems noted, we generally find these simulators to be valuable assets in analyzing many important aspects of HgCdTe detector data. Removing the limitations in calculating low current for the commercial packages would increase their range of validity and usefulness.

APPLICATION OF NUMERICAL SIMULATORS

A few examples which demonstrate the value of numerical models are presented. They all deal with device operation in the diffusion limited regime. The first example models the effect of p/n junction placement relative to heterojunction position on dark current and photocurrent. We also discuss the effect of bias dependent quantum efficiency on R_0A products with background photon flux, and the optimization of device performance in layers with graded band gaps. Figure 7 shows calculations of current-voltage characteristics and quantum efficiency vs wavelength for a heterojunction device as a function of the placement of the p/n junction relative to the heterojunction. The device architecture is that mentioned previously;¹⁶

composition 0.3 cap layer, $2 \times 10^{15} \text{ cm}^{-3}$ n-type base carrier concentration, and a heterojunction width of $0.2 \mu\text{m}$. The designation 0 microns in the figure means that the heterojunction is coincident with the p/n junction; this yields a barrier free heterojunction photodiode for this case. As the p/n junction is displaced into the wide band gap p-type material (negative displacement) relative to the heterojunction, a barrier in the valance band will eventually form. The model shows that a barrier forms for displacement between -0.2 and -0.4 microns. The barrier becomes larger for further displacement. The valance band barrier reduces both dark current and photocurrent, since they both are dominated by minority hole collection from the n-type base material. The calculations show that dark current and photocurrent are proportionately affected, so the barrier will reduce detector

Comparison of HgCdTe Device Models

	Analytic (Rockwell)	HET III (SBRC)	Blaze (Silvaco)	Semica dawn Inc.)
Dimension	1D	1D(2D)	2D(D3)	2D
Recombination	All	SRH+	All	All
Source Code	Yes	Yes	No	No
Device Architecture	Homogeneous	General	General	General
Documentation	Good	Poor	Good	Good
Integrated Graphics	No	No	Yes	Yes
Results: Calculations of Intrinsic Current Mechanisms				
Current				
Diffusion	Okay	Okay-	Okay	Okay
g-r	Okay	Okay-	Limitations*	Limitations*
Tunnel-BB	Okay	Unphysical	Unphysical	Unphysical
QE(λ_p)	Okay	Okay-	Okay-	Okay-
λ_c	Okay	No	(Okay)	Okay

*Low current limitations, likely not related to the current mechanisms;+ incapable of complete predictive simulation of thermal currents.

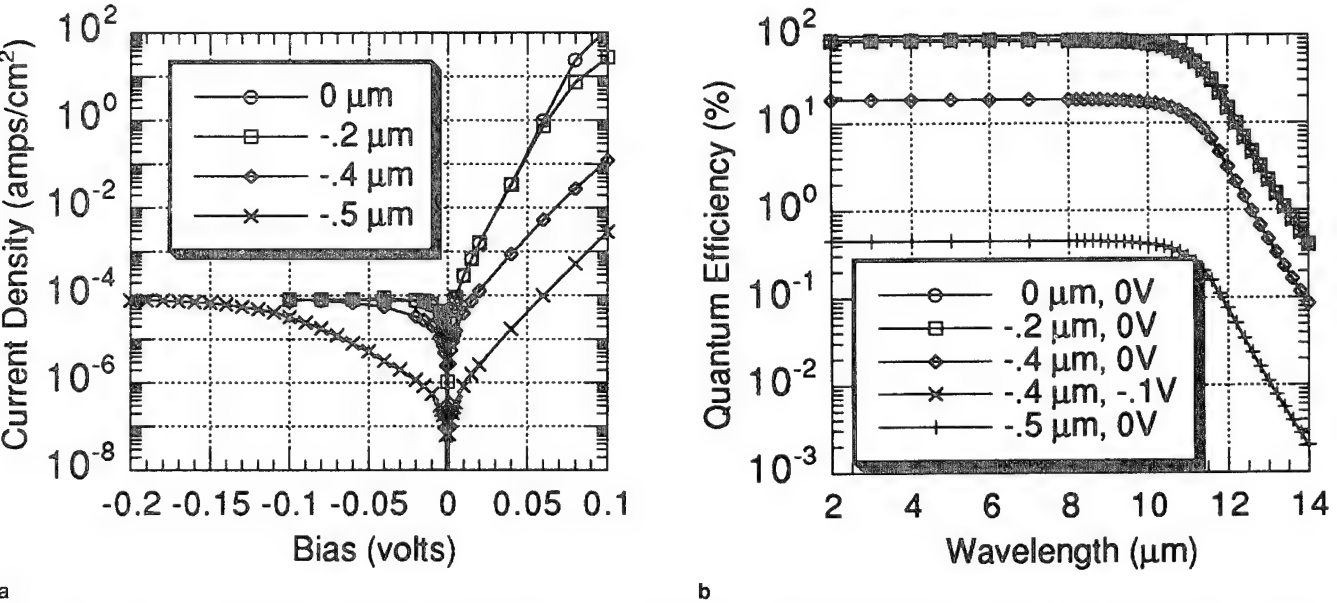
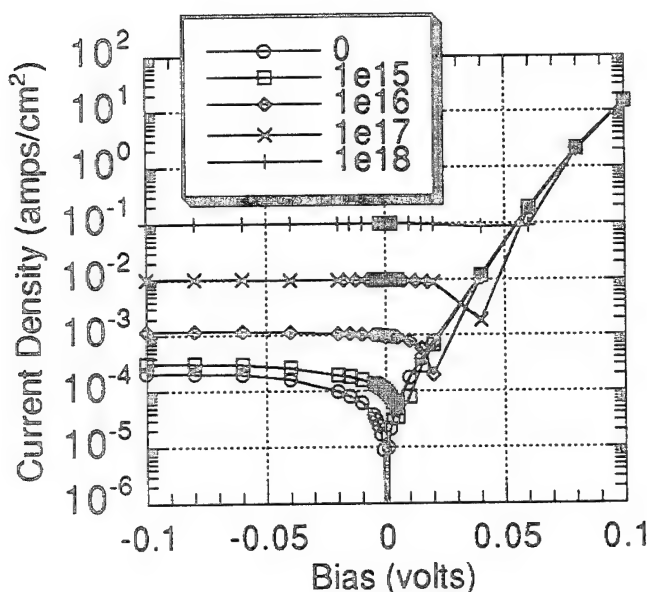
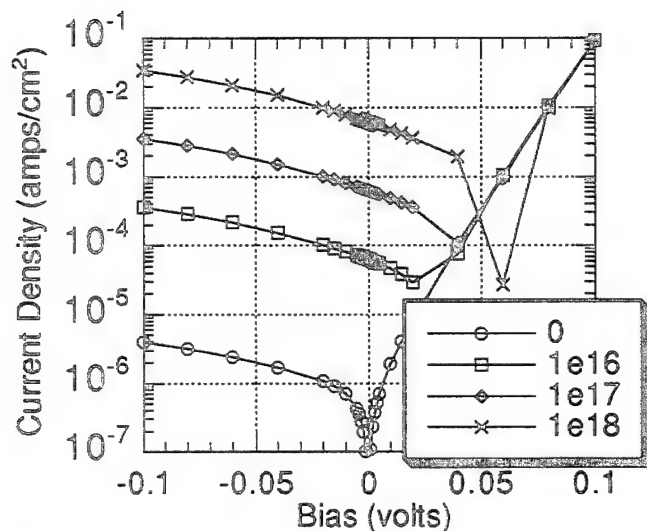


Fig. 7. Calculated I-V characteristics and quantum efficiency vs wavelength for a heterojunction diode as a function of the placement of the p/n junction relative to the heterojunction.



a



b

Fig. 8. Calculated I-V characteristics for a barrier free and a barrier type heterojunction devices at various photon flux densities.

signal-to-noise ratio by the square root of the reduction in either current, since signal is proportional to photocurrent, while noise is proportional to the square root of dark current. Consequently, signal-to-noise ratio can only be decreased for barrier type heterojunctions operated in the diffusion limited regime. This does not mean that the isotype heterojunction is not desirable for the p/n architecture; it is a mistake, though, to try to put the two too close together. Modeling indicates that several μm relative displacement of the p/n junction into the narrow bandgap material is preferred, since then small variations in placement will not substantially affect device performance. The preferred configuration leads to signal-to-noise ratio attained by a one-sided homojunction, without the uniformity problems and performance issues that are inherent in the barrier type heterojunction device.

Devices with barriers, as the $-0.4 \mu\text{m}$ example demonstrates, show bias dependent quantum efficiencies, because increasing reverse bias increases the depletion region width, consequently reducing valance band barrier height. The quantum efficiency increase under reverse bias is offset, however, by corresponding increase in dark current, via the same mechanism; so, at -0.1 volt for the -0.4 micron case, the quantum efficiency and dark current are both nearly the same value, as shown in Fig. 7, as that of the barrier free heterojunction device. The bias dependence of quantum efficiency for such devices will depend critically on several device parameters, such as base carrier concentration, heterojunction width, cap layer composition, and relative placement of heterojunction and p/n junction. This example demonstrates that heterojunctions do not offer inherent performance advantages over homojunctions, and in fact can only reduce performance below that obtained with a homojunction while simultaneously introducing a host of practical problems and demanding extreme control of the technology.

Although our calculations are generally in agreement with those reported elsewhere;¹⁸ for example, in the calculation of band diagrams and the effect of barriers on quantum efficiency, we do not see flux dependent quantum efficiencies,¹⁶ even for barrier type heterojunction devices. In Fig. 8, we show calculated I-V characteristics at various photon flux densities for a barrier free and a barrier type heterojunction device. The curves show flux independent quantum efficiencies for both devices, as indicated by the proportionality of current to photon flux at a given bias voltage (if dark current is subtracted). The quantum efficiency of the barrier type device is much more bias dependent than that of the barrier free device, as indicated by the dependence of photocurrent on bias voltage evident in the right half of the figure. This data suggests that the often observed flux dependence of R_0A products are simply a direct result of bias dependent quantum efficiency. A relationship is easily derived from this concept; $R_0A = 1/(q\Phi d\eta/dV)$, where q is the electronic charge, Φ is the photon flux, and $d\eta/dV$ is the derivative of quantum efficiency with respect to voltage at zero bias. This relationship is easy to check experimentally. This interpretation explains the large variation of flux dependent R_0A products for different devices, the increase in interest in this subject since HgCdTe heterojunction devices became popular, and the experimentally noted inverse flux dependence. The explanation is really not substantially different from the original explanation proposed by Rosbeck et al.¹⁴, considering additional bias dependent quantum efficiency mechanisms which are inherent to heterojunction device physics.

As a final example, we investigate the effect of layer grading on device performance. Although graded layers might seem to have advantages because band gap grading can be used to sweep optically generated minority carriers toward the p/n junction to enhance collection, while simultaneously minimizing the

amount of dark current generating narrow band gap material necessary to achieve a given cutoff wavelength, detectors fabricated in homogenous composition layers are superior. This is demonstrated by optimizing detector signal-to-noise ratio for operation at a particular wavelength, near ten microns in this case, in devices simulated in graded and ungraded HgCdTe. A barrier free p/n heterojunction device in ideal material with fixed doping densities is modeled; layer thickness and material composition were chosen to optimize detector peak wavelength D^* for each device. A compositional fraction grading constant of 0.001/micron was chosen for the graded material. As shown in Fig. 9, D^* (detector limited, zero field of view) is 1.5 times larger in the optimized device in ungraded material. This result is not intuitively obvious. Previous calculations, which have discussed the benefits of grading for quantum efficiency enhancement or dark current reduction, have not been applied to calculate detector signal to noise ratio. The graded material yields a longer cutoff wavelength but does not give better peak wavelength performance. Larger grading constants and longer detector cutoff wavelengths increase the severity of this limitation.

SUMMARY AND CONCLUSIONS

We discussed analytic and numerical modeling of HgCdTe photodiodes and presented examples of their application. Analytic models account remarkably well for a lot of data, implying a reasonable material library and a fair degree of technological maturity. For device architectures that can be modeled by both numerical and analytic models, agreement in many aspects of device performance results, particularly in the calculation of diffusion limited dark current. Limitations of the commercial device simulators prevent calculation of low level currents, particularly at levels relevant to g-r limited dark current; however, HET III and the analytic model are in good agreement in this regime. The numerical models overestimate band-to-band tunneling current and do not provide physically reasonable behavior near zero bias. The limitations on the numerical models can be removed with further software development. Quantum efficiency calculation differences were not so large that experimental discrimination between models would be easily accomplished.

We have obtained some useful results from the numerical simulators. Flux dependent R_0A products can be explained in terms of bias dependent quantum efficiency. Material composition grading is an undesirable feature in an FPA technology. Particularly for high temperature operation, heterojunction detectors can at best equal the performance of well-designed homojunction devices. Heterojunction diodes are well-known to be useful in transistor design because they have high injection efficiency, but there is no corresponding physical reason they offer any advantage over well-designed homojunction diodes for optical detection.

Heterostructures, though, may be of practical ben-

efit for optimization of detector design at these temperatures, but ideally are not required, since the same benefits can also be achieved through the use of high/low junctions, high carrier concentration, or surface passivation. For lower temperature operation, when devices are limited by g-r current or trap assisted tunneling current, numerical modeling indicates that some performance advantage is possible with the heterojunction. The g-r limited case we examined showed less than a factor of two reduction in dark current on changing to a high quantum efficiency heterojunction design; however, it is reasonable to expect some other choice of parameters might make the advantage somewhat larger. Perhaps a greater proportional benefit is to be expected for devices limited by trap assisted tunneling. However, the heterojunction device introduces a host of practical problems, such as poor uniformity and bias dependent quantum efficiency. Also, additional defects associated with the heterojunction itself may not result in a net trap assisted tunnel or g-r current reduction. Diode dependent scatter in the data for devices which are defect limited make clear interpretation of experimental results difficult, but the authors are unaware of any data that favors the heterojunction approach since, at low temperatures, data on the best devices show the same performance for heterojunctions and homojunctions. Although it is plausible to theoretically expect benefit from the heterojunction architecture for devices limited by these two current mechanisms, it will be extremely challenging for the technology to convincingly demonstrate that it can implement the control necessary to use these benefits. Finally, if band-to-band tunneling dominates, it is simpler to reduce the carrier concentration on the lightly doped side of the junction than to introduce a heterojunction. So we recommend that, to increase performance at low temperature, trap assisted tunneling and g-r current be reduced by improving the

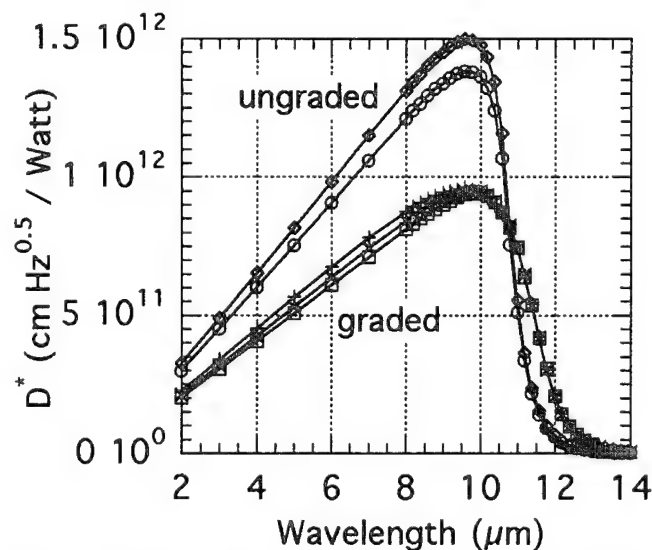


Fig. 9. Comparison of calculated peak wavelength D^* for optimized detectors in compositionally graded and constant composition material.

technology to remove the responsible defects; to improve performance at all temperatures, heterostructures, if used, be kept well away (more than 1 μm) from the photo-sensitive p/n junction.

ACKNOWLEDGMENTS

We thank J. M. Arias' group at Rockwell Science Center, and H. H. Vydyanath's group at Aerojet Electronic Systems Division for providing the HgCdTe detectors. Robert Cottle of Silvaco International, and Daniel Ng of Dawn Technologies, Inc., provided valuable assistance with their respective commercial device simulation packages.

REFERENCES

1. H.J. Hovel, *Semiconductors and Semimetals*, Vol. 11, Solar Cells, (Academic Press, 1975), p. 17.
2. J.P. McKelvey, *Solid State and Semiconductor Physics* (New York: Harper and Row, 1966), p. 421.
3. J.B. Gunn, *J. Electron. Cont.* 4, 17 (1958).
4. S.C. Choo, *Solid State Electron.* 11, 1069 (1968).
5. D.A. Evans and P.T. Landsberg, *Solid State Electron.* 6, 169 (1963).
6. J.L. Moll, *Physics of Semiconductors* (New York: McGraw-Hill Book Co., 1964), p. 253.
7. M. Weiler, *Magneto-optical Properties of HgCdTe Alloys, Semiconductors and Semimetals*, Vol. 16, Ch. 3, (1981), p. 119.
8. A. Rogalski and J. Piotrowski, *Progress in Quantum Electronics*, 12, No. 2/3, 160 (1988).
9. G.L. Hansen, J.L. Schmit and T.N. Casselman, *J. Appl. Phys.* 53, 7099 (1982).
10. G.L. Hansen and J.L. Schmit, *J. Appl. Phys.* 54, 1639 (1983).
11. J.S. Blakemore, *Semiconductor Statistics* (Dover Publications, 1987), p. 221.
12. S.E. Schacham and E. Finkman, *J. Appl. Phys.* 57 (6), 2001 (1985).
13. J.S. Blakemore, *Semiconductor Statistics* (Dover Publications, 1987), p. 263.
14. J.P. Rosbeck, R.E. Starr, S.L. Price and K. J. Riley, *J. Appl. Phys.* 53 (9), 6430 (1982).
15. S.E. Schacham and E. Finkman, *J. Appl. Phys.* 57 (6), 2001 (1985).
16. K. Kosai and W.A. Radford, *J. Vac. Sci. Technol. A* 8 (2), 1254 (1990).

The Magnetic Field Dependence of R_0A Products in n-on-p Homojunctions and p-on-n Heterojunctions from $\text{Hg}_{0.78}\text{Cd}_{0.22}\text{Te}$ Liquid Phase Epitaxy Films

M.C. CHEN, A. TURNER, L. COLOMBO, and D. CHANDRA

Texas Instruments Incorporated, Corporate Research and Development,
Dallas, TX 75265

The analysis of R_0A products as a function of magnetic field in n-on-p diodes using a simple diffusion current model has previously been shown to yield both J_{ep}/J_{total} ratio (the relative contribution of the p-side diffusion current) and μ_{ep} (the minority carrier, electron mobility). In this paper, we report the good agreement between the experimental and theoretical dependence of μ_{ep} on the hole concentration over a wide range between 1×10^{16} and $4 \times 10^{17} \text{ cm}^{-3}$ in n-on-p homojunction diodes fabricated on undoped p-type $\text{Hg}_{0.78}\text{Cd}_{0.22}\text{Te}$ liquid phase epitaxial (LPE) films. The averaged J_{ep}/J_{total} ratio varied between 68 and 90% with the hole concentration. These J_{ep}/J_{total} ratios indicate that other leakage current mechanisms than the p-side diffusion current were not negligible. Also, for the first time, comparative measurements were made on p⁺/n heterojunction diodes consisting of As-doped $\text{Hg}_{0.70}\text{Cd}_{0.30}\text{Te}$ and In-doped $\text{Hg}_{0.78}\text{Cd}_{0.22}\text{Te}$ LPE layers. Unlike a typical change in R_0A products by a factor of 2–3 in n-on-p homojunction diodes, the R_0A products in p⁺/n heterojunction diodes at 7 kG were typically only 2–3% higher than that at the zero field. The typical J_{ep}/J_{total} ratio in p⁺/n heterojunction diodes was about 3–4 %, which confirms the general belief that the p⁺ cap layer, due to the high doping and a larger bandgap, contributes very little to the total leakage current.

Key words: HgCdTe , IR detectors, magnetic field dependence, R_0A products

INTRODUCTION

Schacham and Finkman¹ pioneered the analysis of R_0A products as a function of magnetic field in HgCdTe n-on-p diodes using a simple diffusion current model to deduct the relative contributions of diffusion current from each side of the junction, i.e., J_{ep} (designated for electron diffusion current from p-side) and J_{hn} (designated for hole diffusion current from n-side). They studied the temperature dependence between 13 and 160K of both J_{ep} and J_{hn} in one n-on-p homojunction diode fabricated by ion implantation. At 80K, the J_{ep}/J_{total} ratio of about 67% was obtained. However, Schacham and Finkman arrived at the wrong conclusion that their diodes were "short" diodes with the diffusion length longer than the p-side thickness of about 100 μm (see the analysis from Eq. (1) and on in the next section). Gordon et al.² used the

analysis primarily to extract the minority carrier mobility, μ_{ep} , in the p-type region of so-called "loop-hole" diodes fabricated by ion milling. Although $\text{Hg}_{1-x}\text{Cd}_x\text{Te}$ samples with a wide range of hole concentration were studied from 77 to 300K, μ_{ep} data of only two samples were presented. Gordon et al. also conducted a calculation on μ_{ep} at 77K as a function of hole concentration for x values between 0.2 and 0.3. The discrepancy between the experimental and calculated μ_{ep} values was about 20%.

In this paper, we will concentrate on

- The comparison between the experimental and theoretical dependence of μ_{ep} on the hole concentration in undoped p-type liquid phase epitaxy (LPE) films for the understanding of scattering mechanisms for minority carriers.
- J_{ep}/J_{total} ratios to gauge the importance of other leakage current mechanisms than the p-side diffusion current in n-on-p homojunction diodes.
- Comparative measurements on p⁺/n hetero-

(Received October 4, 1994)

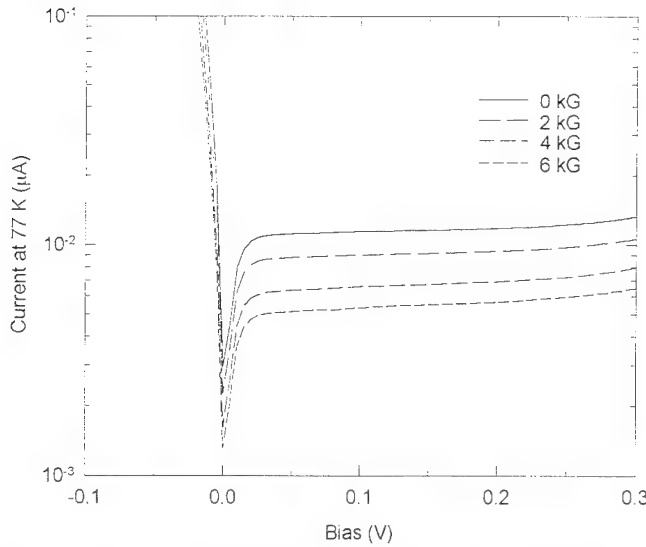


Fig. 1. The I-V curves at 77 K for a typical n-on-p diode from a homojunction device AT-2 at different magnetic fields clearly show the reduction of the reverse leakage current by the magnetic field.

junction diodes to confirm the general belief that the p^+ cap layer contributes very little to the total leakage current.

EXPERIMENTAL

Ion implantation on undoped p-type $\text{Hg}_{0.78}\text{Cd}_{0.22}\text{Te}$ LPE films was used to fabricate n-on-p homojunction diodes. Liquid phase epitaxy films were grown on $\langle 111 \rangle \text{B}$ lattice-matched CdZnTe substrates from Te-rich melts in a dipping reactor. Post-growth anneal under different Hg partial pressures above 300°C produced different levels of Hg vacancies, yielding a hole concentration range between 1×10^{16} to $4 \times 10^{17} \text{ cm}^{-3}$. The thickness of the undoped films in this study was about $50 \mu\text{m}$. The base layers of p^+/n heterojunction diodes were indium-doped $\text{Hg}_{0.78}\text{Cd}_{0.22}\text{Te}$ LPE films, also grown from Te-rich melts in a dipping reactor with a typical doping concentration of about $1\text{--}2 \times 10^{15} \text{ cm}^{-3}$. The cap layers were arsenic-doped $\text{Hg}_{0.70}\text{Cd}_{0.30}\text{Te}$ LPE films grown in Hg-rich melts in a dipping reactor with a typical doping concentration of about $1 \times 10^{18} \text{ cm}^{-3}$. The thickness of the n-type base layers in this study was about $25 \mu\text{m}$. The Cd mole fraction, often referred as the x value, for all the p-type films in n-on-p homojunction diodes was between 0.225 and 0.230, and between 0.220 and 0.225 for n-type base layers in p^+/n heterojunction diodes.

In the simple diffusion current model first used by Schacham and Finkman,¹ the effects of Lorentz force from the magnetic field, B , on the flow of carriers were approximated by substituting the drift mobility with an effective drift mobility:

$$\mu^* = \frac{\mu}{1 + \mu^2 B^2} \quad (1)$$

It is apparent from Eq. (1) that the magnetic field will have negligible effects on heavy holes since their mobility is only about $500 \text{ cm}^2/\text{V}\cdot\text{s}$. At $B = 7 \text{ kG}$, the

value of μB is only 0.035 for holes. Therefore, only the effects of the magnetic field on electron diffusion current from the p-side, J_{ep} , can be observed. For "long" diodes with the diffusion length shorter than the film thickness, J_{ep} at a zero field is:³

$$J_{ep} = \frac{qn_i^2}{p} \sqrt{\frac{k_B T \mu_{ep}}{\tau_{ep}}} \quad (2)$$

where n_i is the intrinsic concentration, p the hole concentration, T the temperature, and τ_{ep} the lifetime. The effects of the magnetic field on J_{ep} can then be expressed as:

$$(J_{ep})_B = \frac{J_{ep}}{\sqrt{1 + \mu_{ep}^2 B^2}} \quad (3)$$

For "short" diodes with the diffusion length longer than the film thickness, J_{ep} at a zero field is:³

$$J_{ep} = \frac{qn_i^2}{p} \frac{d}{\tau_{ep}} \quad (4)$$

where d is the thickness of the p-side. Since the carrier mobility is absent in the expression of J_{ep} for "short" diodes, there should be no effects from the magnetic field on the electron diffusion current. Therefore, there should be no dependence on the magnetic field of $R_0 A$ products of n-on-p diodes with a small p-side thickness.⁴

Leakage currents near zero bias were measured by a Keithly 236 source/measure unit and $R_0 A$ products were deduced by a three-point differentiation method. The diodes, immersed in liquid nitrogen, were oriented so that the junction planes were parallel to the magnetic field. Therefore, the current flow through the junction was perpendicular to the magnetic field. The largest magnetic field used was 7 kG. $R_0 A$ products at each field were then used to calculate the leakage current according to the following expression:

$$J_{\text{total}} = \frac{k_B T}{q R_0 A} \quad (5)$$

Assuming "long"-diode condition for the p-side in both n-on-p homojunction diodes and p^+/n heterojunction diodes in this study, the dependence of J_{total} on the magnetic field can be fitted using:

$$(J_{\text{total}})_B = \frac{J_{ep}}{\sqrt{1 + \mu_{ep}^2 B^2}} + J_0 \quad (6)$$

The three fitting parameters were J_{ep} , μ_{ep} , and J_0 . J_0 is the part of total leakage current which is independent of the magnetic field and can include the n-side hole diffusion current, generation-recombination currents from both the bulk and the surface, and the tunneling current. It will be shown in following sections that while a large variation of J_{total} with the magnetic field allowed very good three-parameter fits in n-on-p homojunction diodes, only two-parameter fits were

feasible in p⁺/n heterojunction diodes due to a small variation of J_{total} with the magnetic field. In the latter case, μ_{ep} was chosen as a fixed parameter.

RESULTS OF n-ON-p HOMOJUNCTION DIODES

Four n-on-p homojunction devices with the hole concentration at 77K at 1×10^{16} , 3×10^{16} , 1×10^{17} , and $4 \times 10^{17} \text{ cm}^{-3}$, respectively, were fabricated. Typically, 15 to 20 diodes were measured in each device. At the maximum magnetic field of 7 kG, R_0A products at 77K were typically two to three times those at the zero field, indicative of the strong deflection on the electron diffusion current due to the Lorentz force. The reduction of the reverse leakage current by the magnetic field is illustrated in Fig. 1. At a reverse bias of 0.3 V, the leakage current at a magnetic field of 6 kG was half that at a zero field. Almost all the R_0A vs B curves can be fitted very well in the scheme using Eq. (5) and Eq. (6) described in the previous section. Such a fit, as plotted in Fig. 2, from a typical diode in device AT-2 with a hole concentration of $3 \times 10^{16} \text{ cm}^{-3}$ yielded $J_{\text{ep}} = 57 \mu\text{A}/\text{cm}^2$, $\mu_{\text{ep}} = 47000 \text{ cm}^2/\text{V-s}$, and $J_0 = 13 \mu\text{A}/\text{cm}^2$. By best-fitting the R_0A vs B curves of every diode measured in each of the four devices, the resulted averaged values and associated standard deviations (numbers following \pm sign) for R_0A , J_{ep} , μ_{ep} , and $J_{\text{ep}}/J_{\text{total}}$ are tabulated in Table I.

The averaged electron mobility in the p-type regions among diodes in each device decreased with increasing hole concentration, changing from 56000 $\text{cm}^2/\text{V-s}$ at $1 \times 10^{16} \text{ cm}^{-3}$ to 47300 $\text{cm}^2/\text{V-s}$ at $4 \times 10^{17} \text{ cm}^{-3}$. In comparison, Schacham and Finkman⁵ used a photo-Hall technique and measured a minority carrier mobility at 77K of about 40000 and 45000 $\text{cm}^2/\text{V-s}$ at $1.4 \times 10^{16} \text{ cm}^{-3}$ for two undoped bulk samples with an α value of 0.225 and 0.230, respectively. To check the validity of the "long" diode assumption in our four n-on-p homojunction devices, the diffusion length at 77K was calculated with the averaged minority carrier mobility data listed in Table I and the minority carrier lifetime data for undoped p-type $\text{Hg}_{0.78}\text{Cd}_{0.22}\text{Te}$ LPE films in our previous work.⁶ The calculated diffusion length at 77K was 38, 16, 8, and 5 μm , respectively, for the four devices listed in Table I. The presumption of "long" diodes was therefore justified.

The averaged $J_{\text{ep}}/J_{\text{total}}$ ratio at 77K, following the same trend as the averaged R_0A product, increased from 69% at $1 \times 10^{16} \text{ cm}^{-3}$ to 90% at $1 \times 10^{17} \text{ cm}^{-3}$, but dropped to 68% at $4 \times 10^{17} \text{ cm}^{-3}$. These $J_{\text{ep}}/J_{\text{total}}$ ratios indicate that although the p-side diffusion current contributed a large part of leakage current in n-on-p

diodes, other contributions, measured as J_0 , from mechanisms such as generation-recombination from both the bulk and the surface, tunneling, and n-side diffusion were not negligible. It should be noted that the possible n-side diffusion current does not come from the implanted n⁺ region, but from n⁻ region formed during the post-implantation anneal.⁷

The data of the dependence of minority carrier mobility on the hole concentration over a range between 1×10^{16} and $4 \times 10^{17} \text{ cm}^{-3}$ offer an opportunity to compare with simple calculations based on Boltzmann statistics. With the density of states for the valence band in $\text{Hg}_{0.78}\text{Cd}_{0.22}\text{Te}$ at about $1 \times 10^{18} \text{ cm}^{-3}$ at 77K, Boltzmann statistics (or nondegenerate statistics) is sufficient for the entire range of the hole concentration of our current interest. As shown by our previous work,⁸ three mechanisms: ionized impurity scattering, polar optical phonon scattering, and alloy disorder scattering also dominate the majority carrier (hole) mobility in p-type $\text{Hg}_{0.78}\text{Cd}_{0.22}\text{Te}$ at 77K. To calculate the minority carrier mobility, one begins with substituting m_e^* (the effective mass of holes) with m_e^* (the effective mass of electrons) in the expressions for these three scattering mechanisms. In addition, the scattering by heavy holes has to be included as fixed scattering centers because of their large mass. So the total impurity concentration, N_i , in Brooks-Herring approximation for ionized impurity scattering is equal to $2p + p$, where the contribution of $2p$ comes from the doubly ionized shallow acceptors associated with Hg vacancies.⁸ The Brooks-Herring

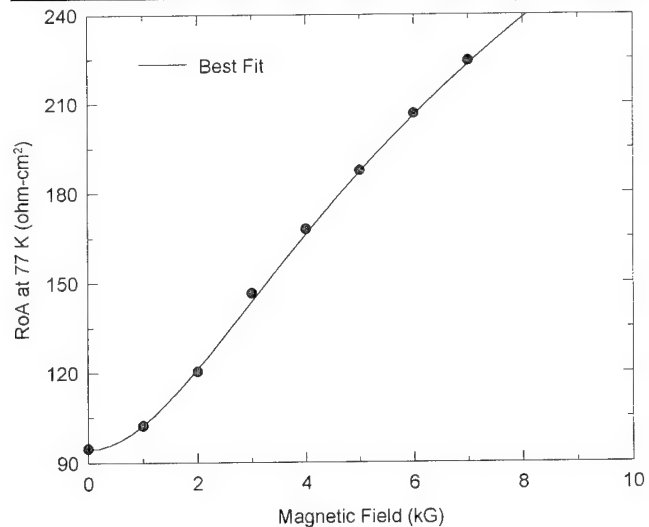


Fig. 2. Measured and best-fitted R_0A products vs B curves at 77K for a typical n-on-p diode from a homojunction device AT-2. The R_0A at 7 kG is about 136% higher than that at the zero field.

Table I. Results of n-on-p Homojunction Diodes

Sample	N_a (cm^{-3})	R_0A (ohm-cm^2)	J_{ep} ($\mu\text{A}/\text{cm}^2$)	$J_{\text{ep}}/J_{\text{total}}$ (%)	μ_{ep} ($\text{cm}^2/\text{V-s}$)
AT-1	1×10^{16}	61 ± 14	77 ± 5	69 ± 16	56000 ± 2300
AT-2	3×10^{16}	83 ± 12	67 ± 8	80 ± 4	51100 ± 3400
AT-3	1×10^{17}	107 ± 10	57 ± 4	90 ± 3	47500 ± 1000
AT-4	4×10^{17}	54 ± 12	87 ± 17	68 ± 19	47300 ± 2800

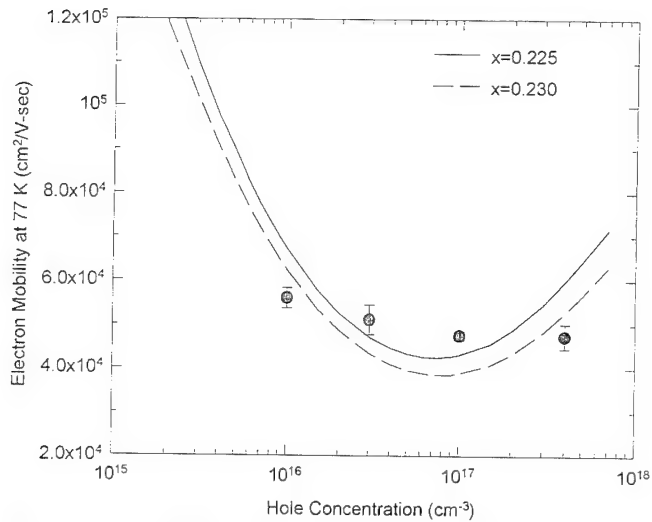


Fig. 3. The averaged minority carrier mobility at 77 K in p-type $\text{Hg}_{0.78}\text{Cd}_{0.22}\text{Te}$ LPE films with a hole concentration ranging from 1×10^{16} to $4 \times 10^{17} \text{ cm}^{-3}$. The solid and dashed lines are calculations for $x = 0.225$ and 0.230 , respectively. The error bars denote the standard deviations.

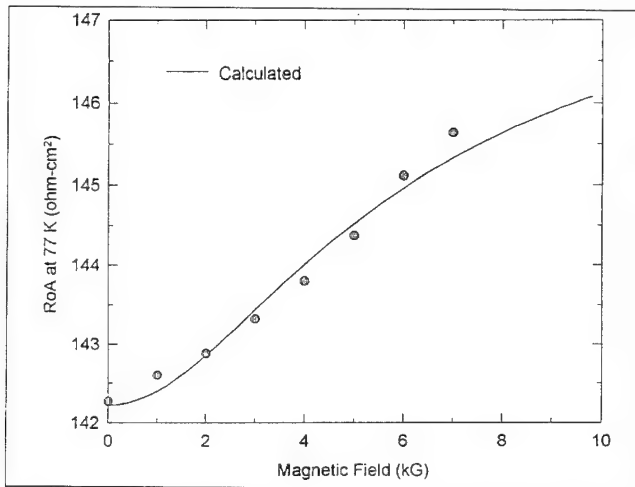


Fig. 4. Measured and calculated R_0A products vs B curves at 77 K for a typical p/n diode from a heterojunction device DC-1. The R_0A at 7 kG is only about 2% higher than that at the zero field.

approximation for electrons as minority carriers can still be expressed as⁸

$$\mu_{II} = 3.284 \times 10^{15} \frac{\epsilon_o^2 T^{3/2}}{N_I (m_e^*/m_o)^{1/2}} \left(\ln(1+b) + \frac{b}{1+b} \right)^{-1} \quad (7)$$

Only the expression for b , a dimensionless parameter reflecting screening, has to be modified slightly to reflect screening from free holes, and is given by:^{9,10}

$$b = 1.294 \times 10^{14} \frac{m_e^* T^2 \epsilon_o}{m_o p} \frac{\mathfrak{S}_{1/2}}{\mathfrak{S}_{-1/2}} \quad (8)$$

where $\mathfrak{S}_{1/2}$ and $\mathfrak{S}_{-1/2}$ are Fermi-Dirac integrals. The

good agreement between the experimental and calculated minority carrier mobility is plotted in Fig. 3. It can be seen that the discrepancy between the data and the mobility range formed by two calculated curves for $x = 0.225$ and 0.230 is less than 10%. As the hole concentration increases above $1 \times 10^{17} \text{ cm}^{-3}$, the calculated minority carrier mobility begins to rise due to the increasing importance of screening, similar to what have been observed in other semiconductors such as GaAs.¹⁰ However, it is also well known that the Brooks-Herring approximation breaks down at the high carrier concentration and the resulted minority carrier mobility is often larger than that calculated by the more rigorous partial-wave phase-shift analysis.¹¹

RESULTS OF p⁺/n HETEROJUNCTION DIODES

In the case of p⁺/n heterojunction devices consisting of As-doped $\text{Hg}_{0.70}\text{Cd}_{0.30}\text{Te}$ cap layers and In-doped $\text{Hg}_{0.78}\text{Cd}_{0.22}\text{Te}$ base layers, most of the leakage current should be due to minority carriers (holes) in the n-type base layers, because of the higher doping and a larger bandgap of the p⁺ cap layers. In the context of Eq. (6), this means a small J_{ep} , and hence a small effect on R_0A products from the magnetic field. Indeed, as shown in Fig. 4 from a typical p⁺/n heterojunction diode in device DC-1, the R_0A product at 7 kG was only 2% higher than that at the zero field. Due to this very small change in the R_0A product vs B curves, it is not possible to conduct the three-parameter fit and yield reasonable values for J_{ep} , μ_{ep} , and J_0 . It is best to reduce the fitting parameters to two. In fitting R_0A product vs B curves with Eq. (5) and Eq. (6), the fit was least sensitive to μ_{ep} . Besides, the experimental data of minority carrier mobility at 77K in p-type $\text{Hg}_{0.70}\text{Cd}_{0.30}\text{Te}$ existing in the literature offers a starting point. Schacham and Finkman¹² determined an electron mobility of about $28000 \text{ cm}^2/\text{V-s}$ at 80K in p-type $\text{Hg}_{0.71}\text{Cd}_{0.29}\text{Te}$ with a hole concentration of $1 \times 10^{16} \text{ cm}^{-3}$ by measuring the travel time of the excess carriers between two ends of the sample. Since our p⁺ cap layers were more heavily doped, a value of $20000 \text{ cm}^2/\text{V-s}$ was assumed for μ_{ep} . The two-parameter fit to the R_0A product vs B curve for a typical p⁺/n heterojunction diode in device DC-1, as shown in Fig. 4 produced a good fit and yielded $J_{ep} = 2.0 \mu\text{A}/\text{cm}^2$, $J_0 = 45.3 \mu\text{A}/\text{cm}^2$, and $J_{ep}/J_{total} = 4\%$. A variation of ± 5000 in the assumed value of μ_{ep} caused a $\pm 10\%$ change in J_{ep} , J_0 , and J_{ep}/J_{total} .

Table II lists the resulted averaged values and associated standard deviations for R_0A , J_{ep} , and J_{ep}/J_{total} of two heterojunction devices by best-fitting the R_0A vs B curves of 15–20 diodes in each device. The averaged J_{ep} in device DC-1 is somewhat misleading since it was distorted by four bad diodes. Most of the diodes in device DC-1 had J_{ep} below $3 \mu\text{A}/\text{cm}^2$ and J_{ep}/J_{total} of about 4%, comparable to what diodes in DC-2 had. The small J_{ep}/J_{total} ratio confirms the conventional wisdom that the p⁺ side in p⁺/n heterojunction device contributes very little to the total leakage

Table II. Results of p-on-n Heterojunction Diodes

Sample	N_d (cm^{-3})	R_0A (ohm-cm^2)	J_{ep} ($\mu\text{A/cm}^2$)	J_{ep}/J_{total} (%)	μ_{ep} ($\text{cm}^2/\text{v-sec}$)
DC-1	6×10^{14}	112 ± 43	17 ± 37	12 ± 21	20000
DC-2	1×10^{15}	180 ± 63	1 ± 0.4	3 ± 1	20000

current. The good fits to R_0A vs B curves with Eq. (5) and Eq. (6) also establishes the validity of the simple diffusion current model in explaining the effects of the magnetic field on R_0A products of p⁺/n heterojunction diodes.

CONCLUSIONS

In summary, we have achieved in this paper

- A good agreement between the experimental data and calculations of the dependence of μ_{ep} on the hole concentration ranging from 1×10^{16} to $4 \times 10^{17} \text{ cm}^{-3}$ in undoped p-type LPE films for the understanding of scattering mechanisms for minority carriers.
- Information that although p-side diffusion current is the largest source of the leakage current in n-on-p homojunction diodes, other mechanisms such as generation-recombination from both the bulk and the surface, tunneling, and n-side diffusion were not negligible.
- Confirmation that the p⁺ cap layer in p⁺/n heterojunction diodes contributes very little to the total leakage current.

REFERENCES

1. S.E. Schacham and E. Finkman, *J. Vac. Sci. Technol.* A7, 387 (1989).
2. N.T. Gordon, S. Barton, P. Capper, C.L. Jones and N. Metcalfe, *Semicond. Sci. Technol.* 8, S221 (1993).
3. M.B. Reine, A.K. Sood and T.J. Tredwell, *Semiconductors and Semimetals*, vol. 18 (New York: Academic Press, 1981), p. 201.
4. Schacham and Finkman made a mistake in Ref. 1 by expressing J_{ep} in magnetic field as proportional to $1/(1 + \mu^2 B^2)$, and fitted their data accordingly. We found that the difference between fits using $1/(1 + \mu^2 B^2)$ and $1/(1 + \mu^2 B^2)^{1/2}$ for electrons will not be noticeable until magnetic field is at 7 kG.
5. S.E. Schacham and E. Finkman, *J. Appl. Phys.* 60, 2860 (1986).
6. M.C. Chen and L. Colombo, 1993 U.S. Workshop on Physics and Chemistry of HgCdTe.
7. L.O. Bubulac, W.E. Tennant, D.S. Lo, D.D. Edwall, J.C. Robinson, J.S. Chen and G. Bostrup, *J. Vac. Sci. Technol. A* 5, 3166 (1987).
8. M.C. Chen and L. Colombo, *J. Appl. Phys.* 73, 2916 (1993).
9. W. Walukiewicz, J. Lagowski, L. Jastrzebski and H.C. Gatos, *J. Appl. Phys.* 50, 5040 (1979).
10. D. Chattopadhyay and H.J. Queisser, *Rev. Mod. Phys.* 53, 745 (1981).
11. J.R. Lowney and H.S. Bennett, *J. Appl. Phys.* 69, 7102 (1991).
12. S.E. Schacham and E. Finkman, *J. Appl. Phys.* 57, 1161 (1985).

Magneto-Transport Characterization Using Quantitative Mobility-Spectrum Analysis

J. ANTOSZEWSKI, D.J. SEYMOUR, and L. FARAONE

Department of Electrical and Electronic Engineering, The University of Western Australia, Nedlands, WA 6009

J.R. MEYER and C.A. HOFFMAN

Code 5651, Naval Research Laboratory, Washington DC 20375

A quantitative mobility spectrum analysis (QMSA) of experimental Hall and resistivity data as a function of magnetic field is presented. This technique enables the conductivity contribution of bulk majority carriers to be separated from that of other species such as thermally generated minority carriers, electrons, and holes populating *n* and *p* doped regions, respectively, and two-dimensional species at surfaces and interface layers. Starting with a suitable first trial function such as the Beck and Anderson mobility spectrum analysis (MSA), a variation on the iterative procedure of Dziuba and Gorska is used to obtain a mobility spectrum which enables the various carrier species present in the sample to be identified. The QMSA algorithm combines the fully automated execution and visually meaningful output format of MSA with the quantitative accuracy of the conventional least-squares multi-carrier fitting procedure. Examples of applications to HgCdTe infrared detector materials and InAs/GaSb quantum wells are discussed. The ultimate goal of this paper is to provide an automated, universal algorithm which may be used routinely in the analysis and interpretation of magneto-transport data for diverse semiconductor materials and bandgap engineered structures.

Key words: HgCdTe, Hall measurements, mobility spectrum analysis, transport properties

INTRODUCTION

Mixed-conduction effects nearly always have a strong influence on the magneto-transport properties of narrow bandgap infrared (IR) semiconducting materials such as HgCdTe.¹ Multiple species due to *n* and *p* doped regions, thermally generated minority carriers, and two-dimensional populations at surfaces and interface layers tend to make significant contributions to the conduction process in addition to the bulk majority carriers. Standard measurements of the resistivity and Hall coefficient at a single magnetic field are of limited use when applied to systems with prominent mixed-conduction, since they

provide only averaged values of both the carrier concentration and mobility, which may not necessarily be representative of any of the individual carrier species. Far more information becomes available if the magneto-transport experiments are performed as a function of magnetic field because, in principle, the data can then be deconvolved in order to obtain densities and mobilities for each carrier species present in the sample.¹⁻³

Traditionally, the conventional technique for analyzing magnetic-field-dependent Hall data is the multi-carrier fitting (MCF) procedure.² However, this technique requires prior assumptions to be made about the number of electron and hole species as well as their approximate mobilities. As a result, injudicious guesses can often lead to misleading and/or ambigu-

(Received October 4, 1994; revised February 7, 1995)

ous results. In order to overcome this shortcoming, Beck and Anderson proposed a novel approach known as mobility spectrum analysis (MSA),⁴ in which an envelope of the maximum conductivity is determined as a continuous function of carrier mobility. While MSA is a fully automated procedure that provides a visually meaningful output format, the information provided by the technique is primarily qualitative rather than quantitative. In particular, it is not possible to obtain a fit to the actual experimental Hall and resistivity data.

In an attempt to overcome these difficulties, Meyer et al.¹ have developed and extensively tested a hybrid mixed conduction analysis (HMCA) procedure, in which the MSA spectrum is used initially to determine the number of carrier species and to roughly estimate their densities and mobilities, and the MCF is then used to obtain a final quantitative fit. The second stage of that procedure is not automated, and results can be expressed only in terms of a discrete number of carrier species with discrete mobilities.

In this work, we discuss the implementation of a quantitative mobility spectrum analysis (QMSA) procedure, which preserves both the visually meaningful output format of the Beck and Anderson MSA technique and the quantitative accuracy of the conventional least-squares MCF result; yet the procedure is entirely automated. The present approach is a variation on the iterative fitting procedure originally developed by Dziuba and Gorska.⁵

Unlike mobility spectrum analysis, which derives only an envelope of the maximum carrier density which may be present with a given mobility, the spectra obtained from this numerical formalism are adjusted so as to optimize the quantitative agreement with the experimental results. The ultimate goal of this work is to develop a comprehensive and fully automated method for quantitatively analyzing and interpreting magneto-transport data; a universal algorithm which is suitable for widespread use as an industry standard. We will address the issues which need to be resolved before this objective can be achieved.

We begin the exposition with brief descriptions of the conductivity tensor for multicarrier systems in the next section and the multi-carrier fitting procedure in the section of that title. In the section on mobility spectrum, we describe the Beck and Anderson MSA and the iterative approach of Dziuba and Gorska. Details of the QMSA approach are then given in the same section.

The Results and Discussion section presents and discusses illustrative results, using the examples of an InAs/GaSb single quantum well grown by molecular beam epitaxy (MBE) and an anomalous HgCdTe alloy sample grown by liquid phase epitaxy (LPE). Convergence issues are also considered in that section. Some concluding comments regarding the suitability and practicality of implementing the QMSA technique as an industry standard are also provided.

MULTI-CARRIER SYSTEMS

The motion of carriers in a Hall sample may be described by the following set of Eq. (1)

$$\begin{aligned} J_x &= \sigma_{xx} E_x + \sigma_{xy} E_y \\ J_y &= \sigma_{yx} E_x + \sigma_{yy} E_y \end{aligned} \quad (1)$$

where $\sigma_{xx} = \sigma_{yy}$ and $\sigma_{xy} = -\sigma_{yx}$ are the longitudinal and transverse conductivity tensor components, respectively, J_x and J_y are the current densities in the x and y directions, respectively, and E_x and E_y are the corresponding electric fields. The experimental Hall coefficient and resistivity are related to the components of the conductivity tensor through the following relations:

$$\begin{aligned} R_H(B) &= \frac{\sigma_{xy}/B}{\sigma_{xx}^2 + \sigma_{xy}^2} \\ \rho(B) &= \frac{\sigma_{xx}}{\sigma_{xx}^2 + \sigma_{xy}^2} \end{aligned} \quad (2)$$

where B is the applied magnetic field in the z direction. For a sample involving more than one type of carrier, the conductivity tensor components can be expressed as a sum over the m species present within the multi-carrier system:

$$\begin{aligned} \sigma_{xx}(B) &= \sum_{i=1}^m \frac{en_i\mu_i}{1 + (\mu_i B)^2} \\ \sigma_{xy}(B) &= \sum_{i=1}^m S_i \frac{en_i\mu_i^2 B}{1 + (\mu_i B)^2} \end{aligned} \quad (3)$$

where n_i and μ_i are the concentration and mobility of the i -th carrier species, respectively, and S_i is $+1$ for holes and -1 for electrons. It is primarily the $1 + \mu_i^2 B^2$ terms in the denominators of Eq. (3) which differentiate the contributions from the various carrier species. The contributions due to higher-mobility carriers (usually electrons) are the first to be "quenched" as B is increased; i.e., once $\mu_i B \gg 1$ a given species exerts far less influence on $R_H(B)$ and $\rho(B)$. This phenomenon provides the field-dependent Hall data with its high degree of sensitivity to the individual mobilities.

MULTI-CARRIER FITTING PROCEDURE

The MCF is a procedure whereby Eq. (2) and Eq. (3) are employed to fit experimental data for $R_H(B)$ and $\rho(B)$. In this method, n_i and μ_i are the fitting parameters and the number of carriers, i , is typically between 2 and 5. The main drawback of the MCF is its arbitrariness. That is, not only must the many parameters in the model be optimized, but a decision needs to be made in advance with respect to what type and how many carriers to assume. The end result is that

the fit to the experimental Hall data is not unique.

MOBILITY SPECTRUM

Mobility Spectrum Analysis

The salient feature of the MSA developed by Beck and Anderson⁴ is that it transforms the experimental conductivity tensor vs magnetic field data into a continuous profile of the carrier mobilities present in the sample. The various electron and hole species then appear as peaks in the mobility spectrum. A major advantage of MSA over the MCF procedure is that it is inherently nonarbitrary; i.e., no prior assumptions are required. The derived spectrum may thus be viewed as simply a mathematical restatement of the original experimental Hall data.

The starting point for the MSA is to allow for the existence within the semiconductor sample of a continuous distribution of hole-like and electron-like carriers of any mobility. Equation (3) can thus be rewritten in integral form:⁴

$$\begin{aligned}\sigma_{xx}(B) &= \int_0^{\infty} \frac{s^p(\mu) + s^n(\mu)}{1 + \mu^2 B^2} d\mu \\ \sigma_{xy}(B) &= \int_0^{\infty} \frac{[s^p(\mu) - s^n(\mu)]\mu B}{1 + \mu^2 B^2} d\mu\end{aligned}\quad (4)$$

where the hole and electron conductivity density functions (i.e., the mobility spectra) are given by

$$\begin{aligned}s^p(\mu) &= ep(\mu)\mu \\ s^n(\mu) &= en(\mu)\mu,\end{aligned}\quad (5)$$

respectively, and $p(\mu)$ and $n(\mu)$ are the hole and electron concentration density functions, respectively. As stated earlier, the goal is to determine the conductivity density functions $s^n(\mu)$ and $s^p(\mu)$. However, the measured $\sigma_{xx}(B)$ and $\sigma_{xy}(B)$ do not uniquely define these density functions. Given values for the conductivity tensor at N different magnetic fields define a $2N$ -dimensional space which has, at most, $2N$ independent basis vectors. Since Eq. (4) defines an expansion of the data in terms of an infinite basis, the expansion cannot be unique. Using a rather complex mathematical formalism, Beck and Anderson were able to obtain unique envelopes $s^n(\mu)$ and $s^p(\mu)$ which represent physical δ -like amplitudes at μ . While this result may not be as valuable as finding unique functions $s^n(\mu)$ and $s^p(\mu)$, it is still very useful in that the various carrier species may at least be identified from the peaks in the envelope spectrum.

Dziuba and Gorska Iterative Approach

A different approach for obtaining the mobility spectrum was proposed by Dziuba and Gorska.⁵ Their more ambitious goal was to derive a quantitatively accurate mobility distribution instead of just an upper-bound envelope. In their approach, the integrals appearing in the conductivity tensor expression of Eq. (4) are approximated by sums of the partial contribu-

tions by carriers having a grid of discrete mobilities:

$$\begin{aligned}\sigma_{xx}(B_j) &= \sum_{i=1}^m \frac{[s^p(\mu_i) + s^n(\mu_i)]\Delta\mu_i}{1 + \mu_i^2 B_j^2} = \sum_{i=1}^m \frac{S_i^{xx}\Delta\mu_i}{1 + \mu_i^2 B_j^2} \\ \sigma_{xy}(B_j) &= \sum_{i=1}^m \frac{[s^p(\mu_i) - s^n(\mu_i)]\mu_i B_j \Delta\mu_i}{1 + \mu_i^2 B_j^2} = \sum_{i=1}^m \frac{S_i^{xy}\mu_i B_j \Delta\mu_i}{1 + \mu_i^2 B_j^2}\end{aligned}\quad (6)$$

where S_i^{xx} and S_i^{xy} have elements defined as follows:

$$\begin{aligned}S_i^{xx} &= s^p(\mu_i) + s^n(\mu_i) \\ S_i^{xy} &= s^p(\mu_i) - s^n(\mu_i)\end{aligned}\quad (7)$$

and the parameter m defines the number of points in the final mobility spectrum.

Using an initial spectrum (first trial function), which was obtained by a simpler approach than that of Beck and Anderson, Dziuba and Gorska were able to solve the set of Eqs. (6) using the Jacobi iterative procedure, in which the diagonal transformation matrix elements $1/(1 + \mu_i^2 B_j^2)$ and $\mu_i B_j / (1 + \mu_i^2 B_j^2)$ are simplified because of the specific choice of the mobility points ($\mu_i = 1/B_i$) in the $s^p(\mu_i)$ and $s^n(\mu_i)$ spectra. Here, B_i is the i -th magnetic field obtained by spline interpolation of the experimental data in order to obtain the required density of points in the spectrum. Moreover, the diagonal elements are used as adjustable coefficients in the iteration process. An important consequence of this specific choice of mobility points is the fact that the mobility range in the spectrum is limited to $1/B_{\max}^{\exp} = \mu_{\min} \leq \mu \leq \mu_{\max} = 1/B_{\min}^{\exp}$, where B_{\min}^{\exp} and B_{\max}^{\exp} are the limits of the magnetic field in the experiment.

The goal of the procedure is to obtain the functional forms $s^p(\mu_i)$ and $s^n(\mu_i)$ which best fit the experimental magnetic field dependencies of σ_{xx} and σ_{xy} . "Nonphysical" results are allowed, since negative values of $s^p(\mu_i)$ and $s^n(\mu_i)$ are often obtained for some regions of the spectra.

Quantitative Mobility Spectrum Analysis

The QMSA approach presented in this paper is based on that of Dziuba and Gorska, with one key modification; that $s^p(\mu_i)$ and $s^n(\mu_i)$ are both constrained to be non-negative at all iteration steps. This is equivalent to requiring that no carriers can contribute negative conductivities. This step circumvents the ill-conditioning of Eq. (6), which can make the direct inversion of that equation meaningless. For definiteness, the MSA envelope (in discrete form) is used as the initial trial function, since the MSA spectrum is known to have approximately the correct overall shape. The final fit to experimental data tends to have lower error when the MSA is used as the first trial function rather than a simpler initial function. However, it is interesting to note that even a zeroed-out initial function (i.e., $s^p(\mu_i) = s^n(\mu_i) = 0$) yields a reasonable final spectrum with only slightly higher error. In the present approach, the mobility range

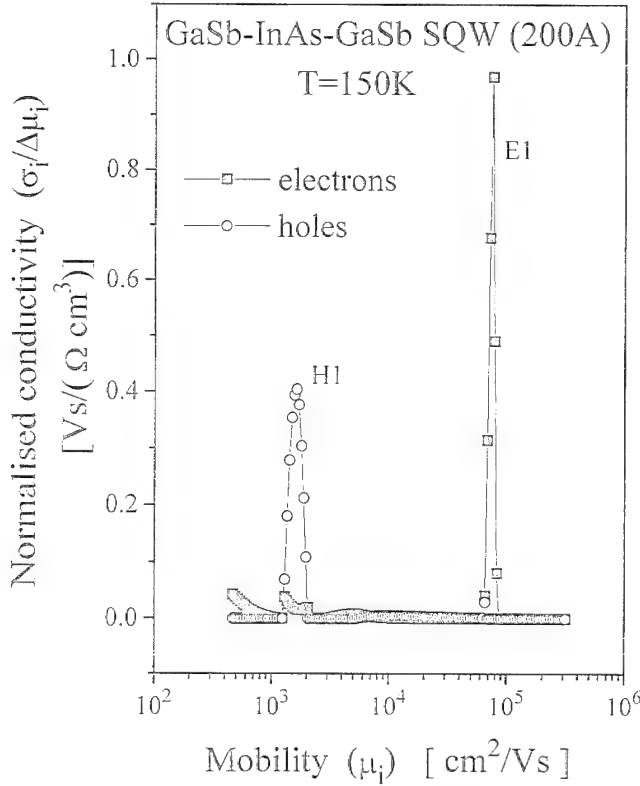


Fig. 1. Normalized $(\sigma_i/\Delta\mu_i)$ mobility spectrum (QMSA) for InAs-GaSb single quantum well at 150K. Two carriers, an electron (E1) in the quantum well and a hole (H1) from the GaSb substrate can be identified.

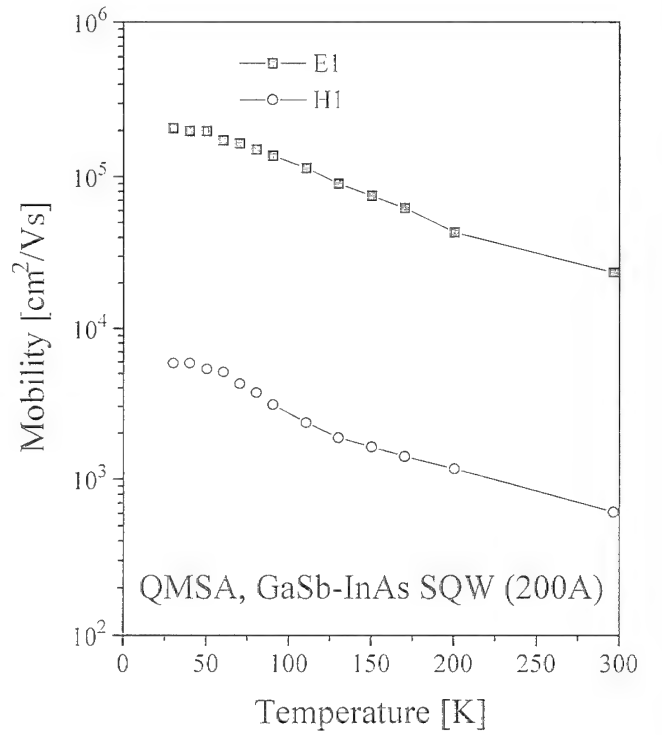
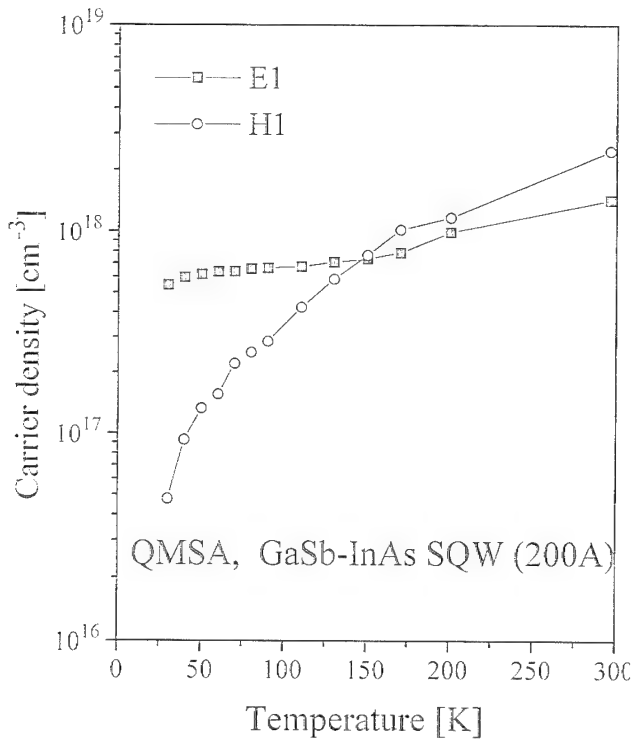
considered by Dziuba and Gorska has been extended to values less than $1/B_{\text{max}}^{\text{exp}}$, which are often of considerable interest in semiconductor characterization, and represent values to which the data have a fairly high degree of sensitivity. A further improvement that has been implemented in the present procedure is in the efficiency with which the iterative solution is obtained in comparison to that employed by Dziuba and Gorska. To solve for S^{xx} and S^{xy} , we first rearrange Eq. (6):

$$S_i^{xx} = (1 + \mu_i^2 B_i^2) \left[\sigma_{xx}^{\text{exp}}(B_i) - \sum_{j=1}^m \frac{S_j^{xx}}{1 + \mu_j^2 B_i^2} \right]$$

$$S_i^{xy} = \frac{(1 + \mu_i^2 B_i^2)}{\mu_i B_i} \left[\sigma_{xy}^{\text{exp}}(B_i) - \sum_{j=1}^m \frac{S_j^{xy} \mu_j B_i}{1 + \mu_j^2 B_i^2} \right] \quad (8)$$

If the values of S_i^{xx} and S_i^{xy} from the previous iteration are substituted into the right-hand side of Eq. (8), and if their new values are used as soon as they become available, the new set of values $S_i^{xx}(k+1)$ and $S_i^{xy}(k+1)$ can be determined from the following Gauss-Seidel iterative procedure

$$S_i^{xx}(k+1) = (1 + \mu_i^2 B_i^2) \left[\sigma_{xx}^{\text{exp}}(B_i) - \sum_{j=1}^{i-1} \frac{S_j^{xx}(k+1)}{1 + \mu_j^2 B_i^2} - \sum_{j=i+1}^m \frac{S_j^{xx}(k)}{1 + \mu_j^2 B_i^2} \right]$$



a

b

Fig. 2. (a) Carrier density and (b) mobility as a function of temperature for the InAs-GaSb single quantum well obtained from QMSA (see Fig. 1); an electron (E1) in the quantum well and a hole (H1) from the GaSb substrate are evident.

$$S_i^{xy}(k+1) = \frac{(1 + \mu_i^2 B_i^2)}{\mu_i B_i} \left[\sigma_{xy}^{exp}(B_i) - \sum_{j=1}^{i-1} \frac{S_j^{xy}(k+1) \mu_j B_i}{1 + \mu_j^2 B_i^2} - \sum_{j=i+1}^m \frac{S_j^{xy}(k) \mu_j B_i}{1 + \mu_j^2 B_i^2} \right] \quad (9)$$

If $S_i^{xx}(k)$ and $S_i^{xy}(k)$ are added and subtracted, respectively, from the right-hand side of the corresponding expressions in Eq. (9), and if the constant ω is introduced such that

$$\begin{aligned} S_i^{xx}(k+1) &= (1 - \omega) S_i^{xx}(k) + \omega \\ &\left\{ \left(1 + \mu_i^2 B_i^2 \right) \left[\sigma_{xx}^{exp}(B_i) - \sum_{j=1}^{i-1} \frac{S_j^{xx}(k+1)}{1 + \mu_j^2 B_i^2} - \sum_{j=i+1}^m \frac{S_j^{xx}(k)}{1 + \mu_j^2 B_i^2} \right] - S_i^{xx}(k) \right\} \\ S_i^{xy}(k+1) &= (1 - \omega) S_i^{xy}(k) + \omega \\ &\left\{ \left(\frac{1 + \mu_i^2 B_i^2}{\mu_i B_i} \right) \left[\sigma_{xy}^{exp}(B_i) - \sum_{j=1}^{i-1} \frac{S_j^{xy}(k+1)}{1 + \mu_j^2 B_i^2} - \sum_{j=i+1}^m \frac{S_j^{xy}(k)}{1 + \mu_j^2 B_i^2} \right] - S_i^{xy}(k) \right\} \end{aligned} \quad (10)$$

then the successive over-relaxation iteration algorithm is obtained in which the coefficient ω controls the convergence speed of the procedure. Although this algorithm is not guaranteed to converge, convergence has in fact been obtained for every one of the many experimental data sets analyzed so far. In the standard iteration procedure (in which $\omega=1$), the mobility spectrum is modified so rapidly that even after the first iteration step the qualitative information contained in the shape of the envelope spectrum is destroyed.

To ensure that such information is preserved, a value of $\omega=0.01$ was chosen in our calculations so that modification of the mobility spectrum was slowed down in the successive iterations. In order to obtain more accurate results, interpolation between the experimental points for $\sigma_{xx}(B)$ and $\sigma_{xy}(B)$ has been carried out using a spline technique, resulting in a density of 50 points per decade. This allows the spectrum to be derived with much higher resolution in comparison to that obtained by Dziuba and Gorska who used only ten points per decade.

It is important to note that the amplitudes of $s^p(\mu_i)$ and $s^p(\mu_i)$ in the QMSA depend on the density of points used for the calculation. Thus, in order to obtain the total conductivity corresponding to the carrier represented by a particular peak, all the amplitudes under that peak must be added together.

RESULTS AND DISCUSSION

It was remarked in the introduction that the QMSA can be applied to any magnetic-field-dependent Hall and resistivity data (as long as the concentrations and mobilities do not depend on magnetic field and quantum oscillations are not prominent). In this section, we present representative results illustrating the

analysis for two dissimilar semiconductor systems: an InAs-GaSb single quantum well whose relatively simple mobility spectrum displays only one electron peak and one hole peak, and an LPE-grown HgCdTe ($x = 0.216$) alloy sample whose more complex spectra will be discussed in more detail.

InAs-GaSb Single Quantum Well

As a first example, we consider results for a GaSb-InAs-GaSb single quantum well with thickness 200Å. Figure 1 presents the QMSA mobility spectrum for the quantum well at $T = 150K$. The spectrum is seen to display sharply resolved peaks corresponding to one electron species (the two-dimensional electron

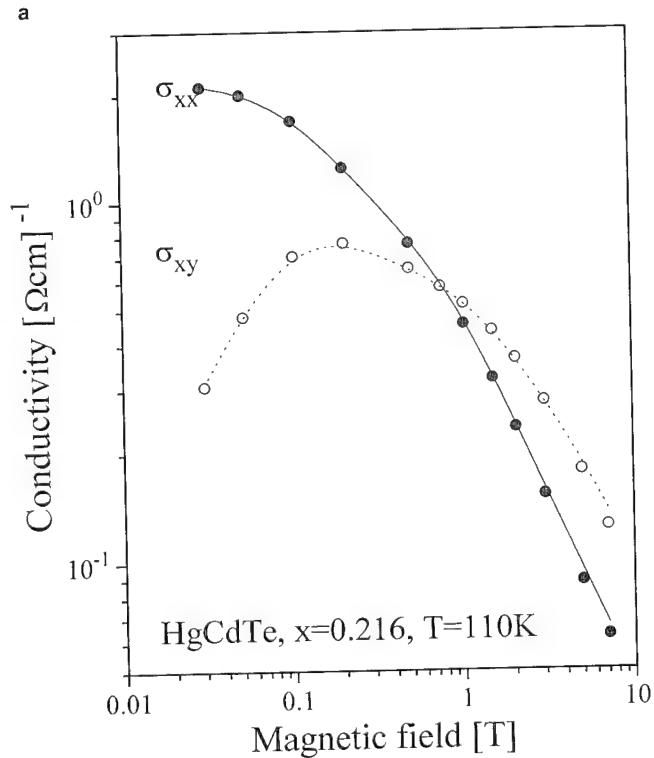
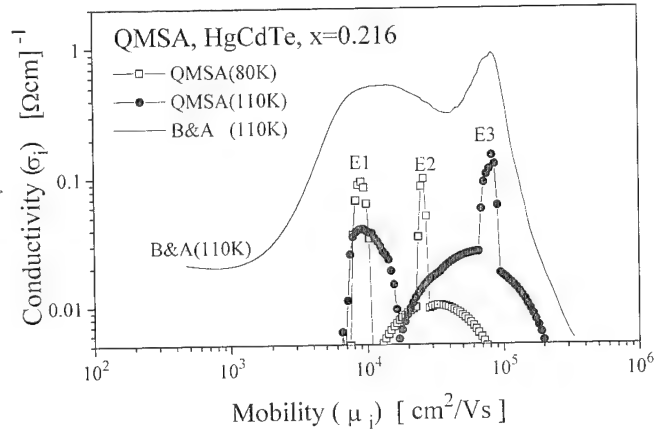


Fig. 3. (a) Mobility spectrum (QMSA) at 80 and 110K, and Beck and Anderson (B&A) envelope at 110K; and (b) experimental (points) and calculated (curves) using QMSA of the conductivity tensor components at 110K for LPE HgCdTe ($x = 0.216$).

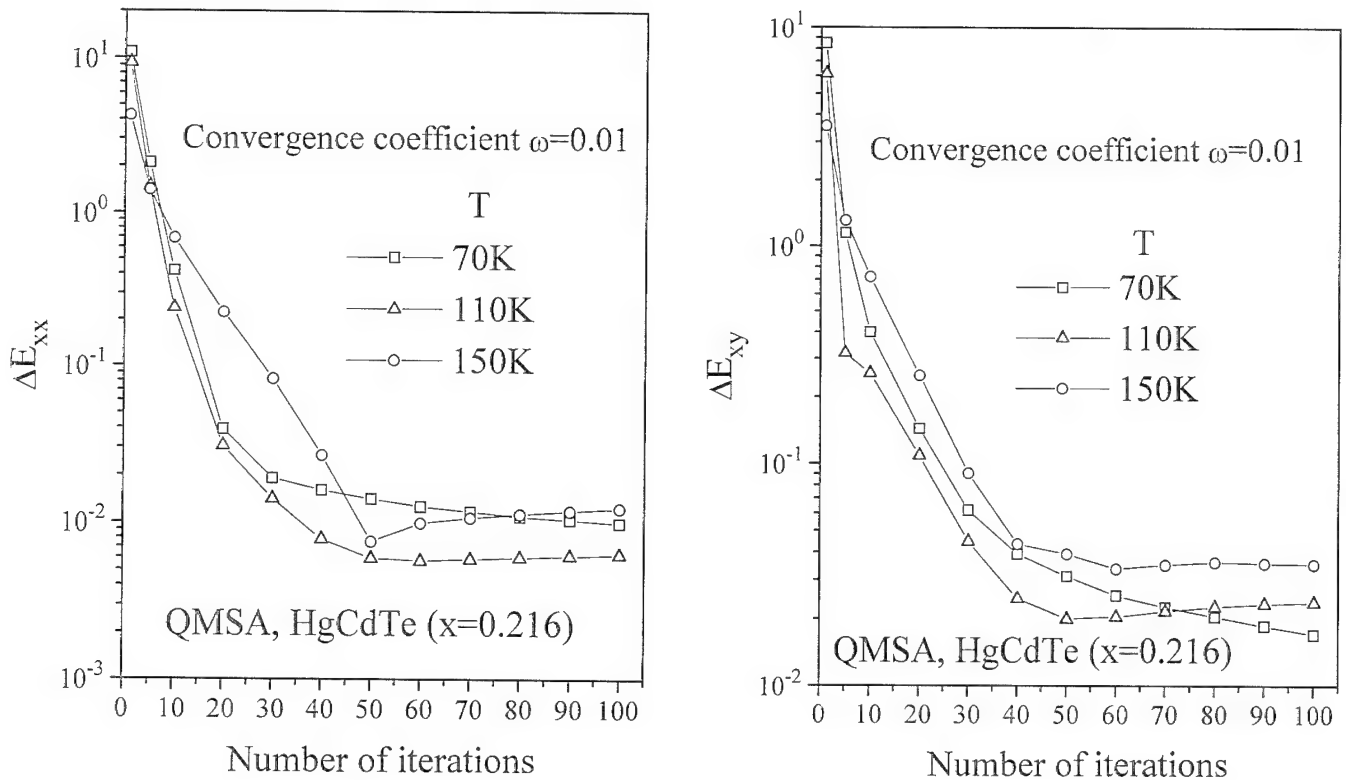


Fig. 4. Convergence in the QMSA iterative procedure according to Eq. (11) for (a) σ_{xx} and (b) σ_{xy} for LPE HgCdTe ($x = 0.216$) at three temperatures: 70, 110, and 150K.

residing in the quantum well, labeled E1) and one hole species (the three-dimensional, bulk, majority carrier in the GaSb substrate, labeled H1). As was mentioned in the section on QMSA, the magnitude of the conductivity contributions creating the QMSA spectrum depends on the density of points in such a way that the total conductivity remains constant. In order to present the results in a form which does not depend on the mobility increment chosen, the spectrum in Fig. 1 has been normalized by dividing the partial conductivity contributions by the mobility increment (i.e., $\sigma_i/\Delta\mu_i$). The net carrier density for a given species can also be obtained, by summing over the incremental contributions under the peak corresponding to that carrier:

$$n = \sum_i \sigma_i / (e\mu_i).$$

Temperature-dependent carrier densities and mobilities for both E1 and H1 were determined from the QMSA spectra at a series of temperatures between 30 and 300K, and are shown in Fig. 2. Note that H1 freezes out in the low-temperature limit. The mobility and concentration results derived from the QMSA procedure are quite similar to those obtained from a conventional MCF fit. The significant difference, however, is that the QMSA spectra were obtained from a fully automated algorithm, whereas the MCF required initial assumptions about the number and types of carrier species to employ in the fitting procedure.

LPE HgCdTe Sample

The second data set to be considered are for an LPE-grown HgCdTe alloy ($x = 0.216$) film provided by Loral. The electrical properties of this sample were anomalous, which probably accounts for the complexity of its mobility spectra. Typical QMSA results for this sample are presented in Fig. 3a, which illustrates the electron spectra for $T = 80$ and 110K (the hole conductivities are much smaller, so we will ignore them in this discussion). Note that the 80K spectrum displays two sharp peaks (E1 and E2), while the 110K spectrum contains two peaks (E1 and E3) plus a broad shoulder where E2 had been (the identification of these three species will be discussed below). The solid line indicated as B&A is the initial, discrete form, of the Beck and Anderson envelope for the iterative procedure. For the 110K data, Fig. 3b demonstrates that the final QMSA fits (curves) to the experimental (points) conductivity tensor components σ_{xx} and σ_{xy} are almost perfect. Although the QMSA mobility spectrum changes dramatically during the iterative procedure, it still preserves the qualitative features of the Beck and Anderson MSA envelope that was used as the initial trial function. However, whereas the MSA spectrum provides only qualitative information, the final QMSA spectrum also yields an accurate quantitative determination of the mobility and density of each electron species.

Figure 4 shows the convergence process for the spectra obtained at temperatures of 70, 110, and

150K. The convergence is measured as an error, defined in the same way for both conductivity tensor components σ_{xx} and σ_{xy} :

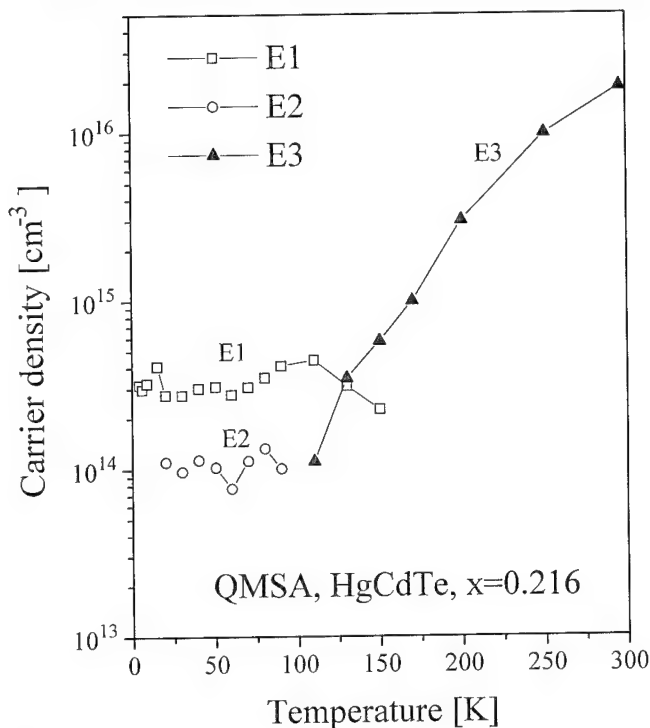
$$\Delta E^2(k) = \frac{\sum_i [\sigma_i^{\text{exp}} - \sigma_i^{\text{QMSA}}(k)]^2}{\sum_i [\sigma_i^{\text{exp}}]^2} \quad (11)$$

where σ_i^{exp} and σ_i^{QMSA} are the experimental and QMSA values, respectively, and k is the iteration step number. For most of the samples analyzed so far, the error $\Delta E(k)$ decreases to its minimum value (best fit) after approximately 50 iterations (with $\omega = 0.01$). A characteristic feature of the error is that it is smaller for the σ_{xx} component (about 1%) than for σ_{xy} component (about 2–4%). This is probably because the experimental data for σ_{xx} are more accurate than those for σ_{xy} (at low magnetic fields, the Hall voltage is an order of magnitude less than the resistivity voltage).

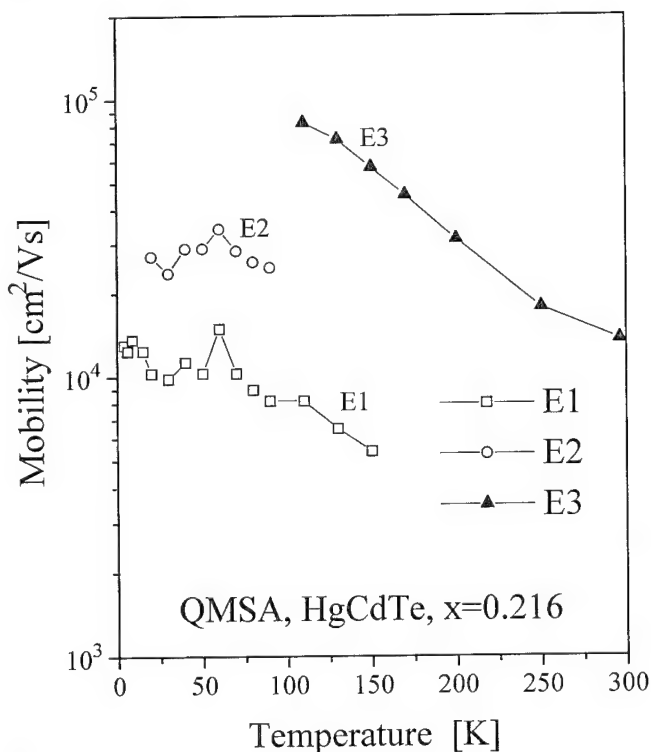
Quantitative mobility-spectrum analysis of the magneto-transport data taken at a number of different temperatures between 4.2 and 300K was used to extract temperature-dependent carrier concentrations and mobilities (see Fig. 5a and 5b, respectively) for all three of the carrier species. Note that whereas both n and μ for E1 and E2 are nearly independent of T , the density for the higher-mobility species E3 increases rapidly with increasing temperature. This is clearly the intrinsically generated electron which occupies the bulk of the HgCdTe epitaxial layer. The two lower-mobility species E1 and E2 therefore reside somewhere else, perhaps at the surface or in the graded-gap buffer region between the CdTe substrate and the HgCdTe film. As such, their carrier concentrations should more properly be represented as sheet densities, which are found to be $5 \cdot 10^{11} \text{cm}^{-2}$ for E1 and $2 \cdot 10^{11} \text{cm}^{-2}$ for E2. Since the E3 species is so dominant that its peak completely obscures the other two at temperatures above 150K, densities and mobilities for E1 and E2 are not shown in Fig. 5 for temperatures in that range.

For comparison purposes, the same data sets were also analyzed by the standard multi-carrier fitting procedure, using the Marquardt-Levenberg nonlinear least-squares curve-fitting algorithm implemented in the MicroCal Origin™ software package. Although the error in fitting the conductivity tensor was relatively small for any MCF calculation employing three or more species, the qualitative behavior of the resulting densities and mobilities was highly dependent on how many carriers were assumed to be present. Assuming three species, for example, at low temperature two of them obviously corresponded to E1 and E2 from Fig. 3a, while the third had a much lower mobility. However, at temperatures above 100K, the highest-mobility species increased its mobility (corresponding to E3) while the intermediate-mobility species appeared to become a composite of E1 and E2. When four species were assumed, the mix became even more complicated, dramatically illustrating the

extreme sensitivity of the MCF to the arbitrary initial assumption concerning species multiplicity. Thus, there is considerable advantage to the elimination of prior assumptions in the QMSA, even though it is not always a straightforward matter to interpret the



a



b

Fig. 5. (a) Carrier density and (b) carrier mobility as a function of temperature for LPE HgCdTe ($x = 0.216$) obtained from the mobility spectrum (QMSA). Three identified carriers indicated as E1, E2, E3.

identity of the various peaks and shoulders which appear in the spectra. In contrast to the standard MCF, the data manipulation phase of the QMSA magneto-transport characterization is clearly differentiated from the interpretation phase.

CONCLUSIONS

We have discussed a new approach to obtaining quantitative mobility and carrier density information from the analysis of field-dependent Hall and resistivity data. Starting with an appropriate initial trial function such as the Beck and Anderson spectrum (in discrete form), the iterative algorithm of the QMSA generates electron and hole mobility spectra which yield almost perfect fits to the experimental conductivity tensor as a function of magnetic field. The spectra obtained may be viewed as an easily interpreted graphical restatement of the input data. It fully quantifies the number of carrier species (from the number of peaks), their type (electrons or holes), and their densities and mobilities. While the QMSA results are often similar to those obtained from a standard multi-carrier fit, the procedure is fully automatic and does not require any initial assumptions.

In most regards, the iterative approach presented in this paper does not differ appreciably from that of Dziuba and Gorska. We have employed a more realistic initial function (the MSA mobility spectrum), significantly increased the density of points in the spectrum, extended the mobility limits, and employed a more efficient iteration algorithm (the successive over-relaxation procedure). In practice, however, the most significant difference is that the convergence has been improved by constraining the partial conductivity contributions to always have non-negative values (which is also more physically reasonable). These refinements have made the technique more practical and reliable to use.

For a PC with a 486 processor, the total CPU time needed to generate the QMSA spectrum for a single

temperature (including experimental data interpolation, the MSA spectrum calculation, and the QMSA itself) is in the order of 2 min. Presently, the only step requiring human intervention is in the determination of carrier densities corresponding to a given mobility peak, since one must choose the range of mobilities to be integrated over for each peak. Ultimately, however, this step could also be automated in more routine cases where the general nature of the spectrum is somewhat known in advance.

Further refinements of the QMSA technique are now under investigation. Also being initiated is a detailed study of how the QMSA performs when it is routinely applied to a large number of samples with widely varying properties. However, preliminary indications suggest that the present form of the procedure is quite suitable for use as an industry-standard tool for analyzing field-dependent Hall characterizations of diverse semiconductor materials and bandgap engineered structures.

ACKNOWLEDGMENTS

We would like to thank Zbigniew Dziuba for many useful discussions and W.A. Beck for supplying the software for the mobility spectrum envelope calculation. We also thank W.I. Wang for supplying the InAs-GaSb quantum well sample and Loral Infrared and Imaging Systems for supplying the anomalous LPE HgCdTe sample. This project was financially supported by The Australian Research Council.

REFERENCES

1. J.R. Meyer, C.A. Hoffman, F.J. Bartoli, D.J. Arnold, S. Sivananthan and J.P. Faurie, *Semicond. Sci. Technol.* 8, 805 (1993).
2. M.C. Gold and D.A. Nelson, *J. Vac. Sci. Technol. A* 4, 2040 (1986).
3. S.P. Tobin, G.N. Pultz, E.E. Krueger, M. Kestigian, K.K. Wong and P.W. Norton, *J. Electron. Mater.* 22, 907 (1993).
4. W.A. Beck and J.R. Anderson, *J. Appl. Phys.* 62, 541 (1987).
5. Z. Dziuba and M. Gorska, *J. Phys. III France* 2, 110 (1992).

Characterization of Molecular Beam Epitaxially Grown HgCdTe Epilayers by Mid-Infrared Interband Magneto-Absorption

P. HELGESEN, R. SIZMANN, T. SKAULI, T. COLIN, H. STEEN, and S. LØVOLD

Norwegian Defence Research Establishment, Division for Electronics,
P.O. Box 25, N-2007 Kjeller, Norway

Interband magneto-absorption is used to characterize molecular beam epitaxially (MBE) grown HgCdTe epilayers. Both the bandgap and the Moss-Burstein shift in n-doped layers are determined from the experiments. A heterostructure sample consisting of four layers with different compositions is also analyzed. Due to the good experimental sensitivity all four bandgaps are determined, in contrast to optical transmission analysis without a magnetic field where only the lowest gap is readily visible. The interband magneto-absorption signal strongly depends on the electron mobility. This has been used as an aid to optimizing the MBE growth conditions of HgCdTe layers on different substrate orientations.

Key words: HgCdTe, interband magneto-absorption, molecular beam epitaxy (MBE), Moss-Burstein shift

INTRODUCTION

Magneto-optical studies of semiconductors in general and HgCdTe in particular are a powerful noncontact and nondestructive tool for determining the electronic band structure. It has been shown that the quasi-germanium model gives a consistent description of the carrier behavior in HgCdTe in the presence of a magnetic field.^{1,2} This technique has been used to determine the symmetry properties of the fundamental extremes as well as the values of the effective mass and g-factor. Most of the previous investigations have been performed on thick bulk samples. Therefore, interband excitations (electron-hole excitations across the bandgap) have mainly been studied in the reflection geometry, and only a few transmission investigations on thin samples exist.^{3,4} In contrast, due to the smaller absorption, intraband (free carrier) excitations like cyclotron reso-

nance have been measured in the transmission mode, and much attention has been paid to this type of measurements.⁵⁻⁸

Recently, we have studied interband magneto-absorption in HgTe/CdTe superlattices with emphasis on the fundamental physical aspects.^{9,10} The rich optical spectra permit a close comparison with theoretically evaluated hole to electron subband transitions. It is also possible to identify structures in the absorption which do not originate from the electronic band, but from impurity levels or interference effects.

In this paper, we describe the use of interband magneto-absorption as a sensitive characterization technique for HgCdTe epilayers. The emphasis is on determining technologically important parameters relevant for device applications. Three major topics are addressed:

- In n-doped layers the absorption edge is shifted to larger energies, the Moss-Burstein shift, as the Fermi energy moves into the conduction band. By interband magneto-absorption both the funda-

(Received October 4, 1994 ; revised February 6, 1995)

Table I. Structural Parameters for the Epilayers Used in This Work

Sample	Nominal Structure	Structure Determined from Magneto-Absorption	Comments
A Single Doped Layer	$d = 6.3 \mu\text{m}$ $x = 0.20$ $n = 4 \times 10^{16} \text{ cm}^{-3}$	$E_G = 44 \pm 5 \text{ meV}$ $E_F = 80 \pm 10 \text{ meV}$ $x = 0.191 \pm 0.003$ $m_c = 0.012 \pm 0.002 m_0$	$n = 9.9 \times 10^{16} \text{ cm}^{-3}$ from Hall measurement. $n = 7 \pm 2 \times 10^{16} \text{ cm}^{-3}$ calculated from the Fermi energy.
B Single Heterojunction	$d_1 = 2 \mu\text{m}, x_1 = 0.23$ $d_2 = 3 \mu\text{m}, x_2 = 0.28$	$E_{G1} = 144 \pm 5 \text{ meV}, x_1 = 0.250 \pm 0.003$ $E_{G2} = 245 \pm 5 \text{ meV}, x_2 = 0.311 \pm 0.003$	undoped single heterojunction with two layers of different composition, x .
C Triple Heterojunction	$d_1 = 10 \mu\text{m}, x_1 = 0.21$ $d_2 = 1 \mu\text{m}, x_2 = 0.225$ $d_3 = 1.5 \mu\text{m}, x_3 = 0.24$ $d_4 = 2 \mu\text{m}, x_4 = 0.255$	$E_{G1} = 96 \pm 5 \text{ meV}, x_1 = 0.221 \pm 0.003$ $E_{G2} = 111 \pm 5 \text{ meV}, x_2 = 0.230 \pm 0.003$ $E_{G3} = 134 \pm 5 \text{ meV}, x_3 = 0.244 \pm 0.003$ $E_{G4} = 159 \pm 5 \text{ meV}, x_4 = 0.259 \pm 0.003$	undoped triple heterojunction with one thick layer with low x and three thin layers with slightly higher x .
D HgTe/CdTe Superlattice	61 Periods $d_w = 82 \text{ \AA}$ $d_b = 30 \text{ \AA}$	$E_G = 20 \pm 5 \text{ meV}$ $E_1 = 485 \pm 5 \text{ meV}$	E_1 is the transition energy to the next higher subband. Sample D has been grown on both (211) and (776) substrate at 170°C simultaneously.
E HgTe/CdTe Multiple Quantum Wells	40 Periods $d_w = 78 \text{ \AA}$ $d_b = 71 \text{ \AA}$	$E_G = 20 \pm 10 \text{ meV}$	E_1 is not resolved. Sample E has been grown on both (211) and (100) sub- strate at 180°C simultaneously.

Note: The nominal values at the left are the design parameters of the structures. d is the layer thickness, n is the carrier density for the n -doped layer, x is the Cd fraction in the $\text{Hg}_{1-x}\text{Cd}_x\text{Te}$ layers, m_c is the conduction band effective mass at the Fermi energy, and d_w and d_b are the superlattice well and barrier width, respectively. The bandgap, E_G , and the Fermi energy, E_F , at the right are determined experimentally, while the composition, x , is calculated from the gap.

mental bandgap and the Moss-Burstein shift (or the Fermi energy) can be experimentally determined. The Fermi energy can also provide information on the carrier density.

- The bandgap of undoped single epilayers can be found by conventional infrared transmission analysis. However, it is difficult to determine the different gaps in heterostructures with this method. We demonstrate that interband magneto-absorption can meet the need for a precise gap determination in heterostructures, by determining all four gaps in a triple heterostructure sample.
- The amplitude of the oscillating interband magneto-absorption signal depends on the electron mobility, independently of the type of doping. The electron mobility is very sensitive to the crystalline quality of the structures. Thus, interband magneto-absorption can be used as an aid to optimize the MBE growth conditions by comparing the magneto-absorption amplitude from structures grown at different conditions.

EXPERIMENTAL

The HgCdTe epilayers were grown in a Riber 32 MBE system on lattice matched CdZnTe substrates with different surface orientations: (111)B 4° misoriented, (211)B, and (100), hereafter referred to as (111), (211), and (100), respectively. Further details about the growth procedures have been published elsewhere.¹¹ Table I gives an overview of the samples used in this investigation.

The interband magneto-absorption is measured in the Faraday configuration using a Fourier transform interferometer coupled to an 11-Tesla superconducting magnet. All measurements are performed at liquid helium temperature. The setup covers the mid-infrared regime from 500 to 5000 cm^{-1} using a HgCdTe detector mounted in the magnet dewar.

RESULTS AND DISCUSSION

Interband Landau level transitions in the Faraday geometry occur with $\Delta n = \pm 1$, where n is the Landau level quantum number of the carriers.¹ The dominating transitions originate from the heavy hole-like valence band Landau levels. The transition probability is generally largest for transitions to the $n = 1$ conduction band Landau level and decreases for transitions to levels with larger quantum number. Due to the large mass, the heavy hole Landau level energies are small compared to the energies of the conduction band Landau levels.

In general, the bandgap is found by extrapolating each Landau level transition energy individually to zero magnetic field. For thick epilayers without any size quantization effects, all Landau level transitions merge at the fundamental gap. The extrapolation is performed using the approximate expression for the conduction band Landau level energy, Eq. (28) of Ref. 1. For bandgap determination, it is not necessary to calculate the Landau level energy, and thus detailed knowledge about band structure parameters like the effective mass and g -factor are not needed. Instead the Landau level transition energies can be

fitted to the expression

$$E_{LL} \equiv \frac{E_G}{2} + \sqrt{\frac{E_G^2}{4} + AB}, \quad (1)$$

where E_{LL} is the Landau level transition energy, E_G is the bandgap, A is a constant including the band parameters, and B is the magnetic field. The valence band Landau level energies are neglected. This method ensures a precise gap determination, also in the case where experimental data close to $B = 0$ are missing. The composition, x in $\text{Hg}_{1-x}\text{Cd}_x\text{Te}$, is calculated from the bandgap using the formula by Hansen et al.¹²

In Fig. 1a, the normalized magneto-transmission is shown for a n-doped HgCdTe layer (sample A of Table I) at various magnetic fields. The normalization is done by dividing the transmission at a certain magnetic-field by the transmission at zero magnetic field, $T(B)/T(0)$. Hence, only magnetic field dependent features in the spectrum are seen. The data without a magnetic field is not normalized. The normalization procedure is described in more detail elsewhere.⁹

Each transmission minimum in Fig. 1a originates from an allowed Landau level transition. Figure 1b shows the Landau fan chart of the measurement data in Fig. 1a. Five different Landau level transitions are resolved. They are labeled and their energy positions are indicated with lines in the transmission curves in Fig. 1a. The structure is n-type doped with indium and has $n = 9.9 \times 10^{16} \text{ cm}^{-3}$ as determined from Hall measurements. Thus, also an intraband Landau level transition (cyclotron resonance) is observed in the experiments. This transition is labeled 1 in Fig. 1.

The interband absorption edge both with and without an external magnetic field is shifted relative to the fundamental gap due to the Moss-Burstein shift.¹³ However, the gap can still be determined by extrapolating the observed Landau level transition energies to zero magnetic field, (see Fig. 1b). In contrast, infrared transmission without a magnetic field only determines the Moss-Burstein shifted gap.¹⁴ For the transition labeled 2 in Fig. 1b, the final state Landau level is partly occupied, and thus this transition cannot be used in the gap determination. The gap is determined to be $E_G = 44 \pm 5 \text{ meV}$.

The Moss-Burstein shift, which is due to the Fermi energy, E_F , in the conduction band, can be found in two different ways from the data in Fig. 1a. The Landau level transitions cease at energies lower than $E_G + E_F$. This is especially prominent for the transitions labeled 2 in Fig. 1b. The energy $E_G + E_F$ can also be identified as the low temperature absorption edge at zero magnetic field. The Fermi energy is determined simply by subtracting the fundamental gap, E_G . Both methods give $E_F = 80 \pm 10 \text{ meV}$ relative to the conduction band edge. It is possible to estimate the carrier density from the Fermi energy, integrating the density of states while taking the conduction band nonparabolicity into account. This gives $n = 7 \pm 2 \times 10^{16} \text{ cm}^{-3}$ in rather good agreement with the value determined from Hall measurements. Thus, interband

magneto-absorption measurement also gives information about the carrier density.

The effective mass at the Fermi energy is determined from the intraband transitions marked with 1 in Fig. 1. Due to the conduction band nonparabolicity, the value varies slightly with the magnetic field, and it should be determined at a very low field value. In this experiment, data for fields below 7 T were inaccessible due to the spectral range of the setup. At 7 T $m_c = 0.012 \pm 0.002 m_0$. This is in good agreement with a theoretically calculated effective mass of $m_c = 0.01 m_0$ at the Fermi energy.¹ Access to experimental data for magnetic fields closer to 0 T would probably even improve the agreement with the theory. The fundamental bandgap, the Fermi energy, and the effective mass for sample A are all listed in Table I.

An example of interband magneto-absorption measurements on a single heterojunction (sample B of Table I) is shown in Figs. 2a and 2b. From the transmission data at zero magnetic field in Fig. 2a, it

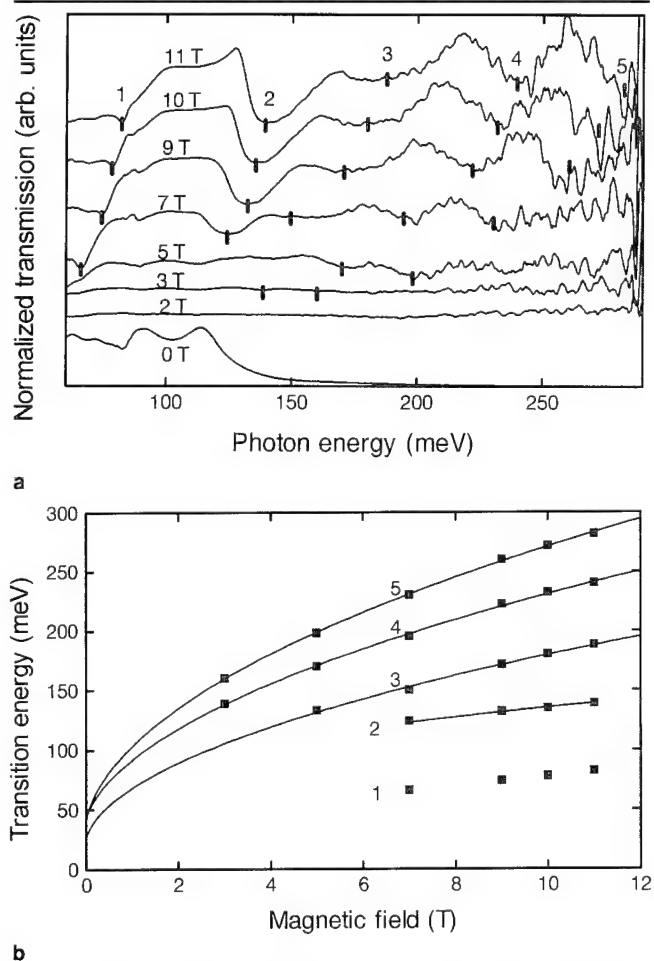


Fig. 1. (a) Normalized transmission for the n-doped HgCdTe layer, sample A of Table I, at several magnetic fields. Each minimum in the transmission corresponds to a Landau level transition. The energy positions of the transitions are marked, and the different transitions are labeled. The 0 T data is not normalized and shown for reference. (b) Landau level fan chart for the same sample. The full lines are fits using Eq. (1) to the experimentally observed Landau level transition energies (squares). The Landau level transitions are marked in accordance with a).

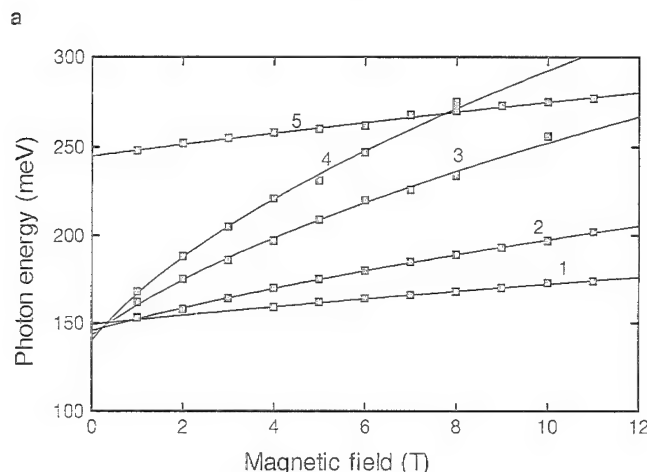
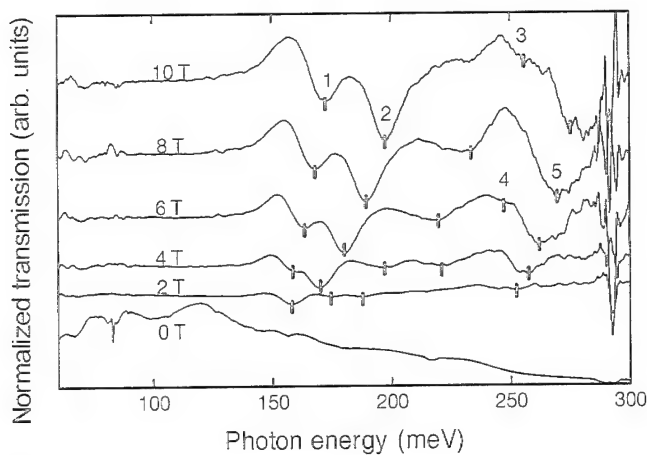


Fig. 2. (a) Normalized transmission for the single heterojunction sample B at various magnetic fields. The transmission curve at $B = 0$ T is not normalized. The identified Landau level transitions are labeled and their energy positions are marked. (b) Landau level fan chart for the same sample, where the fits (full lines) to the experimental results (squares) are extrapolated to zero magnetic field for precise gap determinations in both layers.

is possible to resolve the fundamental gap of the low bandgap material at approx. 140 meV. The bandgap of the second layer is, however, not easily determined from the $B = 0$ data.

With an applied magnetic field the spectra in Fig. 2a consist of a superposition of Landau level transitions in the two layers. At least five different Landau level transitions are resolved. They are labeled and their energy positions are marked at the various magnetic fields in Fig. 2a. The Landau level fan chart is shown in Fig. 2b. For precise identification of the Landau level transitions and their energies, measurements are performed also at intermediate magnetic fields compared to those shown in Fig. 2a. In addition, the Landau level transitions are partly recognized by their fine-structure in the absorption spectra.

By extrapolation, four Landau level transitions are identified as originating from the low gap material. The gap is determined to $E_{G1} = 144 \pm 5$ meV, equivalent to $x = 0.250 \pm 0.003$. The fifth Landau level transition does not extrapolate to the same energy at

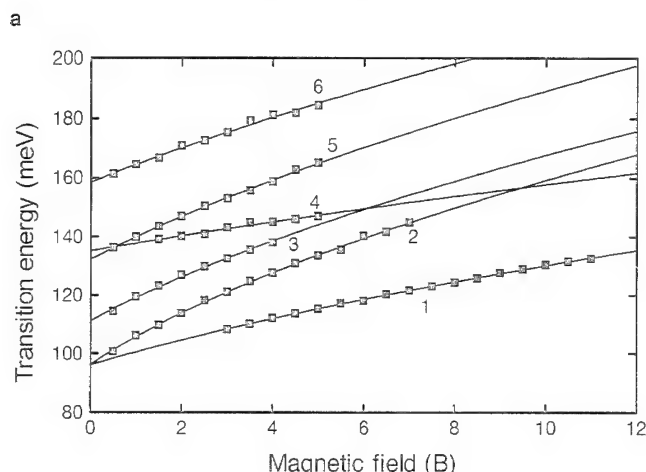
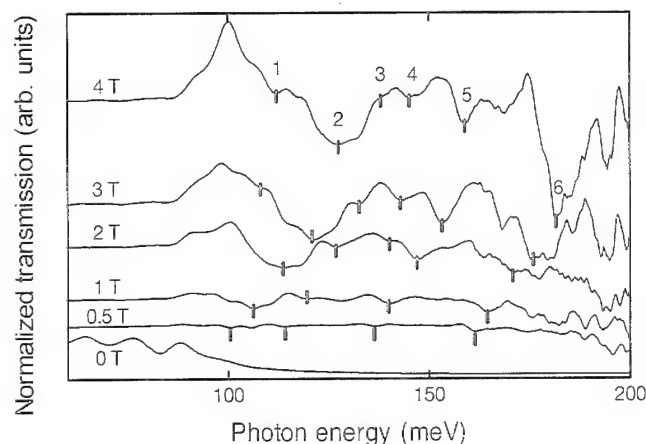


Fig. 3. (a) Normalized transmission for the triple heterojunction sample C (see Table I) at low magnetic fields. The identified Landau level transitions are labeled and their energy positions are marked. The transmission curve at $B = 0$ T is not normalized. (b) Landau level fan chart showing that the bandgap of all four layers can be identified by extrapolation of the Landau level transition energy to $B = 0$.

$B = 0$ and must occur in the layer with higher bandgap. Extrapolation gives a gap energy of $E_{G2} = 245 \pm 5$ meV or $x = 0.310 \pm 0.003$. With this information, it is possible to identify the small structure around 250 meV in the zero field transmission curve of Fig. 2a as the absorption edge of the wide gap material.

Due to the rather thin layers in sample B, it was possible to resolve the absorption edge of both materials also in the absence of a magnetic field. For other structures like photodiodes with a thick (10 μm) low x layer followed by a thin (1–2 μm) layer with slightly larger x , this is definitely not the case. Figure 3 shows interband magneto-absorption measurements for a triple heterostructure (sample C of Table I). The structure consists nominally of a 10 μm layer with $x = 0.21$ grown on top of three thin layers (1.0, 1.5, and 2.0 μm , respectively) with slightly higher x ($x = 0.225$, 0.24, and 0.255, respectively). At zero magnetic field, it is possible to identify the bandgap of the thick layer with low x value in the transmission measurements in Fig. 3a. The absorption edges of the three thin layers are not visible, however.

Several Landau level transitions are observed with an applied magnetic field. At high fields pronounced superposition occurs in the absorption between Landau level transitions in the different layers. At low fields, approximately below 4 T, the situation is simpler. By careful analysis of transmission spectra with magnetic field separation of 0.5 T, at least six different Landau level transitions can be resolved. The fan chart in Fig. 3b shows that their transition energies can be extrapolated to zero magnetic field, giving four different bandgaps. The extrapolation to four different bandgaps are also directly visible in the $B = 0.5$ T transmission measurement shown in Fig. 3a. The measured gaps have also been confirmed by partly etching the thick low x layer and repeating the interband magneto-absorption experiments. The determined layer compositions are very close to the nominal ones. The results are listed in Table I.

The main reason for the ability to resolve Landau level oscillations from all four layers is the large transition probability at the onset of the magneto-absorption or more generally on resonance for a Landau level transition as described previously. At the same time, the off-resonance absorption coefficient is lower than without a magnetic field. This combination opens up the possibility to resolve magneto-absorption features in layers where no information are available from absorption experiments without a magnetic field. However, even with a magnetic field, it is impossible to observe absorption features from all layers in a heterostructure if the composition difference is too large combined with a thick low x layer.

In order to observe pronounced Landau level transitions, the mobility of the electrons, μ , has to fulfill the condition $\mu B > 1$. The observation of clear Landau level transitions down to at least $B = 0.5$ T in Fig. 3a indicates an electron mobility of $\mu > 20000$ cm²/Vs in all four layers of sample C. Another heterostructure with independent indication of a low electron mobility in one of the layers has also been analyzed. In this case, no Landau level transition was observed from the low mobility layer. Thus, only layers with reasonable electron mobility can be analyzed.

The sensitivity to the electron mobility has been used as an aid to optimizing the growth conditions of HgCdTe epilayers, especially superlattice structures. Figure 4a shows the interband magneto-absorption measurements for the superlattice, sample D of Table I. The structure was grown simultaneously on both a (211) and a (111) oriented substrate at a temperature of 170°C. Several Landau level transitions are observed on the sample grown on (211) substrate orientation. In contrast, only the first Landau level transition is observed on the sample grown on (111) orientation. This shows that with the growth conditions used, the structure grown on the (211) orientation has superior electronic quality compared to the structure grown on the (111) orientation. A similar structure has also been grown at a substrate temperature of 190°C. In this case, several Landau level transitions

are observed for both substrate orientations. Thus, for the specific set of growth conditions used, good quality superlattices can be grown over a larger temperature interval on (211) than on (111). Further details about substrate temperature control and the growth procedures are given elsewhere.^{11,15}

A similar comparison between the growth on (211) and (100) has been performed on a multiple quantum well structure (sample E, of Table I). The normalized transmission data are shown in Fig. 4b. For these specific growth conditions, which were optimized for (100), the (100) structure have the best electronic quality. A more comprehensive comparison between the growth on (211) and (100) will be presented elsewhere. These results demonstrate the ability to extract information about the electronic quality from interband magneto-absorption experiments.

CONCLUSIONS

We have demonstrated that interband magneto-absorption is very well suited for noncontact and nondestructive characterization of HgCdTe epilayers.

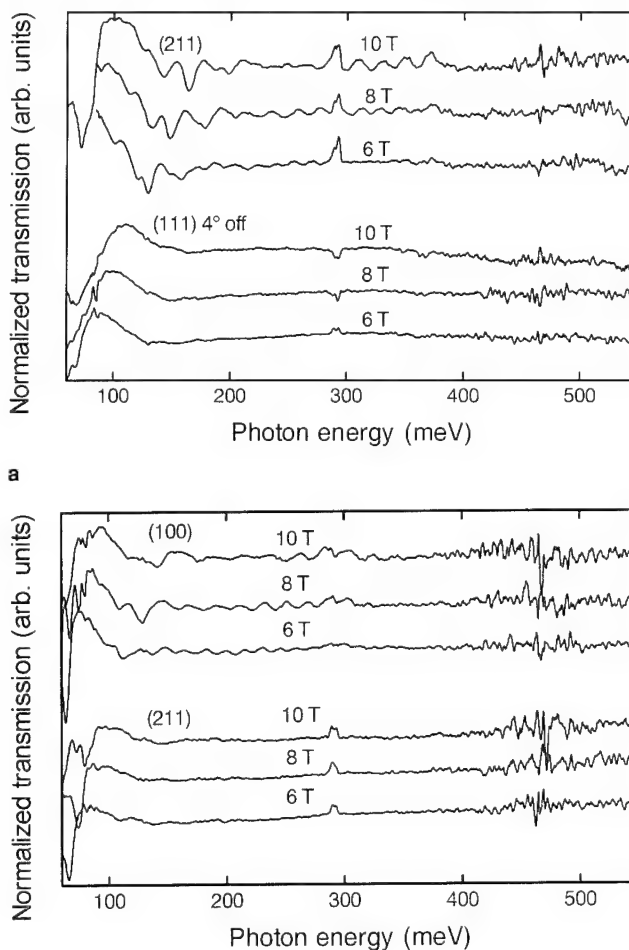


Fig. 4. (a) Normalized transmission at various magnetic fields observed on two superlattices, sample D, grown at 170°C on the (211) and (111) orientations in the same run. (b) Normalized transmission at various magnetic fields for two multiple quantum well structures, sample E, grown on (211) and (100) at 180°C in the same run.

Three main issues have been addressed. In n-doped layers both the bandgap and the Fermi level can be determined. The Fermi level also provides information on the carrier density. The bandgaps in complicated multilayer heterostructures can be precisely found. This has been demonstrated by determining both the bandgap and the composition in a triple heterostructure sample with four different layer compositions. Interband magneto-absorption also serves as a sensitive test of the electronic quality of the epilayers. This has been used as an aid to optimizing the growth conditions for HgCdTe superlattices and quantum wells.

REFERENCES

1. M.H. Weiler, *Semiconductors and Semimetals* Vol. 16, ed. R.K. Willardson and A.C. Beer (New York: Academic Press, 1981).
2. D.G. Seiler, C.L. Littler and M.H. Weiler, *Semiconductors and Semimetals* Vol. 36, ed. R.K. Willardson and A.C. Beer (New York: Academic Press, 1992).
3. Y. Guldner, C. Rigaux, A. Mycielski and Y. Couder, *Phys. Stat. Sol.* 82, 149 (1977).
4. Y. Guldner, C. Rigaux, A. Mycielski and Y. Couder, *Phys. Stat. Sol.* 81, 615 (1977).
5. B. Ellis and T.S. Moss, *Proc. 3rd Int. Conf. Photocond.* 211 (1969).
6. M.A. Kinch and D.D. Boss, *J. Phys. Chem. Solids* 32, 461 (1971).
7. Y.A. Bratashevskii, V.B. Tyutyunnik, K.S. Averyanov and I.M. Nesmelova, *Sov. Phys.-Semicond.* 9, 114 (1975).
8. P. Knowles and E.E. Schneider, *Phys. Lett. A* 65, 166 (1978).
9. R. Sizmann, P. Helgesen, T. Colin, T. Skauli and S. Løvold, *J. Electron. Mater.* (1995) (accepted).
10. R. Sizmann, P. Helgesen, T. Colin, T. Skauli and S. Løvold, *Appl. Phys. Lett.* 64, 881 (1994).
11. T. Colin, D. Minsås, S. Gjøs, R. Sizmann and S. Løvold, *Compound Semiconductor Epitaxy*, 340, ed. C.W. Tu, L.A. Kolodziejewski and V.R. McCrary (Pittsburgh, PA: Mater. Res. Soc., 1994).
12. G.L. Hansen, J.L. Schmit and T.N. Casselman, *J. Appl. Phys.* 53, 7099 (1982).
13. D. Long and J.L. Schmit, *Semiconductors and Semimetals* Vol. 5, ed. R.K. Willardson and A.C. Beer (New York: Academic Press, 1970).
14. The bandgap can be determined from conventional infrared transmission analysis by defining it as the energy where the absorption coefficient is $\alpha = 500 \text{ cm}^{-1}$ after numerically filtering interference effects in the transmission spectrum.
15. T. Skauli, T. Colin and S. Løvold, *J. Vac. Sci. Technol. A* 12, 274 (1994).

Photoluminescence and Raman Studies of High Quality CdTe:I Epilayers

N.C. GILES and JAESUN LEE

West Virginia University, Department of Physics, Morgantown,
WV 26506-6315

T.K. TRAN, J.W. TOMM,* and C.J. SUMMERS

Quantum Microstructures Laboratory, Georgia Tech Research Institute,
Atlanta, GA 30332-0800

Low-temperature photoluminescence (PL) studies of iodine-doped CdTe epilayers have been performed. A compensating acceptor center which gives rise to deep-level PL emission at 1.491 eV is identified. From selective excitation PL studies, we assign this 1.491 eV line to the recombination of an associate donor-acceptor close pair, consisting of nearest neighbor substitutional sodium and iodine atoms ($\text{Na}_{\text{Cd}} - \text{I}_{\text{Te}}$). This neutral defect complex has a localized mode of 36.5 meV, which is much larger than the bulk CdTe lattice mode of 21.3 meV. The electronic energy level associated with this defect is 115 meV below the conduction band. Also, we use a combination of selective excitation PL and Raman spectroscopies to determine the ionization energy of the isolated shallow iodine donor (I_{Te}) in CdTe. We find that the donor binding energy of this anion-site hydrogenic donor is $15.0 (\pm 0.2)$ meV.

Key words: CdTe, donors, photoluminescence (PL)

INTRODUCTION

Substitutional doping of CdTe with iodine¹ on the Te sublattice (I_{Te}) has yielded room-temperature electron concentrations as high as $3 \times 10^{18} \text{ cm}^{-3}$. These n-type CdTe:I epilayers exhibit bright photoluminescence (PL) from liquid helium temperature to room temperature.² Previous PL studies have focused on the near-edge emission related to the shallow iodine (I_{Te}) donor.³ In the present study, we use PL spectroscopy to identify compensating acceptor centers which give rise to deep-level PL emission at 1.491 eV. Also, we use a combination of selective excitation

PL and Raman spectroscopies to determine the ionization energy of the shallow iodine donor (I_{Te}) in CdTe. The hydrogenic donor ionization energy in CdTe has been thought to be 14 meV and indium, a cation-site donor, does exhibit a 14.1 meV donor binding energy.⁴ However, our previous work⁵ suggested that the iodine donor energy is closer to 15 meV. We clarify those results in the present study.

EXPERIMENTAL DETAILS

Photoluminescence studies were performed on a series of CdTe:I epilayers grown by molecular beam epitaxy at Georgia Tech. Above-band-gap excitation for conventional PL experiments was provided by the output from an argon ion laser. The tunable output from a Ti:sapphire laser (Coherent model 899-01) was used in the selective excitation studies. The Ti:sapphire emission energy was measured to within ± 0.03 meV.

*Permanent Address: Humboldt-Universitat zu Berlin, Institut für Physik, Unter den Linden 6, D-10099 Berlin, Germany

(Received October 4, 1994; revised November 29, 1994)

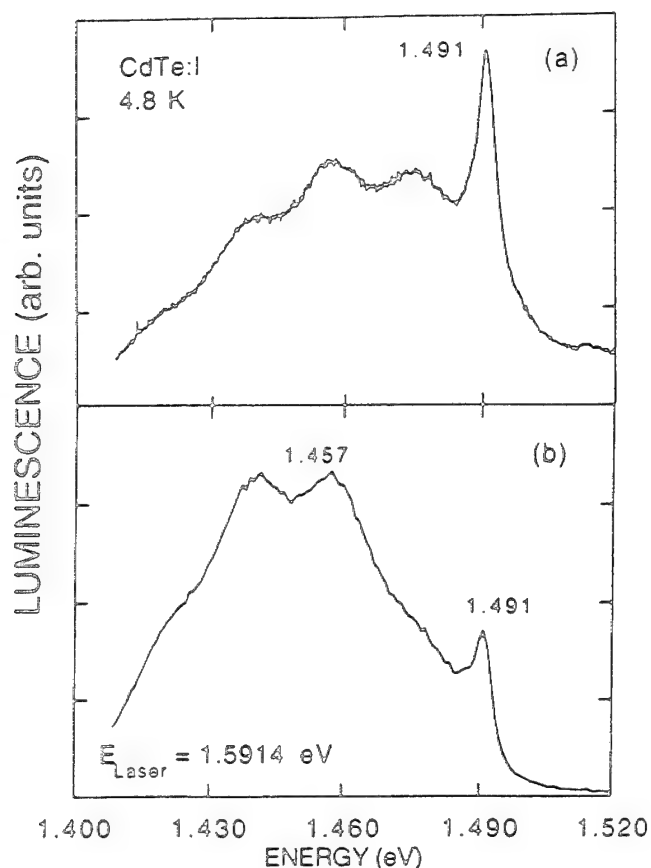


Fig. 1. Deep-level PL at 4.8K from CdTe:I. Curve (a) was taken with 514.5 nm excitation from an argon laser. Curve (b) was taken with below-band-gap excitation at 1.5914 eV and shows the enhancement of the DAP band.

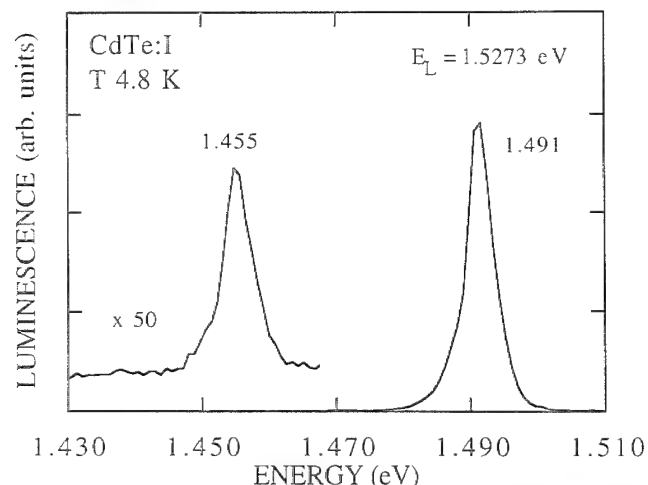


Fig. 2. Photoluminescence spectrum at 4.8K from CdTe:I epilayer using below-band-gap excitation at 1.5273 eV. Localized defect PL at 1.491 eV is accompanied by 36 meV phonon.

Sample temperature was controlled by flowing helium vapor across the sample surface in a Janis SuperVaritemp Dewar. The PL signals were detected with an Instruments SA HR-640 spectrometer and GaAs photomultiplier tube (PMT), and then analyzed with a lock-in amplifier. A Jobin-Yvon Ramanor U1000 double monochromator equipped with a GaAs PMT and photon counting electronics was used to obtain

micro-Raman spectra. In these latter experiments, the 488 nm excitation from an argon ion laser was focused on the sample surface to a spot diameter of about 10 microns using an Olympus BH-2 microscope.

Excitation PL studies were performed using a tunable Ti:sapphire laser (Spectra-Physics model 3900) with output wavelength recorded by an interferometric Burleigh WA-2100S Wavemeter. The sample temperature was maintained at about 10K for the excitation PL studies. The excitation PL signals were dispersed using a Spex 1000M monochromator and detected with a liquid-nitrogen-cooled germanium photodetector.

RESULTS AND DISCUSSION

Low-temperature PL spectra from heavily doped CdTe:I epilayers exhibit deep-level emission in the range from 1.40 to 1.49 eV. These emissions are related to compensating acceptor centers which limit the n-type doping. Figure 1 shows the deep-level PL spectrum at 4.8K for a sample with a room-temperature carrier concentration of $1.3 \times 10^{18} \text{ cm}^{-3}$. The data in Fig. 1a were excited using the above-band-gap 514.5 nm (2.41 eV) output from an Ar⁺ laser. A relatively sharp emission at 1.491 eV is the dominant feature, and a broad band showing several orders of phonon replicas extends from 1.47 to 1.40 eV. Figure 1b shows the spectrum recorded with the incident excitation energy provided by a Ti:sapphire laser tuned to 1.5914 eV, which is below the CdTe band gap but within the range to excite electrons to the shallow iodine donor levels. The intensity of the broad band increases, as is characteristic for distant donor-acceptor pair (DAP) recombination, while the 1.491 eV feature becomes much weaker.

A correlation of growth parameters with the 1.47 eV intensity⁶ shows the deep-level DAP band to be recombination between shallow I_{Te} donors and I_{Te} -cadmium vacancy complexes, or A centers ($V_{\text{Cd}} - I_{\text{Te}}$). The thermal quenching behavior of the integrated PL intensity of the DAP emission gave a value of 125 meV for the iodine A-center ionization energy, which is in good agreement with ionization energies reported for the chlorine A-center ($\sim 120 \text{ meV}$) in CdTe.⁷ The data in Fig. 1 clearly show that the 1.491 eV line is not related to isolated iodine donors.

To identify the nature of the 1.491 eV recombination band, we recorded a series of selective excitation spectra using below-band-gap excitation. Figure 2 shows the spectrum recorded at 4.8K with the incident photon energy tuned to 1.5273 eV, which is well below the iodine (D^0, h) energy in CdTe. The DAP emission is not observed with this low excitation energy. The 1.491 eV line, however, is easily seen and is accompanied by a phonon replica at about 1.455 eV with separation energy of $\sim 36 \text{ meV}$. This replica, or localized mode, was observed under excitation energies from 1.52 eV to near 1.49 eV. The average separation energy between the localized mode and the 1.491 eV PL line was 36.5 meV. This energy is

quite different from the LO phonon energy in CdTe of 21.3 meV.

Excitation PL spectra were recorded at Georgia Tech at sample temperatures of 10K. The data shown in Fig. 3a were recorded while the spectrometer monitored the PL emission at 1.488 eV, which is slightly below the 1.491 eV peak emission. There was no significant resonance as the incident laser light was scanned across the band gap energy at 1.606 eV, and thus this region is not shown explicitly in Fig. 3a. An increase in signal intensity was detected under 1.510 eV excitation, which is 22 meV above the monitoring energy. The data in Fig. 3b was recorded with the spectrometer fixed at 1.455 eV, which is the position of the 36 meV phonon replica. Again, an increase in signal intensity is observed for excitation at 1.510 eV. A slight resonance also is seen at 1.492 eV, corresponding to the main PL line. In both curves (a) and (b), there is a decrease in signal intensity at 1.514 eV. The origin of that decrease is not known at this time. The excitation spectrum recorded with the spectrometer monitoring a portion of the broad A-center DAP band is shown in Fig. 3c. In particular, the excitation spectrum in Fig. 3c was taken while monitoring the emission at 1.400 eV. There is clearly a resonance near the shallow (D^0 , h) energy at 1.59 eV, as expected for DAP recombination.

Returning to the question of the origin of the 1.491 eV emission, we note that it is relatively sharp and has a full-width-at-half-maximum of only 5 meV. Yet this emission is relatively deep, occurring at 115 meV less than the band gap energy. This localization energy is similar to that reported for the ($V_{Cd}-2Cl_{Te}$) neutral defect complex observed in chlorine-doped bulk CdTe.⁸ This neutral defect was described as a double deep acceptor, and localization energies in the range from 0.09 to 0.12 eV were obtained for different chlorine doping levels. Although we have clear evidence for the singly ionized acceptor ($V_{Cd}-I_{Te}$) in the heavily doped films included in our study, the observation of a 36 meV localized mode associated with the 1.491 eV PL strongly suggests that cadmium vacancies are not playing a role.

In addition to the iodine donor atoms, our previous work had revealed the presence of cation-site shallow acceptor impurities, i.e. sodium and/or lithium.⁶ Since the acceptor ionization energies associated with these two impurities are 58.7 and 58.0 meV for sodium and lithium, respectively, it is usually difficult to determine from PL methods which of the two impurity species is present. However, if we assign the 1.491 eV emission to a neutral defect ($A_{Cd}-I_{Te}$), where A represents an acceptor impurity species, we can predict the localized mode by invoking a simple linear diatomic chain model. Here, the force constant is assumed to be unaltered from that of the host lattice, since the defect is electrically neutral. An increased vibrational mode frequency (and thus increased energy) will be produced by a smaller cation impurity mass relative to cadmium. Both lithium and sodium satisfy this condition. Iodine is close to tellurium in mass, and thus is

expected to have negligible effect. The energy of the localized mode, E_{ph} , will depend⁹ on the reduced mass μ according to $E_{ph} \sim \sqrt{1/\mu}$, where $1/\mu = 1/M_1 + 1/M_2$. M_1 and M_2 are the cation-site and anion-site masses. The difference in mass between Na and Cd yields a localized mode of 37 meV, in excellent agreement with our data. The localized mode associated with the lithium impurity is too high in energy. We, therefore, assign the 1.491 eV PL to associate donor-acceptor pairs, consisting of nearest neighbor sodium and iodine atoms ($Na_{Cd}-I_{Te}$). The bright PL at 1.491 eV detected at liquid helium temperatures then is a signature of unintentional contamination with so-

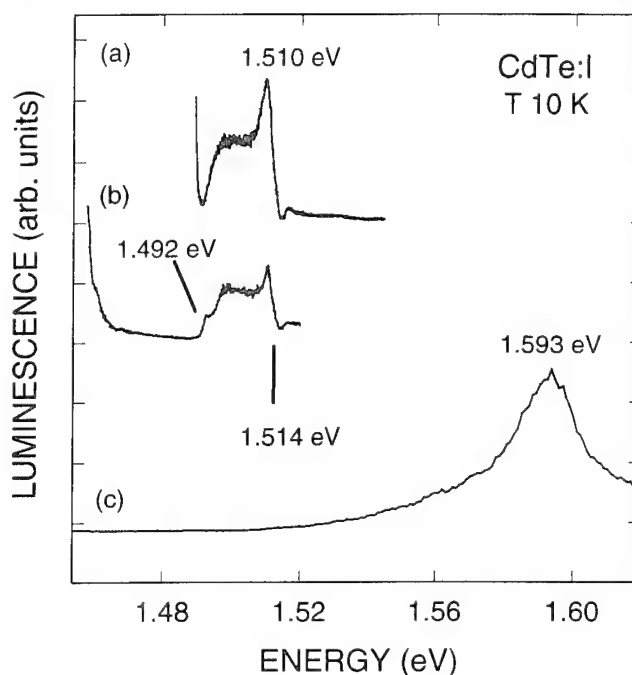


Fig. 3. Excitation PL spectra recorded (a) with spectrometer set to 1.488 eV, just below the maximum of the localized defect PL, (b) with spectrometer set to the localized mode at 1.455 eV, and (c) with spectrometer set to 1.400 eV.

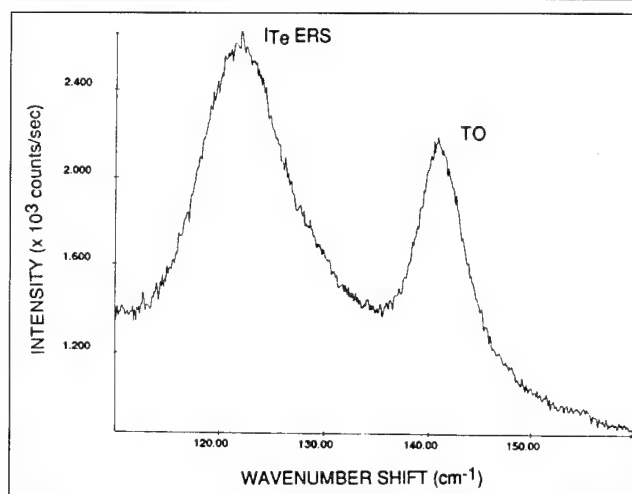


Fig. 4. Micro-Raman spectra at 296K from CdTe:I using 488 nm line from argon laser. Electronic Raman scattering signal due to donors is observed at ~ 122 cm^{-1} . The TO phonon is also observed.

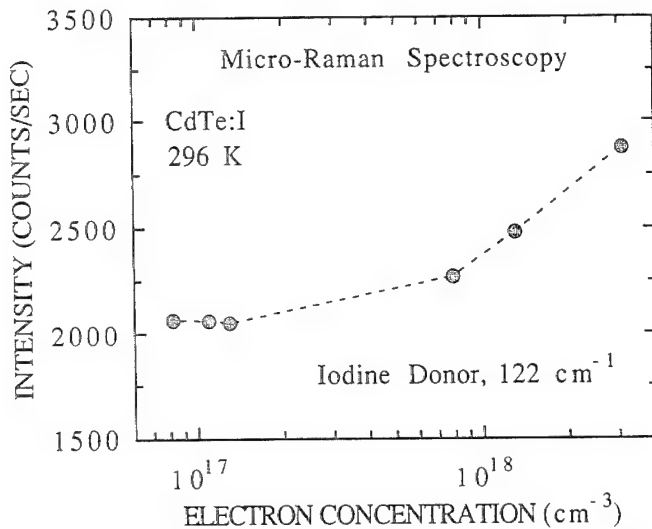


Fig. 5. Dependence of ERS intensity in CdTe:I epilayers on room-temperature carrier concentration.

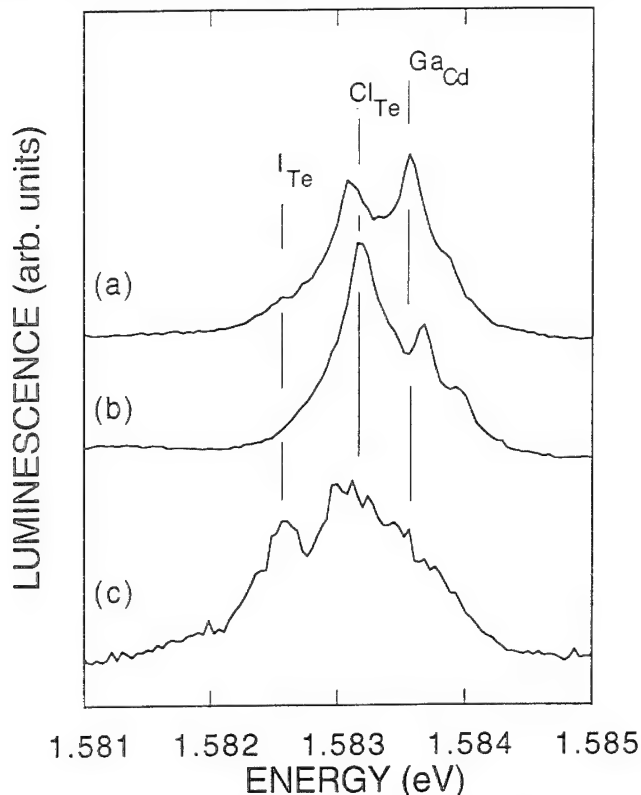


Fig. 6. Selective excitation of two-electron transitions associated with different donors in the CdTe:I epilayers. Incident laser energy was (a) 1.59397, (b) 1.59360, and (c) 1.59336 eV.

dium.

In addition to our study of compensating centers in iodine-doped CdTe, we have performed a series of experiments to more accurately determine the iodine donor ionization energy. Room temperature micro-Raman spectroscopy was used to detect the electronic Raman scattering (ERS) signal associated with the I_{Te} donor. A representative spectrum recorded from a sample exhibiting a room-temperature carrier concentration of $3.1 \times 10^{18} \text{ cm}^{-3}$ is shown in Fig. 4. The

backscattering geometry used in the micro-Raman experiments favors detection of transverse modes. The TO phonon of CdTe is seen at $\sim 142 \text{ cm}^{-1}$. An additional scattering peak is observed at 122 cm^{-1} . The intensity of the emission band at 122 cm^{-1} (15.1 meV) depended on carrier concentration in heavily doped epilayers, as shown in Fig. 5. This lower energy scattering signal is believed to be related to the scattering of light by electrons on donor atoms. This process usually involves electrons undergoing transitions among bound states¹⁰ and may require cryogenic sample temperatures for detection. The width of the ERS band observed at 296K from the CdTe:I epilayers suggests the overlap from several contributing levels. The peak position indicates the iodine donor energy is larger than the 14 meV hydrogenic donor energy normally reported for CdTe. For example, the indium donor ionization energy is 14.1 meV .⁴

We obtained further supporting evidence for a 15 meV ionization energy for isolated iodine donors by performing selective excitation PL experiments on lightly doped epilayers at liquid-helium temperatures. These low-doped epilayers ($n = 10^{14} - 10^{15} \text{ cm}^{-3}$) were grown on GaAs substrates. The liquid-helium PL spectra showed the free exciton emission to be shifted upward in energy to 1.5964 eV , about 1.0 meV higher than the bulk CdTe value. The origin for the increase in recombination energy is elastic strain due to the thermal and lattice mismatch between the CdTe and GaAs.

The output from a Ti:sapphire laser was tuned through the donor-bound exciton recombination region of the CdTe:I/GaAs epilayers. Selective excitation of two-electron transitions (TETs) is manifested by the appearance of sharp emission lines at energies below the bound exciton region given by the donor $1s \rightarrow 2s$ energy differences.⁴ Several distinct two-electron transition lines are observed as shown in Fig. 6 for an epilayer with a carrier concentration of $n = 4 \times 10^{14} \text{ cm}^{-3}$. The data in Fig. 6a was recorded under excitation at 1.59397 eV . Sharp emissions at 1.5836 and 1.5831 eV are produced. In Fig. 6b, excitation at 1.59360 eV results in a more dominant emission at 1.5831 eV . The data in Fig. 6c was recorded under excitation at 1.59336 eV , and a third emission at 1.5826 eV is produced.

As stated above, the PL recombination energies exhibited by the CdTe:I/GaAs epilayers are $\sim 1.0 \text{ meV}$ higher than the unstrained bulk CdTe values. To relate the three TET lines with donor impurities, we correct for the elastic-strain shift in excitonic recombination energies by normalizing the free exciton energy. Thus, an amount of 1.0 meV is subtracted from each of the three resonance emission peaks. The TET resonances thus occur at 1.5826 , 1.5821 , and 1.5816 eV . These emission energies agree well with the values reported⁴ for gallium (1.58272 eV), chlorine (1.58210 eV), and an unknown donor (1.58175 eV). The donor binding energies for gallium and chlorine are 13.8 and 14.5 meV , respectively. The

unknown donor binding energy was about 14.8 meV. The TET observed at the lowest energy in the iodine-doped epilayers is related to the iodine doping, and the 1.5816 eV peak position suggests a donor binding energy of about $15.0 (\pm 0.2)$ meV. The presence of trace amounts of Ga and Cl atoms, unintentionally introduced during growth, can be clearly established. Gallium has diffused from the substrate into the CdTe:I epilayers during growth. The source for chlorine is the tantalum injectors used in the gas source for doping.

SUMMARY

We have identified the origin for PL emission at 1.491 eV in heavily doped CdTe:I as being related to an associate donor-acceptor pair ($\text{Na}_{\text{Cd}} - \text{I}_{\text{Te}}$). This neutral defect exhibits an electronic energy quite distinct from the isolated Na_{Cd} acceptors and I_{Te} donors. It acts as a deep single acceptor with an energy level of 115 meV below the conduction band and has a localized mode of 36.5 meV.

In addition, we focused on determination of the iodine donor binding energy. Room-temperature Raman spectra revealed a peak at 122 cm^{-1} (15.1 meV) whose intensity depended on iodine doping level. We associate this scattering signal with donor electrons undergoing transitions from the ground state (1s) to excited states. To further support a 15 meV binding energy, we obtained two-electron transition spectra from lightly doped epilayers. After accounting for elastic-strain shifts in excitonic recombination energies, the iodine donor transition (1s \rightarrow 2s) appeared at 1.5816 eV. This corresponds to a larger substitutional donor energy (15.0 ± 0.2 meV) than has been reported for any specific donor impurity species in CdTe. Our

study shows that the hydrogenic donor energy for anion sites is closer to 15 meV, as compared with 14 meV for cation-site donors. An unknown donor was, however, observed at 1.5817 eV in bulk CdTe. It may be that the bulk samples were contaminated with iodine in that earlier study.

ACKNOWLEDGMENTS

This work was supported in part by the HgCdTe Flexible Manufacturing Program sponsored by ARPA, contract DAAB07-93-C-U504. The experiments performed at West Virginia University were also partially supported by the National Science Foundation through Grant DMR-9214350.

REFERENCES

1. D. Rajavel and C.J. Summers, *Appl. Phys. Lett.* 60, 2231 (1992).
2. Jaesun Lee, N.C. Giles, D. Rajavel and C.J. Summers, *Phys. Rev. B* 49, 1668 (1994).
3. N.C. Giles, Jaesun Lee, D. Rajavel and C. J. Summers, *J. Appl. Phys.* 73, 4541 (1993).
4. J.M. Francou, K. Saminadayar and J.L. Pautrat, *Phys. Rev. B* 41, 12035 (1990).
5. N.C. Giles, Jaesun Lee, T.H. Myers, Zhonghai Yu, B.K. Wagner, R.G. Benz II and C.J. Summers, *J. Electron. Mater.* 24, 691 (1995).
6. Jaesun Lee, N.C. Giles, D. Rajavel and C. J. Summers, submitted to *J. Appl. Phys.*
7. D.M. Hofmann, P. Omling, H.G. Grimmeiss, B.K. Meyer, K.W. Benz and D. Sinerius, *Phys. Rev. B* 45, 6247 (1992).
8. N.V. Agriskaya, M.V. Alekseenko, E.N. Arkad'eva, O.A. Matveev and S. V. Prokof'ev, *Sov. Phys. Semicond.* 9, 208 (1975).
9. For general discussion, see: Gerald Burns, *Solid State Physics* (Orlando: Academic Press, 1985), Chap. 12, p. 414.
10. M.V. Klein, *Topics in Applied Physics*, 8, ed. M. Cardona (New York: Springer-Verlag, 1975), p. 148.

Status of Te-Rich and Hg-Rich Liquid Phase Epitaxial Technologies for the Growth of (Hg,Cd)Te Alloys

H.R. VYDYANATH

GenCorp Aerojet, 1100 W. Hollyvale Street, Azusa, CA 91702

In this review, we summarize the progress to-date in the technology of $\text{Hg}_{1-x}\text{Cd}_x\text{Te}$ liquid phase epitaxial growth from Hg-rich and Te-rich solutions. Areas of research which need to be pursued to further improve the state of the art in device performance are discussed.

Key words: HgCdTe, liquid phase epitaxy (LPE), Hg-rich and Te-rich LPE

INTRODUCTION

The importance of $\text{Hg}_{1-x}\text{Cd}_x\text{Te}$ as an infrared detector material arises from the tailorability of the band gap from -0.3 eV for the semimetal HgTe to 1.6 eV for CdTe. Also, electrical and optical properties of this pseudobinary compound enable realization of a variety of devices which make it suitable for sensing in a wide spectral region ranging from the visible to beyond $30\text{ }\mu\text{m}$.¹

Liquid phase epitaxial growth (LPE) of $\text{Hg}_{1-x}\text{Cd}_x\text{Te}$ which has been in development since the late 1970s has been recently reviewed by Astles.² Specifics pertaining to Hg rich LPE have been summarized by Tung et al.^{3,4} and Kalisher et al.⁵ Gertner⁶ has discussed epitaxial growth of $\text{Hg}_{1-x}\text{Cd}_x\text{Te}$ including liquid phase epitaxy, vapor phase epitaxy, molecular beam epitaxy and electro epitaxy. A historical perspective of liquid phase epitaxy is presented in great detail in Ref. 5. Rather than repeat the subject matter presented in these excellent papers,¹⁻⁶ we defer the reader to them. Although for the sake of completeness and self-containment, it is impossible to avoid repetition of some of the subject matter already presented in these earlier publications, we hope the reader will benefit from discussion of certain technical details

which we present in this paper and which have not been covered earlier.

In this paper, we shall begin with a brief discussion of the relevant phase diagram details followed by the description of the LPE growth techniques currently in practice. Next, we shall discuss the state-of-the-art characteristics of the $\text{Hg}_{1-x}\text{Cd}_x\text{Te}$ epitaxial material which is attainable with LPE. Because of the importance of multiple layer heterostructure devices and external p-type doping, differences in the incorporation mechanisms of group V dopants for growths from Hg and Te-rich LPE growths will be presented. Recent diffusion work on arsenic doped $\text{Hg}_{1-x}\text{Cd}_x\text{Te}$ will also be covered. The status of the LPE photodiode technology will be briefly reviewed. Finally, areas of additional research which are needed to push the LPE technology further will be discussed; the discussion will include mention of research on silicon based alternate substrates, minimization of Te precipitates and dislocation density in the epitaxial layers and heterostructure interfaces, and finally we present some thoughts on the origin of the native defect related Shockley-Read centers in $\text{Hg}_{1-x}\text{Cd}_x\text{Te}$ and possible annealing conditions to minimize them.

PHASE DIAGRAM DATA

Epitaxial growth of solid $\text{Hg}_{1-x}\text{Cd}_x\text{Te}$ from liquid solutions can be accomplished from metal-rich, Te-

(Received November 10, 1994; revised March 4, 1995)

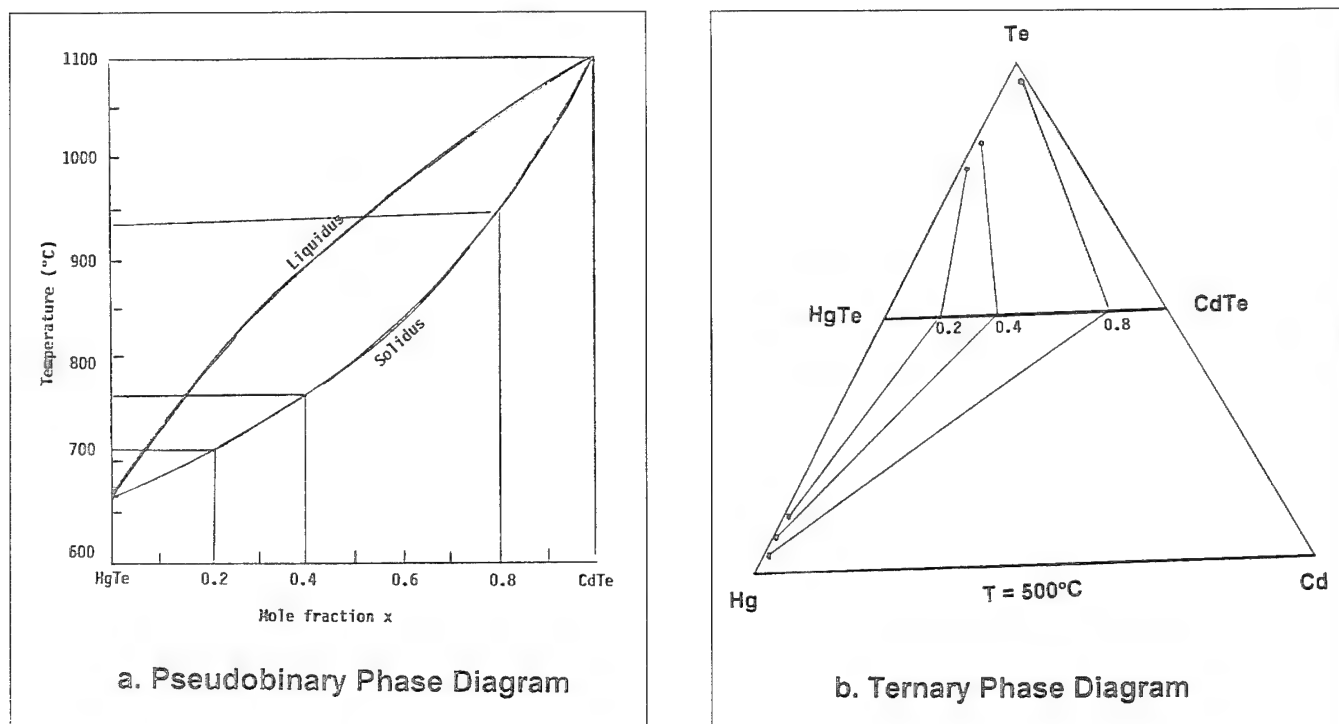


Fig. 1. Liquidus compositions for pseudobinary (Ref. 7) and ternary growths of $\text{Hg}_{1-x}\text{Cd}_x\text{Te}$.

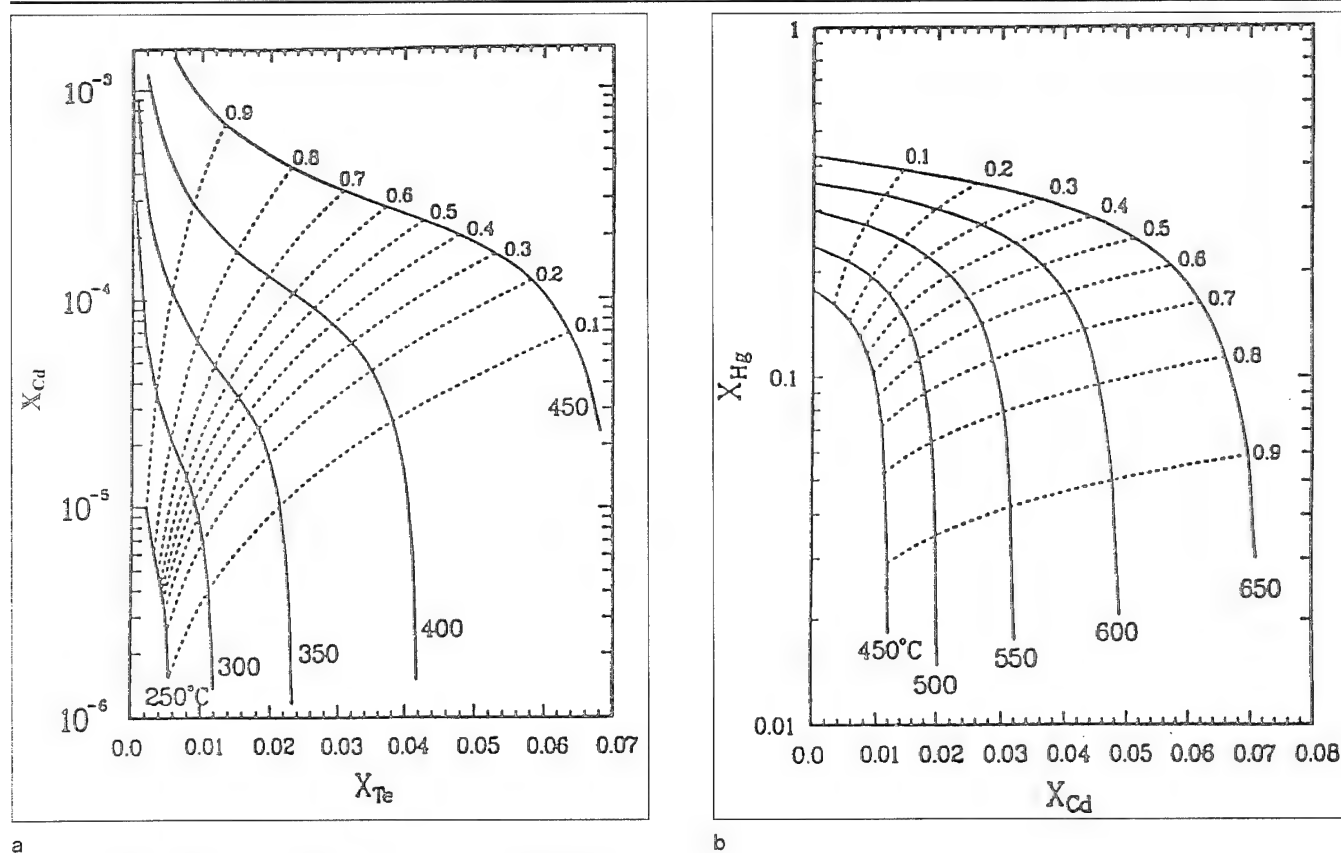


Fig. 2. Liquidus isotherms for Hg-rich (a) and Te-rich (b) growths (Ref. 8).

rich, and pseudobinary solutions. As shown in Fig. 1, for growths from pseudobinary solutions, the Te concentration is fixed at 50% (Fig. 1a).⁷ Hence epitaxial growths of $\text{Hg}_{1-x}\text{Cd}_x\text{Te}$ solids of compositions say $x =$

0.2, 0.4, and 0.8, can be accomplished from pseudobinary solutions only at certain fixed temperatures, whereas, these same growths can be accomplished from ternary solutions at various temperatures and

liquidus compositions. Figure 1b shows the compositions of the metal-rich and Te-rich ternary liquid solutions in equilibrium with $\text{Hg}_{1-x}\text{Cd}_x\text{Te}$ solids of compositions $x = 0.2, 0.4$ and 0.8 at $T \approx 500^\circ\text{C}$. Growths from ternary metal-rich and Te-rich solutions can be carried out at other temperatures also. Figures 2 to 3 show the phase diagram data taken from a recent review paper by Yu and Brebrick.⁸ Astles² provides an excellent list of all the references to the experimental data and theoretical calculations for the phase diagram issues in the Hg-Cd-Te system. Figure 2 shows the liquidus isotherms and solid solution iso concentration lines in the Hg-rich and Te-rich corners at various temperatures. As can be noted from the figure, $\text{Hg}_{1-x}\text{Cd}_x\text{Te}$ solid of composition $x = 0.2$ can be grown at $T = 450^\circ\text{C}$ from a Hg-rich solution containing Cd and Te corresponding to mole fractions $X_{\text{Cd}} = 10^{-4}$ and $X_{\text{Te}} = 0.06$ or from a Te-rich solution containing Hg and Cd with $X_{\text{Hg}} = 0.15$ and $X_{\text{Cd}} = 0.006$. Also evident is the fact that almost pure CdTe(s) grows out of very Hg-rich liquids.

Figure 3 shows the partial pressures of Hg, Cd, and Te_2 along the three phase curves for various $\text{Hg}_{1-x}\text{Cd}_x\text{Te}$ solids in equilibrium with liquid and vapor. At any particular temperature, the $\text{Hg}_{1-x}\text{Cd}_x\text{Te}$ solid coexists with the vapor comprising the constituent elements Hg, Cd, and Te_2 between the limits of partial pressure of Hg, Cd, and Te_2 indicated in Fig. 3. As can be seen from the figure, Hg is the predominant vapor species for almost all compositions of $\text{Hg}_{1-x}\text{Cd}_x\text{Te}$ even under Te-saturated solid solutions. Data presented in Fig. 3 are very essential to design any annealing experiments where the formation of a second phase is to be avoided.

LPE GROWTH TECHNIQUES

The basic principle underlying the growth of $\text{Hg}_{1-x}\text{Cd}_x\text{Te}$ solid from a Hg-rich or Te-rich solution is similar to that of growth of salt crystals from a saturated saline solution. Initially, a saturated solu-

tion of Hg and Cd dissolved in liquid Te (in the case of Te-rich LPE) or that of Cd and Te dissolved in liquid Hg (in the case of Hg-rich LPE) is prepared at a temperature T . This solution is then brought in contact with a substrate such as CdTe or (Cd,Zn)Te. The temperature is then lowered to $T - \Delta T$ so that Hg, Cd, and Te precipitate out of the growth solution onto the substrate. Next, the growth solution is removed leaving a thin crystalline film of $\text{Hg}_{1-x}\text{Cd}_x\text{Te}$ on the substrate. The task of bringing the growth solution and substrate into contact can be accomplished via tipping, dipping, and horizontal sliding techniques.

In the tipping technique, the growth solution and the substrate are held in a graphite boat. Initially, the boat is inclined to keep the growth solution and the substrate separate. The boat is then tipped to flow the growth solution over the substrate for film deposition. After the growth, the boat is tipped again to separate the substrate with the film of $\text{Hg}_{1-x}\text{Cd}_x\text{Te}$, from the growth solution.

In the dipping technique, prior to the initiation of growth, the substrate is held above the growth solution. The substrate is then dipped into the growth solution for $\text{Hg}_{1-x}\text{Cd}_x\text{Te}$ film deposition. After the film deposition, the substrate with the film is removed from the growth solution.

In the horizontal sliding technique, the substrate is held in a stator while the growth solution is held in a slider. To initiate the growth of the film, the slider is moved horizontally to position the growth solution over the substrate. After the growth of the $\text{Hg}_{1-x}\text{Cd}_x\text{Te}$ film, the slider is moved again horizontally to separate the growth solution from the substrate with the epitaxial film on top of it.

Because of the low solubility of Cd and Te in Hg solutions, liquid phase epitaxial growths from Hg-rich solutions require a large quantity of growth solution. Hence, Hg-rich LPE is restricted to growths via the dipping technique, whereas Te-rich LPE growth can be accomplished via any of the three techniques

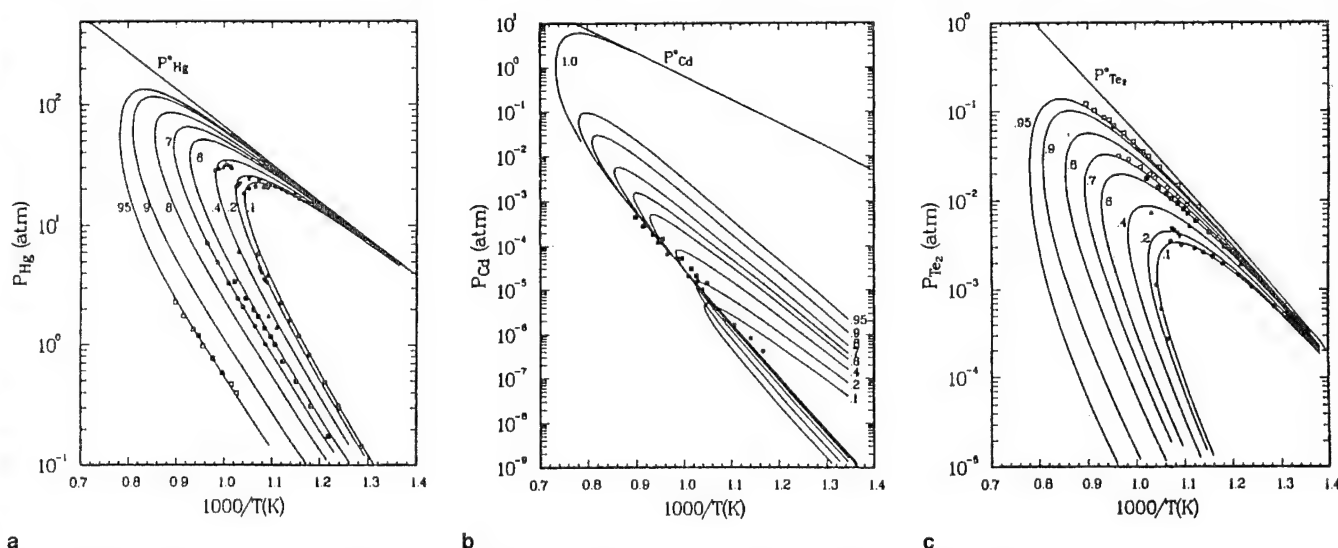


Fig. 3. Partial pressures of Hg (a), Cd (b) and Te_2 (c) along the three-phase curves for various x values of $\text{Hg}_{1-x}\text{Cd}_x\text{Te}$ (Ref. 8).

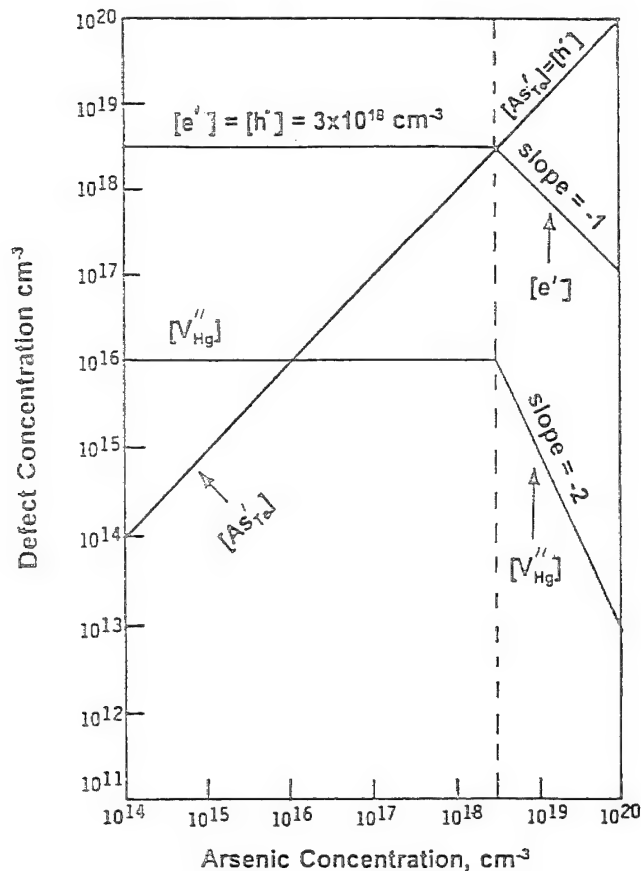


Fig. 4. Expected defect concentrations as a function of arsenic concentration at $T = 450^\circ\text{C}$ under Hg-saturated conditions for $\text{Hg}_{0.9}\text{Cd}_{0.2}\text{Te}$.

mentioned above. Because of the higher Hg pressures involved, growths from Hg-rich solutions need pressurized growth chambers with load locks.⁴ It should be noted that in situ, multilayer heterostructure growth can be more easily accomplished in the slider technique^{9,10} than in the vertical dipping technique.

For LPE growths from Te-rich solutions at 450 to 500°C , the Hg pressure over the growth solution would be a few tenths of an atmosphere. In the vertical dipping system, loss of Hg from the growth solution is suppressed by providing Hg vapor over the growth solution with a Hg reservoir source kept at a lower temperature.¹¹

In the horizontal slider technique such a Hg reservoir has been used by some researchers⁹ whereas others¹⁰ have reported using a HgTe reservoir kept close to the growth solution and in communication with it in the slider boat.

Review by Astles² provides a complete list of references on the various LPE growth techniques described above.

MATERIAL CHARACTERISTICS

In the last decade, outstanding progress has been achieved in the LPE growth of large area, device quality $\text{Hg}_{1-x}\text{Cd}_x\text{Te}$ material. For LPE growth from Hg-rich growth solutions, Tung et al.³ have reported growths of films larger than 32 cm^2 in area with

compositional uniformity of $x = 0.2093 \pm 0.0006$, thickness uniformity of $17.9 \pm 0.4\text{ }\mu\text{m}$ and compositional grading $\Delta x/\Delta t = 0.0018 \pm 0.0001/\mu\text{m}$; up to four of these films ($\sim 120\text{ cm}^2$) can be grown in a single growth run. Comparable compositional uniformity and compositional grading minimization have also been reported for growths from Te-rich solutions. Colombo and Westphal¹² have reported Te-rich LPE growths of $\text{Hg}_{1-x}\text{Cd}_x\text{Te}$ films in excess of 54 cm^2 area with $x = 0.2162 \pm 0.0007$ and $t = 65 \pm 3\text{ }\mu\text{m}$ over such large film areas. Edwall¹³ has reported $x = 0.447 \pm 0.002$ and $t = 13 \pm 1.6\text{ }\mu\text{m}$ over 44 cm^2 area $\text{Hg}_{1-x}\text{Cd}_x\text{Te}$ films grown from Te-rich solutions on sapphire substrates with a layer of CdTe grown by metalorganic chemical vapor deposition (MOCVD) technique. Pultz¹⁴ has reported Te-rich LPE growth of $\text{Hg}_{1-x}\text{Cd}_x\text{Te}$ with $x = 0.169 \pm 0.003$ over 24 cm^2 film areas. Compositional uniformity of $x = 0.2285 \pm 0.0005$ and thickness uniformity of $t = 12.3 \pm 1.3\text{ }\mu\text{m}$ over 6 cm^2 areas have been reported by Edwall¹³ for Te-rich growths on (Cd,Zn)Te substrates using the horizontal slider technique. Absence of capability to stir the growth solution in a slider boat appears to give poorer film thickness uniformity compared to that obtained in the dipping technique.

Very good control of n-type doping has also been reported for both Hg-rich and Te-rich LPE growths. Near 100% donor efficiency has been reported for indium concentrations of up to 10^{17} cm^{-3} .^{4,15} This result is not surprising since the intrinsic carrier concentration is on the order of 10^{18} cm^{-3} ¹⁶ at $T = 450$ to 500°C and only when indium exceeds that concentration will the indium begin to get compensated by Hg vacancies V''_{Hg} and indium-Hg vacancy ($\text{In}_{\text{Hg}}V''_{\text{Hg}}$) pairs.¹⁷ For growths from Te-rich solutions, Colombo et al.¹⁵ have reported excellent reproducibility of indium doping with average concentration of $5.1 \pm 1.9 \times 10^{14}\text{ cm}^{-3}$ and average electron mobility of $1.33 \pm 0.38 \times 10^5\text{ cm}^2/\text{vs}$ at 77 K for a cut off wavelength of $9.86 \pm 0.35\text{ }\mu\text{m}$. Vydyanath et al.¹⁸ have been able to get reproducibility of indium doping concentrations of $6 \pm 1.5 \times 10^{14}\text{ cm}^{-3}$ in nearly a hundred sequentially grown films with average electron mobility of $1.5 \pm 0.5 \times 10^5\text{ cm}^2/\text{vs}$ for a cut off wavelength of $\lambda_{\text{co}} = 10\text{ }\mu\text{m} \pm 0.5\text{ }\mu\text{m}$.

Crystalline quality of films grown from both Te-rich and Hg-rich solutions has been found to be very good. For Hg-rich LPE growth, Kalisher et al.⁵ have reported x-ray rocking curve FWHM less than 40 arcs on the average (silicon four-crystal monochromator, beam size = $1 \times 7.5\text{ mm}^2$) over a film area of 30 cm^2 . They also reported EPD in the films to be the same as that of the lattice matched CdZnTe substrate $\sim 3 \times 10^5\text{ cm}^{-2}$. For Te-rich LPE growths, Colombo and Liao¹⁹ have reported etch pit density ranging from 5×10^4 to $2 \times 10^5\text{ cm}^{-2}$. Also for Te-rich LPE growths, Edwall¹³ has reported EPD of 3×10^4 to $5 \times 10^5\text{ cm}^{-2}$.

Auger limited carrier lifetime has been reported in n-type $\text{Hg}_{1-x}\text{Cd}_x\text{Te}$ material (for $n > 5 \times 10^{14}\text{ cm}^{-3}$) grown from both Te-rich and Hg-rich solutions. For growths from Te-rich solutions, Reine et al.,²⁰ Chen and Colombo²¹ and Edwall¹³ report carrier lifetimes in

excess of $1 \mu\text{s}$ at $T = 77\text{K}$ for $x = 0.21$ to 0.24 and $n \approx 10^{15} \text{ cm}^{-3}$.

In general, for growths from both Te-rich and Hg-rich solutions, carrier lifetime in intentionally doped p-type material has been found to be higher than that in vacancy doped material.²² For Hg-rich growths, Tung et al.³ have reported radiative limited carrier lifetime in arsenic doped $x = 0.3$ material. It has been argued by this group of researchers^{4,5} that the arsenic doping in their material improves the carrier lifetime because of the reduction of native acceptor defects through the mass action effect. Intrinsic carrier concentration in $x = 0.2$ material is on the order of $3 \times 10^{18} \text{ cm}^{-3}$ ¹⁶ at a temperature of 450°C ~ close to the temperature of LPE growth from Hg-rich solutions and only when the arsenic concentration is in excess of $3 \times 10^{18} \text{ cm}^{-3}$ will the crystals become extrinsic. Only after the crystals become extrinsic, the Hg vacancy concentration decreases with increasing arsenic concentration proportional to $[\text{As}]^{-2}$ (Fig. 4). Although the intrinsic carrier concentration for $x = 0.3$ material at $T = 450^\circ\text{C}$ is not known, for the reduction of Hg vacancies via the mass action effect, the intrinsic carrier concentration has to be less than 10^{17} cm^{-3} at $T = 450^\circ\text{C}$. We conjecture that the increase in carrier lifetime due to arsenic doping in their crystals^{4,5} on the order of 10^{17} cm^{-3} and less may not be because of the reduction in the concentration of Hg vacancies via the mass action effect, but simply because of the reduction of all native defects including Hg vacancies subsequent to a low temperature Hg-rich anneal after crystal growth.

DEFECT ANNEALING BEHAVIOR OF LPE FILMS

In principle, point defects may be generated at the interface of the $\text{Hg}_{1-x}\text{Cd}_x\text{Te}$ epitaxial layer and the substrate because of interdiffusion effects and because of the presence of misfit dislocations at the interface which upon climb can act as sources and sinks of point defects. Thus, it is fruitful to examine if the annealing behavior of LPE grown $\text{Hg}_{1-x}\text{Cd}_x\text{Te}$ is different from that of bulk grown material.

Figure 5 shows the 77K hole concentration in unintentionally doped $\text{Hg}_{1-x}\text{Cd}_x\text{Te}$ crystals as a function of the partial pressure of Hg for temperatures ranging from 150 to 655°C . The hole concentration in the crystals is assumed to arise from the native acceptor defects incorporated in the material at the temperature of equilibration.^{16,23} The experimental data shown in the figure for temperatures of 400°C and higher have been taken from bulk crystals and the data for temperatures of equilibration of 400°C and lower have been gathered from LPE films grown from Te-rich solutions. The solid lines in the figure correspond to calculations assuming values of mass action constants for the intrinsic excitation and for the process of a Hg atom leaving the lattice to go into the vapor along with creation of a doubly ionized Hg vacancy and release of two holes to the valence band.¹⁶ The fact that a single set of these mass action constants can

explain the annealing data for LPE films at $T \leq 400^\circ\text{C}$ and for bulk crystals at $T \geq 400^\circ\text{C}$ attests to the fact that the annealing behavior of LPE films is essentially similar to that of bulk grown crystals. Obviously, results shown in Fig. 5 appear to indicate that interdiffusion effects occurring in the epitaxial layers do not affect the carrier concentration at levels of 10^{15} cm^{-3} or higher.

INCORPORATION OF GROUP V ELEMENT ACCEPTOR DOPANTS FOR GROWTHS FROM Hg-RICH AND Te-RICH SOLUTIONS

Replacement of native acceptor defect doping with external acceptor dopants from group I or group V has been of much interest²⁴ because these dopants may be expected to be single acceptors with only one energy level in the forbidden gap, close to the valence band edge whereas the native acceptor defects in $\text{Hg}_{1-x}\text{Cd}_x\text{Te}$ are doubly ionized and the second level could lie close to the middle of the gap and be a potential source of Shockley-Read type recombination centers. Thus, $\text{Hg}_{1-x}\text{Cd}_x\text{Te}$ doped with external p-type dopants which are only singly ionized and whose levels lie close to the valence band edge, when prepared under conditions such that the concentration of the native defects is reduced to a minimum, may indeed have far fewer Shockley-Read type centers than the crystal doped with native defects.

P-type doping with group I or group V elements is also essential in the fabrication of high performance p-on-n photodiodes in multilayer heterostructures.²⁵⁻³³ The only way one can fabricate them is with the use of an external acceptor dopant in the wider band gap layer and a donor dopant in the optically active base layer and to reduce the native acceptor defect concentration to well below the concentration of the dopants. Group I elements are expected to be fast diffusers in $\text{Hg}_{1-x}\text{Cd}_x\text{Te}$ and may result in p-n junctions that are not stable over long periods of time. On the other hand, the large size of the group V elements and hence the low diffusivity of these elements are expected to result in stable and well controlled p-n junctions.

It is for the reasons cited above that it is important to understand the incorporation of group V dopants during LPE growths from Te-rich and Hg-rich solutions.

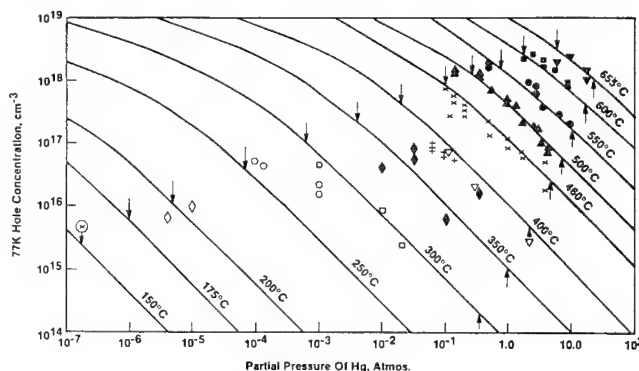
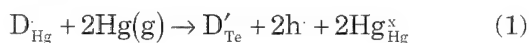


Fig. 5. Comparison of defect anneal results for bulk grown $\text{Hg}_{0.8}\text{Cd}_{0.2}\text{Te}$ crystals with those grown from Te-rich solutions (Ref. 23).

Table I. Electrical Data Showing Evidence of the Amphoteric Behavior of Group V Dopants in $\text{Hg}_{0.7}\text{Cd}_{0.3}\text{Te}$ Films Grown from Te-Rich Solutions³⁴

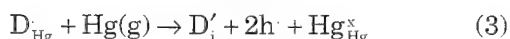
Film No.	Comp.	Dopant and Conc. in the Te-Rich Growth Solution, At. %	200°C Hg-Saturated Anneal		200°C Hg-Saturated Anneal with a 500°C Hg-Saturated Preanneal	
			$ N_A - N_D \text{ cm}^{-3}$ (Variable Temp R_H)	77K Hall Mobility cm^2/Vs	$ N_A - N_D \text{ cm}^{-3}$ (Variable Temp R_H)	77K Hall Mobility cm^2/Vs
109	0.31	P, 0.8	4×10^{16} p type	186		
133	0.30	P, 0.09	1.7×10^{15} n type	3.3×10^4	1×10^{16} p type	111
134	0.30	P, 0.2	2×10^{15} p type	328	4×10^{16} p type	210
100	0.29	As, 1	1.5×10^{14} n type	1.8×10^3	4.4×10^{15} p type	176
121	0.31	As, 10	6×10^{14} n type	1.4×10^4	1.2×10^{17} p type	292
103	0.30	Sb, 0.7	2×10^{13} n type	1.2×10^4	4.5×10^{14} n type	3.7×10^3
117	0.30	Sb, 1.0	1.6×10^{15} p type	172	1×10^{16}	304
118	0.33	Sb, 10.0	4×10^{14} n type	3.6×10^3	1.3×10^{17} p type	196
107	0.29	Bi, 0.95	7×10^{14} n type	4.4×10^4	6×10^{14} n type	2.2×10^4
132	0.27	Bi, 8.7	1×10^{16} n type	2.2×10^4	1.6×10^{15} n type	7.8×10^4
146	0.24	Bi, 0.006	2×10^{15} n type	7.3×10^4	1×10^{15} n type	4.5×10^4
147	0.28	Bi, 0.06	1.6×10^{15} n type	4.2×10^4	9×10^4 n type	3.4×10^4

For growths from Hg-rich solutions near 100% acceptor efficiency has been established for arsenic concentrations of up to high 10^{17} cm^{-3} .³ From a detailed study of the mechanisms of incorporation and behavior of group V dopants for growths from Te-rich solutions, Vydyanath et al.,³⁴⁻³⁶ inferred that all the films doped with group V elements were n-type after a 250°C Hg-rich anneal subsequent to growth. However, these films when subjected to a high temperature preanneal at 500°C under Hg-saturated conditions followed by a 250°C anneal under Hg-saturated conditions showed conversion from n-type to p-type. (Table I). This result led them to conclude that the group V dopants behave amphotERICALLY in epitaxial $\text{Hg}_{1-x}\text{Cd}_x\text{Te}$ grown from Te-rich solutions. They argued that the group V elements P, As, Sb, and Bi are incorporated as donors ($\text{P}_{\text{Hg}}, \text{As}_{\text{Hg}}, \text{Sb}_{\text{Hg}}, \text{Bi}_{\text{Hg}}$) under Te-rich (or Hg-deficient) conditions of growth. Because of the low diffusivity of these elements, subsequent anneal at 200°C under Hg-rich conditions only decreases the concentration of the native acceptor defects without moving these group V atoms from the Hg lattice sites to Te lattice sites. Under conditions of anneal at 500°C under Hg-saturated conditions, they argued that there was enough thermal energy for the transfer of the group V elements from Hg lattice sites to Te or interstitial lattice sites where they act as acceptors. The relevant site transfer reactions and corresponding mass action constants are:



$\text{D} \equiv \text{P, As, Sb, or Bi}$

$$K_{\text{D}_{\text{Hg}}, \text{D}'_{\text{Te}}} = \frac{[\text{D}'_{\text{Te}}][\text{h}]^2}{[\text{D}_{\text{Hg}}]p_{\text{Hg}}^2} \quad (2)$$



$\text{D} \equiv \text{P, As, Sb, or Bi}$

$$K_{\text{D}_{\text{Hg}}, \text{D}'_{\text{i}}} = \frac{[\text{D}'_{\text{i}}][\text{h}]^2}{([\text{D}_{\text{Hg}}]p_{\text{Hg}})^2} \quad (4)$$

The inability to convert Bi-doped films to p-type even with a 500°C Hg-saturated preanneal (Table I) was argued to be due either to the very low diffusivity—lower than that of P, As, and Sb—or to the much lower values of the equilibrium constants $K_{\text{D}_{\text{Hg}}, \text{D}'_{\text{Te}}}$, or $K_{\text{D}_{\text{Hg}}, \text{D}'_{\text{i}}}$ for the site transfer of Bi compared to the values of these same constants for P, As, and Sb.

Finally, the distribution coefficients of the group V elements for growths from Te-rich solutions were evaluated and are shown in Fig. 6 along with the data for growths from Hg rich³⁷ and pseudobinary solutions.³⁸ From the results shown in the figure, it can be noted that the distribution coefficient of group V elements for growth from Te-rich solutions is orders of magnitude lower than that for growths from Hg-rich solutions. This difference was attributed by Vydyanath et al.³⁴ to the activity coefficient of the group V elements being orders of magnitude lower in Te-rich solutions than in Hg-rich solutions.

Amphoteric behavior of arsenic in LPE grown $\text{Hg}_{1-x}\text{Cd}_x\text{Te}$ also finds support from the diffusion work of Chandra et al.³⁹ and Bubulac et al.⁴⁰ Chandra et al.³⁹ found the diffusion coefficient of arsenic to increase with decreasing Hg pressure providing evidence for movement of arsenic via Hg lattice sites. Shaw⁴¹ has analyzed the diffusion data for arsenic in $\text{Hg}_{1-x}\text{Cd}_x\text{Te}$ and has calculated the ratios of the concentration of arsenic donors occupying metal lattice sites to that of arsenic acceptors occupying Te lattice sites (Fig. 7). Shaw's analysis also confirms our earlier findings of the amphoteric behavior of arsenic³⁴⁻³⁶ and the intrinsic behavior of $\text{Hg}_{0.8}\text{Cd}_{0.2}\text{Te}$ ^{16,23,35} at $T \geq 350^\circ\text{C}$ and dopant concentrations $< \text{mid } 10^{18} \text{ cm}^{-3}$. Analysis of this type is extremely useful for the fabrication of p-n junctions with optimum characteristics using arsenic as a dopant in $\text{Hg}_{1-x}\text{Cd}_x\text{Te}$.

LPE Hg_{1-x}Cd_xTe DEVICE TECHNOLOGY STATUS

Hg_{1-x}Cd_xTe LPE technology has matured to a stage of production. Mosaic arrays with pixel densities as large as 1024 × 1024 have been reported in short wavelength infrared (SWIR) (Hg,Cd)Te grown on sapphire substrates from Te-rich solutions;⁴² this technology has also demonstrated mid wavelength infrared (MWIR) arrays with pixel densities as large as 640 × 480.⁴³ Pixel densities as large as 480 × 640 have been reported in LPE long wavelength infrared (LWIR) (Hg,Cd)Te grown from Hg-rich solutions.³ Mosaic arrays with pixel densities ranging from 128 × 128 to 256 × 256 are routinely produced in both Hg-rich and Te-rich LPE grown structures in all spectral bands ranging from SWIR to LWIR regions.⁴⁴⁻⁵¹ Very long wavelength HgCdTe detectors with cut off wavelengths in excess of 18μm have been demonstrated.⁵²⁻⁵⁵ Work cited in Refs. 26, 3, 45, and 53 attests to the production readiness of the multiple layer heterostructure photodiode technology from Hg-rich and Te-rich LPE technologies.

Triple layer heterostructures with capability to produce dual band detector arrays which are sensitive in both mid wave and long wave bands have been developed using Hg-rich LPE.^{3,56}

LPE technology as its state-of-the-art currently stands, can satisfy requirements for most technology applications where device operation at $T \geq 77K$ is needed.

AREAS OF ONGOING RESEARCH

Although LPE Hg_{1-x}Cd_xTe technology is currently capable of providing large density arrays with performance uniformity and operability in excess of 90%, more work is needed to push these limits of performance and operability to near 100%. A significantly larger fraction of work is also needed in pushing the state-of-the-art in the performance uniformity and operability for operation at lower and lower temperatures for sensing and detection under conditions of significantly lower background photon fluxes. Improvements are needed in the material technology to increase the device performance at temperatures where devices become limited by generation-recombination (g-r) centers and tunneling centers. To increase the performance of the devices to near diffusion current limited values in the multilayer heterostructures, improvements in the following critical areas are needed:

- Minimized heterostructure interface dislocation density.
- Minimized extraneous impurities and precipitates in bulk and at heterostructure interface.
- Improved substrate crystalline quality.
- Minimized undesirable native defects in bulk and heterostructure interfaces.

Liquid phase epitaxial growth of (Hg,Cd)Te on an alternate substrate such as silicon is another area of

important research. Difference in the thermal coefficient of expansion between HgCdTe and silicon is a source of problem for large density, large area indium bump bonded hybrids of HgCdTe devices and silicon readout chips particularly when these hybrids have to be thermally cycled. It is believed that this problem can be circumvented by growing HgCdTe directly on silicon and hybridizing to silicon readout chips. This would also make it possible to fabricate much larger area HgCdTe device arrays because of the commercial availability of very large area defect free silicon substrates. In fact, an LWIR HgCdTe mosaic array in a 480 × 640 format has already been demonstrated in LPE material grown from Hg-rich solutions.⁴⁵

Using metalorganic chemical vapor deposition techniques, Kalisher et al.⁵ have grown a thin layer of CdZnTe—on commercially available GaAs/Si wafers—subsequent to which, an LPE HgCdTe layer has been grown from Hg-rich solutions. Research is continuing

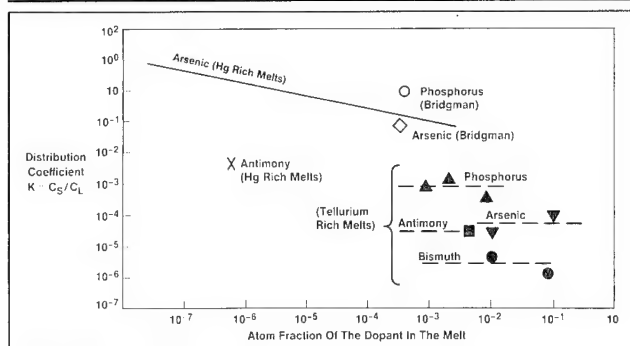


Fig. 6. Distribution coefficient data for group V dopants for growths from Hg-rich, Te-rich, and pseudobinary growths (Ref. 34).

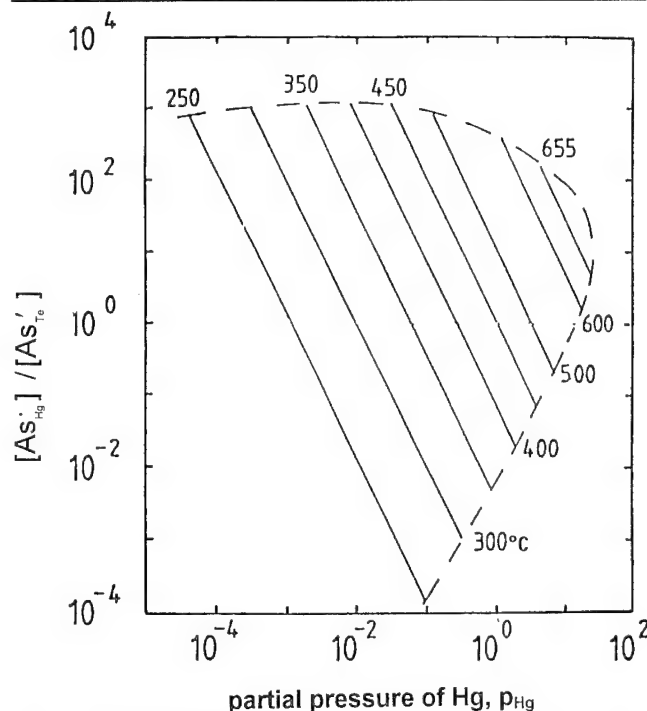


Fig. 7. Calculated ratio of the concentration of arsenic donors ($[As_{Hg}]$) and arsenic acceptors ($[As'_{Te}]$) as a function of temperature and partial pressure of Hg (Ref. 41).

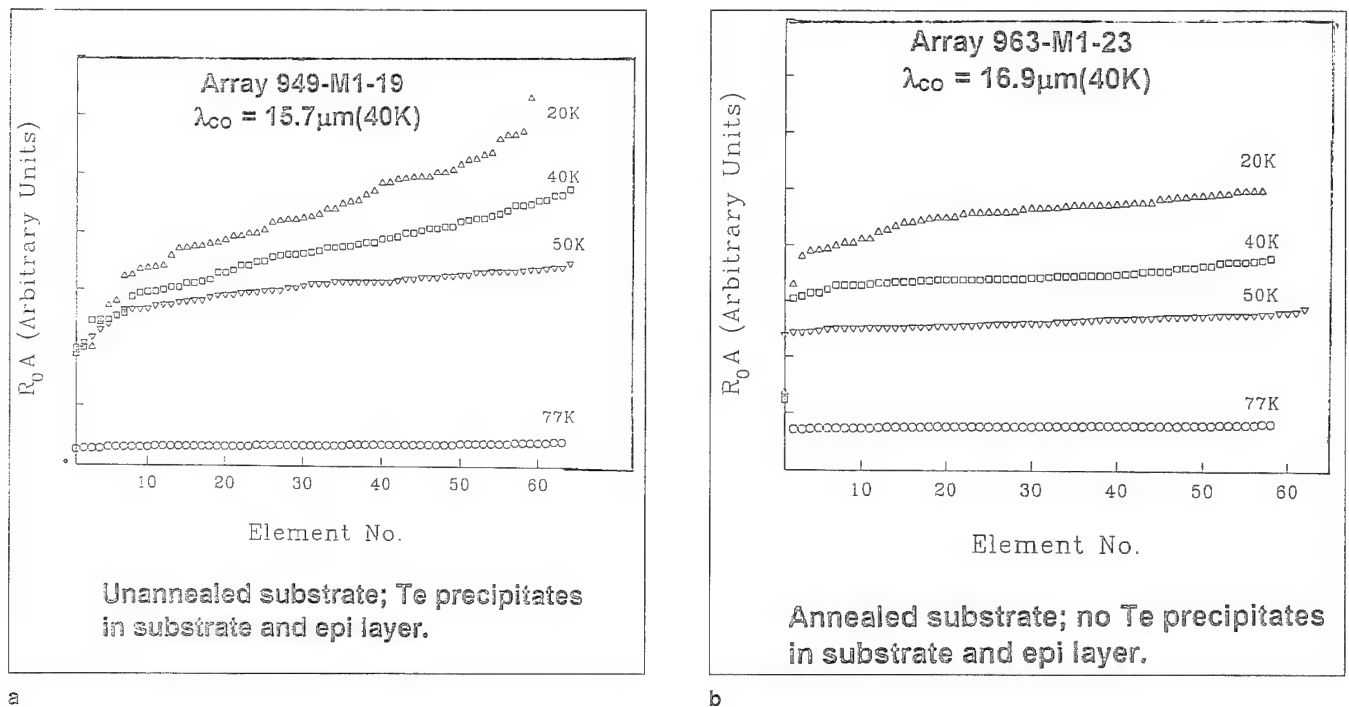


Fig. 8. Demonstration of improved R_0A performance uniformity in devices fabricated in $Hg_{1-x}Cd_xTe$ films grown on annealed (Cd,Zn)Te substrates with no Te precipitates (Ref. 61).

in this area in an attempt to reduce the defect density in silicon based alternate substrates.

Minimization of Heterostructure Interface Dislocation Density

There is ample evidence in literature showing correlation of dislocation density in $Hg_{1-x}Cd_xTe$ epitaxial layers with that of substrates on which these layers are grown. Takigawa et al.⁵⁷ have shown near one-to-one correlation of etch pit density ranging from $<10^5$ cm^{-2} to near 10^7 cm^{-2} of the epitaxial layers with that of the CdTe and CdZnTe substrates. Chandra et al.⁵⁸ have also reported such a correlation.

Takigawa et al.⁵⁷ have also shown correlation of etch pit density with compositional gradient of the heterostructure interface with higher dislocation density in the epitaxial layers with higher compositional grading. Also etch pit density variations as a function of distance from interface indicate the highest density at the interface going up to 10^8 cm^{-2} and dropping to low to mid 10^5 cm^{-2} a few microns on either side of the interface. Lattice matched CdZnTe substrate has yielded the lowest densities of dislocations at the heterostructure interface.⁵⁷

Minimization of Te Precipitates in Substrates and Epitaxial Layers

Wada and Suzuki⁵⁹ have reported on the direct correlation of etch pit density in the substrates with density of Te precipitates.

Vydyanath et al.^{60,61} have developed a step annealing procedure which minimizes the density of Te precipitates in CdTe and CdZnTe substrates. They have also identified thermomigration of liquid Te precipitates in a temperature gradient where these

precipitates move to a region of higher temperature as the principally operative mechanism responsible for the annihilation of the precipitates. They have demonstrated correlation of the presence of Te precipitates in epitaxial layers with that in substrates. Using the step annealing recipe they have demonstrated reduction of Te precipitates in substrates and epitaxial layers.

Finally, they have demonstrated improved device performance uniformity at 40K by reducing Te precipitates in epitaxial layers (Fig. 8). Their work⁶¹ suggests that Te precipitates probably act as generation-recombination centers and also may assist in tunneling thereby producing excessive dark currents in the photodiodes.

It is well established in literature that interdiffusion coefficient between heterostructure layers of $Hg_{1-x}Cd_xTe$ and $Hg_{1-y}Cd_yTe$ depends on composition and increases with decrease in Cd concentration.⁶² This could result in the creation of Te precipitates at the heterostructure interfaces via the Kirkendall effect.⁶³ Based on the fact that Cd diffuses faster in HgTe than Hg does in CdTe, we show in Fig. 9 (schematic) the formation of Te precipitates at the two heterostructure interfaces in a two layer (Hg,Cd)Te heterostructure grown on CdTe or (Cd,Zn)Te substrates.

As can be noted from the figure, Te precipitates will form on the sides of the interface having the larger Cd concentration. The charge states of the diffusing species are also indicated in the figure. It should also be noted that these precipitates can be given rise to, by the climb of dislocations occurring during interdiffusion between the heterostructure layers.

Origin of Native Defect Related Shockley-Read Centers

It is well established in literature⁶⁴ that the minority carrier lifetime in p-type $\text{Hg}_{1-x}\text{Cd}_x\text{Te}$ decreases with increase in Hg vacancy concentration, suggesting that either the Hg vacancy or another native defect whose concentration is coupled to that of the Hg vacancy acts as the Shockley-Read center in limiting the carrier lifetime below the radiative limit. Expression for the single level Shockley-Read limited minority carrier lifetime is given by

$$T_e = T_{no} [1 + \exp(E_F - E_t)/kT] \quad (5)$$

where
$$T_{no} = \frac{1}{C_n N_t}$$

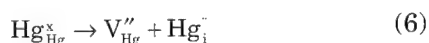
C_n : Capture cross section of electrons; N_t : trap density; E_F : Fermi energy; E_t : trap energy. Examination of Eq. (1) shows that if

$$E_F = E_t, T_e = 2 T_{no} = \frac{2}{C_n N_t} \neq f(\text{temperature})$$

if all traps are ionized.

What this means is that in a temperature range where Hg vacancies are completely ionized and the Fermi level is pinned at the energy level of the Hg vacancies, a temperature independent carrier lifetime should result. Experimental results in literature (Ref. 64) indicate otherwise, thus leading to the inference that Hg vacancies themselves are not the traps but another native defect whose concentration is tied to the concentration of the Hg vacancies—because of the way the crystal is prepared. Indeed, examination of the way in which the crystals have been prepared to vary the Hg vacancy concentration, lends support to our hypothesis. The $\text{Hg}_{1-x}\text{Cd}_x\text{Te}$ samples with different concentrations of Hg vacancies are all prepared under Hg-saturated conditions with the crystals exposed to the highest temperature showing the highest Hg vacancy concentrations. If so, it appears that Hg interstitials whose concentration would track with the concentration of Hg vacancies could be the Shockley-Read centers.

Also, the concentration of the Hg interstitials would be orders of magnitude lower than that of the Fermi level pinning Hg vacancies and thus would explain the temperature dependence of the minority carrier lifetime. The concentrations of Hg interstitials and Hg vacancies are coupled via the Frenkel reaction



where a neutral Hg atom Hg_{Hg}^x occupying a Hg lattice site goes into an interstitial site acting as a double donor Hg_i^+ and leaving behind a vacant lattice site of Hg which acts as a double acceptor V_{Hg}'' . The mass action constant for the Frenkel Reaction (6) is given by

$$K_F'' = \frac{[V_{\text{Hg}}''] [\text{Hg}_i^+]}{[\text{Hg}_{\text{Hg}}^x]} \quad (7)$$

In terms of definition of site fractions indicated by []

$$(\text{square brackets}) [] = \frac{\text{\# of cm}^{-3}}{\text{Total \# of lattice sites}}$$

$[\text{Hg}_{\text{Hg}}^x] \approx 1$ because most of the Hg lattice sites are occupied.

$$\therefore K_F'' = [V_{\text{Hg}}''] [\text{Hg}_i^+] \quad (8)$$

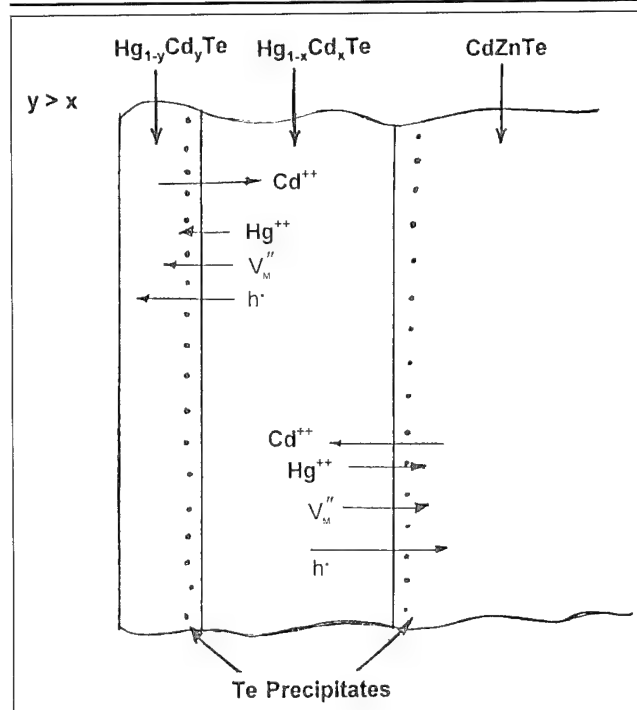


Fig. 9. Compositional interdiffusion and Te precipitate formation near heterostructure interfaces in multilayer $\text{Hg}_{1-x}\text{Cd}_x\text{Te}$ films.

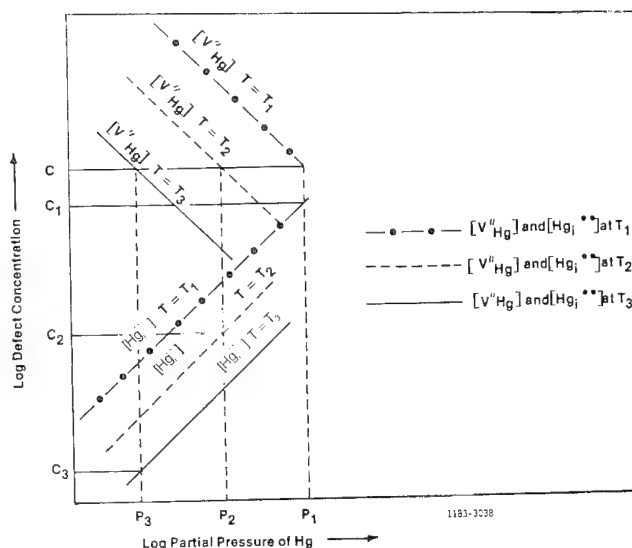


Fig. 10. Variation of the concentrations of Hg vacancies (V''_{Hg}) and Hg interstitials (Hg_i^+) as a function of the partial pressure of Hg in $\text{Hg}_{1-x}\text{Cd}_x\text{Te}$ at different temperatures (schematic).

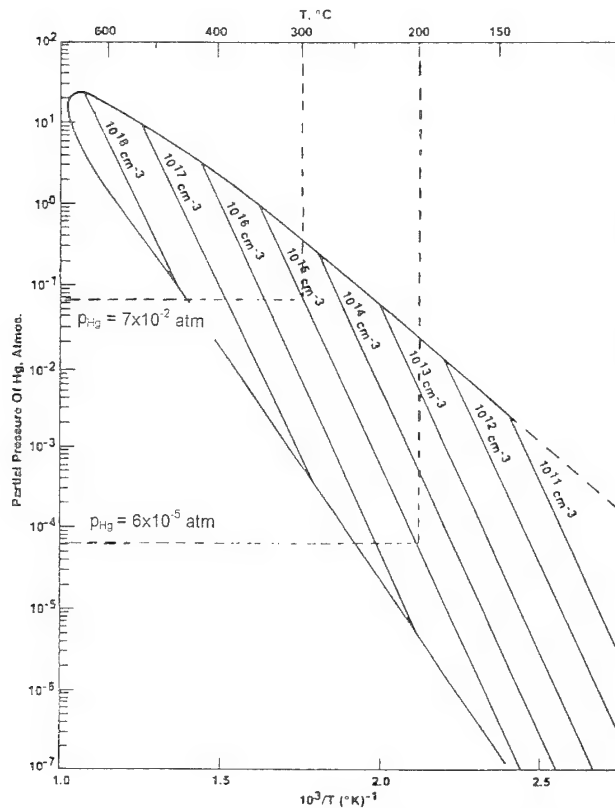


Fig. 11. Iso-hole concentration plot for $\text{Hg}_{0.8}\text{Cd}_{0.2}\text{Te}$ indicating possibility of obtaining identical hole concentration for anneals at two different temperatures and partial pressures of Hg.

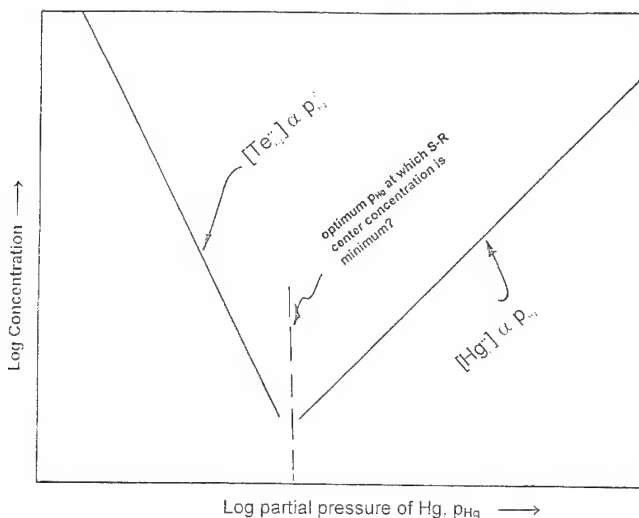


Fig. 12. Variation (schematic) of the concentrations of Hg interstitials (Hg_{\cdot}) and Te antistructure defects (Te_{Hg}) as a function of partial pressure of Hg at a fixed temperature of anneal.

It should be noted that K_F'' is only dependent on temperature and not on partial pressure of Hg. Thus, at a fixed temperature, the value of K_F'' is fixed and when the partial pressure of Hg is varied, the concentrations of V_{Hg}'' and Hg_{\cdot} change in a way that the product of their concentrations remains a constant. Thus, in the samples prepared at higher temperatures under Hg saturated conditions, higher will be the value of K_F'' and higher will be the concentration

of both Hg vacancies and Hg interstitials. Based on this argument, it is easy to see that $\text{Hg}_{1-x}\text{Cd}_x\text{Te}$ samples could be prepared at different temperatures say T_1, T_2, T_3 ($T_1 > T_2 > T_3$), and partial pressures of Hg - p_1, p_2, p_3 ($p_1 > p_2 > p_3$) with the same Hg vacancy concentration C , but with different Hg interstitial concentrations C_1, C_2 , and C_3 ($C_1 > C_2 > C_3$) (Fig. 10); samples prepared at the lowest temperature and lowest Hg pressure would have the lowest concentration of Hg interstitials. If Hg interstitials are the Shockley-Read centers, the minority carrier lifetime in samples prepared at the lowest temperature should be higher than that in samples prepared at the highest temperature even though the Hg vacancy concentration in both samples is the same. Figure 11 shows that in $\text{Hg}_{0.8}\text{Cd}_{0.2}\text{Te}$ crystals a vacancy concentration of $\sim 10^{15} \text{ cm}^{-3}$ can be obtained either with an anneal at $T = 300^\circ\text{C}$ and $p_{\text{Hg}} = 7 \times 10^{-2} \text{ atm}$ or with an anneal at $T = 200^\circ\text{C}$ and $p_{\text{Hg}} = 6 \times 10^{-5} \text{ atm}$, the concentration of Hg interstitial donors with the lower temperature anneal being lower.

The situation may be more complicated than presented here because of the possible occurrence of other sorts of native defects, one example of which is an antistructure donor defect such as Te_{Hg}^m ,^{65,66} where m is an integer representing the degree of ionization of the defect; m can, in principle, take on values from 1 through 4.²³

It can be shown that concentration of these antistructure defects varies as p_{Hg}^{-2} irrespective of their charge state as long as the intrinsic carriers dominate the electroneutrality condition in the crystals²³ and hence as the partial pressure of Hg is decreased, to decrease the concentration of Hg interstitials, the concentration of Te antistructure donor defects increases. Although their concentration is not high enough to be a major species in the charge balance in the crystal, their concentration at low Hg pressures could become significant enough to affect the carrier lifetime. Thus, if Te antistructure defects also could be potential Shockley-Read centers, the optimum preparation condition may be one where the crystal is treated at an intermediate Hg pressure such that the concentration of both Hg interstitial donors and Te antistructure donors is a minimum (Fig. 12). Irrespective of whether the material is p-type or n-type, reduction of these native defect related Shockley-Read centers in the material is expected to result in the improvement of the device performance.

SUMMARY

We have reviewed the state of the art in $\text{Hg}_{1-x}\text{Cd}_x\text{Te}$ material characteristics the current LPE technology is capable of providing from Hg-rich and Te-rich solutions. Areas of ongoing research essential for further development of the technology are discussed.

ACKNOWLEDGMENT

We wish to thank several researchers from various laboratories for generously providing information and advice on material reported in this work. We are

particularly indebted to Drs. T. Tung and S. Johnson of Hughes Santa Barbara Research Center, CA; L. Colombo of Texas Instruments, TX; P. Norton and M. Reine of Loral, MA; and D. Edwall of Rockwell Science Center, CA.

REFERENCES

1. *Semiconductors and Semi-metals*, 18, ed. R.K. Willardson and A.C. Beer (New York: Academic Press, 1981).
2. M.G. Astles, *Properties of Narrow Gap Cadmium-Based Compounds*, emis data reviews series No. 10 P., ed. P. Capper (U.K.: INSPEC, 1994), p. 13.
3. T. Tung, L.V. De Armond, R.F. Herald, P.E. Herning, M.H. Kalisher, D.A. Olson, R.F. Risser, A.P. Stevens and S.J. Tighe, *Proc. SPIE (USA)* 1735, 109 (1992).
4. T. Tung, M.H. Kalisher, A.P. Stevens and P.E. Herning, *Mater. Res. Soc. Symp.* 90, 321 (1987).
5. M.H. Kalisher, P.E. Herning and T. Tung, Submitted to *Progress in Crystal Growth and Characterization* (to be published in 1995).
6. E.R. Gertner, *Ann. Rev. Mat. Sci.* 15, 303 (1985).
7. M.F.H. Micklethwaite, *Semiconductors and Semimetals*, 18, ed. R.K. Willardson and A.C. Beer (New York: Academic Press, 1981), p. 49.
8. T.-C. Yu and R.F. Brebrick, *Properties of Narrow Gap Cadmium-Based Compounds*, emis data reviews series No. 10, ed. P. Capper (U.K.: INSPEC, 1994), p. 55.
9. T.C. Harman, *J. Electron. Mater.* 9, 945 (1980).
10. Y. Nemirovsky, S. Margalit, E. Finkman, Y. Shacham-Diamond, I. Kidron, *J. Electron. Mater.* 11, 133 (1982).
11. S.G. Parker, D.F. Weirauch and D. Chandra, *J. Cryst. Growth* 86, 173 (1988).
12. L. Colombo and G.H. Westphal, *Proc. SPIE (USA)* 2228, 66 (1994).
13. D. Edwall (Rockwell, unpublished).
14. G. N. Pultz (Loral, unpublished).
15. L. Colombo, G.H. Westphal, P.K. Liao, M.C. Chen and H.F. Schaake, *Proc. SPIE (USA)* 1683, 33 (1992).
16. H.R. Vidyantath, *J. Elec. Chem. Soc.* 128, 2609 (1981).
17. H.R. Vidyantath, *J. Elec. Chem. Soc.* 128, 2619 (1981).
18. H.R. Vidyantath and J. Ellsworth, (Aerojet, unpublished).
19. L. Colombo and P.K. Liao, *Proc. SPIE (USA)* 1307, 568 (1990).
20. M.B. Reine, K.R. Maschhoff, S.P. Tobin, P.W. Norton, J.A. Mrczkowski and E.F. Krueger, *Semicon. Sci. Technol.* 8, 788 (1993).
21. M.C. Chen and L. Colombo, *J. Appl. Phys.* 72, 4761 (1992).
22. Y. Nemirovsky and R. Fastow, *Properties of Narrow Gap Cadmium-Based Compounds*, emis data reviews series No. 10, ed. P. Capper (U.K.: INSPEC, 1994), p. 233.
23. H.R. Vidyantath and C.H. Hiner, *J. Appl. Phys.* 65, 3080 (1989).
24. C.E. Jones, K. James, J. Merz, R. Braunstein, M. Burd, M. Eetemadi, S. Hutton and J. Drumheller, *J. Vac. Sci. Technol. A* 3, 131 (1985).
25. C.C. Wang, M. Chu, S.H. Shin, W.E. Tennant, J. T. Cheung, M. Lanir, A.H.B. Van der Wyck, G.M. Williams, L.O. Bubulac and R.J. Eisel, *IEEE Trans. Electron Devices* ED-7, 154 (1980).
26. C.C. Wang, *J. Vac. Sci. Technol. B* 9, 1740 (1991).
27. M. Lanir and K.J. Riley, *IEEE Trans. Electron Dev.* ED-29, 274 (1982).
28. P.R. Bratt, *J. Vac. Sci. Technol. A* 1 1687 (1987).
29. P.S. Nayar, P.B. Ward, P. C. Colter, S.R. Hampton, J.W. Slawinski, L. Fishman, C.M. Callahan and H.R. Vidyantath, *Technical Digest* (San Francisco, CA: IEDM, 1984), p. 385.
30. R.A. Reidel, E.R. Gertner, D.D. Edwall and W.E. Tennant, *Appl. Phys. Lett.* 46, 64 (1985).
31. H.R. Vidyantath, P.B. Ward, S.R. Hampton, L. Fishman, J. Slawinsky, C. Devaney, J. Ellsworth and T. Krueger, *Proc. SPIE (USA)* 686, 12 (1986).
32. K. Kosai and W.A. Radford, *J. Vac. Sci. Tech. A* 8 (2), 1254 (1990).
33. H.R. Vidyantath, P.B. Ward, S.R. Hampton, J.B. Parkinson and B. Klank, *Proc. SPIE (USA)* 1097, 111 (1989).
34. H.R. Vidyantath, J.A. Ellsworth and C.M. Devaney, *J. Electron. Mater.* 16, 13 (1987).
35. H.R. Vidyantath, *J. Vac. Sci. Technol. B (USA)* 9, 1716 (1991).
36. H.R. Vidyantath, *Semicond. Sci. Technol.* 5, S213 (1990).
37. M.H. Kalisher, *J. Cryst. Growth* 70, 365 (1984).
38. P. Capper, J.J.G. Gosney, C.L. Jones and I. Kenworthy, *J. Cryst. Growth* 71, 57 (1985).
39. D. Chandra, M.W. Goodwin, M.C. Chen and J.A. Dodge, *J. Electron. Mater.* 22, 1033 (1993).
40. L.O. Bubulac, D.D. Edwall and C.R. Viswanathan, *J. Vac. Sci. Technol. B* 9, 1695 (1991).
41. D. Shaw, *Semicond. Sci. Technol.* 9, 1729 (1994).
42. L.J. Kozlowski, K. Vural, S.C. Cabelli, A. Chen, D.E. Cooper, D.M. Stephenson and W.E. Kleinhaus, *Proc. SPIE (USA)* 2268, (1994). (To be published.)
43. L.J. Kozlowski, B. Bailey, S.A. Cabelli, D.E. Cooper, I.S. Gergis, C.A. Chen, W.V. McLevige, G.L. Bostrup, K. Vural and W.E. Tennant, *Optical Engineering* 33 (1), 54 (1994).
44. P.R. Norton, *Optical Engineering* 30 (11), 1655 (1991).
45. P.R. Norton, *Proc. SPIE (USA)* 2274 (1994). (To be published.)
46. L.J. Kozlowski, K. Vural, V.H. Johnson, J.K. Chen, R.B. Bailey and D. Bui, *Proc. SPIE* 1308, 202 (1990).
47. R.B. Bailey, L.J. Kozlowski, J. Chen, D.Q. Bui, K. Vural, D.D. Edwall, R.V. Gil, A.B. Vanderwyck, E.R. Gertner and M.B. Gubala, *IEEE Trans. Electron Devices* ED-38, 1104 (1991).
48. L.J. Kozlowski, W.V. McLevige, S.A. Cabelli, A.H.B. Vanderwyck, D.E. Cooper, E.R. Blazejewski, K. Vural and W.E. Tennant, *Optical Engineering* 33 (3) (1994).
49. L.J. Kozlowski, S.A. Cabelli, D.E. Cooper and K. Vural, *Proc. SPIE* 1946, 199 (1993).
50. D.E. Cooper, D.Q. Bui, R.B. Bailey, L.J. Kozlowski and K. Vural, *Proc. SPIE* 1946, 170 (1993).
51. R.E. DeWames, J.M. Arias, L.J. Kozlowski and G.M. Williams, *Proc. SPIE* 1735, 2 (1992).
52. E.E. Krueger, G.N. Pultz, K.R. Maschhoff, S.P. Tobin, P.W. Norton, J.H. Rutter and M.B. Reine, *Mat. Res. Soc. Symp. Proc.* 299 (1993).
53. E.E. Krueger, G.N. Pultz, P.W. Norton, J.A. Mroczkowski, M.H. Weiler and M.B. Reine, *Mat. Res. Soc. Symp. Proc.* 216, 93 (1991).
54. G.N. Pultz, P.W. Norton, E.E. Krueger and M.B. Reine, *J. Vac. Sci. Technol. B* 9, 1724 (1991).
55. M.B. Reine, K.R. Maschhoff, S.P. Tobin, P.W. Norton, J.A. Mroczkowski and E.E. Krueger, *Semicond. Sci. Technol.* 8, 788 (1993).
56. J.A. Wilson, E.A. Patten, G.R. Chapman, K. Kosai, B. Baumgratz, P. Goetz, R. Risser, R. Herald, W.A. Radford, T. Tung and W.A. Terre, *Proc. SPIE* 2274 (1994). (To be published.)
57. H. Takigawa, M. Yoshikawa and T. Mackawa, *J. Cryst. Growth* 86, 446 (1988).
58. D. Chandra, J.H. Tregilgas and M.W. Goodwin, *J. Vac. Sci. Tech. B* 9, 1852 (1991).
59. M. Wada and J. Suzuki, *Jpn. J. Appl. Phys.* 6, L972 (1988).
60. H.R. Vidyantath, J.A. Ellsworth, J.J. Kennedy, B. Dean, C.J. Johnson, G.T. Neugebauer, J. Sepich and P.K. Lias, *J. Vac. Sci. Technol. B* 10, 1476 (1992).
61. H.R. Vidyantath, J.A. Ellsworth, J.B. Parkinson, J.J. Kennedy, B. Dean, C.J. Johnson, G.T. Neugebauer, J. Sepich and P.K. Lias, *J. Electronic Mater.* 22, 1073 (1993).
62. M.F.S. Tang and D.A. Stevenson, *Appl. Phys. Lett. (USA)* 50, 1272 (1987).
63. V. Leute and W. Stratmann, *Z. Phys. Chem.* 90, 172 (1974).
64. V.C. Lopes, A.J. Syllaios and M.C. Chen, *Semicond. Sci. Tech.* 8, 824 (1993).
65. M.A. Berding, M. van Schilfgaarde and A. Sher, *Phys. Rev. B* 50, 1519 (1994).
66. M.A. Berding, A. Sher and M. van Schilfgaarde, *J. Electron. Mater.* 24, 1129 (1995).

Te-Rich Liquid Phase Epitaxial Growth of HgCdTe on Si-based Substrates

F.T. SMITH, P.W. NORTON, P. LO VECCHIO, N. HARTLE, and
M. WEILER

Loral Infrared and Imaging Systems Inc., Two Forbes Rd, Lexington,
MA 02173

N.H. KARAM

Spire Corporation, One Patriots Park, Bedford, MA 01730

S. SIVANANTHAN and Y.P. CHEN

Microphysics Laboratory, Physics Department, University of Illinois at
Chicago, P.O. Box 4348, Chicago, IL 60680

The growth of high quality {111}B oriented HgCdTe layers on CdZnTe/GaAs/Si and CdTe/Si substrates by Te-rich slider liquid phase epitaxy (LPE) is reported. Although the {111} orientation is susceptible to twinning, a reproducible process yielding twin-free layers with excellent surface morphology has been developed. The electrical properties and dislocation density in films grown on these substrates are comparable to those measured in HgCdTe layers grown on bulk CdTe substrates using the same LPE process. This is surprising in view of the large lattice mismatch that exists in these systems. We will report details of both the substrate and HgCdTe growth processes that are important to obtaining these results.

Key words: Heteroepitaxy, HgCdTe, liquid phase epitaxy (LPE)

INTRODUCTION

Silicon-based substrates are attractive for HgCdTe detector arrays because they offer a lower cost, greater mechanical strength, improved thermal expansion match to the Si readout circuit and a more easily scaled manufacturing process when compared with the use of bulk CdTe or CdZnTe substrates.¹⁻³ We will report the growth of high quality {111}B oriented HgCdTe layers on organometallic vapor phase epitaxy (OMVPE)-grown CdZnTe/GaAs/Si and molecular beam epitaxially (MBE) grown CdTe/Si substrates by the use of a Te-rich slider liquid phase epitaxy (LPE) process. A potential problem associated with Si-based substrates is the higher dislocation density expected as a result of the 19% lattice parameter difference between CdTe and Si. A second potential difficulty is

contamination of the HgCdTe by components of the substrate such as Ga or Si. In order for epitaxial HgCdTe layers to be useful for photovoltaic detector arrays, the residual electrically active impurity concentration should be below 2×10^{15} atoms/cm³ and the dislocation density should be below 1×10^6 /cm².

Although the large lattice parameter mismatch between CdTe and GaAs is potentially a problem, it is reduced to 0.7% along one of the <112> directions of the substrate if the CdTe layer takes up the (111) orientation when grown on (100) oriented GaAs.³ A disadvantage of this orientation is that it has been reported that {111} oriented layers of CdTe are extensively twinned, even when grown on CdTe substrates.⁴ Fortunately, we have found, as the case for growth on bulk GaAs substrates,⁵ the use of CdZnTe/GaAs/Si or CdTe/Si substrates tilted a few degrees away from the (100) orientation suppresses twin growth in the CdTe, so that layers with no twin planes intersecting the

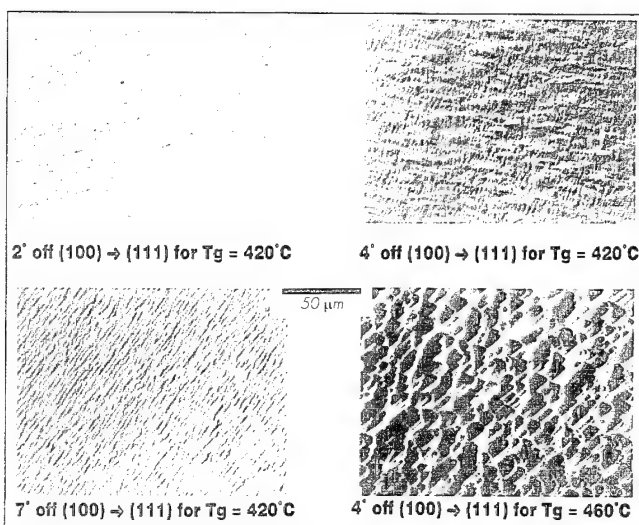


Fig. 1. CdZnTe surface morphology for various Si substrate orientations and deposition temperatures.

CdTe surface, and no twins penetrating the HgCdTe layer, are obtained.⁶

Contamination of HgCdTe layer could result from diffusion of Ga or Si through the CdZnTe or CdTe layer, but we will show that diffusion is sufficiently slow that no appreciable penetration of these elements into the HgCdTe layer occurs during the LPE process. On the other hand, the problem of contamination by these substrate materials from the melt during LPE growth is serious because both GaAs and Si are highly soluble in the Te-rich melt, and Ga and Si are easily incorporated into the growing HgCdTe. Arsenic is much less readily incorporated into HgCdTe from a Te-rich melt so that the GaAs layer is not a significant As impurity source. It is, therefore, necessary to totally encapsulate the substrate outside the growth area to prevent contamination of the melt, using an impervious surface coating or mechanical masking scheme. We will show that the high temperature oxidation of Si produces a very effective encapsulant for this purpose.

RESULTS AND DISCUSSION

Substrates

The substrates used were 2×3 cm rectangles cut from 3" diameter Si wafers. The cutting operation resulted in some chipping of the wafer edges, as well as sharp edges that made conformal coating with an encapsulant difficult. The wafer edges were therefore rounded, either by mechanical abrasion followed by polishing with a diamond slurry or, preferably, by use of a chemical polishing etch. The wafers were then oxidized in a dry oxygen flow at 950°C to give an approximately 150 nm thick oxide coating on all surfaces. A rectangular window was opened in the front side of the wafer by masking the back side plus a 1 or 2 mm wide strip around the perimeter of the wafer with resist, then removing the oxide using hydrofluoric acid solution. Substrate oxidation, photolithography and oxide etching steps were carried

out at Spire Corporation

If a GaAs buffer layer was to be used as an intermediate layer between the CdTe and Si, it was deposited on the Si by OMVPE using trimethylgallium and arsine to a thickness of 0.5 to 2.0 μm , at a reactor pressure of about 76 Torr. These thin GaAs layers were specular and free of cracks. During deposition of the GaAs layer some polycrystalline GaAs specks deposited on the exposed SiO_2 border around the substrate. The average GaAs thickness on the encapsulant was much less than that on the single crystal area, that is the deposition was somewhat selective. The degree of selectivity increased at a high deposition temperature, and for thin GaAs deposits. We will discuss the importance of achieving a high degree of selectivity below.

Deposition of CdZnTe was carried out by OMVPE using a large "pancake" type reactor at Spire Corporation, the Spire model 3000G. The organometallics used were dimethylcadmium, diethylzinc, and dimethyltellurium. The reactor pressure was maintained at 650 Torr. The CdTe/Si wafers were subjected to a brief high temperature bake at about 600°C for 12 m before carrying out the CdZnTe deposition at 420 to 460 °C. The CdZnTe layer was deposited to a thickness of $8 \pm 1 \mu\text{m}$, the Zn concentration was $3 \pm 1.5\%$.

The CdZnTe morphology was found to vary strongly with substrate tilt angle and tilt direction, deposition temperature, and pressure. The surfaces of layers deposited at 420 and 460°C onto substrates tilted 4° toward the Si $\langle 111 \rangle$ direction are shown in Fig. 1. The morphology, uniformity, and orientation of these CdZnTe layers have been described in detail previously.⁶ Recent growth experiments at a lower pressure (300 Torr) have resulted in smoother CdZnTe surfaces. During deposition of the CdZnTe polycrystalline material deposited on the encapsulant around the edges of the wafer, covering the GaAs that had also deposited there.

In addition to affecting the CdZnTe morphology, the Si substrate tilt angle away from the (100) plane was found to affect the growth of twins in the CdZnTe layer. Only lamellar twins with boundaries parallel to the substrate surface were detected either by x-ray or electron diffraction or in cross sections examined by transmission electron microscopy (TEM), in organometallic vapor phase epitaxy CdZnTe layers grown on substrates tilted more than two degrees away from (100).⁶ These lamellar twins do not present a problem for subsequent growth of twin-free HgCdTe layers since no twin boundaries intersect the substrate surface. Lamellar twins were found to be confined more closely to the CdZnTe/GaAs interface as the tilt angle increased, the near-surface region being twin free for a 7 μm thick CdZnTe layer grown on a substrate with a tilt angle of greater than 4°.

Substrates for LPE growth of HgCdTe were also prepared by direct growth of CdTe layers about 8 μm thick onto Si substrates without an intermediate GaAs layer. Silicon substrates with an orientation

tilted about one degree away from (100) were encapsulated as described above and then used for the MBE growth of CdTe layers. Molecular beam epitaxial growth was carried out at the University of Illinois at Chicago. The CdTe grew in an approximately (111)B orientation. X-ray diffraction showed only a small number of lamellar twins close to the CdTe/Si interface. The CdTe surfaces were smooth and specular with at most only a very slight dimpled texture visible at 500X using Nomarski contrast. As with OMVPE growth, polycrystalline deposits of CdTe grew on the SiO₂ encapsulant around the periphery of the substrate, except on the outermost 0.5 mm where growth was shadowed by the substrate holder.

LPE Growth of HgCdTe

Liquid phase epitaxial growth of Hg_{0.79}Cd_{0.21}Te was carried out from a Te-rich melt at about 490°C. The slider method was used with a graphite slider system of conventional design. After heating the system to a few degrees above the intended growth temperature, the melt was saturated by sliding a CdTe wafer underneath it and holding it there for more than 60 m. The CdTe wafer was then slid away from the melt and the melt cooled so as to cause a few degrees of supersaturation. The substrate was then slid under the melt and growth began immediately as a result of the supersaturation. The melt was cooled by a few degrees during an approximately 30 m growth time, after which the substrate was slid away from the melt and the system was cooled to room temperature. The growth sequence and temperature program were controlled by computer.

The surface morphology of the HgCdTe was strongly influenced by the substrate orientation. Figure 2 shows micrographs of the surfaces of 15 to 20 µm thick layers of HgCdTe on both CdTe/Si and Cd_{0.97}Zn_{0.03}Te/GaAs/Si substrates using a Nomarski phase contrast objective. For small tilt angles, one or two degrees, distinct terracing was seen, with the tear-drop shaped features characteristic of heavily terraced LPE surface. For a tilt angle of four degrees a regular wavy appearance was seen, the difference in height from crest to trough, measured with a laser profilometer, is 0.5 to 1 µm. For a tilt angle of seven degrees the surface showed no regular features and was smoother than for a four-degree tilt.

In early experiments using CdZnTe/GaAs/Si substrates, substantial contamination of the melt and of the HgCdTe occurred even though as much as 5°C of supersaturation was used. Electrical measurements

and secondary ion mass spectroscopy (SIMS) analysis showed Ga contamination was occurring at the 10¹⁷ atoms/cm³ to 10¹⁸ atoms/cm³ level, along with Si contamination at a similar level. The SIMS profiles indicated a contamination level that increased toward the wafer surface, clearly establishing that the

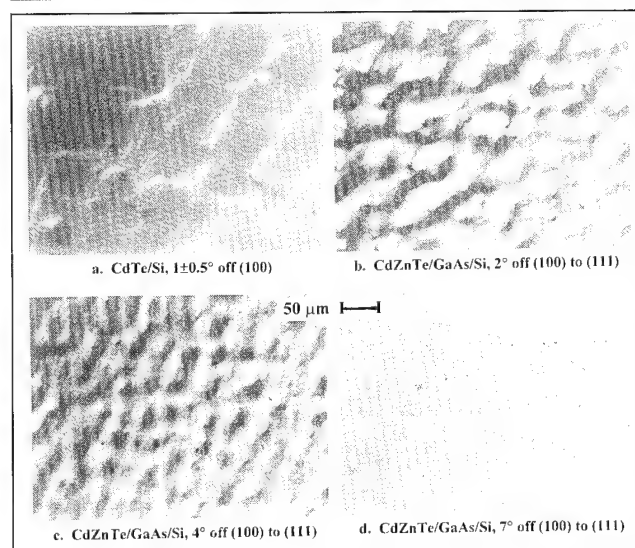


Fig. 2. HgCdTe surface morphology for various substrate types and orientations.

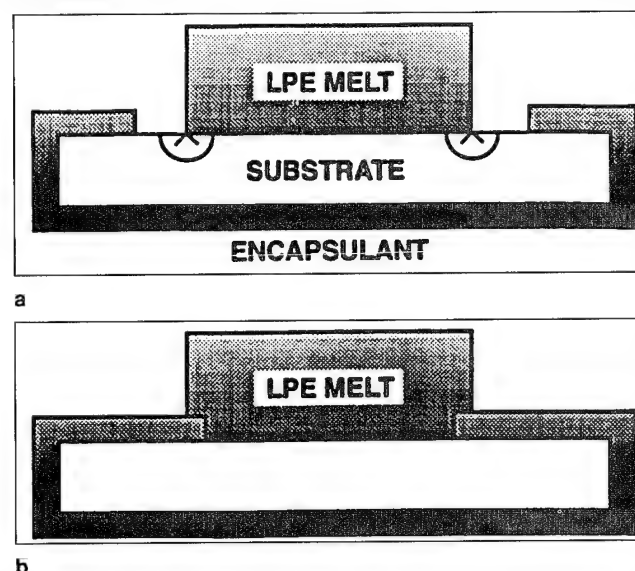


Fig. 3. Relative size of LPE melt and encapsulant window; (a) melt periphery contacts substrate resulting in metback at melt/substrate/vapor junction, and (b) melt periphery contacts encapsulant, metback is prevented.

Table I. Summary of Ga Contamination Results

Process	1.0 µm GaAs Layer	0.5 µm GaAs Layer	Increased Deposition Temperature
Ga atoms on encapsulant (cm ⁻³)	2.4×10^{19}	1.2×10^{18}	$< 1 \times 10^{17}$
Ga atoms (cm ⁻³) in HgCdTe if all on encapsulant enter melt	4×10^{18}	2×10^{17}	$< 2 \times 10^{16}$
Hall electron concentration (cm ⁻³)	1.4×10^{17}	1.5×10^{16}	1.9×10^{15}

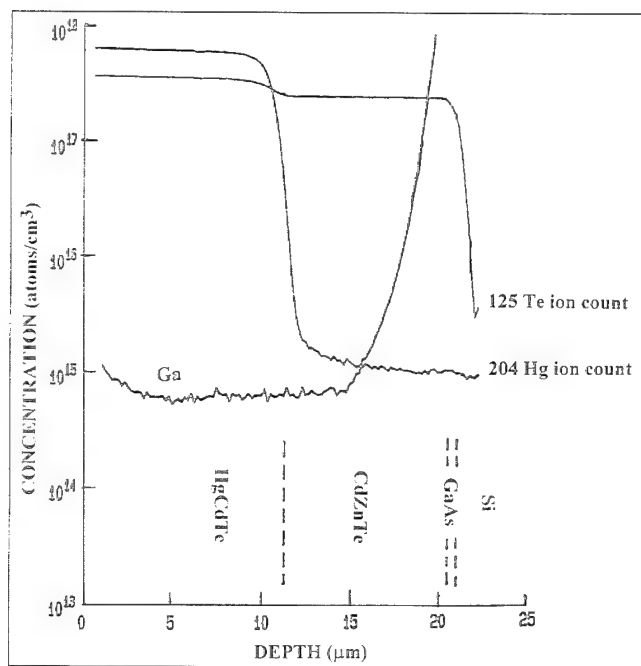


Fig. 4. Secondary ion mass spectroscopy of CdZnTe/GaAs/Si structure.

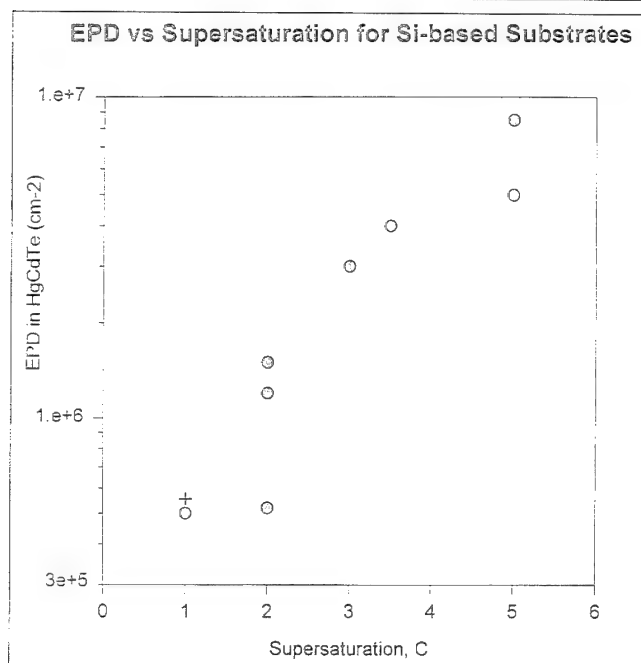


Fig. 5. Etch pit density as a function of supersaturation for LPE HgCdTe on CdZnTe/GaAs/Si (○) and CdTe/Si (+) substrates.

contaminants did not originate at the HgCdTe/substrate interface by diffusion into the HgCdTe. Microscopic examination of the grown films indicated that the melt was dissolving the substrate in a region about 0.2 to 0.5 mm wide around the border of the HgCdTe growth region. Apparently, even though the bulk of the melt was supersaturated, a region near the edge was unsaturated. One possible explanation of this is that Hg was lost by vaporization from the melt periphery, resulting in an increase in the solubility of Cd in the melt. In order to prevent this localized

meltback phenomenon, the width of the encapsulant border around the substrate was increased from 1 to 2 mm. The wider encapsulant prevented the unsaturated region of melt from contacting the CdZnTe layer, which avoided this mechanism of contamination, as shown in Fig. 3.

Subsequent growth runs with a 2 mm border showed a greatly reduced contamination level, but Ga contamination was still found at the 1×10^{17} atoms/cm³ level. Examination showed that most of the polycrystalline material on the encapsulant frame had been dissolved in the melt, and calculations indicate that this could provide sufficient Ga to contaminate the HgCdTe at above this level. Efforts were, therefore, made to eliminate GaAs deposition on the encapsulant border, or to remove it after the deposition process. Reducing the GaAs layer thickness from 1.0 to 0.5 μ m reduced the amount of polycrystalline Ga on the frame by a factor of 20 because of the improved selectivity resulting from the shorter growth time. The reduction in the volume of GaAs on the oxide frame was by counting the specks in selected areas under a microscope and measuring their average diameter. Increasing the GaAs deposition temperature from 675 to 720°C further improved selectivity and reduced Ga contamination. Table I below summarizes these results. The Hall measurements were made after a 96 h anneal at 250°C anneal in saturated Hg vapor. As can be seen the measured donor concentration was always about 10% of the calculated maximum value.

Hall measurements on two HgCdTe layers grown on MBE CdTe/Si substrates gave electron concentrations, after the Hg-rich anneal, of 1.0×10^{15} /cm³ and 1.2×10^{15} /cm³. These layers were grown from a melt that was In doped at a level that gave an average electron concentration of 1.5×10^{15} /cm³ for layers grown on bulk CdZnTe substrates. Secondary ion mass spectroscopy analysis also showed a Si contamination level of less than 10^{15} atoms/cm³ for HgCdTe grown on CdTe/Si substrates.

In order to confirm that the only source of Ga contamination of the HgCdTe was from residual GaAs contamination on the encapsulant, the unencapsulated area of a substrate was masked with photoresist, and the polycrystalline CdZnTe and GaAs were removed using wet etchants. A HgCdTe layer about 10 μ m thick was grown on this substrate using an undoped Te-rich melt. A SIMS analysis profile of the resulting structure was obtained and is shown in Fig. 4. This profile shows the Ga concentration to be below 10^{15} /cm³, and this was confirmed by a measured Hall electron concentration of 3×10^{14} /cm³, with a Hall mobility of 5×10^4 cm²/V.s. The measured Ga concentration increases in the CdZnTe layer, either as a result of Ga diffusion from the GaAs layer or as a result of penetration of some part of the SIMS crater into the GaAs layer. This Hall mobility is about a factor of three below the value expected for HgCdTe with this carrier concentration grown on bulk CdTe substrates, the reason for this discrepancy is not

known.

The growth temperature was kept constant throughout a series of HgCdTe growths on CdZnTe/GaAs/Si substrates, but the amount of supersaturation was varied with the objective of determining whether the amount of contamination would be reduced at high supersaturation. No effect of supersaturation on contamination was detected. The dislocation density in these films was determined by use of the Hahnert and Schenk etch⁷ to develop etch pits in the HgCdTe surface. A relationship was seen between the etch pit density and amount of supersaturation. This relationship is illustrated in Fig. 5. The reduction in dislocation density at the surface of the HgCdTe surface at low supersaturation could result from the fact that the initial growth rate was slower, allowing more time for the formation of an equilibrium misfit dislocation network near the interface with the substrate, so that fewer threading dislocations were formed. The electron mobility for low dislocation density HgCdTe layers grown on CdZnTe/GaAs/Si substrates was close to the value expected for bulk CdTe substrates, the electron concentration and mobility of a $\text{Hg}_{0.79}\text{Cd}_{0.21}\text{Te}$ layer grown using 1°C of supersaturation were $2.8 \times 10^{15}/\text{cm}^3$ and $1.35 \times 10^5 \text{ cm}^2/\text{V}\cdot\text{s}$, respectively.

In order to make a comparison of the utility of Si-based substrates with conventional bulk substrates, a 2 μm thick As-doped HgCdTe p-type cap layer was grown on an In-doped n-type HgCdTe layer about 15 μm thick grown on a CdZnTe/GaAs/Si substrate. The substrate had been prepared under conditions identical with those giving a HgCdTe layer with $n = 1.9 \times 10^{15}/\text{cm}^3$. The p-type layer was grown from a Hg-rich melt by a dipping LPE process. The resulting material was etched to form $60 \times 60 \mu\text{m}$ mesa diodes, gold contacts were formed on the diodes, and the diode surfaces passivated by coating them with a layer of ZnS. The values of R_0A for the resulting diodes ranged from 300 $\text{ohm}\cdot\text{cm}^2$ to over 600 $\text{ohm}\cdot\text{cm}^2$. Figure 6 shows an current-voltage curve for a diode with an R_0A value of 682 $\text{ohm}\cdot\text{cm}^2$. The reverse bias characteristics of these devices were similar to those obtained on bulk substrates. These diodes showed good photoresponse at low temperature, with a cutoff wavelength of 8.6 μm at 80K. A quantum efficiency of about 50% was obtained at this temperature when the diode was illuminated through the Si substrate, which did not have an anti-reflection coating applied to it.

CONCLUSIONS

Good quality {111}B oriented HgCdTe films have been grown on both MBE CdTe/Si and OMVPE CdZnTe/GaAs/Si substrates. Films grown on CdZnTe/GaAs/Si are sufficiently free of Ga contamination by the substrate to make doping control at the $10^{15}/\text{cm}^3$ level possible and have mobilities of above $1 \times 10^5 \text{ cm}^2/\text{V}\cdot\text{s}$. Dislocation densities below $1 \times 10^6/\text{cm}^2$ can be obtained on both types of substrates; and although this value is a factor of three above that obtained using bulk CdTe substrates in the same process, it is

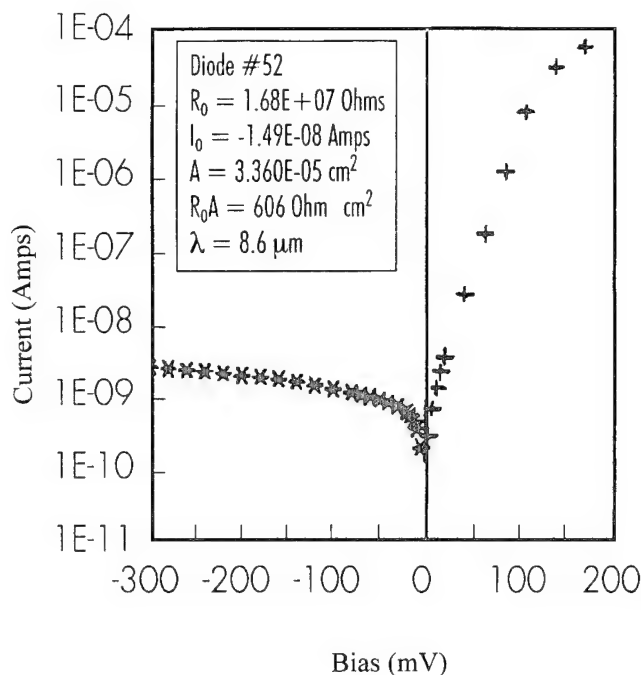


Fig. 6. Current-voltage characteristics of HgCdTe p on n diode on a CdZnTe/GaAs/Si substrate at 80K.

probably low enough that it would not significantly increase dark current in detectors at 80K. It is not clear as yet whether the GaAs buffer layer is having any affect on dislocation density in the CdZnTe layer, or whether use of a lattice matching CdZnTe composition is important, but these factors do not seem to have as large an impact on the dislocation density in the subsequently grown HgCdTe as does the LPE growth process itself. It can be anticipated that further refinements of both the LPE growth conditions, and the substrate preparation process, should lead to further reductions in dislocation density.

The use of a thermally generated oxide on the Si substrate prior to OMVPE or MBE growth has been shown to be effective in preventing contamination of the HgCdTe by the substrate materials, provided GaAs deposition on the encapsulant is avoided. Selective growth of GaAs has been achieved by raising the deposition temperature, and the degree of selectivity can probably be improved further by reduction of the reactor pressure. In any case, the level of contamination that has already been achieved is comparable with the deliberately added dopant concentration.

ACKNOWLEDGMENTS

This work was partially supported by IR&D funds at Loral and by ARPA through Contract No. MDA972-92-C-0076 both at Loral and, through a subcontract, at Spire. The work at Spire was also supported by ARPA Contract No. F-49620-90-C-0090. The work at the University of Illinois was supported by ARPA and by Loral IR&D funds. The authors wish to thank P. Norton and P. LoVecchio (Loral), R. Singer (IDA), and

R. Sudharsanan (Spire) for numerous helpful discussions.

REFERENCES

1. R. Kay, R. Bean, K. Zanio, C. Ito and D. McIntyre, *Appl. Phys. Lett.* 51, 2212 (1987).
2. S.M. Johnson, M.H. Kalisher, W.L. Ahlgren, J.B. James and C.A. Cockrum, *Appl. Phys. Lett.* 56, 946 (1990).
3. R. Triboulet, A. Tromson-Carli, D. Lorans and T. Nguyen-Duy, *J. Electron. Mater.* 22, 827 (1993).
4. M. Oron, A. Raizman, H. Shtrikman and G. Cinader, *Appl. Phys. Lett.* 52, 1059 (1988).
5. G. Feuillet, J. Cibert, E. Ligeon, Y. Gobil, K. Saminadayar and S. Tatarenko, *Mater. Res. Soc. Symp. Proc.* 148, 389 (1989).
6. N.H. Karam, F.T.J. Smith, R. Sudharsanan, A. Mastrovito, J.T. Daly, M.M. Sanfacon, M. Leonard and N.A. El-Masry, *Proc. SPIE Symp. on Optical Engineering and Photonics in Aerospace Sensing*, April 1994.
7. I. Hahnert and M. Schenk, *J. Cryst. Growth* 101, 251 (1990).

Piezoelectric Effects in HgCdTe Devices

C.F. WAN, J.D. LUTTMER, R.S. LIST, and R.L. STRONG

Texas Instruments, Incorporated, Dallas, TX 75265

Piezoelectric effect in long-wavelength infrared (LWIR) HgCdTe has been studied using metal-insulator-semiconductor (MIS) and p-n homojunction devices. A cantilever beam technique was used to measure the shift in flatband voltage in the MIS devices as a function of applied strain, from which piezoelectric constant was derived. This is the first time such a value has been reported in the literature. Subsequent calculation showed that the thermal stress from cryogenic cool (from 300 to 77K) of hybridized infrared devices fabricated on (111) HgCdTe surfaces induced a piezoelectric field of ~ 1840 V/cm. This field is present in the space charge regions in the semiconductor where there is no free carrier. It reinforces the built-field in an n-on-p diode fabricated on the (111)A HgCdTe surface. Thus, the diode is more prone to the thermal stress than one fabricated on the (111)B surface. Electrical measurement of reverse-bias dark currents in HgCdTe photodiodes under applied compressive and tensile stress confirmed the existence of a strain-induced field in the junction.

Key words: HgCdTe, piezoelectric effects, stress, strain

INTRODUCTION

HgCdTe is a narrow-bandgap semiconductor with zinc-blende structure. It is a widely used infrared detector material for photovoltaic detector arrays in the 8–12 μm band. Substantial effort has been expended on large-area focal-plane arrays. These HgCdTe devices are often bump bonded, epoxied, or grown epitaxially on silicon. When the devices are cooled from room temperature to cryogenic temperatures, thermal stresses are introduced due to mismatch in coefficients of thermal expansion of HgCdTe and silicon. In addition, mechanical stresses may be introduced during the device fabrication. This includes the vicinity of windows in dielectric overlayers or around metal gates or contacts. Other stress or

strain may exist near dislocations or other material defects in the HgCdTe.

Stress can induce electric fields and/or surface charges in HgCdTe due to piezoelectric effects. The field may have adverse effects on HgCdTe photodetectors as the narrow bandgap semiconductors are subject to tunnel breakdown and charge redistribution around dislocations, inclusions, and precipitates.¹ The piezoelectric effects have been found to be responsible for shifts in the pinch-off voltage and the saturation current of GaAs field effect transistors (FETs).² In addition, it has been shown to create sufficiently high internal electric fields to modify the electronic structure and optical properties of III-V superlattices.³

Strain effects in HgCdTe have been studied by Weiss and Mainzer.⁴ Significant changes were observed in device characteristics when a strain was applied. Their results suggested a change in n-chan-

(Received October 4, 1994; revised January 8, 1995)

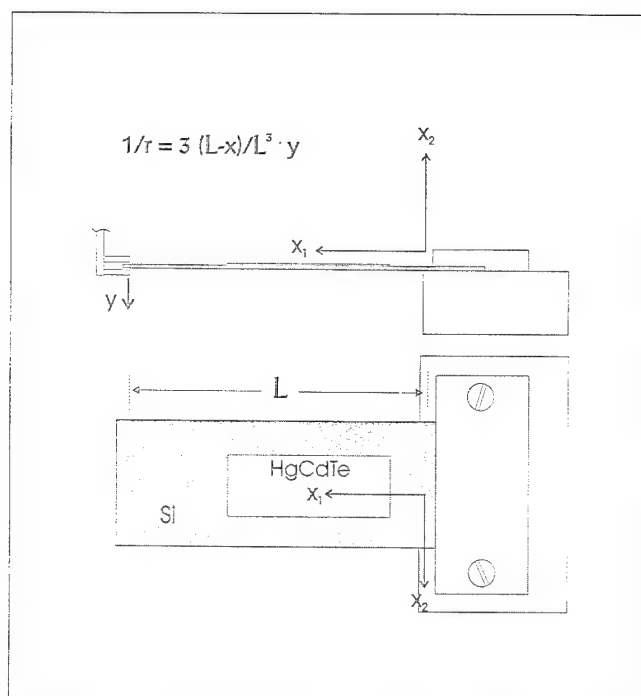


Fig. 1. Schematic diagram of a cantilever beam test fixture.

nel conductivity due either to piezoelectric effects or n-type damage. The piezoelectric constant of HgCdTe, which is needed to assess the piezoelectric effect in HgCdTe, has not been reported in the literature. Conventional measurement techniques such as piezoelectric resonators cannot be used to measure the piezoelectric effect of HgCdTe perhaps because of free-carrier screening. In this study, we used metal-insulator-semiconductor (MIS) and photodiode devices to measure the stress effects. We then extracted the piezoelectric constants, which allowed us to calculate stress-induced electric fields in HgCdTe.

EXPERIMENTAL

Metal-insulator-semiconductor devices and p-n junctions were fabricated on thin slabs ($\sim 10 \mu\text{m}$) of LWIR HgCdTe epoxied to a 20 mil thick silicon substrate. The HgCdTe material was grown epitaxially from solution on [111]-oriented CdZnTe substrates. The MIS devices were fabricated on (111)A surface of n-type HgCdTe, using 1800Å of ZnS as the gate insulator. Donor concentration of the HgCdTe was $\sim 5 \times 10^{14} \text{ cm}^{-3}$. The photodiodes were fabricated on metal-vacancy doped, p-type HgCdTe with acceptor concentration of $\sim 1 \times 10^{17} \text{ cm}^{-3}$. The background impurity was n-type with the donor concentrations of $\sim 5 \times 10^{14} \text{ cm}^{-3}$. The n-region was formed by ion implantation, which converted the p-HgCdTe into n-type by filling the metal vacancies with Hg. A metal field plate was used for controlling the surface potential. Guard diodes were employed to reduce the diffusion current.

A cantilever-beam test fixture was used to apply compressive or tensile strains on the composite. A schematic of the apparatus is given in Fig. 1. Devices nearest the support block were bonded and tested because this region experiences a larger stress when

a load is applied on the free end. The HgCdTe is so thin compared to the silicon substrate that its length change is determined by change in the adjacent silicon surface. From elementary bending theory, the curvature r of the elastically bent cantilever beam at a point x from its support end is⁵

$$1/r = 3(L-x)/L^3 \cdot y, \quad (1)$$

where L is the length of the beam and y is the amount of deflection of the free end. The strain in the thin HgCdTe film attached to the silicon slab is simply the curvature times half the silicon thickness, given by:

$$S = 3t(L-x)/2L^3 \cdot y \quad (2)$$

It is in the direction of the length of the beam.

The cantilever assembly was enclosed in a brass cylinder and immersed in liquid nitrogen during the electrical measurements. Beam deflection was achieved with a rigid clamp attached to a micrometer that allowed bi-directional flexing. The wide gaped clamp could contact either the top or bottom face of the cantilever at the load point. Physical contact between the clamp and the cantilevered beam was determined by monitoring the electrical resistance between the two.

Flatband voltage of the MIS devices and dark current of the diodes were measured as a function of flexing at the liquid nitrogen temperature. A typical test cycle involved bending the HgCdTe/Si composite back and forth with increasing deflection until breakage of Si occurred. The typical incremental change in deflection was ~ 10 mil. The diode devices were tested under optimum field plate bias to eliminate the effect of surface charge. Some of the devices could still be tested after the breakage if the bond wires did not detach from the devices. The results usually restored indicating the flexing is elastic in nature within the range of strain used.

RESULTS AND ANALYSIS

Flatband voltages of the MIS devices were measured as a function of deflection of the beam. They varied linearly with the amount of deflection. The results are reversible indicating there was no plastic deformation during the bending, and the changes were induced by piezoelectric effects. As shown in Fig. 2, applying a tensile stress shifted the flatband voltages toward positive voltage. This means that the electric field generated by tensile stress was in the [111]A direction and that the sign of the piezoelectric constant was positive. The common II-VI semiconductors, such as CdTe or ZnS have positive piezoelectric coefficients, while the common III-V semiconductors have negative ones. The slope or rate of change of the flatband voltage was 1.62 mV per mil of deflection, corresponding to a surface charge of $7.14 \times 10^{-7} \text{ C/m}^2$ per mil of deflection.

Zinc-blende semiconductors have only one independent piezoelectric constant e_{14} due to the symmetries of the crystal structure. Only the shear strains can induce electric polarization; the extensional strains

do not induce polarization.⁶ They can be described by the following equations:

$$P_1' = e_{14} * S_4' \quad (3a)$$

$$P_2' = e_{14} * S_5' \quad (3b)$$

$$P_3' = e_{14} * S_6' \quad (3c)$$

where P_i s are the orthogonal components of the polarization vector, and S_j s are the contracted shear strains. By bending the cantilever beam, strain S_1 along the longitudinal axis x_1 of the beam is generated which can be calculated using Eq. (2), S_2 along the x_2 -axis is zero due to restraint imposed by the silicon substrate, and a strain S_3 is generated in the x_3 direction due to the stretching of HgCdTe in the x_1 direction. S_3 is related to S_1 by a factor of $-v/(1-v)$, where $v = 0.41$, the Poisson's ratio. We have

$$S_1 = 3.81 \times 10^{-5} \text{ per mil of deflection} \quad (4a)$$

$$S_2 = 0 \quad (4b)$$

$$S_3 = -v/(1-v) * S_1 = -0.695 * S_1 \quad (4c)$$

The coordinate system x_1, x_2, x_3 in Fig. 1 does not coincide with that of the HgCdTe unit cell. The [111] direction of the HgCdTe is in the x_3 direction. Tensors in the x_1, x_2, x_3 coordinate system can be transformed into the HgCdTe coordinate system using Euler's angles of $\alpha = 19^\circ$, $\beta = 54.73^\circ$, $\gamma = 45^\circ$, respectively. Then the shear components of the strain tensor (4a)–(4c) become:

$$S_4' = -0.272 * S_1 \quad (5a)$$

$$S_5' = -1.404 * S_1 \quad (5b)$$

$$S_6' = -0.704 * S_1 \quad (5c)$$

The extensional components are not shown since they do not induce polarization as only the shear components S_4' , S_5' , S_6' are capable of inducing piezoelectric effect. Notice we have arbitrarily chosen the projection of x_1' axis on x_1, x_2 plane to be $\phi = 45^\circ$ from the x_1 direction. Although ϕ is dependent on the exact orientation of HgCdTe, it turns out the result is independent of this angle. The polarization vector is by Eqs. (3)

$$P_1' = e_{14} * S_4' = -0.272 * S_1 * e_{14} \quad (6a)$$

$$P_2' = e_{14} * S_5' = -1.404 * S_1 * e_{14} \quad (6b)$$

$$P_3' = e_{14} * S_6' = -0.704 * S_1 * e_{14} \quad (6c)$$

The polarization charge induced on the (111)A surface by this vector is

$$\sigma = n' * P' = 1/\sqrt{3} * (P_1' + P_2' + P_3') = -1.38 * S_1 * e_{14} \quad (7)$$

where n is the unit vector in the [111]A direction. σ is also independent of the azimuthal orientation of the [111]-oriented HgCdTe. Therefore, there is no need to know the exact orientation of (111) HgCdTe liquid phase epitaxy epoxied on the silicon substrate. Substituting the measured value of σ and S_1 in Eq. (7), we obtained $e_{14} = 0.0136 \text{ C/m}^2$, in contrast to 0.034 C/m^2 for CdTe⁷.

For the case of thermal stress generated by the cryogenic cool down from 300 to 77K, the strain components for the (111) HgCdTe are:

$$S_1 = 0.078\% \quad (8a)$$

$$S_2 = 0.078\% \quad (8b)$$

$$S_3 = -2v/(1-v) * S_1 \quad (8c)$$

where again v is the Poisson's ratio of HgCdTe and S_3 is due to contraction of HgCdTe by stretching it in the other two directions. This induces a polarization vector in the x_3 direction for all the azimuth angles of (111) HgCdTe. That is

$$P_1 = P_2 = 0 \quad (9a)$$

$$P_3 = S_3 * e_{14} = -2.93 \times 10^{-5} \text{ C/m}^2. \quad (9b)$$

Thus, the electric field is

$$E_1 = E_2 = 0 \quad (10a)$$

$$E_3 = -P_3 / \epsilon_s \epsilon_0 = 1840 \text{ V/cm} \quad (10b)$$

where ϵ_s is the dielectric constant of HgCdTe, and ϵ_0 is the permittivity. This field is present in the junction depletion region, where there are no free carriers to screen it. The field is in the [111]A direction, in the same direction as the built-in field if an n-on-p diode is fabricated on the (111)B surface. Its strength is quite significant compared to the built-in field of the junction, around 2900 V/cm. On the other hand, if the n-on-p diodes are fabricated on the (111)A face, the thermal-stress induced field is opposite to the direction of the built-in field. The sidewall portions of the junction are not affected in the case of the present planar diodes because the induced field is perpendicular to the built-in field. This leads to a situation where the electric field on the sidewall portion of the

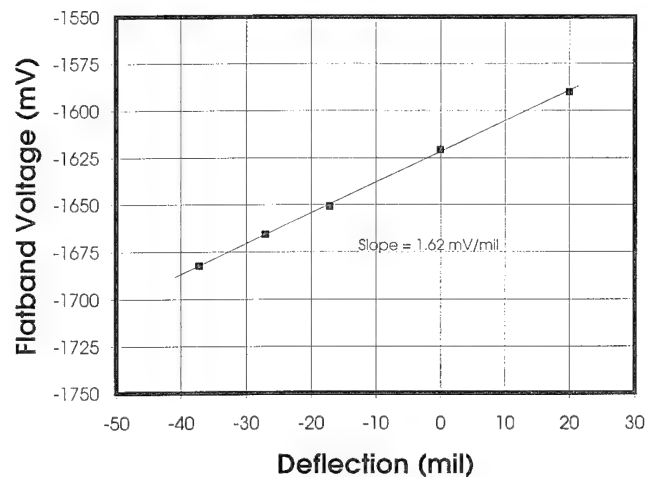


Fig. 2. Flatband voltage of a HgCdTe MIS device as a function of deflection.

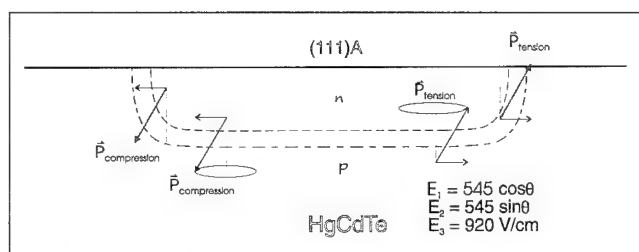


Fig. 3. Polarization vectors generated in HgCdTe by compressive or tensile stresses from bending the HgCdTe/Si hybrid structure.

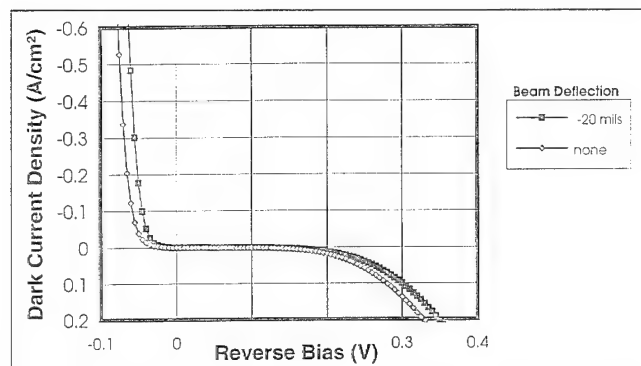


Fig. 4. Effect of bending the HgCdTe/Si hybrid structure on J-V characteristics of diodes built on the HgCdTe.

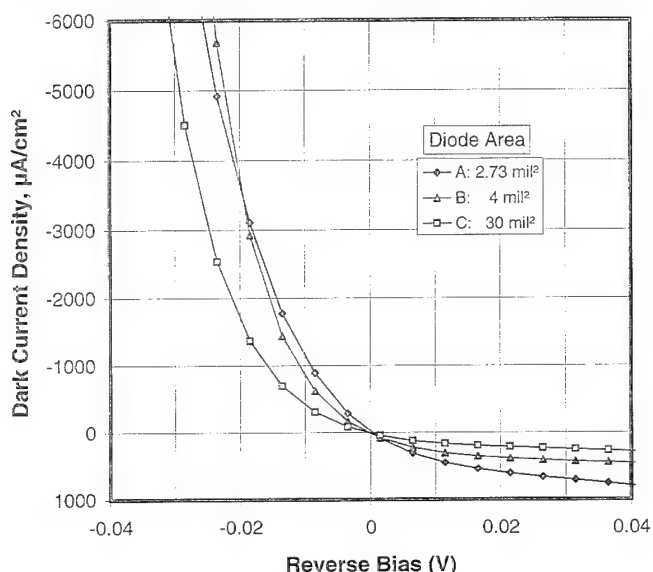


Fig. 5. Current-voltage curves of the diodes used for testing piezoelectric effects in HgCdTe devices.

junction is different from the bottom portion of the junction. If [100]-oriented HgCdTe is used, only extensional strains and no shear strains are generated during cryogenic cool down. Therefore, no piezoelectric polarization will be induced and the diodes built on the [100] surfaces will not be affected. Nevertheless, average good HgCdTe diodes do not show tunnel breakdown until biased to several hundred mV. Therefore, the variations in field may not have significant impact on dark currents. The junctions in mesa diodes do not have sidewalls but the edges of the mesas may be subject to extraneous thermal stresses.

For the case of uniaxial stresses, such as the one applied to the HgCdTe in the present cantilever test system, we can use Eq. (5) and Eq. (6) to calculate the polarization field in the junction. Assuming the amount of deflection was 20 mils, which generates a strain similar to that caused by coefficient of thermal expansion (CTE) mismatch ($\sim 0.078\%$), the induced field becomes

$$E_1 = 545 \cdot \cos\theta \text{ V/cm} \quad (11a)$$

$$E_2 = 545 \cdot \sin\theta \text{ V/cm} \quad (11b)$$

$$E_3 = 920 \text{ V/cm} \quad (11c)$$

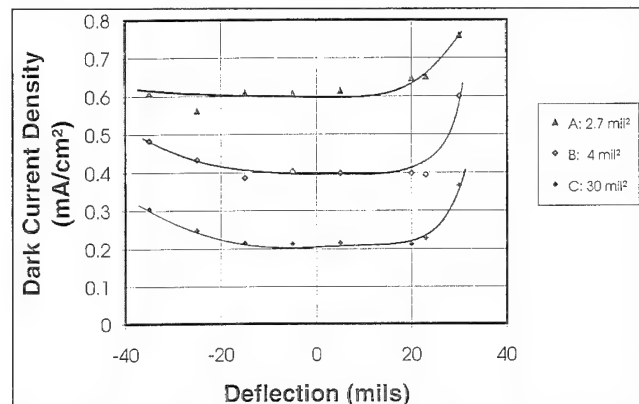


Fig. 6. Dark current densities at 20 mV reverse bias in HgCdTe test diodes under different amounts of tensile and compressive stresses.

where θ is an azimuth angle determined by the orientation of the (111)A HgCdTe. This electric field is not perpendicular to the surface but at a slant angle as shown in Fig. 3. E_3 being the vertical component behaves the same way as the one induced by the biaxial stress but at half the strength. E_1 and E_2 is the lateral component that increases the built-in field on one side of the junction while decreases that on the other. This component reverses direction when the direction of deflection is reversed.

For the case of line stresses such as those created at the edges of insulators or metal field plates, the induced electric field is more complex.² The electric field varies with the distance and angle from the edges and can be quite high. It can change the field in the depletion region and the carrier distribution.

Figure 4 shows the dark current density as a function of reverse bias voltage (J_d vs V) for a planar diode ($\sim 30 \text{ mil}^2$) fabricated on (111)B HgCdTe, measured at two different stress levels. The amounts of deflection were 0 and -20 mils , respectively. The curve shifted toward the right (positive) by $\sim 20 \text{ mV}$ upon compressive stress. This is consistent with a change in the depletion region field from the piezoelectric effects. The amount of shift, however, was smaller than expected.

Figure 5 shows the the dark current density as a function of reverse bias voltage (J_d vs V) for diodes of different areas. The dark current came from the perimeter of the diodes due to generation-recombination (g-r), which was attributed to a high stress in the metal field plate. Figure 6 shows the dark current density of the diodes as a function of the deflection in the cantilever beam. The dark current increased significantly when the cantilever beam was deflected more than 20 mils in the direction of tension, while remaining relatively constant when deflected less than 20 mils. The changes were reversible indicating that no permanent damage was done to the HgCdTe. This can only be explained by the piezoelectric effects. The induced field was too small to change the electronic structure of the HgCdTe. The piezoelectric polarization field upon tension is in the same direction as the built-in field and increases with the amount of deflection. This results in increase in the field-

dependent dark currents and eventual junction breakdown.

The dark current also increased when the cantilever beam was deflected more than 20 mils in the direction of compression. This increase, though less rapidly, cannot be explained by the vertical component of the polarization field, which is opposite to the direction of the built-in field. It can be explained by the horizontal component of the polarization field as shown in Fig. 3. This component increases the built-in field of a certain sidewall portion of the junction and results in an increase in dark current by breakdown mechanisms.

CONCLUSION

We have measured the piezoelectric constant of $\text{Hg}_{0.78}\text{Cd}_{0.22}\text{Te}$ by using a cantilever beam technique. This represents the first time this parameter has been measured to be $\sim 0.0136 \text{ C/m}^2$. This value is small compared with CdTe or other zinc-blende semiconductors. However, hybridized HgCdTe/Si devices can develop substantial amounts of thermal stress from during cool down due to the CTE mismatch or mechanical stress from device fabrication. Electric fields larger than 50% of the built-in field can be induced in the HgCdTe for the hybridized HgCdTe/Si devices from the thermal stress alone. This field can cancel that in the depletion region if the diodes are on (111)A surface and reinforce it if on the (111)B surface. Attempts have been made to assess the effect on diode performance. The results qualitatively agreed with

theory. Reverse-bias dark current in a regular diode can be affected by such a field, especially the diodes with inferior dynamic resistance. Other device parameters such as noise is expected to be affected in a similar fashion, i.e., that diodes with large bias-dependent noise current may show more significant changes in noise under stress. By properly orienting the HgCdTe with respect to strain directions, the effect on device performance may be minimized or improved.

ACKNOWLEDGMENT

The authors wish to thank Brad Hunter for construction of the cantilever test fixture, Joyce Wright for electrical measurements, Art Simmons for providing the MIS devices, and Barbara Brownson and Martha Ohlson for fabricating the photodiodes.

REFERENCES

1. H. Booyens and J.H. Basson, *Phys Stat. Solidi*, (a) 85, 243 (1984).
2. P.M. Asbeck et. al., *IEEE Trans. Electron. Device*, ED-31 (9), 1377 (1984).
3. C. Mailhot and D.L. Smith, *Solid State Comm.* 57, 919 (1986).
4. E. Weiss and N. Mainzer, *J. Vac. Sci. Technol. A* 7(2), 391 (1989).
5. R.F.S. Hearmon, *Applied Anisotropic Elasticity* (New York: Oxford University Press, 1961).
6. W.G. Cady, *Piezoelectricity* (New York: Dover Publication, Inc., 1964).
7. H. Belincourt, *Phys. Rev.* 129, 1009 (1963).

1/f Noise and Material Defects in HgCdTe Diodes

R. SCHIEBEL, D. BARTHOLOMEW, M. BEVAN, R.S. LIST, and
M. OHLSON

Central Research Laboratories, Texas Instruments Incorporated,
MS 150, P.O. Box 655936, Dallas, TX 75265

1/f noise is measured on long wavelength diodes as a function of device geometry, band gap, temperature, diode bias, and anneal temperature for a Te-rich CdTe passivation layer. The results show that for these diodes the 1/f noise is a bulk phenomena due to the modulation of generation recombination current associated with defects formed by the interdiffusion of Te-rich CdTe, and that these defects are located in the junction region. No 1/f noise is observed for the lowest interdiffusion anneal temperature.

Key words: 1/f noise, CdTe passivation, HgCdTe IR diodes

INTRODUCTION

1/f noise is a recurring topic of vital importance to the operation of HgCdTe photodiodes. Several sources of 1/f noise have been suggested: 1/f noise theories proposing modulation of surface tunneling current¹ or surface recombination velocity fluctuations² are motivated by the desire to associate modulation of dark currents (either tunneling or diffusion) with slow processes related to insulator trapping. Many theories for bulk 1/f noise processes based on mobility fluctuations have been proposed³ but are difficult to prove and in some cases conflict with experiment.⁴ In general, it is difficult to envision a slow process such as is required for 1/f noise that takes place in the bulk of homogeneous samples of a narrow band gap semiconductor such as HgCdTe.

One class of candidates for a heterogeneous source of 1/f noise is material defects. Theoretical studies

(such as in Ref. 5) have speculated as to the nature of defects in HgCdTe, and fluctuations in defect states have been proposed as a potential source of 1/f noise.⁶ Empirical relationships between 1/f noise and defects have been observed: Williams⁴ inferred a relationship between flux induced 1/f noise and bulk defects. List⁷ showed that 1/f noise correlated to shallow etch pits, dislocation multiplication, and clustering. In both studies, the defects were unintentionally introduced via material growth.

This work differs in that we study 1/f noise in devices fabricated on material in which defects are intentionally introduced via controlled interdiffusion at the Te-rich CdTe/HgCdTe interface. By intentionally introducing these defects, we are able to draw a more direct correlation between them and the 1/f noise produced.

This study is also different in that it studies the empirical relation between 1/f noise and a number of parameters: interdiffusion anneal temperature (IDT), band gap, temperature, diode bias, and device geom-

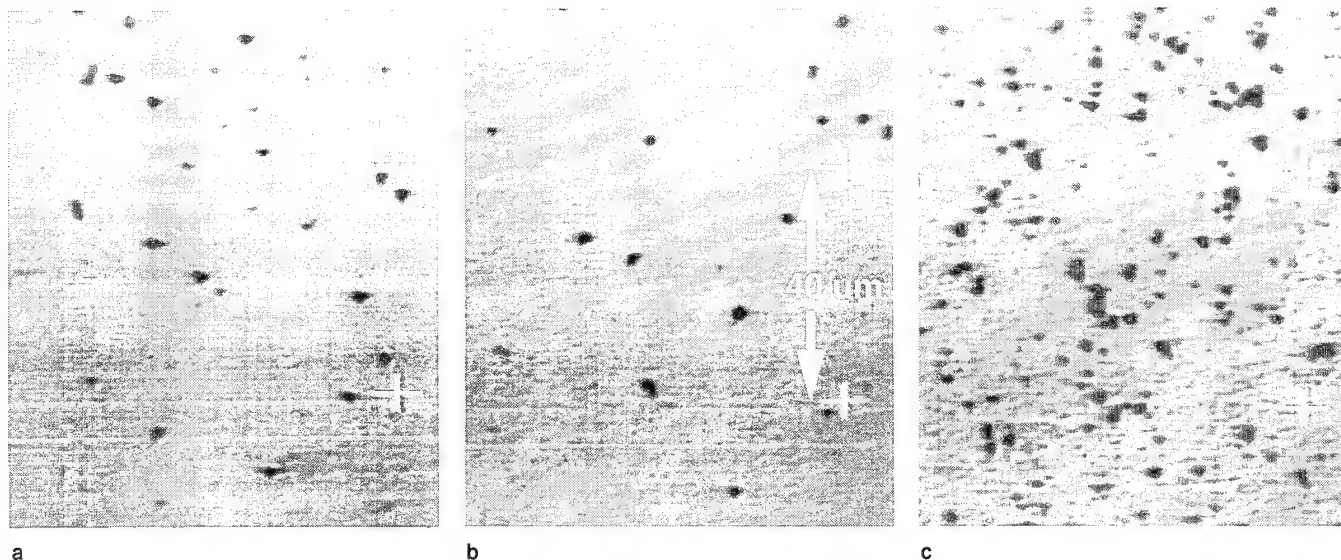


Fig. 1. Photos of defect-etched LPE films, all from the same growth run but receiving different interdiffusion anneals. Distance between crosshairs = 40 μm . (a) Control (b) 300°C interdiffusion anneal, and (c) 400°C interdiffusion anneal.

Table I. Interdiffusion Temperatures and Vacancy Concentration from Hall Measurements

Interdiffusion Temperature ($^{\circ}\text{C}$)	Vacancy Concentration (cm^{-3})
250	2.3×10^{16}
300	8.1×10^{16}
350	1.7×10^{17}
400	4.0×10^{17}

etry. Through correlation of these empirical studies, we are able to better define the nature of the $1/f$ noise and the location of the noise producing centers.

EXPERIMENTAL

In this study, all diodes are formed by ion implantation into thick (greater than 50 nm) long wavelength liquid phase epitaxy (LPE) films. The frontside is passivated with evaporated Te-rich CdTe and annealed in an inert environment prior to ion implantation to set the vacancy concentration. Since no p-type dopants were intentionally introduced into these films, the acceptor concentration is set by the vacancy concentration.

Table I shows the four interdiffusion anneal temperatures (IDT) used in this study and the corresponding vacancy concentrations as determined independently by Hall measurements. This anneal also interdiffuses the front surface and is commonly used throughout the industry to produce a high quality CdTe-HgCdTe interface.

The defects introduced through the interdiffusion of Te-rich CdTe have not been explicitly identified. However, when interdiffused samples are defect etched, larger scale defects—including dislocation clusters and dislocation multiplication—are typically observed on films interdiffused at higher temperatures, but are not evident on films interdiffused at lower temperatures, as shown in Fig. 1. This does not

imply the absence of defects from films interdiffused at lower temperatures, but that finer techniques may be necessary to observe and identify them.

The range of bandgaps and acceptor concentrations covered in this work precludes a detailed discussion of process parameters used in fabricating these devices. However, all diodes were formed by boron implantation through a ZnS/CdTe cap layer at energies from 100 to 150 keV and doses of 10^{14} to 10^{15} cm^{-2} . This was followed by low temperature (100 to 150°C) anneals sufficient to form an n⁻ region dominated by residual donors and hence avoid tunneling currents due to an n⁺/p⁺ junction. All devices had diffusion limited resistance-area products and reverse bias current (measured at 50 mV) at 80K and higher test temperatures.

Noise measurements reported in this study, unless otherwise stated, were made at 50 mV reverse bias. We report the 1 Hz value of the noise current divided by root device area, and refer to this parameter as the noise figure. The following sections show the dependence of the noise figure on geometry, band gap, temperature, interdiffusion anneal, and diode bias.

PARAMETRIC DEPENDENCE OF $1/f$ NOISE

In this section, we present the dependence of the $1/f$ noise on several parameters, including device geometry, band gap, temperature, interdiffusion anneal temperature, and diode bias. All of these measurements were made in the temperature range 77 to 120K. As the results will show, the $1/f$ noise in this range is dominated by a single, thermally activated process. At lower temperatures, other noise sources (associated with tunneling processes) dominate. Consideration of the low temperature processes is beyond the scope of this paper.

Device Geometry

Figure 2 shows relative values of the noise figure

with two different spatial normalizations. One is the noise figure described above—the noise current divided by the square root of the device area. The other is the noise current divided by the square root of the device perimeter. The values reported for each area are median values for about eight to ten devices from the same test bar. The particular data shown in Fig. 2 were taken at 110K on devices from a test bar receiving a 350°C interdiffusion anneal, but the dependences illustrated in Fig. 1 are typical of 300 and 400°C interdiffusion anneals and other test temperatures.

The data show that the appropriate normalization is to device area, clearly illustrating that the 1/f noise has a bulk source. This absence of a perimeter component of 1/f noise also indicates that the interdiffused CdTe interface is relatively noise-free.

Band Gap

Figure 3 shows the median noise figure, measured at 87.3K, for 3×3 mil² devices on several test bars with cutoff wavelengths ranging from approximately 9 to 12 μ m. All test bars received a 300°C interdiffusion anneal. The noise figure clearly increases as the cutoff wavelength increases. For comparison the intrinsic carrier concentration n_i (times a scaling factor of 2.5) is plotted on the same graph. The 1/f noise and the intrinsic carrier concentration have the same dependence on cutoff wavelength. The significance of this dependence is addressed in the Discussion section.

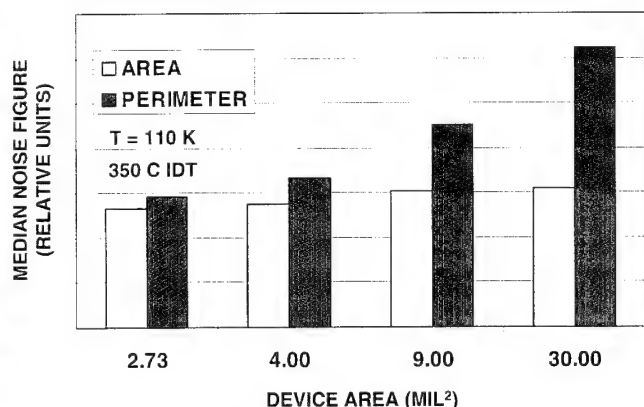


Fig. 2. 1/f Noise and device geometry: noise current normalized to either area or perimeter vs device area. λ_c (77K) = 10.2 μ m. (IDT = Interdiffusion anneal temperature)

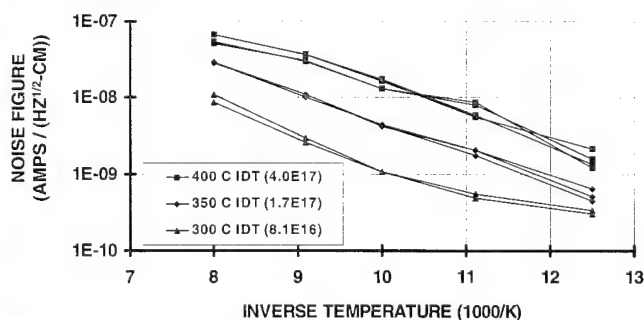


Fig. 3. 1/f noise vs cutoff wavelength.

Temperature

Figure 4 shows the noise figure measured vs temperature for several 5×6 mil² devices on test bars receiving interdiffusion anneals of 300, 350, and 400°C. Clearly the noise is thermally activated and the activation energies are reasonably similar for the three different interdiffusion anneals. A plot of the noise figures vs intrinsic carrier concentration (Fig. 5) shows that, just as for cutoff wavelength, the 1/f noise and the intrinsic carrier concentration have a very similar dependence on temperature.

Interdiffusion Anneal

Figure 6 shows the noise figure plotted vs vacancy concentration for the three highest interdiffusion anneal temperatures (IDT = interdiffusion anneal temperature) considered in this study. While there is clearly a correlation between the 1/f noise and vacancy concentration, this should not be interpreted as

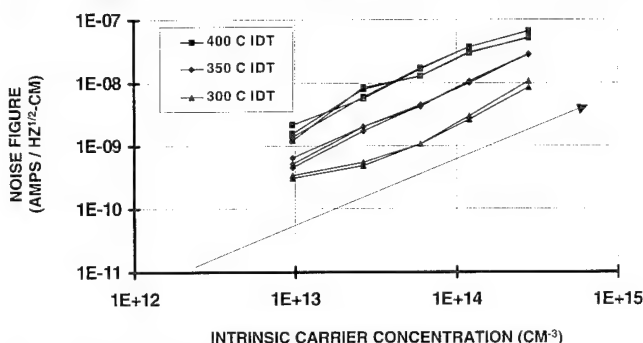


Fig. 4. 1/f noise vs inverse temperature. λ_c (77K) = 10.2 μ m.

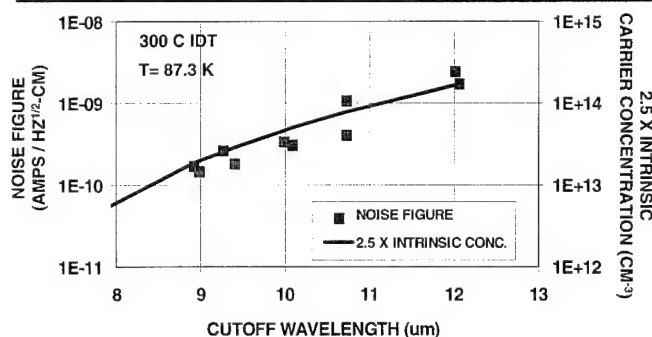


Fig. 5. 1/f noise vs intrinsic carrier concentration. Same data as Fig. 4.

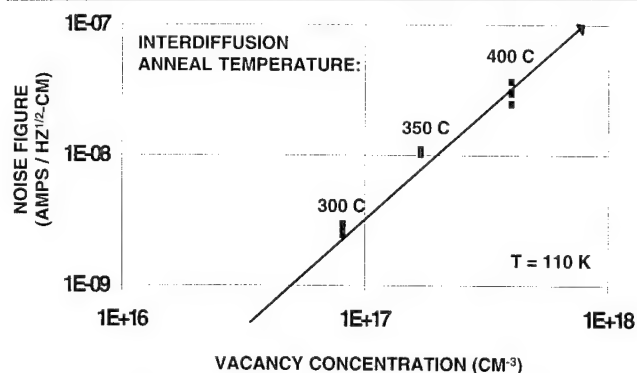


Fig. 6. 1/f noise vs vacancy concentration. λ_c (77K) = 10.2 μ m.

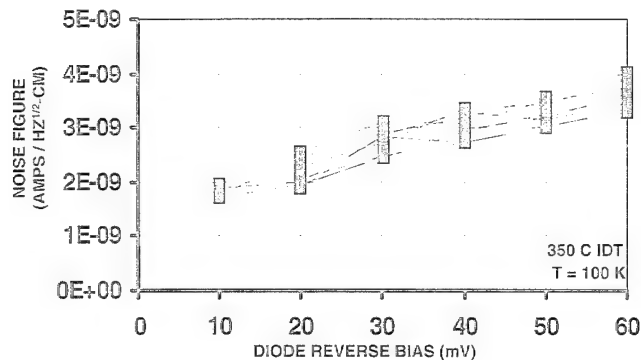


Fig. 7. $1/f$ noise vs diode reverse bias. λ_c (77K) = 10.1 μm .

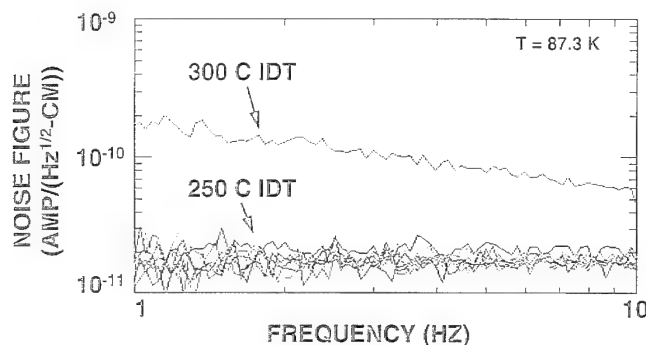


Fig. 8. Noise spectra for devices fabricated on a film receiving a 250°C interdiffusion anneal. (λ_c (77K) = 9.8 μm .) A noise spectrum for a similar device fabricated on a film receiving a 300°C interdiffusion anneal is shown for comparison. (λ_c (77K) = 10.0 μm .)

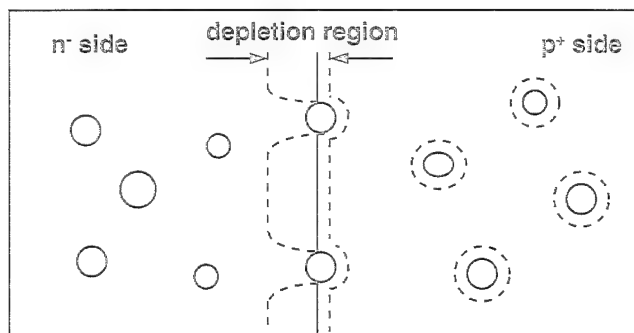


Fig. 9. Schematic showing $1/f$ noise producing defects (in junction).

a causal relationship. The interdiffusion anneal is the driving force behind setting the vacancy concentration and the evidence obtained from defect etching interdiffused samples indicates that it is the driving force behind defect production as well. The data in Fig. 6 suggests that increasing the interdiffusion anneal temperature may enhance the production of $1/f$ related defects more strongly than the production of vacancies.

Diode Bias

Figure 7 shows the noise figure for several devices plotted vs reverse diode bias. The data show a dependence of $1/f$ noise on diode bias, even at biases greater than one or two kT/q . This is significant because any noise carried by a diffusion current would not be expected to have a significant bias dependence past one or two kT/q . The implication is that the spatial

location of defects responsible for $1/f$ noise is not in the neutral n or p regions but in the junction itself. These particular data were taken at 100K on devices from a test bar receiving a 350°C interdiffusion anneal, but the essential features of the bias dependence are typical of 300 and 400°C interdiffusion anneals and other test temperatures.

Results for 250°C Interdiffusion Anneals

Figure 8 shows the noise spectra at 87.3K for several 2×2 mil² devices fabricated on a test bar that received a 250°C interdiffusion anneal. A noise spectrum for a similar device on a film receiving a 300°C interdiffusion anneal is shown for comparison. No $1/f$ noise is observed on the films receiving the 250°C interdiffusion anneal—all devices are shot noise limited. This result was typical of this particular interdiffusion temperature. In fact, the upper limit of the $1/f$ noise on these devices is below that predicted from the trends set by other interdiffusion anneals (such as is suggested by Fig. 6, for example).

DISCUSSION

The parametric dependences discussed in the previous section suggest an empirical model for the $1/f$ noise. The area (as opposed to perimeter) dependence indicates that the source of noise is in the bulk. Furthermore, the fact that it has a significant bias dependence even past a few kT/q indicates that the noise source is in the junction itself not the neutral n or p regions. The strong increase with interdiffusion anneal temperature, coupled with the results from defect etching, support the concept of a defect origin.

The fact that both the temperature and band gap dependence of the $1/f$ noise follow the intrinsic carrier concentration suggests that a generation-recombination current is being modulated. This is further supported by the work of Kraak et al.⁸ He studied grain boundaries (which are commonly associated with arrays of dislocations) in p-type HgCdTe and, using cyclotron resonance, established the existence of inversion layers around these grain boundaries.

The picture that is assembled from these facts is illustrated in Fig. 9. While the interdiffusion process may give rise to defects (such as dislocation clusters and multiplication) throughout the HgCdTe, it is only those defects actually located in the junction that contribute to the $1/f$ noise. Modulation of the generation-recombination current in the depletion regions around these defects (judging from Kraak's results, just on the p side of the junction) gives rise to $1/f$ noise, suggesting a slow process associated with these defects.

The results for the lowest (250°C) anneal temperature suggest that very few defects are created at this temperature or that an essential part of the noise-producing process is absent. The latter possibility may be simply explained by a lower threshold for inversion for lower acceptor concentrations. At such concentrations, the surface around the defects inverts, and the slow processes associated with the

defects will modulate the width of the inversion layer rather than the generation-recombination current associated with the depletion region, so no generation-recombination related 1/f noise will result.

CONCLUSIONS

We have measured 1/f noise on long wavelength diodes fabricated on thick LPE films passivated with interdiffused CdTe as a function of several process, test, and device parameters. The dependence of the 1/f noise on interdiffusion anneal temperature suggests the 1/f noise results from defects introduced by the interdiffusion process, while the dependence of the noise on bias and device geometry show that the responsible defects lie in the bulk and at the junction. Measurements of the temperature and band gap dependence of the 1/f noise suggest that generation-recombination current is modulated to produce the 1/f noise. The absence of 1/f noise at lowest anneal tem-

peratures suggests the absence of noise-producing mechanisms at the lower acceptor concentrations, or the absence of defects at low interdiffusion anneal temperatures.

REFERENCES

1. W. Anderson and H. Hoffman, *J. Vac. Sci. Technol. A* 1, 1730 (1983).
2. R. Schiebel, *IEEE Trans. Electron Dev.* 41, 768 (1994).
3. Van Der Ziel, *IEEE Proc.* 76, 233 (1988).
4. G. Williams, R. Dewames, J. Bajaj and E. Blazewski, *J. Electron. Mater.* 22, 931 (1993).
5. M. Berding, A. Sher and M. Van Schilfgaarde, *J. Electron. Mater.* 24, 1129 (1995).
6. S. Borello and Z. Celik-Butler, *Solid-State Electron.* 36, 407 (1993).
7. R.S. List, R.A. Schiebel and L. Columbo, 1994 IRIS Detector Specialty Group Meeting, Boulder, Co.
8. W. Kraak, J. Kaldasch, P. Gille, Th. Schurig and R. Herrman, *Phys. Stat. Solidi. (B)* 161, 613 (1990).

Characterization of Liquid-Phase Epitaxially Grown HgCdTe Films by Magnetoresistance Measurements

J.S. KIM and D.G. SEILER

Semiconductor Electronics Division, National Institute of Standards and Technology, Gaithersburg, MD 20899

L. COLOMBO and M.C. CHEN

Texas Instruments Incorporated, Dallas, TX 75265

In this paper, we demonstrate that measurements of the magnetoresistance can be used as a valuable alternative to conventional characterization tools to study transport properties of advanced semiconducting materials, structures, or devices. We have measured magnetoresistance on two different systems, namely, three liquid-phase epitaxially grown HgCdTe films and two GaAs-based high-electron-mobility-transistor (HEMT) structures. The results are analyzed by using a two-carrier model as a reference in the context of the reduced-conductivity-tensor scheme. The HEMT data are in quantitative agreement with the two-carrier model, but the HgCdTe data exhibit appreciable deviations from the model. The observed deviations strongly indicate a mobility spread and material complexity in the HgCdTe samples which are probably associated with inhomogeneities and the resulting anomalous electrical behavior.

Key words: HgCdTe, liquid phase epitaxy, magnetoresistance

INTRODUCTION

Measurement of magnetoresistance (referred to as MR for brevity) has been shown in the past to be a valuable tool for studying complex energy bands of semiconductors.¹ It has also been used to extract the carrier mobilities.^{2,3} However, this valuable physical quantity has seldom been used to electrically characterize advanced semiconductor materials, structures, or devices, primarily because of the complexity involved in the analytical expression of the MR. For example, the evaluation of MR involves ensemble-averaging over a third-order power of the relaxation time, while evaluation of the conductivity and Hall coefficient requires only the first- and second-order power ensemble averaging, respectively.¹⁻³ Therefore, the complexity may discourage many workers

from using the MR measurement as a characterization tool, since it masks a simple physical picture needed for the data interpretation. This complexity is inherent and cannot be avoided in general. However, it can be appreciably reduced in special cases of a practical interest, such as shown in this work.

The objectives of this paper are twofold:

- to demonstrate that MR measurements are an alternative characterization tool, and
- to supplement earlier characterization results of GaAs-based high-electron-mobility-transistor (HEMT) structures⁴ and liquid-phase epitaxially grown (LPE) HgCdTe films⁵ via reduced-conductivity-tensor (RCT) measurements.

The magnetoresistance is an extremely useful physical quantity for the electrical characterization of advanced semiconductor materials, structures, or devices.

The MR data obtained from variable-magnetic-field

(Received November 10, 1994; revised January 8, 1995)

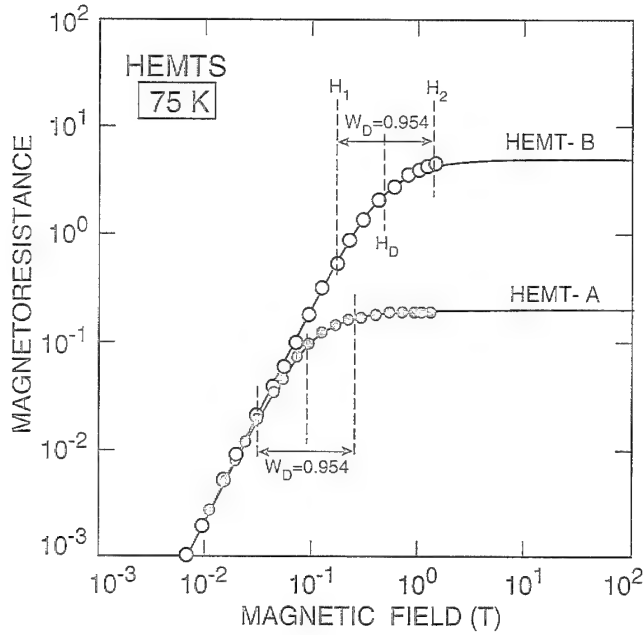


Fig. 1. Magnetoresistance plots for two HEMT vander Pauw structures at 75K. The parameters used in the fits (solid curves) are: $\mu_1 = -13.1 \text{ m}^2/\text{Vs}$, $\mu_2 = -0.30 \text{ m}^2/\text{Vs}$, and $f = 0.167$ for HEMT-A, and $\mu_1 = -13.9 \text{ m}^2/\text{Vs}$, $\mu_2 = -0.32 \text{ m}^2/\text{Vs}$, and $f = 0.868$ for HEMT-B. The value of W_D is calculated from the fits (solid curves).

Hall (VMFH) measurements are analyzed in the context of the two-carrier model of the MR which is based on the RCT scheme.⁴ We take advantage of the simple relationships between the MR, the applied magnetic field, and the relevant physical quantities in the two-carrier model of the MR.⁶ In this paper, we briefly review the formulation of the MR model, particularly the two-carrier model, in the context of the RCT scheme in the next section, followed by interpretation of experimental data in the section on comparison with experimental results. In the last section, we summarize the results of the present MR work.

MODEL FORMULATION

A general treatment of the MR in the RCT scheme is outside the scope of this paper and presented elsewhere.⁶ In this section, we briefly review key aspects of the MR formulated in the RCT scheme. In particular, we present here a detailed description of the two-carrier model of MR, since our interpretation of the experimental results depends primarily on this model.

Magnetoresistance in RCT Scheme

We define the magnetoresistance, M , as a function of the magnetic field, H , as follows:

$$M(H) = \frac{R(H) - R(0)}{R(0)} \quad (1)$$

where $R(H)$ is the longitudinal (parallel to the electric field) element of the resistance tensor; i.e., the sheet resistance, and $R(0)$ is its value at $H = 0$. We have here intentionally used the sheet resistance, $R(H)$, instead of the resistivity to conform with the van der Pauw

measurement configuration used in this work. The experimental value of the sheet resistance $R(H)$ or $M(H)$ can be obtained from the VMFH measurement. On the other hand, the analytical sheet resistance can be expressed in terms of the two components of the conductance tensor as follows:

$$R(H) = \frac{G_{xx}(H)}{G_{xx}^2(H) + G_{xy}^2(H)} \quad (2)$$

where $G_{xx}(H)$ and $G_{xy}(H)$ are the longitudinal and transverse components of the conductance tensor, respectively, and material isotropy is valid. From Eq. (1) and Eq. (2), we can then obtain an analytical expression for the MR. The resulting expression usually is not very effective in correlating the experimentally obtained MR with other transport parameters.¹⁻³ This complication can be alleviated by using the RCT scheme.

In the RCT scheme, the longitudinal element, $X(H)$, and the transverse element, $Y(H)$, of the RCT as a function of the magnetic field are defined as follows for a J -fold multicarrier system:⁴

$$X = G_{xx}(H)/G(0) = \sum_{j=1}^J X_j; \quad Y = G_{xy}(H)/G(0) = \sum_{j=1}^J Y_j \quad (3)$$

where the factor 2 in the original definition⁴ of Y is omitted deliberately for simplicity. For most systems of practical interest, the value of J probably may not exceed three. However, the samples associated with inhomogeneities, in principle, can be considered as an infinity-fold multicarrier system. The two RCT components, X_j and Y_j , for the j^{th} -carrier component in Eq. (3) are given by:⁴

$$X_j = \frac{f_j}{1 + (\mu_j H)^2}; \quad Y_j = \frac{f_j \mu_j H}{1 + (\mu_j H)^2}; \quad f_j \equiv \frac{N_j s_j \mu_j}{\sum N_j s_j \mu_j} \quad (4)$$

where s_j is the sign of carrier charge which is the same as the sign of the mobility, μ ; i.e., $s_j = -1$ for the electrons and $s_j = +1$ for the holes. The unitless parameter f_j can be interpreted as the fractional contribution of the j^{th} carrier to the net conductance where N_j and μ_j are the sheet density and mobility of the j^{th} -carrier component, respectively. The sheet density of the j^{th} -carrier component can be obtained from $N_j = f_j G(0)/(q s_j \mu_j)$, where q is the magnitude of the electron charge. Note that $f_j = 1$ for one-carrier systems. A corollary to this is that $f_j < 1$ for multicarrier systems. From Eq. (1) to Eq. (4), the MR in the RCT scheme can be expressed as:

$$M(H) = \frac{X}{X^2 + Y^2} - 1 \quad (5)$$

The MR can now be expressed as a function of the magnetic field and sets of parameters (f_j , μ_j), each being associated with a particular carrier component in multicarrier systems from Eq. (3) to Eq. (4).

Two-Carrier Model of Magnetoresistance

In order to closely examine the dependence of the MR on relevant variables, we consider here the simplest case, namely, a two-carrier system as an example (one-carrier systems always result in a null MR in the RCT scheme as is seen shortly). The MR for two-carrier systems is given by:⁶

$$M_D(H) = \frac{(\alpha\Delta H)^2}{1 + (\beta\Delta H)^2}; \quad \alpha \equiv \sqrt{f(1-f)}; \quad \beta \equiv (\mu_1/\Delta) - f \quad (6)$$

where $\Delta = (\mu_1 - \mu_2)$ is the mobility difference, and $f \equiv f_1$ (note that $f_2 = 1 - f_1 = 1 - f$). The subscript D here denotes two-carrier systems. Note that both α and β are unitless, which is an attractive characteristic of the MR expression in the RCT scheme. From Eq. (6), it is obvious that the MR of a two-carrier system is proportional to the squares of the mobility difference (Δ) and the magnetic field. Note that the MR is also proportional to $f(1-f)$ ($=f_1f_2$) for two-carrier systems, which provides a simple, clear physical picture. This is not so explicit in the conventional expression.¹⁻³

From Eq. (6), it is easily shown that an ideal one-carrier system should have a null MR since $f = 1$ and hence $\alpha = 0$. Therefore, the two-carrier systems are the simplest, nontrivial case, and hence, we examine in further details the behavior of the MR for two-carrier systems which is represented by Eq. (6). First, we define the transition-field as $H_D = 1/(\beta\Delta)$. In the low-field region ($H \ll H_D$), $M_D(H) \approx (\alpha\Delta H)^2 = f(1-f)(\mu_1 - \mu_2)^2 H^2$ which results in a slope of two in a log-log plot of the MR vs magnetic field (simply called MR-plot). In the high-field region ($H \gg H_D$), a saturation sets in, and the saturation MR is given by $M(\infty) = (\alpha/\beta)^2$.

Another parameter of importance is the transition width which characterizes the transition from the low-to-high field region (see Fig. 1). We define here the transition-width, W , as the logarithmic width of the magnetic field region where the slope of the MR-plot decreases from 1.8 to 0.2 (10% to 90% reduction from the low-field slope of 2.0 for two-carrier systems) as the field increases. This definition results in $W_D = \log_{10}(H_2/H_1) = \log_{10} 9$ for two-carrier systems, where H_1 ($= H_D/3$) and H_2 ($= 3H_D$) are the lower limit and upper limit of the transition region. Note that the transition-field H_D is the logarithmic mid-point of these two limits at which the slope takes a unity value. The value $\log_{10} 9$ (≈ 0.954) is numerically unique to all two-carrier systems and hence can be used as a criterion for the two-carrier system.

Key features predicted by the two-carrier model of MR can be summarized via an MR-plot as follows:

- In the low-field region ($H < H_1$), the MR-plot should exhibit approximately a slope of two; i.e., $M(H) \approx (\alpha\Delta H)^2$.
- In the high-field region ($H > H_2$), the MR-plot should exhibit a saturation. The saturation value of the MR is given by $M(\infty) = (\alpha/\beta)^2$.
- The transition-width should be given by $W_D =$

$$\log_{10} 9 \approx 0.954.$$

All of these features are graphically demonstrated by the HEMT data (Fig. 1), the description of which will follow shortly. On the other hand, the HgCdTe data (Fig. 2) exhibit appreciable deviations which we exploit in the third part of the next section to characterize these LPE samples.

Generalization of Two-Carrier Model

We also review briefly a generalization⁶ of the two-carrier MR model, since it gives insight into the interpretation of the HgCdTe data to be presented below in mobility-spread and HgCdTe samples section. Evaluation of MR in multicarrier systems involving three or more carrier components ($J \geq 3$) is complex. Here we present the implications when the two-carrier model is extended. The extension involves calculation of various inter-carrier coupling coefficients (a two-dimensional matrix) as a function of the corresponding carrier mobilities and f -parameters (carrier concentrations) where the relative magnitude of each coupling coefficient depends on a particular system.⁶ In this atomistic approach of the RCT scheme, any real system can be considered as a near-infinity-fold multicarrier system even though only the contributions of a few dominant carrier components are important. This RCT approach is an alternative to the conventional statistical approach of ensemble averaging. Evaluation of the MR in the conventional method is extremely complex, and the real physical picture is often lost or hidden,¹⁻³ in contrast to the RCT method which often provides a simple physical picture and the ease of numerical calculations. A formal expression of the MR for a J -fold ($J = 1, 2, 3, \dots$) multicarrier

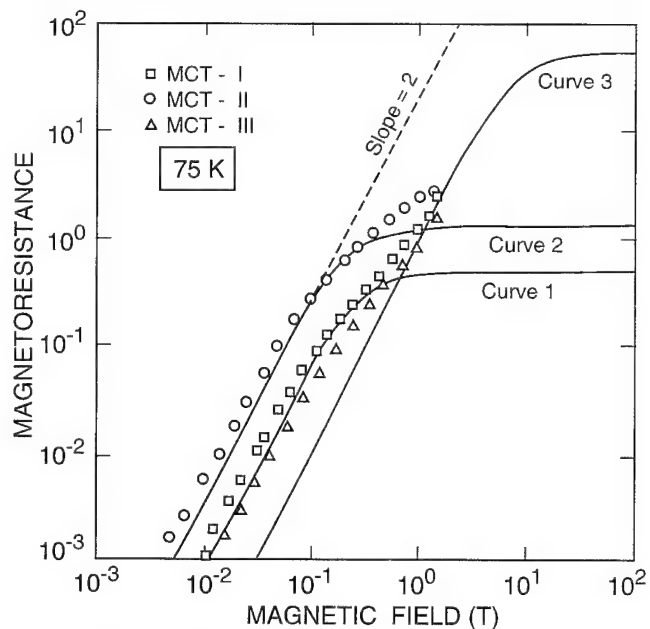


Fig. 2. Magnetoresistance plots for the LPE HgCdTe samples, MCT-I, MCT-II, and MCT-III, at 75K. Symbols and the solid curves represent the experimental data and two-carrier fits, respectively. The parameters used in these fits are extracted from the two-carrier fits of the RCT data. The dashed line represents the H^2 -dependence.

Table I. A List of Parameters Used in Two-Carrier Fits of the Magnetoresistance Data at 75K

Sample	f	μ (m ² /Vs)	Δ (m ² /Vs)	α	β	H_D (T)
HEMT-A	0.167	-13.1	-12.8	0.373	0.857	0.091
HEMT-B	0.868	-13.9	-13.6	0.339	0.154	0.477
MCT-I	0.944	-15.3	-12.0	0.230	0.330	0.252
MCT-II	0.899	-22.3	-19.1	0.301	0.269	0.195
MCT-III	0.681	-1.35	-2.18	0.466	-0.063	7.230

Note: Parameters $f = f_1 = 1 - f_2$, $\mu = \mu_1$, and $\Delta (= \mu_1 - \mu_2)$ are extracted from two-carrier fits of TCT data. The residual errors in the two-carrier fit are less than fractions of 1%; f , α , and β are unitless.

system can be written as follows:⁶

$$M_J(H) = \frac{H^2 \sum_{j=1}^{J-1} a_j H^{2(j-1)}}{1 + \sum_{j=1}^{J-1} b_j H^{2j}} \quad (7)$$

where a_j and b_j are coefficients which depend only on the carrier mobilities and f -parameters (sheet carrier densities). Note that the term H^2 is factored out and the first term in the denominator is unity in Eq. (7). The expression reduces to Eq. (6) for two-carrier systems ($J = 2$) and also results in a null value for an ideal one-carrier system ($J = 1$).

COMPARISON WITH EXPERIMENTAL RESULTS

Measurements

The experimental values of MR used in this paper are evaluated from Eq. (1) by using the sheet resistance data which were obtained from the VMFH measurements. Details of the VMFH technique are described elsewhere.⁴ The samples used in this work are two GaAs-based HEMT structures (HEMT-A and HEMT-B) used in Ref. 4, and three LPE HgCdTe films used in Ref. 5. The three LPE HgCdTe samples are a normal sample (Type I), a mildly anomalous samples (Type II), and a highly anomalous sample (Type III), labeled as MCT-I, MCT-II, and MCT-III, respectively. See Ref. 4 for details of the growth and structure of the HEMTs, and Ref. 5 for the details of the growth and typology for the LPE HgCdTe samples. These samples were in the form of rectangles (approximately 1.0 cm by 0.5 cm for the HgCdTe films and 1.0 cm by 1.0 cm for the HEMT structures), and four ohmic contacts (indium) were formed at the four corners as van der Pauw probes. The film thicknesses of MCT-I, MCT-II, and MCT-III are 85, 64, and 50 μm , respectively, and the alloy x -value is approximately 0.22 for all three samples.

Two-Carrier Model and HEMT Structures

Figure 1 shows the MR-plots at 75K for the two HEMT structures. The symbols and solid curves represent the experimental data and two-carrier fits, respectively. The parameters (f_1 , μ_1 , and μ_2) used to fit the MR data in Fig. 1 are extracted from two-carrier fits of the RCT data.⁴ Table I lists these parameters.

Also listed in Table I are values of α , β , Δ , and H_D which are calculated from those of f_1 , μ_1 , and μ_2 . The absolute errors in the measured MR values are estimated to be less than 0.5% in this work, the main source of error lying in the determination of the value of the zero-field sheet resistance [see Eq. (1)]. Therefore, the size of the symbol representing each data point in Figs. 1–4 is more than sufficient to represent adequately the error range except in the very low-field region (<0.01 T). As shown in Fig. 1, the agreement between the HEMT data (dots) and the two-carrier model (curves) is excellent. The HEMT data meet all the criteria for the two-carrier system described in the section on Two-Carrier Model of MR, i.e., the H^2 -dependence in the low-field region, the presence of the saturation in the high-field region, and a correct value for the transition-width (approximately 0.9 to 1.0) as shown in Fig. 1. A large body of data taken on several HEMT structures (not shown here) exhibits similar general trends as shown in Fig. 1 even though a complete saturation is often not realized because of insufficient field values used in this work (<1.5 T).

The excellent quantitative agreements indicate that the HEMT structures used in this work are nearly ideal two-carrier systems, and the two-carrier model of MR used here is essentially correct and accurately describes real systems of a two-carrier nature. This is expected for the HEMT structures, since all of the main assumptions made in the RCT scheme should be valid for these structures. For example, the HEMT structures are associated with a degenerate system of the two-dimensional electron-gas (2DEG), and the material is isotropic in the xy -plane. It has been already demonstrated that the RCT data taken on these HEMT structures can be explained by using a two-carrier model of RCT.⁴ Therefore, we use the two-carrier model of MR as a reference to interpret the HgCdTe data below.

Mobility-Spread and HgCdTe Samples

Figure 2 shows the MR-plots of HgCdTe data taken at 75K for the three LPE samples, MCT-I, MCT-II, and MCT-III. In contrast to the HEMT data, the two-carrier fit is not very satisfactory for the HgCdTe data. The values of fitting parameters (f , μ_1 , and μ_2) for the two-carrier fits represented by solid curves in Fig. 2 were extracted from two-carrier fits of the RCT data.

Nevertheless, the relevant parameters for the HgCdTe samples are listed in Table I, since some of these parameters have some qualitative significance. As shown in Fig. 2, the HgCdTe data exhibit two features which are markedly different from the HEMT data, i.e., the absence of any indication of saturation and also the absence of the H^2 -dependent region within the field range (0.01 T to 1.5 T) used in this work. [Strictly speaking, the H^2 -dependence and the saturation should occur in the very low and very high field regions, respectively, for any real systems as indicated by Eq. (7).] In particular, the slope of the MR-plot for these HgCdTe samples generally is lower in the low-field region and higher in the high-field region than for the HEMT structures, thus resulting in a transition-width which is too large for two-carrier systems, at least larger than the width of the entire field range used, i.e., $W > 3$. These deviations from the two-carrier criteria for the HgCdTe samples are clearly revealed by poor fits as shown in Fig. 2. We have experienced similar difficulties with the two-carrier model of RCT to fit the RCT data taken on these samples in our earlier work.⁵ This definitively indicates that none of the LPE films used in this work are adequately described by a simple two-carrier system. However, it is interesting to note that, in spite of all these discrepancies, the two-carrier model still can explain qualitatively the relative magnitude of the MR among different samples (see Fig. 2 and Table I). This suggests that some of the behavior of these samples still can be described qualitatively by the two-carrier model as a first-order approximation.

The quantitative disagreements with the two-carrier criteria observed in the HgCdTe samples strongly indicate that these samples are a very complex system. The deviation from the H^2 -dependence in the low-field region, the absence of saturation, and a large transition-width all strongly suggest an appreciable spread in the carrier mobility or a multicarrier nature of these samples. This observation is directly at odds with the conventional wisdom that high-quality n-type HgCdTe samples should be a two-carrier system (or at most, a three-carrier system consisting of electrons, heavy holes, and light holes). Granted the existence of the mobility spread, it is reasonable to assume that mobility values range approximately from that of the primary carrier mobility (easily determined from the RCT fit) to a much smaller value (probably that of the heavy holes). The mobility spread indicated in these samples may result from either the sample inhomogeneities (likely resulting in a continuum distribution) or the discrete multicarrier nature of HgCdTe associated with light holes, heavy holes, electrons, or even surface-layer carriers (resulting in a discrete distribution consisting of several δ -function-like peaks). Nonparabolicity may also contribute to the complex behavior of these samples, but we believe that this effect is minimal and certainly cannot be considered as the primary effect to cause the large mobility spread indicated in this work.

Therefore, neither the two- nor three-carrier mod-

els fit any of the data taken on HgCdTe samples. In order to proceed further, we have made the simplest simulation available which can fit the HgCdTe data, namely, a four-carrier fit for all three samples, all of which are adequate. As an example, the result for the MCT-II data is shown in Fig. 3 where the solid curve represents the four-carrier fit and the dots represent the experimental data replicated from Fig. 2. The parameters used in the simulation are μ $[-30, -10, -3, -1]$ m^2/Vs and $f(0.847, 0.123, 0.019, 0.011)$. We use here the bold-faced vector notation for brevity where the bracket and the parentheses represent the pre-assigned carrier mobilities (μ) and free fitting-parameters (f), respectively. The reason we have used the pre-assigned carrier mobility values μ (a four-parameter fit) is twofold: First, we believe that any fit which involves many free parameters ($J > 3$) is not necessarily unique and may be physically meaningless. Secondly, it is best to choose mobility values which represent reasonably well the mobility spread suggested in the MR data but are still within a reasonable physical picture. Note that the four mobility values chosen decrease successively by about a factor of three from that of the primary carrier component ($-30 \text{ m}^2/\text{Vs}$) which is higher than the value of $-22.3 \text{ m}^2/\text{Vs}$ which is extracted from a two-carrier fit of the RCT data. Similarly satisfactory fits for the MCT-I data and MCT-III data are as follows: the MCT-I data with μ $[-40, -14, -2, -0.1]$ m^2/Vs and $f(0.062, 0.916, 0.018, 0.004)$ which results in a somewhat less satisfactory fit than those of MCT-II and MCT-III, and the MCT-III data with μ $[-5, 4, -1.5, 0.1]$ m^2/Vs and $f(0.382, 0.005, 0.437, 0.176)$. See Table I for comparison with the two-carrier parameters extracted from the RCT data. In reality, the carrier mobility associated with

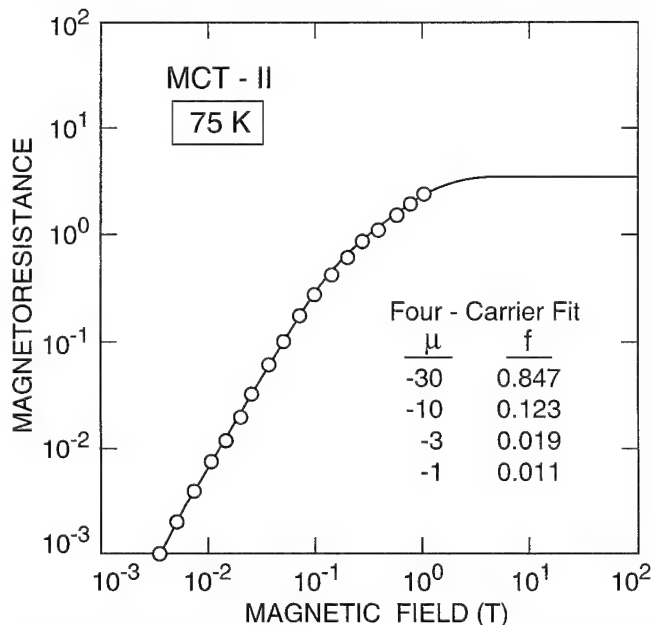


Fig. 3. A four-carrier fit of the MCT-II data shown in Fig. 2. Symbols and the solid curve represent the experimental data and the fit, respectively. The four mobility values are pre-assigned and only the values of the f_i are adjusted in the fit.

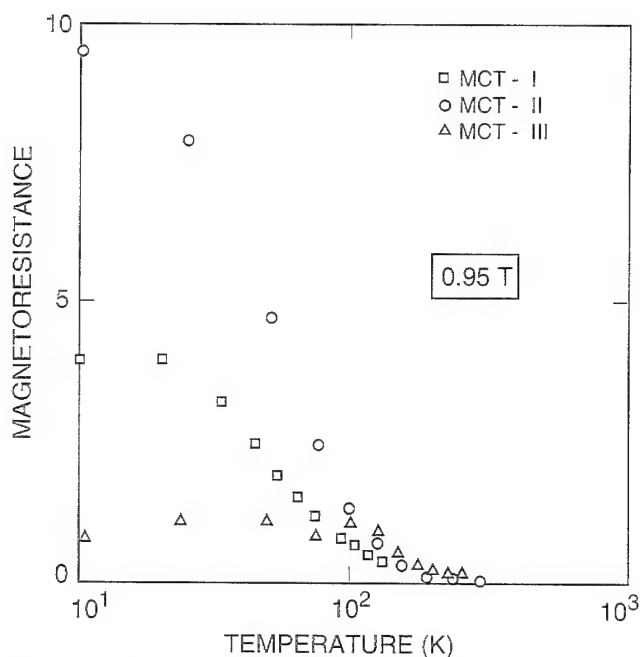


Fig. 4. Magnetoresistance data are plotted vs the lattice temperature for three LPE HgCdTe samples, MCT-I, MCT-II, and MCT-III, at a fixed magnetic field (0.95 T).

inhomogeneities can have either a continuum or discrete (δ -function like) distribution as mentioned already. Therefore, the mobility spread, which is strongly suggested by satisfactory four-carrier fits such as shown in Fig. 3, may be intimately associated with the inhomogeneities in these samples. Inhomogeneities are evoked to explain the anomalous behavior of LPE HgCdTe samples,^{5,7} even though its nature and origin are not very clear presently. We should mention here that Herring⁸ has predicted a contribution of the inhomogeneities to the MR which is proportional to the magnetic field and the variance of the carrier density. His model system assumes a uniform carrier mobility but a position-dependent carrier density. We have not attempted yet to correlate our HgCdTe data to his model mainly due to lack of information of detailed carrier density fluctuations in these samples.

Figure 4 shows the MR plotted vs the lattice temperature at $H \approx 1$ T for the three HgCdTe samples in order to show the difference in the behavior among the three HgCdTe samples. Generally, Type II (mildly anomalous) samples exhibit a larger MR value than Type I (normal) samples, while Type III (severely anomalous) samples show a lower MR value than Type I samples. This trend exists in the low-temperature region (< 100 K) where the magnitude of MR is large as shown in Fig. 4. This can be qualitatively explained from Eq. (6) in a limited field region by using the values of relevant parameters listed in Table I, thus indicating that the two-carrier model of MR also validates qualitatively the typology (based primarily on deviations from an ideal one-carrier system) developed in our RCT work.⁵

SUMMARY AND CONCLUSIONS

Magnetoresistance data obtained by variable-field

Hall measurements and a two-carrier model based on the RCT scheme have been employed to compare two different conduction systems, namely, the LPE HgCdTe films and the GaAs-based HEMT structures. The results demonstrate that magnetoresistance measurements can be used as a valuable tool to characterize semiconducting materials, structures, or devices.

The HEMT data are in quantitative agreements with the two-carrier model, thus validating the utility of the two-carrier model of the magnetoresistance. This also corroborates the result of the reported RCT work⁴ that these HEMT structures are nearly perfect two-carrier systems. The two-carrier model predicts the correct values for the transition-field and the transition-width, and the existence of two limiting cases, namely, the H^2 -dependent (low-field) region and the saturation (high-field) region. The model validated by the HEMT structures is then used as a reference to characterize more complex LPE HgCdTe films.

The HgCdTe data exhibit significant deviations from the two- and three-carrier models. These deviations, namely, the absence of H^2 -dependence and saturation, and a large transition-width, strongly indicate that the HgCdTe films are indeed a complex conduction system. In particular, the large transition-width observed in these samples strongly indicate a large mobility spread or multicarrier nature of these samples. To our best knowledge, we have demonstrated in this work conclusive evidence for the existence of an appreciable mobility spread which may be intimately related to inhomogeneities and anomalous behavior of these samples.

We have demonstrated in this paper that magnetoresistance measurements and subsequent analyses in the RCT scheme can be used to distinguish between a two-carrier system and a more complex system. In particular, they are very useful for the understanding of the sample inhomogeneities and associated anomalous behavior of HgCdTe crystals. They should also be valuable for the electrical characterization of other advanced semiconducting materials, structures, or devices as an alternative to conventional characterization tools.

REFERENCES

1. E.H. Putley, *The Hall Effects and Semiconductor Physics* (New York: Dover, 1960).
2. A.C. Beer, *Solid State Physics, Suppl. 4, Galvanomagnetic Effects in Semiconductors*, ed. F. Seitz and D. Turnbull (New York: Academic Press, 1963).
3. D.C. Look, *Electrical Characterization of GaAs Materials and Devices* (New York: Wiley, 1989).
4. J.S. Kim, D.G. Seiler and W.F. Tseng, *J. Appl. Phys.* 73, 8324 (1993).
5. J.S. Kim, D.G. Seiler, L. Colombo and M.C. Chen, *Semicond. Sci. Technol.* 9, 1696 (1994).
6. J.S. Kim and D.G. Seiler, to be published.
7. M.C. Chen, S.G. Parker and D.F. Weirauch, *J. Appl. Phys.* 58, 3150 (1985).
8. C. Herring, *J. Appl. Phys.* 31, 1939 (1960).

Nondestructive Characterization of $\text{Hg}_{1-x}\text{Cd}_x\text{Te}$ Layers with n-p Structures by Magneto-Thermoelectric Measurements

J. BAARS, D. BRINK, C.L. LITTLER,* and M. BRUDER*

Fraunhofer-Institut für Angewandte Festkörperphysik, Tullastrasse 72,
D-79108 Freiburg i. Br., Germany

The thermoelectric properties of n-type $\text{Hg}_{0.79}\text{Cd}_{0.21}\text{Te}$ (MCT) and of MCT layers with n-p structure have been investigated in transverse ($B \perp \nabla T$) and longitudinal ($B \parallel \nabla T$) magnetic fields ($0 \leq B \leq 16$ kG) using the lateral gradient method at temperatures between 10 and 300 K. The experimental results were analyzed by considering the contributions of electrons and holes to the magneto-thermoelectric effect and the scattering mechanisms involved. The analysis is based on a nonparabolic conduction band and Landau quantization as well as empirical relations for the band gap, the intrinsic carrier density, and the magnetoresistance. For n-type MCT at low temperatures ($10 < T < 30$ K) and weak magnetic fields ($B < 2$ kG), the transverse magneto-thermoelectric effect (TME) was seen to be dominated by electron scattering on ionized defects. Longitudinal acoustic phonon drag was found to affect the TME in strong magnetic fields ($B > 3$ kG) at low temperatures ($T < 20$ K). Longitudinal (LO) phonons were shown to prevail in the electron scattering at higher temperatures ($T > 50$ K) in weak magnetic fields. With increasing magnetic fields, the effect of LO-phonon scattering decreases, and eventually the TME becomes independent of electron scattering. The longitudinal magneto-thermoelectric effect of n-type MCT was also found to exhibit magnetophonon oscillations due to LO-phonon scattering from both HgTe and CdTe phonons. The transverse magnetoresistance (TMR) of the n-type layers in the quantum region has been found to be linearly dependent on the magnetic field. Owing to the TMR of the n-type layers, the variation of the TME of p-n multiple layers with magnetic field is much larger than the variation of the Seebeck coefficient with temperature. Thus, the sensitivity to p-type layers is considerably enhanced compared to that of the Seebeck coefficient. As a result, the TME has proved to be particularly useful in determining the doping and composition of the constituent layers of MCT n-p structures.

Key words: HgCdTe, magneto-resistance, thermoelectric properties

INTRODUCTION

Nondestructive characterization of the doping and composition of $\text{Hg}_{1-x}\text{Cd}_x\text{Te}$ (MCT) layer structures composed of multiple layers of n-type and p-type conduction is important in the design of advanced infrared detector arrays consisting of p-on-n heterodiodes. Hall and conductivity measurements

are widely used to assess the carrier concentration and mobility of semiconductor layers. However, the large electron to hole mobility ratio of MCT considerably impairs this determination whenever a p-type layer coexists with a highly conducting n-type layer. Since the Hall coefficient of multiple layers is a quadratic function of the layer conductivity, the n-type layers dominate the p-type layers, and often the properties of the p-type layers of composite MCT structures are obscured completely. In contrast, the thermoelectric effect (TME) is a linear function of the layer conductance, and therefore it offers a greater characterization potential for multiple MCT layers of different conduction types.^{1,2}

*Permanent address: Department of Physics, University of North Texas, Denton, TX 76203

*AEG-Aktiengesellschaft, INFRAROTMODULE, D-74072 Heilbronn, Germany

(Received October 4, 1994; revised January 25, 1995)

A quantizing magnetic field, applied normal to a multiple-layer sample and the temperature gradient (i.e. in the transverse configuration), has been found to considerably enhance the sensitivity to p-type conduction.³ The resulting transverse current can be viewed as being caused by the drift of the centers of the cyclotron orbits in the temperature gradient. Since the drift velocity of the electrons along the temperature gradient is considerably reduced by the magnetic field, the contribution of holes to the magneto-Seebeck effect is increased relative to that of electrons. Thus, this effect offers a high potential for characterizing thin p-type layers in n-type environments.

Up to now only scarce information on the magneto-thermoelectric properties of MCT has been available. The investigations published so far are mainly dedicated to HgTe. The effective mass of electrons and holes in heavily doped n-type and p-type HgTe have been determined from magneto-thermoelectric measurements, taking into account phonon drag of holes for p-type HgTe.⁴ A large increase of the thermoelectric power has been found for p-type HgTe at temperatures below 30K and has been attributed to phonon drag of holes.^{5,6} Phonon drag of electrons has been proposed for explaining a high negative thermoelectric power measured in pure HgTe samples at low temperatures in quantizing magnetic fields.^{7,8} Also, a singularity found in the thermoelectric power of an MCT sample with $x = 0.14$, has been interpreted as due to phonon drag.⁹ Recently, a sign reversal of the thermopower of an n-type MCT sample with $x = 0.2$ has been observed in quantizing magnetic fields,¹⁰ and this is the only investigation on the magneto-Seebeck effect of MCT in quantizing magnetic fields that we are aware of.

In this study, the magneto-thermoelectric effect of n-type MCT and of MCT p-n layer structures is investigated in greater detail. The thermoelectric properties of the specimens have been investigated in transverse ($B \perp VT$) and longitudinal ($B \parallel VT$) magnetic fields using the lateral gradient method at temperatures between 10 and 300K. The experimental results were analyzed by considering the contributions of electrons and holes to the magneto-thermoelectric effect and the scattering mechanisms involved. The analysis is based on a nonparabolic conduction band and Landau quantization as well as empirical relations for the band gap, the intrinsic carrier density, and the magnetoresistance.

Finally, the TME of MCT layers with n-p structure have been investigated using the lateral gradient method² at temperatures between 10 and 300K. The TME has been found to be of higher sensitivity to p-type layers in an n-type environment than the zero-field Seebeck effect. Therefore, the TME is ideally suited for characterizing constituent p and n-type layers of composite MCT structures.

EXPERIMENTAL

For this study, n-type bulk crystals and epitaxial layers of MCT with $x \approx 0.21$ were used. The bulk

crystals were grown by solid state recrystallization from quenched stoichiometric melts and 0.5 mm thick slices were cut from the bulk crystals parallel to (111) surfaces. The epitaxial layers were deposited from Te-rich solutions on (111)B surfaces of lattice-matched $\text{Cd}_{0.86}\text{Zn}_{0.04}\text{Te}$ crystals using the dipping technique. To convert the as-grown p-type material to n-type, the bulk slices and epitaxial layers were annealed in sealed quartz ampules under saturated Hg vapor pressure at temperatures of 225°C for three to four weeks. Subsequently, the samples were chemomechanically polished using a 0.5% bromine-methanol solution. The annealed epilayers were of uniform composition and had donor densities in the 10^{14} cm^{-3} range, as verified from temperature-dependent Hall-effect measurements and infrared transmission measurements at the fundamental absorption edge. The annealed bulk crystals, which have highly uniform stoichiometry, typically consist of a 200 μm thick n-type skin with donor densities in the low 10^{14} cm^{-3} range and a p-type core about 100 μm thick with acceptor densities in the 10^{16} cm^{-3} range. Prior to the measurements, the samples were subjected to a special electrochemical etch¹¹ to provide clean surfaces of stoichiometric composition and to avoid surface inversion.

The p-on-n MCT heterostructures used for this study were epitaxially grown on $\langle 100 \rangle \text{GaAs}$ substrates by metalorganic chemical vapor deposition (MOCVD) using the interdiffused growth method.^{12,13} The heterostructures consist of three layers: a p-type wide-gap cap layer on top, a p-type narrow-gap absorber, and an n-type narrow-gap absorber on the bottom. All layers are In-doped, and the p-type layers are additionally doped with As. The In and As concentration profiles of the specimens were determined by secondary ion mass spectroscopy (SIMS) performed at Charles Evans Associates. The SIMS Te profiles were used to analyze the heterostructures regarding layer composition and thickness.¹⁴ The compositions of the narrow gap layers were also obtained from infrared transmission measurements of the fundamental absorption edge¹⁵ at temperatures of 77 and 300K.

The thermoelectric effect was measured by employing the lateral gradient method. Details of the arrangement for measuring the thermoelectric voltage by this lateral gradient technique are given in Ref. 2. It is important to note that, since the low temperature glue used is soluble in methanol, the temperature sensors can be removed without damage to the sample. Therefore, the lateral gradient technique is considered to be nondestructive. For the conductivity and Hall-effect measurements the van der Paw method was used. For both methods, Au leads were bonded to Au/In contact pads evaporated at the edges of the rectangular-shaped specimens measuring about $5 \times 12 \text{ mm}^2$. The electrical properties of these contacts on n-type and p-type MCT at temperatures between 15 and 320K were found to be ohmic.

A temperature difference of 1 or 2K across the sample was chosen for determining the Seebeck coefficient between 10 and 50K, and a difference of 5K was used at higher temperatures. The Seebeck coefficient (α) is the differential thermoelectric voltage (DTV) given by the ratio of the measured thermoelectric voltage U_{th} to the temperature difference $T_2 - T_1$ applied to the sample, or $\alpha = U_{th}/(T_2 - T_1)$. The magneto-Seebeck effect was obtained by applying magnetic fields of $0 \leq B \leq 16$ kG to the samples.

THERMOELECTRIC MODEL

Seebeck Coefficient

The DTV or Seebeck coefficient of an isotropic, cubic semiconductor corresponds to the voltage produced by two generators in parallel, the admittances of which are proportional to the conductivity of electrons (e) and holes (h), respectively. In this case, α is given by,¹⁶

$$\alpha = (\alpha_e n \mu_e + \alpha_h p \mu_h) / (n \mu_e + p \mu_h), \quad (1)$$

where the thermoelectric coefficients for electrons and holes, α_e and α_h , have been derived by Devlin¹⁷ from the linearized Boltzmann equation assuming thermally equilibrated phonons. This assumption is justified for MCT at temperatures $T > 30$ K, but it may fail at low temperatures when the interaction between the scattering phonons becomes weaker, owing to their longer wavelength at lower temperatures. Therefore, phonon drag is likely to affect the Seebeck coefficient at temperatures below 30K.⁵⁻⁹ As a result, the model used in preceding studies^{1,2} was limited to temperatures above 30K, and it was restricted to the thermoelectric coefficients $\alpha_{e,h}$, owing to the diffusion of electrons (e) and holes (h) in a temperature gradient. Thus, the coefficients $\alpha_{e,h}$ are given by,

$$\alpha_{e,h} = (k/q) \langle \epsilon \tau_{e,h} \rangle / \langle \tau_{e,h} \rangle - \eta_{e,h}, \quad (2)$$

where $\epsilon = E/(kT)$, $\eta_e = E_F/(kT)$, and $\eta_h = -(E_F + E_g)/(kT)$. The energy E is measured from the edge of the conduction band, E_g is the band gap energy, E_F is the Fermi energy, T is the temperature, k is the Boltzmann constant, q is the elementary charge ($-e$ for electrons and $+e$ for holes), and τ the relaxation time. The kinetic term $\langle \epsilon \tau_{e,h} \rangle / \langle \tau_{e,h} \rangle$ depends on the charge carrier scattering mechanisms involved. Optical phonons are by far the most effective scatterers for charge carriers in MCT, owing to its high ionicity, except at low temperatures ($T < 40$ K) where scattering by ionized defects prevails.⁶ This model uses the kinetic term derived by Devlin¹⁷ for pure optical mode scattering of electrons and holes assuming non-degenerate charge carrier densities, or

$$\langle \epsilon \tau_{e,h} \rangle / \langle \tau_{e,h} \rangle = 2.5 + 0.5/\exp[0.95(\Theta/T)^2] - 0.86(\Theta/T)^{2.5}/\exp(\Theta/T). \quad (3)$$

The Debye temperature Θ is assumed to be equal to the sum of the CdTe-like and HgTe-like longitudinal optical (LO) phonon frequencies of MCT, ω_{LO1} and

ω_{LO2} , weighed by the mole fractions x of CdTe and $1 - x$ of HgTe, respectively, or

$$\Theta = [x \omega_{LO1} + (1 - x) \omega_{LO2}] hc/k. \quad (4)$$

The model includes a single acceptor level of density N_A at an energy E_A above the valence band edge, with a degeneracy factor of four, and fully ionized donors of density N_D . The electron and hole densities, n and p , are determined from the charge neutrality equation together with empirical relations for the temperature and composition dependence of the band gap E_g ,¹⁸ the CdTe-like and HgTe-like LO phonon frequencies ω_{LO1} and ω_{LO2} ,¹⁹ the intrinsic carrier density n_i ,²⁰ and the electron to hole mobility ratio μ_e/μ_h .² This simple model has proven to be adequate for a quantitative description of the thermoelectric properties of p-type and n-type MCT in the temperature range between 40 and 320K.^{1,2}

This model also has been used for characterizing MCT p-on-n heterostructures.² The p-on-n heterostructures have been assumed to be composed of distinct layers with abrupt interfaces. The thermoelectric voltage of a stack of n layers (j) caused by a lateral temperature gradient is equivalent to the voltage produced by n generators in parallel, the admittances of which are the conductances G_j of the individual layers, given by,

$$\alpha_t = \sum_j \alpha_j G_j / G = \sum_j \alpha_j \sigma_j d_j / (\sigma d), \quad (5)$$

where $\sigma = \sum_j \sigma_j d_j / d$ and $d = \sum_j d_j$ are the conductivity and thickness of the total sample, respectively. This linear superposition of the thermoelectric voltages is assumed to be valid in magnetic fields as well. Up to this point, however, the model does not include the effect of an magnetic field.

Magneto-Seebeck Effect

A uniform magnetic field applied to the sample forces the mobile charge carriers in a simple band into circular motion with the cyclotron frequency $\omega_c = |e|B/m^*$ in the plane perpendicular to the magnetic field $B(0,0,B_z)$. The energy of the charge carriers is quantized into discrete Landau levels, given by,

$$E_{l,kz,\pm} = (l + 1/2) \hbar \omega_c + \hbar^2 k_z^2 / (2m^*) \pm (1/2) \mu_B g^* B, \quad (6)$$

where μ_B is the Bohr magneton and g^* is the effective Landé (g) factor.

The magnetic field strongly affects the energies of the highly mobile electrons with small effective masses, whereas the heavy holes are almost unaffected. For example, in MCT at 75K with $x = 0.21$, $\hbar \omega_c \approx 1.5$ meV/kG for electrons and ≈ 23 μ eV/kG for heavy holes ($m_{hh}^* = 0.5 m_0$). Since the drift velocity of the electrons along the temperature gradient is considerably reduced by the magnetic field, the contribution of holes to the magneto-Seebeck effect is increased dramatically relative to that of electrons. Thus, this effect offers a high potential for characterizing thin p-type layers in n-type environments.

In order to include the magnetic field effects, our model must be modified to some extent. Since the

effect on the heavy holes is too small to be detected, only changes arising from electrons must be taken into account. In nonquantizing magnetic fields (i.e., in the classical case), the Fermi energy is not affected by the magnetic field and the total change in the Seebeck coefficient α_e [Eq. (2)] is due to variations of the kinetic term $\langle \varepsilon \tau_e \rangle / \langle \tau_e \rangle$, which depends on the electron scattering. This classical region, therefore, can be used to identify the dominant scattering mechanism. When $\mu B \gg 1$ (the classical high-field region), the kinetic term becomes independent of the scattering mechanisms and attains a limiting value $\langle \varepsilon \tau_e \rangle / \langle \tau_e \rangle = 5/2$, which yields the limit of the magneto-Seebeck coefficient in the classical region, given by,

$$\alpha_e^{\text{lim}} = (k/q) (5/2 - \eta_e). \quad (7)$$

For strong magnetic fields, when $\omega_c \tau \gg 1$ and $\hbar \omega_c \approx kT$, the quantization is pronounced and the Fermi energy is no longer independent of the magnetic field because of the altered density of states. This region is easily reached in low x -value MCT, e.g., for electrons in MCT with $x = 0.21$ in a field of 5 kG, we have $\hbar \omega_c \approx kT$ at 75K.

Using the approximation $\langle \varepsilon \tau_e \rangle / \langle \tau_e \rangle = \langle \varepsilon \rangle$ and Kane's²¹ $k \cdot p$ model for narrow-gap zinc-blende-type semiconductors ($\Delta \gg E_g$), Puri²² derived the following relation for the change in the electronic part of the magneto-Seebeck coefficient in the quantum region beyond its limit in the classical high-field region (i.e., $\Delta \alpha_e(B) = \alpha_e(B) - \alpha_e^{\text{lim}}$);

$$\Delta \alpha_e(B) = (k/e) \left[\ln \sum_{l=0}^{20} x_l^{1/2} e^{-x_l} + \sum_{l=0}^{20} x_l^{3/2} e^{-x_l} \left(\sum_{l=0}^{20} x_l^{1/2} e^{-x_l} \right)^{-1} \right. \\ \left. + (1/2) \ln \left\{ 8P^4 k_B^{-4} / (9E_g^3 kT) \right\} - 1 \right], \quad (8)$$

$$\text{where } 2kT x_l = [E_g^2 + (8/3) P^2 k_B^2 (1 + 1/2)]^{1/2}, \quad (9)$$

$P^2 = E_p \hbar^2 / (2m_0)$ and $k_B^2 = e B / \hbar$. Puri²² showed that this approximation of the electronic contribution to the TME in the quantum limit quantitatively matches the experimental data obtained from measurements on n -type InSb specimens with donor densities in the 10^{13} to 10^{14} cm^{-3} range at temperatures between 6 and 100K. For p -type semiconductors where holes as well as electrons are contributing to the Seebeck coefficient in the quantum region experimental data is still lacking. To include holes in our model, the magnetoresistance must be taken into account.

Transverse Magnetoresistance

In the quantum limit ($E_F < \hbar \omega_c$), all of the transport coefficients except the TME show smooth field dependences which are characteristic of the type of scattering; the TME becomes independent of scattering. For scattering by LO phonons, the transport coefficients may also exhibit resonances due to the magnetophonon (MP) effect. However, disregarding possible MP oscillations for the moment, the transverse magnetoresistance for LO phonon scattering in the quantum limit

is proportional to the cyclotron frequency and thus a linear function of the magnetic induction,²³⁻²⁵

$$\rho_{\perp} / \rho_0 = C \hbar \omega_c / (kT) = C \hbar |q| B / (m_0^* kT). \quad (10)$$

The band-edge effective electron mass m_0^* , is given by^{25,26}

$$m_0 / m_0^* = (2/3) (E_F / E_g) (\Delta + 3 E_g / 2) / (\Delta + E_g). \quad (11)$$

The factor C in Eq. (10) is related to the scattering.²⁴ For other scatterers (e.g. ionized point defects), the transverse magnetoresistance does not linearly depend on the magnetic induction. It is a quadratic or a higher power function of B .^{24,25}

The analysis of the experimental magneto-Seebeck data of p - n layer structures is based on Eq. (5) for the total magneto-DTV and on Eq. (10) for the transverse magnetoresistance. The magneto-DTV of the p -type layers is represented by Eq. (1) and Eq. (2) modified by the magnetoresistance in the quantum limit [Eq. (10)], given by

$$\mu_e / \mu_h = b (\rho_{\perp} / \rho_0)^{-1} \quad (12)$$

where b is the electron-to-hole mobility ratio in the absence of a magnetic field.²

The magneto-DTV due to electron diffusion in the quantum region of nondegenerate n -type layers is described by Eqs. (7), (8), and (9). At temperatures below about 30K phonon drag is likely to occur. Therefore, in addition to the electronic contribution, the phonon drag contribution must be taken into account as well.

Phonon Drag

A phonon flux parallel to the temperature gradient is produced by the temperature difference applied to the crystal. The interaction of phonons with electrons causes momentum transfer from the phonons to the electrons and thus an effective electron flux in the opposite direction as the temperature gradient appears. This phonon drag has to be considered in addition to the electron diffusion in a temperature gradient. In particular, the phonon drag is evident at low temperatures and strong magnetic fields, when the interaction between the phonons becomes weaker and thus the phonons are no longer in thermal equilibrium. The phonon drag has been calculated for isotropic, cubic semiconductors with a simple parabolic band in a quantizing magnetic field by various authors.^{22,27,28}

Puri²² has calculated the phonon drag contribution to the thermoelectric power α_p taking into account two modes of electron coupling to acoustic phonons, i.e. the scattering due to the deformation potential and the piezoelectric mode of scattering. The deformation potential scattering yields a quadratic variation of the thermoelectric power with the magnetic field, whereas for the piezoelectric scattering mode α_p varies linearly with the magnetic field. Experimental α_p data obtained from TME measurements on n -type InSb samples clearly shows a quadratic field dependence at sufficiently low temperatures when the

phonons interact only with the boundaries of the sample. This result is expected since the electron-energy surfaces are isotropic. Thus, based on the expression for the relaxation time of long-wavelength longitudinal acoustic (LA) phonons due to collisions with thermal phonons, given by

$$\tau_q(T) = A/(q^m T^r), \quad (13)$$

and disregarding transverse acoustic phonon scattering, Puri²² derived for the phonon drag contribution to the Seebeck coefficient in the phonon-phonon scattering range:

$$\alpha_p = A' E_d^2 (k/q) (kT)^{-3/2} (m_0^*/m_0)^{1/2} T^{-r} (2k_B T)^{2-m/2}. \quad (14)$$

Here, E_d is the deformation potential constant and A' has only a very weak dependence on the magnetic field and the temperature. A comparison with experimental InSb data yielded $m=1$ and $r=3$. Equation (14) compares well with Khalfin's²⁸ expression for α_p based on $\tau_q = A/(qT^3)$, given by

$$\alpha_p = A^* E_d^2 (k/q) (kT)^{-3/2} (m_0^*/m_0)^{1/2} T^{-3} (2k_B T)^{3/2}, \quad (15)$$

with

$$A^* = (A/\rho) (2m_0)^{1/2} (8\pi)^{-2} [\ln(2\{\hbar k_B s/(4kT)\}^{-2}) - 2.57], \quad (16)$$

where ρ is the density and s is the sound velocity of the crystal. Therefore, for the description of our results, Khalfin's expression (Eq. 15) was used.

RESULTS AND DISCUSSION

N-Type MCT

The magnetic-field dependence and the temperature dependence of the TME of n-type MCT samples with x -values of ≈ 0.21 have been measured. First, the dependences of the TME obtained from DTV measurements of the samples in quantizing magnetic fields will be discussed. Figure 1 presents experimental and calculated variable-temperature DTV data of an n-type MCT sample at 0 and 13.5 kG. The zero field data are well-fitted by the thermoelectric model [Eqs. (1-4)]. The results are also in agreement with those of variable-temperature Hall-effect measurements. The experimental magneto-thermoelectric data for temperatures between 30 and 200K were found to be represented by Eq. 8 for α_e , the magneto-Seebeck coefficient due to the diffusion of electrons in narrow-gap, zinc-blende-type semiconductors in the quantum region. The least squares fit to the experimental data, however, yields a higher value for the donor density and a lower value for x than the fit to the zero-field data. This slight inconsistency may be due to the approximations which underlie Eq. (8), or indicate that higher fields than 13.5 kG are required. At temperatures above 200K, the experimental data

departs from the calculated curve since μB decreases with rising temperatures and thus the electrons deviate from the quantum region. The discrepancy between the experimental data and α_e at low temperatures is caused by phonon drag, as illustrated in Fig. 2. The variation of the experimental TME data with the magnetic field in the quantum limit at temperatures below 20K cannot be fitted unless phonon drag is taken into account. The direct electronic contribution, α_e , together with the phonon-drag contribution α_p [Eq. (8) and Eq. (15)], however, provide an excellent fit of the experimental data, yielding values for the CdTe mole fraction x and the donor density N_D which agree well with those obtained from variable-temperature Hall and infrared-transmission measurements. An average value of $s = 3 \cdot 10^5$ cm/s for the velocity of sound was obtained from the least squares fits which is consistent with the value determined by the elastic constant $c_{11} \approx 6 \cdot 10^{10}$ Nm⁻² of HgTe.²⁵ The fits also yield an average value $AE_d^2 = 3.1 \cdot 10^4$ K³s cm⁻¹ (eV)². Using $E_d = 2.4$ eV for the deformation potential constant, as determined by Gorodilov⁸ from the Bir-

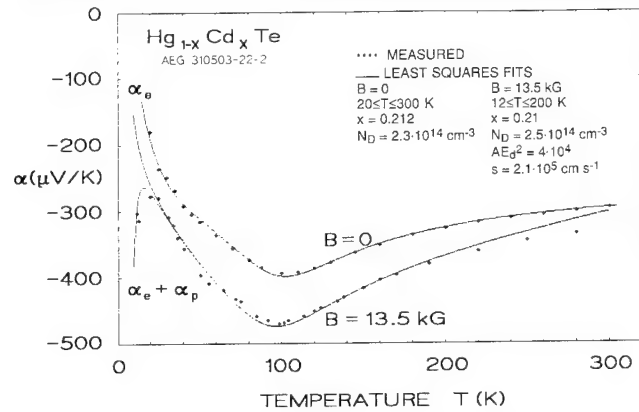


Fig. 1. Seebeck coefficient vs temperature obtained from thermoelectric measurements on an n-type MCT sample at 0 and 13.5 kG. The solid curves are the result of least squares fits to the experimental data (*). The symbols α_e and α_p are the electron and phonon contributions to the Seebeck coefficient, respectively. The fits yielded the parameter values listed in the inserted table.

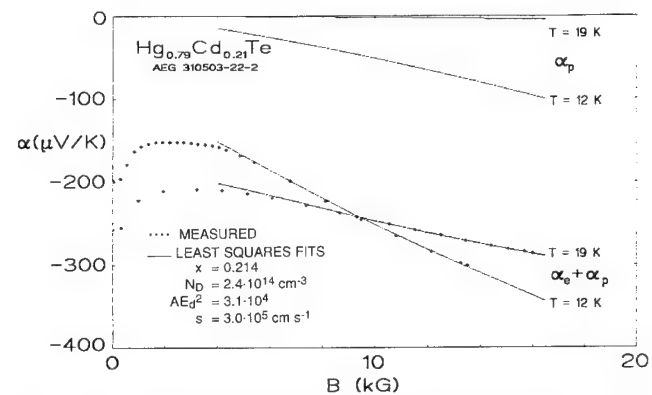


Fig. 2. Seebeck coefficient α vs magnetic induction B of n-type $\text{Hg}_{0.79}\text{Cd}_{0.21}\text{Te}$ at $T = 12.6$ and 18.6 K. The solid curves are the results of least squares fits to the experimental data (*), taking into account phonon drag. The symbols α_e and α_p are the electron and phonon contributions to the Seebeck coefficient, respectively. The field dependence of the phonon drag contribution α_p is shown as well.

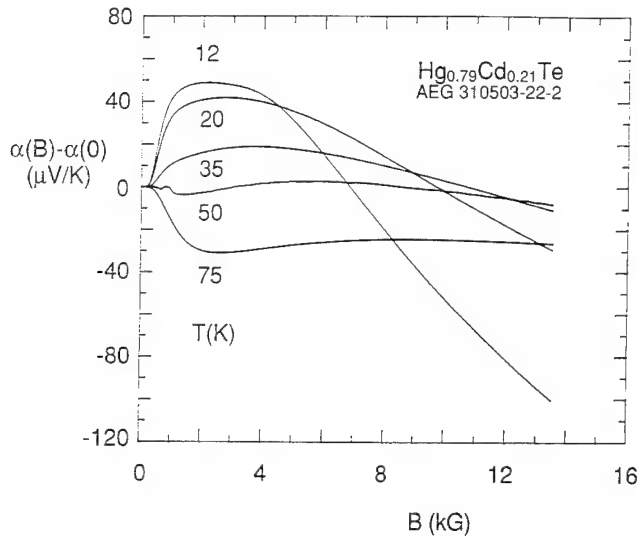


Fig. 3. Change of the TME ($\alpha(B) - \alpha(0)$) as a function of B obtained from measurements on an n-type MCT sample at various temperatures between 12 and 75K.

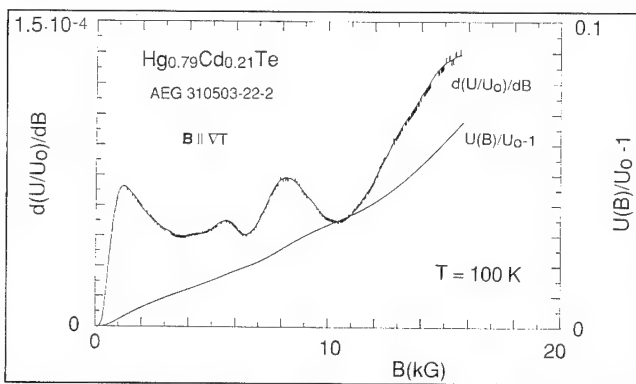


Fig. 4. Relative change ($U(B)/U_0 - 1$) and first derivative ($d(U/U_0)/dB$) of the longitudinal magneto-thermoelectric voltage $U(B)$ normalized to $U(B=0) = U_0$ vs B at $T = 100K$.

Pikus constants, the average relaxation time factor is $A \approx 5.4 \cdot 10^3 K^3 s cm^{-1}$, which compares with the value of $4.37 \cdot 10^3$ found for InSb.²²

The field dependence of the TME in the classical low-field region ($\mu B < 1$, $\hbar \omega_c < kT$) is characteristic of the dominant scattering mechanism as Fig. 3 illustrates. Here the change of the TME as a function of B is shown, obtained from measurements on an n-type MCT sample at various temperatures between 12 and 75K. There is a large positive change at temperatures below 35K and a smaller negative one at temperatures beyond 35K. The maximum change of the TME with the magnetic field in the classical region is given by Eq. (2) and Eq. (7) as

$$\Delta \alpha_e = \alpha_e^{\lim} - \alpha_e(0) = (k/q)[5/2 - \langle \epsilon \tau_e \rangle / \langle \tau_e \rangle]. \quad (17)$$

According to the kinetic term $\langle \epsilon \tau_e \rangle / \langle \tau_e \rangle$ for LO-phonon scattering [Eq. (3)], the maximum change of the TME is negative and of the order of $1 \mu V/K$ at temperatures below 35K. Thus, LO-phonons obviously are not the dominant scatterers at low temperatures. The large positive change, however, can be explained by scattering on ionized point defects. The

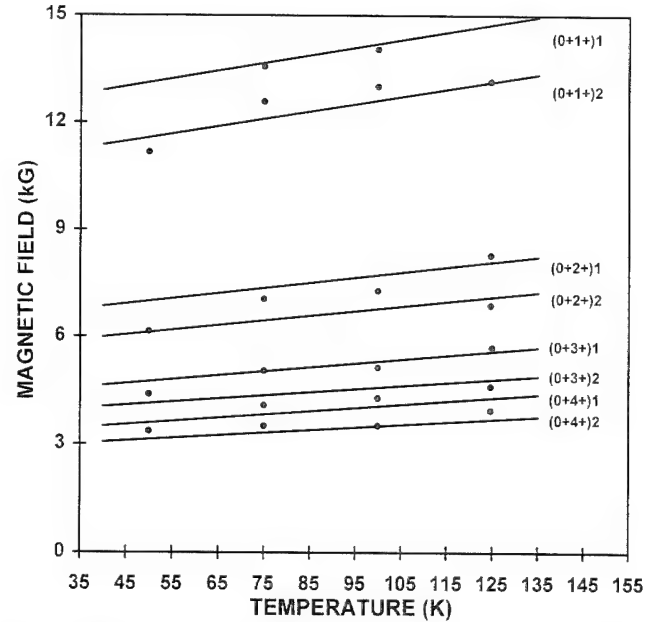


Fig. 5. Magnetic field of magneto phonon resonances vs temperature measured (\bullet) and calculated ($—$) for spin conserving transitions ($0+1+$), and scattering on CdTe-like LO-phonons ($i = 1$) and on HgTe-like LO-phonons ($i = 2$). The measured data is obtained from the second derivative of the LME. It represents minima of the absolute LME. The calculation includes a $\pi/2$ phase shift of the MP resonances to lower fields according to Barker.³⁰

kinetic term for ionized defect scattering¹⁶ ($\langle \epsilon \tau_e \rangle / \langle \tau_e \rangle = 4$) yields a maximum change of the order of $130 \mu V/K$ below 35K. Therefore, ionized defect scattering apparently is the dominant mechanism at low temperatures, whereas LO-phonon scattering prevails at temperatures above 35K.

Oscillations in the longitudinal magnetothermal emf (LME) of the n-type bulk sample have also been seen. These are shown in Fig. 4, where the relative change and the first derivative of the thermoelectric power vs magnetic field at 100K are plotted. These resonances can be described in terms of magneto-phonon (MP) transitions involving both LO HgTe and CdTe phonons, as shown in Fig. 5. The solid lines are the MP transition energies as a function of quantum number and temperature for both the HgTe and CdTe phonons, calculated using Weiler's energy band model,²⁶ and the solid dots are the field positions of the MP resonances. The experimental data were obtained from the second derivative of LME vs B . It can be seen that, for most temperatures and quantum numbers, the MP transitions resulting from interactions of electrons with both the HgTe and the CdTe phonons are unresolved. These MP transitions become resolved at higher fields and temperatures. To fit the MP resonance magnetic field positions to the experimental LME data, it was found that a phase shift of $\pi/2$ to lower fields must be applied to the calculated field positions of the resonances. This phase shift is considerably larger than that predicted by Arora and Peterson,²⁹ and corresponds to the phase shift predicted by Barker,³⁰ confirming his predictions for our experimental conditions.

Past magnetoresistance results³¹⁻³⁴ for low x-value

($x < 0.3$) samples have been described in terms of LO-phonon scattering involving only HgTe phonons. However, the LME results have sufficient resolution to see the contribution due to the CdTe LO phonons as well. Thus, our results also support the premise that both HgTe and CdTe LO phonons are involved in the resonant scattering processes which gives rise to MP resonances in MCT, even at x -values less than $x = 0.3$.

The analysis of the magneto-Seebeck effect of composite structures in particular relies on the transverse magnetoresistance of n-type MCT [Eq. (10)]. Only scarce information on the magnetoresistance of n-type MCT has been available up to now.²⁵ In this study, the transverse magnetoresistance has been investigated between 0 and 12 kG of various n-type MCT samples with donor densities in the low 10^{14} cm^{-3} and electron mobilities in the high $10^5 \text{ cm}^2/(\text{Vs})$ range. For magnetic fields larger than 5 kG, the transverse magnetoresistance of all samples at temperatures between 30 and 100K was found to be nearly proportional to B as illustrated in Fig. 6. From least squares fits to the experimental data, with x and C as adjustable parameters, an average value $C \approx 3$ was obtained for the magnetoresistance factor in Eq. (10), and the x -values yielded agree with those determined by infrared-transmission analysis. This result again confirms that LO-phonon scattering of electrons in MCT is dominant, as already found in the thermoelectric properties at temperatures above 40K.

Composite Structures

The field dependence of the DTV of a bulk n-type

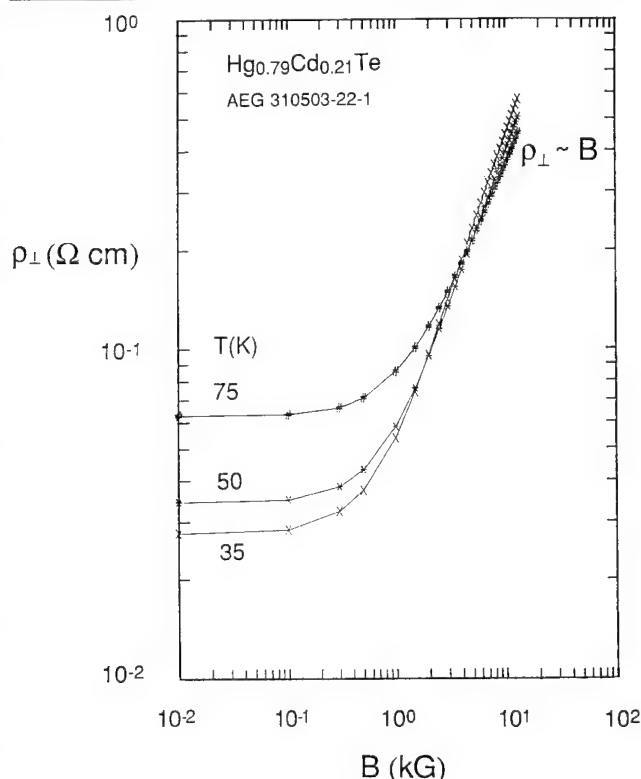


Fig. 6. Resistivity vs magnetic induction B for an n-type MCT sample at various temperatures.

MCT sample with a p-type core at 75K is shown in Fig. 7. It clearly illustrates the dramatic increase in the DTV with the transverse magnetic field applied to this composite p-n structure. To analyze the sample with respect to composition, doping, and thickness ratio of n-type skin to p-type core, it is assumed to be composed of two distinct layers with abrupt interfaces. The mole fraction, x , the donor and acceptor densities, N_D and N_A , of the two layers, the acceptor activation energy, E_A , the magnetoresistance factor C in Eq. (10), and the thickness ratio, d_n/d_p , are considered to be adjustable parameters. The fits yielded the data listed in the table inserted in Fig. 7. The parameter values obtained from the fit to the variable-magnetic-field DTV data compare well with the variable-temperature zero-field DTV data. It is interesting to note that the magneto-DTV analysis yields the same value for C as the analysis of the magnetoresistance. This agreement supports the validity of the magneto-Seebeck analysis based on Eq. (5) and Eqs. (7)–(12).

Subsequently, the p-type core was removed by

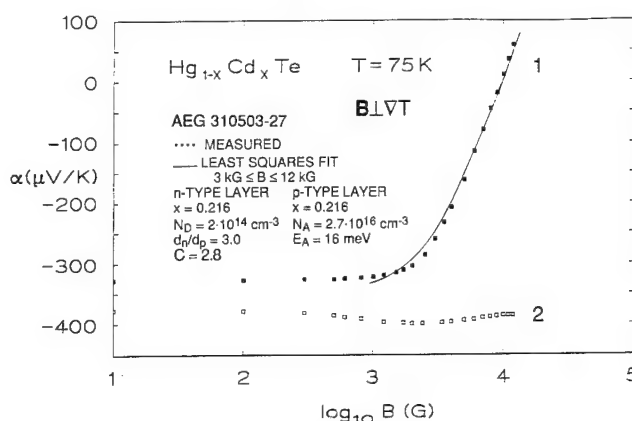


Fig. 7. Seebeck coefficient α vs magnetic induction B of an MCT n-p structure at $T = 75\text{K}$ before (1) and after (2) the p-type layer was removed by etching. The least squares fit to the experimental data of the n-p structure yields x , the donor and acceptor densities, N_D , N_A , the acceptor activation energy, E_A , and the thickness ratio of the n and p-type layer, d_n/d_p , as listed in the inserted table.

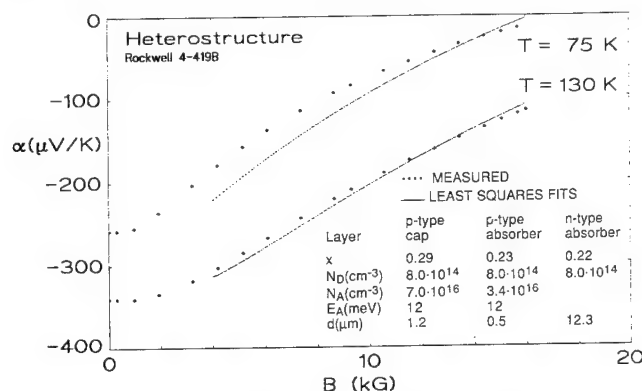


Fig. 8. Magnetic field dependence of the Seebeck coefficient of an p-n heterostructure together with least squares fits to experimental data (*) at 75 and 130K. The least squares fits yield the structural and dopant parameters as listed in the inserted table.

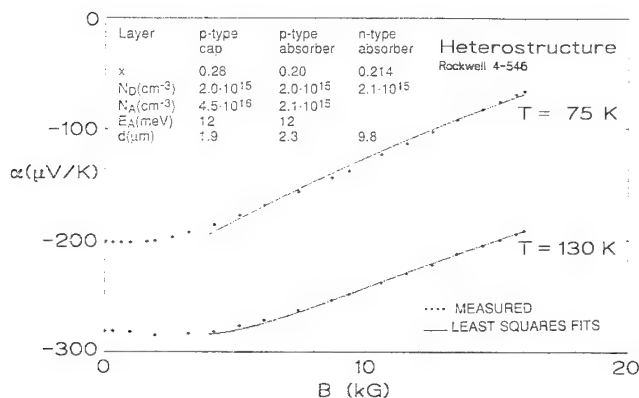


Fig. 9. Magnetic field dependence of the Seebeck coefficient of a p-on-n heterostructure together with least squares fits to experimental data (*) at 75 and 130K. The least squares fits yield the structural and dopant parameters as listed in the inserted table.

etching the sample chemo-mechanically from one side down to a quarter of the original thickness. In contrast to the original sample with the p-type core, the data obtained from variable-field DTV measurements on the thinned specimen exhibit almost no change with the magnetic field, as shown in Fig. 7. The absolute value and the negative sign of the DTV as well as its slight increase with field between 0 and 2 kG is typical of electrons scattered by LO phonons. The x-value and donor density obtained from variable-temperature Hall measurements confirm the results of the magneto-Seebeck analysis.

Figure 8 and 9 present the magnetic field dependence of the Seebeck coefficient of two p-on-n heterostructures together with the least squares fits of the model [Eqs. (5), (7)–(12)] to the experimental data at temperatures of 75 and 130K. For the analysis, the p-on-n heterostructures are assumed to be composed of three distinct layers with abrupt transitions: a p-type wide gap cap on top, a p-type narrow gap absorber, and an n-type narrow gap absorber on the bottom. The mole fractions, x ; the acceptor and donor densities, N_A and N_D , of each layer; and the thickness ratios of the n-type and p-type absorbers to the cap are considered adjustable parameters. Since the thermoelectric model is based on nondegenerate statistics, the analysis must be confined to temperatures for which the Fermi energy is more than 1kT below the conduction band edge of the n-type layer. This is the case for temperatures of 130K and beyond. The model fits very well the variable-field DTV data obtained for 130K. The parameter values obtained from these fits are used to fit the data measured on the samples at 75K. Except for one heterostructure (Fig. 8), the data for 75K is fitted very well, too. There is also agreement with our recently published variable-temperature DTV analyses performed on these heterostructures.² The accuracy obtained from the magneto-Seebeck analysis, however, is considerably higher than that from the zero-field analysis, since, owing to the magnetoresistance of the n-type layer, the effect of variations of the p-type layer parameters on the Seebeck coefficient of p-n multiple layers was

found to be much larger in the presence of a magnetic field than in the absence.

SUMMARY AND CONCLUSION

For n-type MCT at low temperatures ($10 < T < 30\text{K}$) and weak magnetic fields ($B < 2\text{ kG}$), the TME was seen to be dominated by electron scattering on ionized defects. Longitudinal acoustic phonon drag was found to affect the TME in strong magnetic fields ($B > 3\text{ kG}$) at low temperatures ($T < 20\text{K}$). Longitudinal optical phonons were shown to prevail in the electron scattering at higher temperatures ($T > 50\text{K}$) in weak magnetic fields. With increasing magnetic fields, the effect of LO-phonon scattering decreases, and eventually the TME becomes independent of electron scattering. The LME of n-type MCT was also found to exhibit MP oscillations due to LO-phonon scattering of electrons with both HgTe and CdTe phonons.

Finally, the thermoelectric properties of MCT layers with n-p structure have been investigated in transverse ($B \perp VT$) magnetic fields using the lateral gradient method at temperatures between 10 and 300K. The experimental results were analyzed with respect to the relevant structural and dopant parameters, yielding complete information on the heterostructure properties. Thus, the TME has proved particularly useful in determining the doping and composition of the constituent layers of MCT n-p structures. This effect, therefore, offers a high potential for nondestructive characterization of layered MCT, currently used in most FPA infrared detector designs.

REFERENCES

1. J. Baars, D. Brink and J. Ziegler, *J. Vac. Sci. Technol. B* 9, 1709 (1991).
2. J. Baars, D. Brink, D.D. Edwall and L.O. Bubulac, *J. Electron. Mater.* 22, 923 (1993).
3. J. Baars, D. Brink, *SPIE Proc.* 2021, 222 (1993).
4. A. Jedrzejczak and T. Dietl, *Phys. Stat. Solidi. (B)* 76, 737 (1976).
5. V.V. Sologub, V.I. Ivanov-Omskii, V.M. Muzhdaba and S.S. Shalyt, *Sov. Phys. Solid State* 13, 1452 (1971).
6. J.J. Dubowski, T. Dietl, W. Szymanska and R.R. Galazka, *J. Phys. Chem. Solids* 42, 351 (1981).
7. N.A. Gorodilov, L.I. Domanskaya and E.A. Neifel'd, *Sov. Phys. Semicond.* 21, 841 (1987).
8. N.A. Gorodilov, L.I. Domanskaya, E.A. Neifel'd and N.G. Shelushinina, *Sov. Phys. Semicond.* 24, 417 (1990).
9. S.A. Aliev, T.G. Gadzhiev and R.I. Selim-Zade, *Sov. Phys. Solid State* 31, 346 (1989).
10. G.W. Lashkarev, M.V. Radchenko, E.S. Parenskaya, M.S. Nikizin and Ju.I. Rastegin, *Pisma Zh. Eksp. Teor. Fiz.* 53, 411 (1991) (in Russian).
11. M. Seelmann-Eggebert and D. Brink, German Patent DE 40 12 453 A 1.
12. D.D. Edwall, J.-S. Chen, J. Bajaj and E.R. Gertner, *Semicond. Sci. Technol.* 5, S221 (1990).
13. D.D. Edwall, J.-S. Chen and L.O. Bubulac, *J. Vac. Sci. Technol. B* 9, 1691 (1991); D.D. Edwall, L.O. Bubulac and E.R. Gertner, *J. Vac. Sci. Technol. B* 10, 1423 (1992).
14. L.O. Bubulac, D.D. Edwall, J. Chung and C.R. Viswanathan, *J. Vac. Sci. Technol. B* 10, 1633 (1992).
15. E. Finkman and S.E. Schacham, *J. Appl. Phys.* 56, 2896 (1984).
16. R.A. Smith, *Semiconductors* (Cambridge, U.K.: Cambridge University Press, 1964), p. 173.

17. S.S. Devlin, *Physics and Chemistry of II-VI Compounds*, ed. M. Aven and J. Prener (Amsterdam, The Netherlands: North-Holland, 1967), p. 562.
18. D.G. Seiler, J.R. Lowney, C.L. Littler and M.R. Loloee, *J. Vac. Sci. Technol. A* 8, 1237 (1990).
19. J. Baars and F. Sorger, *Solid State Commun.* 10, 875 (1972).
20. G.L. Hansen and J.L. Schmit, *J. Appl. Phys.* 54, 1639 (1983).
21. E.O. Kane, *J. Phys. Chem. Solids* 1, 249 (1957).
22. S.M. Puri, *Phys. Rev.* 139, A995 (1965).
23. V.L. Gurevich and Yu.A. Firsov, *Physics JETP* 13, 137 (1961).
24. L.M. Roth and P.N. Argyres, *Magnetic Quantum Effects, Semiconductors and Semimetals* 1, 199 (1966).
25. R. Dornhaus and G. Nimtz, *Springer Tracts in Modern Physics*, Vol. 98 (Berlin, Germany: Springer, 1983), p. 119.
26. M.H. Weiler, *Semic. Semimet.*, Vol.16 (New York: Academic Press, 1981), p. 141.
27. L.E. Gurevich and G.M. Nedlin, *Sov. Phys. Solid State* 3, 2029 (1962).
28. V.B. Khalfin, *Sov. Phys. Semicond.* 2, 257 (1968).
29. V.K. Arora and R.L. Peterson, *Phys. Rev. B* 9, 4323 (1974).
30. J.R. Barker, *J. Phys. C: Solid State Phys.* 6, L52 (1973).
31. H. Kahlert and G. Bauer, *Phys. Rev. Lett.* 30, 1211 (1973).
32. E.A. Mozhaev, V.I. Ivanov-Omskii, V.A. Mal'tseva, D.V. Mashovets, and R.V. Parfen'ev, *Sov. Phys. Semicond.* 11, 1260 (1977).
33. S.W. McClure, D.G. Seiler, C.L. Littler and M.W. Goodwin, *J. Vac. Sci. Technol. A* 3, 271 (1985).
34. K. Takita, A. Susuki and K. Masuda, *Solid State Commun.* 58, 209 (1986).

Compositionally Graded HgCdTe Photodiodes: Prediction of Spectral Response From Transmission Spectrum and the Impact of Grading

D. ROSENFELD, V. GARBER, V. ARIEL, and G. BAHIR

Kidron Microelectronics Research Center, Department of Electrical Engineering, Technion - I.I.T., Haifa 32000, Israel

We have studied the infrared transmission spectrum and the optical performance of HgCdTe photodiodes containing a linear composition gradient in the active layer. Our objectives were to enable the prediction of the optical performance of a photodiode at 77K, based on the easily and nondestructively measured transmission spectra, as well as to gain a better understanding of the effects of the grading on the optical performance. Consequently, we address three issues here. We first establish improved characterization techniques that can provide accurate values of the necessary material parameters such as gradient in composition. Second, we present a model that can predict the optical response of a diode, based on the material properties and the diode's geometry. Third, we use the above-mentioned model for the theoretical calculations of the effects of the grading and the resulting built-in electric field on the diode's optical response.

Key words: Compositional grading, HgCdTe, infrared (IR) transmission, photodiodes, spectral response

INTRODUCTION

The use of $\text{Hg}_{1-x}\text{Cd}_x\text{Te}$ based heterojunction photodiodes for infrared imaging in the 8–12 μm atmospheric window is well established and needs no elaboration. Most of today's state of the art photovoltaic detectors are fabricated from material grown by liquid phase epitaxy (LPE).^{1–5} Other epitaxial technologies, such as metalorganic chemical vapor deposition (MOCVD)⁶ and molecular beam epitaxy (MBE),⁷ are less mature and are still in the research level. Liquid phase epitaxially grown layers unavoidably contain a gradient in composition of the order of 5 [cm^{-1}]⁸ which results in an almost constant built-in electric field in the quasi-neutral region of about 8 V/cm. While the composition change in LPE layers is always negative (i.e. the Cd fraction reduces as the film

grows), both MOCVD and MBE allow the flexibility of incorporating gradients of various magnitudes and in either direction.

Although, the beneficial effect of the grading on the performance of HgCdTe diodes has already been reported,^{1,5,8} modeling of its influence on the performance of the photodiodes is not fully developed. This is due to the variation of the material's properties along the graded region, which adds a complex spatial-dependent component to the continuity equation. Several iterative numerical computer codes that solve the spatial dependent equation are available. However, they are more difficult to operate and therefore are not widely employed.

In this paper, we present the results of a study of the optical performance of HgCdTe photodiodes containing a linear gradient in composition in the active layer. The objectives of the study are to enable the prediction of the optical performance of photodiode

(Received November 4, 1994; revised January 25, 1995)

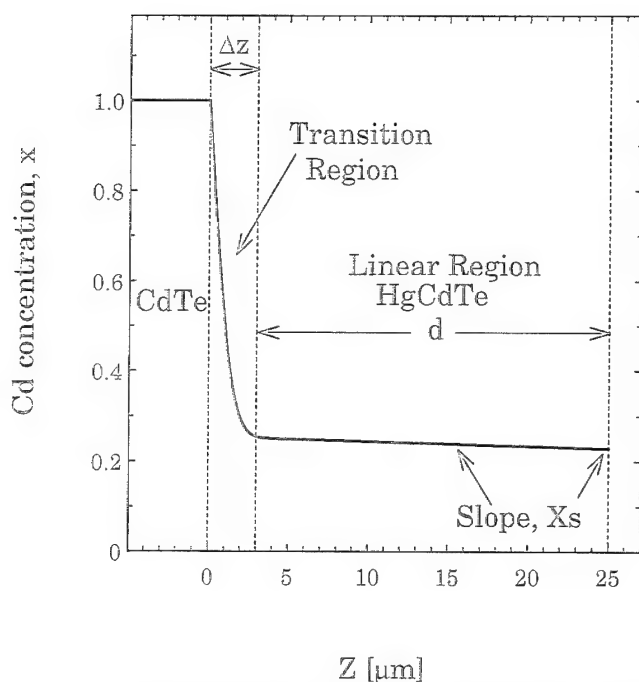


Fig. 1. A schematic description of the composition profile in LPE grown HgCdTe layer.

based on material properties, as well as to gain a better understanding of the effects of the grading and the resulting built-in electric field on the diode's optical performance. To obtain the first goal, two major issues are addressed: the accurate determination of the composition profile from transmission measurements, and the prediction of the 77K spectral response from the obtained profile. Once the spectral response is modeled, the effects of the grading can be theoretically studied. Although we chose to consider $\text{Hg}_{1-x}\text{Cd}_x\text{Te}$ diodes suitable for sensing radiation in the 8–12 μm atmospheric window ($x \approx 0.22$), our results and conclusions are equally applicable to HgCdTe photodiodes of any alloy composition.

At a given operating temperature, the Cd mole fraction (x) is the main property that determines the spectral response. Hence, for a rough estimation of the spectral response and the cut-off wavelength of a homogenous photodiode prior to its fabrication, the x value should be known. Although the composition can be measured directly,^{9,10} most of the characterization techniques are based on indirect measurements of other properties and the use of empirical relations to infer the Cd mole fraction.^{2,10–13} Room temperature infrared (IR) transmission measurements are widely and routinely used. Most of the analysis methods use simple empirical formulas obtained from measurements of homogenous calibration samples. Unfortunately, these empirical formulas cannot be used for the analysis of LPE grown layers in which the material properties vary along the growth direction.

A technique that correlates the transmission spectrum at 300K with the linear composition profile of graded thin layers was published by Hougen¹⁴ in 1989, recently reviewed by Price and Boyd,² and

modified by Liu et al.¹⁵ This technique starts with theoretical calculation of the transmission spectrum by integrating the contributions of thin layers to the absorption process, and then uses fitting procedure to obtain the composition profile from a measured spectrum. In this paper, we present improved fitting procedures as well as a reference to a recently proposed characterization technique based on examining the derivatives of the absorption spectra with respect to the photon energy.¹⁶

Precise knowledge of the composition profile is only one of the parameters needed for an accurate prediction of a diode's optical performance. The other parameters that affect the spectral response can be divided into three major categories: material properties such as surface recombination velocity at the CdTe/HgCdTe interface, minority carrier lifetime and mobility; geometry factors such as optical area and active layer width, and "external" parameters such as the illumination side¹⁷ and the possible existence of anti-reflecting coating layer.

The prediction of the optical performance of LPE photodiodes is even more complicated due to the unavoidable composition gradient which significantly complicates the equations describing the physical phenomena. Hence, we proceed to present a one-dimensional analytical solution of the composition-dependent continuity equation and use the resulting carrier distribution to calculate the diode's spectral response. Using the solution, we present some theoretical calculations which demonstrate the effects of the grading and the built-in electric field on the diode's optical performance.

The paper is organized as follows: the IR Transmission section describes improved experimental procedures for determining the composition profile of graded material from its transmission spectra. The section on Spatial-Dependent Continuity Equation presents a solution of the one-dimensional spatial-dependent continuity equation. In Effects of Grading on Optical Performance, we use the solution to calculate the detector's spectral response and demonstrate the influence of the grading on the diode's performance. In the last section, we summarize our findings.

IR TRANSMISSION

Room temperature IR transmission measurements are the most common characterization techniques used to determine the composition profile. In the case of homogenous material, the transmission spectrum in the range 800–4000 cm^{-1} is measured, and the x value is obtained using one of several methods.^{2,10–13} In the case of LPE heterostructure material with a thin and linearly graded active layer, the procedure of deriving the composition from the measured transmission spectra is more complicated. As the detailed procedure of Hougen has already been experimentally confirmed,¹⁴ reviewed² and slightly modified,¹⁵ we present here the general approach only. To obtain the accurate composition profile, one should start with a general parametric expression for $x(z)$ which contains

both the linearly graded active region and the narrow CdTe/HgCdTe transition region:

x(z) = X_s + S(d - z) + (1 - X_s + Sd) [1 - erf(2z / Δz)] (1)

where X_s, S, d, and Δz are the surface composition, the grading slope, the active layer width and the transition region width, respectively (see Fig. 1). Here we choose to describe the transition profile with an error function which is usually associated with diffusion phenomena. Once the parametric expression is set, the theoretical transmission spectrum for arbitrary values of the parameters can be calculated. This is done using simple multi-layer reflection theory as well as published experimental expressions for the composition dependence of the absorption coefficient α(x), the bandgap E_g(x) and the refractive index n(x). Finally, the theoretical spectrum is compared with the measured one, and the correct values of the four parameters are obtained using a nonlinear iterative fitting procedure. Figure 2 shows an example of Hougen's method: the circles and the dashed line represent a measured transmission spectrum, while the solid curve represent the best fit obtained for X_s = 0.2231, S = 10.53 cm⁻¹, d = 22.6 μm, and Δz = 5 μm. In fact, we found that the result depends strongly on the accuracy of the measured data and on the definition of the error.

Although the above four parameters represent the best fit, other groups of four parameters yield similar results, as can be seen in Table I. While group A was obtained by using four parameters, the other groups were obtained by using a smaller number of param-

eters. In group B, we set the layer width to be 20 μm (previously obtained from the fringes at the 800–1400 cm⁻¹ range). In group C, we set the slope to be 5 cm⁻¹. In group D, we set both d = 20 μm and S = 5 cm⁻¹, and used two parameters in the fitting only. The minor changes in the deviations given in the right column of Table I indicate that all four groups obtained good fit. This is due to the low 'complexity' of the transmission spectrum which is usually given by a smooth monotonic lineshape. In addition, the complex and nonlinear dependence of the absorption process on composition and photon energy, significantly complicate the dependence of the transmission spectra on the above four parameters. Hence, it is possible to obtain several groups of parameters with a small change in the error only. This note is significant since it shows that the accuracy of the method is limited.

To increase the accuracy of the fitting-based methods, one can either reduce the number of fitting parameters or add measured results to raise the

Table I. The Values of the Surface Composition X_s, Compositional Slope S, Active Layer Width d, and Transition Region width Δz, Obtained by Fitting Procedure

	X _s	Slope [μm ⁻¹]	d [μm]	Δz [μm]	Error
A	0.2231	10.5	22.6	5	6.6·10 ⁻²
B	0.2234	10.7	<u>20</u>	0.5	6.8·10 ⁻²
C	0.2269	<u>5</u>	21.8	5.5	7.0·10 ⁻²
D	0.2269	<u>5</u>	<u>20</u>	3.25	7.1·10 ⁻²

Note: Underlined values were kept unchanged during fitting process.

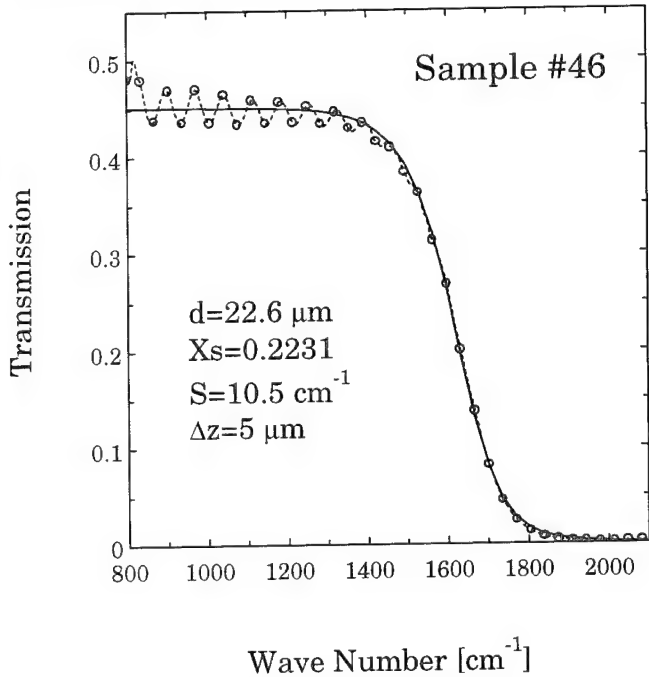


Fig. 2. An example of Hougen's method: circles with dashed line: measured data; solid line: best fit obtained for X_s = 0.2231, S = 10.53 cm⁻¹, d = 22.6 μm, and Δz = 5 μm.

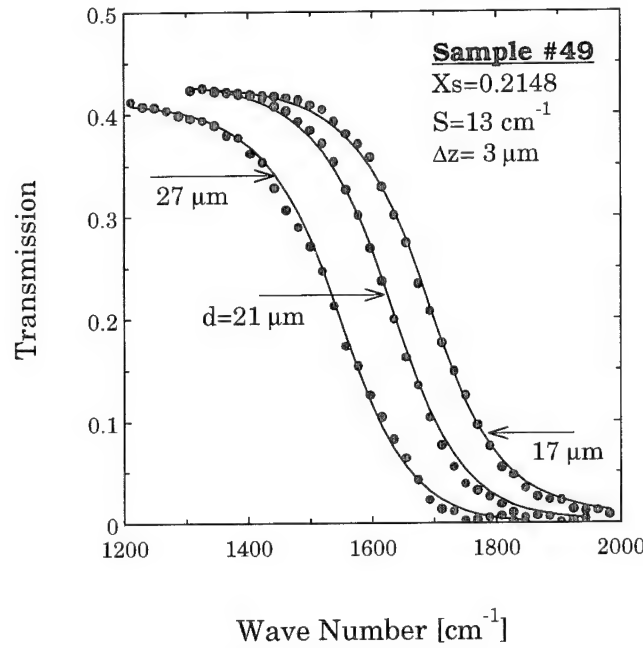


Fig. 3. Transmission spectra of an LPE sample at three different layer widths. Circles: measured data; solid lines: best fit. The best fit values of d, S, X_s, and Δz are also indicated.

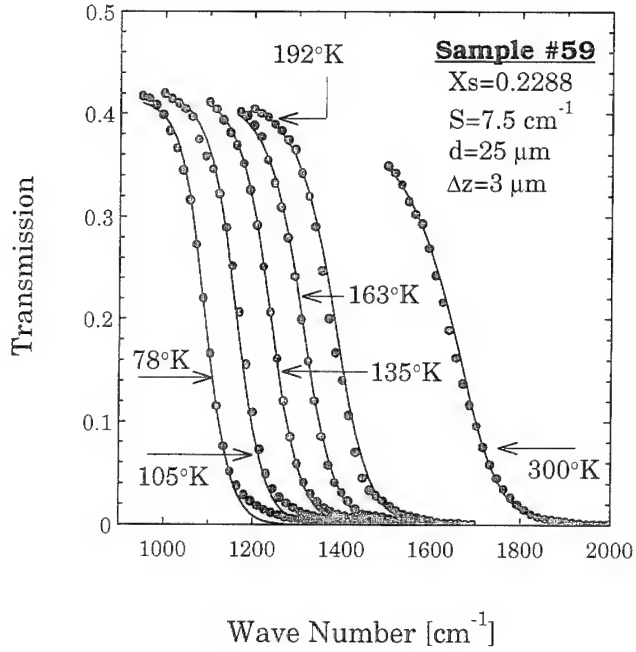


Fig. 4. Transmission spectra of an LPE sample at six different temperatures. Circles: measured data; solid lines: best fit. The best fit values of d , S , X_s , and Δz are also indicated.

complexity of the experimental data. We choose to include additional data obtained by measuring the transmission spectrum of the same sample at either different layer widths or different temperatures. The circles in Fig. 3 represent the measured transmission spectra of one of our LPE samples. The first spectrum is associated with a layer width of 27 μm . The second and third spectra were measured after 6 and 16 μm were etched, respectively. The solid lines represent the theoretical spectra obtained by fitting the model to the three spectra *together*. The parameters associated with the best fit are $S = 13 \text{ cm}^{-1}$, $X_s = 0.2148$ (before etching), and $\Delta z = 3 \mu\text{m}$.

While the procedure described in Fig. 3 is both destructive and tedious, the one described in Fig. 4 is nondestructive and simpler. This figure shows transmission spectra of sample #49 measured at *six* temperatures, between 78 and 300 K. The additional data was added here by changing the temperature rather than by changing the width. Once again, the solid circles represent the measured data, and the solid lines represent the theoretical spectra obtained by fitting the model to the six spectra *together*. The width of the layer (d) was obtained using the fringes at the room-temperature spectrum (not shown in Fig. 4). The values of S , X_s , and Δz were obtained by the fitting procedure and are also given in the figure.

It should be noted here that although we choose to increase the accuracy of the fitting method by including additional data, the accuracy can be also increased by reducing the number of fitting parameters. For instance, the average bandgap and the composition gradient can be obtained by examining the derivatives of the absorption spectra with respect to the photon energy. The details of this recently

developed novel technique, as well as experimental results, are given elsewhere.¹⁶

THE SPATIAL-DEPENDENT CONTINUITY EQUATION

In this chapter, we present a one-dimensional analytical model for the spectral response of linearly graded P-on-n HgCdTe heterojunction photodiode. To simplify the model, we replaced the actual graded CdTe/HgCdTe transition region with an abrupt interface. We assume that a p-n junction is formed either by growing an additional p-type layer with higher Cd concentration, or by As implantation and activation procedure.⁷ We further assume that due to the small thicknesses of space charge region and the upper layer (and the possible wider bandgap), the absorption occurs mostly in the active layer, and hence this region dominates the photocurrent. We also assume that the diodes are large enough and thus two-dimensional effects such as cross-talk do not introduce a large error. In the case of heterostructure, we assume that the electrical junction is located inside the narrow bandgap region and disregard the possible effect of the barrier. Other assumptions will be discussed later.

The steady-state continuity equation in the linearly graded n-type region is:

$$D_p \frac{\partial^2 \Delta P_{ph}}{\partial z^2} - \mu_p E_0 \frac{\partial \Delta P_{ph}}{\partial z} - \frac{\Delta P_{ph}}{\tau_p} + G_L(z, \lambda) = 0 \quad (2)$$

where ΔP_{ph} is the concentration of excess photo-generated minority carriers, $G_L(z, \lambda)$ is their position- and wavelength-dependent generation rate, D_p , μ_p , and τ_p are the minority carrier diffusion coefficient, mobility and lifetime, respectively, and $E_0 = -\partial E_g / \partial z$ is the constant electric field resulting from the linear composition profile and the almost linear dependence of the bandgap (E_g) on composition.¹⁸

In Eq. (2), we assumed that the three properties that characterize the hole (D_p , μ_p , τ_p) are constants. The maximum change in composition in this study is less than 4% along the active layer, and hence the change in D_p and μ_p is minor. The assumption of constant τ_p is weaker and requires more attention. Assuming the n-type layer is of high quality and thus τ_p is dominated by the Auger 1 mechanism, the minority carrier lifetime under low injection conditions can be written as:¹⁹

$$\tau_p \propto P_0 \cdot \tau_{A1}^i \quad (3)$$

where P_0 is the thermally generated minority carrier concentration and τ_{A1}^i is the intrinsic Auger 1 lifetime. In a previous work,²⁰ we showed that when the layer under discussion is n-type and linearly graded, τ_{A1}^i and P_0 demonstrate opposite exponential dependencies upon composition, which drastically decreases the overall composition dependence of τ_p . The resulting composition dependence is weak and therefore can be taken as constant. Hence, when solving the continuity equation in a high quality n-type active

layer, this assumption is valid. However, when dealing with a p type region, in which the lifetime is usually dominated by Shockley-Read-Hall mechanism, some error will be introduced.

Although the weak composition dependence of τ_p was ignored, and D_p and μ_p were assumed to be constant, the spatial dependence of all other material properties such as the absorption coefficient α and the bandgap E_g were not neglected and were included in the term $G_L(z, \lambda)$. When the P-on-n diode is illuminated from the backside with a monochromatic photon flux of wavelength λ , $G_L(z)$ is given by:

$$G_L(z) = -\frac{d\phi(z)}{dz} = \alpha(z, \lambda)\phi_0 e^{-\int_0^z \alpha(u, \lambda) du} \quad (4)$$

where $\phi(z)$ is the photon flux distribution and ϕ_0 is its value at the edge of the absorbing layer.

The minority carrier concentration P_{ph} can be obtained by using the Lagrange method of variable constants together with the boundary conditions.²⁰ Knowing the profile of the photo-generated excess carriers the photo-current J_{ph} can be calculated:

$$J_{ph} = -qD_p \left(\frac{\partial \Delta P_{ph}}{\partial z} \right) + q\mu_p E_0 \Delta P_{ph} \quad (5)$$

Finally, the quantum efficiency $\eta = J_{ph}/q\phi_0$ can be written as:

$$\eta = \frac{(mL_p + \beta)(G_2 - G_1) + \frac{L_p}{L_{eff}}(G_2 - G_1)}{(mL_p + \beta)\sinh\left(\frac{d}{L_{eff}}\right) + \frac{L_p}{L_{eff}}\cosh\left(\frac{d}{L_{eff}}\right)} \cdot \frac{e^{md}}{2} \quad (6)$$

where

$$G_1 = \frac{1}{\phi_0} \int_0^d G_L \cdot e^{-(m+N)u} du \quad (7)$$

$$G_2 = \frac{1}{\phi_0} \int_0^d G_L \cdot e^{-(m-N)u} du \quad (8)$$

$$m = \frac{qE_0}{2kT}; L_{eff} = \frac{L_p}{\sqrt{m^2 L_p^2 + 1}}; \beta = \frac{S_p L_p}{D_p} \quad (9)$$

and where S_p is the surface recombination velocity at the backside, d is the width of the linearly graded n-type active layer, and L_p is the diffusion length given by $L_p = (D_p \tau_p)^{1/2}$. In the case of homogenous material, where $\partial E_g / \partial z = 0$, $E_0 = 0$, $m = 0$ and $L_{eff} \rightarrow L_p$, the above equation reduces to the well-known expression associated with the homogenous junction.^{7,21,22}

Figure 5 shows the quantum efficiency of one of the diodes fabricated on the sample whose properties were previously obtained from the multi-temperature transmission measurement described in Fig. 4. The circles represent the measured spectrum while the solid line represents the prediction of the model based

on $X_s = 0.2288$, $S = 7.5 \text{ cm}^{-1}$, $d = 25 \mu\text{m}$, and $\Delta z = 3 \mu\text{m}$ (see the results of Fig. 4) and on $S_p = 0$. As can be seen, the model predicts well the cut-off wavelength and the photo-current which is roughly related to the area under the curve. However, the model fails to predict the precise wavelength dependence of the quantum efficiency around the cut-off wavelength. This deviation can be explained by two-dimensional effects such as cross-talk or can be the result of errors introduced by our assumptions. To find the source of the error

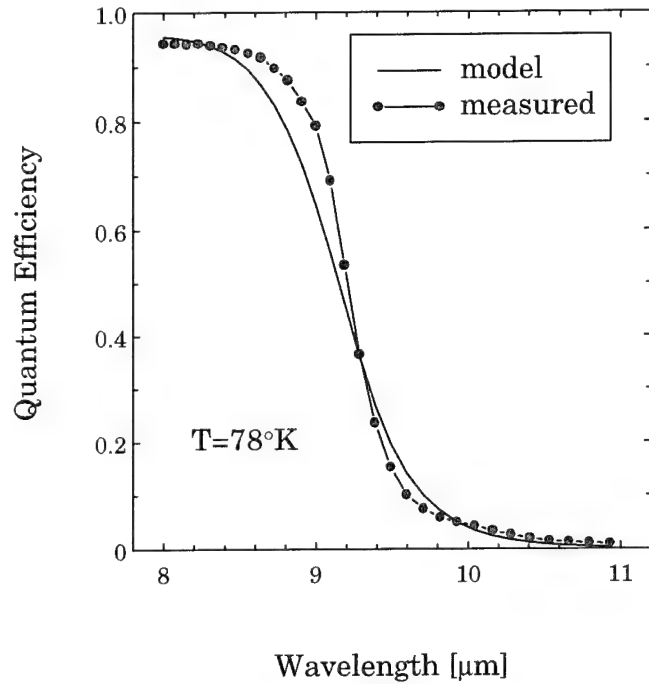


Fig. 5. Quantum efficiency of a diode fabricated on the sample of Fig. 4. Circles: measured data, solid line: model's prediction based on X_s , S , d , and Δz of Fig. 4. $S_p = 0$ is assumed.

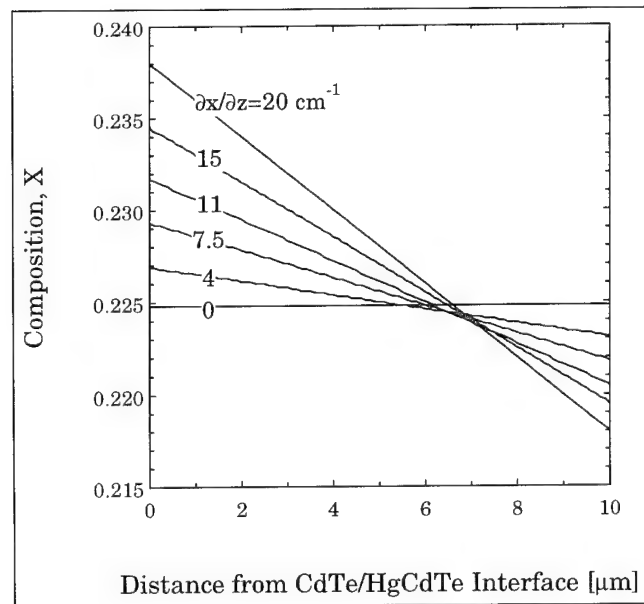


Fig. 6. Six possible composition profiles in the active layer. Slopes are 0, 4, 7.5, 11, 15, and 20 cm^{-1} . Resulting built-in electric fields are 0, 6, 12, 18, 24, and 32 V/cm , respectively.

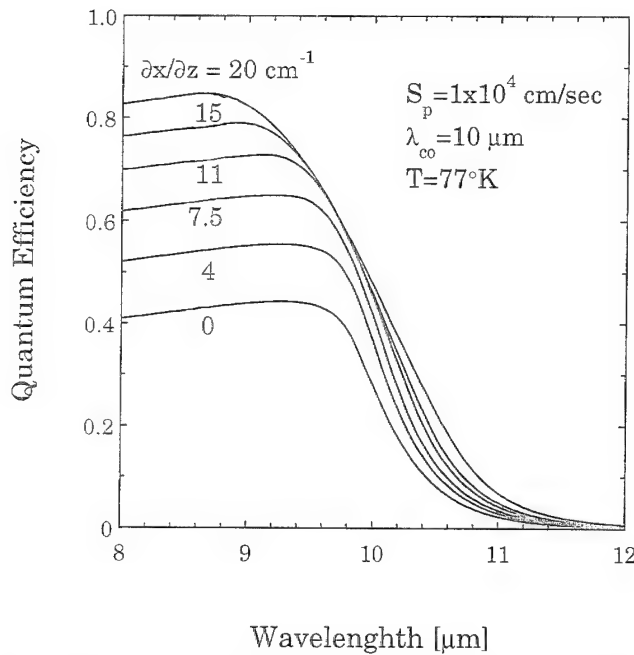


Fig. 7. Calculated spectral quantum efficiency of the diodes of Fig. 7.

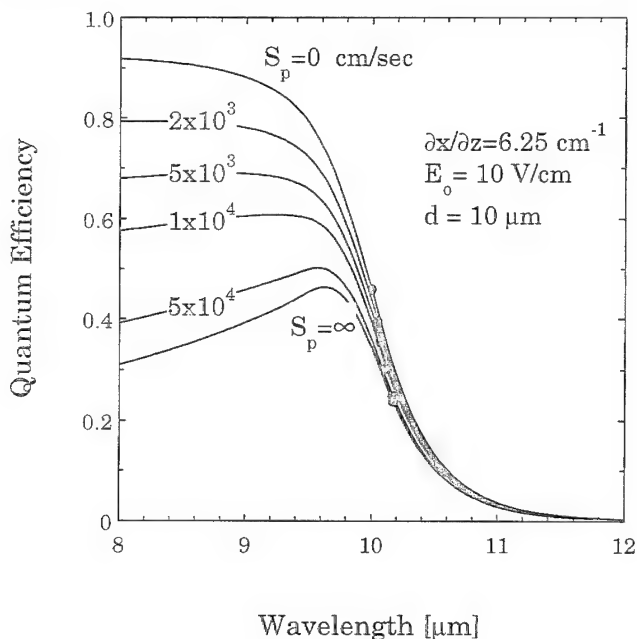


Fig. 8. Calculated spectral quantum efficiency of a photodiode with $\partial x/\partial z = 6.25 \text{ cm}^{-1}$ (built-in electric field of 10 V/cm), with the surface recombination velocity (S_p) as a parameter.

and to improve the model, more experimental data should be collected. Other diodes, fabricated on other structures with different composition profiles, show similar results.

EFFECTS OF GRADING ON OPTICAL PERFORMANCE

Since the model predicts well both the cut-off wavelength and the photo-current, it can be used for analysis, design, and optimization. Here we demonstrate the effects of the grading, surface recombination

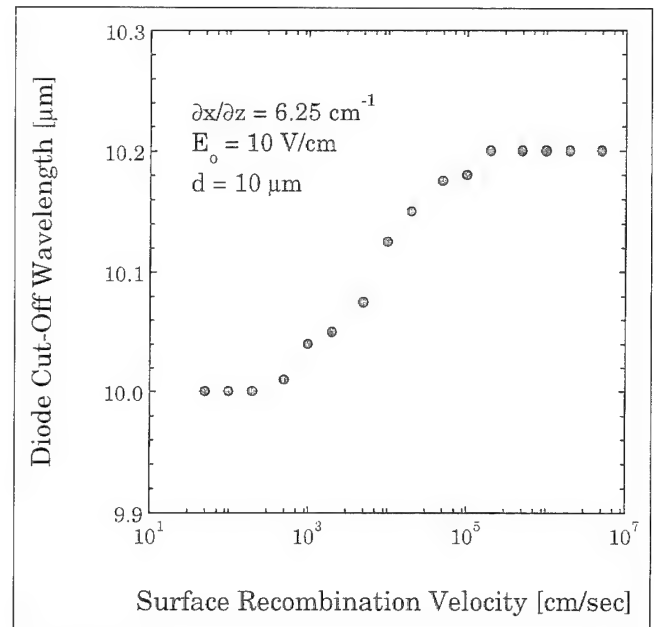


Fig. 9. Cut-off wavelength of a 10 μm linearly graded diode vs backside surface recombination velocity.

velocity, active region width, and other parameters on the diode's photo-current and cut-off wavelength.

Figures 6–9 demonstrate the effects of grading and surface recombination velocity on the spectral response and cut-off wavelength. Figure 6 shows seven possible composition profiles in the active layer associated with slopes of 0, 4, 7.5, 11, 15, and 20 cm^{-1} and built-in electric fields of 0, 6, 12, 18, 24, and 32 V/cm, respectively. Assuming, for example, that the active region is n-type with $\tau_p = 1 \text{ } \mu\text{s}$, $\mu_p = 600 \text{ cm}^2/\text{Vs}$, and $S_p = 10^4 \text{ cm/s}$, all diodes result in cut-off wavelength of 10 μm when operated at 77K and illuminated from their backside. Figure 7 shows the calculated spectral quantum efficiency of the diodes of Fig. 6. The figure shows in the homogenous case the low quality CdTe/HgCdTe interface cause insufficient quantum efficiency of about 40%. However, when the grading slope is raised, and electric fields with higher values are established, the quantum efficiency significantly increases, and the optical performance is greatly improved.

Figures 8 and 9 demonstrate the effect of the surface recombination velocity on diode's performance. Figure 8 shows the calculated spectral quantum efficiency of a photodiode with $\partial x/\partial z = 6.25 \text{ cm}^{-1}$ (built-in electric field of 10 V/cm), with the surface recombination velocity (S_p) as a parameter. As S_p is elevated, the diode's performance is strongly degraded, mostly due to the reduction in the contribution of the shorter wavelengths. However, as the optical performance deteriorates, the cut-off wavelength (λ_{co}) increases (see solid circles). This is due to the particular definition of the cut-off wavelength as the wavelength for which the quantum efficiency reduces to half of its maximal value.¹⁷ Hence, the longer cut-off wavelength results from the degradation in short-wavelength response rather than from improvement in long-wavelength performance. The increase in cut-off

wavelength with the diode's performance degradation is also demonstrated in Fig. 9. The figure shows the cut-off wavelength of a 10 μm linearly graded diode vs the surface recombination velocity at the backside. Three regions are clearly demonstrated; for $S_p < 10^3$ cm/s, the cut-off wavelength is not effected by S_p ; over the range of $10^3 < S_p < 10^5$ cm/s, the curve demonstrates logarithmic dependence on S_p and deviation from 10 μm by up to 0.2 μm . Finally, for $S_p > 10^5$ cm/s, λ_{co} obtains the saturation value of 10.2 μm .

The quantum efficiency given in Eq. (6) is associated with the linearly graded diode illuminated with monochromatic photon flux. However, to properly compare the performance of photodiodes, the contributions of all photons with wavelengths longer than 8 μm and shorter than the cut-off wavelength should be calculated. The relevant parameter is therefore the *weighted average* of the quantum efficiency given by:

$$\eta_{av} = \frac{\int_{\lambda_1}^{\lambda_2} \eta(\lambda) n(\lambda) d\lambda}{\int_{\lambda_1}^{\lambda_2} n(\lambda) d\lambda} \quad (10)$$

where $n(\lambda)$ is the spectral radiant photon emittance of the target given by Plank's radiation law. The use of the weighted average is also appropriate since it is directly proportional to the photo-current by $I_\lambda = qA_{op} \eta_{av} N_o$ [where A_{op} is the optical area N_o is the total number of photons given by the denominator in Eq. (10)]. It should be emphasized here that the values of the weighted average are smaller than these of the quantum efficiency in the shorter wavelength range. This is due to the small contributions of photons in wavelengths close to λ_{co} for which η is relatively low.

Figure 10 shows the average quantum efficiency of a diode with the same material properties as the diode of Figures 6–9, vs the active layer width, with the grading as a parameter. The lowest curve represents the homogenous case. It can be seen that the homogenous diode is associated with an optimal layer width of about 10 μm . However, if the active layer is grown wider, there would be a strong degradation in the quantum efficiency which reduces from 80 to 50%. As the grading slope is raised and stronger built-in electric fields are formed, the degradation is smaller. In the most extreme case presented here where the built-in electric field is of the order of 25 V/cm, the quantum efficiency is completely independent of the layer width.

Figure 11 shows the average quantum efficiency vs the built-in electric field with the surface recombination velocity as a parameter. It seems that in all cases there is a degradation in performance, namely, as the surface recombination velocity increases—the average quantum efficiency decreases. However, in the homogenous case, where no electric field is present, the degradation is by a factor of three, from 90 to 30%. On the other hand, in the outermost case, where strong electric field of 30 V/cm is present, the degradation is significantly smaller, from 90 to about 70%.

SUMMARY

A study of the IR transmission spectrum and the optical performance of HgCdTe photodiodes containing a linear gradient in composition in the active layer, was presented. Three subjects were addressed. First, we suggested improved Fourier transform infrared-based characterization techniques that can provide the composition profile of a graded epitaxial layer. Then, we presented a model that can predict

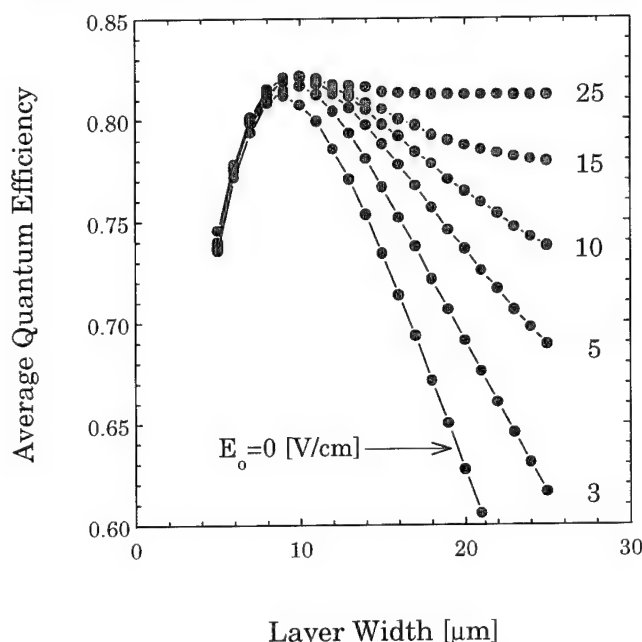


Fig. 10. Average quantum efficiency of a diode with the same material properties as the diodes of Figs. 7–10 vs the active layer width, with the grading as a parameter.

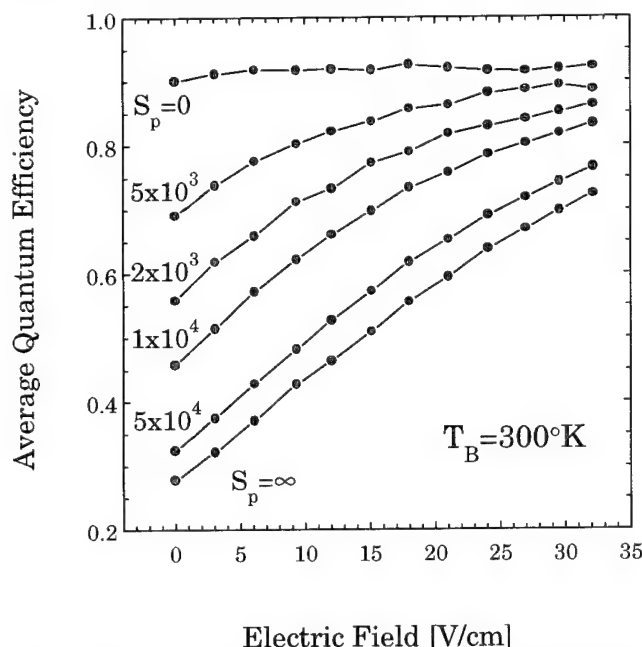


Fig. 11. Average quantum efficiency vs built-in electric field with the surface recombination velocity as a parameter.

the optical response of a diode, based on the obtained composition profile and other properties. In the last section, we confirmed the model and used it to perform theoretical calculations of the effects of the grading and the resulting built-in electric field on the diode's cut-off wavelength and average quantum efficiency. We showed that the major consequence of grading is the reduction of the effects caused by sub-optimal properties.

ACKNOWLEDGMENT

The technical assistance of A. Zohar, S. Dolev, D. Schoenmann, and N. Steinbrecher is acknowledged with thanks.

REFERENCES

1. T. Tung L.V. DeArmond, R.F. Herald, P.E. Herning, M.H. Kalisher, D.A. Olson, R.F. Risser, A.P. Stevens and S.J. Tighe, *Proc. SPIE* 1735, 109 (1992).
2. S.L. Price and P.R. Boyd, *Semicond. Sci. Technol.* 8, 842 (1993).
3. G.N. Pultz, P.W. Norton, E.E. Kroeger and M.B. Reine, *J. Vac. Sci. Technol. B* 9, 1724 (1991).
4. D.D. Edwall, E.R. Gertner and W.E. Tennant, *J. Appl. Phys.* 55, 1453 (1984).
5. M.B. Reine, K.R. Maschhoff, S.P. Tobin, P.W. Norton, J.A. Mroczkowski and E.E. Krueger, *Semicond. Sci. Technol.* 8, 788 (1993).
6. S.J.C. Irwine, *SPIE* 1735, 92 (1992).
7. J.M. Arias, J.G. Pasko, M. Zandian, S.H. Shin, G.M. Williams, L.O. Bubulac, R.E. DeWames and W.E. Tenant, *J. Electron. Mater.* 22, 1039 (1993).
8. S.M. Johanson, D.R. Rhiger, J.P. Rosback, J.M. Peterson, S.M. Taylor and M.E. Boyd, *J. Vac. Sci. Technol. B* 10, 1499 (1992).
9. R. Strong, J. Anthony, B. Gnade, J. Keenan, E. Norbeck, L. Li and C. Helms, *J. Vac. Sci. Technol. A* 4, (1992).
10. W. Micklethwaite, *J. Appl. Phys.* 63, 2382 (1988).
11. V. Kopal, R. Ashokan and V. Dhar, *Infrared Phys.* 33, 39 (1992).
12. N. Oda, T. Kanno, M. Saga, R. Oikawa and Y. Maejima, *J. Cryst. Growth* 117, 193 (1992).
13. E. Finkman and S. Schacham, *J. Appl. Phys.* 56, 2896 (1984).
14. C.A. Hougén, *J. Appl. Phys.* 66, 3763 (1989).
15. K. Liu, J. Chu, B. Li and D. Tang, *Appl. Phys. Lett.* 64, 2818 (1994).
16. V. Ariel, V. Garber, G. Bahir and D. Rosenfeld, submitted to *Appl. Phys. Lett.*
17. D. Rosenfeld and G. Bahir, *J. Appl. Phys.* 72, 3034 (1992).
18. E. Finkman, *J. Appl. Phys.* 54, 1883 (1983).
19. J.S. Blakemore, *Semiconductor Statistics* (Oxford, U.K.: Pergamon, 1962).
20. D. Rosenfeld, V. Garber and G. Bahir, *J. Appl. Phys.* 76, 4399 (1994).
21. Van der Wiele, *Solid State Imaging*, 44 (Nederland: Noordhoff, 1976).
22. H.J. Hovel, *Semiconductors and Semimetals*, vol. 11, ed. R.K. Willardson and A.C. Beer (New York: Academic Press, 1975).

Effect of a Valence-Band Barrier on the Quantum Efficiency and Background-Limited Dynamic Resistance of Compositionally Graded HgCdTe P-on-n Heterojunction Photodiodes

M.H. WEILER and M.B. REINE

Loral Infrared & Imaging Systems, Inc., Lexington, MA 02173

A new analytical model for the bias-dependent quantum efficiency of a HgCdTe P-on-n heterojunction photodiode with a valence band barrier elucidates the important physics of the phenomenon and shows that the background-induced shunt resistance is a result of the same mechanism, that is, a tendency of the light-induced carriers to pile up in the base layer due to the retarding field produced by the barrier. A parameterized version of the model agrees well with experimental current-vs-voltage and noise measurements.

Key words: Band offset, heterojunctions, HgCdTe, quantum efficiency

INTRODUCTION

HgCdTe is well established as the material of choice for fabricating high-sensitivity detectors over a wide range of infrared wavelengths.¹ The most sensitive detectors use heterojunction photodiodes in a wide-gap-P on narrow-gap-n configuration, since the larger gap reduces the dark current contributions from the p-type material.²⁻⁵ Although a number of growth techniques are used for device development, most detector material continues to be grown by liquid phase epitaxy (LPE) because of the combination of large wafer area with consistently high material quality. It has been recognized for some time that with this growth technique it is important to place the increase in the alloy composition between the n-type base and the p-type cap so as to prevent the formation

of barriers to minority carrier transport from the base to the junction depletion region.⁶ The barrier has been shown by numerical modeling to reduce the quantum efficiency.⁷

It has also been recognized for some time that in the presence of strong optical illumination the dynamic resistance of a photodiode fabricated from material of uniform composition (InSb or HgCdTe homojunctions) can be limited by an effective shunt resistance inversely proportional to the strength of the illumination, and that the magnitude of the effect can be calculated using a relatively simple analytical model.^{8,9} The conditions for this effect in solar cells were examined by Lindholm et al.¹⁰ and by Tarr and Pulfrey.¹¹ This effect in compositionally graded HgCdTe heterojunctions has recently been shown by numerical modeling to vary with the heterojunction structure,¹² without invoking additional photogeneration in the depletion region.¹³ However, numerical model-

(Received October 4, 1994; revised January 8, 1995)

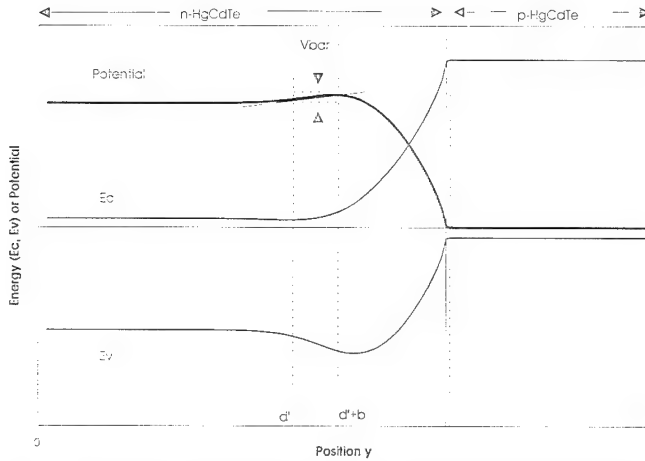


Fig. 1. Schematic representation of the conduction and valence band energies with respect to the Fermi level (upper and lower solid curves) and the electrostatic potential (heavy solid curve) vs position in a compositionally graded heterojunction diode. The n-type base layer is on the left, and the p-type cap layer is on the right. The vertical dashed lines represent the edges of the junction depletion region. The effective height V_{bar} and width b of the barrier are indicated, as well as the linear approximation used to obtain an analytical model for the quantum efficiency.

ing provides only limited insight into the physical origins of this effect and does not show the deep connection between the quantum efficiency barrier and the illumination-limited resistance.

In this paper, we derive a simple analytical model which shows that the heterojunction barrier and the illumination-limited resistance are intimately related effects. In the next section, we first show that a simple two-piece model for the potential in the base layer region, including a retarding field due to the barrier near the depletion region edge, can be solved for an expression for the optically induced carrier density and the quantum efficiency. We then use a depletion region model, including the effects of the alloy composition change on the effective electric potential in the base, to obtain the approximate potential needed to calculate the quantum efficiency. Since the position of the depletion region edge varies with the bias applied to the junction, the model can be used to calculate the bias dependence of the quantum efficiency. It is this bias-dependent quantum efficiency that is the characteristic symptom of the "barrier."

The bias dependence of the quantum efficiency also implies an increase in the photocurrent with increasing reverse bias, which is the characteristic symptom of the bias-limited shunt resistance described by Rosbeck et al.^{8,9} In the case of compositionally graded heterojunction diodes, however, this effect can be one or more orders of magnitude larger than for a homojunction.¹² In the next section, we also show that the diode current noise due to this effect takes the form of increased shot noise at reverse bias rather than thermal noise due to the illumination-dependent resistance. In the section entitled Numerical Model, we show that the quantum efficiency and dynamic resistance from numerical simulations are in qualitative agreement with the analytical model.

In Comparison with Experimental Data, we compare the results of the model with experimental data.

ANALYTICAL MODEL

The purpose of this work is to examine the bias and illumination dependence of the current in a compositionally graded P-on-n heterojunction photodiode. Assuming, for simplicity, that the total diode current is dominated by diffusion effects, it can be written

$$I(V) = -qQ_b A \eta(V) + I_{sat} (e^{qV/kT} - 1) \quad (1)$$

where q is the electronic charge, T the absolute temperature, Q_b the background photon flux, A the diode area, and I_{sat} the saturation current due to diffusion. Since the quantum efficiency η depends on the applied voltage V , there is a term in the inverse resistance, a shunt conductance, proportional to the background Q_b . The conductance is given by

$$\frac{1}{R(V)} = -qQ_b A \frac{d\eta(V)}{dV} + \frac{qI_{sat}}{kT} e^{qV/kT} \quad (2)$$

In this section, we derive an analytical expression for the quantum efficiency of a heterojunction photodiode as a function of the applied bias, in the limit where the heterojunction barrier effects are much larger than the homojunction effect described by Rosbeck et al.^{8,9} The variation of the conduction and valence band energy and of the electrostatic potential are illustrated schematically in Fig. 1 for a backside-illuminated photodiode constructed from a low-doped n-type base region, on the left, with a gradual increase in the alloy composition accompanied by a change in doping to a higher-gap, high-doped p-type cap on the right. If the alloy composition increase occurs too deep in the base region, the valence band energy is forced to decrease, resulting in a barrier to the collection of minority carrier holes generated in the base by the backside illumination. Our objective in this section is to obtain a completely analytical solution for the light-induced carrier concentration and current density due to diffusion from the base. To this end, we first approximate the potential in Fig. 1 as a two-piece function, one with a constant potential, in the bulk of the base layer, and one with a constant retarding field near the depletion region edge, and use this potential to derive an expression for the quantum efficiency as a function of the parameters of this potential. We then derive expressions for the position of the edges of the depletion region and for the potential as a function of position in the base and cap, and then use these expressions to calculate the quantum efficiency as a function of bias. Finally, we derive from these models expressions for the illumination-limited shunt resistance and examine the effect of the barrier on expressions for the diode current noise.

Quantum Efficiency for a Two-Piece Potential

We write the potential in the the linear approximation to the heterojunction as a two-piece function, constant for $0 < y < d'$ and increasing linearly to $y = d'$

+ b, where d' is the distance from the substrate-n-type base layer interface to the onset of the barrier region, and b is the thickness of the barrier region.

$$\psi(y) = \begin{cases} \psi_{\text{base}} & 0 < y < d' \\ \psi_{\text{base}} + E(y - d') & d' < y < d' + b \end{cases} \quad (3)$$

The slope in Eq. (3) corresponds to a constant decelerating field E for the minority carrier holes, and the total barrier height is given by $V_{\text{bar}} = Eb$. We now calculate the junction current in this linear approximation for illumination at the backside of the base layer ($y = 0$). We solve the drift-diffusion equation for the light-induced excess hole density $\Delta p(y)$:

$$D \frac{d^2 \Delta p}{dy^2} + \mu E \frac{d \Delta p}{dy} - \frac{\Delta p}{\tau} = \alpha Q_b e^{-\alpha y} \quad (4)$$

with $D = \mu kT/q$ the ambipolar diffusion coefficient, μ the ambipolar mobility, τ the lifetime of the minority-carrier holes in the n-type base layer, Q_b the (background) optical flux, and α the absorption coefficient. Using Eq. (3), we set $E = 0$ in the bulk of the base layer. We require continuity at $y = d'$ of $\Delta p(y)$ and the light-induced current

$$\Delta J(y) = -qD \frac{d \Delta p(y)}{dy} - q\mu E \Delta p(y) \quad (5)$$

The other boundary conditions are $\Delta p(d' + b) = 0$, at the depletion region edge, and $d \Delta p(0)/dy = 0$ at the substrate interface (no interface recombination).

The general solution to Eq. (4) is of the form

$$\Delta p(y) = \begin{cases} A_1(e^{-\alpha y} + B_1 e^{\kappa y} + C_1 e^{-\kappa y}) & 0 < y < d' \\ A_2(e^{-\alpha y} + B_2 e^{\alpha_1 y} + C_2 e^{\alpha_2 y}) & d' < y < d' + b \end{cases} \quad (6)$$

where $\kappa = 1/L$ (the inverse of the hole diffusion length), and

$$\alpha_1 = -\alpha_0 \pm \sqrt{\alpha_0^2 + \kappa^2} \quad (7)$$

with $\alpha_0 = \mu E/2D = qE/2kT$, and

$$A_1 = \frac{\alpha Q_b \tau}{1 - \alpha^2 L^2} \quad (8)$$

$$A_2 = \frac{\alpha Q_b \tau}{1 + 2\alpha_0 \alpha L^2 - \alpha^2 L^2} \quad (9)$$

The boundary conditions give (at $y = 0$)

$$\kappa B_1 - \kappa C_1 = \alpha \quad (10)$$

and at $y = d' + b$

$$B_2 e^{\alpha_1(d'+b)} + C_2 e^{\alpha_2(d'+b)} = -1 \quad (11)$$

The boundary conditions at the base - barrier region interface give

$$\begin{aligned} & A_1 [e^{-\alpha d'} + B_1 e^{\kappa d'} + C_1 e^{-\kappa d'}] \\ & = A_2 [e^{-\alpha d'} + B_2 + C_2 e^{-2\alpha_0 d'}] \end{aligned} \quad (12)$$

and

$$\begin{aligned} & A_1 [-\alpha e^{-\alpha d'} + \kappa B_1 e^{\kappa d'} - C_1 e^{-\kappa d'}] \\ & = A_2 [-\alpha e^{-\alpha d'} + 2\alpha_0 e^{-\alpha d'} + 2\alpha_0 B_2] \end{aligned} \quad (13)$$

where we have approximated $\alpha_0 \gg \kappa$ ($qV_{\text{bar}}/kT \gg 1$) which gives $\alpha_1 \approx 0$ and $\alpha_2 \approx -2\alpha_0$. The solutions to are, for $\alpha L \gg 1$, for $0 < y < d'$

$$\Delta p(y) \approx \quad (14)$$

$$\frac{Q_b L}{D} \frac{qEL \sinh\left(\frac{d' - y}{L}\right) + kT \cosh\left(\frac{d' - y}{L}\right) (e^{qV_{\text{bar}}/kT} - 1)}{qEL \cosh\left(\frac{d'}{L}\right) + kT \sinh\left(\frac{d'}{L}\right) (e^{qV_{\text{bar}}/kT} - 1)}$$

and for $d' < y < d' + b$

$$\Delta p(y) \approx$$

$$\frac{Q_b L}{D} \frac{kT [e^{qE(d'+b-y)/kT} - 1]}{qEL \cosh\left(\frac{d'}{L}\right) + kT \sinh\left(\frac{d'}{L}\right) (e^{qV_{\text{bar}}/kT} - 1)} \quad (15)$$

The junction current at $y = d' + b$ is calculated according to Eq. (5). The resulting quantum efficiency η is given by $\Delta J(d' + b)/qQ_b$ which is

$$\eta(V) = \frac{1}{\cosh\left(\frac{d'}{L}\right) + \frac{kT}{qEL} \sinh\left(\frac{d'}{L}\right) (e^{qV_{\text{bar}}(V)/kT} - 1)} \quad (16)$$

where we have again made the approximations $\alpha L \gg 1$ and $qEL/kT \gg 1$ and have explicitly included the voltage dependence of V_{bar} for future use.

Representative curves for the quantum efficiency

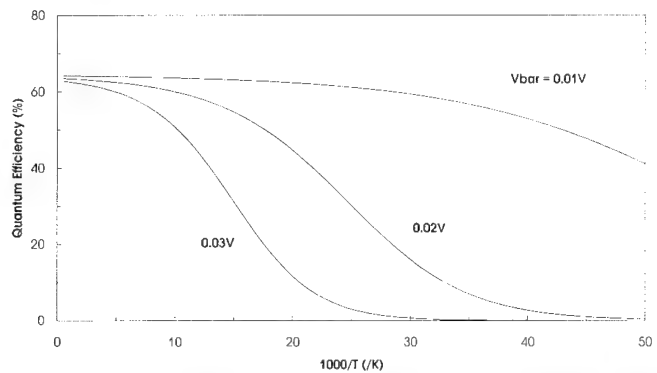


Fig. 2. Quantum efficiency vs inverse temperature for representative parameters: $d' = 15 \mu\text{m}$, $\Delta V = 0.01 \text{ V}$, $L = 15 \mu\text{m}$, and $E = 500 \text{ V/cm}$ ($\Delta E_g = 0.025 \text{ eV}$ and $W = 0.5 \mu\text{m}$).

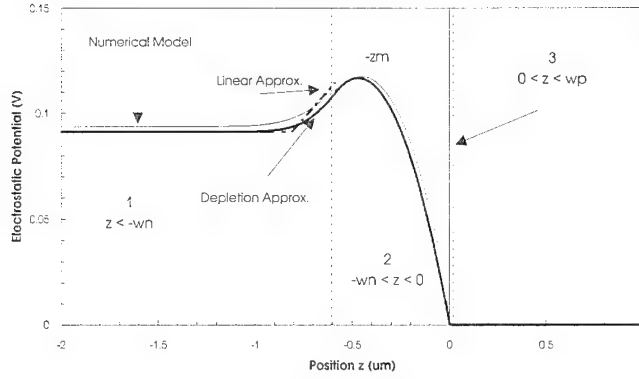


Fig. 3. Electrostatic potential vs position at zero bias from three models: the numerical model (light solid line), depletion approximation (heavy solid line), and linearized analytical approximation (heavy dashed line). The regions of the potential for the depletion approximation are illustrated: Region 1 ($z < -w_n$), Region 2 ($-w_n < z < 0$) and Region 3 ($0 < z < w_p$), where w_n and w_p are the widths of the depletion region in the n-type and p-type layers, respectively.

from Eq. (16) are plotted vs inverse temperature in Fig. 2, with the simplifying assumption that the diffusion length is independent of temperature. For large barriers V_{bar} and/or low temperatures the quantum efficiency does decrease exponentially with inverse temperature when the second term in the denominator of Eq. (16) dominates; however, as discussed by Kosai and Radford,⁶ the decrease is more gradual at more modest ratios of qV_{bar}/kT .

Depletion Approximation for a Compositionally Graded Heterojunction

In order to obtain analytic expressions for the barrier height V_{bar} and average field E in Eq. (16) for a given material structure, we now compare the simple two-piece potential in Eq. (3) to the potential calculated for a compositionally graded heterojunction in the depletion approximation. LoVecchio et al.¹⁴ gave expressions for the depletion approximation for the case of a heterojunction diode including the effects of the alloy composition change on the effective electric potential in the base. Their derivation was based on a model in which there is no valence band offset. Recent experimental evidence suggests that there is, in fact, an offset of about 350 meV at the CdTe-HgTe interface;¹⁵ we assume that this offset varies approximately linearly with alloy composition. Here we give a modified derivation which includes the effect of the valence band offset, and also includes the effect of the variation of the effective mass with position. Figure 3 illustrates schematically the dependence of the potential on position. In this figure, $-w_n$ is the position of the depletion region edge at the n-type base interface, $-z_m$ the position of the maximum in the potential, w_p the position of the depletion region edge at the p-type cap interface, and $z = 0$ the position of the base-cap doping transition (where we have changed coordinates, for convenience, to $z = y - d$).

In Region 1 in Fig. 3 ($z < -w_n$), the position of the conduction band is approximately fixed relative to the Fermi level by the n-type doping, so that as the energy

gap increases the position of the valence band decreases by the same amount, thus increasing the hole electrostatic potential. In the Boltzmann approximation, the potential varies with the position-dependent alloy composition $x(z)$ according to the expression

$$\psi(z) \equiv \psi_1(z) = \frac{kT}{q} \ln \left[\frac{N_a N_d}{n_i^2[x(z), T]} \right] - V_{vo}[x_{cap} - x(z)] - V \quad (17)$$

where T is the temperature, $qV_{vo} = 0.35$ eV is the assumed valence band offset at the CdTe/HgTe interface, x_{cap} is the alloy composition in the bulk of the cap, and V is the bias voltage applied across the junction. The intrinsic carrier concentration is given by the expression of Hansen and Schmit¹⁶

$$n_i(x, T) =$$

$$10^{14} n_{i0}(x, T) E_g^{3/4}(x, T) T^{3/2} \exp[-E_g(x, T)/2kT] \quad (18)$$

where $E_g(x, T)$ is the energy gap given by Seiler et al.¹⁷ (for E_g in eV and T in K):

$$E_g(x, T) = -0.302 + 1.93x - 0.81x^2 + 0.832x^3 + 0.000535 \left(\frac{T^3 - 1822}{T^2 + 255.2} \right) (1 - 2x) \quad (19)$$

$$\text{and } n_{i0}(x, T) = 5.585 - 3.82x + 0.001753T - 0.001364xT \quad (20)$$

If one neglects the variation with x of the prefactors in Eq. (18) (which incorporate the variation of the band-edge density of states or the effective mass) then Eq. (17) reduces to an expression similar to that in Ref. 14

$$\psi_1(z) \approx V_{bi} + E_g[x(z), T] - E_{g1} - V_{vo}[x_{cap} - x(z)] - V \quad (21)$$

where V_{bi} is the junction built-in voltage without a heterojunction (the first term of Eq. (17) for $x(z)$ equal to the base alloy composition) and E_{g1} is the energy gap in the bulk of the base region.

In the spirit of the depletion approximation, we assume that Region 2 of Fig. 3 ($-w_n < z < 0$) has no free carriers so that the potential depends on the density of donors N_d according to the solution to Poisson's equation

$$\psi_2(z) = -\frac{\epsilon N_d}{2q} (z + z_m)^2 + C \quad (22)$$

where ϵ is the dielectric constant (assumed to be independent of alloy composition) and C is a constant to be determined. Similarly, in Region 3 ($0 < z < w_p$)

$$\psi_3(z) = \frac{\epsilon N_a}{2q} (z - z_p)^2 \quad (23)$$

and for $z > w_p$, we define $\psi(z) \equiv 0$.

The conditions that the potential and its derivative be continuous at $z = -w_n$ and w_p are solved to give an expression for the position w_n of the edge of the depletion region in the base

$$w_n^2 - \frac{2\epsilon E_n}{qN_d} w_n = \frac{2\epsilon}{qN_d} \psi_1(-w_n) \quad (24)$$

where $E_n \equiv d\psi(z)/dz$ at $z = -w_n$ is the effective retarding field at the edge of the depletion region, and we have made the approximation $N_a \gg N_d$.

The variation of the alloy composition in an LPE-grown heterojunction where the alloy composition variation is centered around $z = -z_0$ (positive offset z_0 toward the base) is of the form⁷

$$x(z) = x_{cap} - 0.5(x_{cap} - x_{base})\text{erfc}[2(z+z_0)/W] \quad (25)$$

where x_{base} is the composition in the bulk of the base layer, and W is the distance over which the composition change varies from 7.9 to 92.1% of the total change. The erfc dependence results from alloy interdiffusion. When this expression is substituted into Eq. (17) and Eq. (24), the resulting equation can be solved only numerically. We have made such calculations and will compare the results with the numerical models in the next section, but for the purposes of obtaining a completely analytical expression for w_n (which we need to calculate the quantum efficiency analytically) we approximate $E_g(z)$ by a linear variation in an arbitrarily defined region $-z' < z < -z' + W'$ (see Fig. 3):

$$E_g(z) = E_{g1} + \Delta E_g(z+z')/W' \quad (26)$$

where $\Delta E_g \equiv E_g(x_{cap}, T) - E_{g1}$, and the best fit to the analytical model gives W' approximately 1.25 W and $z' \equiv z_0 + W'/2$. With this approximation, and defining the total valence band offset as $V_{v0}' \equiv V_{v0}(x_{cap} - x_{base})$, the linearized potential is given by

$$\psi_1(z) = V_{bi} - V_{v0}' - V + E(z+z') - z' < z, -z' + W' \quad (27)$$

and the retarding field is a constant $E \equiv (\Delta E_g - V_{v0}')/W'$. The solution to Eq. (24) is now

$$w_n(V) = \left[\frac{2\epsilon}{qN_d} (V_{bi}' - V) \right]^{1/2} \quad (28)$$

where we have defined a new effective built-in voltage

$$V_{bi}' = V_{bi} - V_{v0}' + Ez' \quad (29)$$

Eq. (28) is valid as long as $z' - W' < w_n < z'$. The effective potential "barrier" is the difference between the potential at the depletion region edge $z = -w_n$ and that in the bulk of the base, which is

$$V_{bar}(V) = Eb(V) \quad (30)$$

where we have defined a "barrier distance"

$$b(V) = z' - w_n(V) \quad (31)$$

As the reverse bias is increased ($V < 0$), Eq. (28) shows that w_n is also increased (the depletion region moves into the base, away from the alloy composition

increase) thus reducing the barrier distance $b(V)$ which, according to Eq. (30), reduces the barrier voltage $V_{bar}(V)$. According to Eq. (16), this results in an increase in the quantum efficiency at reverse bias. Combining Eqs. (30), (31), and (28) gives

$$V_{bar}(V) = E \left(z' - \left[\frac{2\epsilon}{qN_d} (V_{bi}' - V) \right]^{1/2} \right) \quad (32)$$

which, when combined with Eq. (16), gives an analytical function for the quantum efficiency as a function of the bias voltage V . We will make further approximations to this function in the next major section, in order to compare the model with the results of numerical calculations and, in the section on Comparison with Experimental Data, with experimental data.

Diode Current, Dynamic Resistance, and Noise

We now show that the bias-dependent quantum efficiency immediately gives an illumination-dependent shunt resistance which can be calculated from the same analytical model. The analytical model for the quantum efficiency [Eq. (16) combined with Eq. (32)] gives the following expression for the product of the illumination-dependent shunt resistance $R_A(V)^{12}$ which is the inverse of the first term in Eq. (2) which can be written

$$\frac{1}{R_A(V)} = -I_b(V) \left[\frac{1}{\eta} \frac{d\eta(V)}{dV} \right] \quad (33)$$

and the magnitude of the bias-dependent background current $I_b(V) = q\eta(V)Q_bA$ in Eq. (1):

$$I_b(V)R_A(V) = \frac{2L(V_{bi}' - V)e^{-qV_{bar}(V)/kT}}{\eta(V)w_n(V)\sinh(d/L)} \quad (34)$$

where we have neglected the small dependence of d' on V ($d' \approx d$). We should point out that it is the dependence of d' on V in Eq. (16) that is the source of the effect described by Rosbeck et al.^{8,9} The effect is small in this case only because of the larger effect of the variation of the barrier voltage $V_{bar}(V)$.

At zero bias, we define a background-induced IR product

$$IR_b = - \frac{1}{\left[\frac{1}{\eta} \frac{d\eta}{dV} \right]_{V=0}} = I_b(0)R_A(0). \quad (35)$$

Smaller values of IR_b correspond to larger decreases in the total diode resistance for a given illumination level. For moderate values of qV_{bar}/kT , IR_b decreases exponentially with V_{bar} ; the decrease is more rapid than the decrease in the quantum efficiency η because of the first term in the denominator of Eq. (16). Thus, the reduction in the diode resistance can be a stronger effect than the reduction in the quantum efficiency. In

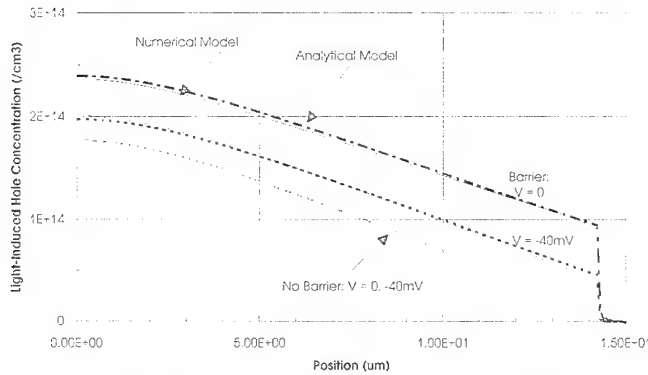


Fig. 4. Light-induced carrier density vs position in the base neutral region for the case of a HgCdTe homojunction (lower curves) and a heterojunction with a barrier (upper curves). The curves were calculated for 0 (solid lines) and -40mV (dashed lines) bias. The curves were calculated using the HET III modeling program except for the heavy lines which were calculated using the analytical approximation for the parameters given in the text.

the limiting case where η is in the strong exponential region, the IR product (for $V = 0$) is given by

$$IR_b \rightarrow \frac{2kTV'_{bi}}{qEw_n} \text{ for } \frac{qV_{bar}}{kT} \gg 1 \quad (36)$$

which is about a factor of kT/qEL smaller than a simplified version of the expression given by Rosbeck et al.⁹ for the homojunction case

$$IR_{b, \text{homojunction}} = \frac{2LV_{bi}}{w_0 \tanh(d/L)} \quad (37)$$

where w_0 is the junction depletion width. (This expression results from the assumptions $\alpha L \gg 1$ and no surface recombination.)

If the bias-dependent shunt resistance were a true resistance the diode current noise would be increased by an extra Johnson noise term. The accepted model for the current noise for a diffusion-limited diode with current given by Eq. (1), if the quantum efficiency η does not depend on bias and there is no illumination-dependent resistance, can be written, at low frequencies,¹⁸

$$I_n^2(V) = 2qI_b + \frac{2kT}{R_0} + \frac{2kT}{R(V)} \quad (38)$$

where $R_0 = R(0)$. Since in reverse bias $R(V)$ increases rapidly (exponentially for diffusion-limited diodes), the last term in Eq. (38) generally becomes very small so that the total current noise decreases in reverse bias.

When η depends on V , one must be careful to separate the noise terms due to the thermal and illumination-dependent inverse resistance terms. The illumination-dependent resistance results simply from differentiating the current vs voltage and therefore does not generate a thermal noise term as do the other resistance terms. The following expression incorporates the shot noise due to the illumination-depen-

dent current and the thermal noise from the "dark" resistance:

$$I_n^2(V) = 2qI_b(V) + \frac{2kT}{R_{dk}(0)} + \frac{2kT}{R_{dk}(V)} \quad (39)$$

where $R_{dk}(V)$ is the dynamic resistance due to the true dark current only (measured with no illumination). If the heterojunction barrier produces a large variation $\eta(V)$, the current noise in large optical backgrounds will be dominated by the shot noise on the background current, which increases with reverse bias; thus in this case the noise will increase, rather than decrease, with reverse bias. We will compare this model with experimental data in the section entitled Comparison with Experimental Data.

NUMERICAL MODEL

Comparison with the Analytical Model

We have used the same numerical modeling program ("HET III") that was modified by Kosai and Radford^{7,19} from the Stanford SEDAN program²⁰ to calculate the quantum efficiency and dynamic resistance to compare with the analytical model described in the previous section. The program solves the coupled Poisson and carrier transport equations for a number of semiconductor materials and device structures; the enhancements by Kosai and Radford⁷ include optical effects and erfc composition profile options. The version of the program we used did not include a valence band offset for HgCdTe. More detailed descriptions are given in Refs. 7 and 20. We did modify the program to incorporate the expression of Seiler et al.¹⁷ for the energy gap as a function of x and T .

Figure 3 compares the electrostatic potential calculated using the analytical model, with and without the linear approximation to the alloy composition, to that calculated using HET III. The assumed base cutoff wavelength was $11\text{ }\mu\text{m}$ at a temperature of 80 K ($x = 0.2185$). The cap-base alloy composition difference Δx was 0.04 with an erfc width W of $0.5\text{ }\mu\text{m}$ centered at an offset z_0 of $0.5\text{ }\mu\text{m}$ (into the base). There was no applied bias. For the numerical modeling the photon wavelength was $8\text{ }\mu\text{m}$ (absorption coefficient $\alpha = 3200/\text{cm}$) and the background flux Q_b was $10^{14}\text{ ph/cm}^2\text{-s}$. The base layer was $15\text{ }\mu\text{m}$ thick and the cap $2\text{ }\mu\text{m}$. The base and cap doping concentrations were 1×10^{15} and $2 \times 10^{17}/\text{cm}^3$, respectively. Fermi-Dirac statistics were used. The base layer hole lifetime τ was calculated using an Auger model giving approximately $1.2\text{ }\mu\text{s}$ in the neutral region. The base layer hole mobility was $745\text{ cm}^2/\text{V-s}$ giving a hole diffusion length L of $23\text{ }\mu\text{m}$. For the analytical models, no valence band offset was used, for consistency with the HET III calculations. There is a small difference between the analytical and numerical potential, and the linearized potential is clearly only a crude approximation. The estimated base layer depletion width w_n is nearly the same for the three models: $0.53\text{ }\mu\text{m}$ for an extrapolation of the carrier density to near 0 in

HET III, $0.54 \mu\text{m}$ for the quasi-analytical model [Eq. (17)] and $0.59 \mu\text{m}$ for the linearized analytical model [Eq. (28)].

A similar comparison of the quantum efficiency η and the IR product IR_b from the numerical and linearized analytical models [Eq. (16) and Eq. (32)], for the same structure as in Fig. 3, for different alloy composition steps $\Delta x = x_{\text{cap}} - x_{\text{base}}$, shows reasonably good agreement, considering that the quantum efficiency in the presence of a barrier is strongly influenced by the exponential term in the denominator of Eq. (16) and that the linearized potential approximation is so crude. As in the case of tunneling, it is very difficult to make accurate calculations when the behavior is dominated by exponential effects. At 80K, a value of the parameter W/W of about two gives the best agreement, instead of the ratio 1.25 which gives the best approximation to the erfc function (Fig. 3). For this case, the quasi-analytical model gives a quantum efficiency of 65% and a zero-background IR product of 0.29 V, compared to 70% and 0.21 V, respectively, from the HET III numerical model.

Calculations for the heterojunction structure for a temperature of 40K show that the zero-bias quantum efficiency is strongly reduced, to 9% from the numerical model, 2% from the quasi-analytical model with W/W equal to 1.25, and the IR product is reduced by an even larger amount, to 0.013 or 0.03 V, respectively. As one might expect, the effects of the barrier at lower temperatures are much stronger and vary more with the alloy composition step.

We have used the HET III model to calculate the variation with position of the photogenerated carrier concentration for a flux Q_b of $1 \times 10^{18} \text{ph/cm}^2\text{-s}$, and have compared the results with the analytical approximation [the solution to Eqs. (10)–(13) substituted into Eq. (6)]. Figure 4 gives the results of the numerical calculation for applied biases of 0 and -40 mV for the case of no barrier ($\Delta x = 0$) and for the above case of $\Delta x = 0.04$, $W = 0.5 \mu\text{m}$, $z_0 = 0.5 \mu\text{m}$. The plots illustrate the dramatic difference between the case with no barrier, with a nearly exponential decrease of the carrier concentration throughout the base, and a small offset at reverse bias which produces only a very small quantum efficiency variation and illumination-dependent shunt resistance, and the case with a barrier where, as described in Ref. 7, the carriers “pile up” in the base and decrease abruptly due to the retarding field in the barrier region. In this case, the reverse bias has a large effect on the light-induced carrier concentration by moving the edge of the depletion region away from the barrier region, reducing the barrier width, hence the barrier height and the carrier pile-up, allowing a larger current to flow into the junction.

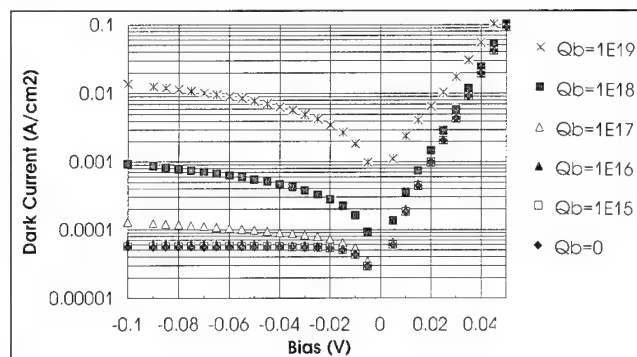
The calculation for the depletion model for the barrier case in Fig. 4 agrees quite well with the numerical model, when the parameters w_n , V_{bar} , and b are adjusted slightly from the linearized approximation. Thus, Fig. 3 and Fig. 4 show that the analytical model describes, at least semi-quantitatively, the

important physics of the effect of a heterojunction barrier on the quantum efficiency, the background-induced shunt resistance, and the photogenerated carrier density.

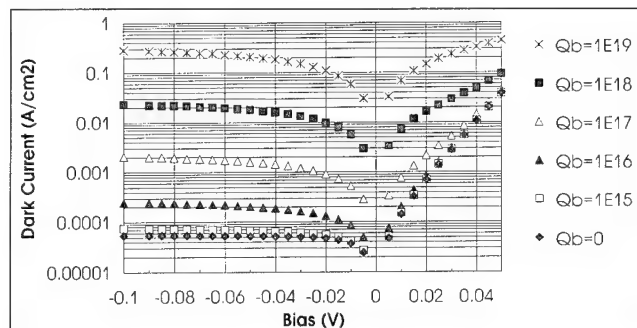
Case Studies

We have used the HET III model to make a detailed assessment of the effect of illumination on a photodiode with and without a heterojunction barrier, and on the temperature dependence of the effect. We have also compared some results with the analytical model.

Figure 5 compares the “dark current” IV curves [$J(V, Q_b) - J(0, Q_b)$] calculated for the two structures used previously, with and without a barrier ($\Delta x = 0.04$ for the barrier case). Both show an background-in-



a



b

Fig. 5. Numerical model results for the “dark” current density $J(V, Q_b) - J(0, Q_b)$ for background illumination fluxes from 0 to $10^{19} \text{ph/cm}^2\text{-s}$ for two structures: (a) homojunction, and (b) heterojunction with a barrier. The parameters of the structures are given in the text.

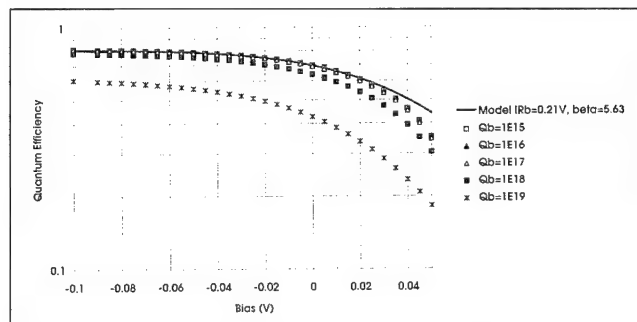
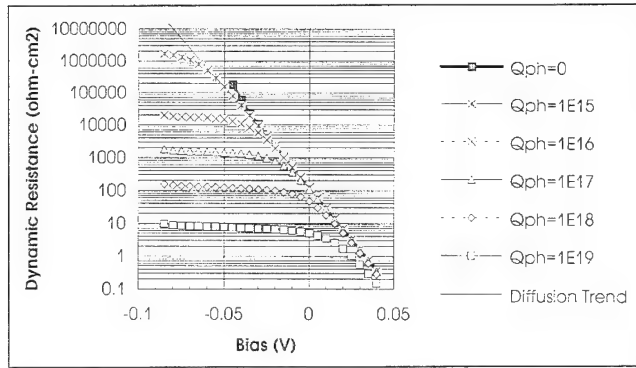
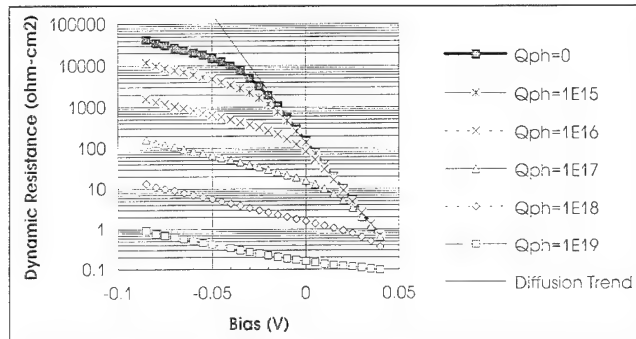


Fig. 6. Numerical model results for the bias-dependent quantum efficiency for background illumination fluxes from 0 to $10^{19} \text{ph/cm}^2\text{-s}$ for the case of a heterojunction with a barrier (Fig. 5b), compared to the analytical model (heavy solid line) with parameters given in the text.



a



b

Fig. 7. Numerical model results for the dynamic resistance-area product vs bias for background illumination fluxes from 0 to 10^{19} ph/cm²-s for the structures given in Fig. 5: (a) homojunction, and (b) heterojunction with a barrier.

duced increase in the current. At a flux of 10^{17} ph/cm²-s, there is only a small increase in the current for the homojunction (about 10^{-4} A/cm² at -0.1 V bias in Fig. 5a) but a much larger increase for the barrier case (2×10^{-3} A/cm² at -0.1 V in Fig. 5b). The quantum efficiency [proportional to $J(V, Q_b) - J(V, 0)$] is approximately independent of bias for the homojunction but, as shown in Fig. 6, varies strongly with bias for the barrier case.

Figure 6 also shows that the quantum efficiency, as expected for a linear device, is independent of flux level up to nearly 10^{18} ph/cm²-s where high level injection effects occur. Figure 6 also shows that the analytical model [Eq. (16)] describes very well the bias dependence of the quantum efficiency, using parameters adjusted to improve the fit. We have rewritten Eq. (16) as

$$\eta(V) = \frac{\eta(-\infty)}{1 + \beta e^{(1+\beta)V/\beta IR_b}} \quad (40)$$

where we have expanded the expression for $V_{bar}(V)$ [Eq. (30)] to give a linear dependence on V . In Eq. (40), the two parameters IR_b and β are, respectively, the zero-bias IR product $I_b(0)R_A(0)$ [Eq. (35)] and the increase of the quantum efficiency at very large reverse bias:

$$\frac{\eta(-\infty)}{\eta(0)} = 1 + \beta \quad (41)$$

In the case illustrated in Fig. 6, the numerical model gives $IR_b = 0.21$ V and $\beta = 0.18$, giving an increase of 18% in the quantum efficiency from 0 to large reverse bias. The analytical model prediction for IR_b is given by Eq. (34) for $V = 0$ and for β the analytical model gives

$$IR_b = \frac{2LV_{bi}' e^{-qV_{bar}(0)/kT}}{w_n(0)\eta(0) \sinh(d/L)} = IR_{b, \text{homojunction}} e^{-qV_{bar}(0)/kT} \quad (42)$$

$$\beta = \frac{kT}{qEL} \tanh\left(\frac{d}{L}\right) e^{qV_{bar}(0)/kT} \quad (43)$$

which gives $IR_b = 0.32$ V and $\beta = 0.27$ (as before, fair agreement with the numerical model).

Figure 7 illustrates the dynamic resistance-area product $R_d(V)A$ calculated numerically from the IV curves in Fig. 5. The resistance at $Q_b = 0$ is similar for the two structures and follows the diffusion trend $\exp(qV/kT)$ for the homojunction and for the barrier case below about 20 mV reverse bias. The background-induced shunt resistance is much lower for the case of the heterojunction with a barrier, with a zero-bias IR product of 0.21 V for the barrier case (Fig. 7b) compared to 11 V (in agreement with the expressions of Rosbeck et al.)⁸ for the homojunction. Thus, the effect of the barrier on the background-induced shunt resistance (about a factor of 50 reduction) can be much stronger than the effect on the quantum efficiency (only about 18% reduction).

COMPARISON WITH EXPERIMENTAL DATA

In order to show that the above calculations can be useful in understanding the quantum efficiency and dynamic resistance of HgCdTe heterojunction photodiodes, we compare the results to a representative set of experimental data. The LPE P-on-n diodes tested were mesa-delineated, backside-illuminated diodes with nominal structural parameters similar to those used in the HET III modeling above. They were grown on CdTe substrates and passivated with CdTe. Because of the limited amount of information available on the detailed heterojunction structure of the diodes tested, and because of the sensitivity of the model to these details, due to the exponential behavior, our goal in this section is to show that the parameterized version of the model can give agreement with the trends of the experimental data.

A long wavelength infrared (LWIR) array, with a cutoff wavelength of 11.39 μ m at a temperature of 77K was tested at a temperature of 40K with four different optical backgrounds ranging from 2.7×10^{15} ph/cm²-s to 1.2×10^{12} ph/cm²-s. At 80K, this array had good but somewhat bias-dependent quantum efficiency, 83% at 0 bias and 95% at -40 mV, from the extrapolation to infinite area of a group of sparse variable-area diodes. The zero-bias large-area quantum efficiency decreased at 40K to 28%. Some of this reduction can be attributed to a reduction in the hole diffusion length L .

There is evidence for a heterojunction barrier for this array, in that the ratio of the optical response at -40 mV bias, to that at 0 bias, averaged 1.15 at 77K and increased to 1.59 at 40K for 35 μm pitch diodes with 20 μm mesas. Also, the zero-bias resistance R_0 was significantly larger at the lowest than at the highest backgrounds (by about three orders of magnitude). Figure 8 plots the inverse of the zero-bias resistance as a function of the zero-bias background current I_b , with a fit to a parameterized version of Eq. (33):

$$\frac{1}{R_0} = \frac{I_b}{IR_b} + \frac{1}{R_{dk}(0)}$$

(44)

Clearly, the fit is very good, using a value for the barrier-induced IR product IR_b of 84 mV for one element and 53 mV for another. In fact, Fig. 8 shows that the “dark” resistance $R_{dk}(0)$, estimated to be about $10^{11}\Omega$, is negligible at all but the lowest backgrounds, so that the product $I(0)R(0)$ at the f/8 background is dominated by IR_b . The variation in IR_b from element to element is probably due to small variations in the barrier height within this array which, because of the exponential dependence, can produce large variations in IR_b and also somewhat lesser variations in the zero-bias quantum efficiency. It should be pointed out that this array was chosen as an example because it had more evidence than usual of such barrier effects.

Figure 9 compares the quantum efficiency of one

element of this array, as a function of reverse bias, to a fit using Eq. (40), with parameters $\eta(-\infty) = 49.5\%$, $IR_b = 55$ mV, and $\beta = 1.08$. The quantum efficiency was calculated by taking the difference between IV curves measured with high and low backgrounds. The fit is excellent up to a reverse bias of about -100 mV, at which point the leakage current became comparable to the background current and a small temperature

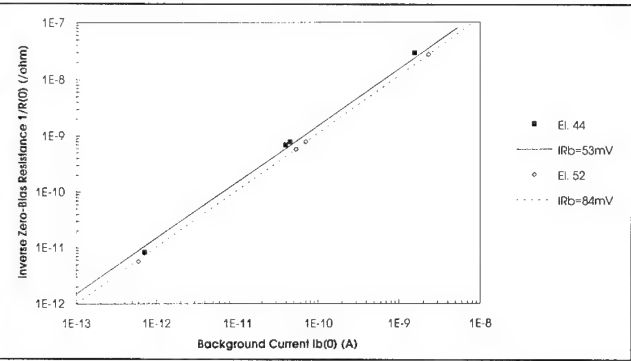


Fig. 8. Plots of the inverse zero-bias resistance $R(0)$ vs the magnitude of the background current I_b for two representative elements of a test array at a temperature of 40K.

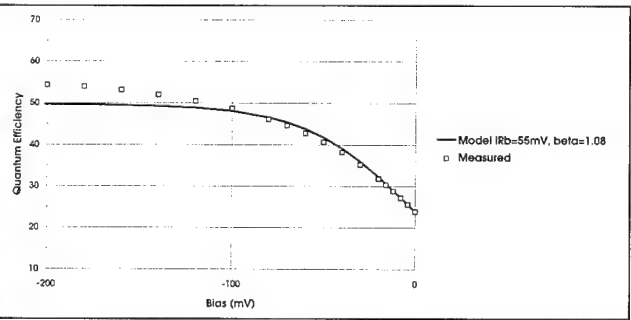


Fig. 9. Quantum efficiency vs reverse bias for one element of the same test array as in Fig. 8, compared to the parameterized model.

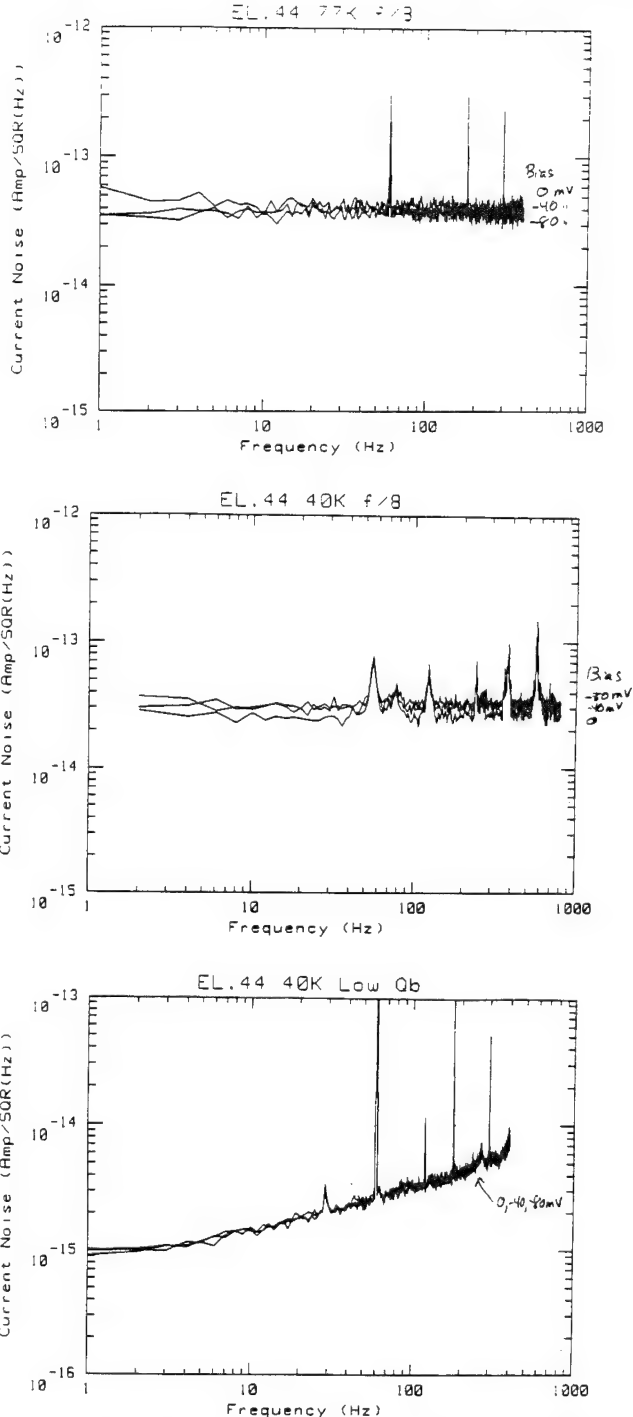


Fig. 10. Current noise vs frequency for one element of the same test array as in Figs. 8–10. (a) $T = 77\text{K}$, f/8 cold shield, (b) $T = 40\text{K}$, f/8 cold shield, and (c) $T = 40\text{K}$, 0.025 in. pinhole with cold spike filter ($Q_b = 1.2 \times 10^{11}\text{ph/cm}^2\text{-s}$).

Table I. Summary of the Noise Measurements in Figure 1

T, f/#	77 K, f/8	40 K, f/8	40K, pinhole
G (V/A)	10 ⁸	10 ⁸	10 ¹¹
I(0) (A)	2.00 × 10 ⁻⁹	1.39 × 10 ⁻⁹	6.36 × 10 ⁻¹³
R(0) (Ω)	3.67 × 10 ⁶	3.62 × 10 ⁷	1.97 × 10 ¹¹
I _n ² (0) calc.	3.3 × 10 ⁻¹⁴	2.7 × 10 ⁻¹⁴	6.2 × 10 ⁻¹⁶
I _n ² (0) meas.	3.3 × 10 ⁻¹⁴	2.7 × 10 ⁻¹⁴	≈ 1.0 × 10 ⁻¹⁵
I(-40mV) (A)	—	2.24 × 10 ⁻⁹	7.76 × 10 ⁻¹³
R(-40mV) (Ω)	1.12 × 10 ⁷	—	2.02 × 10 ¹¹
I _n ² (-40mV) calc.	2.8 × 10 ⁻¹⁴	3.1 × 10 ⁻¹⁴	6.4 × 10 ⁻¹⁶
I _n ² (-40mV) meas.	2.8 × 10 ⁻¹⁴	3.1 × 10 ⁻¹⁴	≈ 1.0 × 10 ⁻¹⁵

Note: Giving for each temperature T and f/# the preamplifier gain G, the measured current I and resistance R at biases of 0 and -40mV, and the calculated current noise I_n at each bias, compared to the measured noise at the same bias. For each of the 40K tests, there are two columns giving the calculations using the noise model which includes the barrier effects [Eq. (38)] based on a shot noise model for the total current, and, for comparison, using the standard model [Eq. (38)] which assumes a thermal origin for the dark current and dynamic resistance. For the 40K, f/8 tests, the shot noise model agrees much better with the measured noise. Because of the small additional noise at 40K with the 0.025 in. pinhole, where there is a small excess measured noise due to shunting effects in the cables and dewar wiring, the measurement is not accurate enough to distinguish between the two models.

difference between the low and high background tests could have resulted in a change in the true "dark" current, rather than a true change in the optically generated current.

Finally, the current noise was measured as a function of frequency to confirm that the illumination-dependent shunt resistance does not in itself generate additional noise. Figure 10 illustrates the current noise spectra for three cases: f/8 cold shield at 77 and 40K, and very low background (0.025 in. pinhole with a cold spike filter) at 40K. Each plot contains three curves, taken at biases of 0, -40, and -80 mV. The results of these tests are summarized in Table I. The gain of the amplifier was 10⁸V/A for the f/8 background cases and 10¹¹V/A for the low background case. At 77K, the noise is dominated by the zero-bias background shot noise and by the detector diffusion current terms and fits the standard noise model [Eq. (38)] very well, with the addition of a term due to the amplifier thermal noise. The noise in Fig. 10a is higher at zero bias than at reverse bias. At the same background but at a temperature of 40K (Fig. 10b), the opposite is true: the noise is dominated by the barrier-induced bias-dependence of the quantum efficiency, so that the noise is indeed larger at reverse than at zero bias, in agreement with Eq. (39) again adding a term due to the amplifier thermal noise. Finally, at 40K and low background (Fig. 10c), neither effect dominates, so that the noise is approximately independent of bias. The increase of the noise with frequency in this case is due to the input amplifier noise voltage, coupled as a current noise by the input cable and dewar lead capacitance, at this very low noise level. There also is a small excess noise due to shunt effects in the cable.

SUMMARY AND CONCLUSIONS

This work has developed a new analytical model which gives fair agreement with numerical models and, more importantly, elucidates the important phys-

ics of the effect of a heterojunction barrier on the quantum efficiency and dynamic resistance of a HgCdTe LPE P-on-n photodiode. A parameterized version of the expression for the bias-dependent quantum efficiency and the barrier-induced shunt resistance agrees well with experimental data and reveals the extent to which these effects are related to each other.

A comparison of the model with experimental data shows that the effect of the barrier becomes much stronger at lower temperatures and for longer cutoff wavelength diodes, and that there can be a large variation in the barrier effects within small areas of the LPE-grown HgCdTe material. This variability may be the source of at least some of the commonly reported increase in the variability of the R₀ product as the temperature is decreased from 80 to 40K.

ACKNOWLEDGMENT

This work was supported in part by ARPA Contract No. MDA972-92-C-0076, monitored by Mr. R. Balcerak, the Atmospheric Infrared Sounder (AIRS) Program (NASA/JPL Contracts No. 958606 and 958970), managed by Mr. Fred O'Callaghan of JPL, and a USASSDC Contract.

REFERENCES

1. W.E. Tennant, C.A. Cockrum, J.B. Gilpin, M.A. Kinch, M.B. Reine and R.P. Ruth, *J. Vac. Sci. Technol. B* 10, 1359 (1992).
2. C.C. Wang, *J. Vac. Sci. Technol. B* 9, 1740 (1991).
3. T. Tung, M.H. Kalisher, A.P. Stevens and P.E. Herning, *Mater. Res. Soc. Symp. Proc.* 90 (1987), p. 321.
4. G.N. Pultz, P.W. Norton, E.E. Krueger and M.B. Reine, *J. Vac. Sci. Technol. B* 9, 1724 (1991).
5. E.E. Krueger, G.N. Pultz, P.W. Norton, J.A. Mroczkowski, M.H. Weiler and M.B. Reine, *Mat. Res. Soc. Symp. Proc.* 216 (1991), p. 93.
6. P.R. Bratt, *J. Vac. Sci. Technol. A* 1, 1687 (1983).
7. K. Kosai and W.A. Radford, *J. Vac. Sci. Technol. A* 8, 1254 (1990).
8. J.P. Rosbeck, I. Kasai, R.M. Hoendervoogt and M. Lanir, *1981 IEDM Proc.*, p. 161.
9. J.P. Rosbeck, R.E. Starr, S.L. Price and K.J. Riley, *J. Appl.*

- Phys.* 53, 6430 (1982).
10. F.A. Lindholm, J.G. Fossum and E.L. Burgess, *IEEE Trans. Electron Devices* ED-26, 165 (1979).
 11. N.G. Tarr and D.L. Pulfrey, *Sol. State Electronics* 22, 265 (1979).
 12. R. Graft, T. Fischer, A. Gray and S. Kennedy, *J. Appl. Phys.* 74, 5705 (1993).
 13. R. Schoolar, *Infrared Phys.* 31, 467 (1991).
 14. P. LoVecchio, M.B. Reine and M.N. Grimbergen, *J. Vac. Sci. Technol. A* 3, 246 (1985).
 15. N.F. Johnson, P.M. Hui and H. Ehrenreich, *Phys. Rev. Lett.* 61, 1993 (1988).
 16. G.L. Hansen and J.L. Schmit, *J. Appl. Phys.* 54, 1639 (1982).
 17. D.G. Seiler, J.R. Lowney, C.L. Littler and M.R. Loloee, *J. Vac. Sci. Technol. A* 8, 1237 (1990).
 18. M.B. Reine, A.K. Sood and T.J. Tredwell, *Semiconductors and Semimetals*, Vol. 18, ed. R.K. Willardson and A.C. Beer, p. 233.
 19. K. Kosai, *J. Electron. Mater.* 24, 635 (1995).
 20. Z. Yu and R.W. Dutton, *Integrated Circuits Laboratory*, Stanford University, 1985 (unpublished).

JOURNAL OF ELECTRONIC MATERIALS

TRANSFER OF COPYRIGHT

To be signed by the author or, in the case of multiple authorship, by at least one of the authors who agrees to inform the others, or, in case of a work made for hire, by the employer. The signed statement must be received by the editor before the manuscript can be accepted for publication.

Copyright to the article by _____.

Submitted under the title _____
is hereby transferred to The Minerals, Metals & Materials Society, Inc. effective if and when the article is accepted for publication in *Journal of Electronic Materials*.

For authors who are employees of the United States Government, the transfer of copyright is understood to be effective only to the extent that such copyright is transferable.

The authors explicitly reserve the following rights:

- All proprietary rights other than copyright, such as patent rights.
- The right to use all or part of this article in future works of their own such as lectures, reviews, textbooks, or reprint books.
- The right to make copies of the authors' own teaching use.
- The right to use figures and tables in future publications, provided explicit acknowledgment is made of their initial appearance in this journal.

Signature _____	Date _____	Phone _____
Address _____		Fax _____
_____		e-mail _____

Journal of Electronic Materials Author Instructions

General Purpose

The *Journal of Electronic Materials* (*JEM*) is published by the Electronic Materials Committee of The Minerals, Metals & Materials Society (TMS) and the Electron Devices Society of the Institute of Electrical and Electronics Engineers. *Journal of Electronic Materials* regularly reports on the science and technology of electronic materials, while examining new applications for semiconductors, magnetic alloys, insulators, and optical and display materials. The journal welcomes articles on methods for preparing and evaluating the chemical, physical, and electronic properties of these materials. Specific areas of interest are electronic memory and logic structures, magnetic-optical recording media, superlattices, packaging, detectors, emitters, metallization technology, superconductors, and low thermal-budget processing. The journal also selectively publishes invited and contributed review papers on topics of current interest to enable individuals in the field of electronics to keep abreast of activities in areas peripheral to their own. Further, *JEM* publishes papers from the annual conference sponsored by the TMS Electronic Materials Committee. It is the journal's editorial intent that the published papers be of interest to nonspecialists and specialists in the field of the particular contribution.

Review Process

Papers for *JEM* are reviewed by two qualified referees to determine suitability. The editor's decision to accept or reject a paper, based on referees' comments, is final. Send three copies of the manuscript key-stroked, double-spaced on 22 × 28 cm (8.5 × 11 in.) paper to the appropriate section or associate editor (see inside front cover). Alternatively, a paper/review/letter can be submitted directly to the editor (see inside front cover), who will assign the manuscript to appropriate section or associate editor (obviously the latter procedure takes longer). Papers dealing with subjects not identified with any particular section or associate editor should be sent to Theodore C. Harman. For letters only, fax one copy to G.B. Stringfellow (801/581-4816), followed simultaneously with two hard copies (one of which includes glossy prints or equivalent). Priority mail is recommended for shortened publication times. The initial submission should state that the contribution is for the Letters section. Authors will be notified when their manuscripts have been accepted for publication.

Stylistic Guidelines

All manuscripts should adhere to the following guidelines:

1. The manuscript, written in English, must be double-spaced throughout, key-stroked on one side of the paper only. Good quality office machine copy is acceptable.
2. Number all pages in sequence.
3. Key-stroke title of article and abstract on a separate first page.
4. The work's significance and its relation to the work of others should be detailed in the Introduction. Major assumptions should be stated and procedures adequately outlined.
5. Key-stroke references, figure captions, and tables on separate pages.
6. Key-stroke references in the style used by technical publications. References should be cited in the text by Arabic numerals as superscripts. Each individual reference should include the names of all the authors, the standard abbreviated name of the journal [see *World List of Scientific Periodicals*, 4th ed. (1960), Butterworths, London], the volume number, the initial page number, and the year of publication in parentheses. For books, the city of publication and the publisher should be given.
7. Use only those figures that are necessary to illustrate the meaning of the text. The text must include a citation of each figure. Original figures must be India Ink line drawings or black-and-white, high-contrast, glossy prints. (Color photographs or photocopies are not acceptable.) Original glossy prints should be submitted along with two sets of copies for the review and should be no larger than 22 × 28 cm (8.5 × 11 in.).
8. Measurements should be given metrically.
9. Submit: (a) the original manuscript and artwork, and (b) two single-sided photocopies of the manuscript and artwork.
10. Each submitted letter (up to six typewritten pages and up to four figures and/or tables) should be accompanied with an abstract of 100 words or less, a key words line, and a transfer of copyright form. The initial submission should state that the contribution is for the Letters section.

Copyright

Submission is a representation that the manuscript has not been published previously and is not currently under consideration for publication elsewhere. A statement transferring copyright from the authors (or their employers, if they hold copyright) to TMS will be required before the manuscript can be accepted for publication. A suitable form for copyright transfer is printed in the back of every January issue and is available from the editor's office and TMS.

Galley Process

Authors will be given the opportunity to review the typeset version of their manuscript. This review should be solely dedicated to detecting typographical errors. Editorial changes and corrections are not to be made at this time. To meet production deadline, a rapid turnaround of these proofs is necessary.

Page Charges and Reprints

Journal of Electronic Materials, like many other scientific and technical journals, depends on author page charges for a significant part of its support. Therefore, a charge of \$110 per printed page is levied for all papers published. One hundred reprints will be supplied without additional charge for every paper on which the payment of these charges is authorized. It is expected that each author or sponsoring institution will contribute fairly to the support of *JEM* through payment of the page charges. However, authors may request a waiver of all or part of the page charges by sending a written request to *JEM*. Instructions and forms regarding page charges, waivers, and reprints will be forwarded from the TMS business office. These and any other special matters related to page charges should be referred to the *JEM* Circulation Department, TMS, 420 Commonwealth Drive, Warrendale, PA 15086; (412) 776-9080; fax (412) 776-3770.

AUTHOR INDEX

Ajisawa, A.	1105	Hasan, J.	1137	Oda, N.	1105
Amir, N.	1161	Hatano, H.	1093	Ohlson, M.	1299
Antoszewski, J.	1255	He, P.	1087	Park, I.H.	1053, 1057
Aoudia, A.	1061	Helgesen, P.	1263	Park, J.W.	1053
Arias, J.M.	1067, 1207	Helms, C.R.	1137, 1219	Park, M.J.	1053, 1057
Ariel, V.	1169, 1321	Hoffman, C.A.	1255	Pasko, J.G.	1067, 1207
Asa, G.	1161	Holander, S.	1137	Pittal, S.	1087
Astles, M.G.	1149	Houlton, M.R.	1149	Pollehn, H.K.	1041
Baars, J.	1311	Jeoung, Y.T.	1053	Reine, M.B.	1077, 1329
Bahir, G.	1169, 1321	Johns, B.	1087	Reisinger, A.R.	1201
Babaj, J.	1067, 1175, 1207	Jones, E.D.	1225	Richter, H.J.	1155
Barnes, S.L.	1077	Karam, N.H.	1287	Richter, V.	1169
Bartholomew, D.	1299	Kawamoto, K.	1093	Robinson, H.G.	1137
Bell, W.	1149	Kawazu, Z.	1113	Rosenfeld, D.	1169, 1321
Benson, J.D.	1041	Keller, R.C.	1155	Schiebel, R.	1299
Berding, M.A.	1119, 1127	Kestigian, M.	1077	Schimert, T.R.	1077
Bevan, M.	1299	Kim, J.M.	1053, 1057	Seelmann-Eggebert, M.	1155
Bhat, I.B.	1039, 1047, 1087	Kim, J.S.	1057	Seiler, D.G.	1305
Blackmore, G.	1149	Kim, J.S.	1305	Seymour, D.J.	1255
Boyd, P.R.	1041	Kim, S.U.	1053, 1057	Shaw, N.	1225
Brigham, R.	1175	Kim, H.K.	1053	Sheng, J.	1175
Brink, D.	1311	Klymachyov, A.N.	1201	Sher, A.	1119, 1121, 1127, 1169
Bruder, M.	1311	Kozlowski, L.J.	1067	Sivananthan, S.	1211, 1287
Bubulac, L. O.	1175, 1207	Krishnamurthy, S.	1119, 1121	Sizmann, R.	1263
Capper, P.	1225	Lange, M.D.	1211	Skauli, T.	1263
Casagrande, L.G.	1189	Lee, D.L.	1183	Smith, F.T.J.	1189, 1287
Case, F.C.	1077	Lee, J.	1269	Song, J.H.	1057
Chandra, D.	1249	Lee, S.B.	1057	Sonoda, T.	1113
Chang, J.M.	1053	Lee, T.S.	1053, 1057	Starr, R.	1077
Chen, A.-B.	1119, 1121	List, R.S.	1293, 1299	Steen, H.	1263
Chen, M.C.	1249, 1305	Littler, C.L.	1311	Strong, R.L.	1293
Chen, Y.P.	1287	LoVecchio, P.	1287	Suh, S.H.	1057
Chun, C.H.	1053	Løvold, S.	1263	Summers, C.J.	1269
Cole-Hamilton, D.J.	1149	Lusson, A.	1061	Takamiya, S.	1113
Colin, T.	1263	Luttmer, J.D.	1293	Tennant, W.E.	1067, 1175
Colombo, L.	1249, 1305	Macleod, B.D.	1183	Tobin, S.P.	1189
Cunningham, B.T.	1183	Maejima, T.	1093	Tomm, J.W.	1269
Dalal, N.S.	1201	Mainzer, N.	1161, 1169	Tran, T.K.	1269
DeWames, R.E. ...	1067, 1207, 1239	Malyutenko, V.K.	1231	Tregilgas, J.	1219
Dhar, N.K.	1041	Malzbender, J.	1225	Triboulet, R.	1061
DiMarzio, D.	1189	Martinka, M.	1041	Turner, A.	1249
Dinan, J.H.	1041	McLevige, W.V.	1175	van Schilfgaarde, M.	1119, 1121, 1127
Dodge, J.	1219	Meléndez, J. L.	1137, 1219	Vanderwyck, A.H.B.	1175
Dudley, M.	1189	Mestechkin, A.	1183	Vitrus, C.M.	1201
Ebe, H.	1143	Meyer, J.R.	1255	Vydyanath, H.R.	1275
Endres, D.W.	1201	Minamide, M.	1093	Wan, C.F.	1293
Faraone, L.	1255	Mitra, P.	1077	Wang, W.-S.	1047
Faurie, J.P.	1211	Mohnkern, L.M.	1201	Weiler, M.H.	1077, 1287, 1329
Ferid, T.	1093	Muller, R.J.	1099	Weiss, E.	1161
Garber, V.	1169, 1321	Mullin, J.B.	1225	Wijewarnasuriya, P.S.	1211
Giess, J.	1149	Murakami, S.	1143	Williams, G.M.	1239
Giles, N.C.	1269	Murthy, S.D.	1087	Wood, C.E.C.	1041
Goren, D.	1161	Myers, T.H.	1201	Wu, J.	1189
Gouws, G.J.	1099	Nemirovsky, Y.	1161	Yanka, R.W.	1201
Graham, A.	1149	Newey, J.	1149	Yasuda, K.	1093
Hails, J.E.	1149	Nishijima, Y.	1143	Young, M.L.	1149
Halepete, S.	1137	Nishino, H.	1143	Zandian, M.	1067, 1175, 1207
Harris, K.A.	1201	Norton, P.W.	1189, 287		
Hartle, N.	1287	Ochi, S.	1113		